Exploration of new geothermal targets in fractured basement context : a multidisciplinary study of the hydrothermal system of Chaudes-Aigues (French Massif Central)

Emmy Penhoët

▶ **To cite this version:**

Emmy Penhoët. Exploration of new geothermal targets in fractured basement context : a multidisciplinary study of the hydrothermal system of Chaudes-Aigues (French Massif Central). Other. Université d'Orléans, 2025. English. ⟨NNT : 2025ORLE1048⟩. ⟨tel-05518961⟩

HAL Id: tel-05518961

https://theses.hal.science/tel-05518961v1

Submitted on 19 Feb 2026

HAL is a multi-disciplinary open access archive for the deposit and dissemination of scientific research documents, whether they are published or not. The documents may come from teaching and research institutions in France or abroad, or from public or private research centers.

L'archive ouverte pluridisciplinaire **HAL**, est destinée au dépôt et à la diffusion de documents scientifiques de niveau recherche, publiés ou non, émanant des établissements d'enseignement et de recherche français ou étrangers, des laboratoires publics ou privés.

HAL Authorization

UNIVERSITÉ D'ORLÉANS

Energie, Matériaux, Sciences de la Terre et de l'Univers
BRGM - ISTO

THÈSE présentée par :

Emmy PENHOËT

Soutenue le : **23 septembre 2025**

Pour obtenir le grade de : **Docteur de l'Université d'Orléans**

Discipline/ Spécialité : Sciences de l'Univers - Géoressources

Exploration of new geothermal targets in fractured basement context:

a multidisciplinary study of the hydrothermal system of Chaudes-Aigues (French Massif Central)

THÈSE dirigée par :

GUILLOU-FROTTIER Laurent	Ingénieur-Chercheur, HDR, BRGM
ARBARET Laurent	Professeur des universités, ISTO

RAPPORTEURS :

MOSCARIELLO Andrea	Professeur, Université de Genève
BRANQUET Yannick	Maître de conférences, HDR, Université de Rennes

---

JURY :

MARTEL Caroline	Directrice de recherche, ISTO, Présidente du jury
LACHASSAGNE Patrick	Directeur de recherche, HSM-UM Montpellier
DUPUY Alain	Professeur des universités, BRGM
LEDESERT Béatrice	Professeure des universités,Cergy Paris Université
MOSCARIELLO Andrea	Professeur, Université de Genève
BRANQUET Yannick	Maître de conférences, HDR, Université de Rennes

Remerciements

“Life is like a box of chocolates, you never know what you’re gonna get.”

Forrest Gump

Cette phrase, empruntée à l’un de mes films préférés, résume assez bien ces 3 années de thèse : une succession de découvertes, d’imprévus, de joies, de doutes et surtout de belles rencontres. Comme toute aventure, cette thèse a été le fruit d’un long cheminement. Pour aboutir il est indispensable d’être guidée, entourée et pour cela je remercie tous ceux qui m’ont accompagnée tout au long de ce parcours.

Je tiens tout d’abord à remercier mes directeurs de thèse. Laurent Arbaret, sans qui cette thèse n’aurait jamais vu le jour. C’est lui qui m’a offert ma première opportunité de stage, puis un second, avant de me proposer un sujet “sur-mesure” parfaitement adapté à mes centres d’intérêt et à mes envies. Sa confiance et son accompagnement m’ont ouvert la porte vers une carrière scientifique. Il a su être présent tout en me laissant la liberté d’orienter mes travaux, il a été un soutien précieux. Ensuite, Laurent Guillou-Frottier, présent au quotidien toujours disponible et qui m’a encouragée à donner le meilleur de moi-même avec bienveillance. Nos échanges réguliers (même plusieurs fois par jour) sont pour beaucoup dans le résultat de mon travail. Leur complémentarité a été un véritable moteur tout au long de ces trois années. On dit souvent qu’une thèse, c’est « 50 % d’encadrement » … et cette expérience en a été la parfaite illustration.

Merci de tout cœur à vous deux, « Laurent et Laurent », pour m’avoir soutenue, accompagnée et encouragée !

Au cours de ces trois années j’ai eu la chance de croiser beaucoup de professionnels, de bénéficier de leurs précieuses connaissances et de leurs conseils éclairés. D’abord, Bernard Sanjuan, dont l’expertise et la rigueur scientifique ont été d’une aide précieuse. Je lui suis reconnaissante d’avoir pris le temps de m’accompagner, de partager et de me transmettre (une petite partie) de son savoir. Au-delà de son rôle d’encadrant, tu as été pour moi une rencontre humaine exceptionnelle. Ta générosité, bienveillance et ton humour ont apporté de la légèreté dans le quotidien parfois intense de la thèse… J’aurais aimé être davantage l’héritière de tes connaissances ! Je tiens également à exprimer ma gratitude à Charles Gumiaux, Angélie Portal et Julien Baptiste pour leur soutien et leur accompagnement. Je n’oublierai jamais les discussions partagées avec chacun d’entre vous après de longues journées de terrain entre gravimètre, alcalinité, fusion partielle ou volcan à Chaudes-Aigues et le fameux « pain-pâté-pinard ».

Je dois souligner que, Chaudes-Aigues ne serait pas la même sans Jacky Pécoul (et cette thèse non plus). Un grand merci à lui pour son aide et sa disponibilité lors de nos visites.

Merci à Yannick Branquet et Andrea Moscariello d’avoir été les rapporteurs de mon travail, à tous les membres du jury d’avoir trouvé le temps dans leurs plannings chargés pour assister à l’exposé de mes recherches et pour les échanges qui ont suivi. Quel beau moment ! (Et oui, je parle pourtant bien de ma soutenance)

Je n’oublie pas les équipes GEM et IMI du BRGM pour leur accueil et leur convivialité tout au long de ces trois années. Même si nos domaines scientifiques étaient très différents — entre métallogénie, économie des ressources minérales et mon « eau chaude », je garderai le souvenir les pauses café du matin, ces moments simples mais précieux où l’on discutait et échangeait bien au-delà de la science. Merci à Max, Alex, Nico, Bryan, Loïc, Anne, Théo, Mamadou, Éric (ou Carlos), Paul et Victoire qui ont apporté de la légèreté à un quotidien parfois stressant. Je souhaite également remercier Emma, arrivée au BRGM en même temps que moi qui est devenue une amie précieuse, ainsi qu’Antoine. Ils m’ont bien souvent permis tous les deux d’oublier la charge de travail.

Je tiens à remercier ma famille, non seulement pour le soutien apporté tout au long de cette thèse, mais aussi et surtout pour leur présence et leurs encouragements depuis le début. Un remerciement tout particulier va à ma mère, ma « moumoune », qui m’a toujours encouragée à faire des études, à donner le meilleur de moi-même et à viser l’excellence. Elle est pour moi un modèle de détermination et de générosité. Je ne pourrai jamais assez te remercier pour tout ce que tu as fait pour moi.

La boîte est désormais refermée… je suis arrivée au bout de ce beau chemin au cours duquel j’ai pu grandir tout le long, pleine d’espoir d’en parcourir un autre tout aussi riche d’expériences et de connaissances !

Merci à tous.

Table of contents

I. Introduction 23

I.1 From mystical beliefs to scientific exploration of thermal resources. 23

I.2 Geothermal energy: classification and exploration 28

I.3 Thermo-mineral springs in France 33

I.4 Overview of current understanding of amagmatic hydrothermal systems46

I.5 Presentation of the study area 55

I.6 Objectives et methods 66

II. Fault zone geometry, a key parameter controlling fluid flow: study of thickness and an intersection zone 71

II.1 Introduction 71

II.2 Contribution of this chapter 73

II.3 Fault Zones Intersections and High-Temperature Geothermal Exploration: 3D Modeling of the Chaudes-Aigues Area (French Massif Central) (Extended Abstract EGC 2025) 75

II.4 Fluid flow in crustal fault zones with varying lengthwise thickness: application to the Margeride Fault Zone (French Massif Central) (published article) 87

III. Inherited structures and hydrothermal upwelling drains: typology of reactivated Variscan faults 127

III.1 Introduction 127

III.2 Contribution of this chapter 128

III.3 Long-lived brittle reactivation of crossing fault networks enhancing upwelling hydrothermal systems: The case study of Chaudes-Aigues spring swarm (to be submitted manuscript) 130

IV. Geochemical characterisation of Chaudes-Aigues springs: hydrothermal system functioning and hidden reservoirs revealed 177

IV.1 Introduction 177

IV.2 Contribution of this chapter 177

IV.3 One hydrothermal system may hide another: Insights from Chaudes-Aigues and nearby springs (published article) 179

V. Infiltration in a weathered granite: regolith impact on hydrothermal systems 242

V.1 Introduction 242

V.2 Defining MGC weathering profile: field study 245

V.3 Impact on fluid flow and thermal regime 249
V.4 Discussion 258
VI. Numerical modelling of the Chaudes-Aigues hydrothermal system: thermal springs simulation and controlling factors analysis 262
VI.1 Introduction 262
VI.2 Contribution of this chapter 263
VI.3 Numerical modeling of thermal springs to investigate controlling factors in amagmatic hydrothermal systems: the Chaudes-Aigues case (French Massif Central) (to be submitted manuscript) 265
VII. Discussion, limits and perspectives 296
VII.1 Multidisciplinary approach 296
VII.2 Synthesis of key findings on Chaudes-Aigues hydrothermal system 298
VII.3 Perspectives for geothermal exploration 301
VII.4 Spring temperature and generating potential: a misleading relation? 303
VII.5 Hydrothermal systems vulnerability to climate change 306
VIII. Conclusions 308
IX. Résumé étendu 312
References 326
Appendices 351
Appendix A: Fault density map methodology 351
Appendix B: Methodology used for 3D thermo-hydraulic modelling. 356
Appendix C: Article published in the review Géologues, June 2024. 358
Appendix D: Extended abstract EAGE GET 2024. 367
Appendix E: Comsol report. 371

Figure list

Figure I.1: Vichy thermal spa “Reine des villes d'eaux”, 1900. Photographic report on the “grands travaux” campaign of 1900: first-class spa and Grand Casino, 1900-1903. M. Laval and Médiathèque Valery-Larbaud (Vichy) collection. 24

Figure I.2: Connections between different aquifers (on the left) and subterranean fires (on the right) at depth. Theories of a 17th-century geologist (Athanasius Kircher, Mundus Subterraneus, 1665). 25

Figure I.3: Thermal baths of Aix-les-Bains, sulphur spring fountain in the hall of the Pétriaux spa complex (Jazé-Pétriau, 2014). 26

Figure I.4: Informative blotter about the thermal waters of Plombières-les-Bains. ... 27

Figure I.5: Photographs, from left to right, of the first fir tree pipes carrying water, the current pipes and the limestone precipitation that eventually clogs the pipes. .. 28

Figure I.6: Different applications of geothermal energy depending on the temperature of the fluids used (source: ADEME, BRGM). 30

Figure I.7: Map of the distribution of geothermal power plants worldwide (after Moeck, 2014). The red lines represent divergent plate boundaries (mid-ocean ridges intersected by transform faults), the green lines represent convergent boundaries (subduction zones), the blue lines represent transform boundaries, the yellow lines represent intracontinental rifts, and the red areas represent active volcanic regions..... 30

Figure I.8: Schematic representation of the thermal water circuit through a deposit (Ladouche B., Négrel P., Vigouroux P., BRGM) 34

Figure I.9: Distribution of thermo-mineral springs (according to the Banque du Sous-Sol, BSSEAU, BRGM) in France. The background map corresponds to the 2M geological map (BRGM). 36

Figure I.10: Distribution of thermo-mineral springs as a function of heat flow in France. Heat flow contours are extracted from the heat flow map of Lucazeau and Vasseur (1989). 38

Figure I.11: Temperature of the 368 springs according to the lithology of the hydrothermal deposit. The deposit is defined using the BSSEAU database (BRGM). If the data is missing, the lithology in which the spring is located is used. 40

Figure I.12: (a) Map showing the distribution of thermal springs in France as a function of topography. (b) Temperature of springs as a function of maximum difference in elevation within a 10km radius of each spring. 42

Figure I.13: (a) Temperature at emergence and (b) percentage of total heat transmitted in a fault zone as a function of its permeability and that of the host rock (Lopez

and Smith, 1995). The temperature is maximum for a specific range of values and decreases outside this range. 44

Figure I.14: (a) Map showing the distribution of thermal springs in France as a function of fault density. (b) Temperature of springs as a function of average fault density within a 10 km radius of each spring. 45

Figure I.15: Distribution of studies on hot springs (title containing ‘hot spring’ or ‘thermal spring’). The classification is based on the main theme of the journals in which the articles were published. 47

Figure I.16: "Evolution of the number of publications per year on topics related to faults ('fault'), fluid flow ('fluid flow' and 'hydrogeology'), the coupling between faults and fluid circulation ('fault' and 'fluid flow' or 'hydrogeology'), and hot springs ('hot spring', 'thermal spring') from 2001 to 2024 (source: Web of Science). 48

Figure I.17: Illustration of subsurface water flows, with infiltration at the highest topographic points and discharge at the lowest Fleming (2004). 49

Figure I.18: Conceptual model of the alteration profile of a Hard Rock Aquifer (HRA) consisting of, from bottom to top: impermeable granite topped by the fractured horizon and an unconsolidated cover (saprolite) (after Lachassagne et al., 2011). 51

Figure I.19: (a) Structure of a fault with a single fault core, (b) structure of a fault zone with several fault cores and damage zones leading to permeability variations (Faulkner et al., 2010). 53

Figure I.20: Location of geothermal systems and optimal exploitation sites according to the structure of the fault zone (after Jolie et al., 2021). 54

Figure I.21: Hydrothermal system in an amagmatic context (after Moeck 2014). 55

Figure I.22: Simplified structural scheme of the Massif Central (Faure et al., 2009). The red dot symbolises the location of Chaudes-Aigues. 56

Figure I.23: (a) Temperature at 30 km depth (mean depth of the Moho), Margeride Granite boundaries are highlighted by the red outline. (b)(c) Approximate temperature evolution around Chaudes-Aigues (modified from Sobolev et al., 1997). 57

Figure I.24: Facies containing ‘horse-tooth’ feldspar phenocrysts in the Margeride Granite 58

Figure I.25: Emplacement model of the MGC, showing the different feeder zones shifted by N150E fault zones (after Talbot et al., 2005). 59

Figure I.26: Fault density map of the MGC (Penhoët et al., 2024), the two fault zones of Malzieu-Saint Flour and Chaudes-Aigues are easily identified by their high density. 60

Figure I.27: Chaudes-Aigues, Cantal (15), France. Several structures are heated by the thermal waters, including the church in the centre, the swimming pool in the foreground and the secondary school on the right of the picture. 61

Figure I.28: « D'azur à la montagne d'or mouvant d'un bouillon d'eaux fumantes d'argent, trois jets de vapeur du même issant de ladite montagne, surmontée de deux fleurs de lys d'or rangées en chef" (Charles d'Hozier, 1696), The Chaudes-Aigues coat of arms can be seen on the front of the 'Gourmet & Glouton' restaurant and in the courtyard of the Geothermia museum. 62

Figure I.29: Some springs in Chaudes-Aigues: (a) The Par spring 82 °C, Le Lavoir 57 °C, La Bonde du moulin 50 °C, Boucharinc 65 °C with its heat exchanger and the La Chaldette borehole (red dot) 35 °C. 63

Figure I.30: (a) Location of the Chaudes-Aigues and La Chaldette thermal springs, (b) Zoom in on the main emergence area, highlighting the main fault zones: N00E in magenta, N030E-50E in blue and N120E-150E in red. 64

Figure I.31: Summary of the different theories proposed since 1906 (Penhoët et al., 2024). 66

Figure I.32: Illustration of the relationship between the chapters of the manuscript. 68

Figure II.1: (a) Location of the MGC and the two main fault zones: (b) the Chaudes-Aigues intersection zone and (c) the variation in thickness of the MFZ. 72

Figure II.2: (a) The Par Spring (82°C), one of the hottest in Europe. (b) Location of the study area simplified geological map. The geometry used for models is highlighted by the black dotted lines. 77

Figure II.3: Geometries and meshes used for the numerical models: (a) simple fault zone, (b) variable-angle X intersection, (c) Y intersection the case of Chaudes-Aigues. 79

Figure II.4: (a) Case of a simple fault zone, for high permeability values (3 10^{-14} m²) the anomaly moves towards the end of the fault zone. (b) Cross-section of the model at the surface, production of 3 potential thermal springs. 81

Figure II.5: (a) X-shaped configuration, 60°, for low permeability values (9 10^{-15} m²) the thermal anomaly is confined at the intersection. (b) Cross-section of the model at the surface, production of one potential thermal spring. 82

Figure II.6: (a) Y-shaped configuration, for high permeability values (3 10^{-14} m²) 3 thermal anomalies are created at the edges of the fault zones. (b) Cross-section of the model at the surface, production of 3 potential hot springs. 83

Figure II.7: (a) Outflow rate corresponding to upwelling zones, (b) maximum surface temperature reached and (c) temperature anomaly at 1000 m depth as a function of fault zone permeability. 84

Figure II.8: (a) Configuration reproducing the location of Chaudes-Aigues springs (K = 10^{-14} m²). (b) Cross-section of the model at the surface, production of an emergence area. 86

Figure II.9: Geological setting of the Margeride Fault Zone (MFZ). Coordinate system: Lambert 93 – RGF93 EPSG:2154. (a) location of the study area. (b) simplified geological map of the Margeride Granitic Complex issued from the 1:1 000 000 geological map of mainland France (BRGM). (c) Simplified map of the study area. Blue lines locate the four selected sections broadly oriented perpendicular to the MFZ and crossing the four major half grabens. Blue dots refer to outcrops on which statistical structural measurements of fractures orientations where performed and that are located as close as possible to the geological sections. Green dots refer to representative locations (Loc_i, see text for details). (d) Close-up map of the northwestern segment of the MFZ along which the Cenozoic Saint Flour Basin emplaced. 92

Figure II.10: (a) Simplified geometry used for parametric studies, with coarse mesh in the embeddings and refined mesh in the faulted zone; the fault zone thickness h varies between 100m to 2500m. (b) Models with a lengthwise variation of the fault zone thickness from 2500 to 50m (prismatic shape). The length of the fault zone, L, has been varied, but the meshes shown here correspond to the results of Figure II.20 and 2.21 where L = 20 km, close to the MFZ. The height of the fault zone is 4 km, and it crops out the surface. 101

Figure II.11 : Equal area projection (lower hemisphere) of primary ductile and magmatic mineral fabrics. (a) Foliations and (b) lineations measured in 57 locations distributed in both UGU and LGU units. Kamb contours in standard deviation. (c) AMS Foliations and (d) lineations of the MGC (modified from Talbot et al. 2005). All stereographic projections are in an equal area lower hemisphere. 104

Figure II.12: (a) Azimuthal (left) and orientation (right) distributions of fractures measured in the UGU and LGU gneissic units. (b) Azimuthal (left) and orientation (right) distribution of fractures measured in the MGC. (c) orientation distributions in three reference sites in the UGU (Loc1), in the MGC (Loc2) and along the MFZ (Loc3, see Figure II.9 for geographical locations). All stereographic projections are in an equal area lower hemisphere. All Kamb contours in standard deviation. 105

Figure II.13 : (a) roadside outcrop located West of Saint-Alban-Sur-Limagnole (Loc4, coordinates: 44.778779205160504, 3.353790900820662) showing the flat-lying joins in the MGC. (b) Orientation distribution of primary fractures and joints in LOC4. 106

Figure II.14: (a) Geological section crossing the Saint-Alban-sur-Limagnole Basin and Chinchazes Basin. Loc 4 refers to flat-lying joints analysis location (see Figure 5a and 5b). (b) Geological section crossing Le Malzieu Basin. For (a) and (b), both scales are in meters. Loc 5 refers to flat lying joints analysis location (see Figure 5a and 5b). All stereographic projections are in an equal area lower hemisphere. All Kamb contours in standard deviation. Principal stress tensors were calculated by using FaultKin software. 108

Figure II.15: (a) Geological section crossing the Chaliers Basin. (b) Geological section crossing the Saint Flour Basin. All stereographic projections are in an equal area lower hemisphere. For (a) and (b), both scales are in meters. All Kamb contours in standard deviation. Principal stress tensor was calculated by using FaultKin software. 110

Figure II.16: (a) Roadside section of the eastern border of the MFZ, East of the Saint Flour graben, depicting the transition from the fresh gneiss with a strongly westward dipping foliation (b, 50m away from the view) to a damaged and altered zones (Loc6, GPS coordinates : 45.0534, 3.1797, location in Figure 1d). (c) Youngest normal, west dipping, faulting event crosscutting the locally mylonitized gneiss. 111

Figure II.17: Field views of the fault core of the MFZ, East of the Saint Flour graben, composed of isolated lenses of fractured gneiss lenses embedded in an altered breccia (Loc7, GPS coordinates: 45.0533, 3.1604, location in Figure 1d). 111

Figure II.18: Fault density map of the study area, the contact between lithologies (black and red lines) correspond to those shown in Figure1. Coordinate system: Lambert 93 – RGF93 EPSG:2154. 113

Figure II.19: Graphs showing the impact of variations in the permeability K and thickness of the fault zone on the value of the maximum thermal anomaly (a), the depth of the 150 °C isotherm (b) and fluid flow velocity (c). 117

Figure II.20: (a) The three convective regimes as a function of fault zone thickness and permeability, black dots represent all the models carried out in order to constrain the regime boundaries (dashed black lines). (b) Three examples of the different regimes as defined in (a). All these experiments have been performed with a fault zone length L equal to 20km. 119

Figure II.21: Results of the models with a lengthwise variation of the fault zone thickness for two permeabilities. 121

Figure III.1: Geological setting of the study area. (a) location of the study area. (b) simplified geological map of the Margeride Granitic complex modified after Talbot et al. (2005). (c) Simplified map of the study area. Coordinates are in Lambert 93. 135

Figure III.2: Geological map of the Chaudes-Aigues area (modified from Gibert et al. 1975). Colored dots correspond to the location of the various observation and structural measurement sites. Lithology at sites is as follow: F is Fault, MGD is Microgranite Dykes, C is Couffour granite, G is Gneiss. Coordinates are in Lambert 93. 140

Figure III.3: Location of the gravity stations on the simplified geological map of the study area. Coordinates are in Lambert 93. 144

Figure III.4: Fault density map of the MGC and its surrounding gneissic units, the black contour delineates the MGC as shown in Figure III.1b. Coordinates are in Lambert 93. 145

Figure III.5: (a) Fault density map between Chaudes-Aigues and La Chaldette (density classes are the same than Figure III.4). (b) Spatial and (c) azimuthal distributions of the lineaments extracted from the DEM analysis in the La Chaldette – Chaudes-Aigues area. (d) Graphs showing the length of lineaments as a function of their azimuth. The studied area corresponds to the red rectangle shown in Figure III.1b. Coordinates are in Lambert 93. 147

Figure III.6: Orientation distributions of fractures measured in most representative sites (a) G-5 and (b) G-4 in the LGU, (c) MGD-3 in a microgranite vein and (d) C-1 in the Couffour Granite. Red line indicates major plane, green secondary, stereographic projections is in an equal area lower hemisphere, all kamb contours are in standard deviation. 148

Figure III.7: (a) Azimuthal distributions of microgranite dykes in the study area. (b) Orientation distributions of fractures measured in the MGD, site MGD-3 (see location in Figure III.2). (c) orientation distributions of altered fractures (n=40) measured in all sites of measurement in MGD, red line indicates major plane, stereographic projections are in an equal area lower hemisphere, kamb contours in standard deviation. (d) N030E altered fracture plan in a microgranite vein (MGD-2, see Figure III.2) showing mineral dissolution (e) not pervasive in the volume. 150

Figure III.8: Panorama of polyphased (ductile to brittle) fault N050E (F2, location in Figure III.2)**.** (b) Strongly deformed gneiss block, with the original foliation fully verticalized. (c) Preserved gneiss block, original foliation remains visible. (d) Two gneiss blocks separated by a discontinuity in foliation, interpreted as a brittle fracture. (e) Vertical quartz vein, several centimetres thick, indicating fluid circulation during the brittle reactivation of the fault. 152

Figure III.9: (a)(d) N050E faults (F3 and F14, see Figure III.2) showing, (b) quartz-sulfide bearing vein in bleached gneiss, (c) close up of the arseno-quartz filling. Apy = Arsenopyrite and Qz= quartz (Following the mineral abbreviations of Warr 2021). (d) silicified gneissic unit and (e) (f) a close up of the oxyde filling. 154

Figure III.10: Outcrop in gneissic unit close to a microgranite vein showing, (b) a N140 normal fault (F5, see Figure III.2), (c) mainly filled with clays. 155

Figure III.11: X-ray Diffractograms obtained for F1, location corresponds to Figure III.2. 156

Figure III.12: Complete Bouguer anomaly map (major contour interval: 1 mGal). LGU corresponds to Lower Gneiss Unit, UGU to Upper Gneiss Unit and MGC to Margeride Granitic Complex. The coordinates are in Lambert 93. 157

Figure III.13: (a) Geological map of the study area and location of gravity stations. (b) Complete Bouguer anomaly map (major contour interval: 2 mGal) and location of the 2D forward modeling of the Chaudes-Aigues area along the L1 (c), L2 (d) and L3(e) cross-sections. 159

Figure III.14: (a) Far field schistosity represented mostly by the biotite foliation measured in the LGU and UGU North of the MGC (modified from Penhoet et al.,

2025a). (b) Schistosity of the LGU measured along the Remontalou river next to Chaudes-Aigues city. (c) isoclinal fold hinge directions affecting the LGU gneisses. Measurements issued from Gibert et al. (1975) and complemented by measurements performed on same outcrops than for (b). (d) Field view on a plane perpendicular to the hinge direction of a isoclinal fold affecting the gneiss of the LGU illustrating the limited amplitude of this folding. 161

Figure III.15: (a) Tectonic timeline summarising the evolution of tectonic stresses (modified from Daffos et al., 2024) to identify the re-activations of structures, 1: Gölke and Coblentz (1996), Mazabraud (2004), 2: Couturié (1979), De Goer de Herve (1991), 3: Ziegler and Dèzes (2007), Bergerat (1985), 4: Blés et al., (1989). (b) Simplified geological map identifying the main drains or barriers near the thermal springs (modified from Gibert et al., 1975). Coordinates are in Lambert 93. 163

Figure IV.1: Location of sampling points on a simplified geological map. The coordinates correspond to the Lambert 93 projection system EPSG 2154. 183

Figure IV.2: Piper diagram. The thermal waters were grouped by geographical location : South Cantal Area (Sainte-Marie, Moulinges, Fontanes), Chaudes-Aigues area (Par 2012, Par 2023, Lavoir 2012, Lavoir 2023, Ban 2012, Ban 2023, Boucharinc, Vialard, Tourette, Poste, Condamines, MTC 2012, MTC 2023, Laval, Loubaresse), Est Margeride area (Mazel, FH, FB1, FB2, Ranc) and West Margeride area (LC 2012, LC 2023). 189

Figure IV.3: (a) Concentrations of bromide, (b) boron as a function of chloride ions. (c) Bicarbonate concentrations as a function of sodium (Na) concentrations. The mixing lines have enabled different reservoirs to be identified, highlighted by three different colours: Green for the Chaudes-Aigues, Orange for the East Margeride and Blue for South Cantal area. 192

Figure IV.4: Deuterium ($\delta^{2}H$) values versus 18-oxygen ($\delta^{18}O$) values in sampled waters. Colors correspond to previously identified groups: Orange for Chaudes-Aigues, Green for Margeride and Blue for Sainte-Marie. Surface waters (streams, rivers) are symbolized by blue crosses. The local meteoric line is based on these points. 194

Figure IV.5: (a) $\delta^{2}H$ and (b) $\delta^{18}O$ concentrations versus chloride concentrations in sampled water. The colours of the dots correspond to the groups identified above: green for the East Margeride group, orange for Chaudes-Aigues and blue for South Cantal. The blue crosses correspond to the rivers or streams sampled, the purple to a stream near Montchanson (Vasseur et al., 1997). 195

Figure IV.6: (a) Inferred recharge elevation of thermos-mineral waters sampled using a regional gradient determined with modern surface water (streams or rivers), Chaudes-Aigues group is represented in orange, South Cantal blue and East Margeride green. (b) Topographic map showing the different supposed impluvium, blue areas correspond to the elevation lower than 850 m a.s.l, grey between 850-1000 m a.s.l, brown higher than 1000 m a.s.l, green above 1400m. Thermo-minerals springs, here represented by yellow circles, correspond to those shown

in Figure IV.1. The MGC boundaries are shown in white dotted lines. The averages are calculated for all the spring values in each group. 198

Figure IV.7: (a) Silica concentration as a function of chloride concentration in sampled water. The green (Margeride group) and orange (Chaudes-Aigues group) lines correspond to the concentrations of chloride of the hot deep reservoir, previously estimated at 56 mg/l and 180 mg/l respectively. Temperature of the two hot deep reservoirs have been estimated, T_{Qz}: Fournier (1977). (b) Zoom on the cluster of points corresponding to the Chaudes-Aigues thermal springs, The Par Spring (Par 2012 and 2023) used for the estimate is highlighted by red dots. 201

Figure IV.8: Estimated reservoir temperatures for the Chaudes-Aigues group using geothermometry. $T_{Na/K}$ (1) : Fournier (1979) ; $T_{Na/K}$ (2) : Michard (1979); $T_{Na/K}$ (3) : Arnórsson et al. (1983) T < 250°C; $T_{Na/K}$ (4) Giggenbach (1988) ; $T_{Na/K/Ca}$: Fournier and Truesdell (1973). The dashed red line indicates the temperature (185°C) of the Chaudes-Aigues reservoir, which has been estimated using numerical modelling (see S2, SM). 204

Figure IV.9: Estimated reservoir temperatures The East Margeride group using geothermometry. $T_{Na/K}$ (1) : Fournier (1979) ; $T_{Na/K}$ (2) : Michard (1979); $T_{Na/K}$ (3) : Arnórsson et al. (1983) T < 250°C ; $T_{Na/K}$ (4) Giggenbach (1988) ; $T_{Na/K/Ca}$: Fournier and Truesdell (1973)..... 206

Figure IV.10: Estimated reservoir temperatures for the South Cantal group using geothermometry. $T_{Na/K}$ (1) : Fournier (1979) ; $T_{Na/K}$ (2) : Michard (1979); $T_{Na/K}$ (3) : Arnórsson et al. (1983) T < 250°C ; $T_{Na/K}$ (4) Giggenbach (1988) ; $T_{Na/K/Ca}$: Fournier and Truesdell (1973)..... 207

Figure IV.11: (a) Concentrations of Sr, (b) Li as a function of chloride ions. Waters groups are highlighted by three different colours: Green for the East Margeride area, Orange for Chaudes-Aigues and Blue for South Cantal area. Surface waters (streams, rivers) are symbolized by blue crosses..... 208

Figure IV.12: (a) $^{87}Sr/^{86}Sr$ ratios as a function of Strontium concentration, (b) $\delta^{7}Li$ values as a function of Lithium concentration in sampled waters. Isotopic values of specific minerals, used in the text, have been added (black arrows, their abscissas are not significant). 210

Figure IV.13: $\delta^{11}B$ values as a function of Boron concentration in the water sampled. Isotopic values of specific minerals, used in the text, have been added (black arrows, their abscissas are not significant). 213

Figure IV.14: 3D block diagram (not to scale) summarizing fluid circulation and the various geothermal reservoirs within the Margeride Granitic Complex. Couffour granite, near Chaudes-Aigues, is represented in orange. The South Cantal group was not represented. 220

Figure IV.15: Model set-up and boundary conditions (see text). Blue and red lines correspond to fixed temperature conditions, where the red one represents the reservoir temperatures. 227

Figure IV.16: Spring temperature as a function of the fault zone permeability, for two distinct basal temperatures and two heat transfer coefficients. Rectangles indicate fluctuating spring temperatures due to periodic hydrothermal pulses. For a basal temperature of 200 °C, temperature around and above 80°C can be reached for a fault zone permeability greater than 6 10^{-14} m². 230

Figure IV.17: Spring temperature and regional heat flow values (bold numbers) as a function of the heat transfer coefficient, for a fault zone permeability of 6 10^{-14} m². Rectangles indicate fluctuating spring temperatures due to periodic hydrothermal pulses. Basal temperatures of 140 °C give regional heat flow values lower than the measured ones. For 170 °C, regional heat flow values are consistent with heat flow data, but spring temperature is too low. For a basal temperature of 200 °C, spring temperature around 70-80°C can be reached, and regional surface heat flow is consistent with measured values. 231

Figure IV.18: a) Role of basal temperature on spring temperature, for two heat transfer coefficients and two values for the fault zone permeability. Rectangles indicate fluctuating spring temperatures due to periodic hydrothermal pulses. b) illustration of hydrothermal convection within the fault zone, for an imposed basal temperature of 185°C, with a fault zone permeability of 6 10-14 m², and with a h value of 0.0005. The maximum recorded temperature at the surface equals 83°C. This image is a zoom around the fault zone and thus isotherms (black contours) are not horizontal on external edges. Color code corresponds to temperature values, from 10°C (blue) to 185°C (red). 232

Figure V.1: Example of a water balance summarising the processes likely to affect the study area. Outputs are shown in red and inputs in blue. 242

Figure V.2: Location of water balance calculation. Background corresponds to the 1M geological map of France. The ««amont»« Bès corresponds to the part outside the box to the south-west and the ««aval» Bès to the north-east. 243

Figure V.3: Weathering profile structure and hydraulic characteristics close and outside a fault zone (faults, veins) according to Lachassagne et al., (2011). The deepening zone increases permeability and facilitates infiltration at depth. 245

Figure V.4: Observation points spatial distribution. The thermo-mineral springs correspond to those previously sampled in chapter III. 246

Figure V.5: Log representing Jurassic deposits on the MGC (modified from Briand et al., 1979). The weathering profile sealed by the Liassic sediments can be seen on these outcrops near Marvejols, (b) on the N88 (44.572, 3.629) and (c) on the D901 (44.540, 3.288). 247

Figure V.6: (a) The fissured horizon (44.711, 3.382), characterised by its horizontal and vertical fractures, (b) the unconsolidated alterites located just above (44.824, 3.076) and (c) a zoom on these (44.826, 3.066), the main altered mineral biotite has disappeared, quartz and feldspars are visible. As mentioned above, near faults, there is a (d) deepening of the profile bringing alterites and fissured layer into contact (44.685, 3.805). 248

Figure V.7: Schematic cross-section (not to scale) of the MGC, the deepening of the profile in the fault zones has not been represented here. Dark pink with crosses corresponds to unweathered granite, light pink to fissured horizon, yellow to alterites (unconsolidated part) and purple to basalts. 249

Figure V.8: Configuration of an Aubrac-type model with the complete weathering profile overlaying the fault zone, with boundary conditions shown (see text). . 251

Figure V.9: (a) Temperatures of potential thermal springs on the surface, (b) depth of maximum temperature anomalies, (c) value of maximum temperature anomalies as a function of fault zone permeability. 253

Figure V.10: Fluid circulation symbolised by the arrows (Darcy velocity) in the case of an Aubrac-type model. (a) Top view, circulation within the alteration profile and (b) cross-section showing interactions with depth. 254

Figure V.11: (a) Convection cells in the fissured horizon, top view and cross-section. (b) Interactions between the surface and deep circulations for low permeabilities, (c) for higher permeabilities. 256

Figure V.12: Fluid circulation symbolised by the arrows (Darcy velocity) in the case of a La Chaldette-type model. (a) Top view, circulation within the alteration profile and (b) top view for higher permeability value. 257

Figure VI.1: Distribution of thermo-mineral springs (according to the Banque du Sous-Sol, BSSEAU, BRGM) in France. The background map corresponds to the 2M geological map (BRGM). 269

Figure VI.2: Distribution of thermal springs as a function of heat flow in France. Heat flow contours are extracted from the heat flow map of Lucazeau and Vasseur (1989). 271

Figure VI.3: Temperature of the 368 springs according to the lithology of the hydrothermal system. 272

Figure VI.4 : (a) Map showing the distribution of thermal springs in France as a function of topography. (b) Temperature of springs as a function of maximum difference in elevation within a 10km radius of each spring. 274

Figure VI.5: (a) Map showing the distribution of thermal springs in France as a function of fault density. (b) Temperature of springs as a function of average fault density within a 10 km radius of each spring. 276

Figure VI.6: (a) Thermal springs distribution in the Massif Central on a 2M geological map (BRGM). (b) Depth of the Moho represented as the thickness of the crust along the AB profile (after Ziegler and Dezès, 2007). 278

Figure VI.7: Geological maps of the (a) MGC cut by the various major fault zones and (b) zoom on the Chaudes-Aigues hydrothermal system. 280

Figure VI.8: (a) Overall geometry of the model with the main faults cutting the Margeride Granite, (b) northern view of the Chaudes-Aigues fault zone crossing

the assumed reservoir at depth. The red dots correspond to the thermal springs used to determine its location (Penhoët et al., 2025b)..... 284

Figure VI.9: (a) Boundary conditions used for all models (with or without topography), (b) zoom on the northern edge of the granite with a reservoir represented as a surface with an imposed temperature. In the case of models without reservoir this condition disappears..... 285

Figure VI.10: Calculation of different flow rates and mixing ratios in numerical models. 286

Figure VI.11: Results of the different models (with/without topography, reservoir): (a) Par spring temperature, (b) La Chaldette spring temperature, (c) mixing coefficients between surface water and deep endmember, and (d) discharge rates at Chaudes-Aigues (see Figure VI.7) as a function of the fault zone permeability. Red dot line indicates the Par Spring or La Chaldette spring values that must be reproduced. 288

Figure VI.12: Final model representing the Chaudes-Aigues hydrothermal system with K_{CA} = 1 10^{-14} m², K_{Aubrac} = 5 10^{-14} m² and h = 0.01 $W.m^{-2}.K^{-1}$. (a) the arrows represent Darcy velocities (m/s) the colour code represents circulation temperatures in the fault zone. (b) Thermal state of the different fault zones in the model with associated isothermal deformations. 291

Figure VII.1: Block diagram illustrating the geothermal systemof Chaudes-Aigues springs (modified from Vasseur et al., 1997). The granitic reservoir is drained to the North thanks to two fluids pathways (greys arrows), while upwelling of hot fluids (orange arrows) is ensured by the dense network of microgranite veins (in orange). 298

Figure VII.2: Functioning of the Chaudes-Aigues hydrothermal system and other hidden systems within the MGC. N50E faults are represented in red and N150E in blue. 301

Figure VII.3: (a) Vision of French geothermal potential in 2018 (BRGM), the grey contours correspond to the main sedimentary basins, the light blue boundaries to continuous reservoirs indicating potential resources and the dark blue to resources assumed/proved to be above 70°C. (b) Vision of global geothermal potential including the sedimentary and crystalline domains. The red lines correspond to the contours of crystalline massifs hosting thermal springs (red dots, T > 50°C). 302

Figure VII.4: Comparison of vertical continuity through two examples: (a) Bagnères-de-Bigorre involving 5 lithologies (Levet et al., 2002) and (b) La Chaldette borehole only drilled in granite (Calvet et al., 2012). Thermal springs are highlighted by the red circles. 304

Figure VII.5: Cold springs locations in France (T ≤ 15°C), some are located close to thermal springs (T > 15°C) and could be the start of a new exploration. 306

Figure IX.1: Distribution of thermo-mineral springs (according to the Banque du Sous-Sol, BSSEAU, BRGM) in France. The background map corresponds to the 2M geological map (BRGM). 313

Figure IX.2: (a) La source du Par (82°C), l'une des plus chaudes d'Europe. (b) Localisation de la zone d'étude (Penhoët et al., 2025a). 314

Figure IX.3: Configuration reproduisant la localisation de Chaudes-Aigues. Coupe à la surface du modèle. 315

Figure IX.4: (a) Calendrier tectonique résumant les différents évènements (Daffos et al., 2024) et les jeux de failles associés, (b) Carte géologique simplifiées représentant les principales failles proches de la zone d'émergence. 317

Figure IX.5: Schéma global de fonctionnement du système hydrothermal de Chaudes-Aigues. 319

Figure IX.6: Coupe schématique (non à l'échelle) du Granite de la Margeride, l'approfondissement du profil dans les zones de failles n'a pas été représenté ici. 321

Figure IX.7: (a) Circulations de fluide au sein de la zone de failles de Chaudes-Aigues, les flèches représentent les vitesses de Darcy et leur code couleur correspond aux températures atteintes. (b) Interactions entre les différents faisceaux de failles et le réservoir. 322

Chapter I:
General introduction

I. Introduction

I.1 From mystical beliefs to scientific exploration of thermal resources.

Thermalism, an age-old practice based on the use of thermal waters for curative purposes, is deeply rooted in European history. The first evidence of the use of thermal waters dates back to Antiquity. In Greece, springs were associated with healing divinities such as Asclepius, while the Romans perfected the practice by building thermal baths throughout the Empire. In France, sites such as Chaudes-Aigues, whose springs (some of the hottest in Europe) reach temperatures of 50°C and one of them close to 82°C, were already being used in the Middle Ages (1332) for heating houses and public baths. The Romans also left an important legacy, building thermal baths in strategic locations such as Aix-les-Bains, Néris-les-Bains and Vichy. These installations reflected not only an interest in health, but also the social and cultural significance of public bathing. These practices spread across Europe, with emblematic sites such as Bath in England and Baden-Baden in Germany. These infrastructures served as both health centres and places of social interaction, illustrating an empirical understanding of the benefits of thermal waters long before the advent of modern science.

I.1.1 The Renaissance and golden age of thermalism in Europe

After a relative decline in the Middle Ages, thermalism revived during the Renaissance, boosted by the rediscovery of ancient texts and growing interest in alternative medical practices. Europe elites flocked to spas like Karlovy Vary in the Czech Republic (formerly Karlsbad, a UNESCO World Heritage Site as one of Europe great spa towns). The town, famous for its 13 springs (the most renowned, Vřídlo, reaching 73°C) attracts figures such as Richard Wagner (Froulikova, 2008) and Georges Clemenceau (Note de Voyage, 1896), who praised the benefits of its mineral-rich waters. A notable French example is Vichy, where Emperor Napoleon III had luxurious facilities built in the 1860s, transforming the town into one of Europe most renowned spas. In the XIX^{e} century, the thermal industry experienced a real industrial boom thanks to the advent of the railways, which made remote sites (such as Vichy

in France) accessible. These resorts became popular holiday destinations for aristocrats and artists, but also for the bourgeoisie in search of health and social prestige.

Figure I.1: Vichy thermal spa “Reine des villes d'eaux”, 1900. Photographic report on the “grands travaux” campaign of 1900: first-class spa and Grand Casino, 1900-1903. M. Laval and Médiathèque Valery-Larbaud (Vichy) collection.

I.1.2 Thermal springs: between mystical powers and popular beliefs

Over the centuries, the expansion of the thermal industry has been based on the effects of thermal waters, which were used by local populations on the basis of beliefs and traditions often based on religion or mysticism. Indeed, thermal waters were often considered miraculous, giving rise to folk and religious stories. For example, the Lourdes Spring in France was quickly known for divine cures, without any scientific explanation until recently (Albert-LLorca, 2005).

Beyond explaining the cures, the origin of the hot springs also caught the imagination of many people. Icelanders associated geysers with manifestations of the ocean goddess anger or with giants living inside them. Other popular theories imagined natural phenomena such as subterranean fires (Figure I.2) or winds coming from the depths of the Earth, also linked to

divine forces. In Campania, the Solfatare springs were associated with gateways to the subterranean world, a place of fire that would explain the hot water on the surface. The Japanese associate them with places where dragons live. In the Middle Ages, alchemists saw mysterious reactions between the 4 elements.

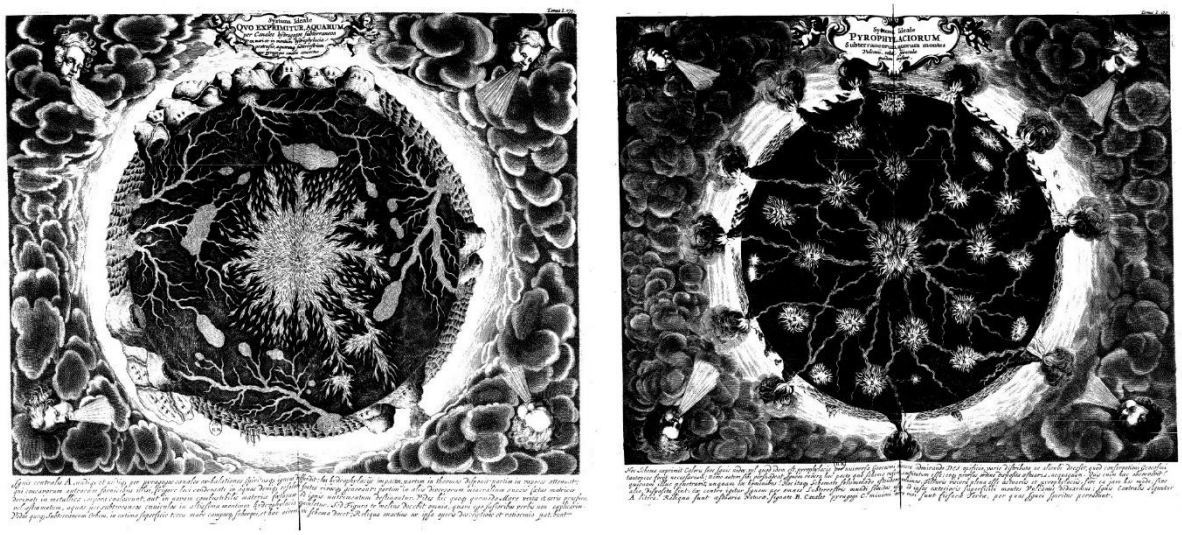

Figure I.2: Connections between different aquifers (on the left) and subterranean fires (on the right) at depth. Theories of a 17th-century geologist (Athanasius Kircher, Mundus Subterraneus, 1665).

I.1.3 From myth to reality

In the 18th century, the composition of thermal waters was the first aspect that attracted the curiosity of scientists. Early analyses revealed the link between the curative effects and the composition of the waters. For instance « *Le soufre subtil contenu dans nos eaux minérales* (de Spa, Belgique) *[…] a été reconnu de tout temps pour béchique, incisif, expectorant ; bon contre l'asthme, les toux violentes & sèches, dans les tubercules du poumon & les ulcères internes dont il adoucit les âcres* » (Joseph Sandberg, Médecin auxdites Eaux, 1780). This association between medicine and chemistry encouraged chemists, doctors and geologists to work together, and from then a precise description was made for each thermal spring. In 1799, Friedrich C. Fuchs published a methodical description of all the waters in the known world. This transition marked the shift from an intuitive perception of the benefits to a scientific validation.

Figure I.3: Thermal baths of Aix-les-Bains, sulphur spring fountain in the hall of the Pétriaux spa complex (Jazé-Pétriau, 2014).

Now that the therapeutic benefits had been demonstrated and explained, it was still necessary to determine the origin of the heat in these thermal springs. At the end of the Age of Enlightenment, people started to pay more attention to the subject, but there were still many questions, and it was difficult to come up with realistic explanations. Authors such as Le Grand d'Aussy and Joseph Hubert Sandberg spoke of ‘underground volcanoes’ or even ‘underground fires’ (Le Grand d'Aussy, 1794).

« Il n’est pas aussi aisé de deviner la cause qui produit la chaleur des eaux thermales. Cette cause est-elle un volcan souterrain ? Comme le prétendent plusieurs naturalistes. Sont-ce des pyrites, ou d’autres matières semblables, en fermentation ? Comme la plupart des chymistes le soupçonnent. Enfin, le liquide ne devient-il chaud, que quand il traverse des filons de houille ? Ainsi que l’a écrit, il y a quelques années, un auteur moderne »

LE GRAND D'AUSSY, Journey made in 1787 and 1788 in the former Upper and Lower Auvergne, now the Puy-de-Dôme and Cantal departments and part of the Upper Loire department (1794).

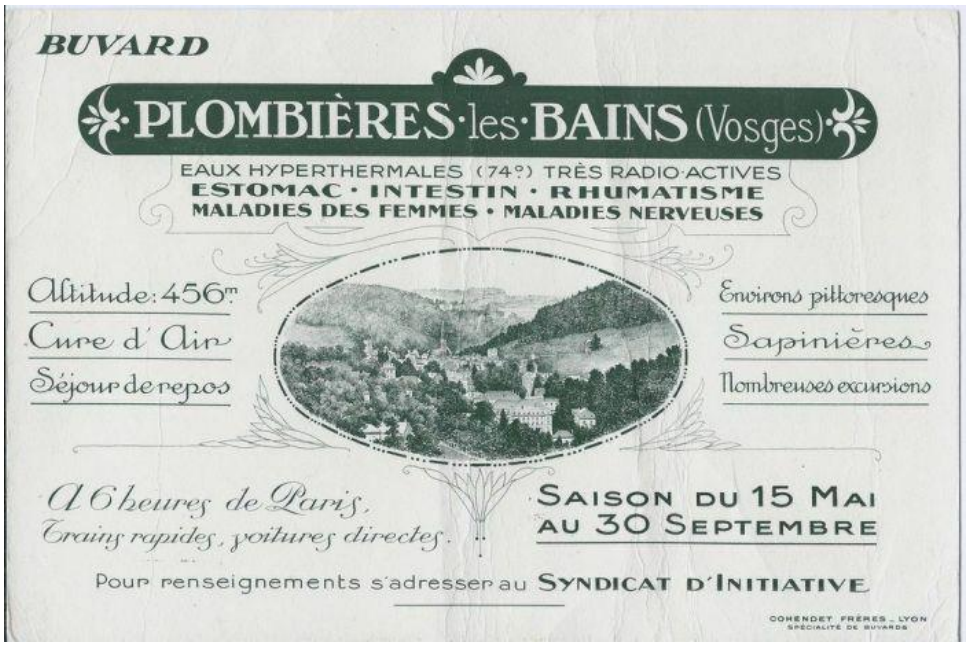

Figure I.4: Informative blotter about the thermal waters of Plombières-les-Bains.

As geological science developed in the XIX^{e} century, an explanation began to be found. Charles Lyell suggested in his book Principles of Geology (1833), that rainwater could infiltrate deep through fractures in order to warm up naturally with the Earth heat. This idea was accepted by many authors of the time, including Robert Busen and Ferdinand von Richthofen (1830-50). In France, the inventory launched in the previous century forced geologists to question the origin of thermal waters. Each thermal spring was now associated with deep circulations, local geothermal gradients allowing the water to be heated at depth. This pioneering work marked an important step in the understanding of geothermal phenomena, establishing a direct link between thermal waters and the Earth internal activity.

I.1.4 Human use of thermal waters

The use of hot water is not limited to the spa industry. It is used for a wide range of activities, including heating and energy production. The district heating system in Chaudes-Aigues is considered to be one of the oldest in the world. Established in 1332, the network is supplied by the 30 springs in the town, in particular the Source du Par, which has a temperature of 82°C. Initially, the pipes carrying the water were made from pine trunks (Figure I.5, Inventory of spa heritage - Route des villes d'eaux du Massif Central). A real spa was only built in the 18th

century, the town plan being to make Chaudes-Aigues ‘the Carlsbad of France’ (Michel Bertrand, medical inspector at Mont-Dore, 1822).

Figure I.5: Photographs, from left to right, of the first fir tree pipes carrying water, the current pipes and the limestone precipitation that eventually clogs the pipes.

Located in Tuscany, Larderello is an emblematic site in the history of geothermal energy. It was here that the first high-temperature geothermal power station was built and opened in 1913. The city benefits from an unusually high geothermal gradient due to plutonic activity. The naturally formed fumaroles are exploited directly by the power station. The total installed capacity is estimated at 800 MW (equivalent to the power of a nuclear reactor), representing more than 10% of Tuscany electricity needs (Enel Green Power).

I.2 Geothermal energy: classification and exploration

I.2.1 Geothermal energy categories and characteristics

Geothermal energy uses heat directly from the underground to produce energy or satisfy thermal needs. This renewable resource plays a key role in the energy transition, offering a clean, sustainable alternative to fossil fuels. Depending on the temperature of the fluids extracted, geothermal energy can be divided into four main categories: high temperature, medium temperature, low temperature and very low temperature, each adapted to specific uses (Figure I.6).

Very low and low-temperature geothermal energy

Low-temperature geothermal energy uses fluids at temperatures below 90°C. It is mainly used for domestic heating, swimming pools or small-scale industrial purposes (the town of Chaudes-Aigues mentioned above is an example of all these uses). This category also includes very low-temperature geothermal energy, used with geothermal heat pumps (PAC) for heating and cooling (Figure I.6). The aquifers targeted are shallow (2.5 km deep at most) and in sedimentary terrain.

Schools are using this sustainable resource. ENSEGID, an engineering school in Bordeaux, uses a reversible geothermal doublet to heat in winter and cool in summer. The targeted fluid is at a depth of 70 m at a temperature of 15°C.

Moderate-temperature geothermal energy

Medium-temperature resources (90°C to 150°C) are mainly used for direct applications, such as heating industrial buildings or for agricultural use (Figure I.6). The aquifers targeted are deeper, up to 4km in sedimentary zones.

This type of geothermal energy is used in Iceland, where it provides 90% of building heating.

High-temperature geothermal energy

This category covers geothermal resources with a temperature above 150°C. It is mainly used for electricity generation (Figure I.6). High-temperature geothermal power plants exploit reservoirs located at great depth (often in volcanic regions). Many are located in volcanic areas or at the edges of tectonic plates.

Two examples of high-temperature (HT) geothermal power plants exist in France. The first is the Bouillante plant in Guadeloupe, which uses a reservoir at 250°C to generate 15 MW of electricity. Then there is the Soultz-Sous-Forêts plant in Alsace, where the Enhanced Geothermal System (EGS) generates 1.7 MW from reservoirs at 200°C.

However, as concepts have evolved, new studies tend to show that high-temperature geothermal reservoirs are not limited to the geological contexts mentioned above.

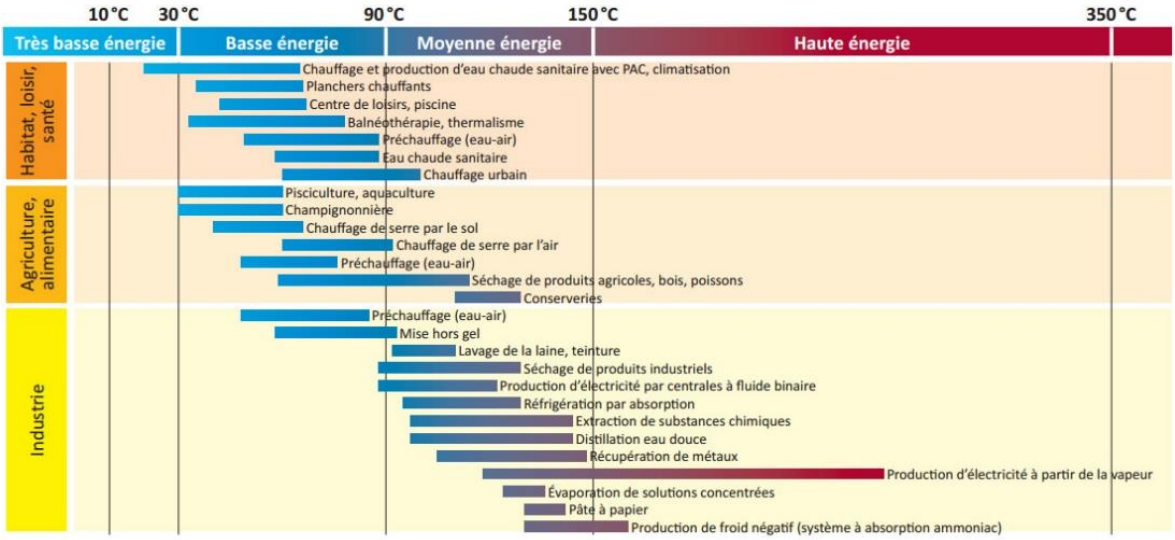

Figure I.6: Different applications of geothermal energy depending on the temperature of the fluids used (source: ADEME, BRGM).

I.2.2 Historical geothermal sites

Today known and exploited geothermal systems are associated with very specific geodynamic contexts. In 2014, Moeck proposed a set of favourable criteria (geodynamic contexts, heat transfer mode) for high-temperature geothermal deposits. His work was later supplemented by Jolie *et al.* (2021).

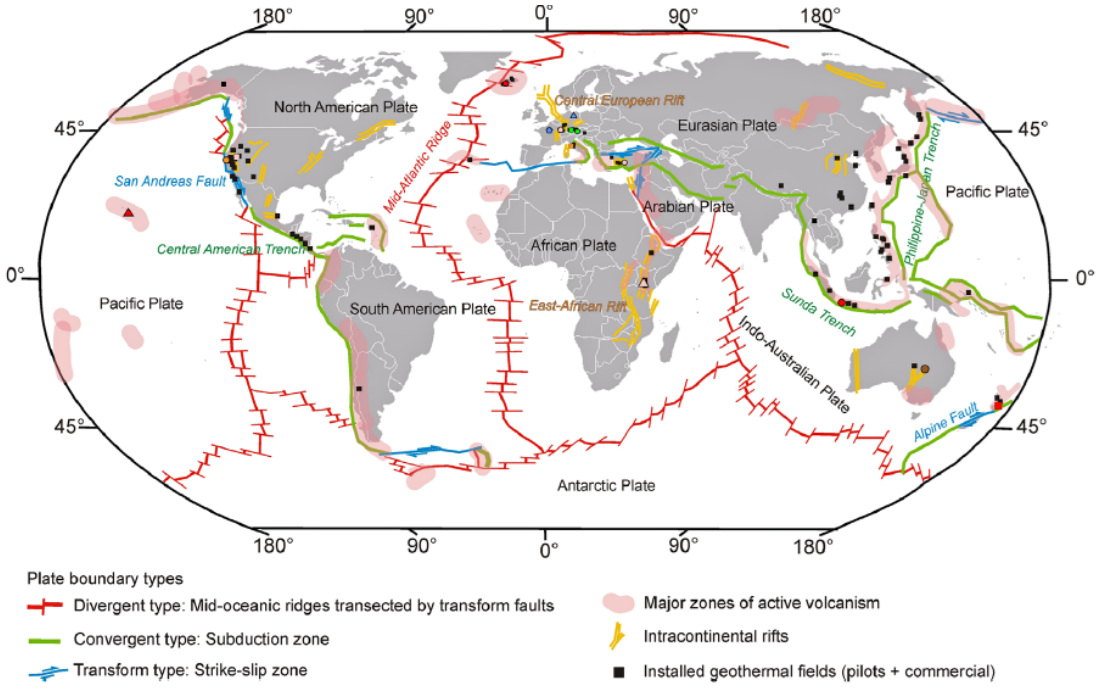

Figure I.7: Map of the distribution of geothermal power plants worldwide (after Moeck, 2014). The red lines represent divergent plate boundaries (mid-ocean ridges intersected by transform faults), the green lines represent convergent boundaries (subduction zones), the blue lines represent transform boundaries, the yellow lines represent intracontinental rifts, and the red areas represent active volcanic regions.

Figure I.7 shows that high-temperature geothermal systems are confined to specific geodynamic contexts. These correspond to rifting zones (extension), magmatic zones (Iceland) or amagmatic zones (Basin and Range), subduction zones often accompanied by volcanic arcs (New Zealand) and also plate boundaries associated with transform faults (San Andreas Fault). The Geysers, located in California, is the largest geothermal complex in the world, with an installed capacity of 1,517 MW (Geysers.com). Thanks to this capacity, around 1 million homes can be supplied with electricity. The power station initially exploited steam from a geothermal reservoir located at a depth of 2 km, reaching a temperature of 235°C (McLaughlin and Donnelly-Nolan, 1981; Thompson and Guderson, 1992). In the north-west, the reservoir is thought to reach 400°C at a depth of 3 km (Garcia *et al.*, 2016; Peacock et al., 2020). Another example is the Hellisheiði power station in southern Iceland. It produces 303 MW of electricity and 133 MW of heat (Sigfússon et al., 2018). Boreholes at depths of between 1,000 and 2,800 metres (Franzson et al., 2005) exploit fluids reaching 280°C (Geirsson, 2006). Geothermal power stations have also been developed near hot spots, such as the Pahoa power station in Hawaii, which produces around 30 MW per year. Located near the Kilauea volcano, it directly extracts heat from the volcanic hot spot. This plant accounts for 30% of the island renewable energy (Puna Geothermal Venture). All these sites have one thing in common: a heat flow anomaly. It follows that geothermal exploration used to target the so-called «abnormally hot» areas.

However, as mentioned above, these contexts are very specific, so the potential for developing HT geothermal energy is limited. New studies are now focusing on geothermal systems with no obvious surface manifestations (no hot springs, fumaroles). These are known as blind geothermal systems (Faulds *et al.*, 2010; Hanson *et al.*, 2014; Brown *et al.*, 2020; Craig *et al.*, 2021). Exploration is now based on indirect methods such as geophysics, structural geology and geochemistry. The new criterion used to define these new targets is permeability anomalies. One important consequence is that fault zones and their intersections become zones of high interest (Faulds *et al.*, 2010).

I.2.3 New geothermal targets: crustal fault zones in basement rocks

Faults are key structures that control fluid flow in the Earth crust (Sibson 1987; Hickman *et al.*, 1995; Curewitz and Karson, 1997; Baietto *et al.* 2008). Understanding the impact of faults on fluid flow is crucial not only for groundwater management but also for geothermal energy production. These faults may be isolated or interconnected, forming a complex network reaching great depths. Crustal fault zones (CFZ) are large-scale structures, both in terms of width and depth, since they are rooted at the ductile-fragile boundary (10-20 km deep, 300-400°C), but also in terms of thickness (from a few metres to several kilometres).

Depending on their permeability, CFZ can be either efficient drains facilitating fluid flow (Caine *et al.*, 1996, Gudmundsson, 2000; Patterson *et al.*, 2018a, 2018b; Patterson and Driesner, 2021), or barriers impeding flow (Bense *et al.*, 2008; Penhoët et al., 2025a-2025b). In contrast to the geodynamic contexts described above, CFZ are abundant on the planet surface. Numerous examples can be cited in France, in the French Massif Central (Duwiquet 2019; Penhoët et al., 2025a), Germany (Achtziger- Zupančič *et al.*, 2017), Spain (Faulkner *et al.* 2003), Finland (Bischoff *et al.*, 2024). Crustal fault zones, by increasing the natural permeability of rocks, open up new prospects for exploring basement rocks (granites) long considered to be devoid of potential since they are impermeable. Currently, their exploitation is based on the use of Enhanced Geothermal Systems (EGS) and the hydraulic stimulation of deep fractures (artificial increase in permeability). Authors have shown that even at very great depths, fractures can remain open and greatly increase the permeability of granitic rocks (Stober 2007; Bischoff *et al*., 2024). Throughout the world, fractured granites have already been identified as geothermal deposits, which may include surface indicators such as thermal springs (Lefort and Jutier, 1862; Richards et al., 1992; Vasseur et al., 1997; Bucher et al., 2009; Craig et al., 2013; Schimdt et al., 2018). Despite the numerous CFZ in the basement domain, they have only very recently been identified as potential HT deposits, and their exploration and exploitation therefore remain very limited.

I.3 Thermo-mineral springs in France

I.3.1 Definitions: hot springs, thermal, thermo-mineral…

For centuries, naturally hot springs have fascinated scientists and local populations. Nevertheless, the very definition of a “thermal” or “hot” spring varies depending on the discipline, the geographical context and even its use.

A spring

In hydrogeology, a spring is defined as « *l’eau qui sourd, l’eau qui sort de terre* » (Palissy, 1580; Dict. Trévoux, 1771; Larousse, 1874; Littré 1877). A spring is the place where underground water naturally emerges from the ground. It corresponds to the intersection between the lower limit of an aquifer (impermeable layer at the base) and the surface of the ground (topography).

« Hot » springs

In 2003, Allan Pentecost of King College London asked his colleagues how they would define a hot spring (Pentecost, 2003), a cold spring or even a thermal spring. The results reflect the most common classifications.

The first definition indicates that a spring can be defined as hot if its temperature is superior to that of the human body (36.7°C). In the opposite case, it is a cold source. As the perception of hot and cold is achieved by a human being, the reference then becomes universal.

The second definition states that a source can be defined as hot when its temperature is higher than the average annual temperature of the area around the source. This concept can lead to different classifications depending on the region, since average annual temperatures vary.

A third proposal defines a hot spring as a natural resurgence of water heated by the geothermal gradient or located near an active volcanic system. This time it is a phenomenon that is used as a criterion.

« Thermal » springs

There is no clear definition of thermal waters. The *Guide qualité pour la ressource en eau minérale* (BRGM, 2004) indicates that they are distinguished from hot waters by their high mineral content and a temperature significantly higher than the average atmospheric temperature. They are therefore often referred to as 'thermo-mineral'. In order to describe them precisely, two classifications exist. The first is based on the temperature:

- Cold waters: less than 20 °C.
- Hypothermal water: from 20 to 35 °C.
- Thermal waters or mesothermal: from 35 to 50 °C.
- Hyperthermal waters: above 50 °C.

The composition is then used to define the chemical facies in a Piper diagram:

- Rich in calcium and sulphates: Calcium sulphate facies.
- Rich in chlorides and sodium: Sodium chloride facies.
- Rich in bicarbonate and sodium: Sodium bicarbonate facies.

Next, it is possible to define a thermo-mineral water 'deposit'. This is made up of an impluvium (rainwater supply and infiltration zone), a transit zone (deep circulation, where the water is enriched with ions) and the emergence zone.

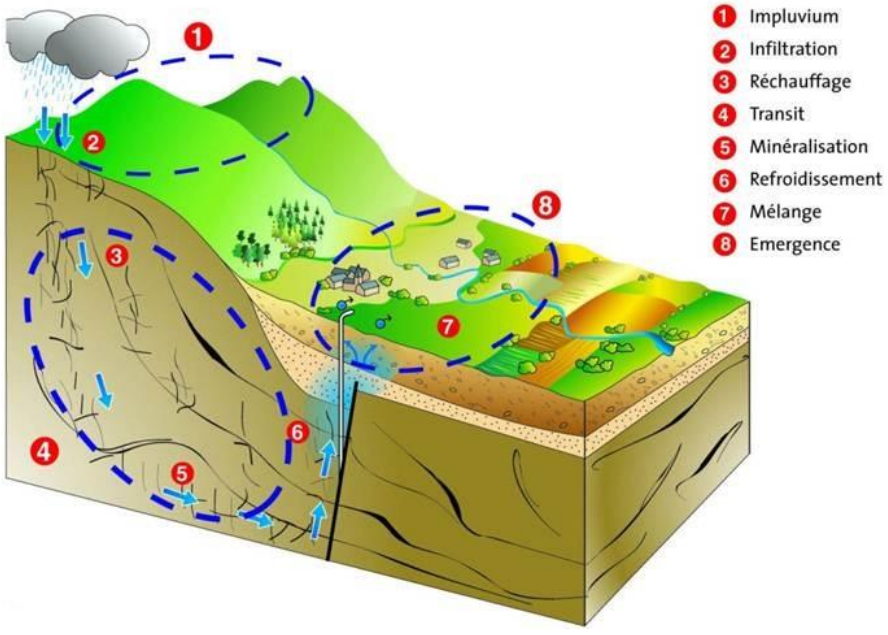

Figure I.8: Schematic representation of the thermal water circuit through a deposit (Ladouche B., Négrel P., Vigouroux P., BRGM)

From a more economic point of view, thermal water could also mean any water, regardless of temperature, used in a health care establishment (santé.gouv).

I.3.2 Distribution of thermo-mineral springs in France.

In the following chapters of this thesis, we consider a spring to be thermal if its temperature is above the annual average. In France, the average annual temperature was 14.4°C in 2023 and 14.5°C in 2022 (French National Temperature Indicator, Infoclimat). A spring can therefore be considered to be thermal if its temperature exceeds 15°C. Using this definition, more than 368 springs have been identified in France (Banque du Sous-Sol, Annales des Mines 1998). The springs have been divided into two categories: between 15-50°C ‘hot’ springs and between 50-85°C ‘very hot’ springs.

Thermo-mineral springs are mainly located in the Pyrenees, the Massif Central and the Alps. However, there are also a few in eastern France and Corsica, and just one in Brittany (Figure I.9). The aim here is to determine whether the distribution of these springs is purely random, or whether it is influenced by a number of specific geological factors.

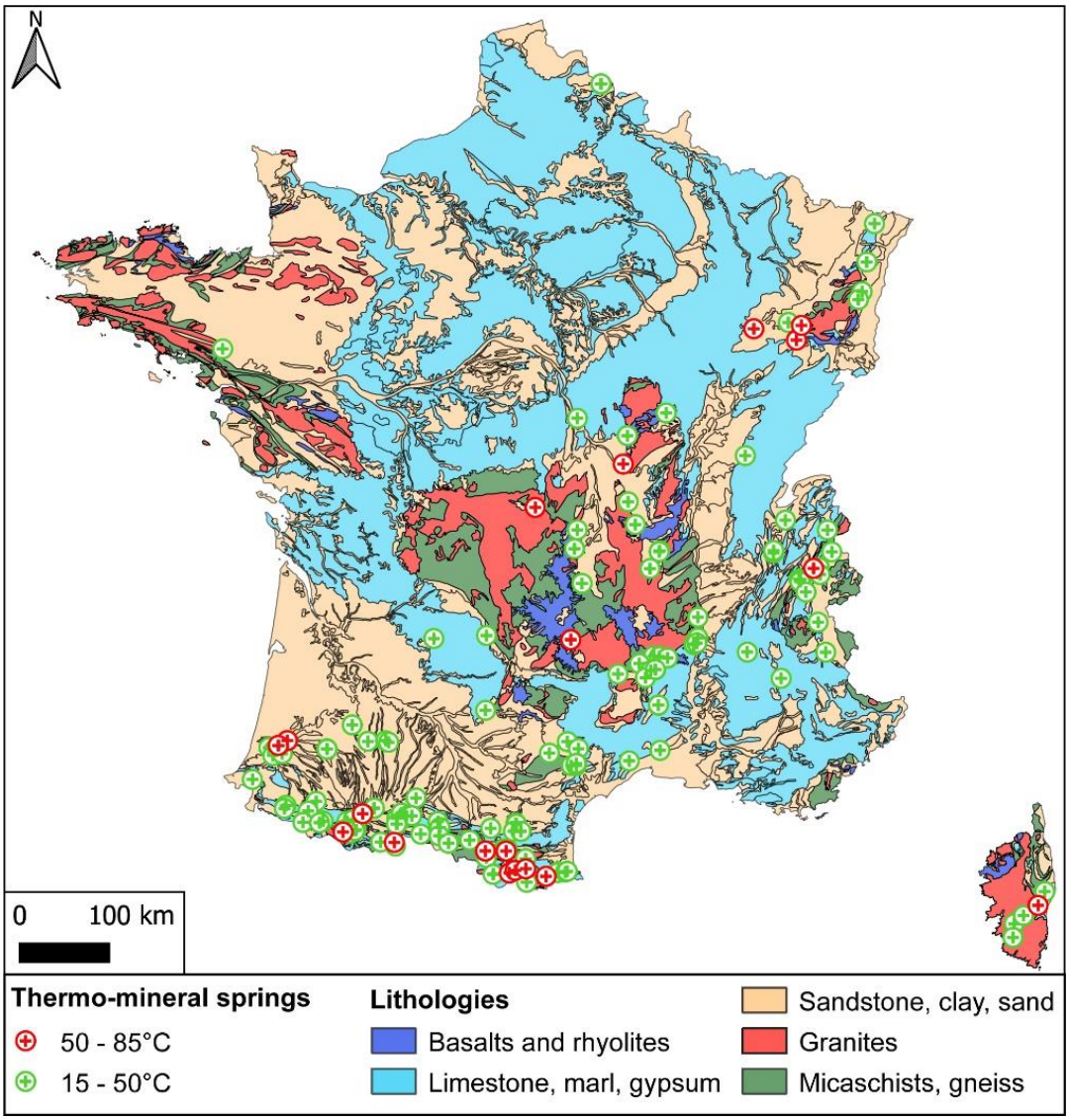

Figure I.9: Distribution of thermo-mineral springs (according to the Banque du Sous-Sol, BSSEAU, BRGM) in France. The background map corresponds to the 2M geological map (BRGM).

Determinants of thermo-mineral spring distribution

The study by Tamburello *et al.* (2022) explores the distribution of hot springs in relation to endogenous factors (heat flow, volcanism, tectonic constraints, etc.) and exogenous factors (topography, precipitation values, climatic variations, etc.) on a global scale. His work demonstrates that heat flow, topography and the presence of volcanism, as well as an extensive stress regime, play a major role. Based on these results, this section aims to analyse the distribution of hot springs in mainland France.

Firstly, the location of hot springs will be analysed in terms of heat flow, the historical criterion guiding geothermal exploration. We will then look at the impact of the lithology of the deposit

(using the definition given above). The link between sources and topography will be studied using a calculated maximum gradient. The final factor will be the density of faults in the immediate vicinity of the springs.

Heat flow

Figure I.10 illustrates the heat flow map of France. It is based on the study of Vasseur (1982), supplemented by Lucazeau and Vasseur (1989). The flux measurements come from both shallow boreholes and deep oil boreholes, combined with pre-existing databases. Once the values had been corrected (to eliminate climatic, topographical and groundwater circulation effects) and the thermal properties of the rocks were known (heat production, thermal conductivity), an interpolation map was produced. As the heat flux measurements were point measurements, the interpolation was able to smooth out extreme values and therefore over or underestimate the data.

In France, some regions have an average heat flux, notably Brittany, the Pyrenees, Provence and the Alps, with values between 60-80 $mW.m^{-2}$. While these heat flux values are not very abnormal, the fact is that mountainous regions (Pyrenees, Alps) are very rich in thermal springs. Most of these springs have temperatures between 15-50°C, but some have temperatures above 50°C.

The Massif Central, the Rhône basin and Alsace have much higher heat flow values (100 $mW.m^{-2}$). These areas are characterised by numerous thermal springs, including one of the hottest in Europe (Source du Par, Chaudes-Aigues). In addition, there are thermal springs at Plombières-les-Bains, Luxeuil-les-Bains and Bourbonne-les-Bains, most of which exceed 50°C. The springs are less abundant than in the previous case, but on average hotter.

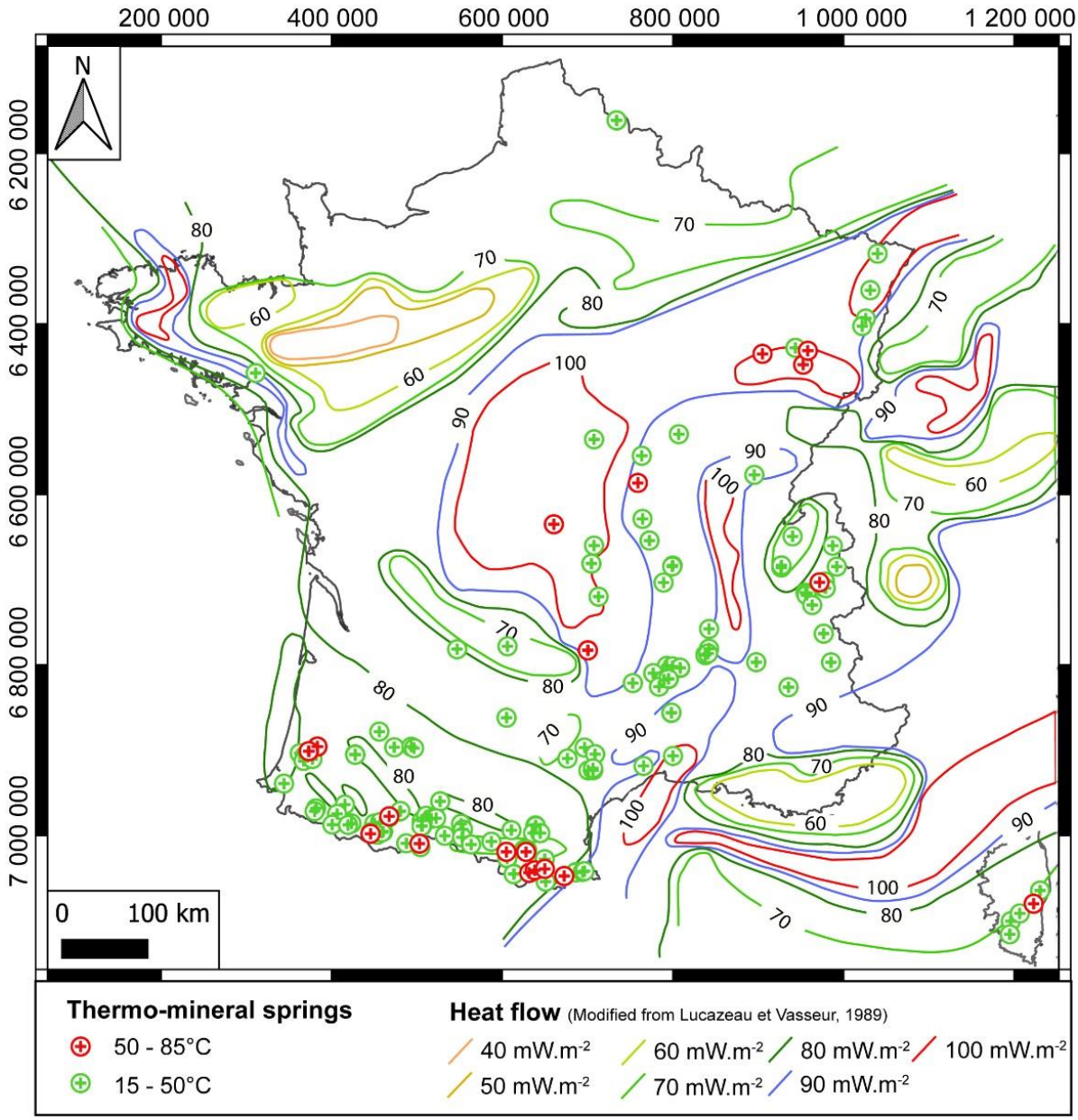

Figure I.10: Distribution of thermo-mineral springs as a function of heat flow in France. Heat flow contours are extracted from the heat flow map of Lucazeau and Vasseur (1989).

The thermal source-heat flux relationship is not that simple. When we compare the heat flow values, represented by the isolines, with the location of the thermal springs, we can see that a high heat flow value does not lead to a very high emergence temperature (Morbihan, Rhone basin). By contrast, regions with low heat flux can produce very hot springs, as in the Pyrenees (Table 1.1, T > 50 °C).

City	Name	Flow rate (m3/h)	Temperature (°C)
Chaudes-Aigues	Par	12	80
Ax-les-Thermes	Rossignol -supérieur	6.3	77.8
Nyer	Saint André	19.5	75
Ax-les-Thermes	Saint Roch	0.04	72
Ax-les-Thermes	Viguerie	4	70
Ax-les-Thermes	Grande Sulfureuse	7.2	69.2
Ax-les-Thermes	Etuve de l'Hopital	3.6	69
Ax-les-Thermes	Puits d'Orlu ancienne	4.6	66.5
Plombières-les-Bains	Robinet Romain	0.5	66.2
Plombières-les-Bains	Vauquelin	0.2	66

Table I.1: The 10 hottest springs in France (BSS EAU and Annales des Mines 1998). The springs at Chaudes-Aigues and Plombières-les-bains are located on heat flow anomalies. Those at Nyer or Ax-les-Thermes in the Pyrenees, conversely, are associated with normal values.

Although heat flow is an initial approach to analysing the distribution of thermal springs in France, it is not sufficient. In order to refine this analysis, other criteria such as fault density, topography and lithology of the deposits will also be taken into account in the following sections.

Hydrothermal deposit lithology

As previously defined, a hydrothermal deposit includes the water infiltration, transit and emergence zones. The lithologies on the 2M geological map (Figure I.9) and those cited in the inventory (BSSEAU BRGM, Annales des Mines 1998) have been grouped into four categories:

- Sedimentary rocks: sandstone, clay, sand, limestone, marl and gypsum.
- Granites.
- Metamorphic rocks: micaschists, gneiss, schists.
- Volcanic rocks: basalts and rhyolites.

Of the 368 springs counted, 2 are volcanic, 159 granitic, 56 metamorphic and 151 sedimentary (Figure I.11).

The granite deposits have both the largest number of springs and some of the highest temperatures, with a maximum of 77.8°C (Source Rossignol, Ax-Les-Thermes). The average temperature of these springs is 41°C (Figure I.11). Metamorphic rocks also host very hot

springs reaching 82°C (Source du Par, Chaudes-Aigues), with an average value of 37°C (Figure I.11). Sedimentary rocks have a large number of springs, but their temperatures are lower, averaging 30°C, with a maximum of 62°C (Bourbonne-les-Bains, Source no. 10) (Figure I.11). The few springs associated with volcanic rocks are relatively cold (27°C on average), with a maximum temperature of 28°C (Source Saint-Martin, Chamalières).

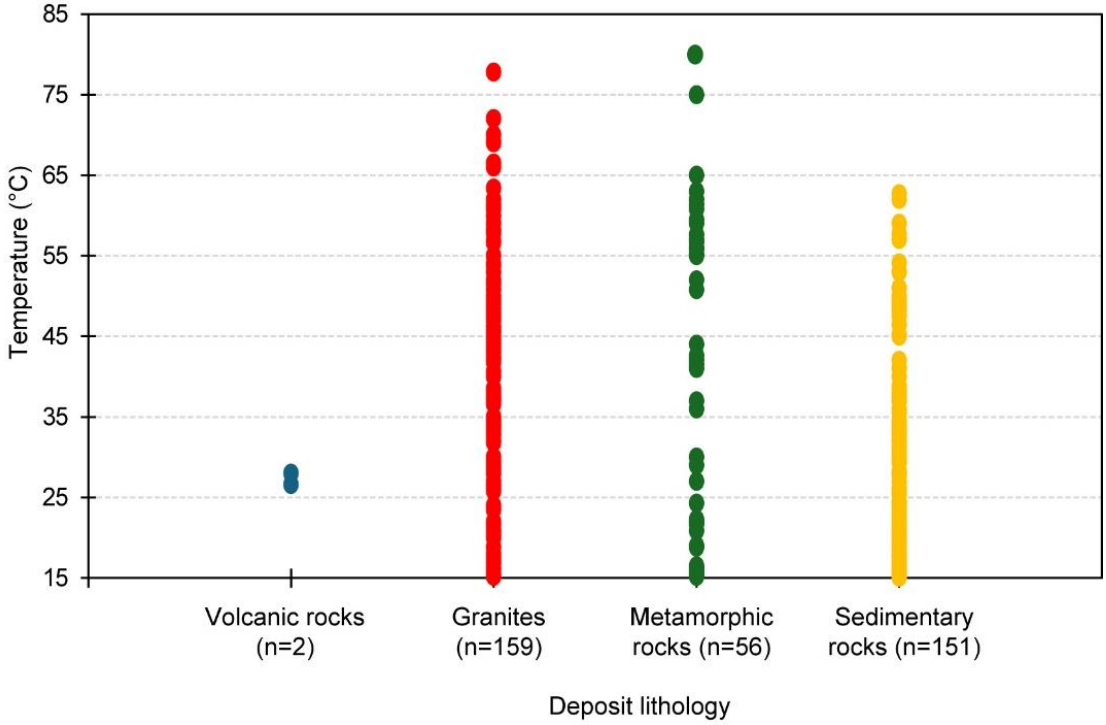

Figure I.11: Temperature of the 368 springs according to the lithology of the hydrothermal deposit. The deposit is defined using the BSSEAU database (BRGM). If the data is missing, the lithology in which the spring is located is used.

The deposit lithologies in the database (BSSEAU and Annales des Mines 1998) are based on field reports carried out on each spring. When the data is available, it will be used. Conversely, when the deposit is not provided, the spring lithology of the 2M geological map will be considered. This can lead to uncertainties such as the Chaudes-Aigues springs, which are located in metamorphic units but associated with a granitic reservoir (Vasseur *et al.*, 1997). As the data does not appear in the inventory, these are considered to come from a metamorphic deposit.

Topography and elevation change

To identify the influence of topography, the maximum difference in altitude surrounding each spring was calculated. Within a 10 km radius, the difference between the maximum altitude

and the altitude of the spring was calculated. Identified as a key parameter in fluid circulation, topography controls both fluid infiltration but also the distribution of thermal springs at the surface (Taillefer *et al.*, 2018).

The results fall into two groups (Figure I.12). The first group covers small gradients (less than 1,500 m), with an average temperature of 32°C and a maximum temperature of 80°C (gradient of 644 m). All four types of deposit are represented. The second group, with a higher altitude difference (between 1,500 and 2,900 m), has a higher average value (39 °C) and a maximum of 77.8 °C. Here, granitic and metamorphic rocks predominate.

It should be noted that the temperature of springs linked to sedimentary rock is not directly linked to gradient. In fact, the emergence temperature varies little as the difference in altitude increases or decreases. Temperatures in springs linked to basement rocks (granites and metamorphic rocks), in contrast, do not behave in the same way. More springs emerge when the gradient is high (the second group mentioned above) at higher temperatures. These types of deposits are therefore more influenced by the surrounding topography.

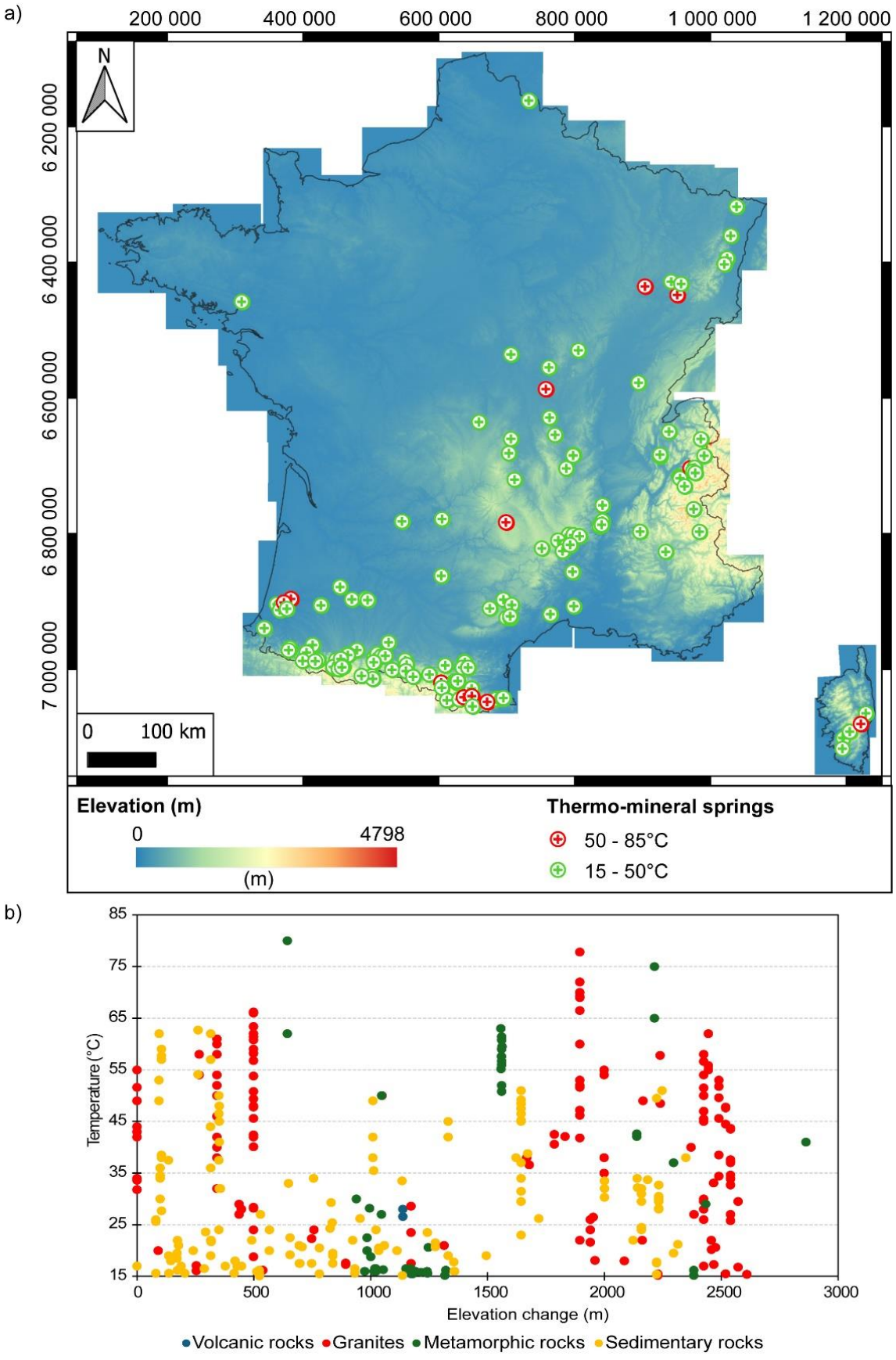

Figure I.12: (a) Map showing the distribution of thermal springs in France as a function of topography. (b) Temperature of springs as a function of maximum difference in elevation within a 10km radius of each spring.

Fault density

The influence of fracturing density was studied using a fault density map. Within a radius of 10 km, the average value of cumulative fault length has been chosen. The method used to produce this map is detailed in Appendix A and in Penhoët *et al.* (2025).

The results show that an optimum fracturing density permits the highest source temperatures to be reached (Figure I.14). The highest temperatures (up to 82°C) are found between 50 km and 100 km of cumulative length. For lower densities, the springs are numerous but their maximum temperature decreases, with values not exceeding 65°C. Conversely, for more densely faulted areas (> 100 km), there are few springs and temperatures are even lower. These do not exceed 55°C. However, it should be noted that for these density values, the minimum temperatures are high (35°C compared with 15°C for the previous groups). This phenomenon, which may seem counter-intuitive, is explained below.

This phenomenon can be directly related to the concept of permeability, as faults are natural drains that allow meteoric surface water to infiltrate at depth, but also to rise quickly to create hot springs at the surface. The calculated fault density therefore provides an initial estimate of the area permeability. Thermo-hydraulic modelling has shown that there is a window of optimal permeability values (of the host rock) that allows the highest spring temperature values to be reached (Figure I.13, Lopez and Smith, 1995). In our case, using the fracture density calculated around the emergence zone, a similar behaviour appears. If the fault density is too low, the permeability is assumed to be low, and the hot fluids rise slowly, in small volumes, and cool. As a result, surface springs will be cold. Inversely, when the fracturing density is very high, the area becomes favourable to the infiltration of dense, cold fluids because it is very highly permeable. By contrast, with an intermediate fracturing density, the area becomes permeable

enough to allow the fast ascent of hot fluids in large volumes, but not permeable enough to allow the infiltration of cold fluids. In this configuration, hot springs appear.

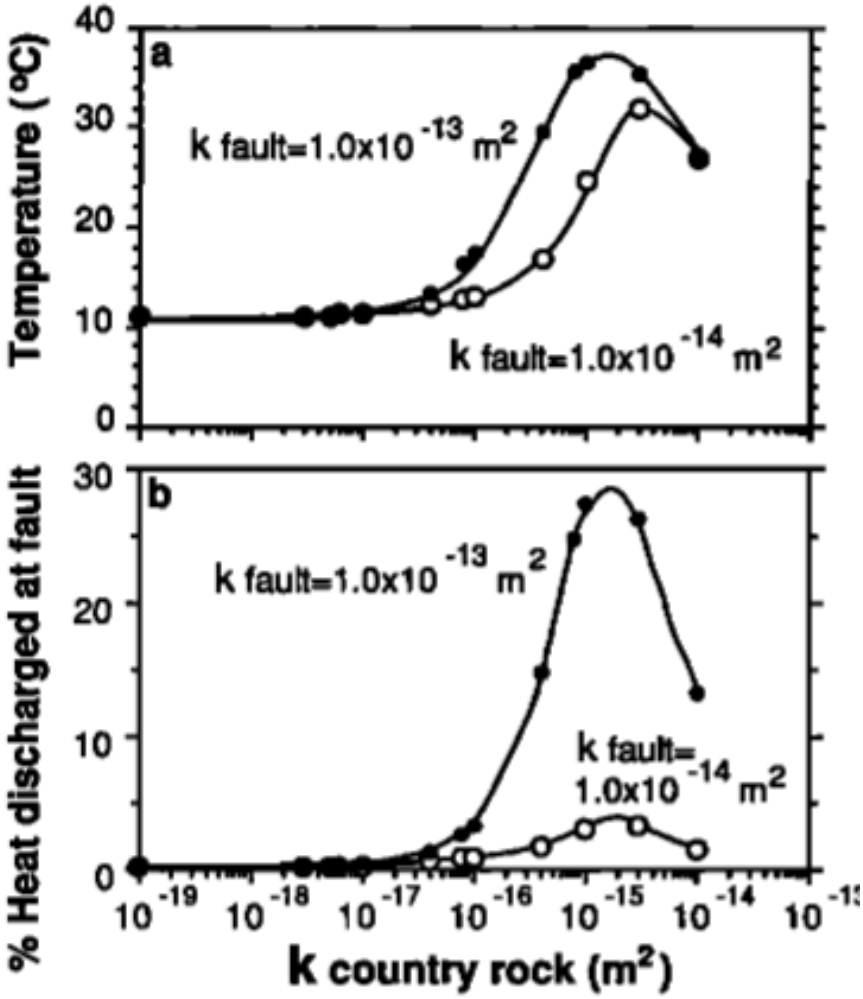

Figure I.13: (a) Temperature at emergence and (b) percentage of total heat transmitted in a fault zone as a function of its permeability and that of the host rock (Lopez and Smith, 1995). The temperature is maximum for a specific range of values and decreases outside this range.

As regards reservoir lithologies, it can still be seen that the temperatures of springs in sedimentary environments are not directly affected by fracturing. They range over all values. Basement rocks, however, are confined within the window of optimum cumulative length values mentioned above. Outside this range of values, the temperature of the springs falls significantly.

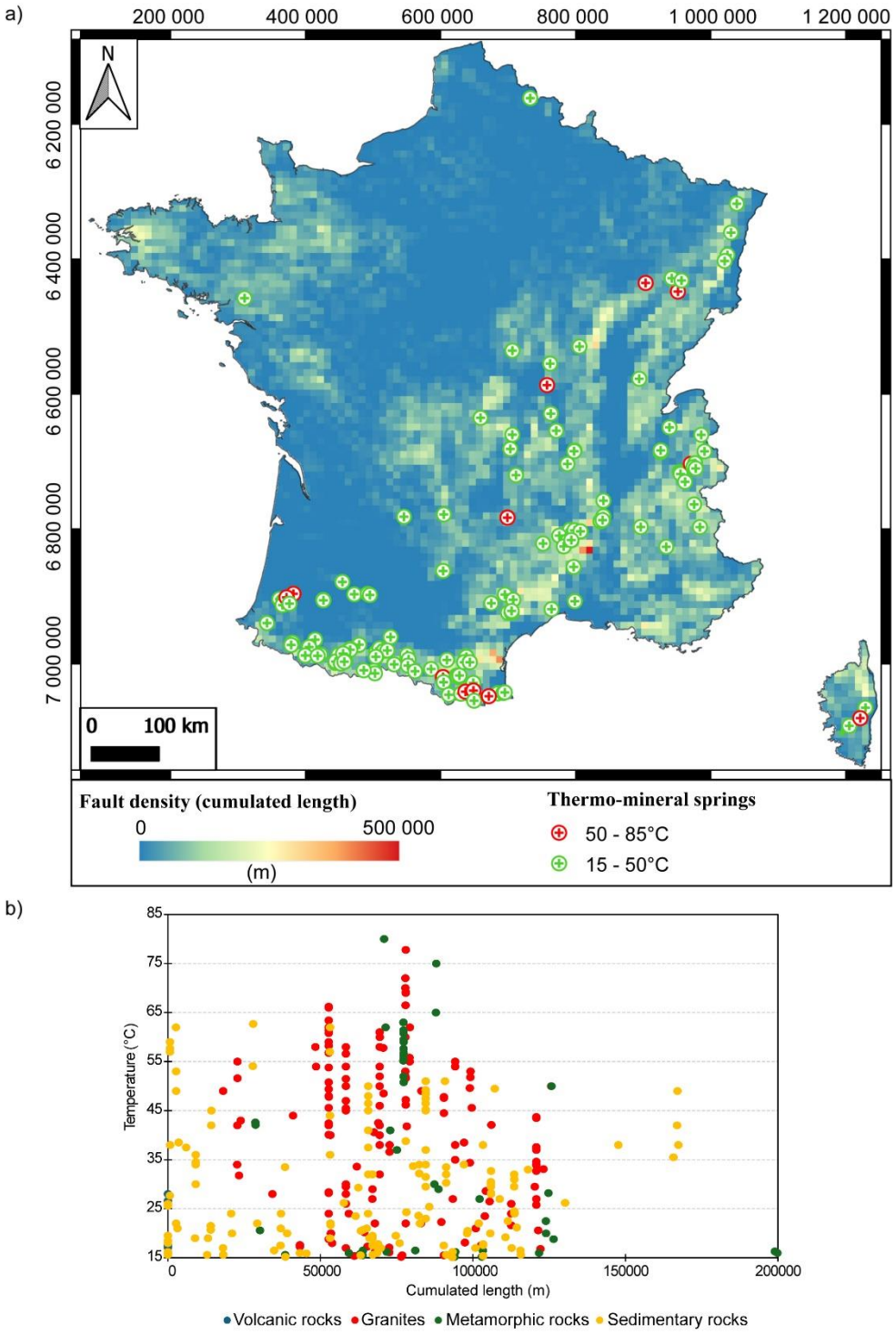

Figure I.14: (a) Map showing the distribution of thermal springs in France as a function of fault density. (b) Temperature of springs as a function of average fault density within a 10 km radius of each spring.

Synthesis

The above descriptions demonstrate the complex relations between hot springs, heat flow, lithologies, elevation changes and fault density. As we saw, none of these parameters by itself can control the presence of a hot spring or its temperature. Instead, a combination of several

criteria appears to be favourable. For example, mountainous regions made up of basement rocks, combining a high gradient and high fracture density, have a large number of hot springs. Conversely, basin areas (Aquitaine or Paris), with few faults and a fairly flat topography, have few thermal springs. These two examples are valid whatever the heat flux measured (e.g. low flux value in the Pyrenees but high in the south of the Paris Basin). However, the Alps and Corsica represent an initial counterexample to this system: even with high altitudes, basement rocks and strong fracturing, the number of thermal springs remains limited.

This preliminary study has shown that the presence of thermal springs is determined by a complex interaction between several parameters.

In this case, the hydrothermal system associated with one of the hottest springs in Europe, Chaudes-Aigues, will be our study area. This specific site will provide an understanding of the interactions between topographic gradient, heat flow and fracturing.

This part of the introduction has been used in a scientific publication corresponding to chapter VI.

I.4 Overview of current understanding of amagmatic hydrothermal systems

I.4.1 Bibliometric analysis: current research on hot springs

A simple experiment was carried out to get an initial idea of the state of knowledge about hydrothermal systems. On the Web of Science site, basic statistics were compiled on the number of publications dealing mainly with hot springs (key words ‘hot spring’ and ‘thermal spring’ in the title). The graphs shown illustrate the dynamics of scientific research through changes in the number of publications by discipline and over time.

Microbiology, and more generally biology, is the discipline with the greatest interest in hot springs, with more than 629 publications recorded since 2001. Thermal springs are home to extremophilic micro-organisms, offering an insight into the limits and adaptation of life while helping to understand the origin of life. Their study also sheds light on the search for

extraterrestrial life in astrobiology, as they may contain physico-chemical conditions resembling the extreme environments of other planets.

The geosciences, conversely, have only 370 publications on the subject. Within these, the majority of published articles are devoted to the study of the composition of thermal waters, with water geochemistry recording the most publications (215, Figure I.15). Next come publications proposing multidisciplinary studies, which may combine structural geology, geochemistry, geophysics and numerical modelling. Publications in geology and geophysics are far less represented, with 75 and 19 respectively.

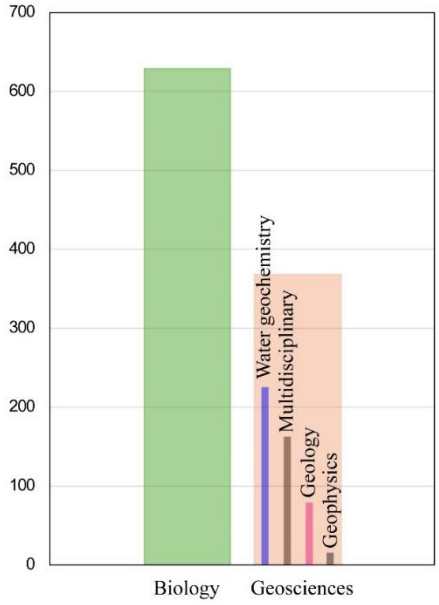

Figure I.15: Distribution of studies on hot springs (title containing 'hot spring' or 'thermal spring'). The classification is based on the main theme of the journals in which the articles were published.

Since 2002, the number of articles published on hot springs has increased slightly, although there is no significant growth (Figure I.16, 21 articles in 2001 compared with 48 in 2024). A slight decrease can even be seen since 2020. The same phenomenon can be observed for publications dealing with fluid circulation ('fluid flow' or 'hydrogeology' in the title of the publication), although their number is greater. Fault or fault zone publications, in contrast, have increased steadily since 2001 (Figure I.16), with the number of publications rising from 350 to 1,155 between 2001 and 2024. Since 2020, however, there has been a slight plateau. Some of the study of faults remains fragmented, however, with the number of publications dealing

with their impact on fluid circulation (‘fault’, ‘fault zone’ and ‘fluid flow’ or ‘hydrogeology’) remaining low (less than 150 publications in 2024). Yet this topic is fundamental to geothermal exploration and the identification of new targets. Other renewable resources, such as CO2, are enjoying greater popularity. In 2024, 1,645 publications were recorded in the Geosciences category (compared with 90 on hot springs).

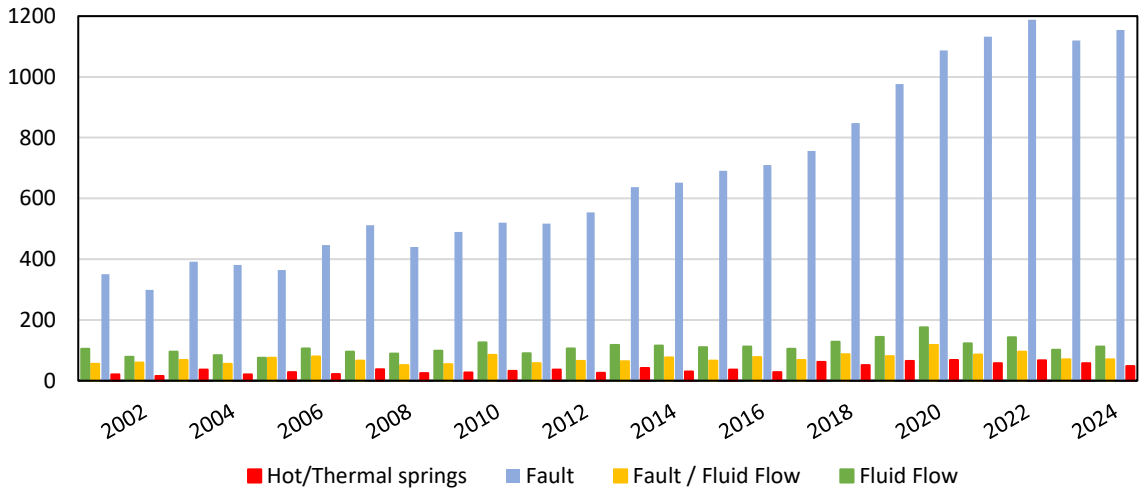

Figure I.16: "Evolution of the number of publications per year on topics related to faults ('fault'), fluid flow ('fluid flow' and 'hydrogeology'), the coupling between faults and fluid circulation ('fault' and 'fluid flow' or 'hydrogeology'), and hot springs ('hot spring', 'thermal spring') from 2001 to 2024 (source: Web of Science).

While few in number, existing studies on springs have led to a better understanding of how hydrothermal systems work and to the identification of key control factors, which are explained below.

I.4.2 Impluvium and infiltration at depth

A high-altitude fractured basement...

Thermal springs are the final expression of a long circulation of meteoric water at depth. In continental hydrothermal systems, water infiltration at high altitude is largely controlled by the presence of fragile fault systems, which play a fundamental role in structuring groundwater flows (Sibson, 1987; Hickman *et al.*, 1995; Curewitz and Karson, 1997; Baietto *et al.* 2008, Haines *et al.*, 2016). Their dip (Duwiquet *et al.*, 2021), thickness (Penhoët et al., 2025a) or orientation in relation to regional constraints (Barton *et al.* 1995; Mckenna and Blackwell 2004;

Faulds *et al.* 2010; Haines *et al.* 2016, Duwiquet *et al.*, 2022) make these structures highly permeable, allowing meteoric water to infiltrate deeply and quickly into the Earth crust.

Topography is a key factor in these flow processes, imposing a hydraulic gradient that favours the circulation from topographic highs towards discharge zones located at lower altitudes. Here, fluids can emerge as hot springs (Taillefer *et al.*, 2018, Carbajal Martinez *et al.*, 2024). Darcy law (Darcy, 1856) describes fluid flow in porous media, and is written as follows:

$$Q = KA\frac{\Delta H}{L} \tag{I.1}$$

with Q (m^3/s) the flow rate, K ($m.s^{-1}$) the hydraulic conductivity, A (m^2) the surface area through which flow occurs. ΔH/L, the hydraulic gradient, quantifies the variation in hydraulic head H (m, piezometric level) over the distance L (m) of the flow. For natural flows, the piezometric level corresponds to the altitude, so we speak of a topographical gradient, which means that flows are directly guided by the topography. In addition, the deeper the flow, the higher the infiltration altitude.

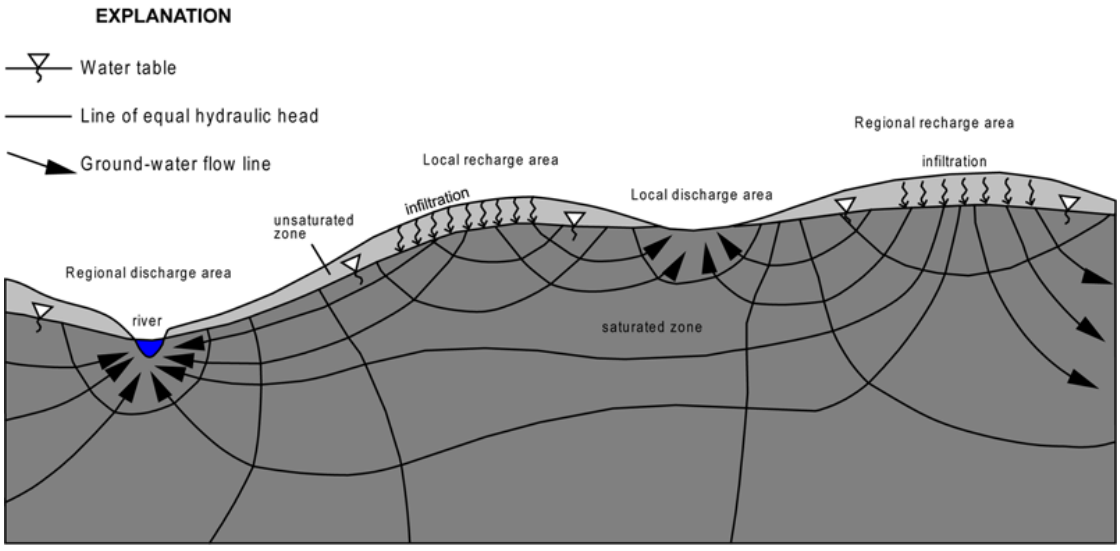

Figure I.17: Illustration of subsurface water flows, with infiltration at the highest topographic points and discharge at the lowest Fleming (2004).

As shown in Figure I.17, flows can be local, with discharge points close to the infiltration zone (local discharge area), or regional, with fluids reaching the valleys (regional discharge area). The common feature is the discharge to a low topographic point. Thus, one source may drain several infiltration areas. When the transport of matter is controlled by a pressure gradient, it

is called advection. In orogenic domains, for example, this 'advective' or forced convection leads to the formation of hot springs (Moeck 2014; Jolie *et al.*, 2021; Taillefer, 2018).

But also weathered

Chemical, tectonic and climatic alteration of the basement rocks (granite) is another key element in these systems. Supergene reactions lead to the formation of a regolith several hundred metres thick, often highly porous and permeable (Maréchal *et al.*, 2004; Dewandel *et al.*, 2006; Lachassagne *et al.*, 2011). Regolith acts as a great subsurface aquifer (Lachassagne *et al.*, 2011), allowing the infiltration of large volumes of water and facilitating its storage prior to transit to deeper reservoirs through fault zones (Wyns *et al.*, 2002; Dewandel *et al.*, 2006; Lachassagne *et al.*, 2011). A weathering profile can be divided into several horizons with different hydraulic properties. At the top, the unconsolidated, clay-rich saprolite or alterite is produced by secondary mineralogical reactions, and the original structure of the rock is no longer recognisable (Dewandel *et al.*, 2006). This layer can reach hydraulic conductivities of the order of 10^{-6} $m.s^{-1}$ and porosities of 5%, acting as a composite aquifer. Below this is the fractured horizon, characterised by intense horizontal and vertical fracturing, density of fractures decreases with depth (Houston and Lewis, 1988; Maréchal *et al.*, 2003a; Wyns *et al.*, 2004, Dewandel *et al.*, 2006). These fractures are not caused solely by tectonics, but also by the weathering of the rock (Wyns *et al.*, 1999, 2004; Lachassagne *et al.*, 2011). This aquifer level reaches very high hydraulic conductivity values (10^{-5} $m.s^{-1}$). The bottom limit is made up of impermeable bedrock, k ~10^{-10} $m.s^{-1}$ (excluding fracturing, Stober and Bucher, 2007). As shown in Figure I.18, in densely faulted zones, a deepening of the profile can occur and create a discontinuity in the weathering profile. These corridors have different hydraulic properties to the above-mentioned horizons and act as infiltration drains for meteoric water towards depth (Wyns, 2004).

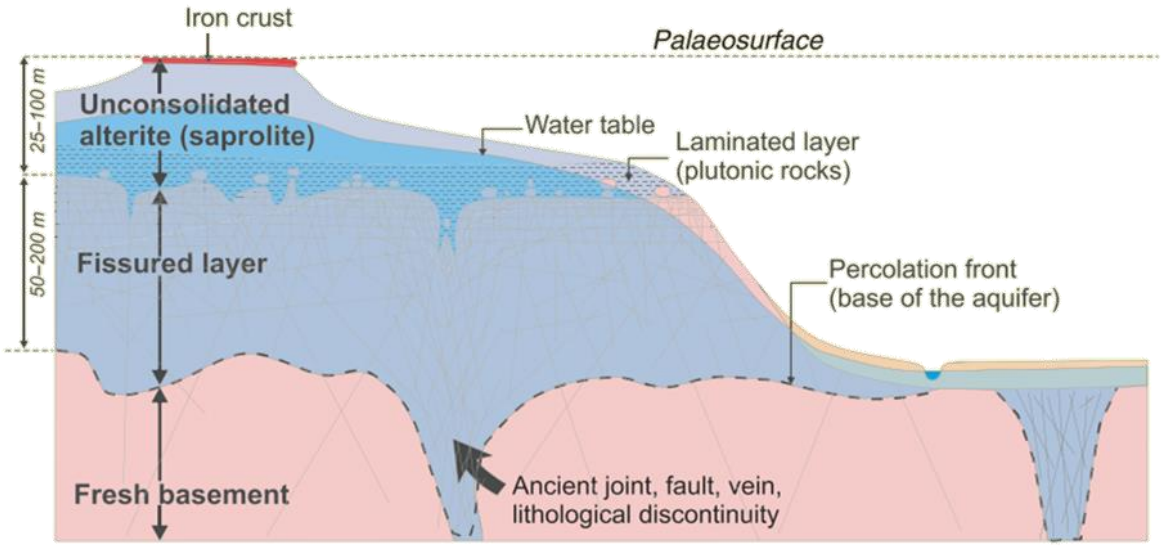

Figure I.18: Conceptual model of the alteration profile of a Hard Rock Aquifer (HRA) consisting of, from bottom to top: impermeable granite topped by the fractured horizon and an unconsolidated cover (saprolite) (after Lachassagne et al., 2011).

The interactions between these different elements - topography, fault networks and basement weathering, shape the dynamics of hydrothermal flows on a crustal scale. Significant recharge at altitude, coupled with circulation at depth within fractures and faults, ensures the renewal and movement of fluids, thus influencing temperatures, chemical compositions and the spatial distribution of hydrothermal springs at the surface.

I.4.3 Deep hydrothermal circulation and heat transfert

Heat source

Continental hot springs draw their heat from several processes, their relative importance varying according to the geological context. In an amagmatic context, two main mechanisms can heat groundwater: basal mantle heat flow and radioactive decay within crustal rocks.

In tectonically stable regions, the crust is thick and undeformed, and the heat flow at its base averages 30 $mW.m^{-2}$ (Jaupart and Mareschal, 2007). At the surface, the average heat flow measured is 65 $mW.m^{-2}$ (Jaupart and Mareschal, 2007). In tectonically active zones (rifts, recent orogenic zones), however, crustal thinning can generate a higher mantle flow, resulting in a surface heat flow ranging from 80 to 120 $mW.m^{-2}$, a value that increases even more in a volcanic context (Pollack *et al.*, 1993).

In addition to this basal heat flux, a crustal contribution is produced by the decay of radioactive isotopes of uranium (U), potassium (K) and thorium (Th). Heat production is around 2 $\mu W.m^{-2}$ (Jaupart *et al.*, 2007), but in granitic rocks, heat production is more significant. Its value can reach up to 7 $\mu W.m^{-3}$ and even 10-20 $\mu W.m^{-3}$ for granites with high heat production (Turcotte and Schubert, 2014).

Heat transfer mechanisms

Conduction is the dominant heat transfer mechanism in the continental crust, involving rocks considered as impermeable (10^{-18} - 10^{-20} m²). According to Fourier law, the heat flux q ($W.m^{-2}$) depends on the temperature gradient T (K) and rock thermal conductivity k ($W.m^{-1}.K^{-1}$):

$$\vec{q} = -k.\vec{\nabla}T \quad \text{(I.2)}$$

Conduction does not involve any movement of matter, so it does not create thermal springs, but can simply heat deep aquifers over a very long time. This is not the most efficient way of transferring heat, as the thermal conductivity of rocks varies very little. In addition, a thermal disturbance occurring at the base of the crust (30 km) will take more than a million years to affect the surface.

As rock permeability increases, fluid circulation velocities increase. For high permeability values (10^{-15}-10^{-12} m²), in particular due to faults or a high fracture density, the convective regime can be set up. Heat is transferred mainly by fluids. As the density of fluids depends on temperature, cold fluids (higher density) infiltrate and hot fluids (lower density) ascend. This phenomenon can be expressed simply by Archimede law:

$$F_b = \Delta\rho \cdot g \cdot V \quad \text{(I.3)}$$

Where Fb is the buoyancy force (N), $\Delta\rho$ is the variation in fluid density (kg.m-3) with temperature ($\Delta\rho=\rho0\cdot\alpha(T-T0)$), g is the gravitational acceleration, V (m3) is the fluid volume and α is the thermal expansion coefficient of the fluid (K-1). According to Darcy law stated above, if permeability increases, flow rate and Darcy velocity both increase. Convection is therefore a very efficient heat transfer mechanism. The convective regime leads to the highest thermal

spring temperatures, and this phenomenon is directly linked to the increase in permeability. Forster and Smith (1989) and Lopez and Smith (1995) showed that there is a favourable permeability window to maximise spring temperatures (see Figure I.13). Nevertheless, if permeability becomes too high, particularly in fault zones, a transient regime can be reached with unsteady convection. The cells then move into the permeable zone and the temperature anomalies generated are lower (Lopez and Smith, 1995; Guillou-Frottier *et al.*, 2013; Penhoët et al., 2025a). Once again, permeability appears to be the key parameter controlling fluid flow.

I.4.4 Genesis of thermal springs

Hydrothermal systems, and more specifically thermal springs, are strongly linked to crustal fault zones (Curewitz and Karson, 1997). They control the infiltration and circulation of fluids, but also their resurgence, by forming efficient drains allowing them to rise quickly without losing the heat they have acquired. Understanding the brittle structure around an emergence zone is fundamental. As mentioned above, the permeability of a fault zone depends on its dip, thickness, orientation with respect to regional constraints and also its structure (intersection, termination), making the hydrothermal deposit location dependent on these parameters (Figure I.20). The very internal structure of a fault zone shows variations in permeability. On the one hand, there are the highly argillaceous fault cores, considered impermeable, and on the other, the damage zone, whose permeability is much higher (Figure I.19). A fault zone presents an irregular alternation of these two components, resulting in a complex organisation.

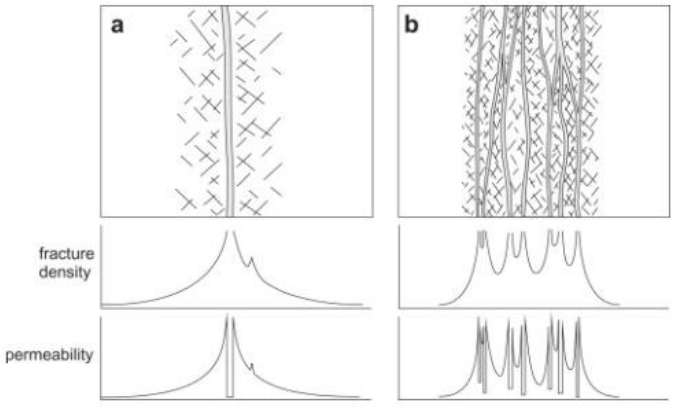

Figure I.19: (a) Structure of a fault with a single fault core, (b) structure of a fault zone with several fault cores and damage zones leading to permeability variations (Faulkner et al., 2010).

Hydrothermal systems are mainly located at the terminations of fault zones (Figure I.20a) or close to areas of interaction between several fault zones, such as intersection (Curewitz and Karson, 1997; Person *et al.*, 2012; Walter 2016; Wu *et al.*, 2023; Figure I.20c), relay (Figure I.20b) and strike-slip areas (Faulds, 2010; Figure I.20f). Permeability is a key parameter that controls hydrothermal system spatial distribution (Gleeson and Ingebritsen, 2016).

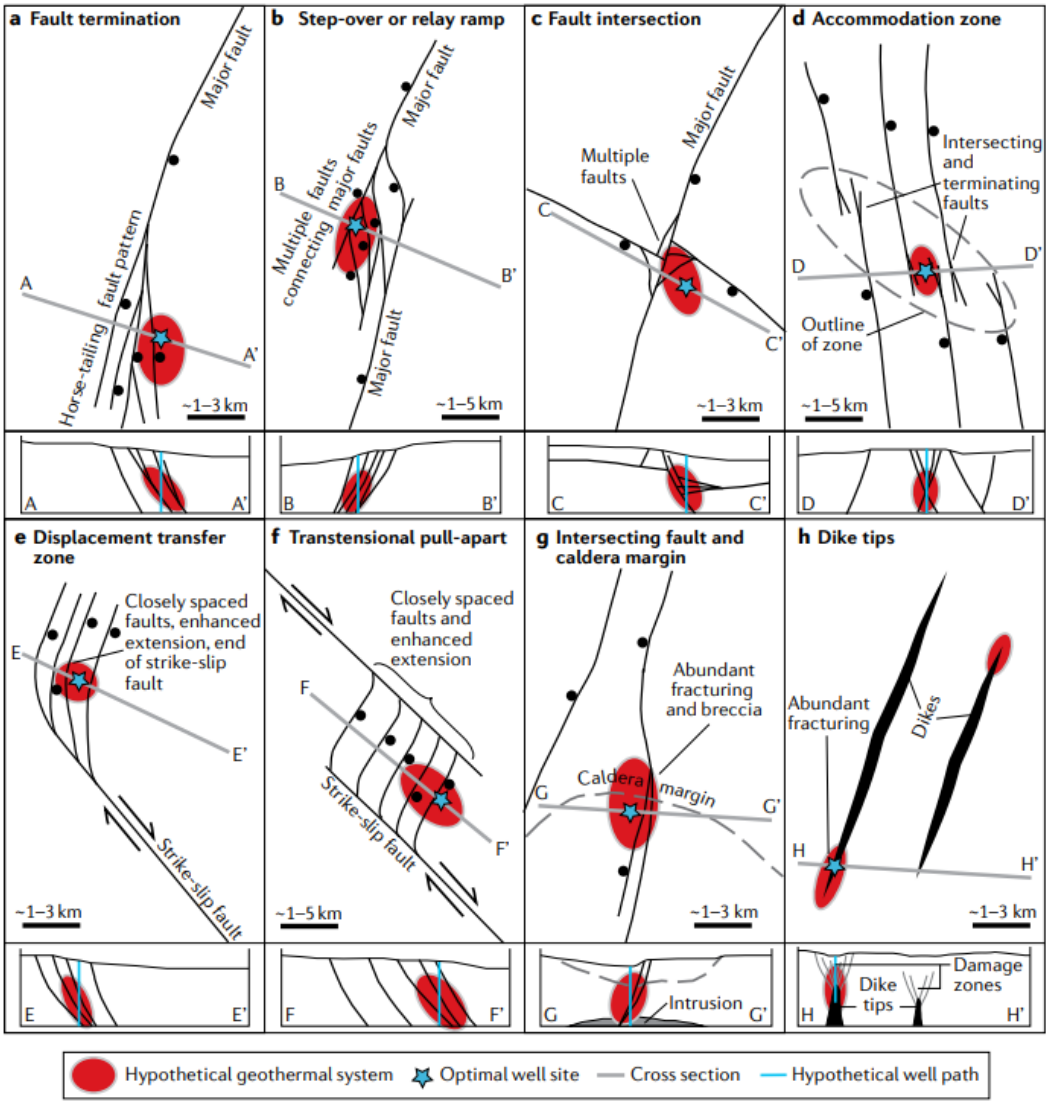

Figure I.20: Location of geothermal systems and optimal exploitation sites according to the structure of the fault zone (after Jolie et al., 2021).

In a nutshell, meteoric fluids infiltrate at the topographic high points, often characterised by strong fracturing that facilitates infiltration at depth. As the fluids flow at depth, guided by the topographic gradient and faults, they heat up thanks to the local geothermal gradient. These

hot fluids, with low density, will rise due to buoyancy forces in highly permeable areas, the fault zones again, at low altitudes. Figure I.21 summarises all these processes.

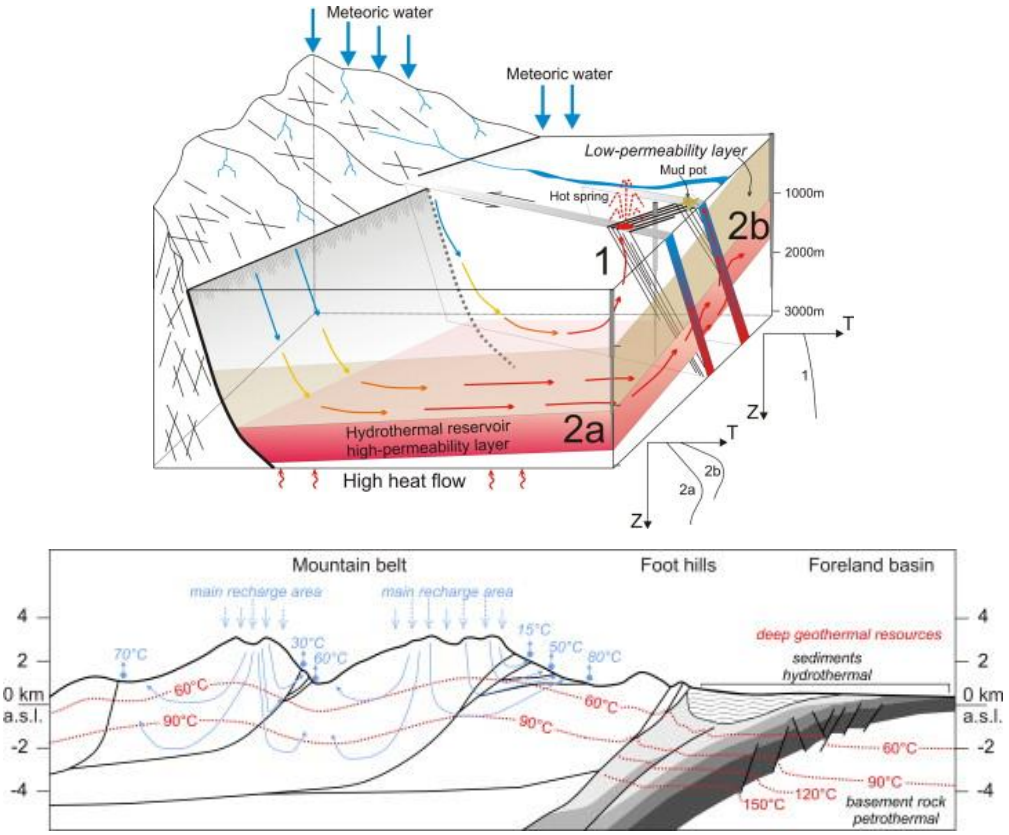

Figure I.21: Hydrothermal system in an amagmatic context (after Moeck 2014).

Having examined the main factors controlling continental hydrothermal systems in an amagmatic context, we can now apply them to a specific case. The Chaudes-Aigues area is a relevant example, where these mechanisms are particularly well illustrated: heat flow anomaly, topographic gradient, crustal fault zone, fault intersection and supergene weathering.

I.5 Presentation of the study area

I.5.1 Recent geological evolution of the Massif Central, its thermal implications

In this introduction, the Variscan history of the Massif Central will not be detailed, although it plays a fundamental role in the current structuring of the region. Indeed, the main fault orientations N030E-50 and N120-150 structuring the study area, typical of regional fracturing, originate from this ancient heritage. These aspects will be detailed in sections II and III. From a hydrothermal point of view, the key factor is the reactivation of these structures over

geological time to maintain their high permeability values. From a thermal point of view, this period provides very little information, as the hydrothermal system lifetime is limited to a few thousand years, which is negligible compared with the time scale of Variscan events.

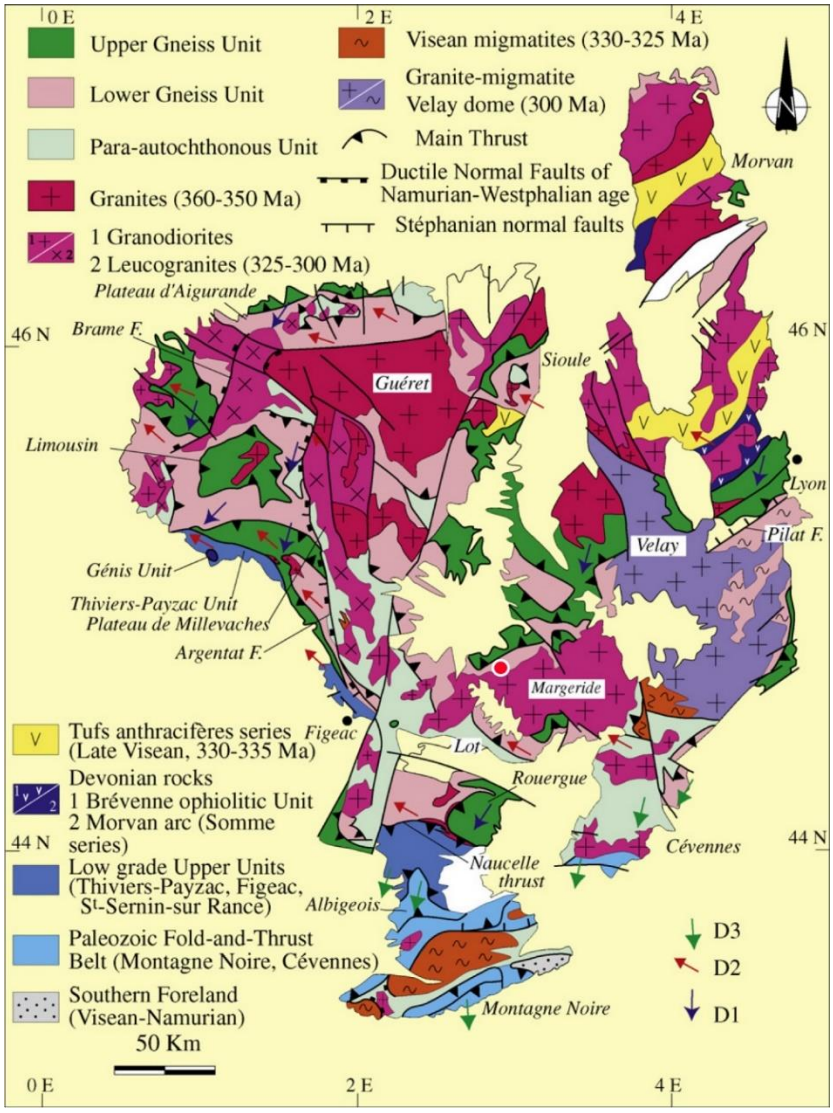

Figure I.22: Simplified structural scheme of the Massif Central (Faure et al., 2009). The red dot symbolises the location of Chaudes-Aigues.

Tertiary events are fundamental to understanding the actual thermal state of our study area. At the end of the Cretaceous and during the Palaeocene, a compressive phase led to a lithospheric bulge in Europe (Ziegler *et al.*, 2007). During the Eocene, an extensional phase developed across Europe, forming a series of sedimentary basins (European Cenozoic Rift System, Ziegler 1992). Evidence of this phase can be seen in the southern Massif Central such as the Limagne (Michon and Merle 2001; Dèzes *et al.* 2004; Merle *et al.* 2023) or the

Malzieu basin (De Goer de Herve *et al.*, 1990). The origin of this extensive phase is still discussed (Michon and Merle, 2001; Michon *et al.* 2003; Michon and Merle, 2005; Dèzes *et al.* 2004; 2005). Authors agree, however, that a mantle thermal anomaly caused crustal thinning beneath the Massif Central. Lucazeau *et al.* (1984), as an example, interpreted this as the creation of a mantle diapir, which provided an additional mantle heat flux of around 25-30 $mW.m^{-2}$. As a result, the total mantle contribution reaches 60 $mW.m^{-2}$ in the area (compared with 30 $mW.m^{-2}$ on average), leading to the anomaly described in Figure I.10).

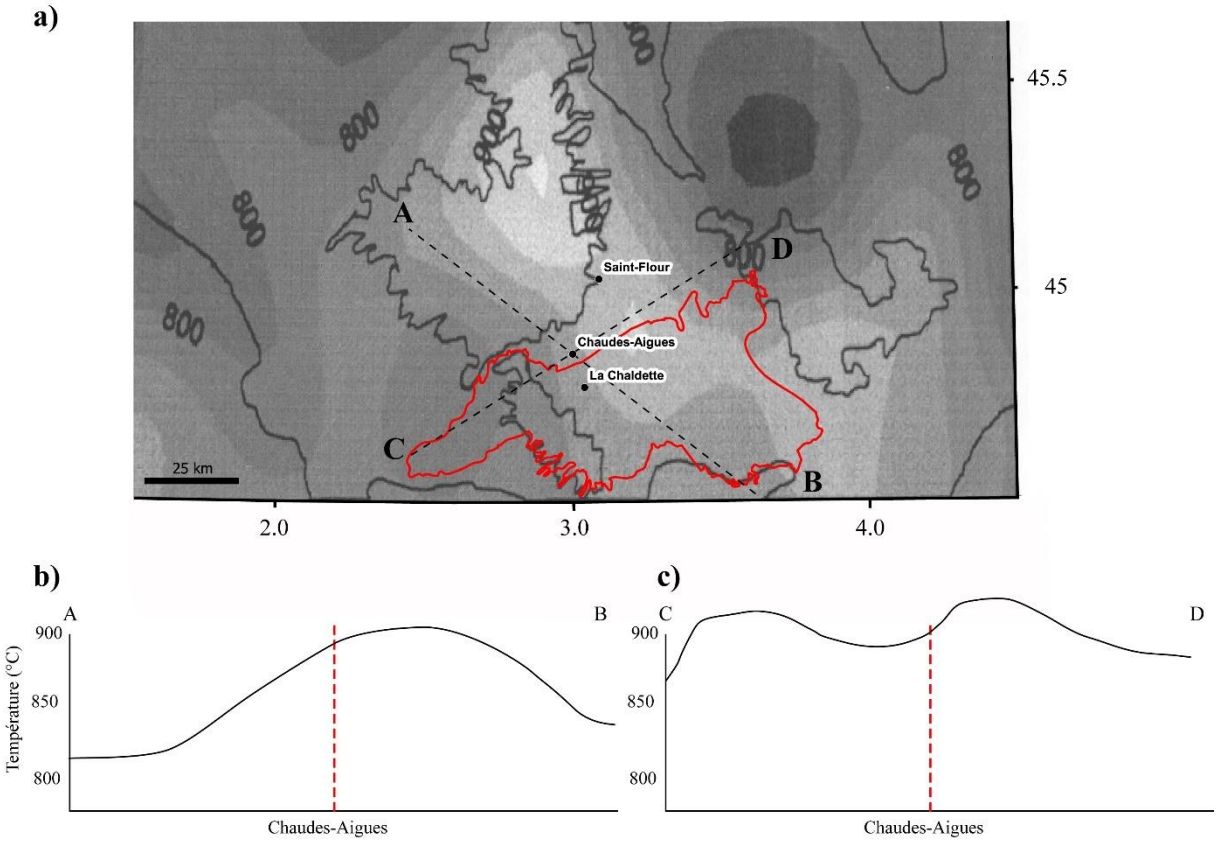

Figure I.23: (a) Temperature at 30 km depth (mean depth of the Moho), Margeride Granite boundaries are highlighted by the red outline. (b)(c) Approximate temperature evolution around Chaudes-Aigues (modified from Sobolev et al., 1997).

Nearby volcanic edifices such as the Cantal and Aubrac are fairly far from our study area, which eliminates them as potential heat sources. The Aubrac, a basaltic massif, and even the Cantal have no surficial magma chambers, and since heat propagation by conduction is slow, their potential contribution would be negligible.

I.5.2 Margeride granitic complex

Margeride granitic complex (MGC) is a massive pluton covering more than 3,200 km² across four French departments: Cantal, Lozère, Aveyron and Haute Loire, and is covered by more than 16 geological maps at 1:50,000 scale. It is one of the major plutons of the Massif Central (Figure I.22, Talbot, 2003). The Margeride Granite was emplaced during an extensive phase at the end of the Carboniferous, 323 ± 12 Ma ago, within the Lower Gneiss Unit (UIG) and Upper Gneiss Unit (USG) (Couturié 1979; Talbot et al., 2005). The main facies is composed of a porphyritic monzogranite, known for its “horse tooth” feldspar phenocrysts (Figure I.24). This facies is crossed by numerous later leucogranites and quartz veins (Talbot et al., 2005).

Figure I.24: Facies containing ‘horse-tooth’ feldspar phenocrysts in the Margeride Granite.

The MGC can be divided into several parts that are directly linked to the N150 fault beams that cross it. The emplacement model proposed by Talbot et al. (2005) indicates the existence of three main NE-SW-trending feeder zones, which first experienced an extensive phase followed by pull-apart play. N150 senestrial faults subsequently allowed them to coalesce, resulting in the formation of the pluton (Figure I.25).

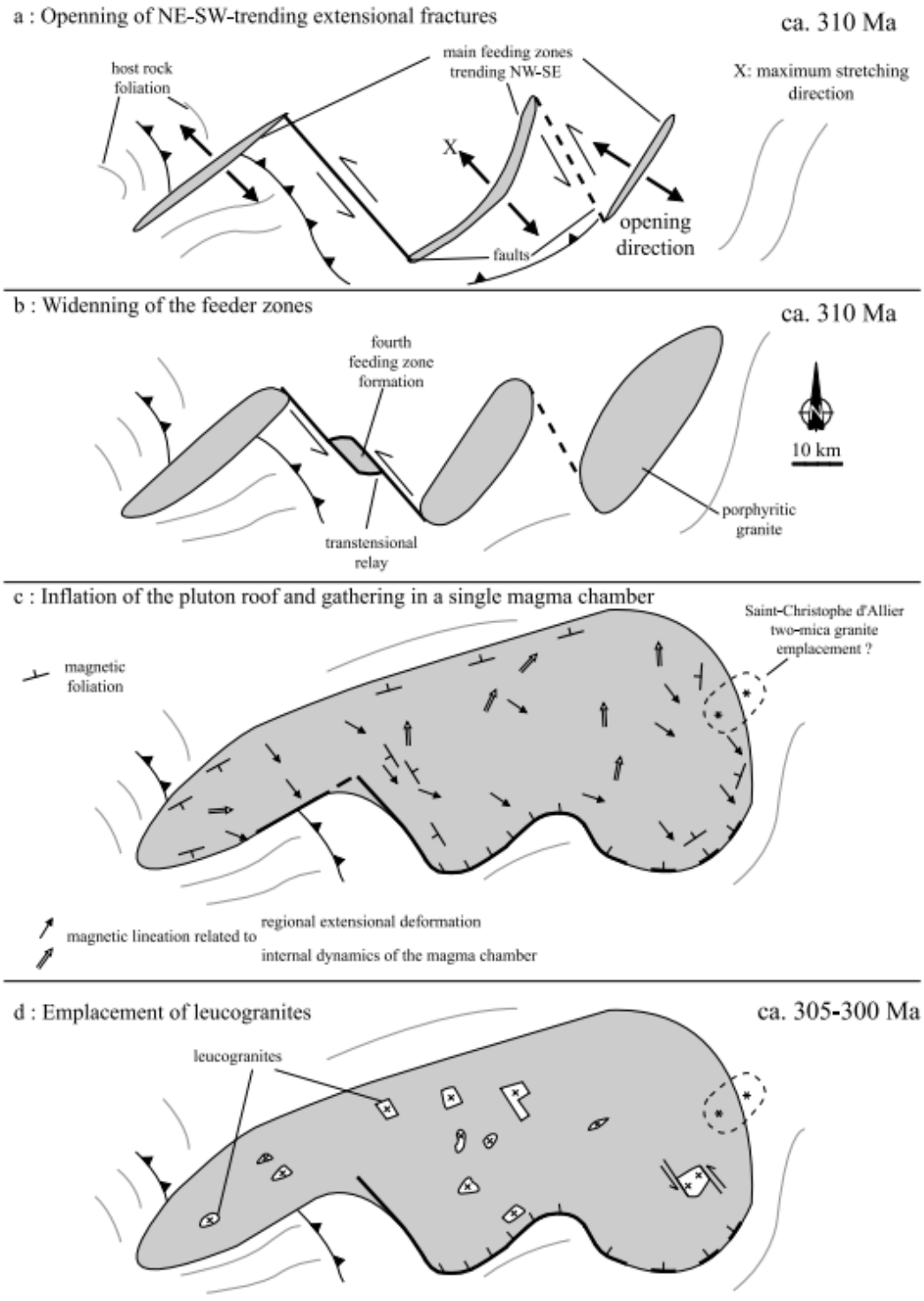

Figure I.25: Emplacement model of the MGC, showing the different feeder zones shifted by N150E fault zones (after Talbot et al., 2005).

The MGC shows several signs favourable to fluid circulation: numerous quartz, porphyrite and microgranite veins. These, together with the numerous faults, could constitute potential drains for fluids. The pluton is marked by a high fracture density, with N150E-trending faults being the most represented. Two areas appear to be particularly fractured (Figure I.26), the first close to

its north-eastern edge and corresponds to the Margeride fault. Its thickness strongly varies from a few metres at its southern end to a fault zone more than 2.5 km thick at Saint-Flour (De Goer de Herve et al., 1990). Further west, to the south of Chaudes-Aigues, a new N150E fault zone can be identified. This one is 2.5 km thick and crosses the granite in its entirety (Burg and de Goer de Herve, 1991). Its northern termination is marked by an intersection with two other Variscan fault zones, the first and main one oriented N030E-50 and the second N0.

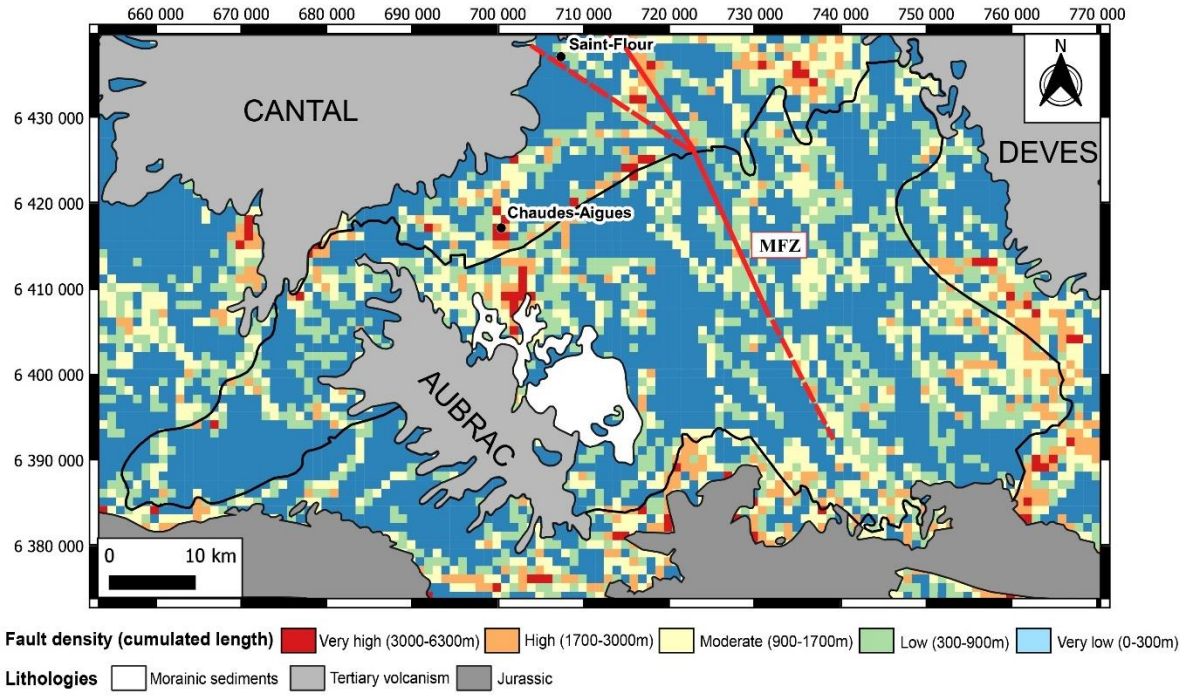

Figure I.26: Fault density map of the MGC (Penhoët et al., 2024), the two fault zones of Malzieu-Saint Flour and Chaudes-Aigues are easily identified by their high density.

These fault zones are ideal for the circulation of fluids, as evidenced by the reactivation of N140-150 oriented faults in the Cenozoic, which led to the upwelling of basalts (Figure I.26) forming the Aubrac massif (De Goer de Herve et al., 1994) and the Julianges plateau (Couturié, 1972). In addition, to the east, the small sedimentary basins of Le Malzieu, Saint-Alban-sur-Limagnole and Saint-Flour demonstrate the reactivation of these faults (Penhoët et al., 2025a).

I.5.3 Chaudes-Aigues, true to its name

Figure I.27: Chaudes-Aigues, Cantal (15), France. Several structures are heated by the thermal waters, including the church in the centre, the swimming pool in the foreground and the secondary school on the right of the picture.

Located in the south of the French Massif Central, in the Cantal département (15), Chaudes-Aigues (Figure I.27) owes its distinction to a unique feature: its 32 thermal springs, which are among the hottest in Europe. This hydrogeological characteristic shaped the history and development of the town, making Chaudes-Aigues a pioneering example of the use of natural hot springs for therapeutic purposes, but above all for geothermal purposes. The town's very urban planning has been organised around this resource, with houses built directly on the springs to directly exploit their heat and ensure natural thermal comfort throughout the year. In addition, as mentioned above, a heating network using spring water was set up as early as 1332, making Chaudes-Aigues the first town in the world to use this technology. This ingenious system used wooden pipes (fir trees) sealed together with clay to spread hot water from the springs to the houses, heating homes and other buildings such as the church.

Far from the social effervescence of Vichy, Chaudes-Aigues is known as a more discreet spa. Its geographical isolation may have limited its expansion over time. Nevertheless, the town still

preserves a strong identity linked to its exceptional heritage: the pioneering use of geothermal energy. Their attachment to the thermal springs can still be seen today on their coat of arms, which can be seen in several places around the town (Figure I.28).

Today, as renewable energies develop, the town may be regaining interest. In order to heat as many public buildings as possible, the town is looking to optimise the circulation of hot water.

Figure I.28: « D'azur à la montagne d'or mouvant d'un bouillon d'eaux fumantes d'argent, trois jets de vapeur du même issant de ladite montagne, surmontée de deux fleurs de lys d'or rangées en chef" (Charles d'Hozier, 1696), The Chaudes-Aigues coat of arms can be seen on the front of the 'Gourmet & Glouton' restaurant and in the courtyard of the Geothermia museum.

The 32 springs at Chaudes-Aigues (Figure I.29) have temperatures ranging from 50 to 82°C. In addition to its high temperature, the Par Spring, said to be the hottest in Europe, has a constant flow rate throughout the year of 250 $L.min^{-1}$ (Vasseur et al., 1997). The total flow from all the springs is 500 $L.min^{-1}$ (Vasseur et al., 1997). There are two groups of springs. The first, on the left bank of the Remontalou and in the heart of the village, is the Par group, made up of around twenty springs (the number is difficult to determine precisely because the springs have been taken over by the residents). On the right bank, further south, is the Ban group, with 7 springs and a borehole supplying the spa (Bérard et al., 2002).

Further south, 10km away, the Chaldette thermal spring (Figure I.30a) used to be collected from the old-village washhouse. Nowadays, the thermal baths collect hot water (35°C) directly from a 65 m deep inclined borehole (Figure I.29).

Figure I.29: Some springs in Chaudes-Aigues: (a) The Par spring 82 °C, Le Lavoir 57 °C, La Bonde du moulin 50 °C, Boucharinc 65 °C with its heat exchanger and the La Chaldette borehole (red dot) 35 °C.

The springs are located in an incised valley carved out by the Remontalou river, at 750 m a.s.l, and are surrounded by a number of topographic high points. To the north, the volcanic edifice of the Cantal (1,800 m a.s.l.), to the south-west the Aubrac plateau (1,470 m a.s.l.), to the east the Margeride Mounts (1,550 m a.s.l.) and to the south the southern edge of the Granite (1,500 m a.s.l.). As these peaks are relatively far from the town (35km, 30km, 40km and 30km respectively), the topographic gradient is low.

The Chaudes-Aigues emergence zone is located in the lower gneiss unit at the end of a thick N150E fault zone containing the La Chaldette spring. The immediate vicinity of the springs is marked by the intersection of three Variscan fault bundles (Figure I.28b, N0E, N030E-050E, N120E-150E), marked by numerous mineralisations and microgranite veins (Figure I.30a and b, Gibert et al., 1975; De Goer de Herve et al., 1990). These traces of past fluid circulation, without any reactivation, may now inhibit fluid flow.

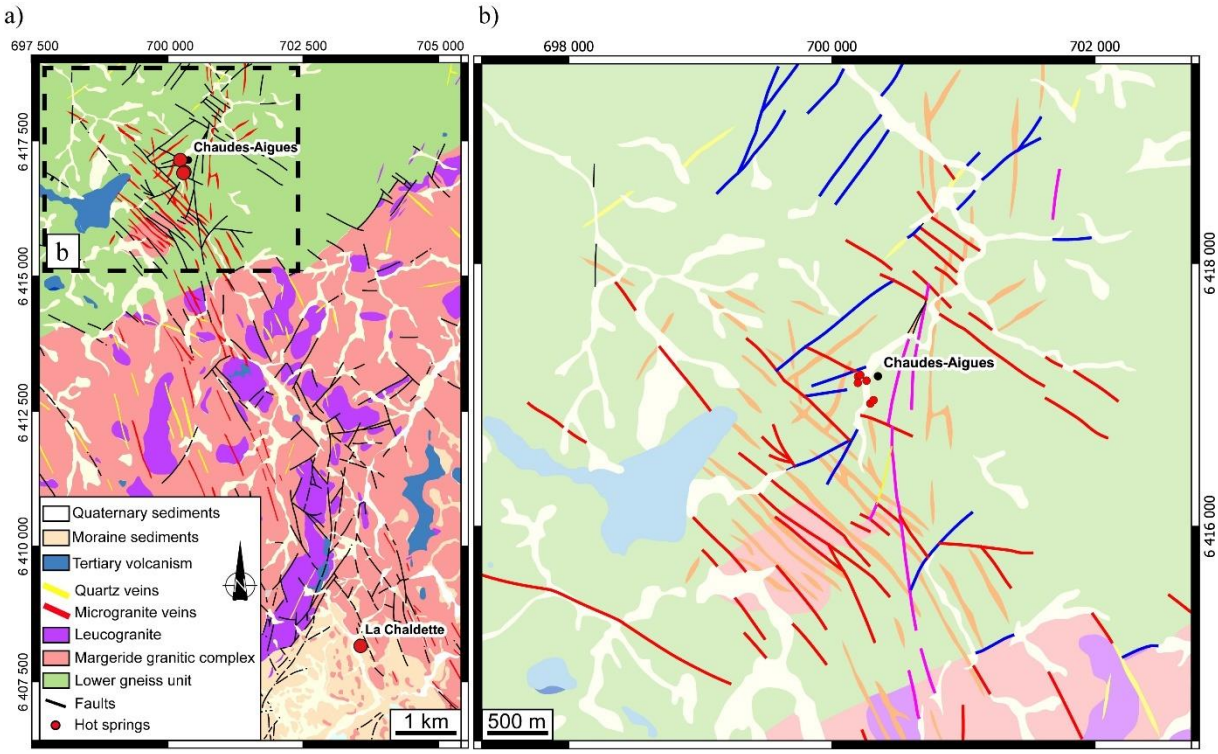

Figure I.30: (a) Location of the Chaudes-Aigues and La Chaldette thermal springs, (b) Zoom in on the main emergence area, highlighting the main fault zones: N00E in magenta, N030E-50E in blue and N120E-150E in red.

Since 1906, several authors hypothesized about the origin of the springs and the hydrothermal system functioning. De Launay (1906) first hypothesis, put forward in 1906 (Figure I.31a),

suggests that the water comes from the town immediate surroundings, i.e. from the metamorphic rocks. The 300 m difference in altitude is thought to be the driving force behind the flow. Thanks to the joints in the gneisses, the water would infiltrate to a depth of 2,500 m to reach a reservoir located beneath the town. The microgranite veins, although separate at the surface, would join at depth to form a single conduit.

Then, Aubignat (1949) (Figure I.29b) specified that the springs originated in the Pliocene and added that the structure of the Cantal volcano was conducive to the fast infiltration of water at depth. The heat source would come from deep volcanic material. In 1973, Henou (Figure I.31c) indicated that the reservoir was located at 2000 m depth. The drains of the system would once again be the microgranite veins.

Cailleaux et al. (1976) then Fouillac and Michard (1981) focused mainly on the water chemical composition. They demonstrated that the water in the Chaudes-Aigues springs was the result of a mixture of a deep hot endmember and cold meteoric water. The authors agree on a reservoir temperature of 175 to 200°C.

Vasseur et al. (1997) completed previous work with geology, geophysics and simplified analytical modelling to propose a first complete functional model of the hydrothermal system involving two parallel circulations (Figure I.31d). The microgranite veins would be the ascending drains allowing the water to rise. The MGC to the south of Chaudes-Aigues, due to its altimetry, fracturing and physical continuity, would constitute the main impluvium zone.

The shallow circuit would drain cold surface water, infiltrating both from the volcanic Aubrac massif and from the Margeride Mounts. These waters would reach 2,000 m depth before reaching Chaudes-Aigues.

The second circuit would follow the first, but this time at a depth of 5,000 m to reach an initial deep reservoir. Its temperature would be between 180 and 200°C. This water would mix with the first in an intermediate reservoir at a depth of 2,000 m, corresponding to a mixing zone. Mixing proportions would be 40% deep endmember and 60% surface water.

However, there are still a number of uncertainties to be clarified, such as the location of the impluvium zone, the deep reservoir and the deep-water pathways. The origin of the volumes of water flowing into the city also remains undetermined. Vasseur et al. (1997) suggest that the Würm glaciers were responsible for the high flow rates from the springs. This hypothesis needs to be confirmed, and so the transfer time of the water within the system. In addition, the La Chaldette thermal spring has not been included in the model.

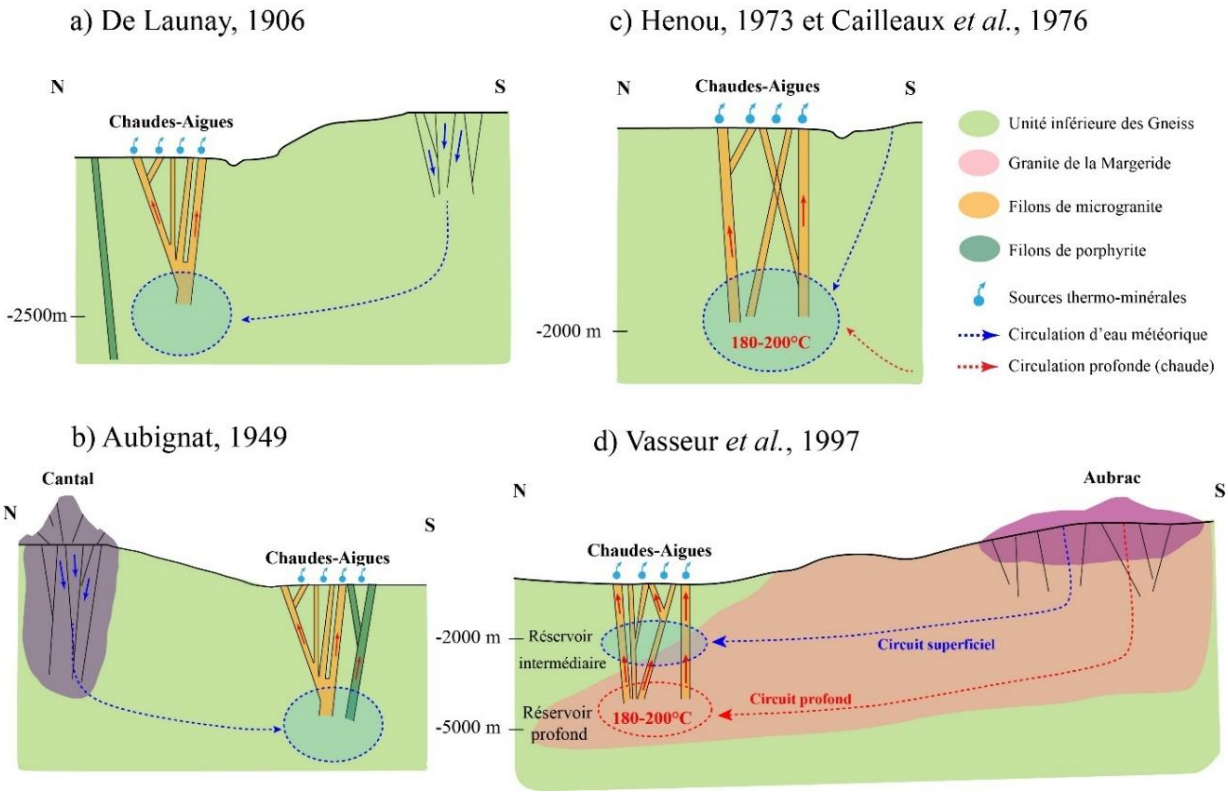

Figure I.31: Summary of the different theories proposed since 1906 (Penhoët et al., 2024).

I.6 Objectives et methods

The study of this hydrothermal system is aimed at identifying new targets for high-temperature geothermal exploration. Here, the key is to determine the controlling factors that determine the functioning of hydrothermal systems in a fractured basement area. To this end, the following questions will need to be answered:

- Where is the impluvium of the Chaudes-Aigues thermal springs located? Which structures allow the water to infiltrate deeply? How and where do the fluids accumulate?

- Which structures ensure the fast ascent of fluids to the surface? How do fault zones interact with each other? Are there barriers to fluid flow?
- What is the heat source that explains thermal springs and their temperatures?
- What factors influence the location of hot springs?
- Is the system controlled by topography?
- Why are there 30 thermal springs in the town?
- Does the thermal spring La Chaldette, 10 km further south, belong to the same system? Are there several reservoirs?

In order to characterise this complex system, we rely on various complementary approaches. The integration of several disciplines is essential to understand the mechanisms controlling fluid circulation as a whole. Structural geology is used to identify and understand the brittle structure of the system (main faults, secondary faults, tectonic heritage, permeability of structures). Water geochemistry characterises the reservoir by providing information on water origin, temperature and fluid residence time. Geophysical methods (gravimetry) provide imagery of deep structures and enable certain reservoir properties to be estimated. Finally, hydrogeology is fundamental to understanding recharge, flows and interactions between different lithologies. This field data will be used to feed thermal-hydraulic numerical models by constraining the key reservoir parameters (permeability, major structures), in order to propose a robust conceptual model of the Chaudes-Aigues hydrothermal system.

This study aims to better understand the Chaudes-Aigues hydrothermal system using a multidisciplinary approach that combines structural geology, geophysics, geochemistry, and numerical modeling.

First, Chapter II examines the geometry of fault zones and its impact on fluid circulation. This investigation focuses on the two major fault zones of the MGC: the Chaudes-Aigues intersection zone and the Margeride Fault Zone. These two geometrical configurations are used to study the influence of fault zone thickness and fault intersections on fluid flow. Chapter

III focuses on characterizing the upwelling drains used by thermal waters. An analysis of fracturing at both regional and local scales is carried out to identify the main fault families and reconstruct their evolution through geological time. Chapter IV aims to characterize the geochemistry of thermal waters. Based on major elements and isotopic data, this aim is to determine the origin of the waters, their infiltration zone, as well as the nature and temperature of the deep reservoir. It also provides a first estimate of the system residence time. The impact of the granitic weathering profile (regolith) on both fluid flow and thermal regime is then explored. The alteration of the MGC is first characterized and then analysed using numerical modeling to assess its potential influence on hydrothermal system behaviour (Chapter V). Chapter VI integrates the findings from the previous chapters into 3D thermo-hydraulic models of the hydrothermal system. Numerical modeling is used to replicate Chaudes-Aigues thermal springs and to analyse the influence of key parameters such as topography and the presence of a deep, high-temperature reservoir. Finally, a general discussion will take place regarding the limitations of the applied methodology. Then, more broadly, how this study can pave the way for new a new geothermal exploration.

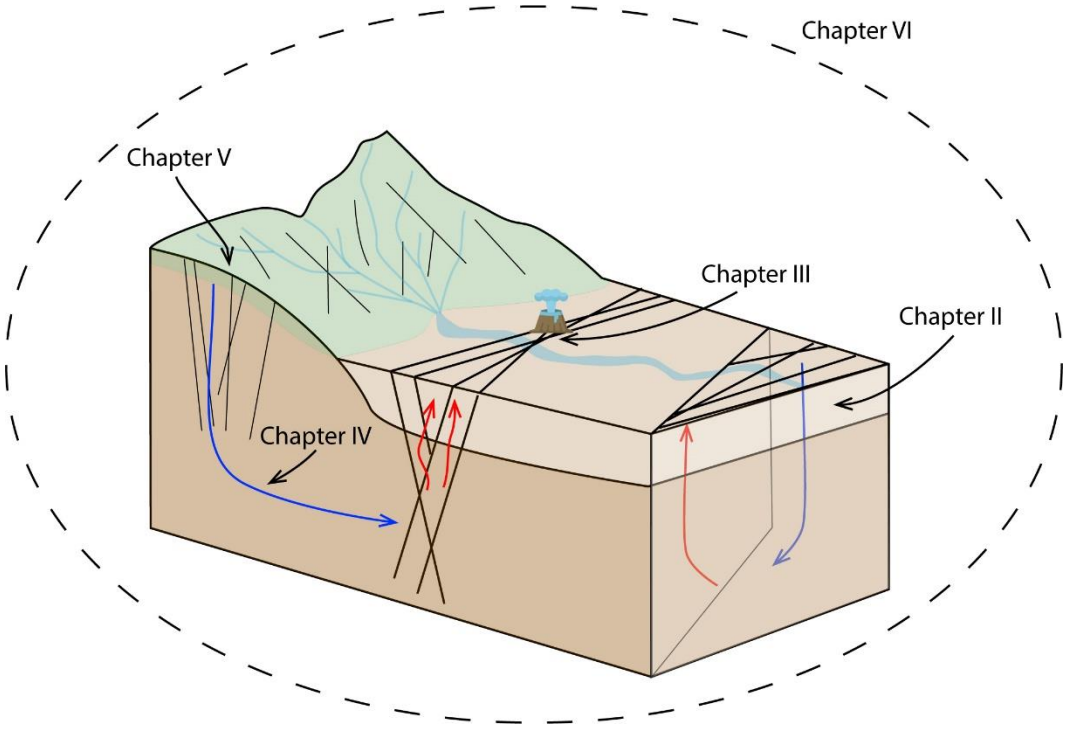

Figure I.32: Illustration of the relationship between the chapters of the manuscript.

Chapter II: Fault zone geometry, a key parameter controlling fluid flow: study of thickness and an intersection zone.

II. Fault zone geometry, a key parameter controlling fluid flow: study of thickness and an intersection zone.

II.1 Introduction

The Margeride Granitic Complex (MGC) presents two crustal fault zones with unique geometric features (Figure II.2). Geometry parameters controlling the fault zone permeability and thus possible thermal anomalies have already been identified such as their dip (Duwiquet et al., 2021) or orientation in relation to regional constraints (Barton et al. 1995; Mckenna and Blackwell 2004; Faulds et al. 2010; Haines et al. 2016, Duwiquet et al., 2022). As well as the intrinsic geometry of the fault zones, the interactions between them are also important. The location of a hydrothermal system depends directly on the geometric relationships between different fault zones (Faulds et al., 2010; Jolie et al., 2021, see Chapter 1 Figure I.20). The two zones studied in this chapter provide an opportunity to determine the impact of new parameters such as thickness and the intersection between two fault zones.

First, Chaudes-Aigues thermal springs are located in the basement made of metamorphic units close to the northern edge of the MGC (Figure II.2b). On a regional scale, the area is characterized by a very high fracturing density (Penhoët et al., 2025a, their Figure 18). The emergence area is located at the intersection of three, including two main fault zones forming a complex Y-shaped structure. The first fault zone, N140E, characterized by the presence of another thermal spring (La Chaldette, 35°C), is more than 2.5 km thick and 10 km long. The second, oriented N50, is relatively thinner (1.5 km) but is highly pronounced in the topography, as evidenced by the orientation of the valley. The river, the Remontalou, is deviated from its initial orientation (N150E) by these faults (Figure II.1b). These Variscan directions have been reactivated many times since the Paleozoic to the present day (Penhoët et al., 2025a). The third trend, which is less significant than the previous ones, corresponds to several faults and fractures oriented N00E.

Then, located 25 km east from Chaudes-Aigues, the Margeride Fault Zone (MFZ) thickness lengthwise direction varies significantly, from 50 m in the south to over 2 500 m in the north

(Saint-Flour, Figure II.2c). It is one of the main fault zones intersecting the Margeride Granitic Complex (MGC) with the Chaudes-Aigues-La Chaldette one. In the case of the MFZ, the only surface indicator is the Coren-Les-Eaux Spring (10 km north of Saint-Flour), where geochemical studies indicate a deep reservoir reaching 220°C (Fouillac, 1983). Consequently, it might be possible that this thickest part of the fault zone could host a potential «hidden» thermal anomaly.

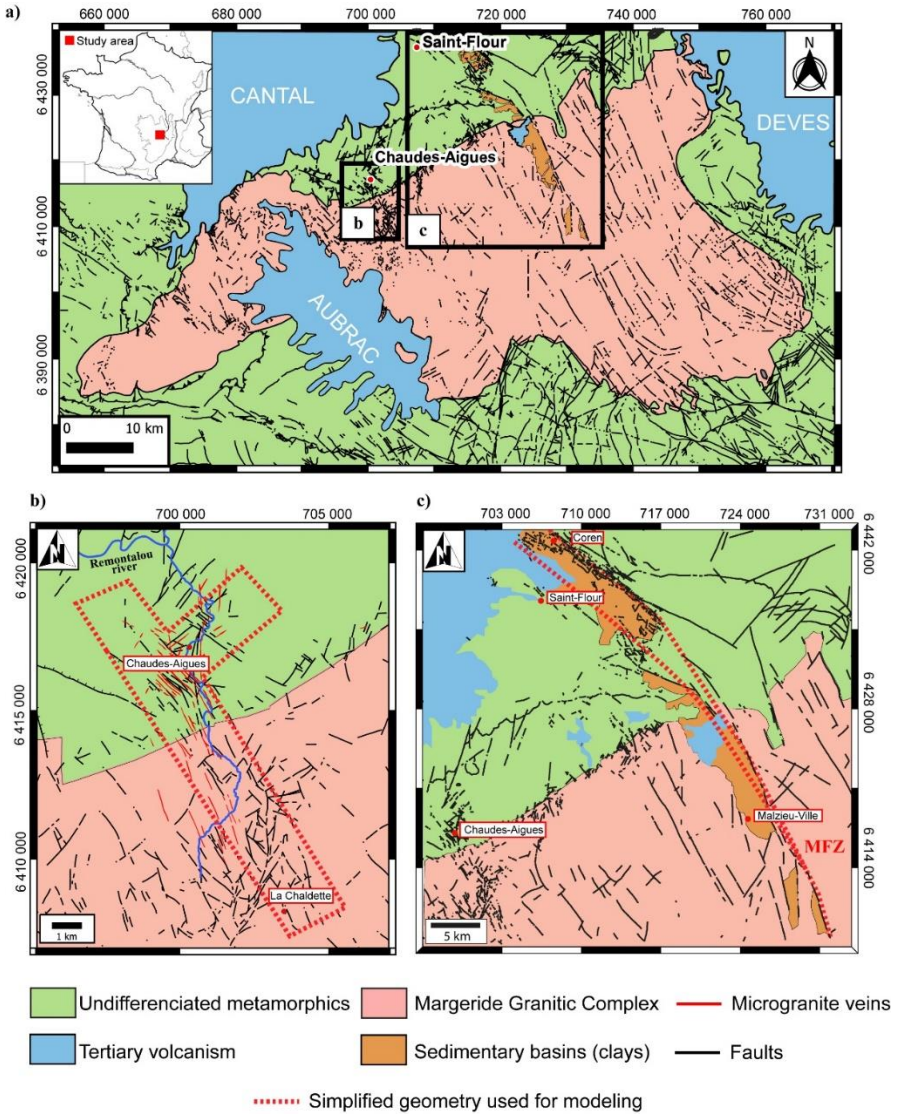

Figure II.1: (a) Location of the MGC and the two main fault zones: (b) the Chaudes-Aigues intersection zone and (c) the variation in thickness of the MFZ.

The aim here is to use Chaudes-Aigues intersection and the MFZ as demonstrators to quantify the impact of a varying fault zone geometry on fluid flow, thickness in the first case and intersection for the second. In these two studied areas, structural data were acquired in the

field to identify the main fault families and their evolution over time to identify potential reactivations. These field observations were also used to determine the precise maximum thickness of the MFZ. Then, 3D numerical models were used to quantify the impact of these geometries on fluid flow. Equations and procedure are common for all the models (Chapter 2, 4 and 5), and detailed in Appendix C and following articles.

II.2 Contribution of this chapter

The intersection parametric study reveals that all fault configurations generate positive surface temperature anomalies, favouring thermal spring formation. Simple fault zones produce hotter springs but with low flow rates, even for high permeability values. In contrast, intersecting faults, especially with small angles, result in higher flows (up to 40 l/s at 30°), due to increased infiltration volume, but yield cooler surface temperatures. Furthermore, thermal convection sets in more easily in intersections, occurring at lower permeabilities, unlike simple faults. Applied to Chaudes-Aigues, the simplified Y-shaped model reproduces the spring location but underestimates both temperature and flow rate. Indeed, effects of topography-driven flow or mechanical-induced flow, which are not taken into account, may play an important role (Taillefer et al 2018; Duwiquet et al 2024).

Using the MFZ, it has been possible to study several processes with a direct impact on fluid flow. In particular, the interactions between the thickness of a fault zone, fluid circulation and the convective regime have been quantified. In fact, this study showed that thin fault zones are more likely to produce multiple low anomalies at shallow depths. Very thick fault zones behave in the opposite way, producing a single positive temperature anomaly of greater magnitude at greater depths. The thermal regime of the fault zone is directly affected by the variation in thickness. The greater the thickness, the greater the range of stable convection (single, strong temperature anomaly). In addition to permeability, the thickness of the fault zone therefore appears to be a key parameter to be taken into account. Finally, fault zones with a geometry similar to the Margeride fault (longitudinal variation in thickness) seem to always have a positive temperature anomaly at the thickest end.

These initial results are limited but confirm that the geometry of a fault zone is a key parameter with a strong impact on fluid flow. These studies could have identified two areas of high geothermal potential. First, the Chaudes-Aigues area with a lot of surface indicators (hot springs), may host a shallow positive thermal anomaly. Then, the MFZ could host a positive temperature anomaly at its northern end, as suggested by the Coren source. However, these data still need to be supplemented by more realistic numerical models that include current regional constraints, especially as the MFZ is changing orientation. Topography should also be incorporated into the models. A more detailed structural study would also be required to identify potential past fluid circulation.

II.3 Fault Zones Intersections and High-Temperature Geothermal Exploration: 3D Modeling of the Chaudes-Aigues Area (French Massif Central) (Extended Abstract EGC 2025)

Fault Zones Intersections and High-Temperature Geothermal Exploration: 3D Modeling of the Chaudes-Aigues Area (French Massif Central)

Emmy Penhoët,[1,2] Laurent Guillou-Frottier,[1,2] Laurent Arbaret,[2] Charles Gumiaux[2]

[1]BRGM, Georesources Division, Orléans, France
[2]ISTO, UMR 7327, University of Orléans, CNRS, BRGM, Orléans, France
Corresponding author: e.penhoet@brgm.fr

Extended abstract to be presented at the European Geothermal Congress, Zurich, Switzerland, 8-10 October 2025.

Keywords: Fault zone, intersection, hot springs, numerical modeling, geothermal energy.

Abstract

This study investigates the role of fault zone intersections in enhancing geothermal potential, focusing on the Chaudes-Aigues hydrothermal system in the French Massif Central. Located at the intersection of major Variscan fault zones, the site hosts over 30 hot springs, including the Par Spring (82 °C). Despite the low natural permeability of crystalline rocks, intersecting fault zones are thought to significantly increase fluid flow and heat transport. To assess this, we conducted a series of 3D numerical models simulating different fault zone configurations (single fault zone, X-shaped, and Y-shaped geometries), varying intersection angles and permeability values. Results reveal that fault intersections facilitate thermal convection at lower permeabilities than single fault zones. X-shaped and Y-shaped configurations enhance flow compared to isolated fault zones, although they may lead to cooler surface temperatures at the extremities due to dominant cold inflows at higher permeabilities at the intersection. Back to the Chaudes-Aigues case, the Y-shaped model explains the spring emergence location but underestimates surface temperatures and flow rates. Our findings highlight the structural influence of fault intersections on geothermal systems and offer new insights for targeting high-temperature resources in amagmatic, crystalline settings.

Introduction

Currently, French geothermal power plants are limited to tectonically active areas such as the Rhine graben (Soultz-sous-Forêts) or magmatic zones (Bouillante, French West Indies). In order to increase the number of new geothermal resources (heat or power), geothermal exploration must move towards other geological contexts, such as basement areas. However, direct exploitation remains complex because of low porosity and permeability values (Achtziger-Zupancic 2017).

Fault zones are known to increase permeability locally, and their effects on fluid circulation and temperature anomalies have been documented (Forster and Smith, 1989; Barton et al. 1995; Faulds et al. 2010; Guillou-Frottier et al., 2020; Duwiquet et al., 2021; Penhoët et al., 2025a). Few studies exist on fluid circulation at the intersection of faults (Person et al., 2012; Patterson et al., 2018), even though these are shown to increase permeability and concentrate fluid flow (Curewitz and Karson, 1997; Craw 2000; Micklethwaite and Cox, 2006; Bense et al., 2013). Contrary to the Person et al. (2012) study where faults are 10-20 m wide, we studied the intersection of “fault zones”, which differ from “faults” by their large width (several hundreds of meters,).

To enhance the understanding of the geothermal potential of these unusually permeable targets, our study will concentrate on the Chaudes-Aigues hydrothermal system. Located at the intersection of 2 major Variscan fault zones as illustrated by dashed black lines in Figure II.2b, the town is known for hosting 30 hot springs (e.g. the Par Spring, with an emerging fluid temperature of 82°C, Figure II.2a) that would be supplied by a deep reservoir whose temperature would reach over 190°C (Fouillac, 1983; Vasseur et al., 1997). Spring temperatures range from 50 to 82°C, with a total flow rate of 500 l/min (8 l/s), constant throughout the year. This configuration provides a demonstrator for understanding the impact of fault zone intersection on fluid circulation and the hydrothermal system. Our study aims to determine whether the structural particularity of the emergence area could explain the temperatures and flow rates of the springs.

Geological setting

The Chaudes-Aigues thermal springs are located in the basement made of metamorphic units (Vanderhaeghe et al., 2020) close to the northern edge of the Margeride Granite emplaced 323 Ma

ago by NW-SE faults (playing the role of feeder zone, Talbot et al., 2005). On a regional scale, the area is characterized by a very high fracturing density (Penhoët et al., 2025a). The emergence area is located at the intersection of 3, including 2 main fault zones forming a complex Y-shaped structure. The first fault zone, N140, characterized by the presence of another thermal spring (La Chaldette, 35°C), is more than 2.5 km thick and 10 km long. The second, oriented N50, is relatively thinner (1.5 km) but is highly pronounced in the topography, as evidenced by the orientation of the valley. The river, the Remontalou, is deviated from its initial orientation (N150E) by these faults. These Variscan directions have been reactivated many times since the Paleozoic to the present day (Penhoët et al., 2025a). The third trend, which is less significant than the previous ones, corresponds to several faults and fractures oriented N0. These trends are even more visible due to the numerous microgranite and quartz veins present in the study area (red segments in Figure II.2). These fault zones have been reactivated several times over geological time (De Goer de Herve et al., 1990; Faure 1995; Penhoët et al., 2025a).

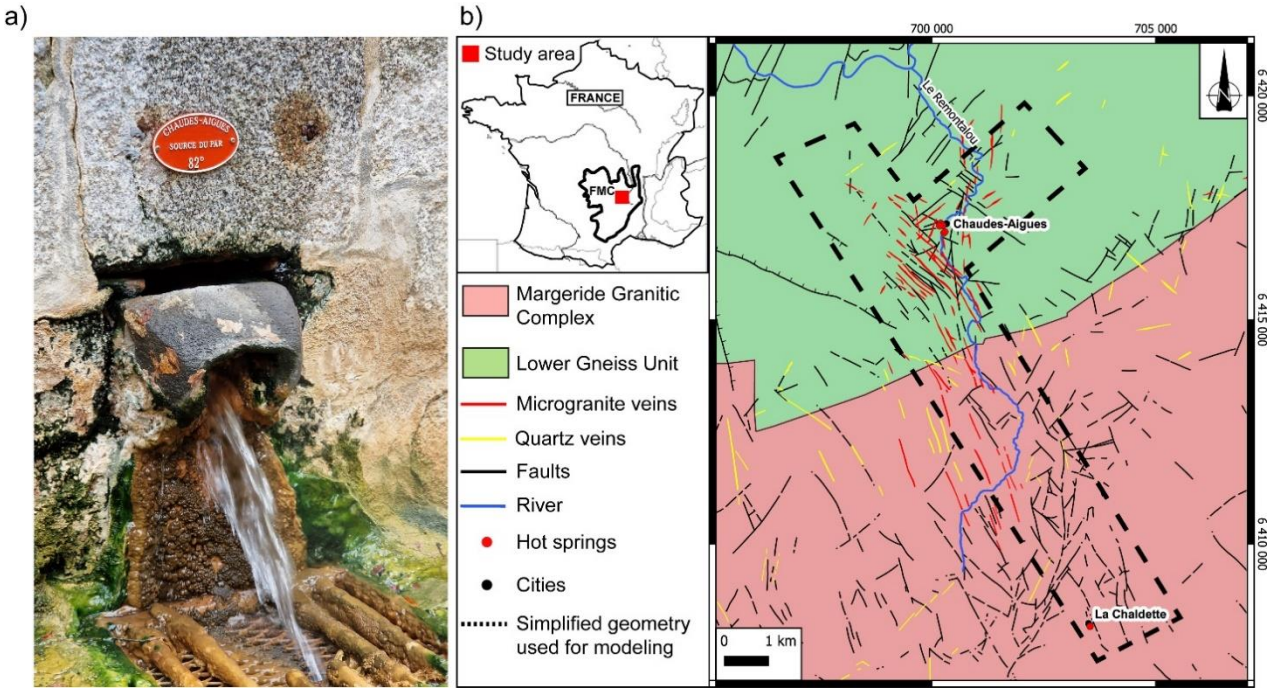

Figure II.2: (a) The Par Spring (82°C), one of the hottest in Europe. (b) Location of the study area simplified geological map. The geometry used for models is highlighted by the black dotted lines.

Methods

Chaudes-Aigues corresponds to a sector with a possible high geothermal potential. As demonstrated in previous studies, the geometry of the fault zone, more specifically its thickness over height ratio, directly influences the setting up of thermal convection (Malkovsky and Magri 2016, Duwiquet et al., 2024; Penhoët et al., 2025a).

This site will be used for parametric studies. Using Comsol Multiphysics, Darcy law was coupled with heat transfer equation and mass conservation as in Guillou-Frottier et al. (2013).

Meshing and geometry

The first series of models corresponds to a single fault, 15 km long, 1 km wide and 5 km thick, zone with no intersection (Figure II.3a). Dimensions are the same for all configurations. Next, X-shaped models (Figure II.3b) were made to represent an intersection. The angle between the two fault zones forming the X is variable (Figure II.3b). Finally, the specific case of Chaudes-Aigues is illustrated by a Y-shaped model with a 90° angle between the two fault zones (Figure II.3c).

For parametric study, a simplified parallelepidic geometry is chosen for the fault zone and the basement. The size of mesh elements is based on permeability value. In areas of low permeability (host rocks), the mesh element size is coarse but extremely fine in the fault zone (high permeability) (Figure II.3).

Boundary conditions

For all models, a mixed thermal condition is imposed at the surface of the fault zone (single, X or Y) to reproduce potential thermal variations corresponding to hot springs (Magri et al., 2015; Taillefer et al., 2018, 2024). It is given by:

$$Q = h\,(T_0 - T) \quad (1)$$

where Q is the surface heat flow, h a heat transfer coefficient and T_0 the fixed temperature at the surface, away from the fault zones. The value h (heat transfer coefficient), controlling this equation, is supposed to reproduce (i) a surface heat flux of 100 mW/m² under conductive conditions and (ii) a temperature that could reach ~80 °C at the spring emergence. Outside

the fault zones, a surface temperature of T_0 of 10°C is applied. The basal heat flux is imposed at 85 mW/m² and bulk heat production is imposed at 3 mW/m^3 to reach the measured surface heat flow of 100 mW/m² in the French Massif Central (Lucazeau et al., 1984). The surface pressure is equivalent to the atmospheric pressure (10^5 Pa), and its value increases gradually with depth. A no flow condition was imposed on the lateral sides and bottom of the model. Lateral boundaries are thermally insulating.

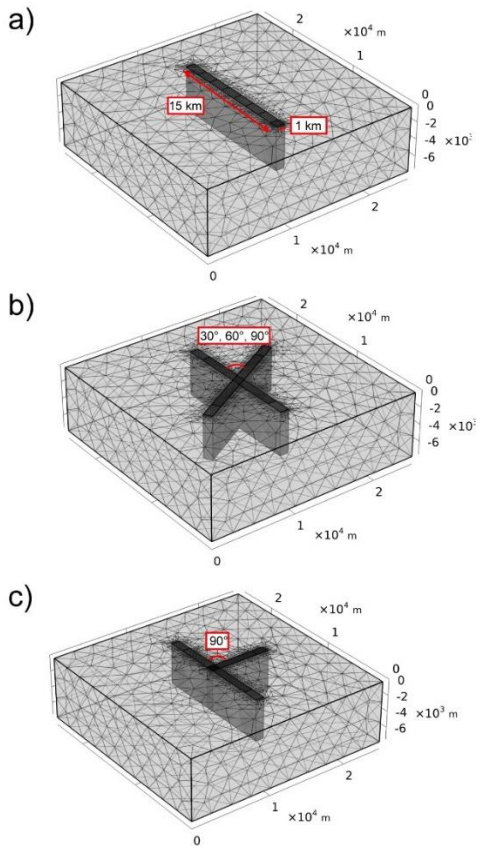

Figure II.3: Geometries and meshes used for the numerical models: (a) simple fault zone, (b) variable-angle X intersection, (c) Y intersection the case of Chaudes-Aigues.

Physical properties

Fluid dynamic viscosity is a function of temperature following the equation of Smith and Chapman (1983) or Rabinowicz et al. (1998). The density of water is also a function of pressure and temperature (Guillou-Frottier et al., 2020). The main unknown in our models remains the permeability. The Margeride Granitic Complex is considered (without fracturing) as impermeable (10^{-18} m²).In the natural environment, however, the permeability of fractured rock can reach values of the order of 10^{-13} m² (Brace 1984; Evans et al. 1997; Sonney and Vuataz

2009; Ranjram et al. 2015; Walter 2016; Achtziger-Zupancic et al. 2016 & 2017; Neuzil 2019), so the value assigned to the fault zone will vary. With depth, the increase in pressure tends to seal the fractures, and a decrease in permeability with depth is therefore applied (Garibaldi et al., 2010).

Results

A series of numerical experiments has been performed with different angles between fault zones (30 to 90°), geometries (simple, X-shaped and Y-shaped) and different fault zone permeabilities. Temperature field, positive thermal anomalies (defined as the excess temperature when compared to the conductive regime), velocity field, and convective patterns, are recorded. In order to calculate the flow rates at the surface, the surface of the models is divided into small zones, which are only used for flow rate calculations. The flow rate is calculated at the final time step as an integral of velocity field over the small surfaces of the fault zone. The results for the simple fault zone are shown in Figure II.4, the X-shaped intersection models in Figure II.5 and the Y-shaped intersection models in Figures II.6 and II.8. Details of the various calculations are given in Figure II.5.

Single fault zone

In our configuration, above a permeability of 3 10^{-14} m², convection starts up and temperature anomalies appear. They first appear at the center of the fault zone, then as permeability increases, they become unstable and move from the center to the edges of the fault zone (Figure II.4). High temperatures anomalies between 44 and 50°C appear at shallow levels (200-210 m). The temperatures of potential thermal springs are high, reaching 57°C at a flow rate of 10 l/s (52°C and 9l/s in Figure II.4b). At depth, e.g. 1500 m, positive temperature anomalies remain visible, with values around 30°C.

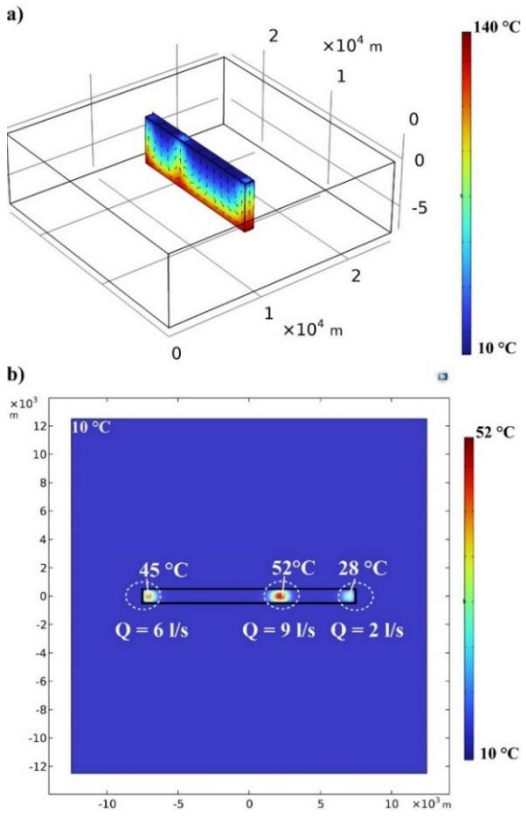

Figure II.4: (a) Case of a simple fault zone, for high permeability values (3 10^{-14} m²) the anomaly moves towards the end of the fault zone. (b) Cross-section of the model at the surface, production of 3 potential thermal springs.

X-shaped configurations

In order to reproduce several natural cases, three different angles of intersection were tested: 30, 60 and 90°. In terms of locating positive temperature anomalies, the 3 types of models produced the same results. When the permeability value is low, lower than 3 10^{-14} m², hot upwellings are concentrated at the intersection of fault zones (Figure II.5). The ends then correspond to infiltration zones dominated by cold flows. However, as the permeability value increases, positive anomalies are found at the 4 ends of the fault zones. The surface common to the two fault zones, the intersection, becomes a major infiltration zone.

In addition, the results in terms of positive temperature anomaly values, thermal springs and flow rates differ. The 30° angle produces relatively low surface temperatures, reaching a maximum of 44.2°C for 3 10^{-14} m² (average of 20.4°C). The associated outflow rates corresponding to these temperatures are high, reaching up to 40 l/s. Maximum temperature anomalies at depth are confined to rather shallow depths, 400 m on average. The associated values reach a maximum of 46. 2°C. When the angle is at its maximum, 90°, the springs

produced are slightly different. Surface temperatures are higher, up to 53°C, but with lower flow rates (30 l/s maximum). The maximum positive temperature anomalies are deeper and higher than for the previous configuration, reaching up to 55.7°C at average depths of 545 m. The 60° model produced intermediate results. Surface temperatures are lower at an angle of 90° but higher than the angle of 30°. The flow rates show the same behavior as the deep anomalies (temperature and depth).

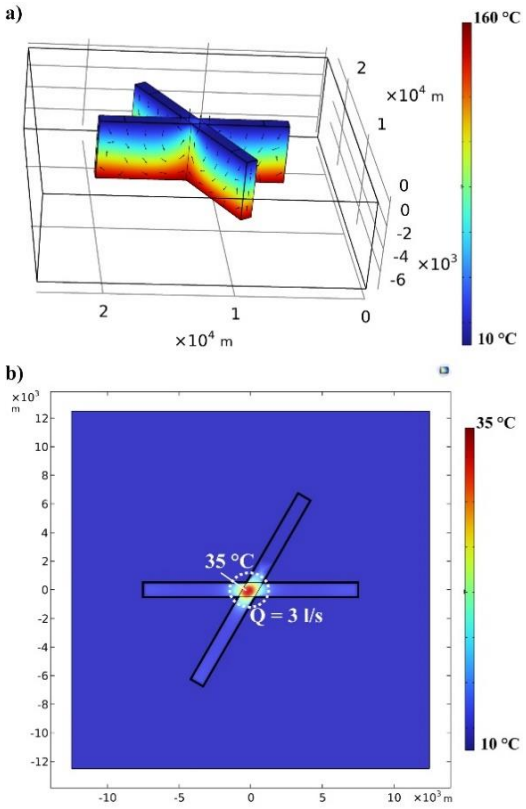

Figure II.5: (a) X-shaped configuration, 60°, for low permeability values (9 10^{-15} m²) the thermal anomaly is confined at the intersection. (b) Cross-section of the model at the surface, production of one potential thermal spring.

Y-shaped configuration

The Y-shaped configuration shows similar behavior as the X-shaped models, with an angle of 90°. For low permeability values (8 10^{-15} m²), the positive temperature anomalies are deep and of low amplitude at the intersection of the two fault zones. As permeability increases, they intensify and become more surficial, forming at the 3 extremities of the model (Figure II.6). They reach a maximum value of 48°C at a depth of 650 m (10^{-14} m²). Beyond this value, cold downward flow becomes the predominant feature (Figure II.6) and the positive anomaly values

decrease. At the surface, the highest temperatures reached are up to 55°C and an associated flow rate of 25 l/s (see green curve in Figure II.7).

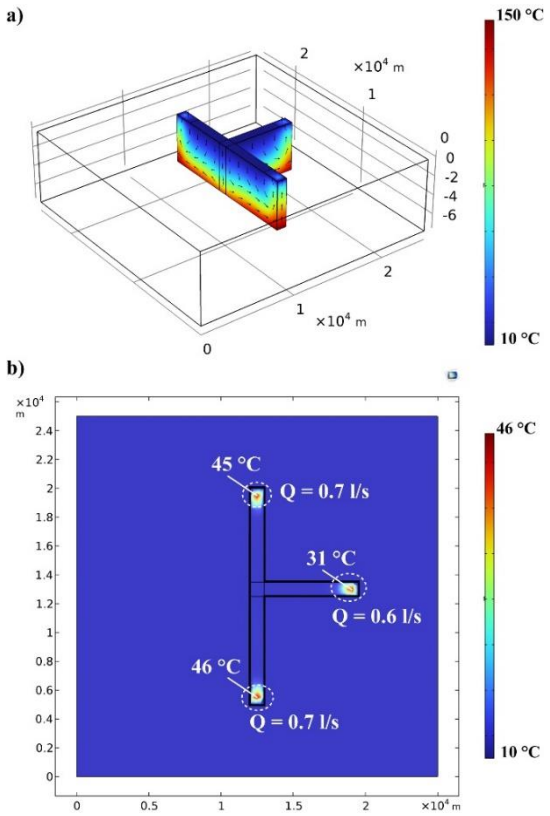

Figure II.6: (a) Y-shaped configuration, for high permeability values (3 10^{-14} m²) 3 thermal anomalies are created at the edges of the fault zones. (b) Cross-section of the model at the surface, production of 3 potential hot springs.

Discussion

Springs characteristics

All the configurations tested generate positive temperature anomalies at the surface, and therefore the production of potential thermal springs. However, the characteristics of these springs are not identical for an intersection of fault zones or a single fault zone.

In the case of a simple fault zone, the flow rates from the springs remain low despite the increase in the permeability of the fault zone. The maximum value reached is 10 l/s, which remains low (purple, Figure II.7a). However, this low flow rate also results in the highest spring temperatures, reaching 57°C.

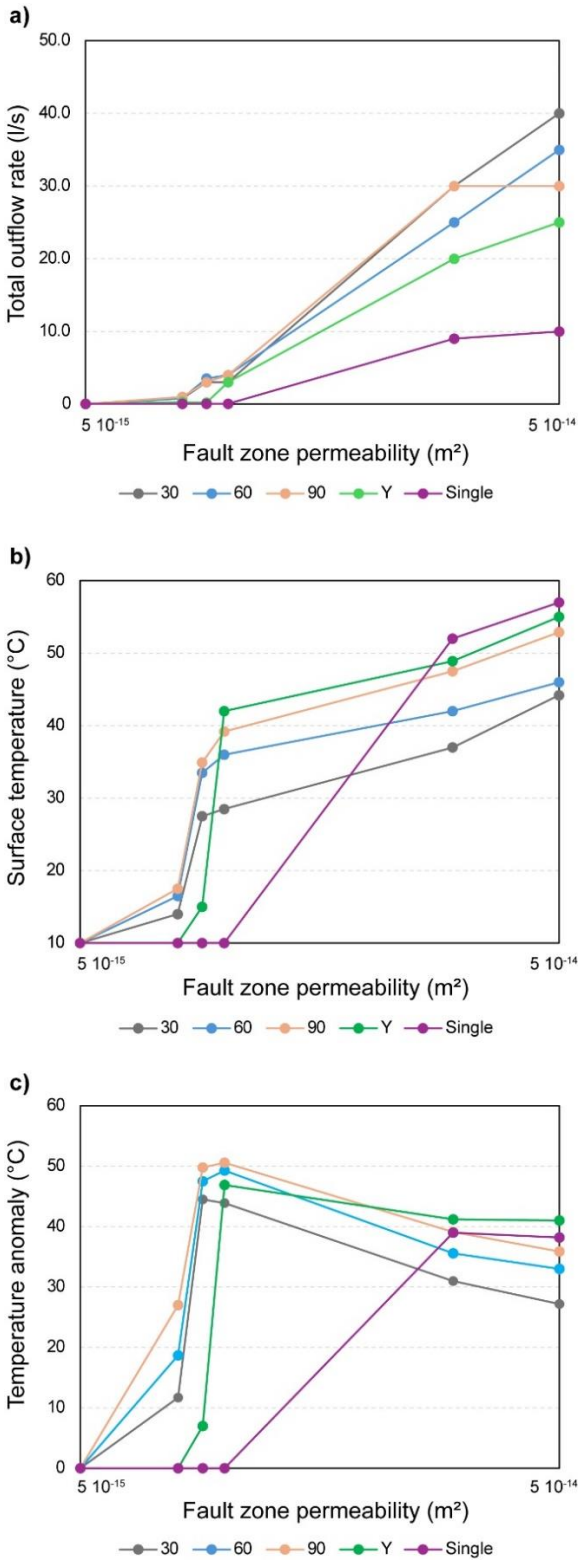

Figure II.7: (a) Outflow rate corresponding to upwelling zones, (b) maximum surface temperature reached and (c) temperature anomaly at 1000 m depth as a function of fault zone permeability.

The X-shaped configurations clearly show the impact of the intersection angle on fluid flow. The smaller the angle, the greater the outflow rates from potential springs (Figure II.7a). Flow rate from a 30° intersection is higher than that from a 90° intersection, although the difference

remains small for a permeability of 3 10^{-14} m², 40 l/s compared with 25 l/s respectively. The differences in outflow between a single fault zone and an intersection are primarily due to geometry. In fact, the geometry of the intersection doubles the volume of a potential infiltration zone, which considerably increases outflow rates. On the other hand, this advantage can quickly become disadvantageous when permeability increases with the preponderance of cold flows. When it comes to surface temperature, the opposite is observed. For any value of permeability, the greater the angle, the higher the positive temperature anomalies Figure II.6b). The 90° configuration gives the highest spring temperature of 53°C.

To summarize, simple fault zones are thought to produce hotter thermal springs but with low flow rates, unlike intersection zones, which are colder but have higher flow rates.

Set up of thermal convection

In parallel with these observations, it is possible to see that the intersection of fault zones facilitates the onset of convection. The simple fault zone produces temperature anomalies only for very high permeability values (K > 3 10^{-14} m²). In the case of Y or X intersections, convection starts at low permeabilities (as low as 8 10^{-15} m²). This phenomenon can be seen directly in Figure II.7c, where deep anomalies are first produced by fault intersections.

Implications for Chaudes-Aigues area and limits

The Chaudes-Aigues emergence area has been reproduced with the Y-shaped configuration. The results are intermediate, with lower temperature anomalies than a simple fault and lower flow rates than an intersection. For low permeabilities (8 10^{-15} – 10^{-14} m²), it is possible to reproduce a spring located at the intersection of the two fault zones (Figure II.8a). If the location is correct, the associated flow rates remain too low (0.001 - 3 l/s, Figure II.8b) as well as the surface temperature (15 - 43 °C, Figure II.8b).

These results show that geometry has an influence on flow rates and emergence temperatures, but that it is not the only parameter. Particularly in the case of Chaudes-Aigues, located in a mountainous area, topography must be taken into account. In addition, the

reservoir supposed to be at 190°C at a depth of 5 km (Vasseur et al., 1997) has not been reproduced here.

Conclusions

This study highlights the key role of fault intersections in controlling geothermal fluid flow and surface thermal anomalies. Intersections allow convection to occur at lower permeabilities than isolated faults, leading to higher discharge rates despite lower surface temperatures.

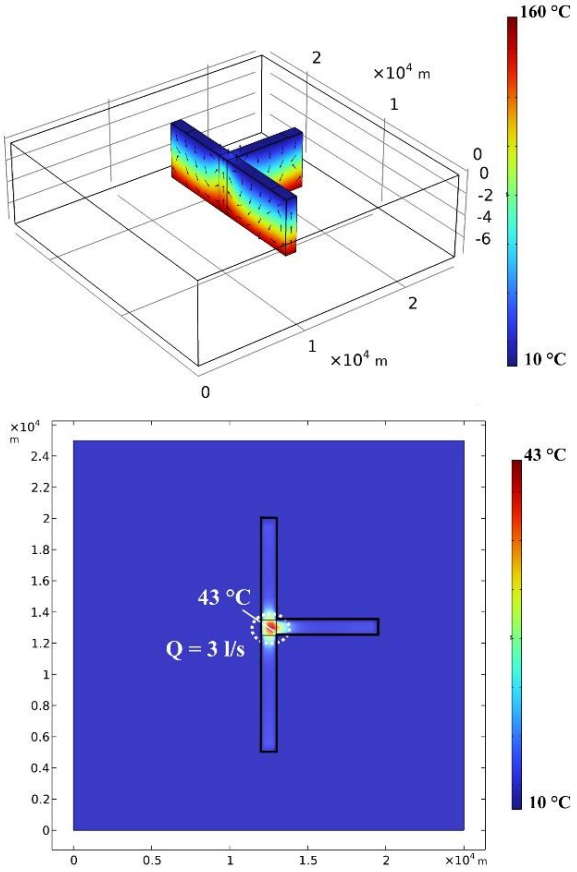

Figure II.8: (a) Configuration reproducing the location of Chaudes-Aigues springs (K = 10^{-14} m²). (b) Cross-section of the model at the surface, production of an emergence area.

The geometry of the intersection influences both flow intensity and heat distribution. At Chaudes-Aigues, the Y-shaped structure explains the spatial pattern of springs but not the full extent of flow and temperature, suggesting deeper thermal inputs or topographic effects. These results underline the importance of incorporating regional structural complexity into models and geothermal exploration.

II.4 Fluid flow in crustal fault zones with varying lengthwise thickness: application to the Margeride Fault Zone (French Massif Central) (published article).

Fluid flow in crustal fault zones with varying lengthwise thickness: application to the Margeride Fault Zone (French Massif Central)

Emmy Penhoët[1,2], Laurent Arbaret[2], Laurent Guillou-Frottier[1,2], Hugo Duwiquet[3],

Charles Gumiaux[2], Mathieu Bellanger[4].

1 : BRGM, Georesources Division, 45060 Orléans, France.

2 : ISTO, UMR 7327, Université d'Orléans, CNRS, BRGM, 45071 Orléans, France.

3 : ENGIE, Geothermal Division, 1 place Samuel de Champlain, Faubourg de l'Arche, 92930 Paris la Défense, France.

4 : TLS-Geothermics, 91 Chemin de Gabardie, 31200 Toulouse, France.

Manuscrit published in Geothermal Energy, 13:6, 2025, https://doi.org/10.1186/s40517-025-00334-9

E-mail adresses : penhoetemmy@gmail.com , laurent.arbaret@univ-orleans.fr , l.guillou-frottier@brgm.fr , hugo.duwiquet@engie.com , charles.gumiaux@univ-orleans.fr , mathieu.bellanger@tls-geothermics.fr

Corresponding author: Emmy Penhoët, BRGM, Georesources Division, 45060 Orléans, France, E-mail address: penhoetemmy@gmail.com

Abbreviations :

Margeride Fault Zone : MFZ

Bureau de Recherches Géologiques et Minières : BRGM

Institut des Sciences de la Terre d'Orléans : ISTO

French Massif Central : FMC

Lower Gneiss Unit : LGU

Upper Gneiss Unit : UGU

Margeride Granite Complex : MGC

European Cenozoic Rift System : ECRIS

Abstract

Crustal fault zones, holding promise as potential geothermal reservoirs, remain largely untapped and unexplored. Located in the southern Massif Central, France, the Margeride Fault Zone (MFZ) varies in thickness (lateral extension perpendicular to the fault plane) from 100 m to over 2500 m. Reactivated several times under different stress regimes since the Variscan orogeny, this zone is characterized by an intense alteration and fracturing. As a result, the multiple reactivations of the fault zone has maintained permeability, leading to favourable conditions for fluid circulation. Structural measurements and geological cross-sections were used to precisely constrain thickness and geometry of the fault zone. North of the MFZ, the Coren thermal spring indicates reservoir temperatures of about 200 - 250 °C, hinting at the possible existence of a temperature anomaly. To investigate this geothermal potential, 3D numerical models simulating fluid circulation within a fault zone were conducted. Various configurations were explored, altering fault zone thickness and permeability for two key geometries. The first geometry, which manipulated the width of the fault zone along its length, demonstrated a direct correlation between fault zone thickness and amplitude of thermal anomaly. Thinner faults (< 500 m) exhibited multiple weak positive thermal anomalies, while thicker faults (> 500 m) tended to develop a single, substantial positive thermal anomaly. In the second examined geometry, where fault zone thickness increased longitudinally, a consistent positive temperature anomaly emerged at the thickest section of the fault zone.

Depending on the permeability value, an additional anomaly may develop but will migrate laterally towards the thinnest part of the fault zone. This multi-disciplinary approach, combining numerical modelling and field measurements, presents a predictive methodology applicable to geothermal exploration in analogous basement domains. In our case, it has shown that the northern end of the Margeride fault zone could represent an area that needs to be explored further in order to assert its high geothermal potential. Our numerical models will increase understanding of how fault width and geometry impact the geothermal potential of the Margeride Fault zone and similar areas in crystalline basement.

Keywords

French Massif Central, Margeride Fault Zone, Thickness Variation, 3D Numerical modeling, Fault density, Structural measurements.

Introduction

In High-Temperature geothermal systems (T > 150 °C) where thermal convection dominates, deep hot fluids require highly permeable pathways to reach the surface (Manning and Ingebritsen 1999; Ledésert et al. 2009; Ingebritsen and Appold 2012; Ingebritsen and Gleeson 2014; Moeck 2014 ; Caspari et al. 2020, Jolie et al. 2021). These conduits can be faults or fractures networks or alteration pathways (Lowell 1975; Berkowitz 2002; Simms & Garven 2004, Bischoff et al. 2024) in which thermally-driven convective circulation may develop. In the last decades, 2D and 3D numerical models of fluid flow in permeable fault zones have been performed to better constrain the key parameters that control the circulation of fluids and heat within the fractured system but also in the surrounding rocks (López & Smith 1995; Bächler et al. 2003; Patterson et al. 2018; Duwiquet et al. 2022). At the scale of the fault zone, most significant parameters are the permeability and thickness of the damaged zone, its horizontal and vertical extension, and inclination and orientation of the fault with respect to the regional stress field (Duwiquet et al. 2021). Indeed, many studies have shown that the faults affected by an extensional regime are excellent upwelling conduits for deep fluids (Barton et al. 1995; Mckenna and Blackwell 2004; Faulds et al. 2010; Haines et al. 2016, Roche et al. 2018). Thickness of the fault zone plays also a role in the triggering of thermal convection, as

demonstrated theoretically by Malkovsky and Magri (2016). In terms of geometry, crustal fault zones that are sufficiently thick (fault zone thickness greater than 100 m) and long (length greater than 1 km) with a displacement of 100-150m are more likely to host fluid circulation (convection), as proposed by Guillou-Frottier et al. (2024). Ultimately, topography is also a key parameter to consider in geothermal exploration since lateral pressure gradients may control how the meteoric fluids travel through the first kilometers of the crust (Forster and Smith 1989; Barton et al. 1995; Taillefer et al. 2018, Alt-Epping et al. 2021, Carbajal-Martinez et al. 2024).

In purely crustal context, because of the time evolution of the direction and intensity of the stress field, faults zones often show multiple successive brittle reactivations. It results in the development of relatively thick fault zones whose permeability could be maintained over time. Conversely, recent faults zones that experienced a small number of brittle events without a significant change in the stress conditions may remain relatively narrow. Therefore, geothermal exploration in highly fractured crustal setting should include the identification of thick polyphased faults and the knowledge of their brittle evolution (Mitjanas et al. 2024).

To investigate the impact of the brittle evolution and consequent fault zone thickness on the geothermal potential of crustal fault zones, we selected the Margeride Fault in the French Massif Central. The French Massif Central is characterized by a large-scale surface heat flow anomaly (100-110 mW m^{-2}, over several hundreds of km Lucazeau and Vasseur 1989). When the radioactive component of surface heat flow is removed, the remaining mantle heat flow would be around 60 mW m^{-2} (Lucazeau et al., 1984) beneath the Cenozoic grabens and the volcanic areas, implying temperatures above 200 °C at a depth of 5 km (see Figure 5 in Lucazeau et al. 1984). Numerous crustal fault zones or permeable fault clusters exist in the Massif Central (Pontgibaud fault zone, Duwiquet et al. 2019; border faults of the tertiary Limagne Basin, Calcagno et al. 2014; Chaudes-Aigues fault network, Vasseur et al. 1997). In the Saint Flour area (Figure II.9), the Margeride Fault is the result of a long-lived brittle history since the Carboniferous. Consequently, the Margeride fault is made of a complex network of gouge alternating with damage zones, that we refer hereafter as the Margeride Fault Zone

(MFZ). Furthermore, the MFZ has the particularity of having an increasing thickness from south-east to north-west.

Aside from the structural geology arguments, a thermo-mineral spring is located in the thickest part of the MFZ. The "Font de Vie" spring at Coren-les-Eaux, (10 km north of Saint-Flour) is found in the gneissic bedrock. Even if the spring is cold at the surface (10 °C), it is nevertheless highly mineralized (7 g L^{-1}), and geothermometers indicate at depth a reservoir temperature of 220 °C (Fouillac 1983).

We performed structural measurements of the regional brittle structures network in the granitic and gneissic surrounding rocks and in the Margeride Fault Zone itself. We particularly focused along four sections striking perpendicularly to the MFZ and centered on the associated cenozoic grabens. Results have been used to constrain the 3D numerical models where the variation in thickness from south-east to north-west is taken into account.

Given the few studies on the effects of varied fault widths on fluid and heat transfer (see however Duwiquet et al. 2024), our work based on key points such as the brittle evolution of the fault zone, and on numerical models will help to constrain the identification of new potential geothermal targets.

Geological setting

The regional-scale crustal fault zone used as a study-case consists of the Margeride Fault Zone (named MFZ hereafter) located in the central part of the French Massif Central (Figure II.9). The French Massif Central is essentially inherited from the Variscan collisional orogen whose successive ductile to brittle orogenic events range from the late Silurian (ca. 410 Ma) to the early Permian (ca. 300 Ma, Faure 1995; Vanderhaeghe et al. 2020). In addition, from the late Paleozoic to present-day, this granite and gneiss basement has suffered successive tectonic brittle events (Blès et al. 1989; Faure et al. 1995; Merle et al. 2023).

The MFZ crosscuts several variscan lithologies: a late variscan granite (named the Margeride Granite Complex hereafter) and its country rock composed of two Paleozoic gneissic series.

In addition, Oligocene half grabens developed at the contact of the MFZ evidence its brittle cenozoic reactivation (Figure II.9).

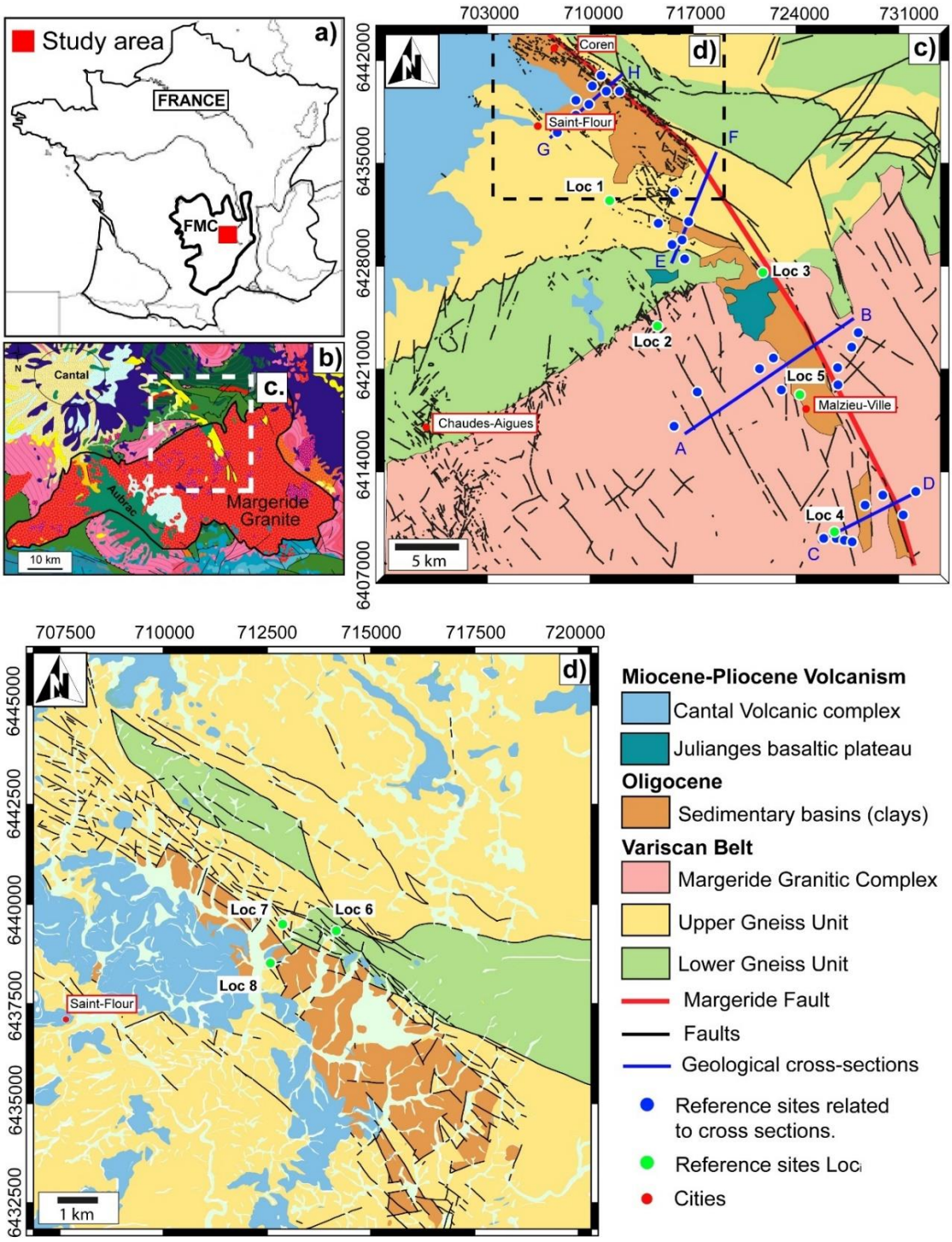

Figure II.9: Geological setting of the Margeride Fault Zone (MFZ). Coordinate system: Lambert 93 – RGF93 EPSG:2154. (a) location of the study area. (b) simplified geological map of the Margeride Granitic Complex issued from the 1:1 000 000 geological map of mainland France (BRGM). (c) Simplified map of the study area. Blue lines locate the four selected sections broadly oriented perpendicular to the MFZ and crossing the four major half grabens. Blue dots refer to outcrops on which statistical structural measurements of fractures orientations where performed and that are located as close as possible to the geological sections. Green dots refer to representative locations (Loc$_i$, see text for details). (d) Close-up map of the northwestern segment of the MFZ along which the Cenozoic Saint Flour Basin emplaced.

The metamorphic units

In the Saint Flour-Le Malzieu area (Figure II.9c), the metamorphic formations related to the Devonian to early Carboniferous, south verging, ductile shearing are represented by the Lower and Upper Gneiss units (named respectively LGU and UGU hereafter; Vanderhaeghe et al. 2020; Figure II.9). The UGU is made of retrogressed granulite composed by garnet-bearing diatexites associated with metatexites. The LGU consists mainly in micaschistes, paragneisses and orthogneisses that suffered greenschist to amphibolitic metamorphism. The contact between the two units is interpreted as a main shear zone between two stacked nappes (Burg and Matte 1978).

The Margeride Granitic Complex (MGC)

The 323 ± 12 Ma old Margeride Granite Complex (MGC, red area in Figure II.9c) emplaced during a late carboniferous extensional event as a laccolith within the LGU and UGU series (Couturié 1979; Talbot et al. 2005). The main facies are composed of a porphyritic monzogranite crosscut by late leucogranites and quartz dykes. The emplacement model proposed by Talbot et al. (2005) involves four NE-SW trending feeding zones that played either as pull-apart or extensional gashes controlled by sinistral NW-SE trending faults. Mineral lineations developed during the magmatic emplacement are homogenously oriented SE-NW with a shallow dip to the NW (Talbot et al. 2005) it implying a syn-orogenic emplacement within a NW-SE extensional regional stress field (Vanderhaeghe et al. 2020).

The MGC shows several signs favorable to the circulation of fluids. There are numerous quartz, porphyrites and microgranites dykes which could be potential pathways for fluids. Evidence come from the reactivation of N140E brittle fractures that that allow the upwelling of basaltic melts during the Cenozoic (Julianges plateau described by Couturié (1972), Figure II.9b). Fifteen km to the West of Saint-Flour (Figure II.9c), the granite has been suggested as a hydrothermal reservoir associated with the Chaudes-Aigues thermal springs, based on the above criteria (Cailleaux et al. 1976; Vasseur et al. 1997).

The Margeride Fault Zone (MFZ)

The MFZ is a major crustal fault zone whose age and multiphase history remain poorly documented. Broadly, the MFZ could be divided into two segments: The northern segment that begins south of the Saint Flour Basin (Figure II.9) is composed of a ~N130E trending, 15-kilometer-long and up to 2500-meter-thick network of brittle faults that overprint a similarly oriented, preexisting ductile fault zone affecting the LGU and UGU series. Its northwestward extension is occulted by the basaltic lava flows of the mio-pliocene Cantal stratovolcano. This structure is easily visible in the topography since there is an important slope break between the Margeride plateau culminating at an elevation of1400 m to the East and the Malzieu Basin at 800 m to the West. The age of the early ductile event is not determined. However, its orientation, parallel to the mineral lineations in the UGU and LGU series, together with the fact that it does not propagate to the south into the Margeride granite point out that this ductile event ended before 320 Ma. It could therefore be attributed to the first major ductile extension of the late Variscan period (Faure 1995).

The second southeastern segment transects the Margeride granite. It is composed of a ~N150E trending brittle fault system. The thickness of the MFZ is not observable in the field. However, the minimum distance between the outcropping continental sediments and the unfractured granite visible along the Malzieu and Saint-Alban Basins highlights a thickness of 100 meters, at most. The lengthwise connection with the northern segment takes place near the Chaliers Basin where the transition from N160E to N140E trending along both faults and grabens are obvious (see Figure II.9, Burg and De Goer de Herve 1990).

Late Variscan and Mesozoic brittle overprint

During the late Variscan period (330-280 Ma), the region experienced successive major extensions. First, a NW-SE extension related to the syn-collisional extension that affected the ductile part of the crust. Second, a NE-SW extension (Faure 1995; Daffos et al. 2024). The latest variscan-related event was a North-South compression that progressively became East-West during the Stephanian (Blés 1989). This North-South compression generated a

conjugate brittle system made of N140E-N170E dextral and N010E-N050E sinistral strike-slip faults, associated with N80-N120 inverse faults. At the end of the Paleozoic, the Variscan range was peneplaned.

Tectonic events associated with the opening of the Atlantic and Ligurian oceans are understood to have little effect on the study area, as evidenced by an accentuated peneplain process during the Mesozoic

Cenozoic extension and uplift

In the late Cretaceous and Paleocene, an intraplate compression involved a buckling of the lithosphere and reactivation of pre-existing crustal discontinuities (Ziegler et al. 2007). During the Eocene, an east-west extensional regime developed over the Massif Central with the establishment of the European Cenozoic Rift System (ECRIS; Michon and Merle 2001; Dèzes et al. 2004; Merle et al. 2023). Although the origin of the ECRIS remains debated (Michon and Merle 2001; Michon et al. 2003 & 2005; Dèzes et al. 2004 & 2005), all authors agree that a mantle thermal anomaly started during the Paleocene and caused thinning of the lithosphere beneath the FMC. It resulted in the implementation of N140E to N0E elongated grabens, from North to South of the FMC, the northernmost being the Limagne Basins.

In the study area, four half grabens are located along the western side of the MFZ. From the South to the North, they comprise the Saint-Alban Basin, the Malzieu Basin, the Chaliers Basin and the Saint-Flour Basin (De Goer De Herve et al. 1990; Figure II.9). Sedimentation was predominantly detrital. All Basins are limited on their eastern edge by the MFZ, along which subsidence was limited as the thickness of the continental sediments has been estimated to a maximum of 150 meters (De Goer De Herve et al. 1990). The western edges of these half-grabens are not marked by major faults, leading to their asymmetric geometry. In the Malzieu Basin, this asymmetric structure is outlined by the present course of the Truyère River (not shown in Figure II.9).

During the Upper Miocene, the Massif Central was subjected to a regional uplift due to a NW-SE directed compression (Mazabraud et al. 2005). It resulted in the active erosion of the peneplaned surface leading to the formation of the Truyère valley.

Present-day regional stress field

According to Mazabraud et al. (2005) the current stress field in the French Central Massif implies a NW-SE compression, which means that fractures oriented in this direction could play as tensions gashes. Indeed, favourably oriented faults will be those that enable fluid circulation (Barton et al. 1995; Mckenna and Blackwell 2004, Faulds et al. 2010, Duwiquet et al. 2022). Thus, the two segments of the MFZ, which varies in strike by 30°on average, will possibly react differently in this regional stress field.

Geothermal setting of the Malzieu area

Surface and mantle heat flow

Along the MFZ, several surface heat flow values have been published (Lucazeau and Vasseur 1989). They are consistent as a heat flow value of 96 mW m^{-2} is found in the North (Saint Flour area, site “Saint Michel”, NGHF Database, Lucazeau 2019) while a heat flow of 102 mW m^{-2} is obtained in the south (“Aumont Aubrac” site, Lucazeau 2019). A geothermal gradient of 31 °C km^{-1} has been measured for the first site and 34 °C km^{-1} for the second. However, these sites correspond to shallow boreholes (depth of 150 m), where measured temperatures could be affected by paleoclimatic disturbances. Consequently, we chose two others neighboring heat flow sites in the FMC (Auriat and Villechabrolle), with depths of 1000 and 650m, respectively. These two boreholes show deep unperturbed temperature gradients of 30 and 32 °C km^{-1} respectively. These values are consistent with the average temperature gradient of the FMC.

The large-scale surface heat flow anomaly of the FMC has been interpreted by Lucazeau et al. (1984) as a mantle diapir bringing an additional mantle heat flow of 25-30 mW m^{-2}, thus leading to a total mantle heat flow around 60 mW m^{-2} in the area.

Radiogenic heat production

Decades ago, four boreholes were drilled by the INAG (National Institute for Astronomy and Geophysics) in the MGC to collect core samples and to measure the temperature gradient. Heat production measurements on these core samples indicate values varying between 2.76 μW m^{-3} and 4.32 μW m^{-3}. The value finally retained is 3.75 μW m^{-3} (Bayer et al. 1982). For the metamorphic units, samples taken over the FMC point to a mean value of 2.5 μW m^{-3} (Lucazeau and Vasseur 1981).

Methods

Brittle structures analysis

In order to constrain the brittle structures affecting the MGC and its surrounding gneissic basement outcrop-scale measurements at key sites were combined with regional scale fault density analysis methods, as detailed below.

Outcrop-scale structural measurements

We performed outcrop scale fractures analysis on 57 references sites, 31 of them being distributed along, and as close as possible to, the four selected cross sections (Figure II.9c). Theses sections are perpendicular to, and crosscut, the MFZ. In addition, they are centered on the four cenozoic half-grabens. In each location, from 50 to 200 measurements were performed according to the size of the outcrops. Low dipping joints, i.e. dipping less than 15°, were not considered in these locations as they more likely relate to either exfoliation or unloading joints. Nevertheless, two additional stations were selected to characterize the change in attitude of these flat-lying joints approaching Le Malzieu graben.

Due to the absence of adequately sized and representative outcrops, measurements were not conducted within the continental sedimentary series filling the grabens.

Regional scale fault density

A regional scale faults density analysis has been performed on an assemblage composed of the four geological maps covering the study area, namely N°789-Saint-Flour (De Goër de Herve et al. 1990), N°790-Langeac (Bouiller et al. 1986), N°813-Chaudes-Aigues (Burg et al. 1991), N°814-Saugues (Couturié 1979). We digitized faults by applying a grid consisting of

500 meters wide square cells. The cumulative length values per cell were divided into 5 classes using the natural breaks of the distribution histogram (Jenks algorithm implemented in QGIS; Jenks 1967).

Primary mineral structures analysis

In addition to the analysis of brittle structure, mineral foliation and lineation developed in the two gneissic units were measured at 57 stations distributed over the area. Foliations and lineations in the MGC are issued from Talbot et al. (2005). Talbot et al. (2005) evidenced the close correspondence between the magnetic fabrics and the mineral fabrics in the granite. Both magmatic and ductile foliations were used to properly define the fractures type developed in the MGC and the surrounding basement, respectively, as they may overlay on primary joints (Marre 1986). In igneous rocks, three main type of primary joints, which are orthogonal to each other and guided by the orientation of inherited mineral foliation and lineation, may develop (Cloos 1922): the Q joints (cross fractures) that are perpendicular to the mineral lineation, the S-joints (longitudinal fractures) that are perpendicular to the foliation and parallel to the lineation, and finally, the L joints that are parallel to the foliation (Marre 1986).

Numerical Modeling

The thickening of the MFZ, from the Le Malzieu to the Saint-Flour areas may have an impact on the possibility for thermal convection to occur within the permeable fault zone. Before investigating by numerical modeling whether thermal convection can occur in various parts of the Margeride fault zone, a simple analytical approach is presented below.

Estimate of Rayleigh number

Thermal convection occurs if the Rayleigh number Ra (ratio of driving versus resisting forces, depending on physical properties, medium geometry, and temperature contrast) exceeds a critical value Ra_c (e.g. Turcotte and Schubert, 2002, chap. 9.9). For an infinite porous layer with constant temperature conditions on top and bottom boundaries, this Ra_c value equals $4\pi^2$ (Lapwood 1948).

For a fault zone of a finite width, the critical value (Ra_c) has been studied by Malkovsky and Magri (2016) through a linear stability analysis and for a temperature-dependent fluid viscosity. For a fault zone with a half-width over height ratio Δ, they showed that for an averaged temperature gradient, the critical Rayleigh number writes:

$$\mathrm{Ra_c} = 2.466\left[\left(\frac{8.19}{\Delta}\right)^{5/4} + (4\pi^2)^{5/4}\right]^{4/5} \quad (1)$$

In our case, the average temperature gradient hypothesis is valid since values around 30 °C km^{-1} have been measured (see above). For a constant viscosity case, the coefficient 2.466 in equation (1) is replaced by 1 (see Malkovsky and Magri 2016), and the classic $4\pi^2$ value is recovered as soon as the half-width over height ratio (Δ) is large (i.e. for an infinite width). For a finite fault zone thickness, the critical Rayleigh number is larger than $4\pi^2$.

Assuming that the Margeride fault zone height is 5 km (which corresponds to the gneiss-granite transition according to Talbot et al. 2005), fault zone half-width can be estimated at 50 m for the Malzieu area while it reaches 1250 m in the Saint-Flour area. The associated Δ values are thus 0.01 and 0.25, respectively. It follows that the two critical Rayleigh numbers for Le Malzieu and Saint-Flour areas equal:

$$\mathrm{Ra_c(Malzieu)} = 2056$$

$$\mathrm{Ra_c(Saint-Flour)} = 155$$

In other words, the thick deformation zone in the Saint-Flour area may easily host thermal convection since the critical Rayleigh number is small. For given physical conditions and petrophysical properties, one may observe thermal convection in the Saint Flour deformation zone while these conditions will not lead to thermal convection in the Le Malzieu area.

In the following, different fault zone geometry (thicknesses and lengths) and different physical properties will be tested through numerical modeling of heat and mass transfer within a finite-width permeable fault zone. Numerical models were performed with the Comsol Multiphysics™ software.

3D models

As demonstrated by Malkovsky and Magri (2016), the establishment of a convective regime depends directly on the morphology of the fault zone and more precisely on its thickness and height. A parametric study where fault zone thickness and fault zone permeability are varied is first presented. In order to study the impact of the varying thickness in the longitudinal direction, fault zone with a prismatic shape is then studied.

As in Guillou-Frottier et al. (2013) Darcy' law was coupled with heat transfer equation and mass conservation. Several variables such as thermal conductivity, heat capacity, porosity, rock density (see Table II.1) necessary for modeling were estimated thanks to field observations and literature data.

Boundary and initial conditions

At the upper surface, a temperature of 10 °C was fixed. According to regional data, a constant heat flux of 85 mW m^{-2} is imposed at the base of the model (Lucazeau and Vasseur 1989). An averaged heat production rate of 3 µW m^{-3} (see previous section on radiogenic heat production rate) is assumed in the entire domain The lateral borders were thermally insulated (host rocks). A geothermal gradient of 30 °C km^{-1} was imposed as an initial condition. The equivalent thermal conductivity is deduced from the above thermal conditions (heat flow, temperature gradient and heat production), leading to a value of 2.8 W m^{-1} K^{-1}, consistent with thermal conductivity measurements in the area (Lucazeau et al., 1984).

The surface pressure is equivalent to the atmospheric pressure (10^5 Pa), and its value increases gradually with depth. A no flow condition was imposed on lateral sides and bottom of the model (host rocks).

Meshing and geometry

(a) (b)

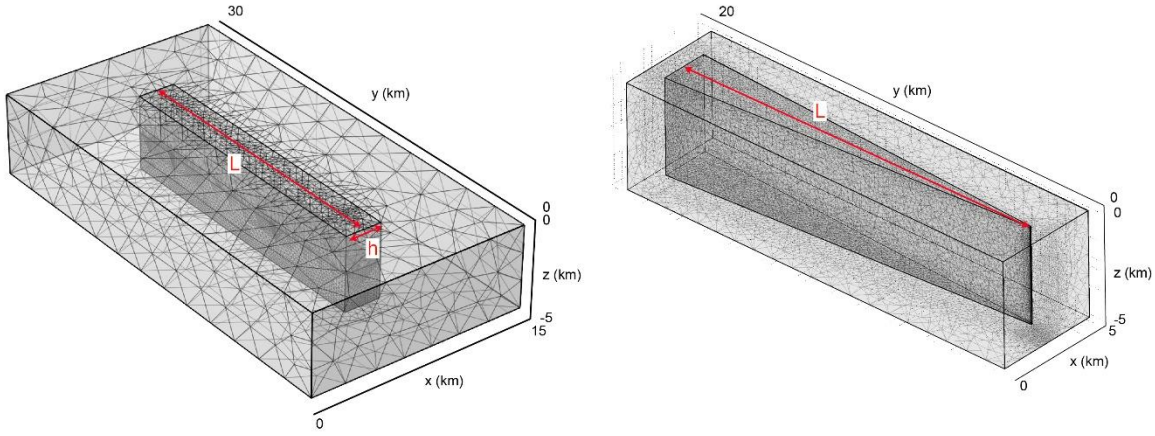

Figure II.10: (a) Simplified geometry used for parametric studies, with coarse mesh in the embeddings and refined mesh in the faulted zone; the fault zone thickness h varies between 100m to 2500m. (b) Models with a lengthwise variation of the fault zone thickness from 2500 to 50m (prismatic shape). The length of the fault zone, L, has been varied, but the meshes shown here correspond to the results of Figure II.20 and 2.21 where L = 20 km, close to the MFZ. The height of the fault zone is 4 km, and it crops out the surface.

For the parametric study, a simplified parallelepidic geometry is chosen for the fault zone and the basement (Figure II.10a). The size of mesh elements is based on the permeability value. In areas of low permeability (host rocks), the mesh element size is coarse (minimum size 100 m) but extremely fine in the fault zone (high permeability) (maximum 20 m). The same mesh features have been used for the prismatic shape.

Variable physical properties

For the fluid, here supposed as pure water, the dynamic viscosity (Pa.s) is a function of temperature T(°C), such that:

$$\mu(T) = 2.414.10^{-5}.e^{\frac{570}{(T+133)}} \quad (2)$$

following Smith and Chapman (1983) and Rabinowicz et al. (1998).

The density of water is also a function of pressure and temperature, such that:

$$\rho_f(T,P) = 1006 + (7.424 \times 10-7 \times P) + (-0.3922 \times T) + (-4.441 \times 10-15 \times P^2)) + (4.547 \times 10-9 \times P \times T) \quad (3)$$

$$+ (-0.003774 \times T^2)$$

$$+ (1.451 \times 10 - 23 \times P^3)$$

$$+ (-1.793 \times 10 - 17 \times P^2 \times T)$$

$$+ (7.485 \times 10 - 12 \times P \times T^2)$$

$$+ (2.955 \times 10 - 6 \times T^3)$$

$$+ (-1.463 \times 10 - 32 \times P^4)$$

$$+ (1.361 \times 10 - 26 \times P^3 \times T)$$

$$+ (4.018 \times 10 - 21 \times P^2 \times T^2)$$

$$+ 7.372 \times 10 - 15 \times P \times T^3)$$

$$+ (5.698 \times 10 - 11 \times T^4)$$

Equation (3) is based on a polynomial fit of experimental data, as developed by Launay (2018) and published in Guillou-Frottier et al. (2020).

The main unknown in the modelling approach remains the permeability value for each formation found in our study area. The MGC and the two metamorphic units are considered, in the absence of fracturing, as impermeable. The permeability values in common rocks vary between 10^{-18} m² and 10^{-13} m² (Brace 1984; Evans et al. 1997; Sonney and Vuataz 2009; Ranjram et al. 2015; Walter 2016; Achtziger-Zupancic et al. 2016 & 2017; Neuzil 2019), which leaves a wide range of possibilities. Here we will attempt to better constrain qualitatively the permeability using structural measurements, field observations and fault density estimates.. The increase in pressure at depth tends to seal the fractures and thus causes a decrease in the permeability of the units. This phenomenon can be described by the following equation :

$$K_u(z) = K_{0_u} . e^{\frac{-z}{\delta}} \quad (4)$$

where $K_u(z)$ is the permeability of each unit (m²), K_{0_u} is the highest permeability (from 10^{-15} m² to 5 10^{-14} m² in the fault zone, and 10^{-18} m² in the host rocks) reached by the unit (at the surface) and z is the depth (m) (Garibaldi et al. 2010). The length δ (m) characterizes the intensity of the decrease in permeability with depth. A δ value of 2000m has been chosen.

	Porosity	Permeability K_0 (m^2)	Matrix thermal conductivity (W/m.K)	Density (kg/m^3)	Matrix heat capacity (J/kg.K)	Heat production (W/m^3)	Fluid thermal conductivity (W/m.K)	Fluid heat capacity (J/kg.K)
Fault zone	0.20	$10^{-15} – 5\ 10^{-14}$	3.30	2700	1000	x	0.6	4200
Bulk	0.05	10^{-18}	2.80			$3\ 10^{-6}$		

Table II.1: Parameters used for rocks and fluid in 3D modelling. These values have been obtained from different studies (Smith and Chapman 1983, Rabinowicz et al. 1998, McKenna and Blackwell 2004, Guillou-Frottier et al. 2013, Taillefer 2017, Duwiquet et al. 2019).

The following numerical results correspond to final state (steady state or pseudo steady state regimes) of 2 Myr of transient evolution. Initial conditions reproduce a conductive regime and at t > 0, permeabilities are effective.

Results

Structures analyses

Primary ductile and magmatic structures

In the two gneissic units the mineral foliations show a similar distribution marked by two plane populations. The main population corresponds to a N065 trending mean plane that dips to the North-West by 33° (Figure II.11a). The secondary population yields a mean foliation oriented N105E and dipping to the North by 64°. In contrast the lineation measured on these two associated foliation populations yield a mean lineation constantly trending N100E and plunging to the Northwest by 20° (Figure II.11b). This N100E regional stretching lineation is known to be developed over the southern metamorphic nappes of the French Massif Central (Faure 1995). These two associated foliations, characterized by different dips but close strike directions represent flanks of asymmetric folds developed in both gneissic units.

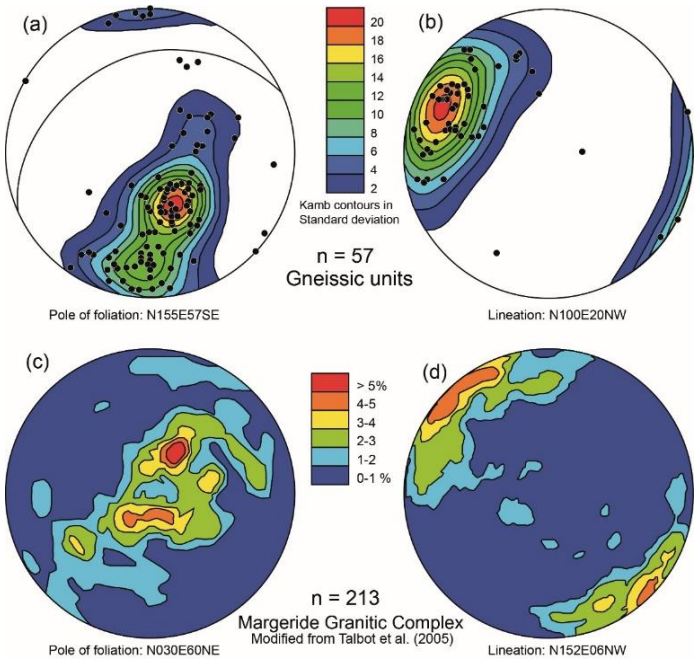

Figure II.11: Equal area projection (lower hemisphere) of primary ductile and magmatic mineral fabrics. (a) Foliations and (b) lineations measured in 57 locations distributed in both UGU and LGU units. Kamb contours in standard deviation. (c) AMS Foliations and (d) lineations of the MGC (modified from Talbot et al. 2005). All stereographic projections are in an equal area lower hemisphere.

These ductile structures of Eo-Variscan age are characterized by a first N100 direction, which is the regional stretching lineation and is also widely developed in the southern metamorphic nappes of the Massif Central (Faure 1995).

In the MGC, field measurements of mineral foliation and lineation are difficult to achieve, as the granite appears macroscopically isotropic (no visible magmatic foliation). Nevertheless, Talbot et al. (2005) measured the magnetic foliations and lineations by applying the anisotropy of magnetic susceptibility technic and they considered them as closely representative of the magmatic mineral foliation and lineation, respectively. Talbot et al. (2005) evidenced magnetic foliations weakly dipping either to the NE or the SW, leading to a ~N45E trending pole girdle (Figure II.11c). In contrast, the tied magnetic lineations are well organized as they are almost horizontal with an average trending direction of N130E to N160E (Figure II.11d).

Regional fracture analysis

Regional fracture network analysis was performed by combining 57 locations distributed in the study area. For a sake of simplification and as most of the fractures exhibit a strong dip, strike directions are also presented in rose diagrams together with lower hemisphere projections

(Figure II.12a and 2.12b). Among these locations, three reference sites have been selected as they best illustrate the fracture network in both UGU and LGU gneissic units, the MGC and finally, in a location close to the MFC (Figure II.12c; locations in Figure II.9).

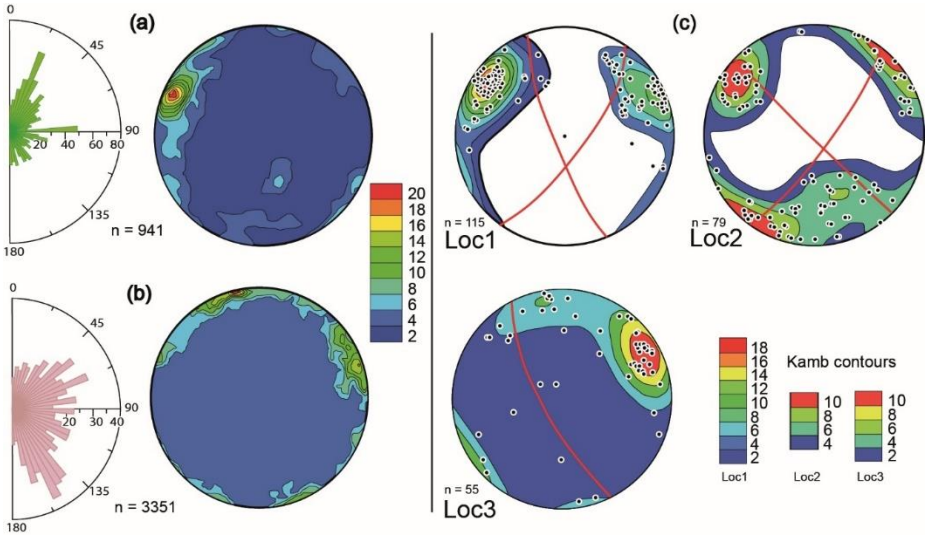

Figure II.12: (a) Azimuthal (left) and orientation (right) distributions of fractures measured in the UGU and LGU gneissic units. (b) Azimuthal (left) and orientation (right) distribution of fractures measured in the MGC. (c) orientation distributions in three reference sites in the UGU (Loc1), in the MGC (Loc2) and along the MFZ (Loc3, see Figure II.9 for geographical locations). All stereographic projections are in an equal area lower hemisphere. All Kamb contours in standard deviation.

In the LGU and UGU units, 941 fractures were measured (Figure II.12a). The main population is represented by N20E to N30E trending, almost vertical, fractures. A second population is composed of well oriented N90E trending planes. Two minor, more distributed, N45E and N140E trending populations complete this fracture network. The main population is well represented in the selected reference site Loc1 (Figure II.12c), in which the second population trend N70E. In the MGC, 3345 fractures were measured (Figure II.12b). The main population is composed of vertical fractures trending from N140E to N160E. The second population is even more scattered as it is formed of vertical fractures with strikes ranging from N45E to N80E. This fracture network organization is well expressed in the reference site Loc2 (Figure II.12c). Approaching the MFZ, the fracture network changes (Loc3, Figure II.12c). Only one population represented by well-organized N150E to N160E trending fractures is found. This fracture network is parallel to the MFC at this location (Figure II.9).

Flat lying joints

Flat lying, joints are commonly observed in the MGC. These joints could be related to either L joints or unloading joints. A reference site outcrop West of Saint-Alban-Sur-Limagnole (Loc 4, Figure II.13a; see location in Figure II.9c). In this outcrop, a main vertical, N120E trending, fracture population is crosscut by, regularly distributed, flat-lying joints (Figure II.13b). Approaching the grabens, and more particularly near Le Malzieu graben, the attitude of the joints changes. This is particularly notable in the Porte des Fées Canyon where the attitude of the joints is clearly visible in the landscape (Loc5, Figure II.13c; see location in Figure II.9c). In this location two vertical, N170E and N60E trending fracture populations are crosscut by N160E trending joints gently dipping to the East of 12° (Loc 5, Figure II.13d).

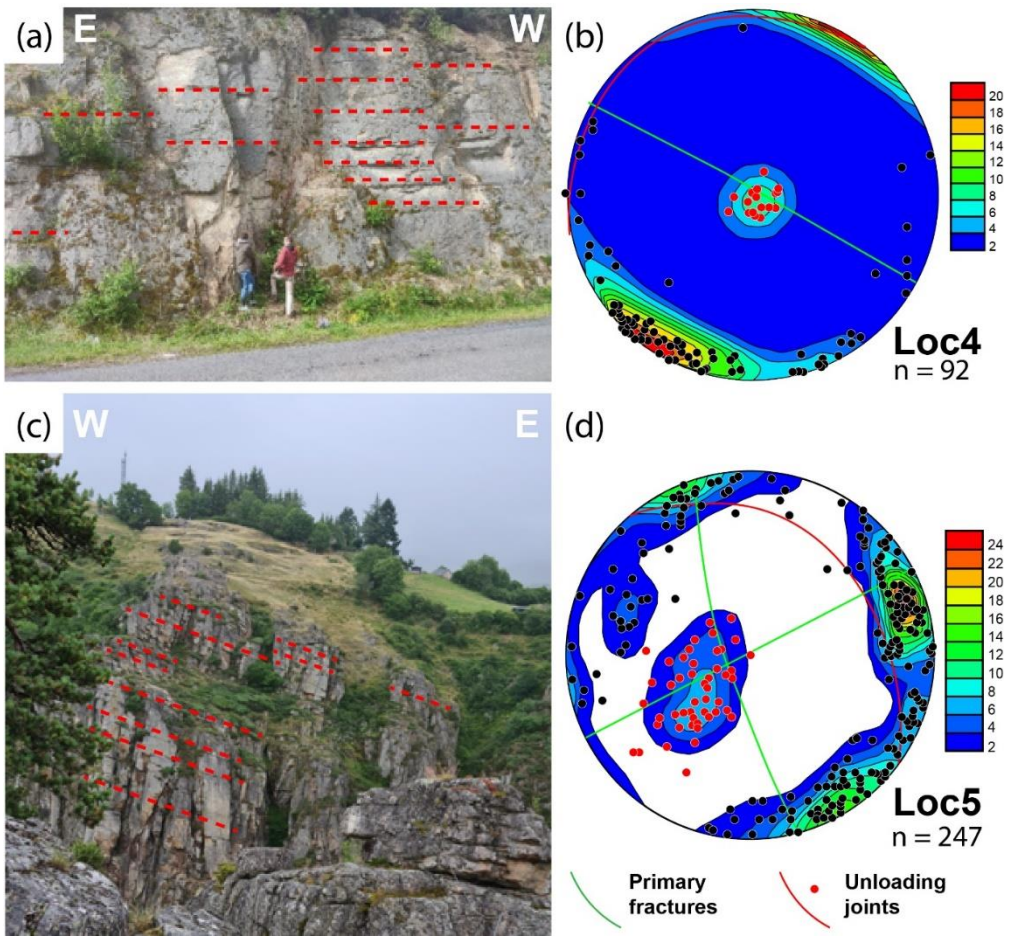

Figure II.13: (a) roadside outcrop located West of Saint-Alban-Sur-Limagnole (Loc4, coordinates: 44.778779205160504, 3.353790900820662) showing the flat-lying joins in the MGC. (b) Orientation distribution of primary fractures and joints in LOC4.

Four cross sections perpendicular to the MFZ and centered over the four sedimentary Basins were designed. Two are located in the MGC to the South (Saint-Alban sur-Limagnole and

Chinchazes Basins; Le Malzieu Basin; Figure II.14) and two are located in the LGC/UGC gnessic basement to the north (Chaliers Basin; Saint Flour Basin; Figure II.15) (locations in Figure II.9c). No outcrop appropriated for statistical fracture analysis were found in the oligocene sediments of the grabens.

Seven reference sites are distributed near the section crossing over the two Basins of Saint-Alban-sur-Limagnole and Chinchazes (Figure II.14a). Among them, site 41 was dedicated to flat lying joints analysis (Loc 4, Figure II.13a and 2.13b). Two main populations of fractures are recognized. Northeast of the Basins, A N050E to N070E trending family is associated with a N100E family. Both are vertical in average. Stress tensor analysis in location 49 indicates that a horizontal East-West main regional stress field was responsible for this conjugate fault system (Figure II.14a). These fracture families are present westward and around the sedimentary Basin while they progressively rotate to form N110E and N170E trending, strongly dipping, fractures population in the westernmost location (location 50, Figure II.14a). Secondary fracture family comprise N170E to North-South planes that were only observed in locations 40 and 43.

Eight references sites document the fracture distribution along the section crossing over Le Malzieu Basin (Figure II.14b). Among them, site 37 was dedicated to flat-lying joint analysis (Loc 5, Figure 5c and 5d). The two main vertical fractures family trending N050E to N070E and N100E to N150E, respectively, are present all along the section. Stress tensor analysis in sites 63 and 52 indicate that a horizontal NW-SE main regional stress field was responsible for this conjugate fault system (Figure II.14a). Secondary fractures comprise N020E to North-South vertical planes (sites 51 and 55) while N090E trending vertical fractures are observed in sites 54 and 52 (Figure II.14b).

The MFZ is not outcropping along the two sections. Therefore, the thickness can only be estimated by using indirect evidence. Along the eastern border of the Chinchazes Basin, the undeformed granite outcrop less than hundred meters from the oligocene continental sediments filling the graben (outcrop location: 44.7826, 3.4158). This apparent low thickness

is consistent to those proposed for the segment of the MFZ bordering Le Malzieu Basin (Couturié 1972).

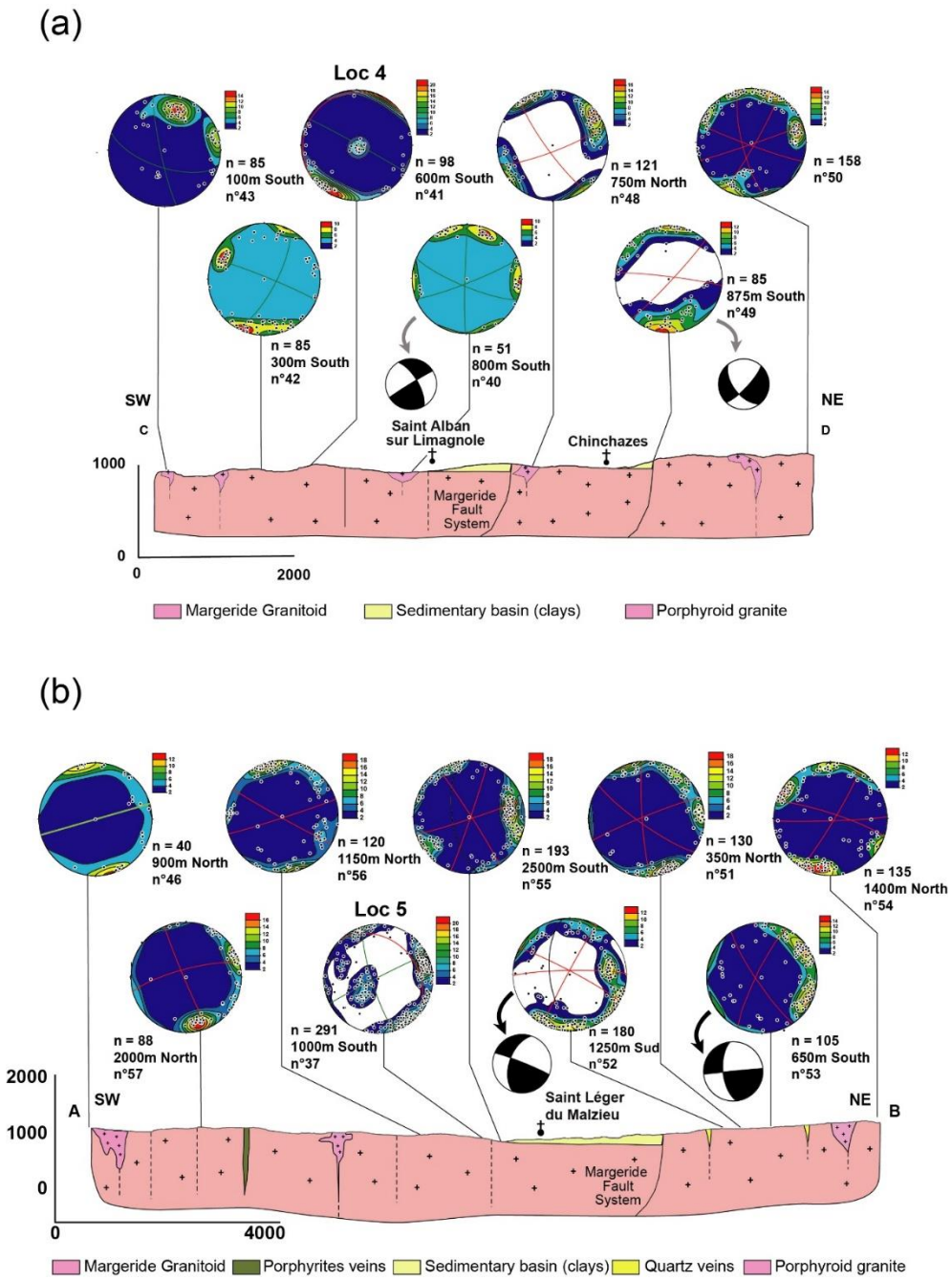

Figure II.14: (a) Geological section crossing the Saint-Alban-sur-Limagnole Basin and Chinchazes Basin. Loc 4 refers to flat-lying joints analysis location (see Figure 5a and 5b). (b) Geological section crossing Le Malzieu Basin. For (a) and (b), both scales are in meters. Loc 5 refers to flat lying joints analysis location (see Figure 5a and 5b). All stereographic projections are in an equal area lower hemisphere. All Kamb contours in standard deviation. Principal stress tensors were calculated by using FaultKin software.

Further to the North, the Chaliers Basin is emplaced in the LGU-UGU units (Figure II.15a). 7 reference sites are distributed along the section. To the East of the MFZ bordering this graben the gneisses are affected by North-South to N030E highly dipping fractures only associated

occasionally with a secondary, almost East-West trending, fracture population (Sites 18 and 17; Figure II.15a). West of the graben, near Chaliers village, these two fracture populations are also present. Conjugate N010E and N160E fault system was found near the contact with the continental sediments filling the graben (Site 24, Figure II.15a). Stress tensor analysis yields a horizontal NW-SE main regional stress field similar to the one obtained near Le Malzieu graben (Figure II.14b), all being compatible with a broadly N070E-directed horizontal extension.

The northern last section crosses over the Saint Flour Basin (Figure II.15b). East of the graben, the LGU outcrops along the road of Montchamp (Margeride plateau, Figure II.16a). From the East to the West, the gneiss that exhibits a N120E trending, 80° West dipping, foliation (Figure II.16b), is progressively affected by an increasing ductile deformation that becomes more pervasive with evidence of mylonitisation while approaching the border of the graben. This ductile deformation is crosscut by distributed brittle normal faults almost parallel to the ductile foliation (Figure II.16c). 8 reference sites for fracture analysis are distributed along the section. To the East, fracture analysis evidence two populations formed of N010E to N030E fractures associated with N100E fractures, both being vertical (Sites SF7, Figure II.15b). These two populations are also present westward where they progressively rotate from 20° clockwise approaching the border of the graben. This zone of about 500 meters thick is composed of isolated lenses of intensively fractured gneiss lenses and quartz veins embedded in an argilised breccia (Figure II.17). Within the graben, these two populations are present but from place to place, one take precedence over the other. In location SF4 (Figure II.15b), N040E trending fracture is the main population while to the West, the N120E to N140E trending fractures become the only population (location SF5 and SF8, Figure II.15b).

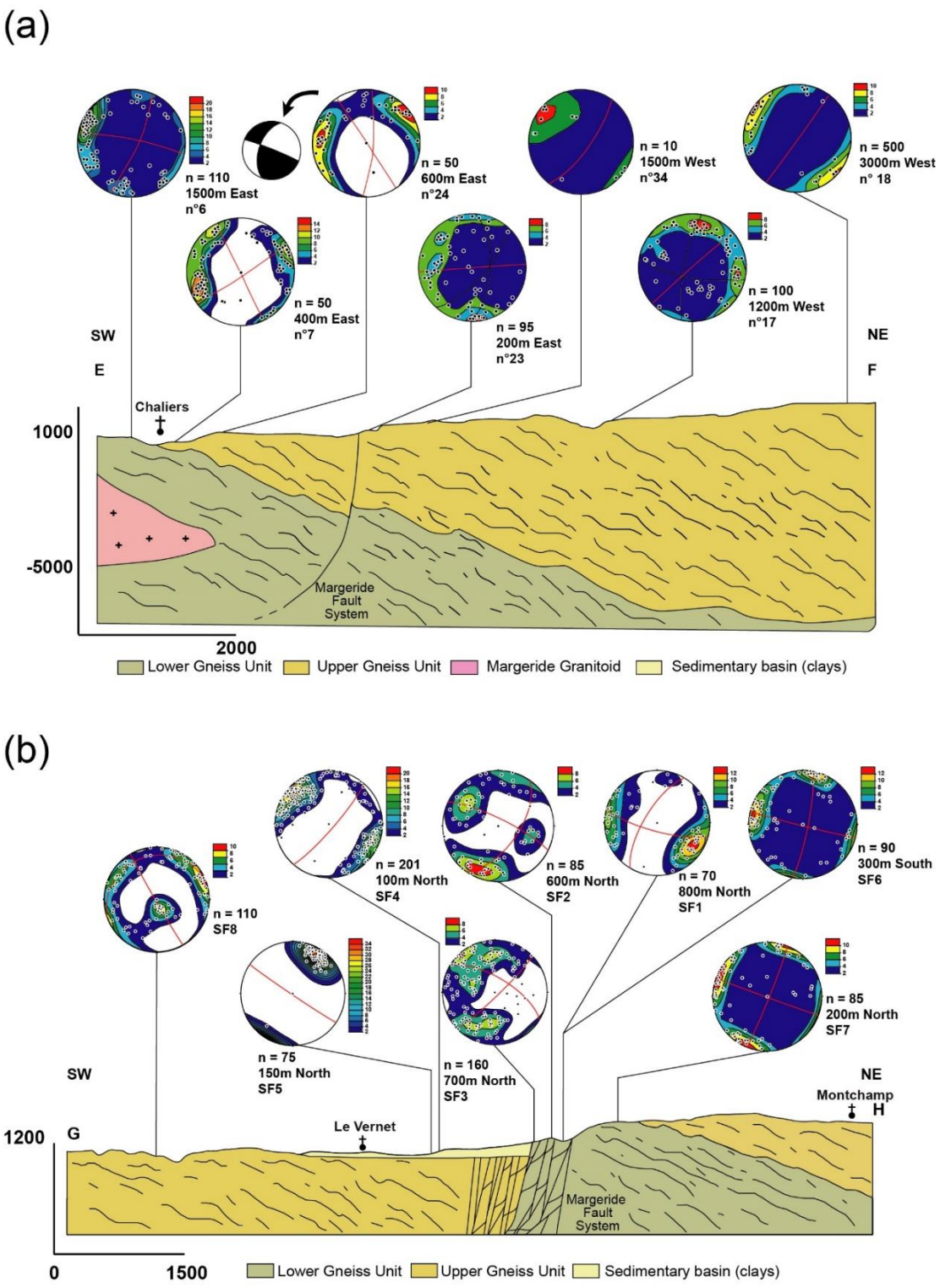

Figure II.15: (a) Geological section crossing the Chaliers Basin. (b) Geological section crossing the Saint Flour Basin. All stereographic projections are in an equal area lower hemisphere. For (a) and (b), both scales are in meters. All Kamb contours in standard deviation. Principal stress tensor was calculated by using FaultKin software.

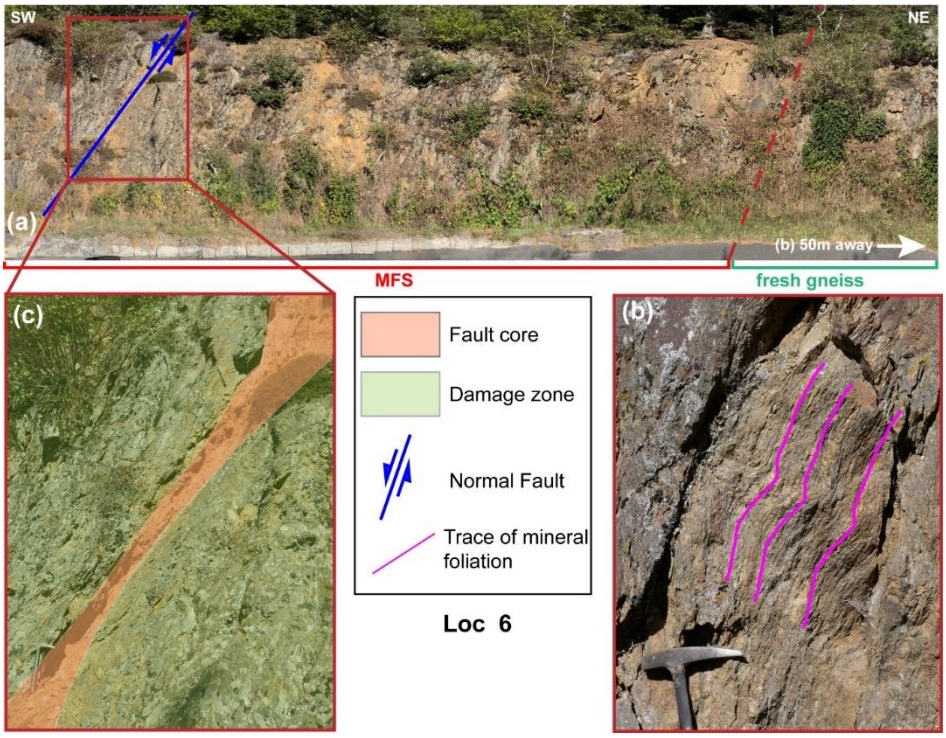

Figure II.16: (a) Roadside section of the eastern border of the MFZ, East of the Saint Flour graben, depicting the transition from the fresh gneiss with a strongly westward dipping foliation (b, 50m away from the view) to a damaged and altered zones (Loc6, GPS coordinates : 45.0534, 3.1797, location in Figure 1d). (c) Youngest normal, west dipping, faulting event crosscutting the locally mylonitized gneiss.

Figure II.17: Field views of the fault core of the MFZ, East of the Saint Flour graben, composed of isolated lenses of fractured gneiss lenses embedded in an altered breccia (Loc7, GPS coordinates: 45.0533, 3.1604, location in Figure 1d).

Regional fault density

The fault density distribution complements the outcrop scale fracture analyses performed along the four main geological sections by evidencing regional scale major fault zones.

In the MGC, low to moderate fault densities domains form N140E trending faults closely parallel to the MFZ and distributed over the granitic massif (Figure II.18). An exception comes from the Chaudes-Aigues area, 20 km. South-West of our study area, where the fault density is very high forming also a N140E trending lineament but that propagate northwestward in the LGU near Chaudes-Aigues, a city known for its hot springs swarm (De Goër de Herve and Burg 1991). It should be noticed that the fault density remains low along the trace of the MFZ, which is an additional argument for a thin core zone forming this segment emplaced in the MGC.

The second domain comprising moderate to high fault density is formed by the N045E trending contact between the MGC and the LGU (section between Chaudes-Aigues area and Le Malzieu Basin, Figure II.18). On the contrary, East of the MFZ, the contact between the MGC and the basement is not marked by a significant fault density.

In the North-East, the gneissic units show several N045E trending lineaments of moderately fault densities.

Finally, the larger domain formed of very high fault density of faults corresponds to the N120E directed segment of the MFZ bordering the Saint Flour Basin (Figure II.18). Its maximum width is about 2500 meters.

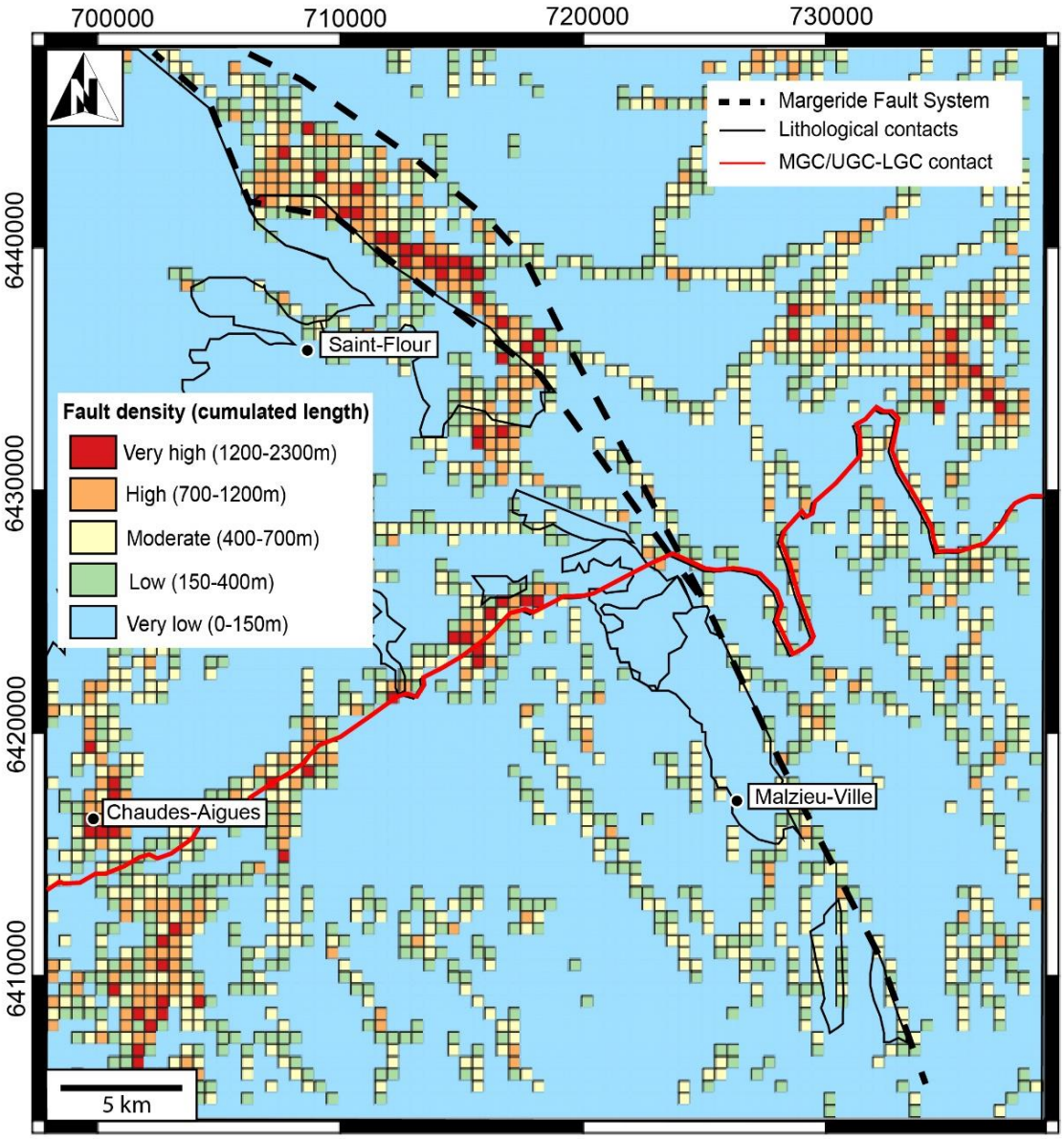

Figure II.18: Fault density map of the study area, the contact between lithologies (black and red lines) correspond to those shown in Figure1. Coordinate system: Lambert 93 – RGF93 EPSG:2154.

Synthesis

By combining field observation and fracture network analysis at outcrop scale with regional fault density analysis we can draw up the structural constraints of the magmatic and tectonic history of the region since the Variscan period that led to the lengthwise change in thickness and orientation of the MFZ.

The southeastern segment of the MFZ is emplaced in the MGC and is composed of a, N140Etrending, narrow fault zone of possibly less than 100m thick (this study, Couturié 1972). This orientation, found over the magmatic body in the form of distributed lineaments of high

fault density (Figure II.18), corresponds also to the direction of the four main feeding zones that opened as transtensional sinistral relays and that lead to the emplacement of the 310-300 Ma old MGC (Talbot et al. 2005). Magmatic fabrics recorded these directions of emplacement with N150E trending lineations on roughly flat foliations (Figure II.11c and II.11d). Consequently, longitudinal primary joints are vertical and strike N140E to N150E. Such longitudinal joints were reactivated, shortly after the cooling of the main granitic facies and until 290 Ma, leading to the successive emplacement of microgranites, then microporphyrite, and finally, quartz dykes (De Goër de Herve and Burg 1991). Stress tensor analysis on conjugate fault system is compatible with a horizontal NW-SE principal stretching axis (Figure II.14). Such direction prevailed during the late carboniferous contemporaneously with dykes' emplacement, but also during the Pliocene, a period during which the region experienced an intense uplift and a subsequent erosion (Ziegler and Dèzes 2007, Daffos et al. 2024).

The northwestern segment of the MFZ is emplaced in the UGU and LGU and is composed of a, N120E trending, up to 2500 thick fault zone (this study, De Goër de Herve and Tempier 1988). De Goër de Herve and Tempier (1988) showed that a N140E trending and vertical, muscovite-rich, mylonitic shear zone affected the gneisses of the two units, before the Visean, i.e. before the emplacement of the MGC. This vertical, sinistral strike-slip fault, continued to operate as a brittle fault, particularly during the Stephanian; leading to a thick fault zone formed of densely fractured and argilised preexisting mylonites (Figure II.17, De Goër de Herve and Tempier 1988).

All these variscan brittle structures were reactivated during the two successive active extension events during the Oligocene and then the late Miocene (De Goer De Herve et al. 1990). Reactivation as normal faults of both N140E trending primary joints and similarly oriented late variscan faults in the granite together with reactivation of the thick fault zone in the LGU-UGU led to the subsidence of the four half-grabens. These normal movements along west dipping faults, to the east, and evidence of quasi stratigraphic unconformable contact on the underlying granite, along western edges. To explain this geometry, Couturié (1979) and De Goer De

Herve et al. (1990) proposed a listric geometry of the eastern boundary faults of the Basins, which are themselves subsiding in a "Roll-Over" fashion (Figure II.14). Change in attitude of the flat lying joints near le Malzieu graben is an additional evidence for a "Roll-Over" rotation of about 12° (Figure II.13). Finally, during the Mio-Pliocene compressive recession (Merle and Michon 2001), N40 trending fractures played as vertical relays leading to the present-day "piano key" geometry of the grabens along the MFZ (Couturié 1979, De Goer De Herve et al. 1990).

The high density of faults (Figure II.18) and the various reactivations of fragile structures indicate that the MFZ could have a high permeability value. Several studies have shown that the permeability of fault zones can reach values of the order of 10^{-13} m² and ever more (Neuzil et al. 2019, Scibek 2020). In our study we will therefore use a range of values from 10^{-15} m² to 5 10^{-14} m².

The MFZ, that comprises a southern N140E trending, thin fault zone, branching to the northwest to a 2500 m thick fault zone represents a study case of crustal fault zone with lengthwise change in thickness. The influence of this geometry on the thermal regime and upward fluid transfer is approached by numerical modeling.

Numerical modeling

The entire numerical procedure has been previously tested with several benchmark experiments, including the 3D benchmark tests of Magri et al. (2017), as detailed in Guillou-Frottier et al. (2020).

Sensitivity analysis

A series of numerical experiments has been performed with different fault zone thicknesses (100 to 2500 m) and different fault zone permeabilities. Temperature field, positive thermal anomalies (defined as the excess temperature when compared to the conductive regime), velocity field, and convective patterns, are recorded.

The value of the maximal thermal anomaly depends on the thickness of the fault zone (Figure II.19a). The optimum thickness (1000 m) for achieving the highest thermal anomaly value (55 °C) is not the largest since, the value reached for a fault zone thickness of 2500 m is 52 °C. However, if we compare the temperature anomalies produced at the same depth (1000m), this time it is the thickest fault zones that generate the highest values: 48 °C for 2500 m compared with 35 °C for 500 m (see dashed red line in Figure II.19a). The impact of thickness is directly observed. For a fixed permeability value (K), for example at K = 3 10^{-14} m² (star symbol in Figure II.19a), the temperature anomaly values produced are not the same. Thickest faults, over 1000 m, produce higher anomaly values than thinner faults. At low permeabilities (7 10^{-15} m², circle symbol in Figure II.19a), the anomaly increases with thickness. On the contrary, for higher permeabilities (5 10^{-14} m²), an optimum thickness of 1000 m appears. For thicker or thinner faults, the anomalies decrease. Thick fault zones will be more favorable for deep anomalies generating higher temperatures than superficial anomalies in thinner fault zones.

The depth of the 150 °C isotherm also varies with the fault zone thickness (Figure II.19b). For low permeability (5 10^{-15} m²), heat conduction dominates, and the depth is common to all models. When the permeability value increases, two distinct behaviors emerge for thin faults (100-1000 m) and thick faults (1700-2500 m). In the first case, the depth of the 150 °C isotherm decreases as permeability increases, reaching 3800 m for a fault zone thickness of 500 m.In the second case, convection operates, cold downwellings take over upwellings and causes this boundary to deepen below 4000 m. It appears that a thick permeable zone favors the downward flow of cold fluids and causes the fault zone to cool. The variation in thickness shows that for fine faults (< 1000 m), a rise in the 150°C isotherm will lead to a high increase in the permeability of the fault zone (3 10^{-14} m²). The same phenomenon can be observed for thick faults, but with permeability values an order of magnitude lower.

For a better understanding of the different thermal regimes, the fluid flow velocities have been recorded (Figure II.19c). Velocity values depend on the width of the fault zone. The greater the thickness, the higher the maximum velocity. When h = 2500 m, velocities reach 9 10^{-8} m s^{-1}

compared to 10^{-11} m s^{-1} for 100 m or 2 10^{-8} m s^{-1} for 500 and 1000 m. Two behaviors again stand out in terms of the increase in these velocities as permeability increases. The finer fault zones (500-100 m) show a curve that can be divided into two areas: a first part with a small increase from 10^{-15} m² to 7 10^{-15} m² and a second part with a higher slope up to 5 10^{-14} m². For thicknesses greater than 500 m, the curve splits into several portions and leads to higher values. Once again, reasoning with a fixed permeability directly highlights the role of thickness variation. For a permeability of 10^{-14} m², a 500 m fault zone has a velocity of 10^{-11} m/s compared with 5 10^{-8} m/s for a 2500 m fault zone. This difference, of three orders of magnitude, indicates that at a fixed permeability, the thickness of the fault zone is crucial for the establishment of a convective regime.

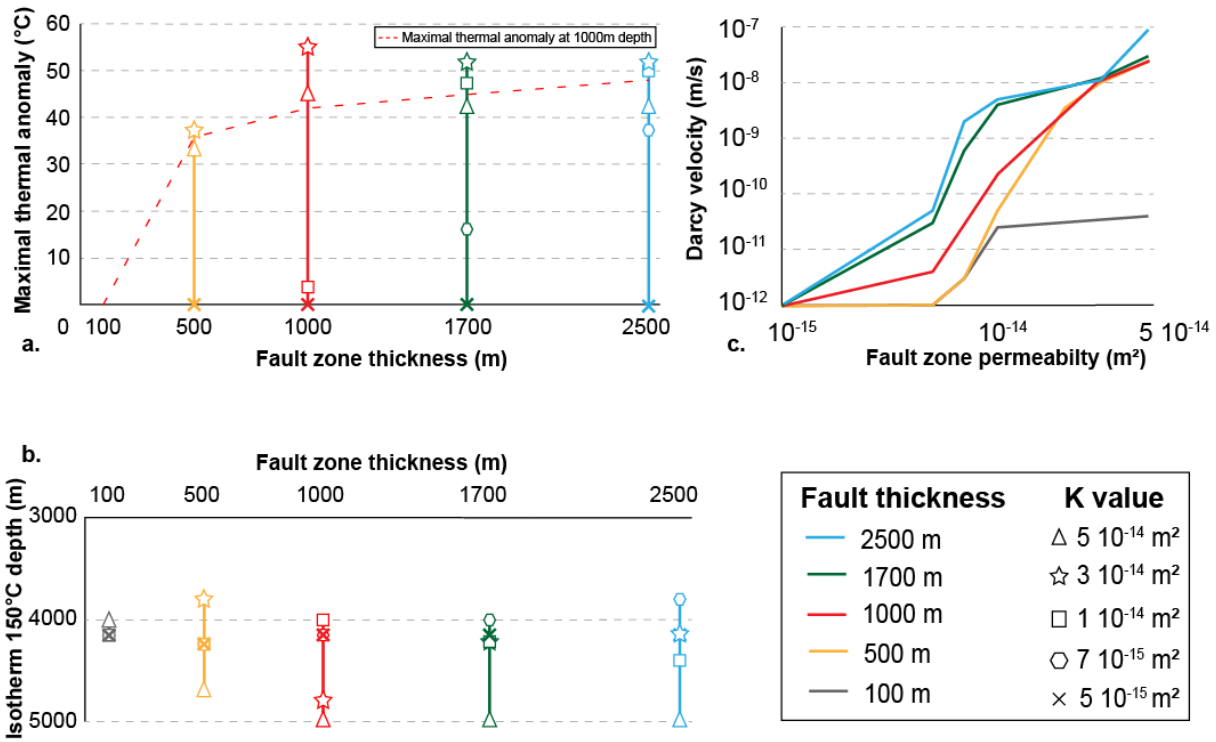

Figure II.19: Graphs showing the impact of variations in the permeability K and thickness of the fault zone on the value of the maximum thermal anomaly (a), the depth of the 150 °C isotherm (b) and fluid flow velocity (c).

The results of the various models can be divided into one conductive and two convective regimes. The first group represents the configurations leading to a conductive regime (green area, in Figure II.20). The associated fluid flow velocities are very low, around 10^{-12} m s^{-1}, and isotherms remain horizontal (no temperature distortion).

When permeability increases, fluid velocities also increase, and thermal convection is triggered. The first convective regime corresponds to a steady-state single upwelling (II, yellow area, in Figure II.20). As described in other studies (e.g. Zhao et al. 2003; Guillou-Frottier et al. 2020) the upwelling zones exhibit a triangular-like pattern. Fluids rise in the center of the structure and are bordered by two large downwellings on each side. Fluid circulation velocities are higher than in the previous case, between 2.5 10^{-9} m s^{-1} (500 m thickness) and 9 10^{-8} m s^{-1} (2500 m thickness). Positive maximum thermal anomalies range from 38 °C (500 m) to 55 °C (1000 m).

The second convective regime presents several convection cells evidenced by several zones of upwelling (III, orange area, in Figure II.20). This regime has already been highlighted in other studies. As permeability increases, the wavelength between the upwelling zones decreases (Guillou-Frottier et al. 2020). In our case, two upwellings appear and move laterally, along the longitudinal direction (transient regime). In the case illustrated on bottom-right of Figure II.20 (fault zone thickness of 500 m and permeability of 3 10^{-14} m²), two upwelling zones are visible, bordered by downward flows. Here again, the upwelling exhibits a triangular like pattern, as described in Guillou-Frottier et al. (2020). Since permeability decreases with depth, cold dense fluids move more easily from the most permeable zone (surface) and become predominant over hot upwellings, which start to rise in the less permeable zone (bottom). This phenomenon gives them a triangular shape, with upwellings edges “eroded” by cold downwellings. One consequence is that the generated temperature anomalies have lower values. Fluid flow velocities vary between 1 10^{-8} m s^{-1} and 9 10^{-8} m s^{-1}.

The boundaries between the different domains are not horizontal lines, indicating that these regimes are directly dependent on the thickness of the fault zone. The boundary between the conductive regime and the first convective regime decreases with thickness (between blue and yellow areas, Figure II.20a). At a fixed permeability, the development of convection is favored when the thickness of the permeable zone increases.

For fine fault zone (< 500 m), the establishment of a type III convective regime appears to be directly affected by the variation in thickness. For a permeability of 5 10^{-14} m², a fault 100 m thick will be in a conductive regime, one 250 m thick in convective regime II and one 500 m thick in regime III. However, beyond 500 m, the limit seems to be guided more by permeability. As the thickness increases, the permeability value that allows the third regime to be reached also increases. For a fixed permeability value, the limit becomes almost horizontal (between orange and yellow areas, Figure II.20a). A wider range of stability is observed, for thickness greater than 500 m, leading to single steady-state upwelling (yellow area, see Figure II.20a). For fault zones less than 250 m thick, conduction is the dominant regime (for realistic permeabilities). Indeed, for thin fault zones, convection occurs only for high permeability (e.g. for h = 100 m, K = 5 10^{-13} m²) in transient regime, so that the third regime is favored. Furthermore, a stationary system is difficult to achieve, which leads directly to the third regime (orange area, Figure II.20a).

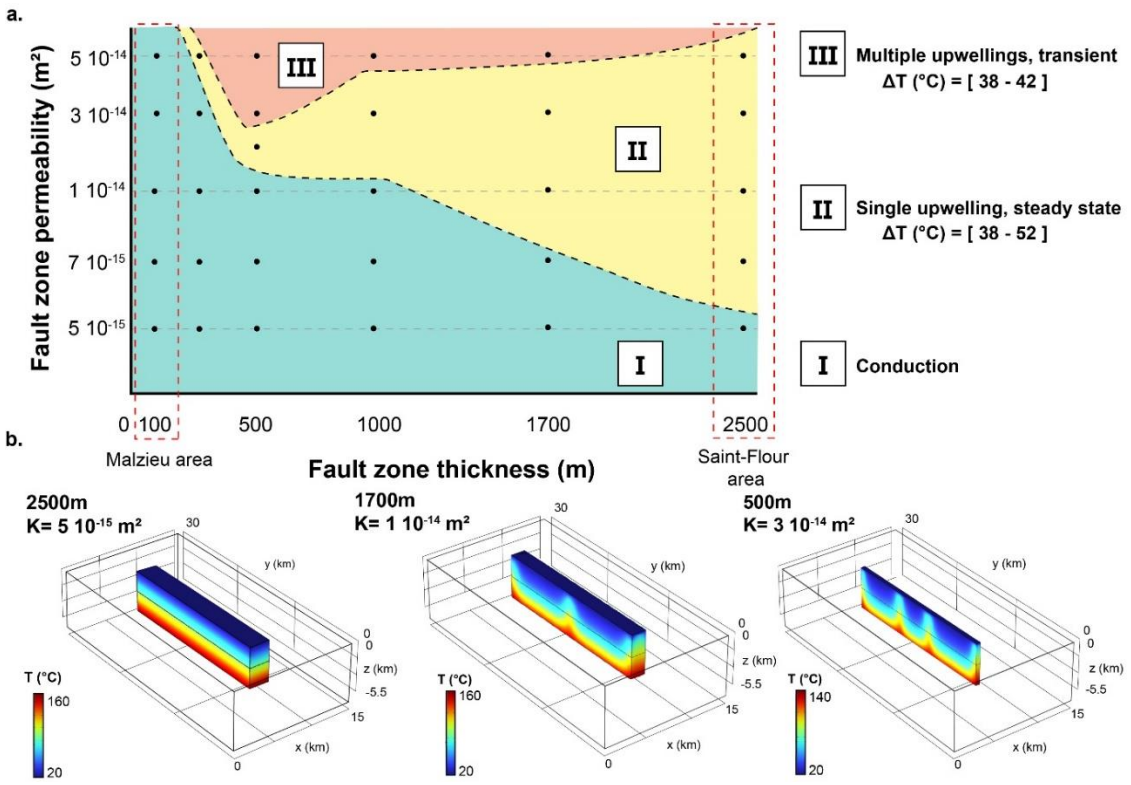

Figure II.20: (a) The three convective regimes as a function of fault zone thickness and permeability, black dots represent all the models carried out in order to constrain the regime boundaries (dashed black lines). (b) Three examples of the different regimes as defined in (a). All these experiments have been performed with a fault zone length L equal to 20km.

Models with a lengthwise variation of the fault zone thickness

Field evidence as well as fault density distribution (Fig 10) underline the north-westward thickening of the MFZ. Numerical models of Figure II.21 include a lengthwise varying thickness, from 70 m (bottom right of the fault zone) to 2500m (upper left). The maximum fault zone permeability K_{F0} equals 8 10^{-15} m² in Figure II.21a, and 1.5 10^{-14} m² in Figure II.21b. In addition to temperature field illustrated as in Figure II.20, positive thermal anomalies ΔT are represented by isosurfaces separated by 10 °C (see colour bars). In both experiments, there is no thermal anomalies in the thinnest parts of the fault zone, where isotherms flatten (conductive regime). On the opposite, a thermal anomaly is always present around the thickest part of the fault zone (convective regime). Its amplitude can vary with time but not its location. Experiment of Figure II.21a reaches a steady-state 1.5 Myr after the beginning of the experiment. On the opposite, experiment of Figure II.21b exhibits a quasi-periodic behaviour, where thermal anomalies migrate laterally towards the thinnest zones (black arrows). At t_0 + 500 kyr, three thermal anomalies are visible, including the fixed one around the thickest part of the fault zone. With time, the central one decreases in amplitude and disappears, while the third one increase in amplitude, as shown at time t_0 + 2 Myr. The dashed black arrows indicate the new incipient upwelling, which will also migrate toward the thinnest zone. Top views on the right of Figure II.21b illustrate the thermal diffusion of the anomaly within the embeddings.

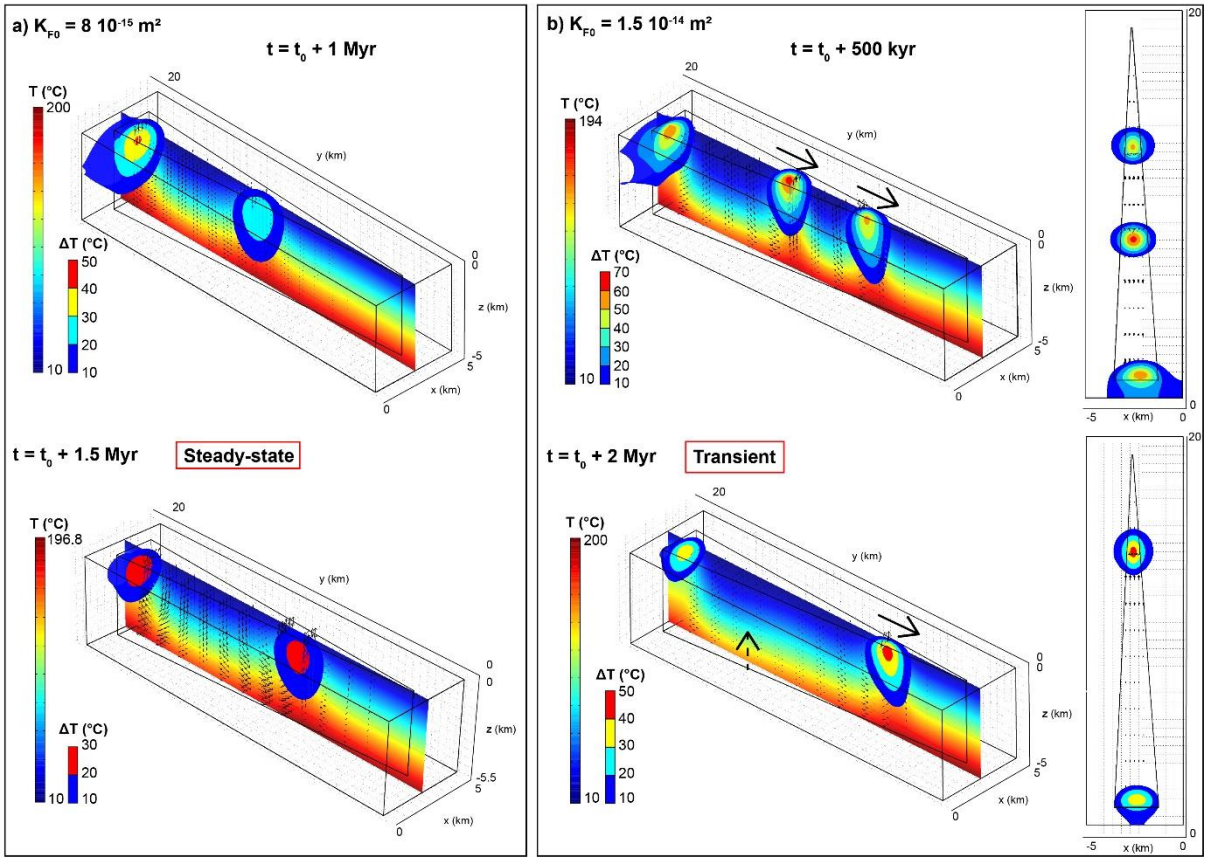

Figure II.21: Results of the models with a lengthwise variation of the fault zone thickness for two permeabilities.

Discussion

Exploration using a multidisciplinary approach

The aim of this work was to study the effects of the progressive thickening of a simple fault towards a thick fault zone on the circulation of fluids at depth. Structural measurements in the field were used to constrain qualitatively the intensity of fracturing and the thickness of the fault zone. These data have been used directly in the 3D dynamic models to demonstrate the direct impact of thickness on convective dynamics. Our numerical results indicate that deep anomaly values (1000 m depth) increase with thickness (Figure II.19c). Furthermore, thick fault zones (> 500 m) are more likely to host stable convective systems. Finally, the latest models have demonstrated the existence of a positive temperature anomaly (Figure II.21), whatever the permeability used, at the thickest end of the fault zone. In order to achieve full coupling between field exploration and dynamic modelling, the measured orientations would still have to be used in a model incorporating the current stress regime of the study area. Such models,

which are beyond the scope of this study, need a thermo-hydro-mechanical coupling approach (e.g. Duwiquet et al., 2021, 2022).

Controlling fluid fow factors depend on the thickness of the fault zone

As expected, the higher permeability leads to an increase in the number of upwelling in the fault zone (Rabinowicz 1998, Guillou-Frottier et al. 2020). The first boundary shown in Figure II.20 between the conduction domain and a single upwelling (blue and yellow areas) seems logical since the increase in width coupled with the increase in permeability is favourable to the development of convection (Magri Malkovsky 2016). Presented as the parameter governing fluid flow, permeability does not appear to be the only controlling parameter for the regimes shown in Figure II.20. In fact, as the width of the fault zone increases, so does the yellow area represent stable convection. Indeed, it appears that a thick fault zone allows the development of steady-state convection. We might therefore assume that fault zones less than 500 m thick are mainly governed by permeability, but that this is no longer true for thicker fault zones.

Edge effects and transient regime

Concerning the transient aspect of the third regime (zone in red, Figure II.20), this migration of upwelling zones appears to be due to the dimensions of the fault zone. Indeed, different lengths of the fault zones have been tested (L = 15, 20, 50 km) and edge effects have been observed. When fault zone length is compatible with the convective wavelength associated with a given permeability (e.g. Guillou-Frottier et al., 2020, their Figure 1), then a steady-state regime establishes. If the length of the permeable zone and the wavelength of the upwelling zones are not compatible, the convective pattern is not stable and the upwelling migrates laterally towards the thinnest parts of the fault zone, then disappearing and followed by a new incipient upwelling around the center of the fault zone, which will migrate with time (dashed arrow in Figure II.21b). It is however important to point out that whatever the convective regime, the thermal anomaly located at the thickest part of the fault zone does not migrate and remains fixed in space and time.

Geothermal potential of the Margeride Fault Zone

The advantage coupling field observations and modelling (define the brittle of the study area to determine the state of permeability and ultimately use thermal modelling) is that it can be used to provide assistance before the exploration phase, making it possible to predict areas with high geothermal potential. The use of numerical models has already confirmed the possibility to identify exploitable areas independently of other exploration methods, as for the Rittershoffen area, close to the Soultz-sous-Forêts geothermal site (Upper Rhine graben, France) (Guillou-Frottier et al. 2013). In our case we have shown that thick fault zones are more likely to develop stable convection leading to high temperature anomalies (Figure II.20). Models with a lengthwise thickness variation indicate that a positive temperature anomaly persisted at the thick end of the fault zone. The thin end is not affected by convection movements. Following these results, a positive temperature anomaly of 50 to 70 °C could be expected in the thickest part of the fault zone, or in the intermediate part at a depth of around 1000 m. These models tend to show that high-temperature geothermal exploitation would be unsuitable in view of the temperatures reached (between 100 and 120 °C at a depth of 1000 m). However, the results obtained here are encouraging, given that a temperature of 10 °C is imposed at the surface of the model (see Boundary Conditions section), which could considerably minimise the value of the anomaly due to the imposed cooling.

Studies such as those by Eldursi et al. (2023) and Duwiquet et al. (2022) have also shown that the orientation of the fault zone fundamentally influences fluid circulation. According to Mazabraud (2005), the zone is currently undergoing NW-SE compression, leading to the opening of similarly oriented structures. The northern part of the MFZ (Saint-Flour) therefore appears to be favorably oriented (N120E on average), unlike the southern part (Malzieu, N150E). Finally, the presence of the Font-de-Vie Spring at Coren-les-Eaux is an important indicator, since it indicates a reservoir at a depth of over 220 °C (Fouillac 1983).

Our numerical approach applied to the MFZ should be improved by more realistic (stress regime, boundary condition, topography) modelling. Nevertheless, it indicates that geothermal

exploration should focus primarily on the north of the study area (Saint-Flour), while the south of the zone show a very low potential (Malzieu).

Conclusions

The MFZ is a natural laboratory, enabling us to study a range of processes that have a direct impact on fluid circulation. Using this example, it was possible to quantify the impact of the thickness of a fault zone on fluid circulation and convective regimes. Thin fault zones will be more likely to produce multiple upwellings with weaker, shallower anomaly values. At the opposite, it will be more common to obtain a single higher and deeper anomaly in thick fault zones. It therefore appears that in addition to permeability, the thickness of the fault zone becomes a fundamental parameter to be taken into account. Last, we showed that, for fault zones with longitudinal thickening, the thickest extremity will always be affected by a positive temperature anomaly.

This method has identified a potential area for more extensive exploration in crystalline basement. However, some elements still need to be included in dynamic models. The current stress field is not taken into account, nor is the change in orientation of the MFZ. Finally, the fault zone is marked by a major jump in topography (around 600 m) that could influence fluid circulation. These new elements will help to refine the geothermal potential of the study area.

Chapter III: Inherited structures and hydrothermal upwelling drains: typology of reactivated Variscan faults.

III. Inherited structures and hydrothermal upwelling drains: typology of reactivated Variscan faults

III.1 Introduction

Fault density around Chaudes-Aigues thermal springs is very high. In fact, they are located at the intersection of three fault zones, in order of importance, N150E, N50E and N0E (Gibert et al., 1975; De Goër de Herve, 1991). These directions are underlined by the presence of microgranite veins, especially to the west of the town, and quartz veins. Historically, these microgranite veins have been proposed as the main drains in the system, allowing deep hot water to reach the surface quickly (Launay, 1906; Aubignat 1949; Vasseur et al., 1997). Only one study, made by Gibert et al., (1975), described precisely the brittle architecture of this area. He pointed out the multiple reactivations of these structures over geological times and indicated that the intersection of the two major fault zones N050E and N150E would create areas of concentrated fracture and high permeability which is directly linked with the existence of the 30 hot springs (Gibert et al., 1975). However, there are still uncertainties as to the identification of the ascending drains.

This chapter, corresponding to a manuscript submitted to the Journal of Volcanic and Geothermal Research, is dedicated to the analysis of the brittle structuration of the emergence area. The first step is to characterise the fault and fracture networks in order to determine the main fault families and their dynamics over time in order to identify potential reactivation. A typology of the various faults in the vicinity of the town was drawn up in order to identify potential drains. A gravimetric campaign was carried out to characterise the geological structures located directly beneath the springs studied. The aim of this approach is to obtain a precise geometry and distribution of the formations at depth, in particular the location of the Margeride granite, the Couffour granite and the lower gneiss unit. These results will make it possible to assess the lithology likely to host a potential reservoir.

III.2 Contribution of this chapter

A simple analysis of fault density across the MGC identified two highly fractured zones: Chaudes-Aigues and Saint-Flour with the MFZ (Chapter 2). This analysis highlighted the presence of major faults N140-150E, forming fault zones several kilometres long, concentrated in particular around the Chaudes-Aigues and La Chaldette springs.

Analysis of the lineaments shows a distinct structural segmentation between the gneissic metamorphic units to the north and the MGC to the south. The lineaments of the MGC are longer, dominated by a N140E orientation, while those of the gneissic units are more varied in distribution. The topography of the MGC plateau is less irregular, with the exception of the N040E-trending valley of the River Bès near La Chaldette.

Microstructural analysis shows that the fractures measured are predominantly vertical, with two main populations combined: N020E and N140E in the LGU and Couffour units. In the MGC, the main fracture has a N170E orientation, similar to that observed near Chaudes-Aigues.

The faults near the springs can be divided into three groups. Firstly, the N030E-N050E faults, characterised by, initially ductile, thick damage zones. These faults were reactivated several times since the late variscan period in a brittle context with clearly identified zones of fluid circulation

Gravimetry highlights the complex geometry of the MGC, with the north termination of the granite body close to the surface below Chaudes-Aigues. The geometry of the Couffour granite has been imaged for the first time, although its density remains very close to that of the MGC.

In the light of these different results, it appears that Chaudes-Aigues is a system mainly controlled by the heritage of Variscan faults. The N050E ductile faults, which were inherited and then reactivated, are thought to be the main upwelling channels for the thermal waters. These deep and thick brecciated faults would intersect the roof of the granite just below. This configuration suggests that the MGC could act as a hydrothermal reservoir. One of the reports

from the boreholes used to supply the thermal baths mentions the presence of a mylonitised fault just below the spring (source du Ban). The hypothesis that the town is located on a large N050 fault is supported by the orientation of the valley, as the Remontalou is itself deviated from its N150E direction at this point. The zone of intersection with the N150E faults further reinforces the permeability of the system

The microgranite veins were identified as the main drains of the system (Vasseur et al., 1997). However, only a few potential traces of past hydrothermal circulation along N030E fractures have been identified in the microgranite veins reenforcing the assumption that N050E faults are the major drains.

III.3 Long-lived brittle reactivation of crossing fault networks enhancing upwelling hydrothermal systems: The case study of Chaudes-Aigues spring swarm (submitted manuscript)

Long-lived brittle reactivation of crossing fault networks enhancing upwellings in hydrothermal systems: The case study of Chaudes-Aigues spring swarm

Emmy Penhoët[1,2], Laurent Arbaret[2], Angélie Portal[1], Charles Gumiaux[2], Maxime Picault[1], Albane Canva[1], Béatrice Ledésert[3], Nicolas Maubec[1], Séverine Caritg[1], Laurent Guillou-Frottier[1,2]

Manuscript submitted in Journal of Volcanology and Geothermal Research

1 : BRGM, F-45060 Orléans, France.

2 : ISTO, UMR 7327, Université d'Orléans, CNRS, BRGM, F-45071 Orléans, France.

3 : CY Cergy Paris Université, Géosciences et Environnement Cergy, 1 Rue Descartes, Neuville-sur-Oise, 95000, France

E-mail adresses : e.penhoet@brgm.fr, laurent.arbaret@univ-orleans.fr , charles.gumiaux@univ-orleans.fr, a.portal@brgm.fr, m.picault@brgm.fr, n.maubec@brgm.fr, l.guillou-frottier@brgm.fr

Corresponding author at: Guillou-Frottier Laurent, BRGM, F-45060 Orléans, France.

E-mail address: l.guillou-frottier@brgm.fr

Abbreviations :

Bureau de Recherches Géologiques et Minières : BRGM

Institut des Sciences de la Terre d'Orléans : ISTO

French Massif Central: FMC

Lower Gneiss Unit: LGU

Upper Gneiss Unit: UGU

Margeride Granite Complex: MGC

Microgranite dyke: MGD

SM: Supplementary Material

Abstract

Identifying the structures that allow hydrothermal fluids to rise from a deep reservoir to surface thermal springs is a major geothermal challenge. Faults play an ambivalent role in this process: they can be effective drains or, on the contrary, impermeable barriers, depending on their geometry and their reactivation over geological time. The locations of thermal springs are directly linked to these structures, their architecture and particularly in fault zones intersections. Exploring this variability is essential to constrain the circulation mechanisms in geothermal systems.

The Chaudes-Aigues hydrothermal system, French Massif Central, is a particularly suitable natural laboratory for exploring the relationship between faults and fluid flow. It is characterised by more than 30 thermal springs, some of the hottest in Europe (up to 82°C for the Par Spring), located at the intersection of three Variscan fault zones: N150E, N050E and N00E. These intersections create networks of concentrated fractures, likely to act as preferential conduits for fluid flow. Despite these structural indications, the precise upwelling drains remain poorly identified. This study, aimed at identifying these drains, combines field structural analysis, fault density mapping, lineament analysis and gravity inversion modeling. Fault density mapping reveals a clear contrast across the study area. The southwestern Margeride Granitic Complex (MGC) shows sparse faulting, while its northeastern extent exhibits high fault density in N150E-oriented corridors, particularly near Chaudes-Aigues and La Chaldette. Outcrop-scale fault zone analysis reveals three major types. One of them, made of thick ductile-to-brittle N050E

trending shear zones, assumed to be highly permeable, would be the main upwelling drains of the system. Gravity modeling reveals that the MGC would be located at shallow depth beneath the thermal springs. Altogether, results demonstrate that inherited ductile fabrics, reactivated fault systems, and fracture connectivity exert first-order control on granite emplacement and hydrothermal flow. These findings refine the structural model of the Chaudes-Aigues system and highlight the critical role of tectonics in geothermal fluid circulation. This hydrothermal system illustrates how inherited structures may act either as impermeable barriers or efficient drains, once reactivated, a duality that controls the location and persistence of thermal springs

Keywords

French Massif Central, Chaudes-Aigues, Permeability, Fault reactivation, Fault zone, Hot springs, Fault density, Structural measurements, Gravity profiles

Introduction

Crustal fault zones are critical features in the Earth crust that control subsurface fluid flow (Sibson 1987; Hickman et al., 1995; Curewitz and Karson, 1997; Baietto et al., 2008). Depending on their permeability structure, faults can be either efficient drains facilitating fluid migration or barriers impeding flow. Understanding fault behaviour in relation to fluid flow is crucial for geothermal energy production, hydrocarbon exploration, groundwater management. Studies have shown that key parameters such as structural characteristics : thickness, length or dip (Malkovsky and Magri, 2016; Duwiquet et al., 2021, 2024; Guillou-Frottier et al., 2024; Penhoët et al., 2025a), mechanical features: fault orientation related to stress field (Barton et al. 1995; Mckenna and Blackwell 2004; Faulds et al., 2010; Haines et al. 2016; Roche et al., 2018; Duwiquet et al., 2021), and chemical properties: dissolution, precipitation or sealing (Morrow et al., 2001; Zhang et al., 2008, Ledésert et al., 2010) can affect fluid circulation in a fault zone. All these characteristics have to be considered to understand the interaction between fluid-flow and a fault zone. These parameters could evolve over time and changing geological conditions. Beyond these parameters, the internal structure of the fault zone will directly influence fluid flow. Fault zone permeability is highly heterogeneous and depends on fault zone architecture, which generally consists of a low-permeability fault core surrounded by

higher-permeability damage zones (Caine et al., 1996; Faulkner et al., 2003, 2010). The fault core, often composed of fine-grained gouge and cataclasite or mylonite, tends to act as a barrier to flow, whereas the damage zones, characterized by fractures and breccias, can serve as conduits (Caine et al., 1996; Sibson, 1996; Faulkner et al., 2010; Duwiquet et al., 2021). However, these barriers and conduits behaviours correspond to dynamic processes since fault slip, mineral precipitation or dissolution can affect fault permeability over time (Evans et al., 1997; Eichhubl et al., 2009; Bense et al., 2013).

One mechanism that prevents faults from becoming permanently sealed and allows permeability value to remain high is fault reactivation. Reactivation occurs when stress conditions induce slip along pre-existing fault planes, often breaking mineral seals, dilating fractures, and enhancing fluid migration pathways (Wibberley and Shimamoto, 2003; Micklethwaite and Cox, 2004).

In geothermal or volcanic settings, fault-fluid interactions are further complicated by high temperature and chemically reactive fluid. Elevated temperatures amplify processes such as mineral dissolution and precipitation, which modify fault permeability (Fournier, 1989; Rowland and Sibson, 2004; Fisher and Harris, 2016).

Thermal springs are frequently associated with fault zones that act as drains enabling deep hot fluids to reach the surface (Lowell 1975; Berkowitz 2002; Simms & Garven 2004) and even influence their locations (Faulds et al., 2010). Some studies have shown that they are particularly located at fault intersection (Curewitz and Karson, 1997; Person et al., 2012; Belgrano et al., 2016). These heated fluids can be originated from deep geothermal reservoirs (Vasseur et al., 1997; Taillefer et al., 2018; Duwiquet et al., 2019; Carbajal-Martinez et al., 2024). Furthermore, faults influence hydrothermal circulation by connecting heat sources (e.g., magmatic bodies or radiogenic rocks) with near-surface aquifers, facilitating the emergence of high-temperature springs. The interaction between fault and hydrothermal systems is therefore a key driver in the genesis and sustainability of geothermal systems.

This study focuses on the Chaudes-Aigues hydrothermal system (French Massif Central), a unique natural laboratory characterized by high-temperature thermal springs (up to 82°C for The Par Spring), which are among the hottest natural springs in Europe. Springs are located at the intersection of two major faults sets striking N030E-050E and N120E-150E and which developed during the Variscan orogeny (Gibert et al., 1975; De Goer de Herve, 1991). Gibert et al. (1975) precisely described the brittle architecture of this area and pointed out the multiple reactivations of these structures from Variscan times; the intersection of these two major faults' sets would create areas of concentrated fracturing and high permeability which is directly linked to the of 30 hot springs occurrences (Gibert et al., 1975). Yet, identification of the drains through which the thermal fluids flow is still uncertain up to now. Springs are thought to originate from deep circulation within fractured crystalline basement rocks (De Launay, 1906; Aubignat, 1949; Henou, 1973; Vasseur et al., 1997). Vasseur et al. (1997) proposed that the fluids are meteoric in origin, infiltrating at high altitudes before being heated at depth. A mix between meteoric fluids and a deep circulation would occur at 2.5 km depth with a reservoir temperature of 175-200°C (Cailleaux et al., 1976; Fouillac and Michard, 1981). Numerous vertical microgranite dykes are proposed to be the drains through which hydrothermal fluids rise rapidly and in large volumes (Vasseur et al., 1997).

This study aims to investigate crustal fault zone permeability and its role in controlling fluid flow, focusing on the link between faults sets architecture, stress conditions, reactivation processes, and fluid-rock interactions. The Chaudes-Aigues geothermal system has been developed into Variscan basement units showing a long-lived tectonic history from Variscan times up to date. It is an ideal site to investigate fault-controlled hydrothermal flow, fault reactivation, and permeability evolution. Structural measurements of the brittle structures throughout the granitic and gneissic Variscan units have been systematically performed around the springs. A typology of the faults is established in order to characterize potential drains. To constrain the subsurface structures geometry, four Bouguer anomaly gravity profiles have been surveyed and modelled in the emergence area.

Geological settings

The hot springs swarm emerge in the city of Chaudes-Aigues (central part of the French Massif Central) (Figure 1) and is located in Paleozoic gneissic series (Figure 1c). Few kilometres south outcrops the late variscan Margeride Granite Complex (MGC, Talbot et al., 2005). From the late Paleozoic to present-day, this crystalline basement has suffered successive tectonic brittle events (Blés et al. 1989; Faure et al. 1995; Merle et al. 2023).

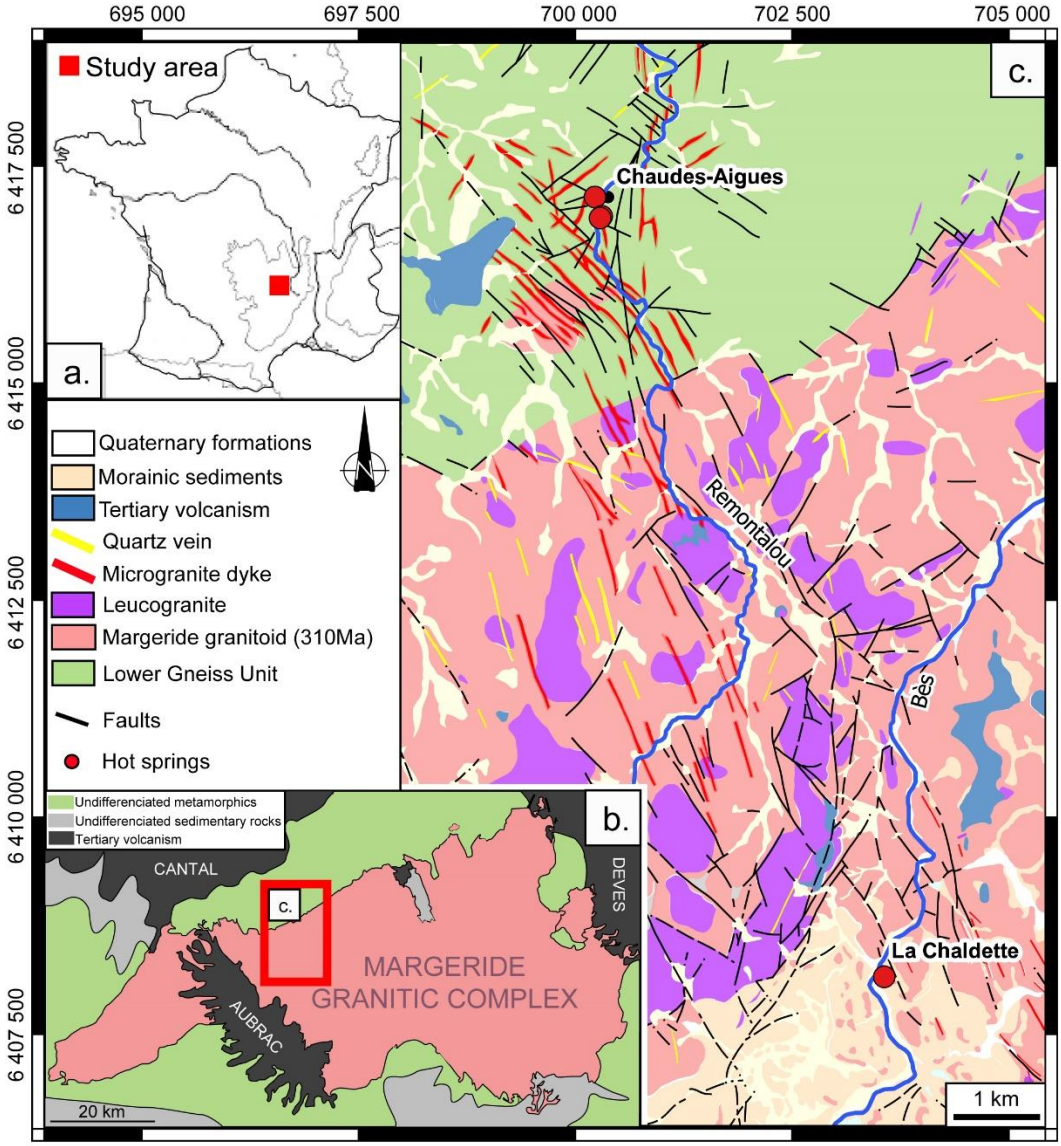

Figure III.1: Geological setting of the study area. (a) location of the study area. (b) simplified geological map of the Margeride Granitic complex modified after Talbot et al. (2005). (c) Simplified map of the study area. Coordinates are in Lambert 93.

Metamorphic units

In the Chaudes-Aigues area, the metamorphic formations are represented by the Lower and Upper Gneiss units (named respectively LGU and UGU hereafter; Vanderhaeghe et al. 2020;

Figure III.1c). The contact between the two units is interpreted as a main shear zone between two stacked nappes (Burg and Matte, 1978). The UGU consists of retrograded granulites while the LGU consists mainly of micaschists, paragneisses and orthogneisses (Penhoët et al., 2025a). The mineral foliation of the gneisses strikes N065E and dips to the Northwest by 33° and is locally folded leading to a secondary foliation plane oriented N105E and dipping to the North by 64° (Penhoët et al., 2025a).

Plutonic massifs

Two plutonic granitic bodies are identified in the studied area: The large Margeride Granite Complex (MGC) occupying 2500 km^2 to the South and the Couffour granite outcropping southwest of Chaudes-Aigues city as a small body (Figure III.1c).

The MGC emplaced 323 ± 12 Ma ago (U/Pb age on monazite, Pin, 1979), during a late carboniferous extensional event, as a laccolith within the LGU and UGU series (Vachette et al., 1979; Couturié, 1979; Faure 1995; Talbot et al., 2005). Its main facies is composed of a porphyritic monzogranite. Talbot et al. (2005) show that Magmatic lineations are homogenously oriented SE-NW and slightly plunging to the NW (Talbot et al. 2005). They proposed that the pluton emplaced along four SW-NE trending feeding zones that played either as pull-apart or extensional gashes linked to subvertical, left-lateral SE-NW striking faults. Besides, the regional gravimetric study performed by Talbot et al. (2005) has constrained the overall 3D geometry of the pluton showing a mostly horizontal footwall at about 5 kilometres depth. However, the geometry of the north-western contact near the city of Chaudes-Aigues remains poorly constrained at the study scale from Talbot et al. (2005).

The small biotite-bearing monzonitic Couffour Granite has been interpreted either as an apophyse of the Margeride laccolite or as a later intrusion (Burg et al., 1991). Bellon and Gibert et al. (1975) determined an age of emplacement around 270 Ma (K/Ar dating method), which supports the second hypothesis. The geometry at depth of the Couffour granite remains unconstrained.

Magmatic and hydrothermal veins

Several vein networks are recognised in the Chaudes-Aigues area. The oldest veins emplacement event identified in the region is represented by brecciated, quartz and pyrite-bearing veins. These mineralized veins of 330 ± 40 Ma in age were mined alongside the Bès river, South-East of Chaudes-Aigues, during the early 20th century (Bellon and Gibert, 1975; Burg et al., 1991).

The most represented vein population is made of, up to 20 m wide and few kilometres long, microgranite dykes, dated at around 265 ± 8 Ma (middle Permian, K-Ar whole rock analysis, Bellon and Gibert, 1975). They crosscut both the MGC and its metamorphic basement (orange lines in Figure III.1c). In the MGC they form a, 17km long by 3 km wide, ~N160E directed swarm (Burg et al., 1991). The thermal spring of La Chaldette is located on the south-eastern branch of this dike swarm (Figure III.1c, De Goer De Herve et al., 1994). Near Chaudes-Aigues, three contemporaneous dyke populations are distinguished on the basis of their respective main orientations (Gibert et al., 1975; Figure III.2): 1. The main population is composed of N130E to N140E striking dykes that represent the north-westward propagation of the dike swarm emplaced to the South in the MGC and that crosscut the Couffour granite; 2.a population made of vertical, N040E to N090E striking, dykes emplaced North of the city; and finally, 3. low dipping, North striking, dykes are associated with the second population, East and North-east of Chaudes-Aigues.

The latest veins population emplaced in the study area is represented by porphyrite and quartz veins (Burg et al. 1991). Porphyrite form rare veins mostly oriented N150E-N170E. Quartz veins are mostly oriented N030E-060E, few of them being oriented N150E-160E. These hydrothermal paleo-circulations date back to extension events from the Triassic to the Upper Jurassic (De Goer De Herve et al., 1994). They are mainly confined to the MGC and do not extend into the metamorphic units. They intersect and may shift the granitic dykes mentioned above.

Late and post-Variscan Brittle history

Regional scale crustal discontinuities

Successive major brittle deformation events affected the study area since late-Variscan (Faure 1995; Daffos et al., 2024). From Namurian to Permian, the region experienced a compressional event, characterized by a progressive rotation of the principal shortening axis, horizontal, from N-S to E-W trending (Faure, 1995). During the N-S compression, a conjugate brittle system composed by N140E-N170E dextral and N010E-N050E sinistral strike-slip faults associated to N080E-N120E thrust faults developed (Penhoët et al., 2025a). These directions were reactivated during the successive emplacement of the three dyke generations (microgranite, porphyrites, and then quartz).

Throughout the Mesozoic, no significant new brittle tectonic activity was recorded in the region (Blés, 1989). However, the yet-distant E-W extension related to the opening of the Atlantic Ocean and Ligurian Sea during the Jurassic may have reactivated pre-existing structures in the study area (Blés et al., 1989; Penhoët et al., 2025a).

During the late Cretaceous and the Paleocene, an intraplate compression phase with N-S horizontal principal shortening occurred, involving a buckling of the lithosphere and reactivation of preexisting crustal discontinuities (Ziegler and Dèzes, 2007; Daffos et al., 2024). The late Variscan brittle structures were significantly reactivated during the Cenozoic (De Goer De Herve et al., 1990). During the Eocene and the Oligocene, the European Cenozoic Rift System developed (Dèzes et al., 2004; Michon and Merle, 2001; Michon et al., 2003). This major event, whose origin remains debated, resulted in a major E-W extensive phase with the implementation of broadly N-S oriented grabens such as the basins located all along the Margeride Fault Zone, East of the study area (Penhoët et al., 2025a). In the meantime, the volcanic activity took place in the region: since the Miocene, post-rift volcanism spreads throughout the region forming three volcanic units: the Cantal stratovolcano to the North-West, and the monogenic basaltic fields of Aubrac to the West and of Devès to the East (Figure III.1b). It is worth noting that in both monogenic volcanic fields, N140E striking Variscan faults were used as drains during the basaltic ascent leading to strombolian edifices alignments (De

Goer De Herve et al., 1994). Since the early Pleistocene, the regional stress conditions correspond to a NW-SE compression, still active nowadays (Mazabraud et al., 2004).

Chaudes-Aigues area brittle network

Gibert et al. (1975) carried out a detailed structural study of the Chaudes-Aigues area (Figure III.2). From 358 to 330 Ma, a ductile to brittle compressive phases resulted in the folding of the gneisses followed by the emergence of two conjugate, N140E-150E and N40-50E striking reverse faults (Gibert et al., 1975). During the Middle Permian, an extensive phase resulted in the emplacement of the above described microgranitic veins. The microgranite dike swarm near Chaudes-Aigues shows three directional families forming a Y-shaped pattern in map view: N140E striking dykes crosscut the MGC, to the south. A main, N120E-striking dykes set crosscut the Couffour granite, to the North, while a secondary, N40E-striking branch propagates in the surrounding gneisses, northeast of the city (Figure III.2). In the later swarm, vertical dykes locally branch with the shallow westward dipping, mainly ~North striking sills emplaced along the foliation of the gneisses. Gibert et al. (1975) suggested that the veins emplaced along pre-existing brittle discontinuities.

Following Gibert et al. (1975), late brittle events are characterised by (i) undated reactivation of North-South faults during a ~N010E compression involving mainly horizontal movements, with a sinistral/dextral inverse component and (ii) an extensive Cenozoic phase reactivating N120E-140E directed faults as normal faults.

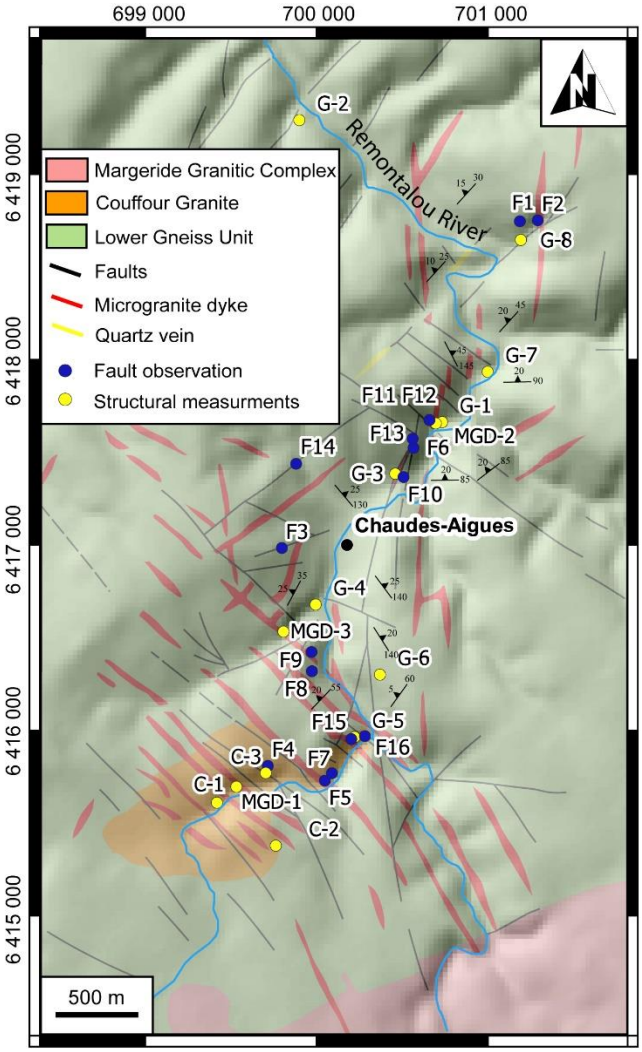

Figure III.2: Geological map of the Chaudes-Aigues area (modified from Gibert et al. 1975). Colored dots correspond to the location of the various observation and structural measurement sites. Lithology at sites is as follow: F is Fault, MGD is Microgranite Dykes, C is Couffour granite, G is Gneiss. Coordinates are in Lambert 93.

Geothermal evidence

The study area is characterised by the presence of a geothermal swarm of thirty hot springs all located in the city of Chaudes-Aigues with the exception of La Chaldette hot spring that emerge 8 kilometres further South (Figure III.1). Temperatures of theses hot springs range from 50 to 82°C. The total flow rate is a constant 500 l/min throughout the year. The Par Spring, one of the hottest in Europe, alone has a flow rate of 270 l/min (Cailleaux et al., 1976; Michard, 1981; Vasseur et al., 1997). The houses are built directly on the springs, most of them being taped for urban heating (Henou, 1973; Bertrand et al., 1977). As a consequence, the spatial relationships between the springs and the fault network are not outcropping. However, Gibert et al. (1975) suggested that the thermal waters flowed upwards along pre-existing N140E

fractures. In addition, Vasseur et al. (1997) suggested that microgranite dykes may behave as main drains. According to different geothermometers, the fluids would reach 200°C (Cailleaux et al., 1976; Michard et al., 1981) at 2 500 metres depth according to Vasseur et al. (1997). A more recent study on geochemical signatures of the Chaudes-Aigues thermal springs indicate a reservoir temperature of 190 +/- 10 °C (Penhoët et al., 2025b)

Methods

Fault Fracture Density based on geological maps

A spatial analysis of fault density is performed on an assemblage composed of 20 distinct published sheets of the French 1:50,000 scale geological map covering the MGC. A regular grid consisting of 500 meters wide square cells was generated. Cumulative length of the faults' trace intersected by each cell is computed and 5 density classes are identified based on the natural break values from the distribution histogram (Jenks algorithm implemented in QGIS; Jenks, 1967).

Lineaments analysis

A regional-scale analysis of lineaments has been performed using Digital Elevation Model (DEM). Data are in raster grid format with a 25 m pixel spatial resolution and a maximum vertical accuracy of 2.5 m (IGN, 2011).

Lineaments can be shown as alignments of topographic highs, lows, or slope breaks. If considering only the ones with a minimum length, these linear shapes, defined as regional lineaments, represent topographical features that can have various geological meanings: fractures, ductile shear zones, cleavage and foliation trajectories, contacts between two lithologies or dikes, depending on the spatial resolution of the DEM used.

In order to define regional lineaments only, it is necessary to focus on linear structures of significant minimum length (several hundred meters).

Lineaments are manually digitized using artificial illumination from four directions (N45, N135, N225, N315) to the DEM raster data with QGIS software (QGIS.org, 2024). The digitizing process was conducted within a zoom range in the GIS software, corresponding to scales from

1: 25,000 to 1:80,000 on the computer display, in order to detect topographic lineaments at a scale compatible with the available 1:50,000 geological maps.

To mitigate user dependency in this manual analysis, a comparison was performed among different operators lineament detections. Only common or similar lineaments (both in location and trend of the segments) were considered for further analysis and interpretation.

Outcrop-scale structural measurements

Micro-structural analysis is performed in 15 sites or stations (GPS coordinates in SM1) in order to estimate the paleo-stress. The stations are spatially spread to include all the lithologies surrounding the springs: LGU, MGC, CG and MGD. According to the size of the outcrops, from 50 to 200 measurements are made in each station. Because of the absence of outcrops, measurements were not conducted in the direct vicinity of the springs, within the city of Chaudes-Aigues. Joints dipping less than 15° were not considered in these locations as they may potentially relate to either exfoliation or unloading joints.

Mineralogical analyses by X-Ray Diffractometry (XRD)

8 hand samples of gouge material filling representative fault cores crosscutting the Couffour gneiss, MGC and Couffour granite were sampled for XRD analyses. The analyses were carried out on the fine fraction (< 2 µm). This fraction was collected by sedimentation, using Stokes' law. The samples were suspended in deionised water and left to settle for 90 minutes. The particles in the top of the suspension were then pipetted and deposited on a glass slide (oriented preparation). Oriented preparations were analysed under two conditions: 1) after being dried at 50 °C and 2) after solvating overnight in an ethylene glycol atmosphere as outlined by Moore and Reynolds (1989). The second step is designed to saturate the interlayer spaces of the swelling clay minerals with ethylene glycol molecules. The basal (00l)-diffraction pattern of swelling clay minerals varies as a function of numerous factors such as the interlayer-cation type. The XRD pattern of the oriented preparations were collected using a BRUKER D8 Advance X-ray diffractometer equipped with a Cu Kα radiation (λ = 1.54056 Å) operating at 40 kV and 40 mA and a fast multichannel LynxEye XE-T detector. Data were

collected from 2.5 to 35 °2θ, with a step of 0.03 °2θ and a count time of 288 seconds per step. Data treatment was carried out using DIFFRAC EVA V7.1 software (Bruker).

Gravity study

Complete Bouguer anomaly

The Margeride granite has already been the subject of several gravimetric surveys (Agshahi 1979; Pétrequin 1979; Van de Meulebrouck 1983; Talbot et al. 2005), but these were aimed at determining the overall geometry of the pluton and did not cover the area of this study. New gravity measurements have thus been performed along three profiles in order to better image the structures at depth beneath the Chaudes-Aigues thermal springs (**Figure III.12**a). A first (L1) is oriented from southwest to northeast and lies on the LGU unit, crossing the Couffour granite and the Chaudes-Aigues area faults' set. Profiles L2 and L3 intersect the contact between the LGU and the MGC, at right angle in map view, in order to image the shape and extent sinking of this major contact. Profile L2 also intersects both the Couffour granite and the Chaudes-Aigues area faults' set. . Profile L1, besides targeting the MGC, enables the geometry at depth of the Couffour granite to be investigated.

141 gravity stations have been measured using two Scintrex CG-6 Autograv™ gravimeters. The stations were spaced approximately 200 meters apart along-strike of the profiles. Measurements were taken during acquisition programs that ran from 2.75 to 9.75 hours. Each program began and ended at a single reference station in Chaudes-Aigues for the two apparatus. At each station, gravimetric readings consisted of at least two 30-second measurements, or more if the instrument was inclined or there was high ambient noise (wind, traffic, etc.). To determine data reproducibility, 18 stations were reoccupied over several programs (i.e., 12.8% repeats). The repeated measurements exhibit a normal distribution centered around zero, with a standard deviation of 0.010 mGal.

The determination of station coordinates and elevation was carried out using differential GNSS systems (Trimble Geo XH6000 with a Zephyr II antenna). The recorded data were corrected through post-processing in relation to a reference station located within 20 kilometers of the

study area (SCDA station of the IGN permanent GNSS network) using GPS Pathfinder Office software (v.5.90-65535). The result is an average accuracy of 0.03 meters in planimetry and 0.05 meters in altimetry.

Standard gravity data processing techniques were applied to derive the complete Bouguer anomaly, incorporating both free-air and Bouguer corrections. A reference density of 2.6 g/cm³ was chosen for the Bouguer and terrain corrections consistent with the basement geology. Terrain corrections were calculated from 50 m to 10 km around each gravity station using the 25 m resolution BD ALTI® DTM (IGN), and from 10 to 167 km using 250 m resampled grids based on the same DTM and the Bathymetric DTM of the Golfe du Lion – Côte d'Azur (Shom, 2015). Gravimetric data were processed using Oasis Montaj software (2024.2).

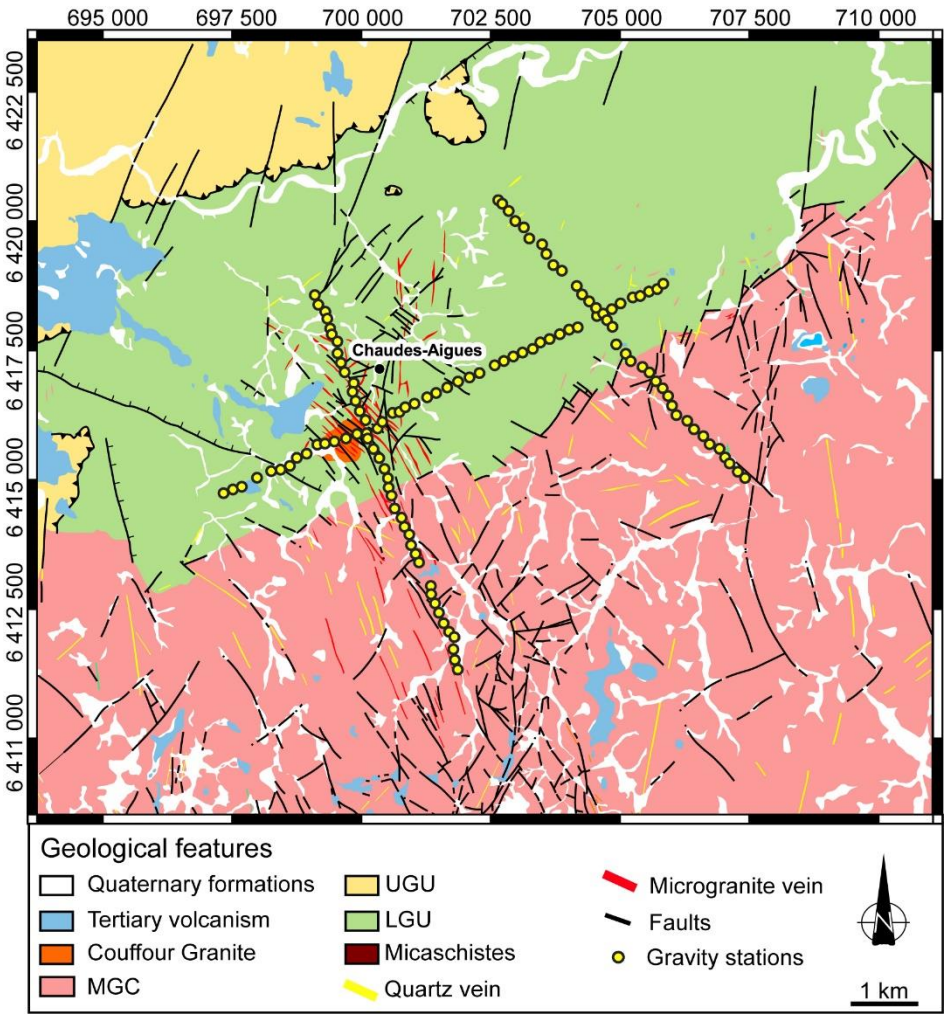

Figure III.3: Location of the gravity stations on the simplified geological map of the study area. Coordinates are in Lambert 93.

2D forward modelling

2D forward modeling involves simulating density distributions in the subsoil section that best fits the observed data along the profile, in this case, the complete Bouguer anomaly (Figure III.12). This modeling process is a practical tool for enhancing subsurface geometrical models by incorporating insights from geological data and additional geophysical methods. The 2D forward models were produced using the GM-SYs module in Oasis Montaj along acquisition profiles L1 (Figure III.13a), L2 (Figure III.13b), and L3 (Figure III.13c). The first model was built on line L1 and is based on the geological model of Talbot et al. (2005) and De Goer de Herve et al. (1994). The L2 and L3 models were then built based on the L1 model while ensuring 3D consistency of the structures.

The models use density values of Gébelin et al. (2006): 2,780 km/m^3 for the UGU, 2,720 km/m^3 for the LGU, 2,750 km/m^3 for the micaschists and 2,640 km/m^3 for the MGC. In the absence of known data, a density of 2,640 km/m^3 was assumed for the Couffour granite, which is equivalent to the density of the MGC.

Results

Brittle structure analysis

Regional Fault Density

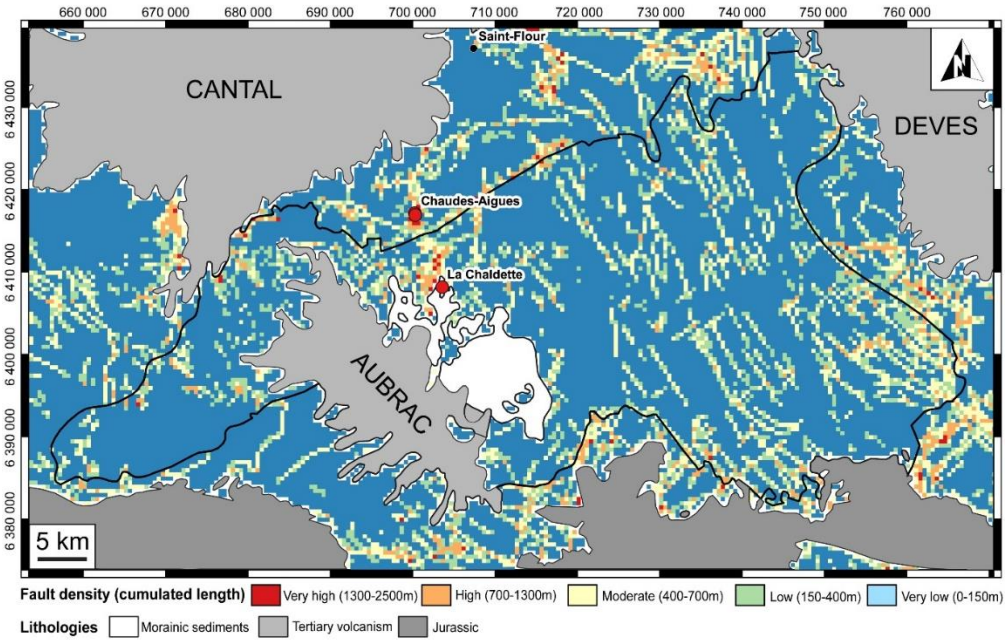

Figure III.4: Fault density map of the MGC and its surrounding gneissic units, the black contour delineates the MGC as shown in Figure III.1b. Coordinates are in Lambert 93.

Most of the MGC exhibits low faults density values, in particular in its southwestern area, West of the Aubrac volcanic province (Figure III.4). To the East, moderate to high faults density areas form N140E striking and distributed lineaments of several kilometres long (Figure III.4). Two, high to very high, and up to 5 km wide, fault density domains are located nearby the thermal cities of Chaudes-Aigues and La Chaldette (Figure III.5a). Both connect to form a large N140E striking lineament.

Two areas of high fault density are also highlighted within the country rocks of the MGC: near Saint Flour city (northern edge of the map), high fault densities correspond to the Margeride fault system (Penhoët et al., 2025a). The second area is composed of two N050E directed lineaments, northeast of Chaudes-Aigues, that overlap with both the contacts between LGU and UGU, and between MGC and LGU (Figure III.4).

Finally, two other high fault density areas are identified in sedimentary covers. One is located south of the Cantal volcanic complex while the second cover a wide zone southeast of the studied area (Figure III.4). They affect the Cenozoic and Mesozoic sedimentary lithologies, respectively.

Regional lineament analysis

Lineament analysis is performed on an area of about 115 km^2 integrating the high-density fault trend between La Chaldette and Chaudes-Aigues swarm springs (Figure III.5b).

Gneissic units

220 lineaments were detected in the UGC and LGC metamorphic units located north of the analysed area (Figure III.5b). The average length of the lineaments is 330 meters while the lineaments exceeding 1000 meters, either oriented North-south or East-west, are rare (Figure III.5c, d). Three main subpopulations are recognized (Figure III.5c). The first subpopulation is composed of N160E to N000E lineaments. A significant number of theses lineaments are located near Chaudes-Aigues (Figure III.5b). The second subpopulation is composed of well-defined N090E lineaments, most of them representing thalwegs of tributaries of the Remontalou river, north of Chaudes-Aigues (Figure III.1). The last subpopulation is composed

of lineaments distributed over the analysed area and whose orientations scatter from N020E to N070E.

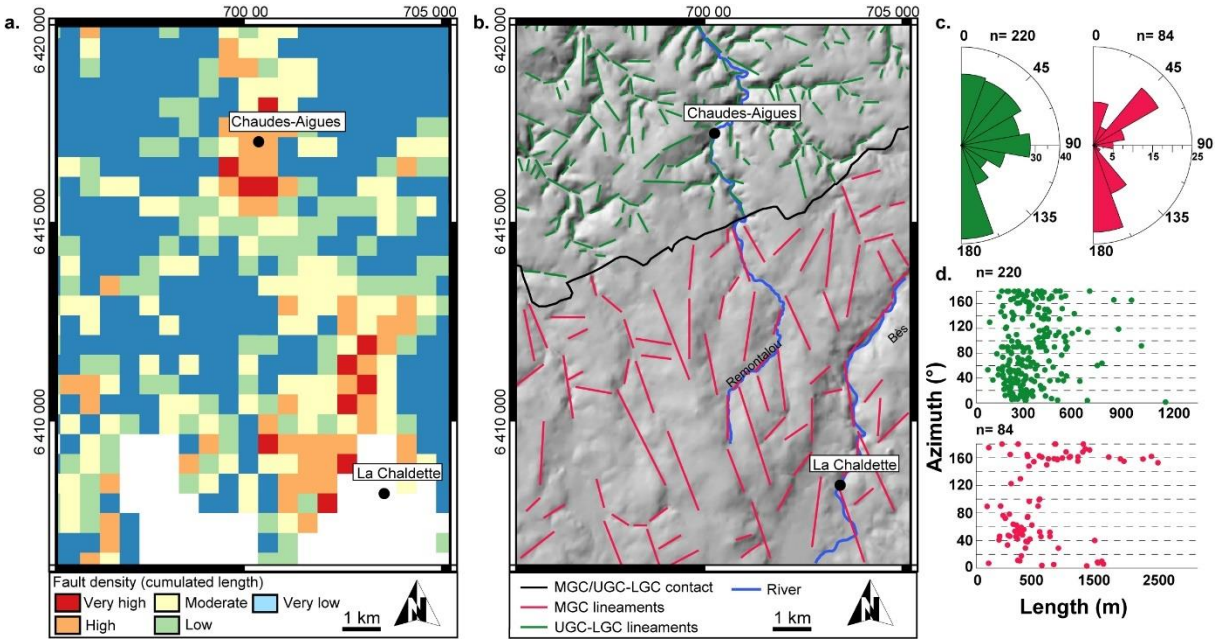

Figure III.5: (a) Fault density map between Chaudes-Aigues and La Chaldette (density classes are the same than Figure III.4). (b) Spatial and (c) azimuthal distributions of the lineaments extracted from the DEM analysis in the La Chaldette – Chaudes-Aigues area. (d) Graphs showing the length of lineaments as a function of their azimuth. The studied area corresponds to the red rectangle shown in Figure III.1b. Coordinates are in Lambert 93.

Margeride Granitic Complex

84 lineaments were detected in the MGC located South of the analysed area (Figure III.5b). The average length of these lineaments is 960 meters, lineaments exceeding 1000 meters are rather common. They are constituted mainly by N140E directed lineaments (Figure III.5d). Two main subpopulations are identified (Figure III.5c). The first subpopulation is composed of N140E to North-South lineaments, and the second one is composed of N040E to N055E striking lineaments (Figure III.5c). These two subpopulations are present and relatively well distributed over the MGC unit. Overall, the topography of the MGC plateau appears less rugged than the one developed in the gneissic units (Figure III.5b). An exception arises near La Chaldette where an alignment of lineaments oriented N040E, locally anastomosing with North-South segments, propagate North-eastward. It corresponds to the well-marked valley of the Bès river (Figure III.5b).

Regional fracture analysis

15 locations distributed in the study area were selected to perform outcrop-scale fracture population analysis in all units, namely, LGU, Couffour Granite, MGC and MGD.

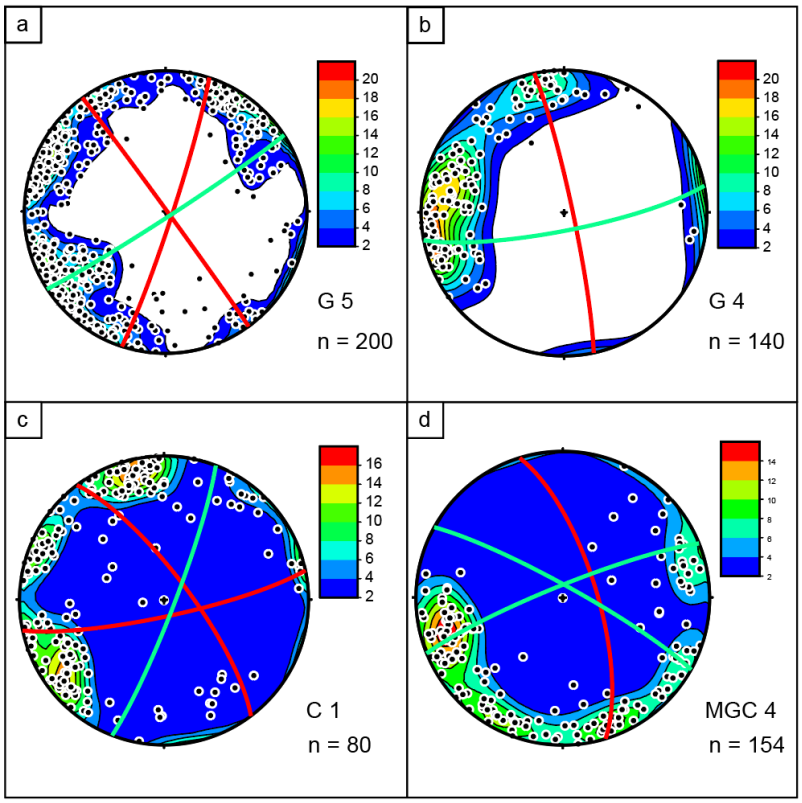

Figure III.6: Orientation distributions of fractures measured in most representative sites (a) G-5 and (b) G-4 in the LGU, (c) MGD-3 in a microgranite vein and (d) C-1 in the Couffour Granite. Red line indicates major plane, green secondary, stereographic projections is in an equal area lower hemisphere, all kamb contours are in standard deviation.

Lower Gneissic Unit

950 fractures were measured in the LGU. With few rare exceptions, most fractures are vertical to steeply dipping (Figure III.6 and SM2, SM3 and SM4). As illustrated by two representative locations/sites (Figures 6a and 6b), two main conjugate populations are commonly found among the N140E directed main fault network crosscutting the Couffour granite (site G5, location in Figure III.2). They correspond to N020E striking fractures associated with N140E striking fractures. Despite the absence of shear sense indicators (striaes) these directions are compatible with a North/North-West to South/South-East directed, horizontal paleo main stress. A third, less represented ~N050E striking population is also evidenced (Figure III.6a). Near the Spring swarm of Chaudes-Aigues (Site G4, location in Figure III.2), only two main

fracture populations are recognized based on their orientation measurements: most of the fractures are oriented N170E while few fractures are oriented N080E (Figure III.6b).

Couffour Granite

Fracture analysis performed in the Couffour granite (Site C1, location in Figure III.2) highlights three fracture populations, two of which exhibiting closely similar mean orientation to those measured further south in the LGU (site G5 described above), i.e. N140E, N020E (Figure III.6c). The third population deviates from site G5, as this fracture population is, on average, oriented N080E. The minor population in the Couffour granite corresponds to the N020E striking fractures.

Margeride Granitic Complex

The measurements were carried out in the MGC, near La Chaldette hamlet (site MGC4, location in Figure III.2). The fracture network affecting the granite is composed of three population but with a unique principal population characterised by a mean N170E orientation (Figure III.6). This population of fractures has the same orientation as the main population identified in the LGU near Chaudes-Aigues city (Site G4, Figure III.6; location in Figure III.2). Two minor vertical fracture populations are also identified with respective N070E and N120E striking.

Microgranite dykes

Particular attention has been paid on fractures affecting the microgranite dykes as they are commonly considered as the main hydrothermal drains (Vasseur et al., 1997 and references therein). The strike orientation of microgranite dykes emplaced in both the MGC, the LGU and the Couffour granite is computed from the 1:50,000 geological map (De Goer de Herve, 1991) which is based, in the studied area, on the detailed mapping of Gibert et al. (1975, Figure III.2). Four populations are identified: the most represented one corresponds to N150E striking dykes on average (Figure III.7a). Theses dykes are located south of the area, in the LGU at the vicinity of the contact with the MGC, and in the MGC itself (Figure III.2). The second population includes the ~N130E striking dykes on average (Figure III.7a). Corresponding dykes crosscut

the LGU and the Couffour granite, west of Chaudes-Aigues city (Figure III.2). The third population is much less represented but comprises N040E dykes emplaced in the LGU West and North of Chaudes-Aigues (Figure III.7a and 2). These three populations are composed of highly dipping to near vertical dykes. Finally, the last population include North-South directed veins characterized by a moderate dip of about 50° to the West (Gibert et al., 1975). Field observations, in particular near Chaudes-Aigues city, show that the granitic magmas propagated contemporaneously within fractures opened along all the recognized directions as a connected network during a single magmatic event (Gibert et al., 1975 and MGD3 location Figure III.2).

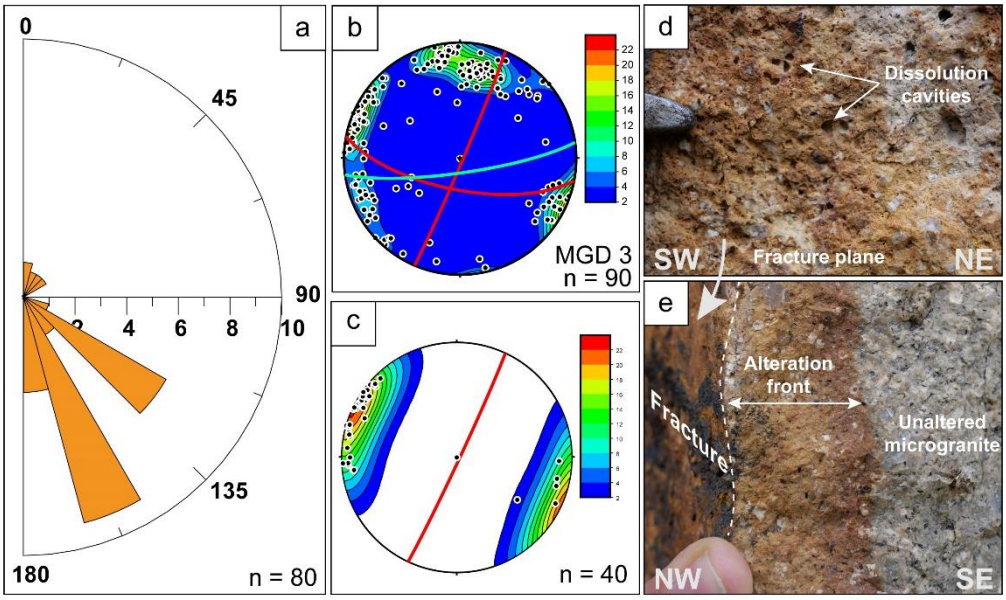

Figure III.7: (a) Azimuthal distributions of microgranite dykes in the study area. (b) Orientation distributions of fractures measured in the MGD, site MGD-3 (see location in Figure III.2). (c) orientation distributions of altered fractures (n=40) measured in all sites of measurement in MGD, red line indicates major plane, stereographic projections are in an equal area lower hemisphere, kamb contours in standard deviation. (d) N030E altered fracture plan in a microgranite vein (MGD-2, see Figure III.2) showing mineral dissolution (e) not pervasive in the volume.

Representative fracture population affecting the microgranite dykes can be observed at the triple junction between the N160E, N130E and N040E connected veins in map view (site MGD3, location in Figure III.2). Two main populations are identified (Figure III.7b). They comprise well-represented ~N030E vertical fractures associated to ~N100E striking, highly South dipping fractures (Figure III.7b). A third second-order population can be recognized with ~N085E striking sub-vertical fractures. The stereographic poles projection of the two last

populations (N100E and N085E) suggests that these two populations may possibly represent a single class of fractures (Figure III.7b).

Paleo-fluids circulations can be observed along some fracture planes but exclusively along N030E striking, vertical fractures (Figure III.7c). Traces of fossilized fluid-rock interactions correspond to dissolution cavities; rectangular shape of which indicating feldspar dissolution (Figure III.7d). Quartz is preserved on the surface of these planes. In addition, extensive traces of iron oxidation affect the fractures concerned. This oxidation forms an alteration front that locally propagates within the microgranite at up to 3 cm away from the fracture (Figure III.7e).

Faults zones typologies

The fault zones are investigated by analysing several characteristics in the field including the thickness and fracturing intensity of damage zones, fabric, the development of clay-filled gouges and the emplacement of sulfur-bearing quartz veins within faults core. Particular focus was placed on the fault network that is well-exposed near the Chaudes-Aigues spring swarm along the Remontalou River. Three main typologies of fault zones, affecting either the LGU or the Couffour granite, have been identified.

Thick ductile to brittle fault zones

The first population of faults comprises several hundred meters thick, N050E striking, vertical fault zones characterised by preserved evidence of primary ductile deformation. These only affect the LGU. An example of such faults is well outcropping to the north of the studied area (F2 fault, location in Figure III.2) fault where a well-developed damage zone of over 200 metres thick is pretty well exposed (Figure III.8a). Several fault cores composed of clay-rich vertical, less than one-meter-thick, gouges are identified over the fault zone (Figure III.8b and c). Some of these gouges wrap around preserved blocks in which gneiss of the LGU protolith exhibit well preserved mineral foliation without any intensive alteration or fracturing (Figure III.8c and d). Foliation may randomly be tilted from place to place due to relative blocks rotation, but most show a highly dipping foliation that is also often folded (Figure III.8d). The mineral foliation of the LGU protolith outcropping in the vicinity of the fault strike N050E with a shallow dip the

North-west. This suggests that the gneiss has suffered a primary intense ductile deformation crosscut before a brittle deformation as the primary folding was overprinted to produce the isolated, less deformed block, most of them being verticalized. Finally, the late event identified in the fault core is represented by the emplacement of a vertical and half-metric, sulphide-rich, quartz-bearing vein (Figure III.8e).

Water seepage is extensively observed over the outcrop, particularly on vertically foliated blocks. This suggests a present-day high permeability of these F2 faults.

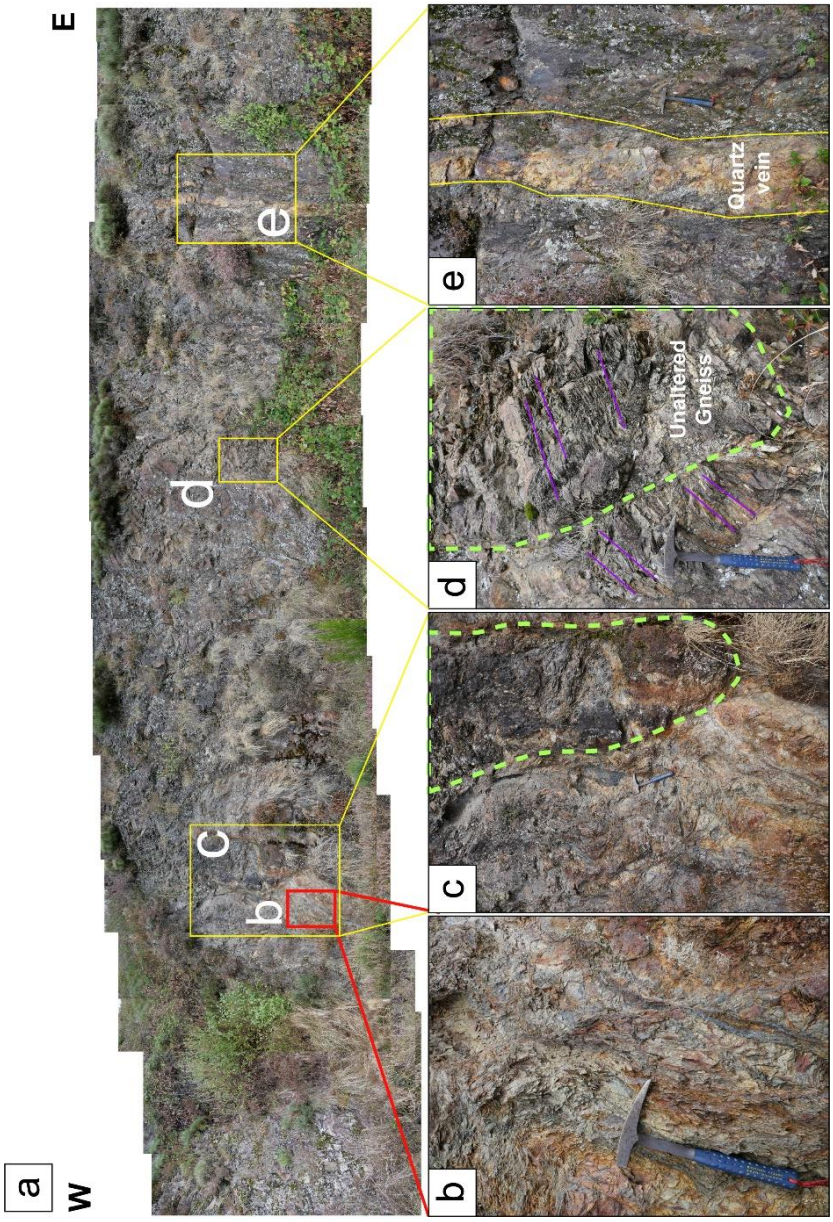

Figure III.8: Panorama of polyphased (ductile to brittle) fault N050E (F2, location in Figure III.2)**.** (b) Strongly deformed gneiss block, with the original foliation fully verticalized. (c) Preserved gneiss block, original foliation remains visible. (d) Two gneiss blocks separated by a discontinuity in foliation, interpreted as a brittle fracture. (e) Vertical quartz vein, several centimetres thick, indicating fluid circulation during the brittle reactivation of the fault.

Sulfides bearing quartz veins

Several sulfides bearing quartz veins cross-cutting preexisting faults are observed in the study area. The most representative examples are shown in Figure III.9. The most abundant mineralisation is composed of pyrite and arsenopyrite. Two populations of distinct striking of sub-vertical veins exist: a first population of 20 cm thick N00E to N020E striking veins is well exposed South of Chaudes-Aigues along the Remontalou river (abandoned mines of Sansard village, Pierrot et al., 1971). A second population corresponds to thicker quartz veins that can locally reach more than one-meter-thick and which are emplaced along the N050E brittle faults outcropping North and Northeast of Chaudes-Aigues. Most of the quartz veins are limited in extension along the trend of the fault as illustrated by the fault F3 (Figure III.9a and b, location in Figure III.2) in which quartz bears arsenopyrite (Figure III.9c). In contrast, extensive silicification is observed in other N050E trending faults. A well outcropping example is given by the fault F14 (Figure III.9d, e and f, location in Figure III.2). The quartz veins of several meter thick and of about one kilometre of horizontal extension has nearly fully replaced the brecciated gneiss of the fault gouge.

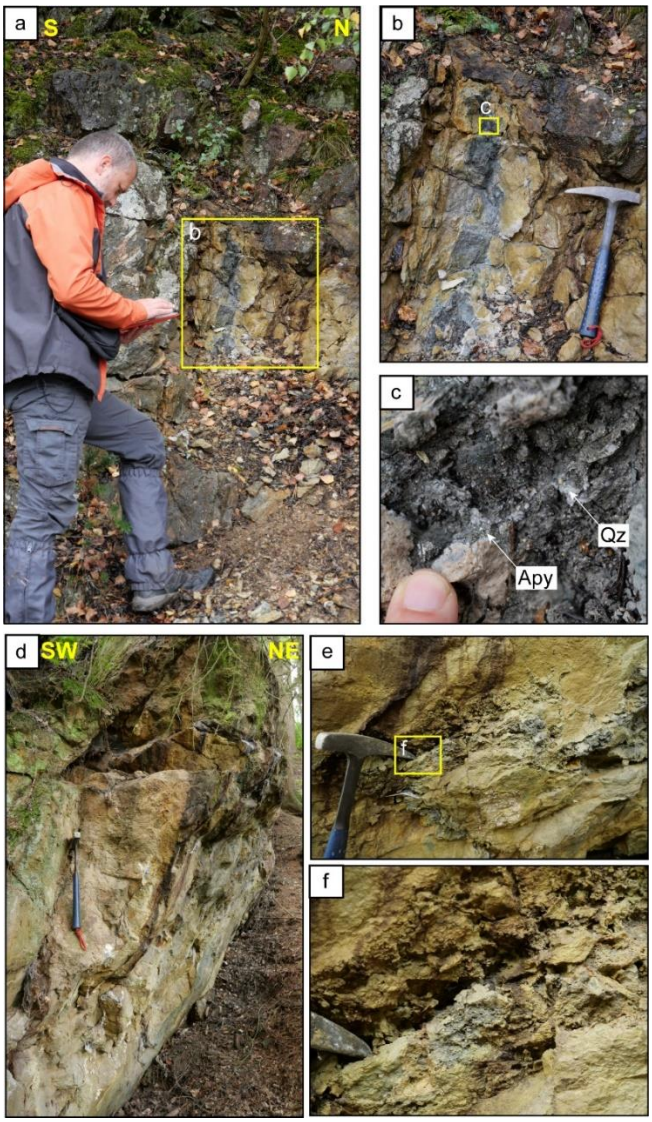

Figure III.9: (a)(d) N050E faults (F3 and F14, see Figure III.2) showing, (b) quartz-sulfide bearing vein in bleached gneiss, (c) close up of the arseno-quartz filling. Apy = Arsenopyrite and Qz= quartz (Following the mineral abbreviations of Warr 2021). (d) silicified gneissic unit and (e) (f) a close up of the oxyde filling.

Clay-bearing fault gouges

The third type of faults recognised corresponds to meter thick ones whose core is formed by clay-rich gouges (Figure III.10a, b and c). They are particularly well developed in the N140E directed fault swarm, West of Chaudes-Aigues, in which they affect the Couffour granite, the gneisses and more rarely the microgranitic veins.

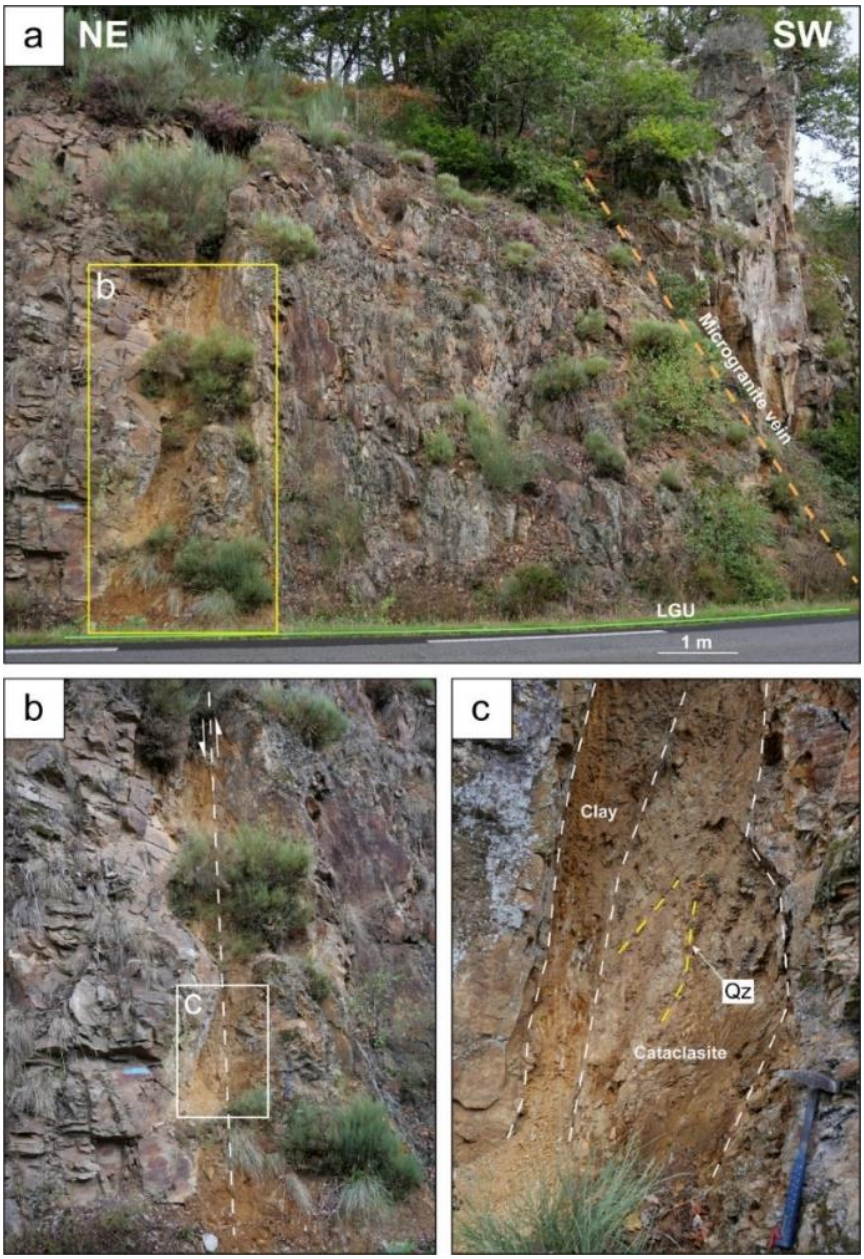

Figure III.10: Outcrop in gneissic unit close to a microgranite vein showing, (b) a N140 normal fault (F5, see Figure III.2), (c) mainly filled with clays.

X-Ray Diffraction analysis

6 samples of fault core clays were analysed by XRD. All the spectra are available in SM5. The filling of F1 shows a mixture of several clay phases (Figure III.11). Mineralogical analyses carried out on the < 2 µm fraction identify different types of clay minerals. This sample contains several clay minerals: smectite, chlorite/smectite mixed layered, illite/micas phase and kaolinite (Figure III.11). Of these minerals, smectite and the chlorite/smectite mixed layered are swelling; the positions of their diffraction peaks shift after treatment with ethylene glycol, unlike those of illite/micas and kaolinite.

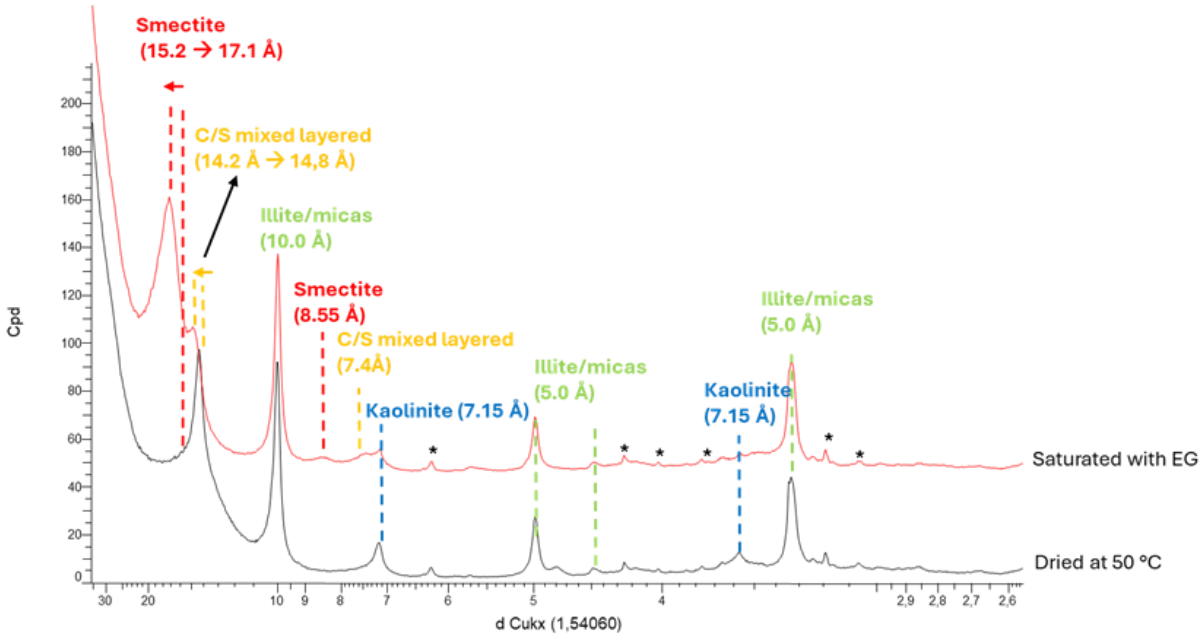

Figure III.11: X-ray Diffractograms obtained for F1, location corresponds to Figure III.2.

X-ray diffractograms of the fine fraction of the F1 sample obtained before (dried at 50°C) and after saturation with ethylene glycol (saturated with EG). C/S mixed layered means Chlorite/smectite mixed layered. Peaks with asterisk correspond to non-clay phases such as feldspar and quartz.

A similar mineralogy based on smectite and illite is found in all of the samples, with some additional minerals such as I/S and C/S mixed layered, kaolinite, talc and chlorite for F1 and F4.

<u>Geometry of the emergence zone at depth</u>

Residual Bouguer anomaly

The measured complete Bouguer anomaly values range from -68 to -55 mGal. As the interpolated map (Figure III.12) and the measured profiles (Figure III.13) show, the Bouguer anomaly values is marked by a NNW-SSE decreasing gradient though not perfectly

perpendicular to the mapped geological contact between gneiss units and the MGC. A very low-value signal rises northward to the southwest of the study area along line L2.

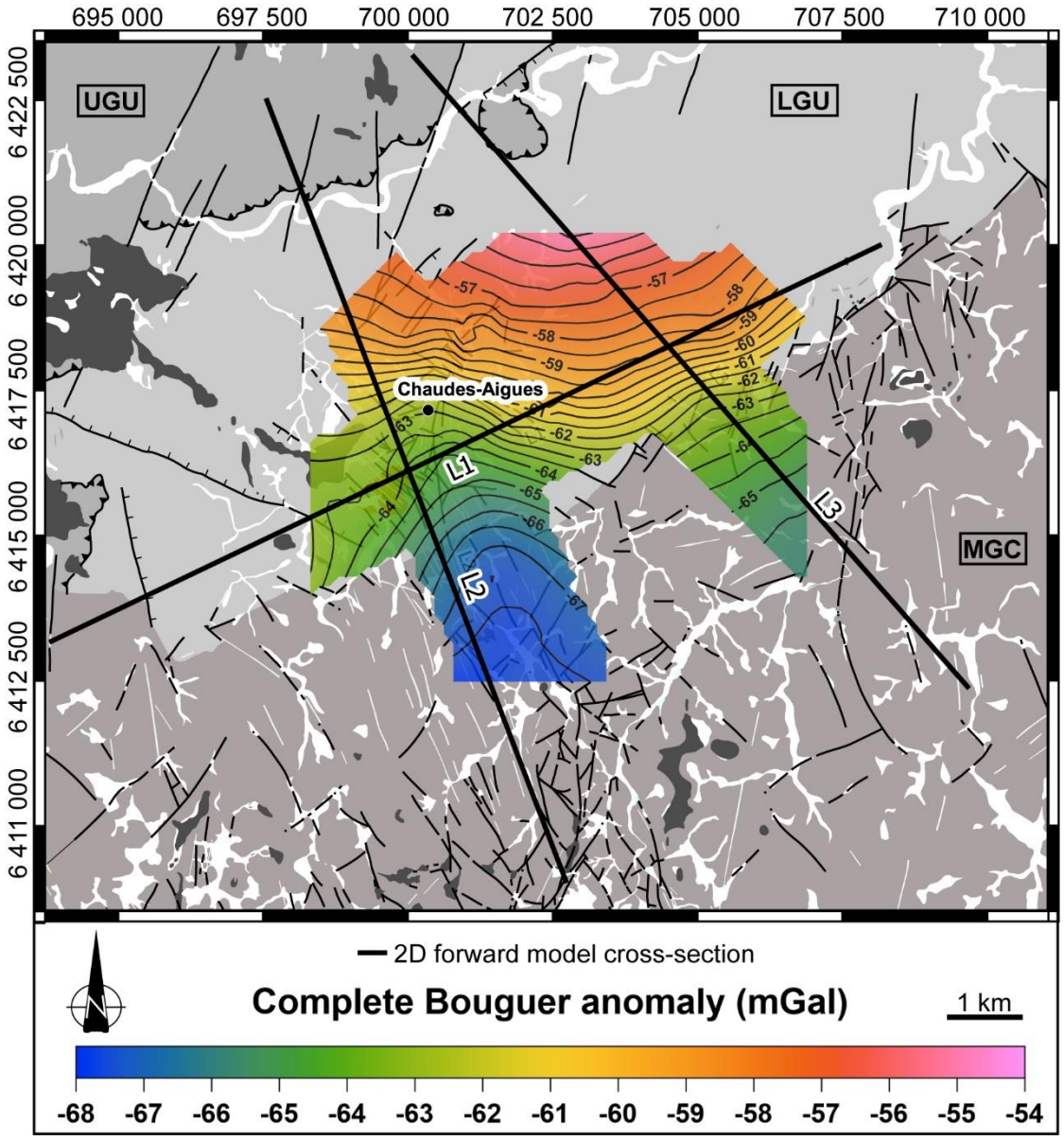

Figure III.12: Complete Bouguer anomaly map (major contour interval: 1 mGal). LGU corresponds to Lower Gneiss Unit, UGU to Upper Gneiss Unit and MGC to Margeride Granitic Complex. The coordinates are in Lambert 93.

2D modelling

Sections L2 and L3 (Figure III.13b, c) both exhibit a rather large (approximately 10 mGal), continuous and consistent Bouguer anomaly decrease from NNW to SSE which must correspond to the effect of a deep seated and significant density contrast between rock units. Forward 2D modelling results in both sections in (i) a northward extension of the MGC to depth, below the outcropping gneisses and (ii) bulbous, bow-shaped geometry of the contact. The

larger gradient displayed to the NNW of the L2 profile, from 0 to ~2000 m, highlights a shorter (~4 500 m), thicker (~5 500 m) and shallower (<300m depth) granite extension within the gneisses with a steeper northern contact (Figure III.13b). In contrast, the shallower anomaly gradient observed in profile L3 can be modelled by a quite long and deep granite bulb extension within the LGU, towards the NNW. In details, its thickness ranges from 5000 meters (m) to a few hundred meters (m) and the granite extends to depth more than 5500 m north of the outcropping contact zone (Figure III.13c, located at 4000 m distance along the cross-section). The ENE-oriented thinning of the hidden and buried part of the MGC within the LGU is clearly evidenced by the Bouguer anomaly map (Figure III.12). In profile L3, the Bouguer anomaly value shows a quite abrupt slope break between abscissas 3200 m and 4300 m (Figure III.13c). This highlights that the ENE-oriented thinning of the granite is discontinuous with the granite roof sinking 1500 m over 650 m. It is not worthy that such structural discontinuities are not highlighted along NNW striking cross-sections (see Figures 13 b and c) Section L1 (Figure III.13a) confirms the geometry of the MGC. In this section, the gravimetric gradient changes polarity at the 3100-meter abscissa. This change is explained by the MGC deepening to 2,000 meters. These discontinuities in the geometry of the MGC roof contact can be interpreted as marking offsets along faults roughly trending North to NW. However, these are difficult to precisely outline due to the data resolution of the gravity survey.

The minimum Bouguer anomaly value observed along profile L1 (Figure III.13a) is interpreted to reflect the presence of low-density granitic rocks at a very shallow depth or at the surface. This zone correlates well with the outcropping Couffour pluton, indicating that this small body caps the deep northern extension of the MGC. Nevertheless, the use of a uniform density for both distinct geological units prevent any modelling of the contact geometry and, consequently, any highlighting of the emplacement mechanism of the younger Couffour granite within the MGC.

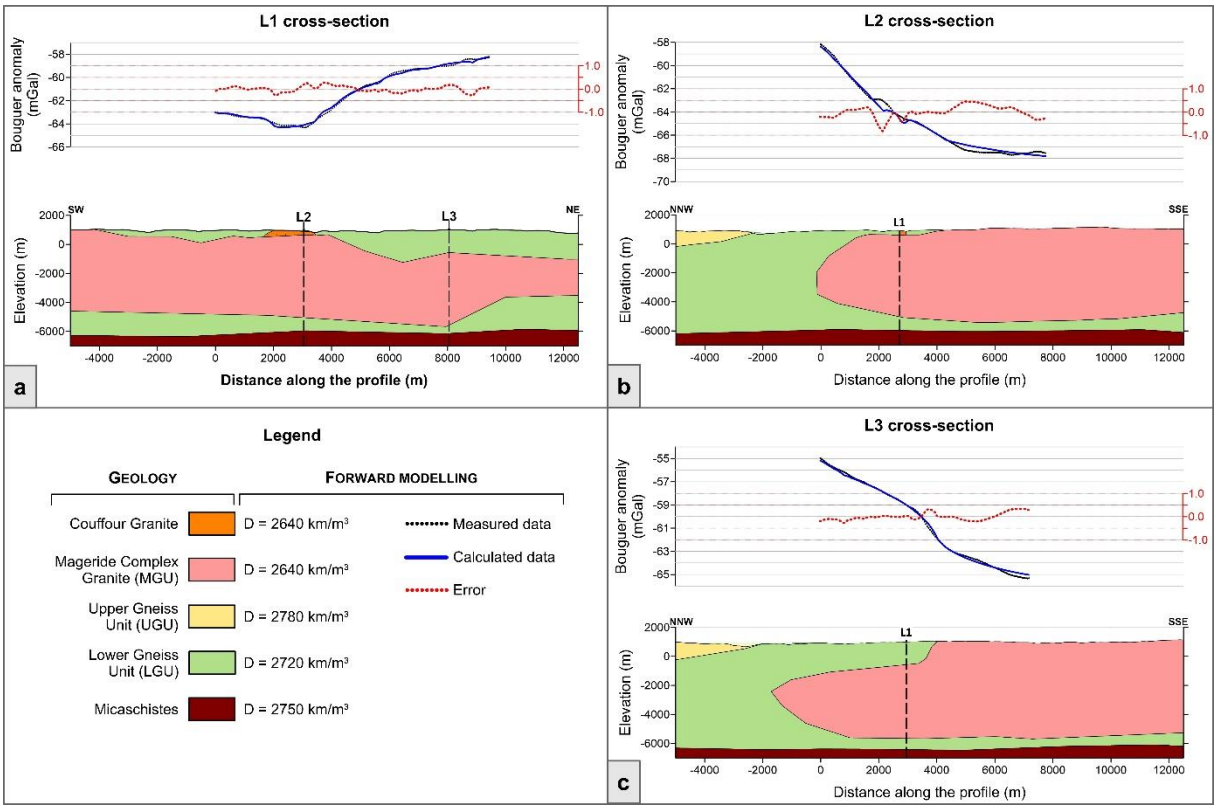

Figure III.13: (a) Geological map of the study area and location of gravity stations. (b) Complete Bouguer anomaly map (major contour interval: 2 mGal) and location of the 2D forward modeling of the Chaudes-Aigues area along the L1 (c), L2 (d) and L3(e) cross-sections.

Discussion

Location and nature of the reservoir in the hydrothermal system

From a hydrogeological and geochemical point of view, the MGC has been identified as the main reservoir of the Chaudes-Aigues hydrothermal system (Vasseur et al., 1997; Penhoët et al., 2025b). The N140E-trending fault zone between La Chaldette and Chaudes-Aigues area drains the water from the southern part of the MGC to its northern edge, where the fluids are concentrated. Our gravity survey (Figure III.13b, c) clearly shows the wedge-shaped northern termination of the MGC within the metamorphic gneissic units at depth, below the Chaudes-Aigues area. This result is consistent with the proposed geometry of this termination proposed by Vasseur et al. (1997) and confirmed by the regional scale gravity survey conducted by Talbot et al. (2005). Our gravity model indicates that the MGC lies at a shallow depth beneath the Chaudes-Aigues springs. In addition, we have evidenced that the Couffour granite outcropping, located approximately one kilometre South-West of Chaudes-Aigues, is connected to the termination of the MGC at depth.

Clay mineral assemblages identified by X-Ray Diffraction (XRD) analyses on fault gouge samples near the springs (Figure III.9) include illite, smectite, chlorite, and interstratified phases. These assemblages are consistent with temperatures in the range of 180 – 240 °C, as observed in other active hydrothermal systems (Bouchot et al., 2010; Beauchamps et al., 2019; Fulignati, 2020) and support the reservoir temperature previously inferred at 190°C from geochemical geothermometric calculations (Vasseur et al., 1997; Penhoët et al., 2025b).

Inherited structures and fault reactivation shaping fluid flow pattern in the Chaudes-Aigues area

Since the late Variscan period (330 – 280 Ma), the region experienced several ductile, and then, brittle deformation phases. The primary ante-carboniferous ductile regional deformation affecting the LGU is represented by a regularly oriented pervasive schistosity characterised by, on average, a N046E trending mineral foliation plane dipping 17° to the North-West (Penhoët et al., 2025a; Figure III.14a). While the ductile fabric is almost monocline across the area, foliation looks particularly folded nearby Chaudes-Aigues where the foliation's orientation in the LGU is statistically slightly more dispersed with projected poles aligning along a NE-SW girdle compatible with a N315 shallowly plunging hinge line on average (Figure III.14b). In addition, compiled measurements of hinge fold lines performed along the Remontalou river together with those collected by Gibert et al. (1975) indicate a well-defined N300-directed, nearly horizontal, hinge fold line on average (Figure III.14c). Most of the folds exhibit a low amplitude (Faure et al., 2001 and 2009, Figure III.14d). The last ductile event recognised over the region consisted of N050E striking shear zones that are characterised by a thick central damaged zone in which the foliation is verticalized and parallelised to shear planes and highly deformed as mylonitic deformation may locally be observed (F2, Figures 8 and 15). During the Mid-Carboniferous the region experienced an extensional phase that affected the ductile part of the crust. This resulted into the thinning of the continental crust leading to the transition from ductile to brittle regional deformation (Faure, 1995). This resulted in the development of a conjugate fault system comprising N140-170E and N010-N050E faults, both of which are well developed in the study area (Blés, 1989). At 310 Ma, the MGC has been interpreted to emplace

along three NE-SW trending feeder zones, which were controlled by dextral N140 faults that allowed pull-apart type opening (Talbot et al. 2005). The Late Carboniferous period was characterised by a compression of North-South striking maximum shortening, which was responsible for the formation of a conjugate fracture system comprising N140-170E striking dextral and N010-N050E striking sinistral faults, as well as the emplacement of microgranite and quartz veins (De Goer de Herve, 1991). The Couffour Granite has not yet been dated, but since it is crosscut by the microgranite dykes, it cannot correspond to the latest magmatic event in the area.

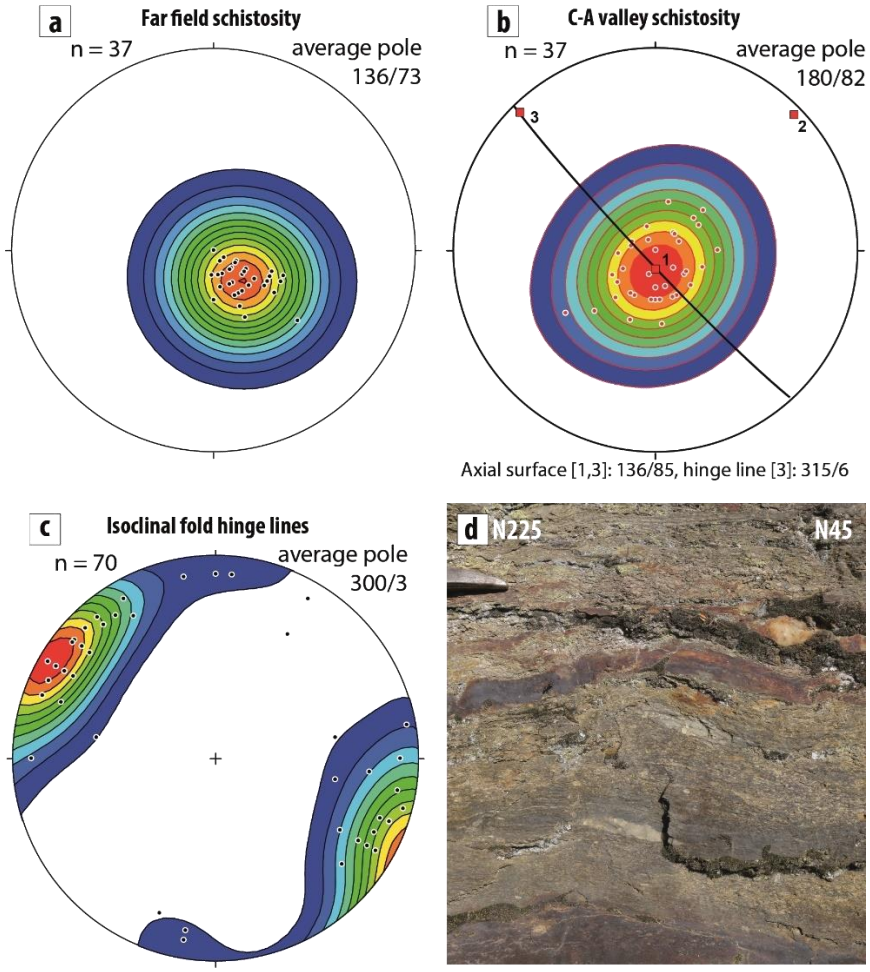

Figure III.14: (a) Far field schistosity represented mostly by the biotite foliation measured in the LGU and UGU North of the MGC (modified from Penhoet et al., 2025a). (b) Schistosity of the LGU measured along the Remontalou river next to Chaudes-Aigues city. (c) isoclinal fold hinge directions affecting the LGU gneisses. Measurements issued from Gibert et al. (1975) and complemented by measurements performed on same outcrops than for (b). (d) Field view on a plane perpendicular to the hinge direction of a isoclinal fold affecting the gneiss of the LGU illustrating the limited amplitude of this folding.

The Mesozoic period was characterised by a relatively calm tectonic activity during which the structures were reactivated and used for the upwelling of mineralised fluids (Santouil, 1980;

Blés et al., 1989). The observed sulphide-bearing quartz veins (see Figure III.7) are present along N00E-trending faults (Pierrot et al., 1971). An intraplate compression phase begun during late Cretaceous and Palaeocene, leading to the brittle reactivation of pre-existing Late Variscan faults (Ziegler and Dèzes, 2007); It resulted in the reactivation of N150E and N050E striking steeply dipping faults as, respectively, left-lateral and right-lateral strike-slip movements (Ziegler and Dèzes, 2007). This brittle reactivation leads to the cataclasis of both microgranite dykes and quartz veins that were formerly emplaced along these faults (Figure III.15). Then, the latest brittle event led to the N030E-directed fracture planes along which dissolution patterns are visible (Figure III.7). Then, during the development of the European Cenozoic Rift System (ECRIS; Michon and Merle, 2001; Dèzes et al., 2004; Ziegler and Dèzes 2007; Merle et al., 2023), the East-West oriented general extension resulted in the reactivation of the N150E striking faults set as normal faults and the development of localised graben basins, particularly along the Margeride Fault Zone crosscutting the MGC, east of the studied area (Penhoët et al., 2025a). Nowadays, the French Massif Central is subjected to a NW-SE compression (Figure III.15a, Mazabraud et al., 2004; Baize et al., 2013).

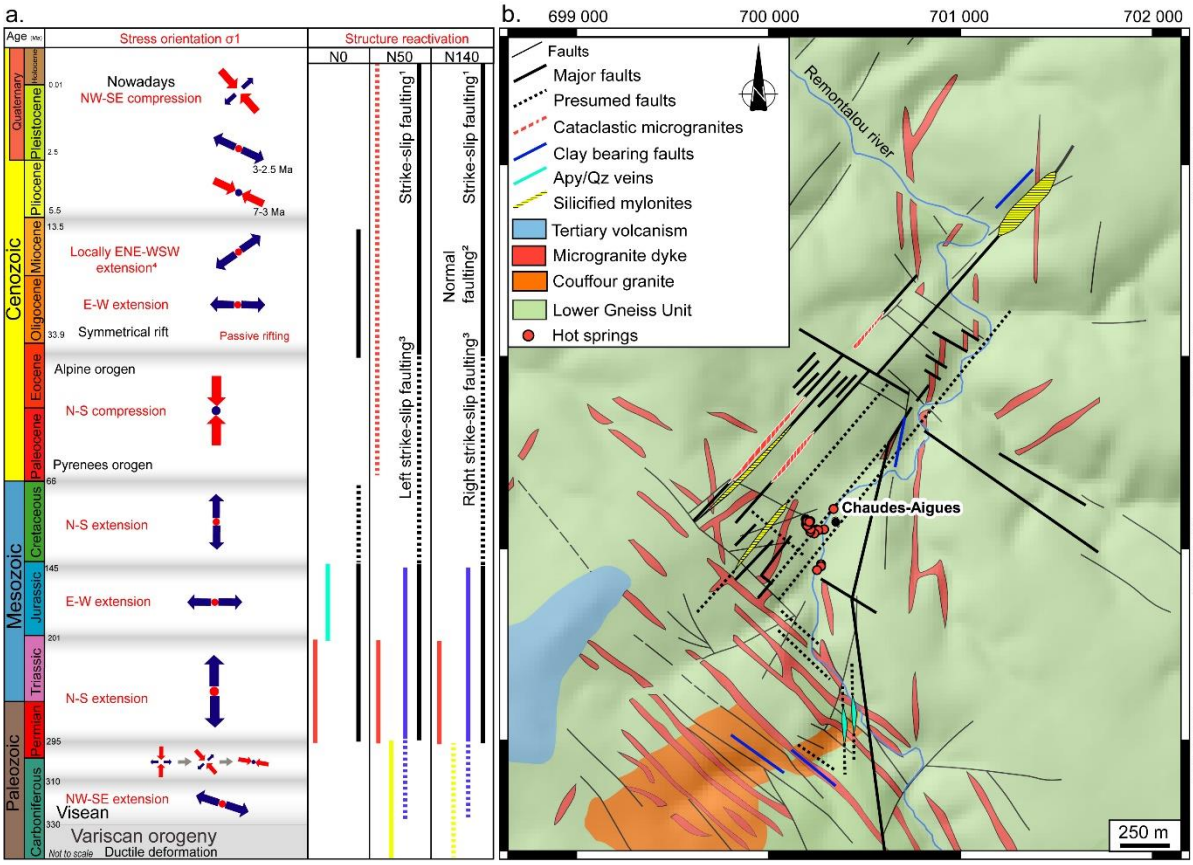

Figure III.15: (a) Tectonic timeline summarising the evolution of tectonic stresses (modified from Daffos et al., 2024) to identify the re-activations of structures, 1: Gölke and Coblentz (1996), Mazabraud (2004), 2: Couturié (1979), De Goer de Herve (1991), 3: Ziegler and Dèzes (2007), Bergerat (1985), 4: Blés et al., (1989). (b) Simplified geological map identifying the main drains or barriers near the thermal springs (modified from Gibert et al., 1975). Coordinates are in Lambert 93.

All this evidence suggests that the specific nature of the spring swarm of Chaudes-Aigues in terms of location and flow rate are the results of a combination of structural features, acting either as drains or barriers, and topographic factors.

Firstly, the brittle network affecting the LGU, the Couffour granite and potentially the MGC at depth is composed of the intersection of three fault networks: N150E, N050E and N0E (Figure III.15b). These three fault directions were already active during the late Palaeozoic during which microgranite, and then quartz, veins emplaced (De Goer de Herve, 1991; Figure III.15b). All have been repetitively reactivated since the carboniferous. In particular, the N050E faults, initially developed as decametric thick ductile shear bands appear nowadays as brecciated, highly permeable, and still active drains (Figure III.8). Although no outcropping evidence of faults were found in the vicinity of the spring swarm of Chaudes-Aigues, a borehole located on the south bank of the Remontalou in Chaudes-Aigues (BSS001YWBT,

https://infoterre.brgm.fr/page/banque-sol-bss), evidenced a silicified mylonite at 65m depth. In addition, the general N150E to N140E orientation of the Remontalou river to the South, in the MGC, clearly changes approaching Chaudes-Aigues to redirect N050E along a ~2 km segment to flow again, downstream to the North, along a N140E direction in the LGU. This two-kilometre-long lineament most probably expresses the influence of a major crustal weakness compatible with a major N050E fault zone belonging to the similarly oriented fault network outcropping North of the city (Figure III.15b). In addition, chlorite-bearing fault gouges, indicative of the highest temperatures, were identified specifically at the intersection zone of the fault zones and along the N050E mylonitized shear zones, reinforcing the interpretation that these structural features act as primary hot fluid conduits within the Chaudes-Aigues hydrothermal system. This is consistent with the concept that intersections between fault zones often form “interaction damage zones,” where localized dilation and enhanced fracture connectivity promote fluid flow (Peacock et al., 2017).

Secondly, in contrast to previous models, this study shows that microgranite dykes do not appear to act as the main fluid drains in the system, as evidenced by the low indicators of fluid circulation along these structures (Figures 7d, 7e). The N030E-oriented fracture planes, which show dissolution features, must correspond to tensional gashes compatible with a NW–SE striking σ_3 axis. These stress conditions align with the Namurian extensional phase structural setting (315 Ma, Figure III.13a) even though microgranite dykes along these structures postdate this period (265 ± 8 Ma, Bellon and Gibert, 1975). An alternative extensional phase likely occurred during the Late Pliocene, providing a more recent timing for the fluid circulations observed. Therefore, these microgranite dykes may instead act primarily as barriers to fluid flow rather than as conduits. Furthermore, it is worth noting that many N050E trending faults are locally formed of silicified mylonites (Gibert et al., 1975) that may act as barriers to during the over deepening of the river since the Pliocene uplift of the French Massif Central. Berio et al. (2025) showed that hydrothermal silicification can strongly reduce fault zone porosity and permeability, reinforcing their role as hydraulic barriers. Silicified mylonites in the Chaudes-

Aigues area act as barriers that restrict northward fluid flow, as shown by the deflection of the Remontalou River. We assume that the same barrier effect is likely to occur at depth. This supports the idea that silicified mylonites in the Chaudes-Aigues area limit fluid flow northward, contributing to the observed river deflection.

Thirdly, our geophysical survey has evidenced the vertical geometry with limited horizontal extension of the Couffour granite whose root is probably encased in the MGC. This highly fractured granite is therefore an additional potential drain through the LGU. Its contribution as drain for the upwelling of the deep fluids is consistent with the composition of the waters at Chaudes-Aigues (Penhoët et al., 2025b).

Finally, the springs swarm of Chaudes-Aigues is located in a strongly incised valley which has developed since the Pliocene uplift (De Goer de Herve, 1991; Malcles et al., 2020). The geographic link between hydrothermal emergences and minimum topographic levels, the latter being often related to thick structural damage zones, is commonly reported in crustal settings (Taillefer et al., 2018 and references therein).

Consequently, our results allow localising the main upwelling path for hot fluids at the intersection of three major sets of continuously reactivated, and then permeable, oblique faults since almost 290 Ma. the deep hot fluids reservoir is most probably localised in the Northern extension of the MGC below the gneiss units, as imaged by Bouguer anomaly modelling. From depth, the highly fractured Couffour granite, which is imaged as rooted in contact of the MGC roof, may enhance the permeability while near the surface the barriers formed by quartz veins and microgranite dykes to the North, together with the minimum topographic represented by the incised valley, may control the final fluid rise expressed nowadays by the dense springs swarm in the city of Chaudes-Aigues.

Conclusions

This study provided an overall view of the structural organisation of the Chaudes-Aigues system, combining structural geology and geophysics. We have shown that the main reservoir is located in the northern termination of the MGC located at shallow depth beneath the town.

The reservoir temperature, estimated at 190°C, is corroborated by the mineralogical assemblage of fault gouges, indicating deep hydrothermal circulation.

The N050E-trending ductile and then brittle faults are the main drains of the hydrothermal system. Their intersection with the N150E fault zone concentrates and focuses fluid flow. Contrary to some previous hypotheses, the microgranite dykes do not act as conduits: rather, they constitute potential barriers, as do the large silicified mylonites located to the north of Chaudes-Aigues, which limit the upwelling of fluids.

Finally, the current location of the hot springs in the incised Remontalou valley illustrates the combined influence of topography and tectonic structures favourable to fluid circulation. These results confirm that the distribution of hydrothermal upwellings are the result of a complex interaction between structural inheritance, tectonic reactivation and topographic control.

Supplementary Materials

SM1: Microstructural measurement stations location.

Name	Longitude	Latitude
UG-1	3.010894	44.85939
UG-2	3.001198	44.874008
UG-3	3.007709	44.856896
UG-4	3.002305	44.850565
UG-5	3.004943	44.844146
UG-6	3.006671	44.847173
MGD-1	2.996915	44.841742
MGD-2	3.010459	44.85933
MGD-3	3.000112	44.849249
C-1	2.995597	44.840974
C-2	2.999591	44.838893
C-3	2.998918	44.842407
C-4	3.048846	44.777339
UG-7	3.013989	44.861826
UG-8	3.016245	44.868213

SM2: Structural measurements in Gneissic units.

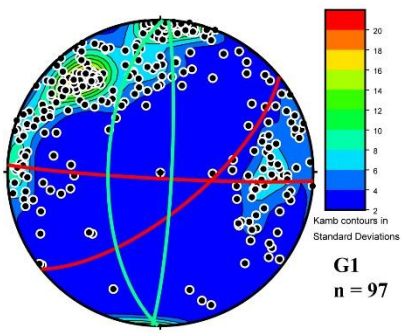

G1
n = 97

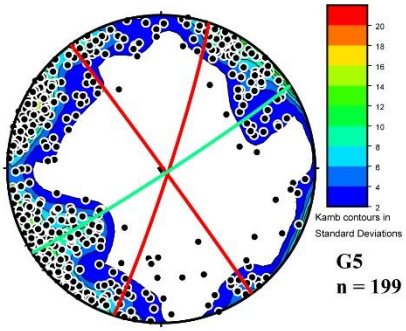

G5
n = 199

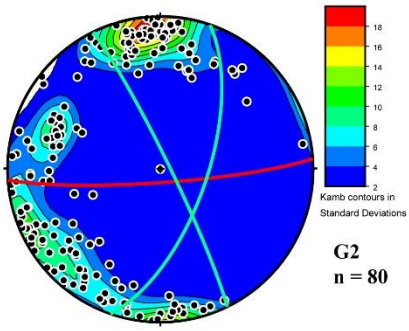

G2
n = 80

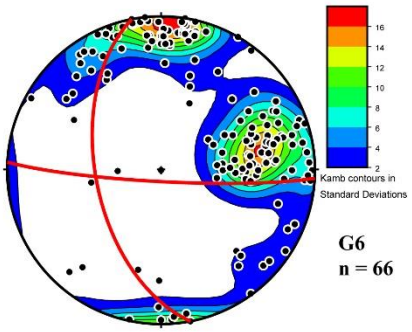

G6
n = 66

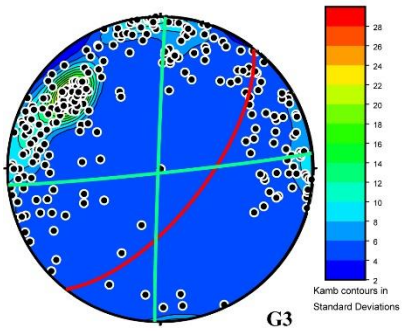

G3
n = 117

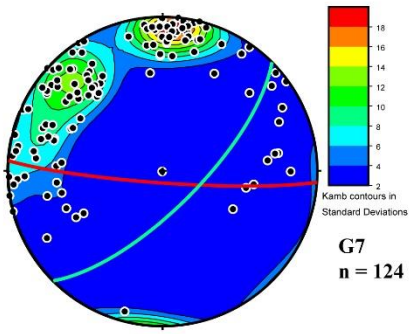

G7
n = 124

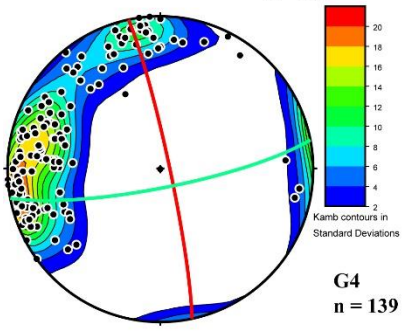

G4
n = 139

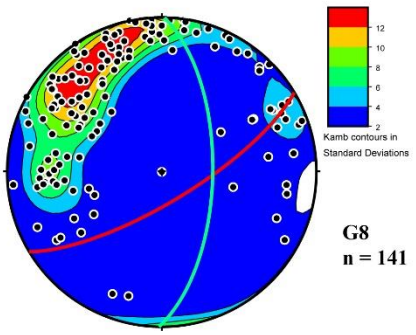

G8
n = 141

SM3: Structural measurements in the Couffour Granite.

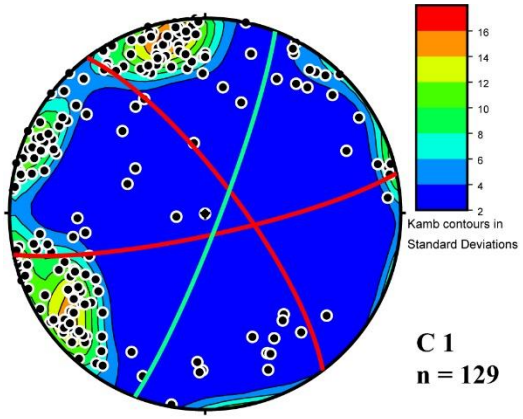

C 1
n = 129

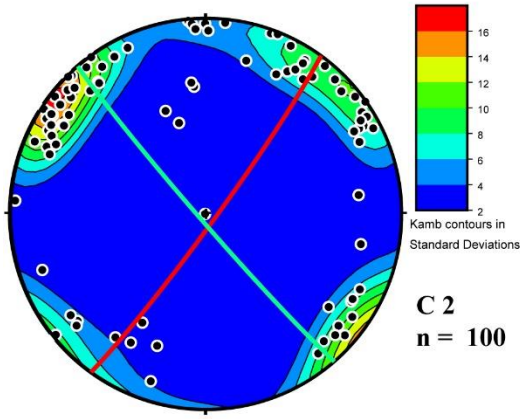

C 2
n = 100

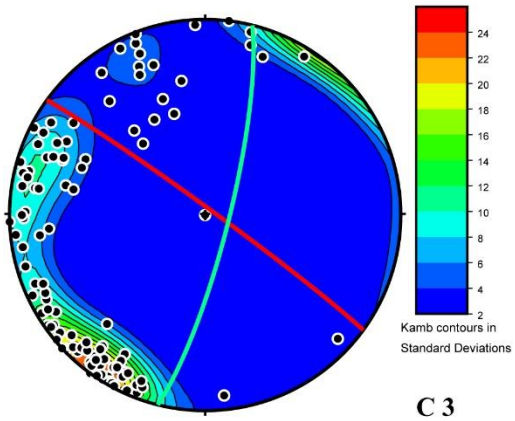

C 3
n = 87

SM4: Structural measurements in the Microgranite Dykes.

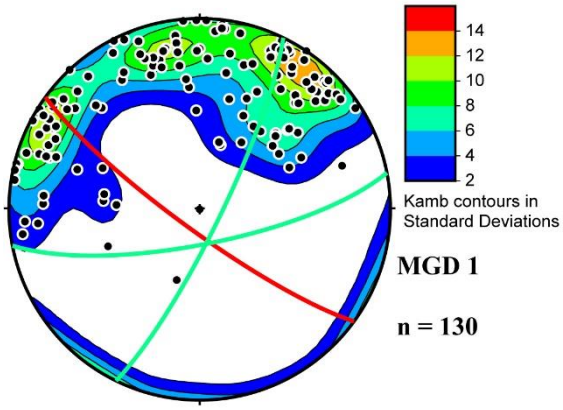

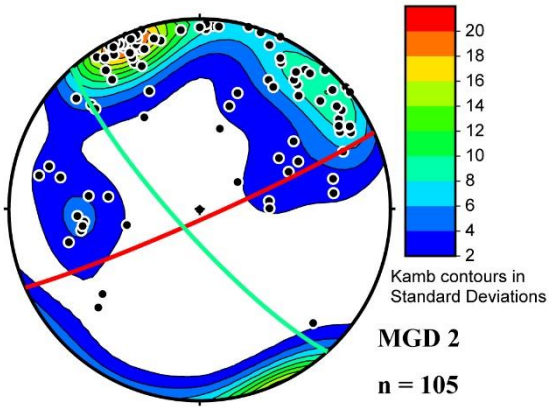

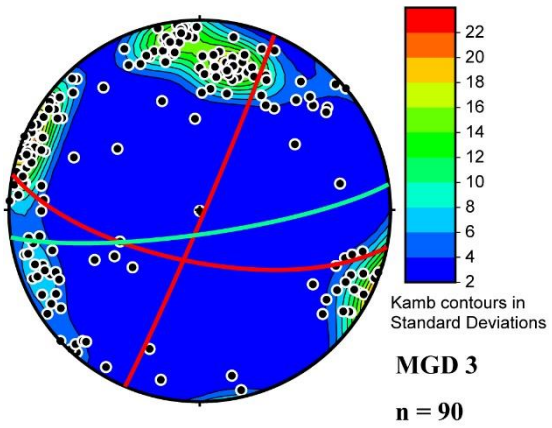

SM5: DRX spectra

Fault F1:

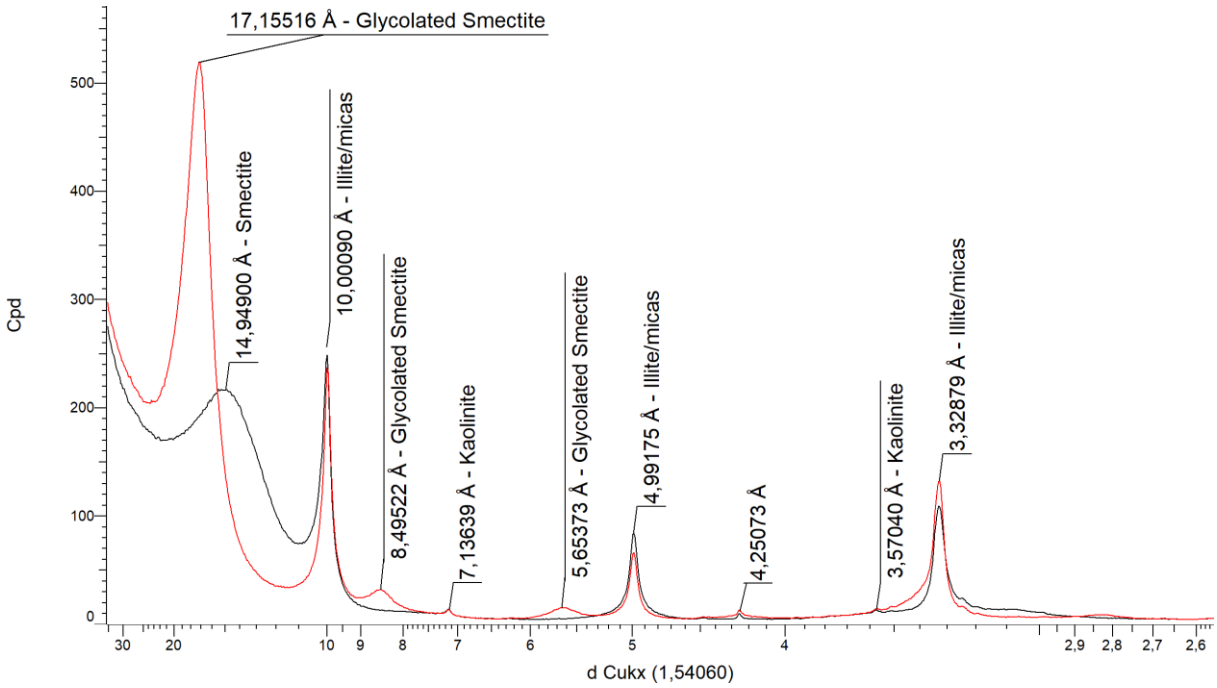

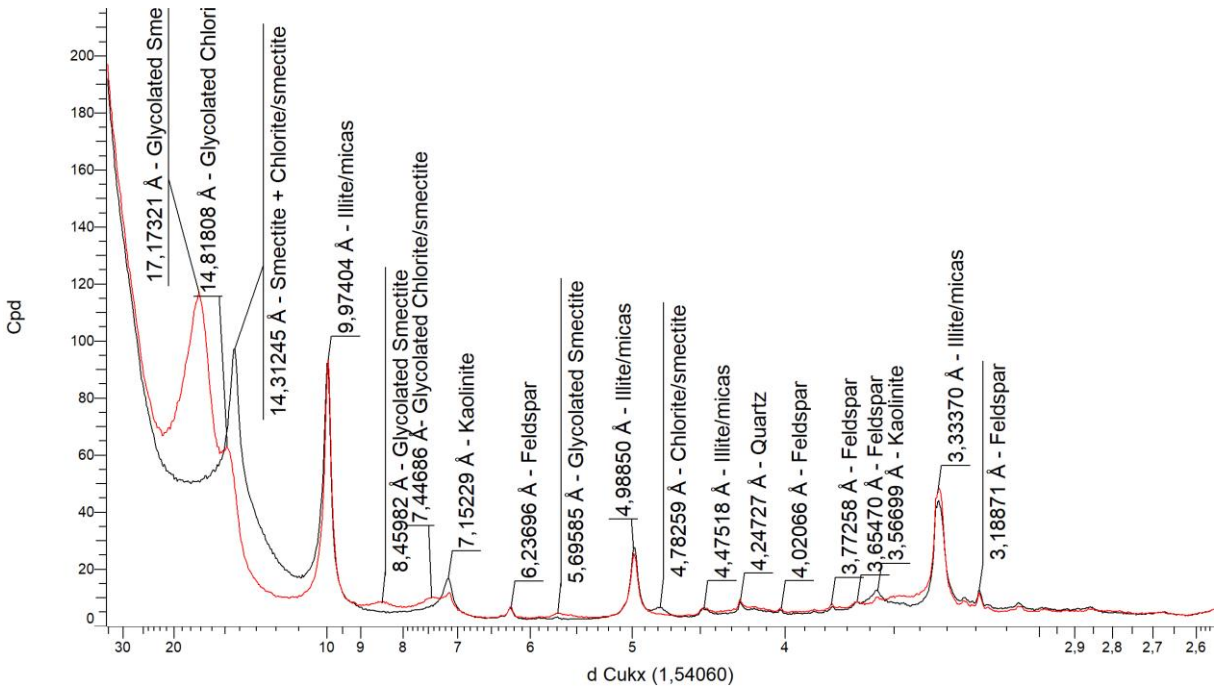

Fault F2:

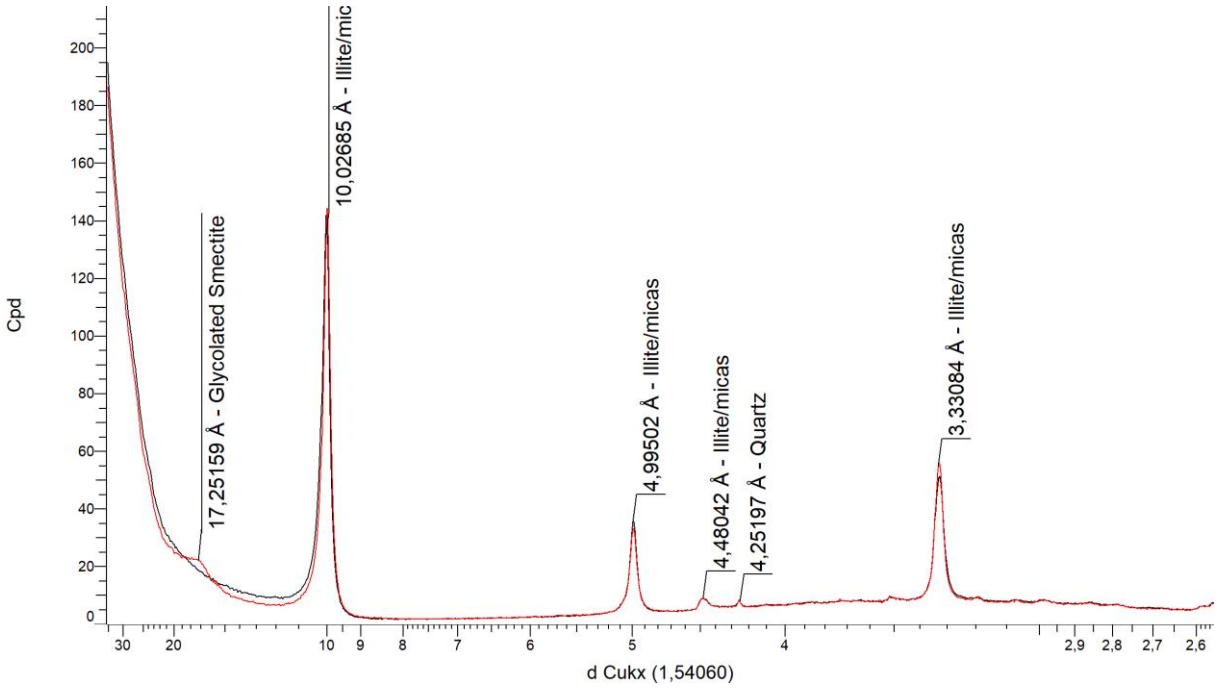

Fault F4:

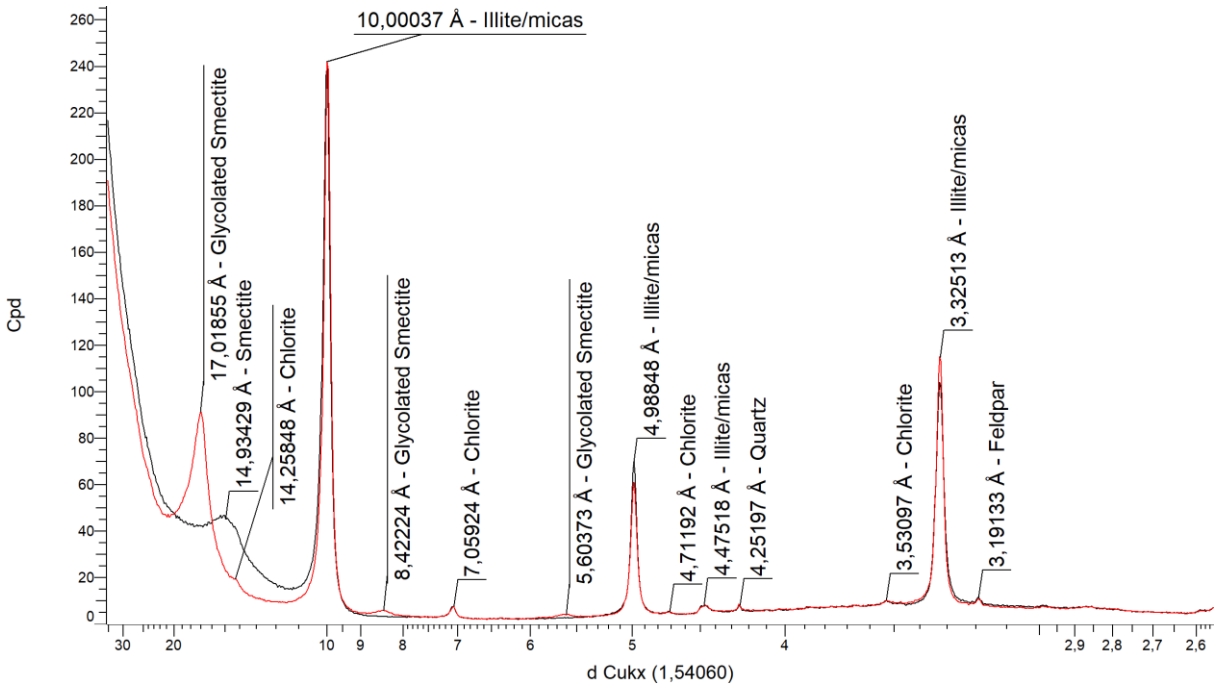

Fault F5:

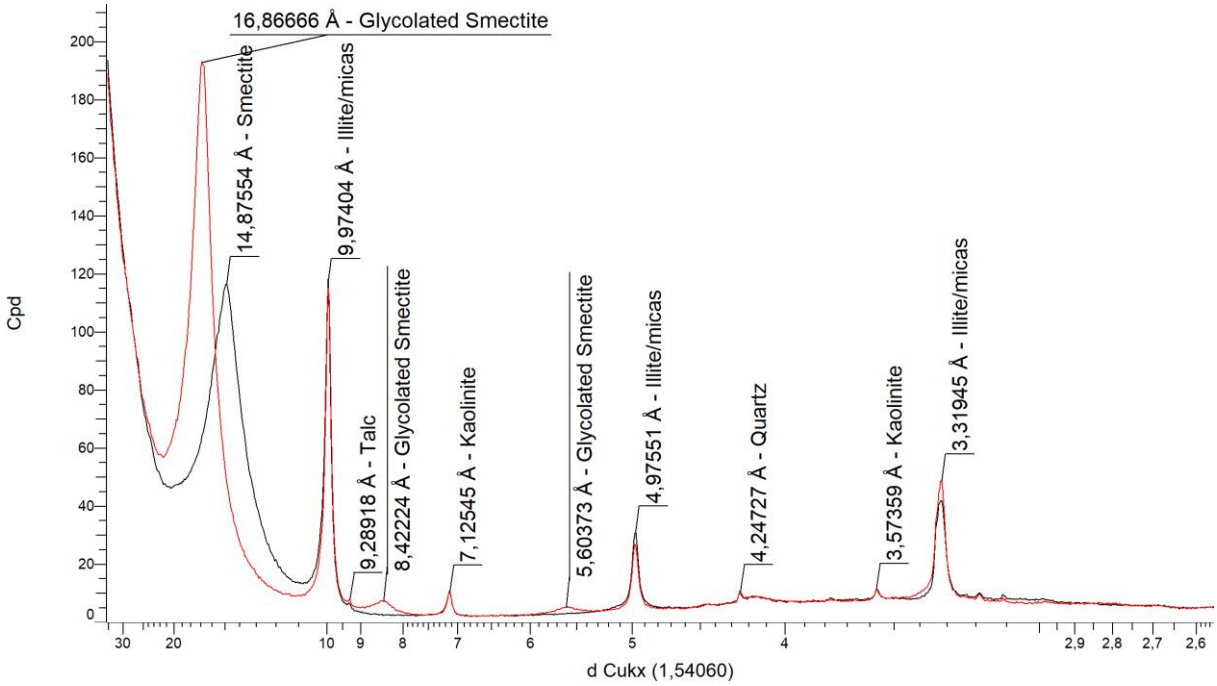

Fault F6:

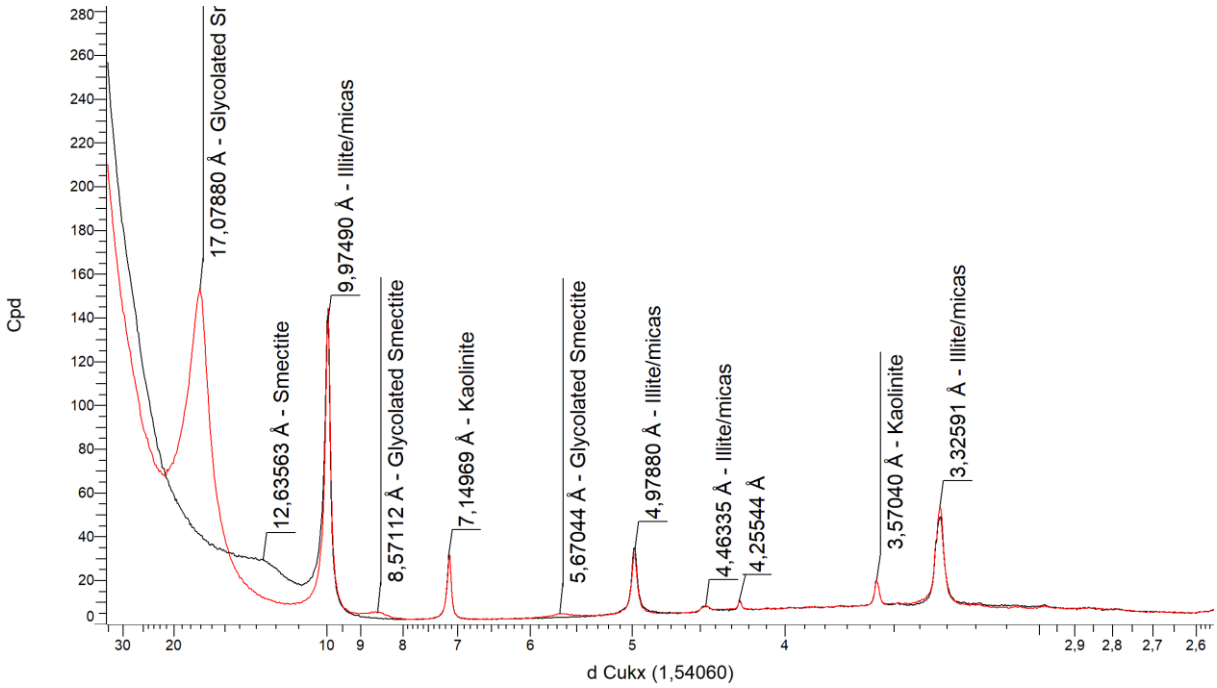

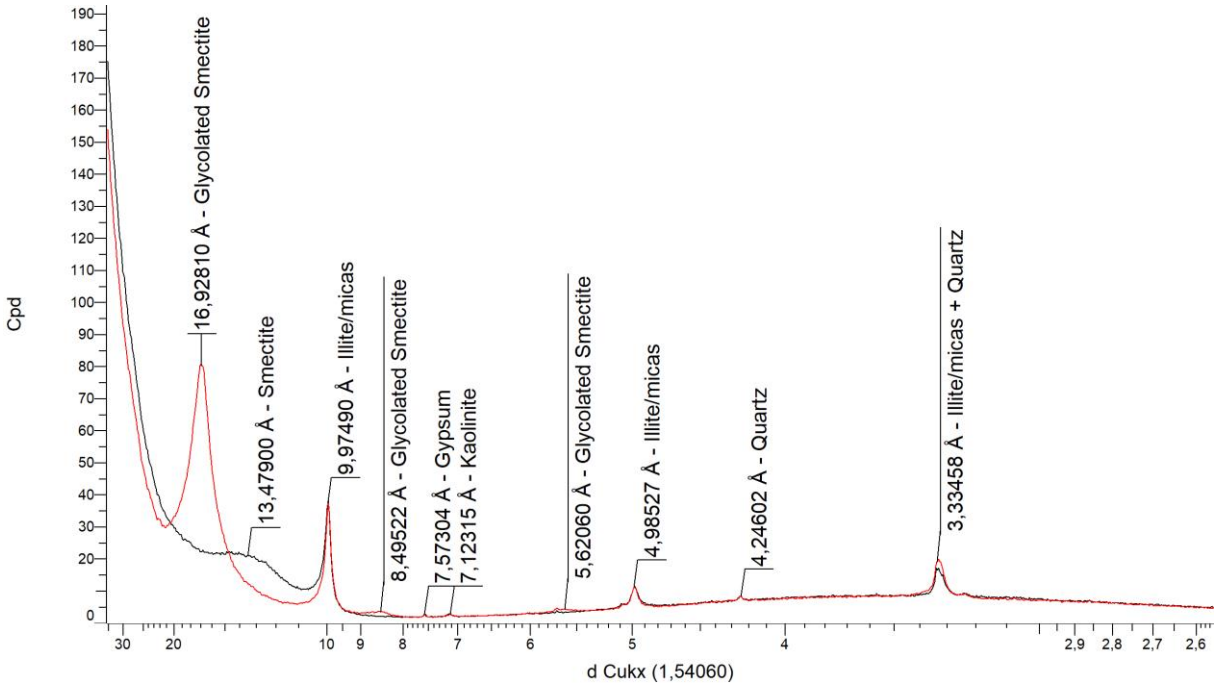
Cpd
16,92810 Å - Glycolated Smectite
13,47900 Å - Smectite
9,97490 Å - Illite/micas
8,49522 Å - Glycolated Smectite
7,57304 Å - Gypsum
7,12315 Å - Kaolinite
5,62060 Å - Glycolated Smectite
4,98527 Å - Illite/micas
4,24602 Å - Quartz
3,33458 Å - Illite/micas + Quartz
d Cukx (1,54060)

Chapter IV: One hydrothermal system may hide another: implications for the Chaudes-Aigues hydrothermal system.

IV. Geochemical characterisation of Chaudes-Aigues springs: hydrothermal system functioning and hidden reservoirs revealed

IV.1 Introduction

The thermal springs at Chaudes-Aigues have been the subject of several geochemical studies, which have shown that the water is a mixture of surface water and a deep reservoir, whose temperature has been estimated from 175 to 200°C (Cailleaux et al., 1976; Michard et al., 1981). Vasseur et al. (1997) specify the proportions of the mix, indicating a dilution of 60%. Isotopic analyses cannot be used to determine the precise impluvium zone, as the altimetry of the Cantal, Aubrac and Margeride Mounts are relatively close. Very few data are available on La Chaldette spring, and its connection with the Chaudes-Aigues springs remains unclear.

This chapter corresponds to a manuscript published in Geothermics. The aim of this work is to characterise the hydrothermal system. Several springs located around Chaudes-Aigues were sampled to delimit the hydrothermal system. The first step was to identify the different groups of waters using major elements, and thus to spatially delimit Chaudes-Aigues hydrothermal system. These will be used to highlight mixing phenomena between several samples. Next, stable isotopes can be used to determine the origin of the water and its infiltration zone. Geothermometric calculations provide an initial approach to determine the temperature of the deep reservoir supplying the Chaudes-Aigues springs. To precisely determine this value, these results will be supplemented by geochemical modelling (thermodynamic equilibria), thermo-hydraulic modelling and isotope fractionation reactions. By reconstructing the hydrothermal deposit from the impluvium zone to the emergence zone, this study has provided an overall view of the system.

IV.2 Contribution of this chapter

By characterising several MGC springs, the hydrogeological context of Chaudes-Aigues was defined and better understood. This ‘large-scale’ sampling highlighted the existence of different hydrothermal systems within the MGC.

The first supplies the springs in the south of the MGC (Mazel, Fontaine Basse, etc.), the second the Chaldette spring and the last the Chaudes-Aigues springs (town, Montchanson, Loubaresse, etc.). Infiltrated in the immediate vicinity, the Margeride springs are the result of a mixture of surface water (45%) and a deep reservoir (55%). Its temperature is estimated at approximately 120°C. The low density of faults could explain the cold surface temperature. Secondly, water from the Chaldette, which is also mainly meteoric, is estimated to reach 110°C at depth. The convergence of geothermometers indicates that the water infiltrating the southern edge of the granite is in equilibrium with the surrounding rock. This circulation could take place in the altered horizon of the Margeride granite (regolith, see chapter 5).

Regarding the Chaudes-Aigues springs, as mentioned in previous studies, the water comes from a mixture between a surface component and a deep endmember. The various results indicate that meteoric water infiltrates mainly into the southern edge of the MGC and is drained towards the town thanks to a favourable topographical gradient and a thick N150E fault zone. The composition of this surface water is similar to the La Chaldette spring. In addition, part of the water in Chaudes-Aigues comes from a deep reservoir, located partly beneath the town and extending some ten kilometres to the north-east. Using various methods, its temperature has been estimated at 190°C. This deep endmember is also thought to be a mixture of mantle water (mainly gaseous) and meteoric water.

These initial findings have identified several potential geothermal reservoirs within the MGC. However, as this study primarily focused on the Chaudes-Aigues area, further analyses and field investigations are needed to fully assess the geothermal potential of the granite body as a whole. With respect to the Chaudes-Aigues hydrothermal system, this work both confirms previous studies and reduces existing uncertainties, while also providing new insights.

IV.3 One hydrothermal system may hide another: Insights from Chaudes-Aigues and nearby springs (published article)

One hydrothermal system may hide another: Insights from a geochemical exploration of Chaudes-Aigues and nearby springs (French Massif Central)

Emmy Penhoët[1,2], Bernard Sanjuan[1], Laurent Guillou-Frottier[1,2], Manuel Moreira[2], Laurent Arbaret[2].

Manuscript published in Geothermics, 133 (2025) 103476,

https://doi.org/10.1016/j.geothermics.2025

1 : BRGM, F-45060 Orléans, France.

2 : ISTO, UMR 7327, Université d'Orléans, CNRS, BRGM, F-45071 Orléans, France.

E-mail adresses : e.penhoet@brgm.fr , b.sanjuan@brgm.fr, l.guillou-frottier@brgm.fr , manuel.moreira@cnrs-orleans.fr , laurent.arbaret@univ-orleans.fr

Corresponding author: Emmy Penhoët, BRGM, F-45060 Orléans, France.

E-mail address: e.penhoet@brgm.fr

Abbreviations :

Bureau de Recherches Géologiques et Minières: BRGM

Institut des Sciences de la Terre d'Orléans: ISTO

Lower Gneiss Unit: LGU

Upper Gneiss Unit: UGU

Margeride Granite Complex: MGC

Cantal volcanic complex: CVC

Total Dissolved Solids: TDS

Supplementary material: SM

Abstract

Granitic-hosted hydrothermal systems offer valuable insight into deep fluid circulation mechanisms in amagmatic contexts. This study focuses on the Chaudes-Aigues hydrothermal system in the French Massif Central, which hosts one of the hottest natural springs in Europe (Par Spring, 80-82 °C). Our work aims to better constrain the functioning of the system, including reservoir temperature, recharge zone, and fluid pathways. A combined approach of water geochemistry (major elements, isotopes) and thermo-hydraulic numerical modelling was applied. Using 22 thermal springs distributed across the Margeride Granitic Complex (MGC) and the Cantal Volcanic Complex (CVC) the temperature of Chaudes-Aigues reservoir has been estimated and is thought to reach 190 ± 10 °C, validating and refining previous estimates. Isotopic and geochemical tracers point to a meteoric origin, with the recharge area most likely located along the southern edge of the MGC, connected to the emergence zone via a thick N150E fault zone. This study redefines the Chaudes-Aigues system as fully amagmatic and structurally controlled. Other geothermal reservoirs have also been identified within the Margeride Granitic Complex, with temperatures exceeding 100 °C, indicating a broader geothermal potential of the area. Furthermore, this study highlights the potential for identifying similar hidden geothermal systems in other fractured granites with limited surface manifestations, offering new perspectives for high-temperature geothermal exploration in Europe.

Keywords

Chaudes-Aigues, French Massif Central, granite, thermal springs, geochemistry, isotopes, numerical modelling, multi reservoir.

Introduction

Hydrothermal systems hosted in granitic context provide valuable insights into the interplay between heat transfer, fluid circulation, and structural controls in the Earth's crust. Unlike magmatic (recent volcanic) systems where heat is derived from active intrusions, these amagmatic geothermal systems rely on different mechanisms (e.g. Moeck, 2014; Jolie et al., 2021). They imply deep fluid circulation, where meteoric waters infiltrate along fault zones, are heated at depth before ascending through areas of high permeability and then emerge at low topography points (Lopez and Smith,1995; Sonney and Vuataz, 2009; Alt-Epping et al., 2021; Stober et al., 2022).

Granite-hosted hydrothermal systems are critically influenced by structural factors, particularly faults and fracture networks, which control fluid circulation and pathway in the crust (Sibson, 1987; Hickman et al., 1995; Curewitz and Karson, 1997; Baietto et al. 2008, Yoshida et al., 2009; Koike et al., 2015; Haines et al., 2016). Faults act as primary conduits, enabling the deep penetration of surface waters and their subsequent ascent to finally emerge as thermal springs. The thermal and geochemical characteristics of these systems are controlled by lithological properties, the depth of fluid circulation, and the tectonic activity of fault zones.

This study is focused on exploring the hydro-geochemical processes occurring in geothermal systems in granitic settings, with the example of the Chaudes-Aigues hydrothermal system in the French Massif Central. Renowned for hosting one of the hottest natural springs in Europe (The Par Spring, 80-82°C, Vasseur et al., 1997), the functioning of the hydrothermal system, which results in a total of 30 thermal springs, remains imprecise and incomplete. The waters have been identified as a mixture between a meteoritic component and a hot deep reservoir (Cailleaux et al., 1976; Vasseur et al., 1997). This phenomenon complicates the estimation of reservoir temperature, which has been estimated between 175 and 195°C (Cailleaux et al.,

1976; Michard et al., 1981; Vasseur et al., 1997). Similarly, the impluvium (infiltration area) has not really been identified, although the Aubrac plateau has been suggested by Vasseur et al. (1997). More generally, dynamics of hydrothermal systems leading to the emergence of hot springs has been rarely studied (see however Vasseur et al., 1997; Magri et al., 2016; Taillefer et al., 2018; Dupuy et al., 2021; Carbajal-Martinez et al., 2024).

The objective of this work is to significantly improve the understanding of the functioning of the Chaudes-Aigues hydrothermal system by determining the temperature of the deep reservoir and its dimensions. Additionally, it aims to resolve uncertainties regarding the recharge area of the system. To answer all these questions, a combination of water geochemistry and thermo-hydraulic modelling was carried out. First, 22 thermo-mineral springs were sampled (Figure III.1), including springs located in the middle of the Margeride Granitic Complex (MGC) and others on the southern side of the Cantal volcanic complex (CVC). By studying the major components, we were able to isolate several waters groups and then determine the temperature of the associated deep reservoirs using geothermometric calculations and geochemical modeling. Stable isotope analysis allowed to remove the uncertainty on the location of the impluvium. To better constrain the temperature of the reservoir feeding the Chaudes-Aigues springs, a parametric study was carried out using simplified thermo-hydraulic numerical models reproducing surface heat flow as well as spring temperatures.

Hydrogeology of the study area

Geological settings

At Chaudes-Aigues, the thirty thermal springs are located near the northern edge of the Margeride Granitic Complex (MGC), central part of the French Massif Central (Figure IV.1). This area is characterized by a complex geological history, including Variscan orogeny processes and subsequent extensional tectonics during the Mesozoic and Cenozoic. The MGC was emplaced into the Variscan basement, made of metamorphic units (LGU and UGU), during the late Carboniferous (~300 Ma) (Talbot et al., 2005). Its emplacement is associated with post-orogenic extension and is accompanied by a network of fractures and faults that have

been reactivated during subsequent tectonic episodes (Talbot et al., 2005; Penhoët et al., 2025a). This geological context is further developed in Penhoët et al. (2025a).

Two volcanic edifices are present in the study area, the Cantal Volcanic Complex (CVC) to the North-West and the Aubrac plateau to the South-West. The Cantal stratovolcano was mostly built between 13 and 2.9 Ma, i.e. from the Middle Miocene to the Upper Pliocene (Nehlig et al., 2001). The slope visible in our area is made up of debris avalanche deposits, overlain by supracantalian basalts, which correspond to the last flows emitted (De Goer de Herve et al., 1994). The Aubrac plateau is made of subalkaline to alkaline basalts or basanites (De Goer de Herve et al., 1994; Couturié al., 1994), these flows were produced entirely during the Upper Tortonian, between 8.7 and 7 Ma, with some Messinian recurrences dated up to 6 Ma (De Goer de Herve et al., 1994). Its thickness is lower than 100 m on the entire peripheral edge and is estimated at 300 m below the three highest peaks (De Goer de Herve et al., 1994).

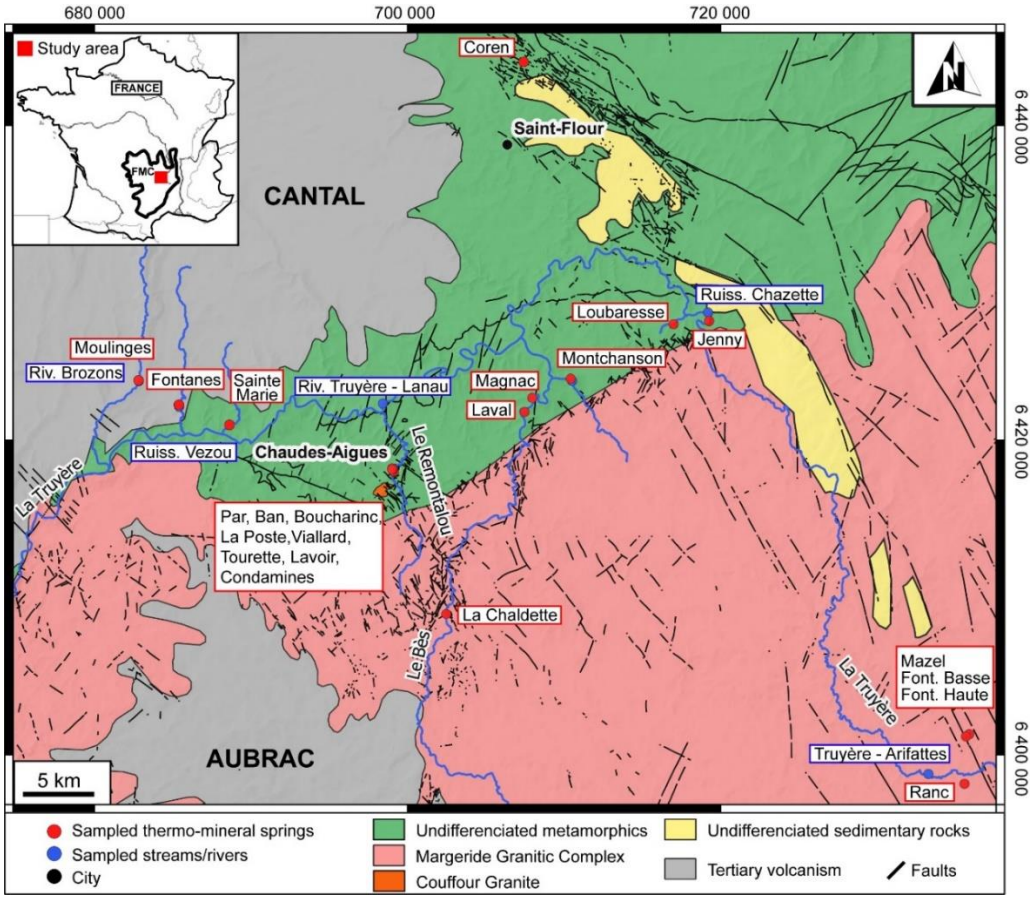

Figure IV.1: Location of sampling points on a simplified geological map. The coordinates correspond to the Lambert 93 projection system EPSG 2154.

Hydro and thermal settings

The 30 thermal waters of the Chaudes-Aigues area emerge at temperatures between 50 and 80-82°C, this latter value being measured several times in the last decades and showing slight variations. The emergence area, in the gneissic units, is characterized by a high density of brittle structures (Figure IV.1). The springs are located at the edges of major NW-SE fault systems crosscut by 2 other Variscan fault zones (Gibert et al., 1975, De Goer De Herve, 1991; Penhoët et al., 2025a). These NW-SE faults intersect the whole MGC, creating a favourable setting for hydrothermal activity. These high-permeability areas, due to brittle deformation fracturing, facilitate the infiltration of meteoric water and its interaction with the granite at depth. Further south in the MGC (10 km), located in the same NW-SE fault zone, another thermal spring, the “La Chaldette” spring emerges at 32.5°C in the granite laccolith. Since 1995, the borehole “Les Granits”, drilled at a depth close to 75 m, near the thermal spring, and reaching a temperature of 34°C, has replaced this spring as the water supply for today’s spa. Its link with the Chaudes-Aigues hydrothermal system has never been clearly identified in the literature (De Goer de Herve et al., 1994; Calvet et al., 2012).

Numerous cold springs exist at the surface of the MGC (Figure IV.1). The Mazel springs (Fontaine Basse, Fontaine Haute and le Ranc) are located in its southern part. The only available information is given by Négrel et al. (2000), who have determined, using isotopes analysis, that these waters originate from a deep circulation in the MGC. On the southern Cantal side, the Moulinges, Sainte-Marie and Fontanes cold springs have not been studied before. This large-scale sampling, including the cold springs far from Chaudes-Aigues, will enable the hydrothermal system lateral extension to be delineated.

From a thermal point of view, Chaudes-Aigues is a suitable case study of geothermal system in granite environment. Although the springs are surrounded by two volcanic systems, the CVC and Aubrac, it is difficult to assert that the heat source of the system comes from a magmatic context. In fact, no study has confirmed the existence of a present-day potential magma chamber in the CVC. The differentiated magmas are thought to come from more than 20 km

below the surface (Nehlig et al., 2001). In the case of Aubrac plateau, made of basalts (De Goer de Herve et al., 1994), magma ascends via dykes without the need of a magma chamber. Chaudes-Aigues can therefore be considered as an amagmatic system. According to Vasseur et al. (1997), the thermal gradient is around 30-35°C/km, and a regional heat flow of around 110 mW/m^2 has been estimated (Lucazeau et al., 1984). Heat production resulting from the radioactive decay of the sub-horizontal granitic laccolith (around 3.8 mW/m^3, Lucazeau et al. 1984) release, for a thickness of 7 km, the amount of 27 mW/m², i.e. 24 % of the surface heat flow. As suggested by Lucazeau et al. (1984), mantle heat flow is anomalously high beneath this part of the French Massif Central, reaching values around 60 mW/m^2.

Past and present models of the Chaudes-Aigues hydrothermal system

Models describing the hydrothermal system at Chaudes-Aigues have evolved over time. De Launay (1906) proposed that the water came from the gneissic plateau near the town and seeped down to a depth of 2 500 m before rising, under the effect of pressure, through the microgranite veins. Henou (1973) refined this theory by locating the reservoir at 2 000 m depth, with the drains still being the microgranite veins. Subsequent geochemical studies carried out by Cailleaux et al (1976), followed by Michard et al. (1981), suggested a mixture of deep warm water and colder surface water. The temperature of a deep reservoir has been estimated at around 175 to 200°C, on the basis of water chemistry data and use of chemical geothermometers as well as geochemical modelling of water-rock-gas interaction processes. Vasseur et al. (1997) proposed the first simplified diagram of the hydrothermal system, including infiltration zone, fluid pathways and emergence conditions. According to their model, two distinct water circuits would coexist within the MGC: a surficial, where cold waters infiltrate from the Aubrac and Margeride mounts or the CVC and reach 2 000 m depth. Another part of the water would flow through a deep path reaching 5 000 m depth. These two circuits would mix in an intermediate reservoir at a depth of 2 000 m, with an estimated proportion of 40 % deep hot water from a geothermal reservoir at 190 ± 10°C and 60 % shallow cold water.

Sampling and analytical methods

The water and gas samples presented here were collected in two field campaigns. The first in 2011-2013 (unpublished data collected by BRGM) and the second in 2023 (this study). Same methods for sampling and analyses have been used for both.

Water samples

A total of 32 water samples was collected including 27 samples of thermo-mineral waters and 5 samples of surface waters (see Table S1 in Supplementary Material, SM, and Figure IV.1). Collection of the fluid samples in the field was accompanied by appropriate on-site measurements such as fluid temperature, conductivity, pH, Redox potential, alkalinity and H_2S detection. The temperature, conductivity, pH and redox potential measurements were performed on the raw fluid samples using a WTW portable multiparameter measuring device and the corresponding electrodes, whereas alkalinity was analysed using HCl titration on fluid samples filtered at 0.45 µm. Absolute uncertainty concerning the pH measurements was 0.05 pH units and relative uncertainty concerning the other parameters varied from 5% to 10%, depending on the parameter and the range of measured values. For the parameters measured using the WTW portable device and the corresponding electrodes, absolute and relative uncertainties are given in their instruction manual.

Collection and conditioning of all the water samples followed the classical procedures recommended for each of the chemical and isotopic analyses to be performed. Thus:

- For the chemical analysis of major anions and some trace elements, such as Cl, SO_4, Br, F, NH_4 and PO_4, the water samples were filtered at 0.45 µm and collected in 100 ml polyethylene bottles.

- For the chemical analysis of major cations, the water samples were filtered at 0.45 µm, then acidified using Suprapur HNO_3 and collected in 100 ml polyethylene bottles.

- In order to avoid silica precipitation, the samples of hot water for dissolved silica analysis were collected in 50 ml polyethylene bottles and immediately diluted by a factor of 10 using Milli-Q water.

- For the chemical analysis of the other trace elements, such as B, Sr, Li, Ba, Mn, Fe, Al, Cs, Rb, Ge, As, Nd, Ag, Cd, Co, Cr, Cu, Ni, Pb and Zn, as well as for the isotopic Li and Sr analyses, the water samples were filtered at 0.1 µm, then acidified using Suprapur HNO_3 and collected in 100 ml polyethylene bottles.

- For the isotopic analysis of B, the water samples were filtered at 0.1 µm, then acidified using Suprapur HNO_3 and collected in 1 l polyethylene bottles.

- Untreated fluid samples for the isotopic analysis of D and ^{18}O in the water and of ^{13}C in the carbon dioxide were collected in 100 ml and 1 l polyethylene bottles, respectively.

- For the isotopic analysis of ^{18}O and ^{34}S in the dissolved sulphate, cadmium acetate was added to the water samples collected in 2 l polyethylene bottles.

All the chemical analyses for both major and trace elements in the collected water samples were done in the BRGM laboratories using standard water analysis techniques such as Ion Chromatography (IC), Inductively Coupled Plasma-Atomic Emission Spectroscopy (ICP-AES), Inductively Coupled Plasma-Mass Spectrometry (ICP-MS), Flame Emission Spectrophotometry, and Colorimetry. Depending on the concentration of the species in solution, the relative analytical uncertainties vary from 2 to 5% for major species and from 10 to 15% for trace and infra-trace elements.

The isotopic analyses of the water samples (δD and $\delta^{18}O$ of the water, $\delta^{18}O$ and $\delta^{34}S$ of the dissolved sulphate, $\delta^{13}C$ of the carbon dioxide, plus the $\delta^{7}Li$, $\delta^{11}B$ and $^{87}Sr/^{86}Sr$) were also performed in the BRGM laboratories using Thermo Ionization Mass Spectrometry and Neptune Multi Collector ICP-MS. More details relative to the BRGM analytical procedures are given in Millot et al. (2011). Deuterium and oxygen-18 isotope analyses were systematically carried out on all sampled water points. Values for Li, ^{11}B and the $^{87}Sr/^{86}Sr$ isotope ratio were determined at most sampling points. Values for ^{34}S et ^{18}O of dissolved sulphates and ^{13}C of dissolved CO_2 were measured on only a few selected samples.

The absolute uncertainty for the δD and $\delta^{18}O$ analyses of the water samples was ± 0.8‰ and ± 0.1‰, respectively. The absolute uncertainty for the $\delta^{18}O$ and $\delta^{34}S$ analyses of the dissolved sulphate was ± 0.1‰ and ± 0.3‰, respectively, while for the $\delta^{13}C$ analyses of the carbon dioxide, it was ± 0.1‰. The external reproducibility of the $\delta^{7}Li$ and $\delta^{11}B$ analyses was estimated at around ± 0.5‰ and ± 0.3‰, respectively, and the in-run precision of the $^{87}Sr/^{86}Sr$ ratio was generally better than ± 10×10^{-6} (2 σm, where σm is the standard error of the mean).

Gas samples

Gas samples were collected in specially designed glass flasks. Only two samples of non-condensable gases associated with the thermo-mineral waters of the Lavoir and Magnac have been sampled without significant atmospheric contamination. The corresponding chemical analyses (CO_2, N_2, O_2, He, H_2, H_2S, Ar, CH_4, ethane, propane, butane and pentane) were carried out by gas chromatography at the BRGM laboratories. These chemical analyses were also carried out on one gas sample extracted from the water of the Montchanson spring, after acidification with nitric acid. The relative analytical uncertainty of the measurements is 3%, except for He, H_2 and H_2S gases, where it is 5%. In addition, mass spectrometry analyses of $\delta^{13}C$ bound to free carbon dioxide were carried out on these three samples in BRGM laboratories. The absolute uncertainty on these measurements is ± 0.1‰.

Analyses of helium and neon abundances as well as of the isotopic ratio (R/R_a = $(^3He/^4He)_{sample}/(^3He/^4He)_{atmospheric}$) were carried out in the noble gas laboratory of the Institut de Physique du Globe de Paris (IPGP) on the first two samples of non-condensable gases. These analyses were performed using the ARESIBO mass spectrometer. Absolute analytical uncertainties on R/R_a isotope ratios range from ±0.007 to ±0.02, depending on the helium abundance. The R/R_a isotope ratio was also measured on dissolved gases in the water from the Montchanson thermo-mineral spring. The absolute analytical uncertainty is ±0.02.

Analytical results

Water chemistry and isotopes

The analytical results obtained for major and trace species are reported in SM Tables S4 and S5, respectively. The ionic balance (I.B.) values, all below 5%, suggest good analytical quality for major species.

The studied thermo-mineral waters are all carbo-gaseous, with emergence temperatures ranging from 2.2°C (Mazel Spring in Margeride) to 80°C (Par Spring in Chaudes-Aigues) and variable TDS values ranging from 0.4 g/l (Loubaresse Spring) to 4.8 g/l (Fontaine Basse 1, FB 1). In the Piper diagram shown in Figure IV.2, most thermo-mineral waters have a sodium-bicarbonate facies. Springs of the Margeride Est group and some of the Chaudes-Aigues area (Loubaresse, Jenny and Laval) deviate from this trend and correspond to sodium chloride facies. The Condamines spring (Chaudes-Aigues area) is alone in the calcic and magnesian chloride sulphate facies.

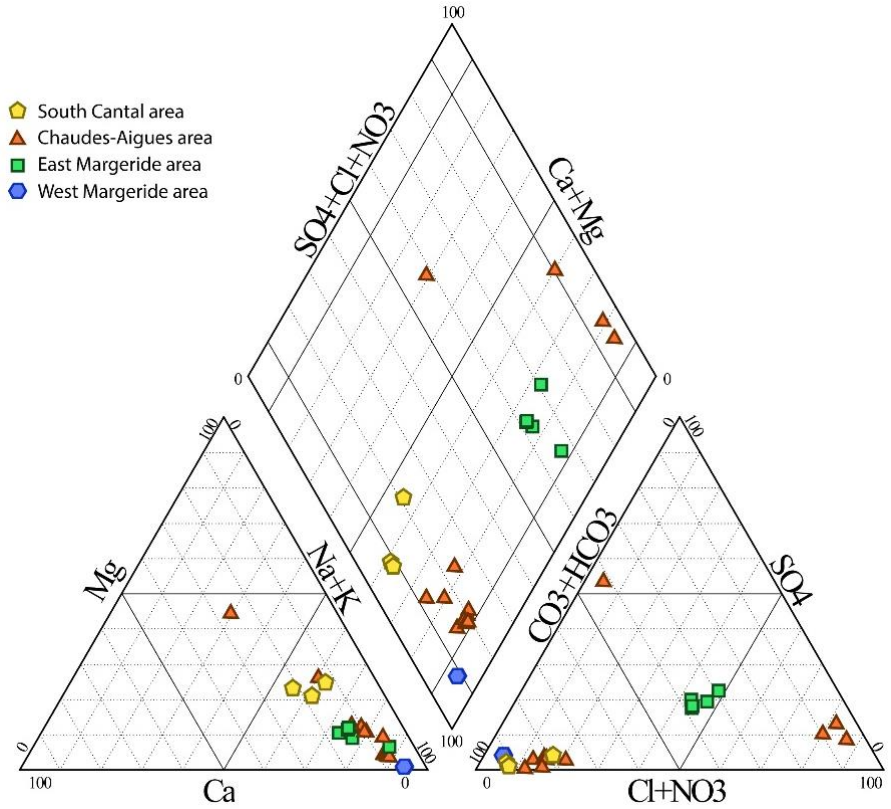

Figure IV.2: Piper diagram. The thermal waters were grouped by geographical location : South Cantal Area (Sainte-Marie, Moulinges, Fontanes), Chaudes-Aigues area (Par 2012, Par 2023, Lavoir 2012, Lavoir 2023, Ban 2012, Ban 2023, Boucharinc, Vialard, Tourette, Poste, Condamines, MTC 2012, MTC 2023, Laval, Loubaresse), Est Margeride area (Mazel, FH, FB1, FB2, Ranc) and West Margeride area (LC 2012, LC 2023).

According to Beaucaire et al. (1987), the major components of carbo-gaseous waters (Na and HCO_3) and soluble elements such as Cl, Br and B are mainly acquired in the deep reservoir

and are only subsequently affected by mixing processes with surface waters. Concentration ratios of these elements remain constant over large areas. These ratios can therefore be used to classify thermo-mineral waters into different groups, depending on the deep reservoir to which they belong.

Fig 3a and 3b represent, respectively, bromide concentrations and boron concentrations as a function of chloride concentrations. Figure IV.3c represents bicarbonate ions as a function of sodium. Three main groups of thermo-mineral waters belonging to different deep reservoirs can be identified. These generally correspond to the geographical location of the springs.

The first group includes the waters from the thermo-mineral springs of Chaudes-Aigues area, mainly located on the northern edge of the MGC (see Figure IV.1), with Cl/Br mass ratios ranging from 361 to 515 (Figure IV.3a). These waters also present values from 36 to 76 for the Cl/B mass ratio values (Figure IV.3b) and similar HCO_3-Na ratios (Figure IV.3c). If the thermal water of La Chaldette (LC 2012 and 2023) indicates a similar HCO_3/Na ratio to that of the Chaudes-Aigues waters, its Cl/Br and Cl/B mass ratio values (312-253 and 31-27, respectively) are relatively lower.

A second group of waters is made up of thermo-mineral springs of the South Cantal area (Figure IV.1, Sainte-Marie, Fontanes and Moulinges), with Cl/Br and Cl/B mass ratio values ranging from 484-518 and 172-271, respectively (Figs. 3a and 3b). Their comparable HCO_3/Na ratio values are the highest ones of the 3 groups (Figure IV.3c) and linked to their low measured pH values (5.76-6.19). They suggest relatively high-pressure of associated CO_2 gas. This could be due to their proximity with the CVC.

The third group gathers the East Margeride thermo-mineral springs (Fig.1, Mazel, Fontaine-Haute, Fontaine-Basse 1, Fontaine-Basse 2, Ranc), with Cl/Br mass ratio values ranging from 171 to 323 (the lowest, Figure IV.3a). Cl/B mass ratio values range from 94 to 157 (Figure IV.3b). Their HCO_3-Na ratio values are similar and lie between those of the waters from the two other groups (Figure IV.3c).

The existence of these three groups and linear correlations suggests processes of mixing between endmembers of deep, and therefore hotter waters, and surface cold waters, as these endmembers rise to the surface.

The isotopic analysis results are given in SM Table S6 and will be interpreted in the discussion section.

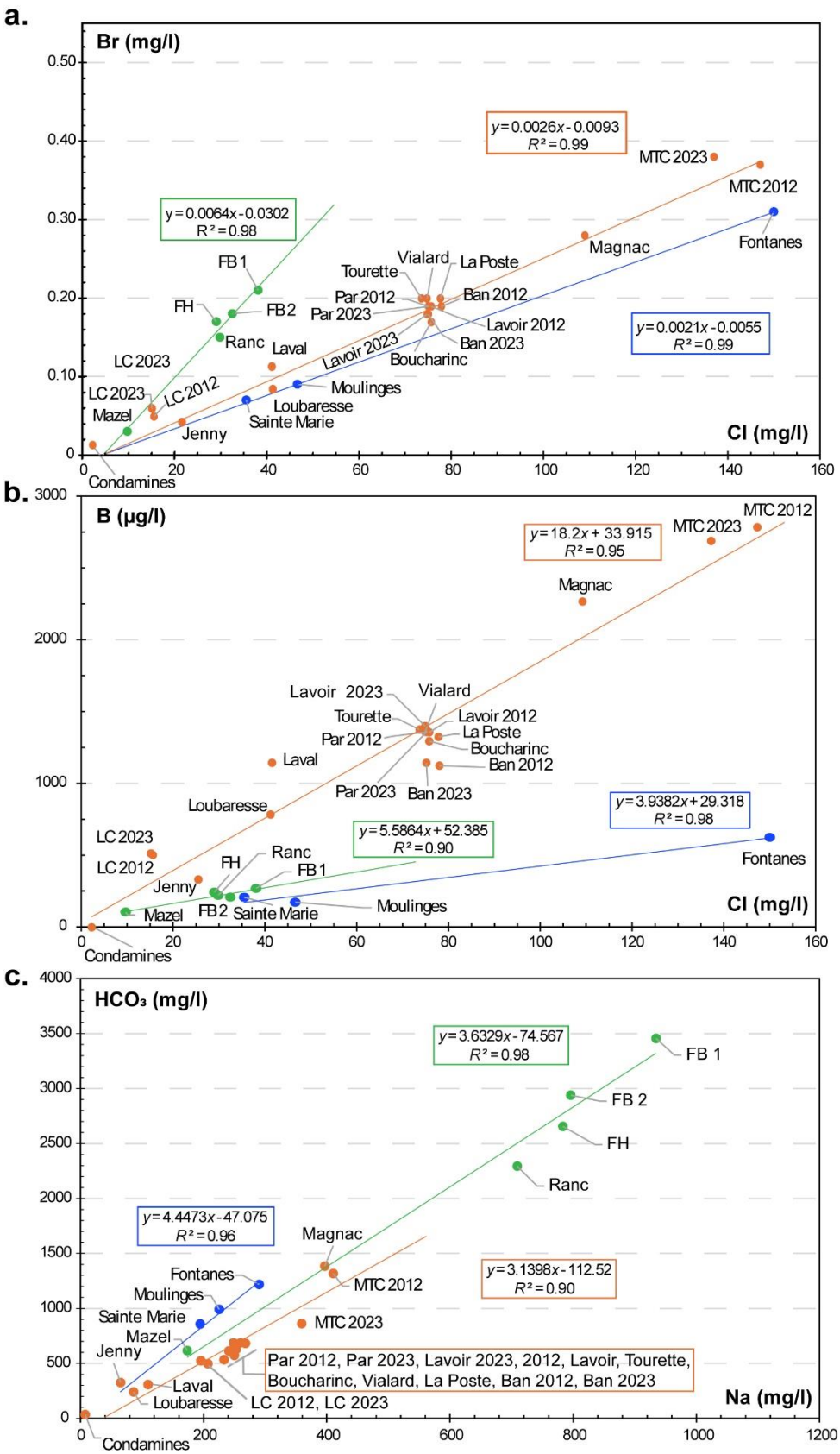

Figure IV.3: (a) Concentrations of bromide, (b) boron as a function of chloride ions. (c) Bicarbonate concentrations as a function of sodium (Na) concentrations. The mixing lines have enabled different reservoirs to be identified, highlighted by three different colours: Green for the Chaudes-Aigues, Orange for the East Margeride and Blue for South Cantal area.

Gas chemistry and isotopes

All the obtained results are reported in the SM Table 5. As shown in this table, the non-condensable gases associated with the waters of the two thermo-mineral springs that were correctly sampled (Lavoir and Magnac springs) are mainly CO_2. The methane concentrations of 0.08 and 0.04%, respectively, are relatively low. Slight contamination by air, most probably during sampling, which contributes small quantities of nitrogen, oxygen and argon, is observed for these gas samples.

Discussion

Origin of thermo-mineral waters

Stable isotopes in water provide information about the origin of water (Craig, 1961; Blavoux, 1995). Using the six surface water samples taken, a Local Meteoric Water Line (LMWL) was drawn, parallel to the Global Meteoric Water Line (GMWL; Craig, 1961). Its equation is shown in Figure IV.4.

The different groups of waters are distributed around the GMWL, indicating their meteoric origin. Waters from the South Cantal group (blue dots, see Figure IV.4) and the East Margeride (green dots, see Figure IV.4) are located on the local meteoric line, with some points shifted slightly to the left, indicating a possible interaction with CO_2 (Ferrara et al., 1965; Ferronsky and Poliakov, 1982; Karolyte et al., 2017). Most of the waters from the Chaudes-Aigues group is located to the right of the GMWL. This shift may be due to interactions with relatively hot waters and/or low water-rock ration values (high water-rock interaction processes).

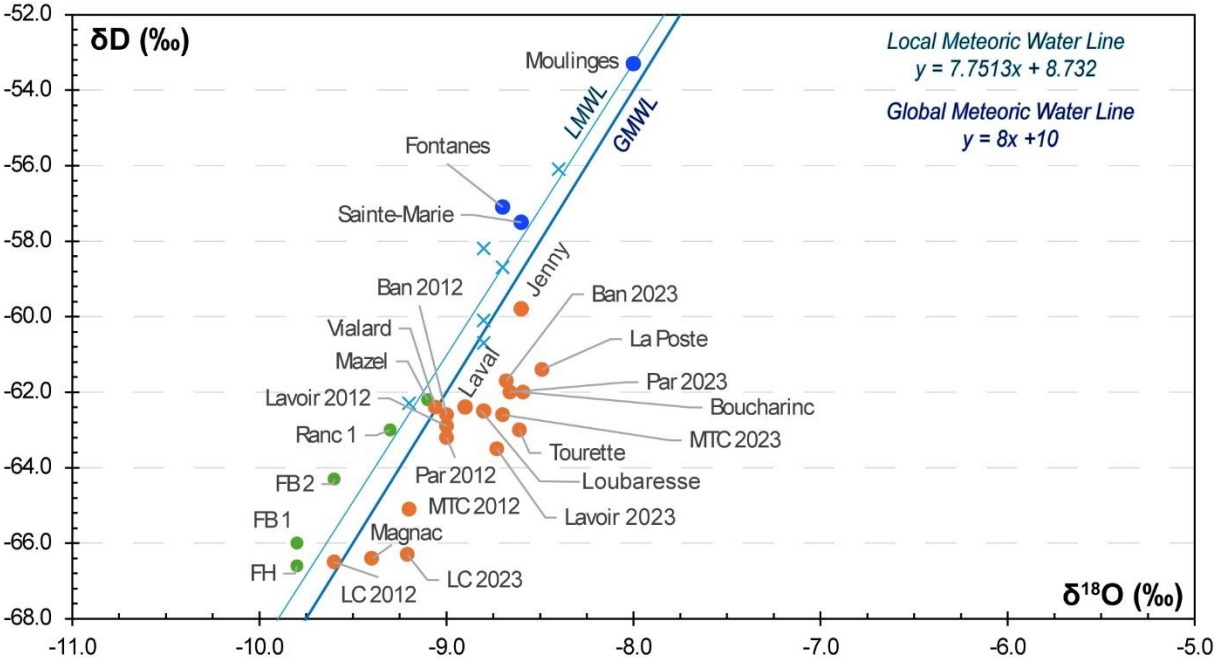

Figure IV.4: Deuterium (δ^2H) values versus 18-oxygen ($\delta^{18}O$) values in sampled waters. Colors correspond to previously identified groups: Orange for Chaudes-Aigues, Green for Margeride and Blue for Sainte-Marie. Surface waters (streams, rivers) are symbolized by blue crosses. The local meteoric line is based on these points.

Fig 5a and 5b, representing O and D isotopic values as a function of Cl concentrations, mobile species, also suggest that most of the studied water samples are the result of mixing processes. Except Magnac spring, waters of the Chaudes-Aigues group would therefore be the result of a mixture of surface component, the composition of which would be close to that of present-day meteoric water (blue crosses) and an endmember of deep and hot water from the geothermal reservoir. The Montchanson water (MTC 2012) is the closest to the isotope composition and chloride concentration of this deep hot endmember. These results confirm the studies carried out by Vasseur et al. (1997). The Magnac water would be also the result of a mixing of this endmember and cold surface water, but with a lower isotope signature than that of the present-day meteoric waters (Figure IV.5a and 5b). This could also be the case for the La Chaldette water, for which the contribution of the endmember of deep and hot water would, however, be much less significant than for the Magnac water. La Chaldette water would be mainly made up of surface waters.

The waters of the East Margeride group are also the result of a mixture of current surface waters (blue crosses), identical to those of the Chaudes-Aigues group, with a deep component, which is different this time.

For the South Cantal group, made up of only 3 springs, the Fontane spring has the most mineralized water (including the Cl concentration of 150 mg/l) and could have the isotope signature and chloride concentration closest to the deepest and hottest water endmember of this group.

Using mixing lines, we can estimate the composition of the reservoir. Here the deep poles would have a concentration of 180 mg/l and 56 mg/l for the Chaudes-Aigues and Margeride groups respectively (Figure IV.5a and 5b).

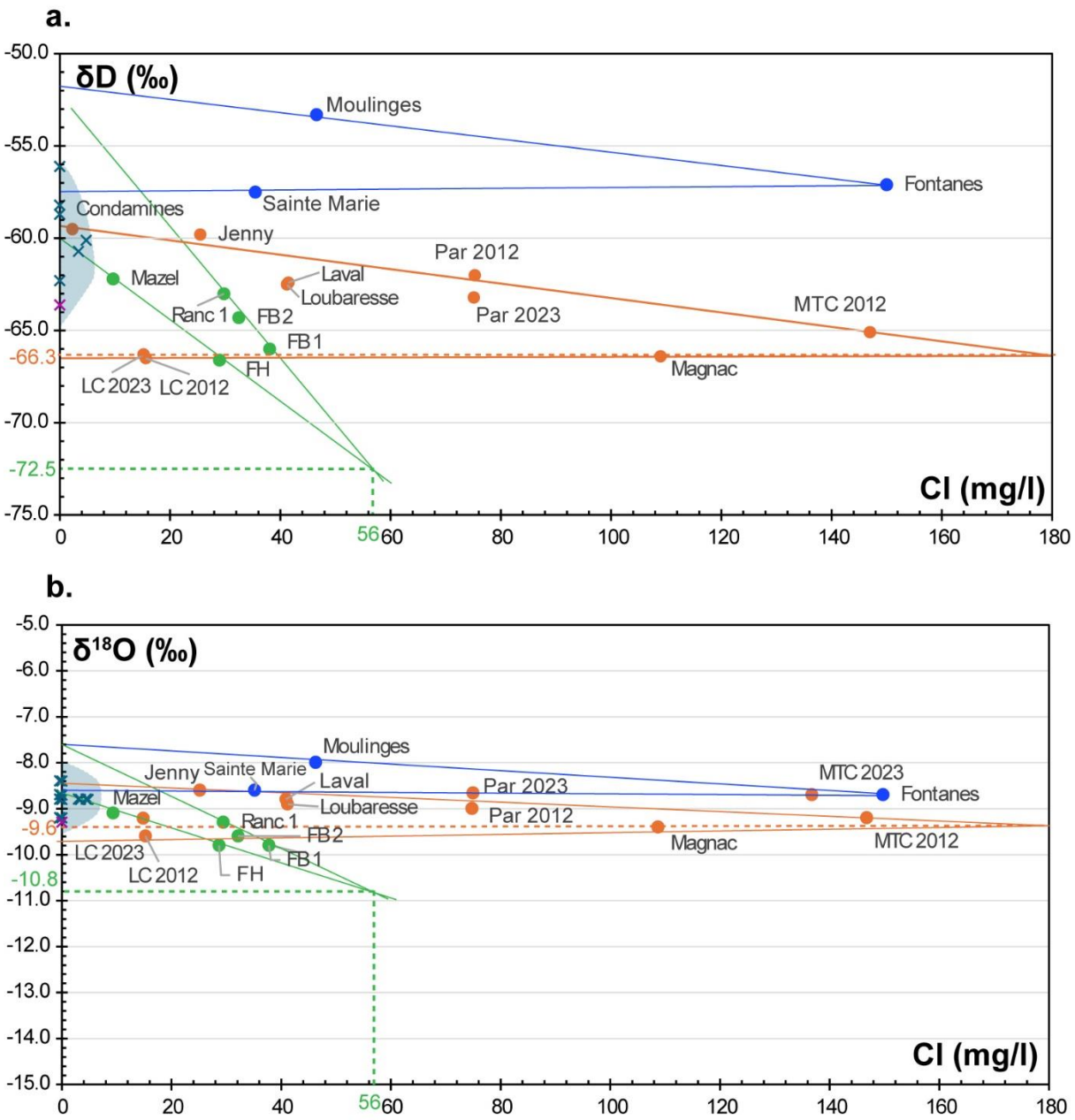

Figure IV.5: (a) δ^2H and (b) $\delta^{18}O$ concentrations versus chloride concentrations in sampled water. The colours of the dots correspond to the groups identified above: green for the East Margeride group, orange for Chaudes-Aigues

and blue for South Cantal. The blue crosses correspond to the rivers or streams sampled, the purple to a stream near Montchanson (Vasseur et al., 1997).

Chloride ions are mobile species that are involved in very few chemical reactions, so they can be used as tracers to identify dilutions. Using the deep compositions previously estimated, it is possible to calculate the mixing proportions of the studied springs. As mentioned above, the water from the Montchanson spring is the closest to the reservoir, representing on average 80% of its composition (Table 1). Conversely, the rest of the springs in the Chaudes-Aigues group are more diluted, with an average of 60% meteoric waters (Table 1). Water from the La Chaldette spring is mainly meteoric water, with less than 10% coming from a deep component (Table 1).

The group of East Margeride springs contains less diluted water, with an average of 60% deep reservoir water (Table 1). Only the Mazel Spring is predominantly surface water (83%).

In the case of the group of South Cantal springs, Fontanes water is the closest to the deep hot endmember.

	Springs	Deep Reservoir (%)	Meteoric water (%)
Chaudes-Aigues	Par	42	58
	Magnac	61	39
	MTC	82	18
Margeride	Mazel	17	83
	FH	52	48
	FB 1	68	32
	FB 2	58	42
	Ranc	53	47
South Cantal	Sainte Marie	24	76
	Moulinges	31	69

Table IV.2: Estimation of the percentages of deep pool and surface water originally constituting the water of the thermal springs sampled. The percentages are calculated using the chloride ion compositions estimated using Fig 5a and 5b, 180 mg/l and 56 mg/l respectively for the Chaudes-Aigues and East Margeride groups. For the South Cantal group, Fontanes is supposed to be the deep endmember.

Using oxygen isotopes, it is possible to determine the altitude at which water has infiltrated (Taillefer et al., 2018; Dupuy, 2021; Carbajal-Martinez et al., 2024). Using surface water samples, a local isotopic gradient can be calculated (see Figure IV.6a). Elevation values were

calculated using a local gradient based on surface water samples. The equation is shown in Figure IV.6a.

The springs in South Cantal group have the lowest altitudes (blue dots in Figure IV.6a). Using the isotopes, water is supposed to come from 625 to 700 m a.s.l. The Chaudes-Aigues springs (orange dots in Figure IV.6a), for their part, indicate infiltration altitudes ranging from 650 to 1300 m a.s.l. The dilution of thermal water has little effect on altitude, and the composition of the deep endmember (-9.6‰, see Figure IV.5b) indicates an altitude of 1300 m a.s.l. The springs in the MGC (East Margeride group, green dots in Figure IV.6a) come from the highest altitudes, 1000 - 1450 m a.s.l.

Using average values for the South Cantal, Chaudes-Aigues and East Margeride groups, we find: 675 m, 900 m and 1250 m respectively. These altitudes were compared with a digital elevation model to try and identify possible feeding areas for each group. As can be seen from Figure IV.6b, the impluvium of the Sainte-Marie group may correspond to the immediate environment of the springs (grey area). The southern slopes of the Cantal and the right bank of the Truyère correspond to these altitudes. For the Chaudes-Aigues springs, the feed zone appears to be further away. In fact, the eastern or western part of the MGC or the CVC in its upper part may correspond to the altitudes mentioned above. For the Mazel springs, the even higher altitude reduces the surface area available. The eastern part of the MGC, close to the springs, has consistent altitudes. Further away, the Cantal and the south-western end of the MGC also reach 1400 m a.s.l.

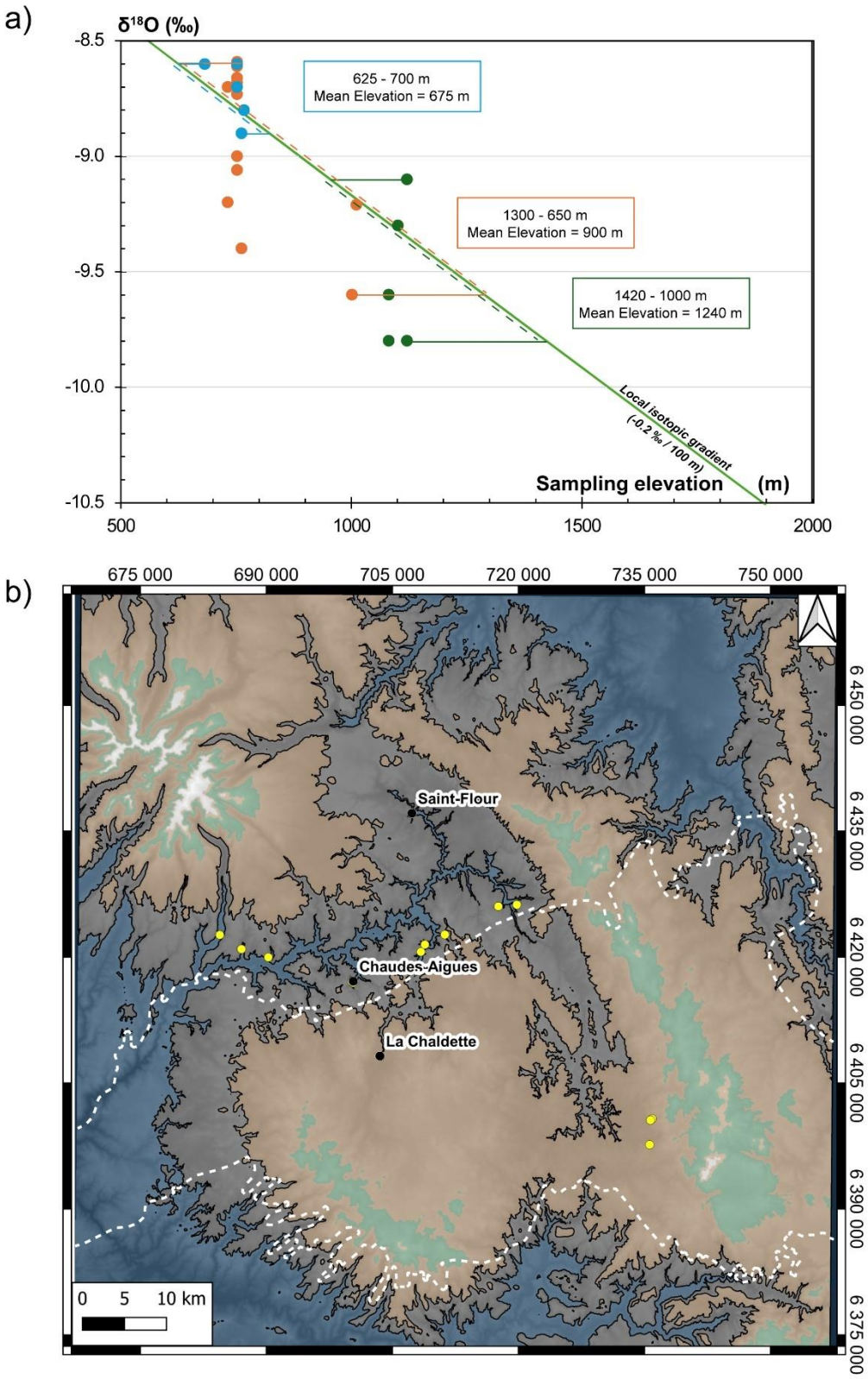

Figure IV.6: (a) Inferred recharge elevation of thermos-mineral waters sampled using a regional gradient determined with modern surface water (streams or rivers), Chaudes-Aigues group is represented in orange, South Cantal blue and East Margeride green. (b) Topographic map showing the different supposed impluvium, blue areas correspond to the elevation lower than 850 m a.s.l, grey between 850-1000 m a.s.l, brown higher than 1000 m a.s.l, green above 1400m. Thermo-minerals springs, here represented by yellow circles, correspond to those shown in Figure IV.1. The MGC boundaries are shown in white dotted lines. The averages are calculated for all the spring values in each group.

Since altimetry cannot eliminate neither the CVC nor the Aubrac or the southern edge of the MGC, the hydrogeological characteristics of the region must be considered. The CVC is separated from the Chaudes-Aigues springs by a natural barrier: the Truyère river. It seems unrealistic that the flows would be deep enough to avoid it. Furthermore, the structure of the Lower Gneiss Unit, located between the volcano and the springs, is unfavourable as their foliation is generally oriented towards the north (Penhoët et al., 2025a). A final reason against this would be the sedimentary basin (Aurillac basin) beneath the volcano (Nehlig et al., 2001), which would be more likely to retain fluids.

Concerning the Aubrac, although it is made up of very deep drains (basalts upwellings), it does not seem to be the best candidate either. Due to its highly fractured nature and the presence of volcanic rock, the plateau is an area of high permeability and therefore high infiltration. Eighty-nine springs (including seasonal ones) have been counted here (Bourlier et al., 2005). However, like the CVC, it remains at a significant distance (more than 20 km) from the Chaudes-Aigues springs. Although the vertical circulation of fluids seems to be confirmed, the geological map does not show any structures enabling fluids to be transported to Chaudes-Aigues. Finally, no evidence of basalt or other volcanic products was found in the water analyses. Consequently, the amagmatic characteristic of the Chaudes-Aigues hydrothermal system is strengthened.

Reservoir temperature

In hydrothermal contexts, it is common practice to use chemical and isotopic geothermometers to estimate the reservoir temperature of emerging thermal spring waters. These thermometric relationships using the chemical and isotope compositions of these waters are based on empirical, semi-empirical or experimental relations derived from known or unknown chemical equilibrium between water and minerals taking place in the geothermal reservoir. They assume that these waters have reached a thermodynamic equilibrium at depth and that this equilibrium has not been altered during their ascent to the surface.

Since 1965, numerous chemical and isotope geothermometers have been proposed in the literature. Among the most used are geothermometers such as Silica (Quartz or Chalcedony; Fournier, 1977; Michard, 1979), Na-K (Fournier, 1979; Arnórsson et al., 1983; Giggenbach, 1988; Michard, 1983; 1990), Na-K-Ca (Fournier and Truesdell, 1973), K-Mg (Giggenbach, 1988), Na-Li (Fouillac and Michard, 1981; Kharaka et al., 1982) and $\delta^{18}O_{H20\text{-}SO4}$ (Lloyd, 1968; Mizutani and Rafter, 1969; Zheng, 1999; Boschetti et al., 2011).

Group of the Chaudes-Aigues thermal waters

Given that all waters in the Chaudes-Aigues group all seem to be the result of a mixture between an endmember of deep hot water from the geothermal reservoir and surface waters (Figs. 4a, 4b, 4c, 6a and 6c), we will only attempt to estimate the temperature of this endmember. The Par thermal spring, which indicates the highest temperature of discharge and has a relatively high flowrate, has probably the water for which the Cl and SiO_2 concentrations are the least affected other than by the mixing process (depletion or enrichment in dissolved silica by mineral precipitation or dissolution reactions, for example). As the Cl concentration of the deep hot endmember from the geothermal reservoir was previously determined (180 mg/l), we can therefore calculate its corresponding concentration of dissolved silica, using the following relationship:

$$[\mathrm{SiO2}]_{reservoir} = [\mathrm{SiO2}]_{Par} \frac{[\mathrm{Cl}]_{reservoir}}{[\mathrm{Cl}]_{Par}} \quad (1)$$

This results in a concentration of dissolved silica of the order of 200-220 mg/l (see Figure IV.7).

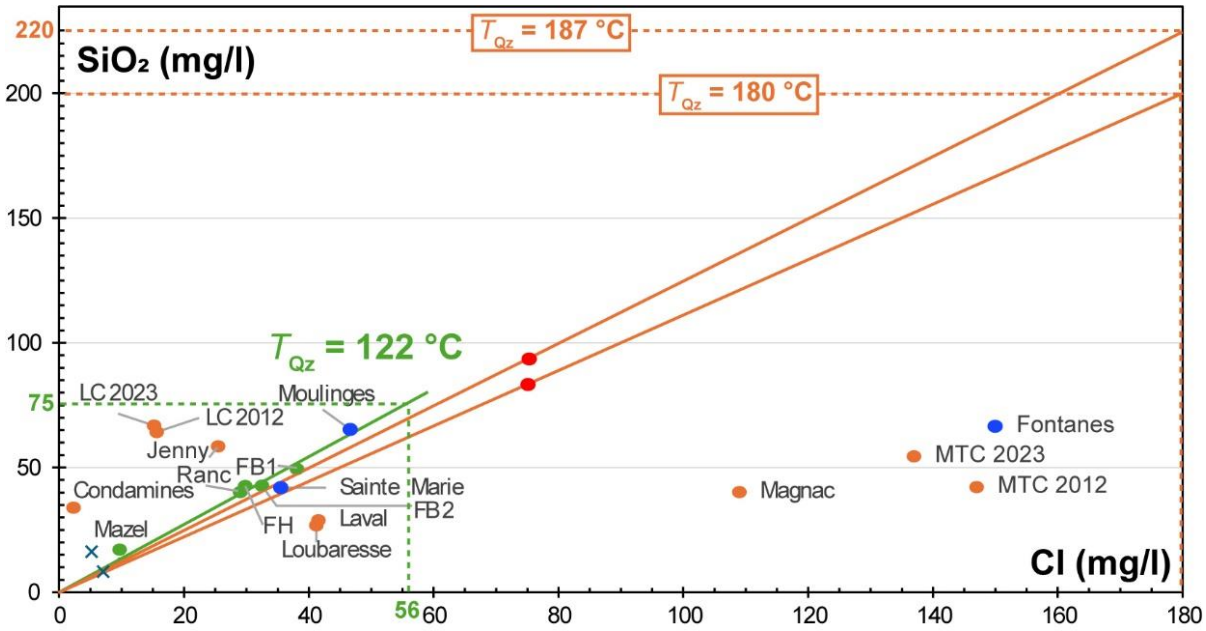

Figure IV.7: (a) Silica concentration as a function of chloride concentration in sampled water. The green (Margeride group) and orange (Chaudes-Aigues group) lines correspond to the concentrations of chloride of the hot deep reservoir, previously estimated at 56 mg/l and 180 mg/l respectively. Temperature of the two hot deep reservoirs have been estimated, T_{Qz}: Fournier (1977). (b) Zoom on the cluster of points corresponding to the Chaudes-Aigues thermal springs, The Par Spring (Par 2012 and 2023) used for the estimate is highlighted by red dots.

Using the Quartz-geothermometer (Fournier, 1977; Michard, 1979), the temperature of the deep hot endmember in the geothermal reservoir can be then estimated at 180-190°C.

This estimation is very close to those using the geothermometers such as Na-K (Michard, 1983; Arnórsson et al., 1983) and Na-K-Ca (Fournier and Truesdell, 1973), which give values of 193-202°C, 202-213°C, and 192-196°C, respectively, for the Par water samples (see SM Table S8 and S1).

The K-Mg geothermometer defined by Giggenbach (1988) gives a very underestimated temperature value (98°C), but this is not surprising as it is known that, unlike the hot waters which are depleted in magnesium, the cold surface waters can be rich in this element (Michard and Roeckens, 1983; Guo et al., 2019) and can disturb the chemical equilibrium of the hot waters with their deep reservoir, during the process of mixing between these waters.

Among the $\delta^{18}O_{H20\text{-}SO4}$ thermometric relationships applied on the Par water sampled in 2011, only those determined by Zheng (1999) and Boschetti et al. (2011), give values of temperature of 164°C and 171°C, close to those estimated using silica-quartz, Na-K and Na-K-Ca

geothermometers, but slightly lower. The other relationships determined by Mizutani and Rafter (1969) and Lloyd (1968) yield lower estimates (142 and 149°C, respectively).

Despite the uncertainties on the chemical analyses as well as on the isotope values, these estimates of reservoir temperature for the Chaudes-Aigues geothermal system, taken as a whole, are very close to that made by Cailleaux et al. (1976) and Vasseur et al. (1997) of 190 ± 10°C that can be considered as the most appropriate one.

During the ascent of gaseous hot waters to the surface, the concentrations of many chemical species can be considerably modified either by reactions of dissolution linked to the high cold aggressiveness of CO_2-rich waters, or by reactions of precipitation due to cooling and degassing of the solutions. Consequently, some variations in temperature estimates for each of the Chaudes-Aigues springs are to be expected, depending on the time taken to reach the surface, cooling processes, and the extent of mixing with surface waters, as shown in Table S8 (SM) and Figure IV.8.

Geochemical modelling (see details in S1, SM) support the consistency of our geothermometric results and confirm that the chemical composition of the deep fluid from the Chaudes-Aigues geothermal reservoir, before mixing with cold surface waters (see Table 2), is controlled at 190°C by an equilibrium reaction with respect to a mineralogical assemblage constituted, at least, of Quartz, K-Feldspar, Albite, and Illite (Muscovite). The CO_2 pressure values at 190°C estimated using these pH values and HCO_3 concentration range from 2.3 to 3.4 bar (2.8 bar for pH = 7.0 ± 0.1).

At this temperature in the reservoir, the deep fluid is also in equilibrium with respect to Laumontite, which could control the calcium concentration if this element is only affected by the process of mixing with cold surface waters and no other process. As we have seen that magnesium was most probably enriched by mixing with surface waters, we can estimate its concentration in the reservoir water before mixing if we assume that it is controlled by the Chlorite-Albite-Muscovite equilibrium reaction at 190°C and if we use the K-Mg thermometric

relation proposed by Giggenbach (1988), which is based on this equilibrium reaction. In this case, the concentration of Mg would be of the order of 0.15 mg/l.

Group	*T* °C	pH	Na mg/l	K mg/l	Ca mg/l	Mg mg/l	Cl mg/l	SO_4 mg/l
Chaudes-Aigues	180 -200	6.92 - 7.08	610 - 653	68 - 72	50 - 54	0.10 - 0.20	175 - 185	210 - 215
Margeride	80 - 120	6.00	1370 - 1380	50 - 60	220 - 230	15 - 20	50 - 60	

Table IV.3: Estimated composition of the deep endmembers based on previous dilution coefficients. For the South Cantal, the deep endmember has the composition of Fontanes spring.

Reservoir temperature beneath the Chaudes-Aigues thermal waters has also been estimated by numerical simulations of hydrothermal convection within a permeable fault zone (see SM S2). Appropriate thermal boundary conditions allowed to reproduce spring temperature (80 - 82°C) and surface heat flow (110 mW/m²) for a reservoir temperature of 185 °C at a depth of 5 km, thus confirming the previous estimated temperatures using geothermometers and geochemical modelling.

La Chaldette thermal water

The thermal water from the La Chaldette drillhole, which is located in the granite basement, can be considered as a particular case. Even if a small contribution of deep hot water from the Chaudes-Aigues geothermal system cannot be ruled out (of the order of 10%) and most of the fluid is constituted of surface water, most of the values of reservoir temperature estimated using chemical and isotope geothermometers are relatively comparable and range from 85 to 140°C (see Table S8, SM and Figure IV.8). This result suggests that this water is close to the full chemical equilibrium with respect to the reservoir rocks at a temperature of 110 ± 20°C. Its pH value estimated at this temperature (7.33) is higher than for the Chaudes-Aigues thermal waters and its associated CO_2 pressure (0.093 atm) is much lower. Consequently, this fluid is less aggressive towards the rocks it encounters as it rises to the surface and presents far fewer risks of CO_2 outgassing and scaling deposits. Very probably, it retains almost all of its chemical

composition resulting from equilibrium reactions at 110°C with respect to the rocks of its geothermal reservoir, which is also colder and shallower than that of Chaudes-Aigues.

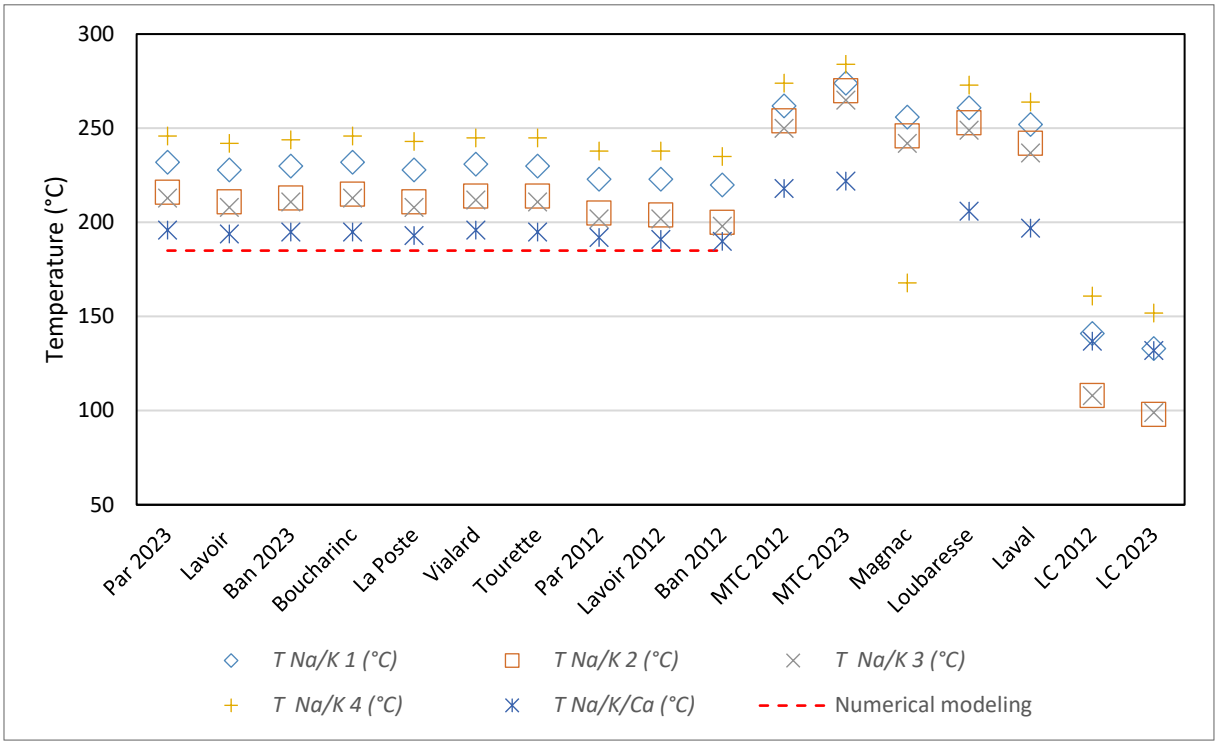

Figure IV.8: Estimated reservoir temperatures for the Chaudes-Aigues group using geothermometry. $T_{Na/K}$ (1) : Fournier (1979) ; $T_{Na/K}$ (2) : Michard (1979); $T_{Na/K}$ (3) : Arnórsson et al. (1983) T < 250°C; $T_{Na/K}$ (4) Giggenbach (1988) ; $T_{Na/K/Ca}$: Fournier and Truesdell (1973). The dashed red line indicates the temperature (185°C) of the Chaudes-Aigues reservoir, which has been estimated using numerical modelling (see S2, SM).

Group of the East Margeride waters

For the thermo-mineral waters in this group, the same approach as that applied to the waters from the Chaudes-Aigues springs can be used to determine the concentration of silica in the deep hot endmember, before mixing with surface waters, and at the same time estimate its temperature. A chloride concentration of around 56 mg/l corresponds to a silica concentration of 75 mg/l (Figure IV.7). Here again, it can be estimated that there was no precipitation of silica before and after mixing of the waters, the concentration of dissolved silica being relatively low. In the Icelandic volcanic environment, Arnórsson (1975) showed that Quartz was the controlling phase above 170°C, and by Chalcedony below 125°C. In the waters from granitic environment studied by Michard (1990), the transition temperature is close to 100°C. In general, waters with aquifer temperature of < 80°C equilibrates with Chalcedony, but some low-temperature waters can also equilibrate with Quartz. In the 80 - 100°C temperature range,

silica concentrations are intermediate between Quartz and Chalcedony solubilities. Depending on whether the Chalcedony or the Quartz geothermometer (without vapour loss) is used, temperatures of 90 - 93°C (Fournier, 1977; Arnórsson et al., 1983) to 122°C (Fournier, 1977) are estimated for the deep endmember of the East Margeride waters.

This temperature range is close to the values estimated using the Na/K thermometric relationships proposed by Michard (1990) and Arnórsson et al. (1983) for thermal waters with temperature values ranging from 25 to 150°C. Using the chemical composition of the deep endmember (see Table 2), these estimates are 108 and 113°C, respectively. The isotopic compositions of the springs indicate a temperature between 68 and 79.5°C (Table S8, SM). Consequently, for the East Margeride thermo-mineral waters, the temperature of their deep reservoir can be estimated at 100 ± 20°C. If we assume that the Mg in the reservoir water before mixing is controlled by the Chlorite-Albite-Muscovite equilibrium reaction at this temperature and use the K-Mg thermometric relation proposed by Giggenbach (1988), based on this equilibrium reaction, its concentration would be then close to 18 mg/l.

If we consider, like Sarazin et al. (1986), that the pH value of the Mazel water is the less affected by outgassing, because this water is the most diluted by the shallow waters before reaching the surface, we can estimate a pH value close to 6.00 for the deep reservoir water at 100°C, using the pH value measured at the discharge of the Mazel spring (6.19 at 2.2°C) and the previous approximate relationship proposed by Michard et al. (1981). The associated CO_2 pressure is then calculated to be close to 14.9 atm. This order of magnitude of CO_2 pressure, between 10 and 15 atm, is quite common in many places in the Massif central (Michard et al., 1987). Numerous geothermometers give either higher or lower temperature estimates (see Table S8, SM, and Figure IV.9), which are probably due to secondary reactions taking place during the ascent of the aggressive and unstable CO_2-rich water of the deep geothermal reservoir towards the surface (probable reactions of mineral dissolution and scaling precipitation due to degassing of CO_2).

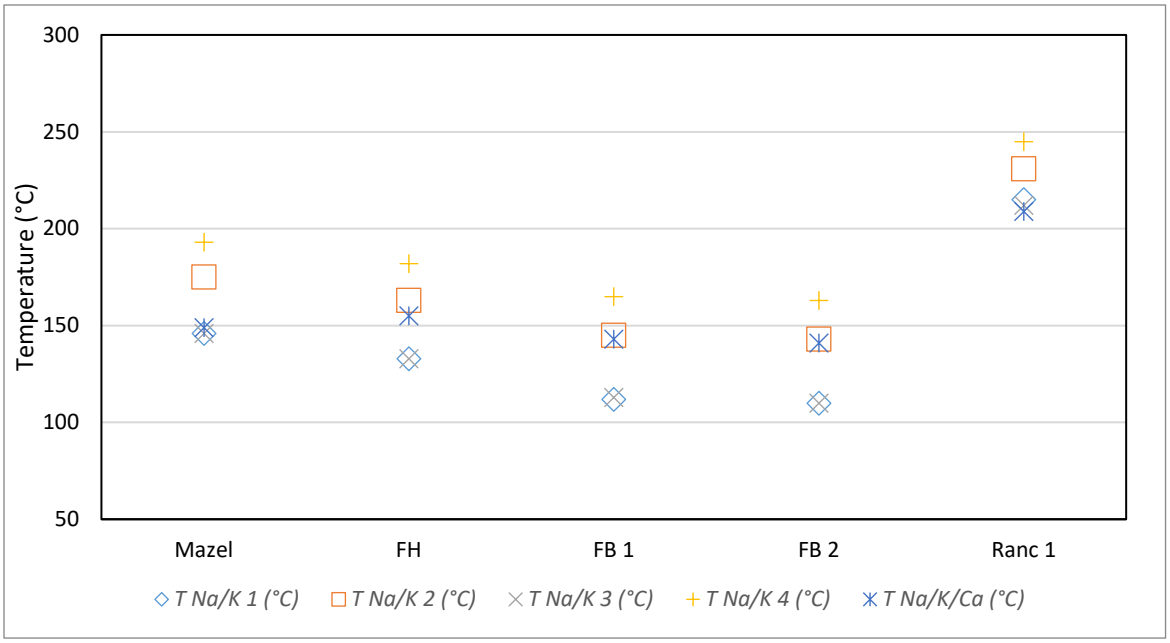

Figure IV.9: Estimated reservoir temperatures The East Margeride group using geothermometry. $T_{Na/K}$ (1) : Fournier (1979) ; $T_{Na/K}$ (2) : Michard (1979); $T_{Na/K}$ (3) : Arnórsson et al. (1983) T < 250°C ; $T_{Na/K}$ (4) Giggenbach (1988) ; $T_{Na/K/Ca}$: Fournier and Truesdell (1973).

Group of the South Cantal thermal waters

For the Sainte-Marie, Fontanes and Moulinges thermo-mineral waters in this group, the chemical geothermometers give relatively different temperature estimates (see Table S8, SM and Figure IV.10), which are probably due to the significant changes in a large part of the chemical composition of these acidic and aggressive CO_2-rich waters between the deep reservoir and the surface, which may also degas or mix with surface waters, particularly as regards species such as potassium, calcium and magnesium.

For these waters, the reservoir temperature is evaluated at 130 ± 15°C, mainly based on the temperatures estimated for the Fontanes thermo-mineral water, using the silica-Quartz geothermometer (Fournier, 1977), the Na-K thermometric relationships proposed by Michard (1990) and Arnórsson et al. (1983), and the $\delta^{18}O_{H20\text{-}SO4}$ isotope thermometric relationships defined by Lloyd (1968), Boschetti et al. (2011) and Zheng (1999), which give relatively concordant values of 116°C, 127 and 138°C, and 129 and 120°C, respectively. As mentioned before (see Figure IV.4 and 5), the Fontane water could be mainly constituted of deep CO_2-rich fluid coming from the geothermal reservoir, which cooled and partially interacted with neighbouring rocks as it rose to the surface.

At the reservoir temperature of 125°C, the pH value was calculated to be close to 5.80, using the lowest pH value (5.76) measured at the discharge of the three thermal springs. The associated CO_2 with the Fontanes water was then calculated to be around 8.7 atm in the reservoir conditions, confirming the high quantities of CO_2 accompanying these waters.

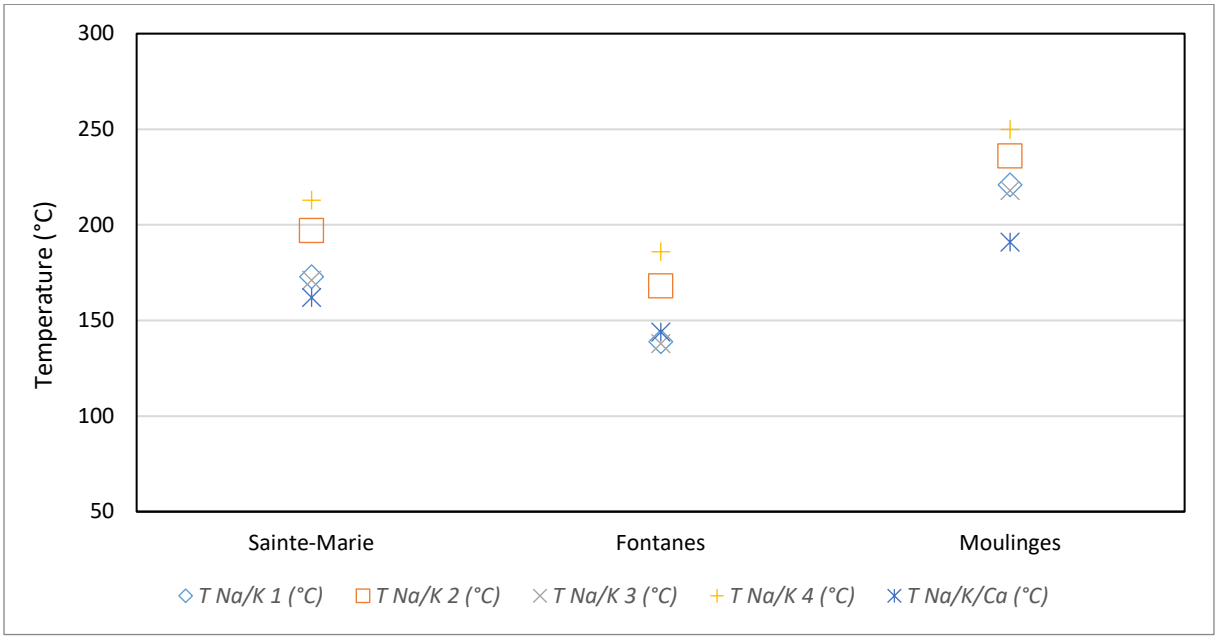

Figure IV.10: Estimated reservoir temperatures for the South Cantal group using geothermometry. $T_{Na/K}$ (1) : Fournier (1979) ; $T_{Na/K}$ (2) : Michard (1979); $T_{Na/K}$ (3) : Arnórsson et al. (1983) T < 250°C ; $T_{Na/K}$ (4) Giggenbach (1988) ; $T_{Na/K/Ca}$: Fournier and Truesdell (1973).

Isotopic signatures of the thermal waters

As the CO_2- rich deep thermo-mineral waters are aggressive due to their low pH value, they can interact with the rocks they encounter as they rise to the surface and be enriched in trace elements. They can also degas at the surface, causing scaling deposits such calcite, which can trap trace elements. In addition, these waters can mix with cold shallow waters. Consequently, unlike bromide and boron, numerous trace elements such strontium and lithium have not always a conservative behaviour, due to chemical re-equilibration processes, and it is difficult to know what their concentration was in the deep water of the geothermal reservoir. Frequently, the use of Sr, Li and B isotopes can help to better understand the processes controlling these elements and their behaviour. They can be useful tracers of water-rock interaction processes and of mixing of waters from different origins.

Strontium and Lithium signatures

Fig 11a and 11b indicate that the group of East Margeride waters, which is completely located in the granitic complex, is very enriched in strontium and lithium, compared to the other groups, while the isotopic values of these two elements are tighter (0.712964 - 0.718803 and 1.4 - 5.5 ‰, respectively), except for the Par, Ban and Lavoir thermo-mineral waters from Chaudes-Aigues, which have higher values of $^{87}Sr/^{86}Sr$ ratio ranging from 0.721948 to 0.721996, and the Moulinges water from the South Cantal area, which indicates a lower value of 0.711970 (Table S5, SM).

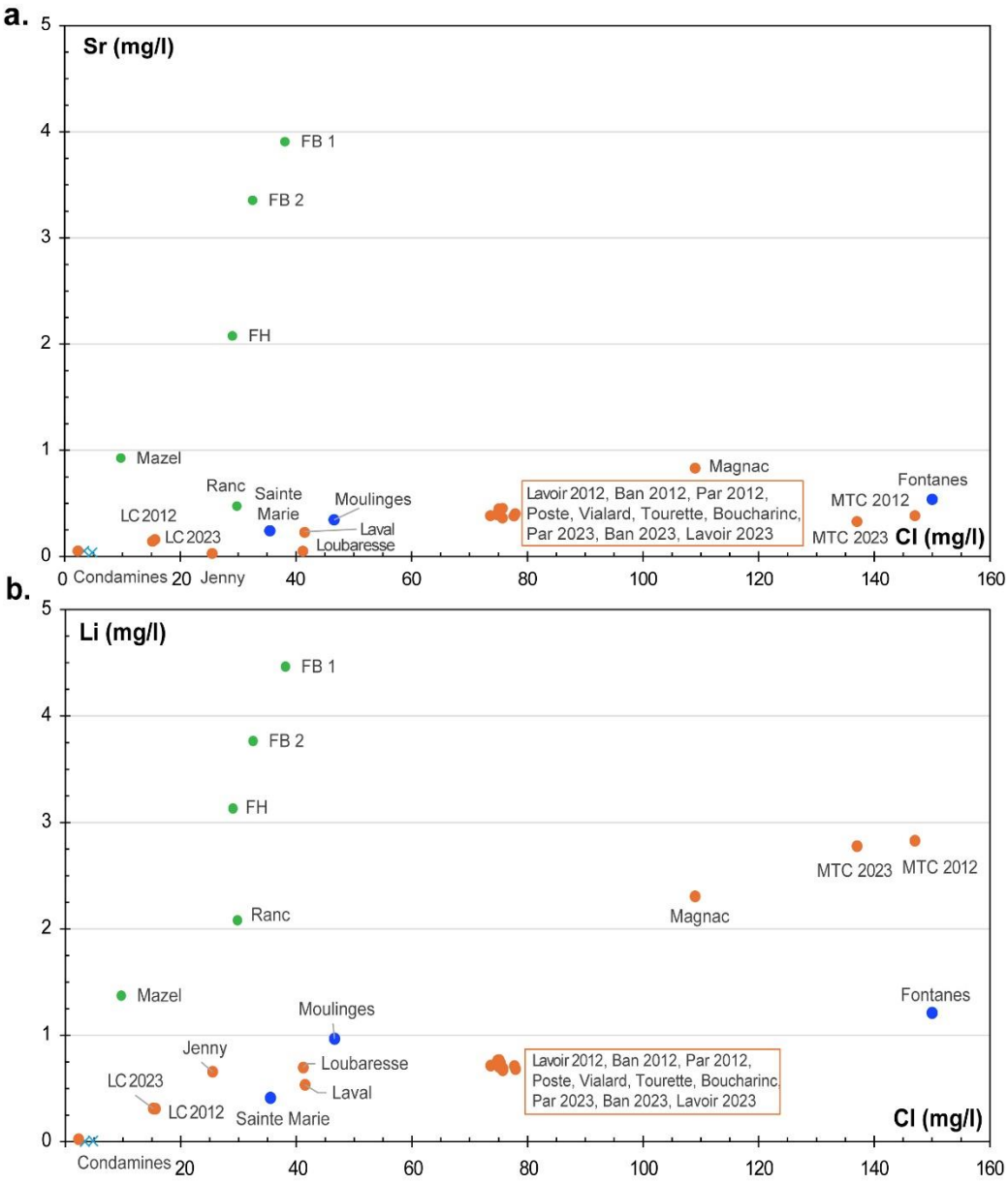

Figure IV.11: (a) Concentrations of Sr, (b) Li as a function of chloride ions. Waters groups are highlighted by three different colours: Green for the East Margeride area, Orange for Chaudes-Aigues and Blue for South Cantal area. Surface waters (streams, rivers) are symbolized by blue crosses

In these two Figures, except the Ranc water, the East Margeride fluids seem to confirm the mixing between a deep saline endmember water and surface dilute waters. For the waters of the other groups, this is much less obvious. The high amounts of Sr and Li observed in the East Margeride waters compared to those of the other waters (Figure IV.12a and 12b), must be probably associated to changes of granite mineralogical facies, given that their estimated reservoir temperature is the lowest one.

In their study on thermal and mineral waters from Hercynian granites in Portugal, Marques et al. (2012) determined $^{87}Sr/^{86}Sr$ ratio values between 0.710599 and 0.731496, which represents a similar but larger range of values than that of our study. They noted that many of these values were close to the Sr isotopic ratios of the plagioclases of the local granitic rocks (0.71261 - 0.72087 and 12b) and not to those of the whole granitic rocks (0.735697-0.789683).

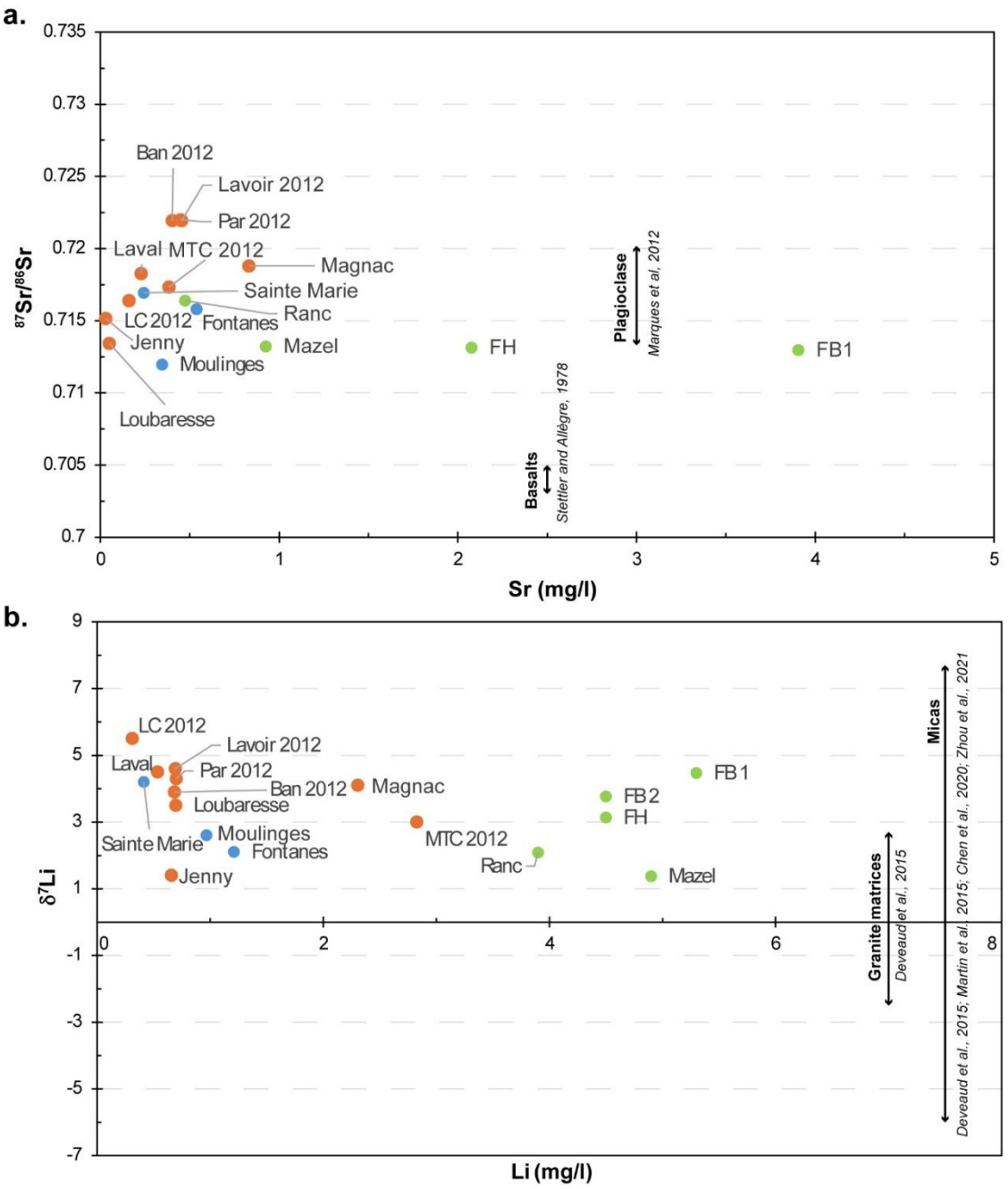

Figure IV.12: (a) $^{87}Sr/^{86}Sr$ ratios as a function of Strontium concentration, (b) δ^7Li values as a function of Lithium concentration in sampled waters. Isotopic values of specific minerals, used in the text, have been added (black arrows, their abscissas are not significant).

These results seem to be supported by the study carried by Zuddas et al. (1995) relative to granite-fluid interaction processes, who found that the Sr concentration and the $^{87}Sr/^{86}Sr$ ratio values in the waters depended on the dissolution of the minerals from the granite, such as plagioclase, biotite, K-feldspar. Based upon dissolution of feldspars under controlled laboratory conditions, Brantley et al. (1998) observed that plagioclase dissolved at relatively fast rates and could release significant Sr into solution, giving a Sr isotopic signature to the solution close to that of the plagioclase. Franklyn et al.

(1991) had already concluded, in their study based on groundwater $^{87}Sr/^{86}Sr$ ratios in the Eye-Dashwa Lake pluton, in Canada, that the Sr isotope ratios of the deep groundwaters were mainly the result of interactions with minerals such as plagioclase.

As noted by Marques et al. (2012), in open fluid systems, the time for reaction between plagioclase and water is short and, thus, the Sr isotopic signature of the fluids reflects the hydrolysis of plagioclase with low $^{87}Sr/^{86}Sr$ ratios rather than dissolution of the whole rock (Franklyn et al., 1991; Mc Nutt et al., 1987, 1990). However, radiogenic Sr from weathering of biotite and K-feldspars may be effectively removed from various granitic weathered systems (Blum et al., 1994; Zuddas et al., 1995) and usually, K-feldspars and biotite, which have high Rb contents, indicate higher $^{87}Sr/^{86}Sr$ ratios.

The highest Sr isotopic values analysed in the Par, Ban and Lavoir waters could indicate that these processes of K-feldspar and biotite dissolution have a greater contribution in the Sr contents of these waters.

For the Moulinges water, which has the lowest $^{87}Sr/^{86}Sr$ ratio, its location in the Cantal volcanic deposits, characterized by Sr isotope signatures close to 0.703 - 0.705 in the host basalt environment (Figure IV.12a), and their influence on the chemical composition of this water, could be put forward to explain this value (Stettler and Allègre, 1978).

In an experimental study of Li isotope fractionation between Li-mica and aqueous fluids from 300 to 500°C, carried out by Wunder et al. (2007), the T-dependence of the Li-isotope fractionation was approximated by the following equation:

$$\Delta^7\mathrm{Li}_{\mathrm{Li}\frac{\mathrm{mica}}{\mathrm{water}}} = \delta^7\mathrm{Li}_{\mathrm{Li-mica}} - \delta^7\mathrm{Li}_{\mathrm{water}} = -4.52\left[\frac{1000}{T(\mathrm{K})}\right] + 4.74 \quad (2)$$

We can also write:

$$\delta^7\mathrm{Li}_{\mathrm{Li-mica}} = \delta^7\mathrm{Li}_{\mathrm{water}} - 4.52\left[\frac{1000}{T(\mathrm{K})}\right] + 4.74 \quad (3)$$

If we apply this equation to the Par water at 190°C, which is the estimated reservoir temperature, we find a value of -0.72 ‰ for the corresponding solid phase, using the δ^7Li analysed in this water (4.3 ‰, Table S6, SM). For the La Chaldette water, this value is -1.56 ‰, at 110°C. For the Mazel - Fontaine Basse 1 water, this value is -2.07 ‰, at 100°C, and for the Fontanes water, this value is -4.51 ‰, at 125°C.These values are very different from those that can be calculated using other rare equations relative to Li fractionation existing in the literature, like those between clinopyroxene (synthetic spodumene) and aqueous fluids from 500 to 900°C (Wunder et al., 2006) and between basalt and diluted seawater from 25 to 250°C (Millot et al., 2010). For the first equation, we find respective values of -3.17 ‰ at 190°C, -4.05 ‰ at 110°C, -4.57 ‰ at 100°C, and -7.00 ‰ at 125°C. For the second equation, these values are: -4.55 ‰ at 190°C, -6.89 ‰ at 110°C, -7.64 ‰ at 100°C, and -9.52 ‰ at 125°C

The δ^7Li values calculated for the solid phases using the equation of Li isotope fractionation between Li-mica and aqueous fluids defined by Wunder et al. (2007) for the thermo-mineral of this study, at the estimated reservoir temperatures, seem to be those that are most in line with the literature data found for micas (δ^7Li values from -6.0 to 7.7 ‰; Deveaud et al., 2015; Martin et al., 2015; Chen et al., 2020; Zhou et al., 2021; see Figure IV.12b). These results suggest that micas are the main lithium-bearing minerals in the different geothermal reservoirs of this study and the temperatures estimated for these reservoirs are quite good. Except for the Fontanes water (Figure IV.12b), these results are consistent with those obtained by Teng et al. (2004) on the average upper continental crust of 0 ± 2 ‰ and on granite matrices (-2.5 to 2.7 ‰; Deveaud et al., 2015). According to Deveaud et al. (2015), most pegmatite and granite δ^7Li signature range from -2 to 2 ‰. For the Par water, the δ^7Li value of -0.72 ‰ calculated for the solid phase suggests that Li-rich pegmatite (δ^7Li values ranging from -1.0 to 10 ‰; Chen et al., 2020) could carry this element.

Boron signatures

Unlike lithium and strontium, boron often indicates a conservative behaviour in the thermal waters. The Cl-B diagram of the Figure IV.3b enabled us to distinguish the different groups of

thermo-mineral waters of this study. The d11B values vary greatly from one group to another, with only those in the South Cantal and East Margeride showing the highest values (positive values) in Figure IV.13.

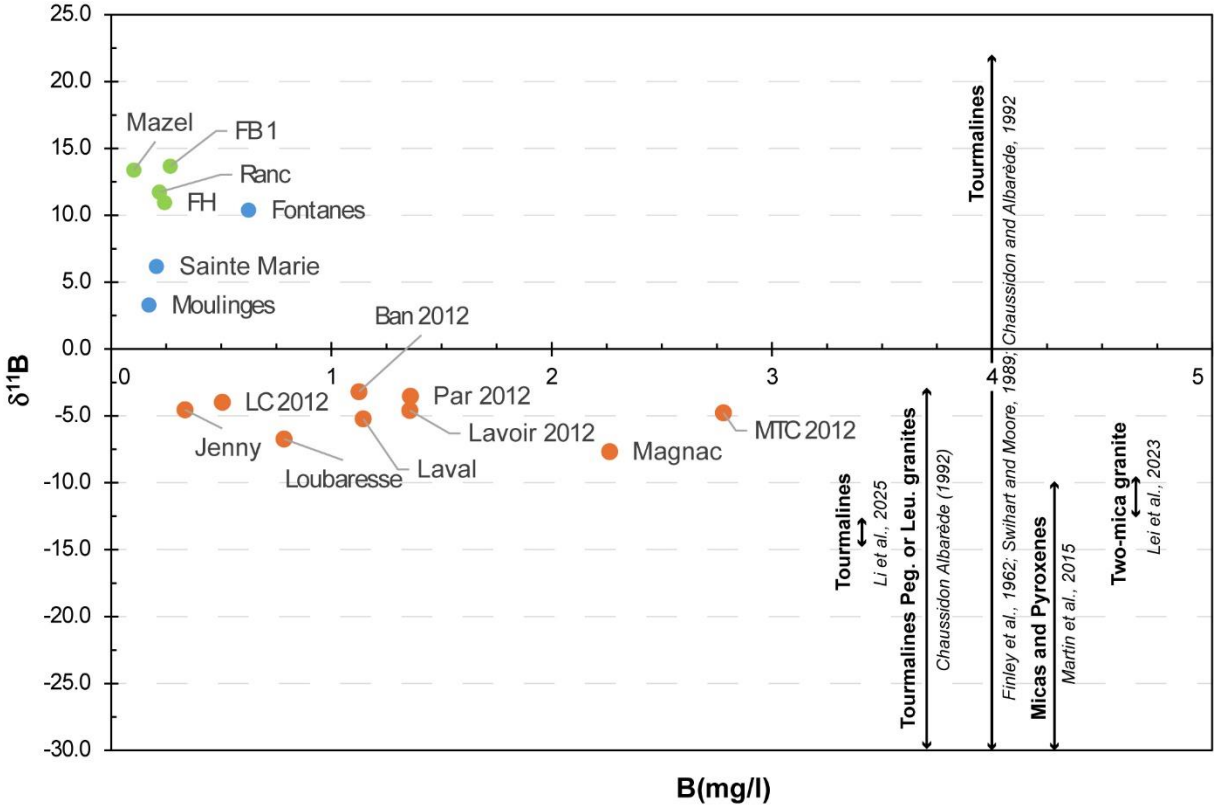

Figure IV.13: $\delta^{11}B$ values as a function of Boron concentration in the water sampled. Isotopic values of specific minerals, used in the text, have been added (black arrows, their abscissas are not significant).

As for Li isotopes, a similar approach can be used for boron isotopes. Two equations of boron isotope fractionation have been proposed in the literature by Williams et al. (2001) relative to the illitization of Smectite at 300 and 350°C, and by Wunder et al. (2005) for micas-clays melt between 25°C and 1000°C. These respective equations are as follows:

$$\Delta^{11}B_{\frac{\text{mineral}}{\text{water}}} = \delta^{11}B_{\text{mineral}} - \delta^{11}B_{\text{water}} = -10.12\left[\frac{1000}{T(\text{K})}\right] + 2.44 \quad (4)$$

$$\Delta^{11}B_{\frac{\text{mineral}}{\text{water}}} = \delta^{11}Li_{\text{mineral}} - \delta^{11}Li_{\text{water}} = -10.69\left[\frac{1000}{T(\text{K})}\right] + 3.88 \quad (5)$$

We can also write:

$$\delta^{11}B_{\text{mineral}} = \delta^{11}B_{\text{water}} - 10.22\left[\frac{1000}{T(\text{K})}\right] + 2.44 \quad (6)$$

and:

$$\delta^{11}B_{mineral} = \delta^{11}B_{water} - 10.69\left[\frac{1000}{T(K)}\right] + 3.88 \quad (7)$$

If we apply these two equations to the Par water at 190°C, which is the estimated reservoir temperature, we find respective values of -22.94 and -22.73 ‰ for the corresponding solid phases, using the $\delta^{11}B$ analysed in this water (-3.53 ‰, see Table S6, SM). For the La Chaldette water, these values are -27.95 and -28.00 ‰, respectively, at 110°C. For the Mazel - Fontaine Basse 1 water, these values are -11.01 and -11.10 ‰, at 100°C, and for the Fontanes water, these values are -12.60 and -12.59 ‰, at 125°C.

All these isotopic values are lower than those analysed by Martin et al. (2015) in micas and pyroxenes ($\delta^{11}B \geq$ -9.9 ‰), but most of them are in the range observed in the continental crustal rocks ($\delta^{11}B$ from -30 to 22 ‰; Finley et al., 1962; Swihart and Moore, 1989; Chaussidon and Albarède, 1992).

The low $\delta^{11}B$ values calculated for the Par and La Chaldette waters could be explained by the relatively abundant presence of tourmaline described in the sub-alkaline Muscovite, Biotite and Tourmaline leucogranites. These granites are generally fine-grained rocks, often aplitic, but frequently with pegmatitic zones, and clearly posterior to the Margeride granite, which they cross, forming numerous generally sub-vertical veins no more than ten metres wide, like in the Chaudes-Aigues thermal area, or sub-horizontal sheets often several tens of metres thick (Couturié, 1977; Bayer et al., 1982). In the pegmatitic zones, we mainly find (Couturié, 1977):

- xenomorphic Quartz;
- Albite and perthitic K-Feldspar, rarely self-morphing, which sometimes form masses of up to several cubic metres,
- blades of Muscovite and, more rarely, Biotite;
- very common black Tourmaline (Schorl), of needle packs arranged in parallel that can weigh several kilos;
- automorphic Cordierite, entirely phyllitised, in stocky prisms 1 to 2 cm in diameter;

- pink andalusite, in prisms 1 to 2 cm in diameter.

Presence of Tourmaline was also observed in the clear facies of the Margeride granite (Couturié, 1977). Tourmaline is the most abundant boron-bearing mineral in the crust (Barth, 1993). Chaussidon and Albarède (1992) have studied tourmalines by ion microprobe. They found a wide range in $\delta^{11}B$ values of -29.9 to -2.9 ‰ for Tourmaline minerals hosted in granites, pegmatites and aplites, which covers the entire range of the values calculated in our study. The most positive $\delta^{11}B$ values were found in Li-rich Tourmalines, while schorl was the most depleted in ^{11}B, which is concordant with the mineralogical observations in the leucogranites of our study, especially in the pegmatitic areas.

Chaussidon and Albarède (1992) determined their lowest $\delta^{11}B$ values (-29.9 to - 20.5‰) in Tourmalines from Archean pegmatitic granites, in Swaziland, Southern Africa, and from Bouaflé granite, in Ivory Coast, Africa, which are comparable values with those calculated for the solid phases relative to the Par and La Chaldette waters. The presence of sub-vertical veins of leucogranite with pegmatite areas, enriched in Micas, in the Chaudes-Aigues area, could also explain the highest $^{87}Sr/^{86}Sr$ ratios observed in this study (see previous sub-section about strontium signature).

Relative to the Mazel - Fontaine Basse 1 and Fontanes waters, similar $\delta^{11}B$ values for solid phases were reported by Chaussidon and Albarède (1992) in the range of - 16.3 to -10.3 ‰ in Tourmalines from Gangotri and Manaslu leucogranites, in high Himalaya, from Soublaké granite, in Ivory Coast, Africa, from pegmatitic dike, in Niger, Africa, and from banded aplite in layered pegmatite, in Swaziland, Southern Africa. Li et al. (2025) determined B isotope compositions of tourmaline ranging from -14.8 to -12.6 ‰ in Li-poor pegmatites in the Mufushan granitic batholith, South China.

Given all these results, it could be concluded, in our study, that $\delta^{11}B$ values in the thermo-mineral waters mainly depend on temperature and the amount of Tourmaline in the granite rocks. However, the behaviour of the B isotope fractionation is probably more complex

because the data relative to the Mazel - Fontaine Basse 1 and Fontanes waters can be also compatible with the B isotopic values reported by Lei et al. (2023) in their study on samples of two-mica granite and Biotite granite from the Huayang-Wulong granite suite (South Qinling, Central China). For Biotite in Biotite granite, these authors determined δ^{11}B values ranging from -12.7 to -9.6 ‰ and this value was -12.0 ‰ in two-mica granite. Note that Muscovite had systematically lower δ^{11}B values than Biotite by more 5-8 ‰. Feldspar + Quartz had δ^{11}B values of -13.1 to -9.6 ‰ for Biotite granite and -12.6 ‰ for two-mica granite, slightly lower than Biotite from the same granite samples.

Finally, Williams et al. (2007) proposed the following geothermometer based on intracrystalline boron isotope partitioning in Illite-Smectite:

$$T(°\mathrm{C}) = \frac{\left(\delta^{11}\mathrm{B}_{\mathrm{tetrahedral}} - \delta^{11}\mathrm{B}_{\mathrm{interlayer}} + 30\right)}{0.05} \quad (8)$$

This approximate formula suggests that the interlayer sites of Illite-Smectite preserve the B isotopic composition of water at the temperature that produced the authigenic Illite. If we apply this geothermometer using the B isotopic data of the Par Spring, we can then estimate a temperature of 212°C, which is slightly higher than that given for the geothermal reservoir, using the other geothermometers (T = 190 ± 10°C). For the other geothermal systems (La Chaldette, Mazel - Fontaine Basse 1 and Fontanes), using this same formula, we find the respective estimations of reservoir temperature of 121°C, 106°C and 140°C, which are also relatively concordant with those previously estimated using the other geothermometers (110°C, 100°C and 130°C).

Gas origin

The ^{3}He/^{4}He ratios measured on the non-condensable or dissolved gases give a rough estimate (considering possible kinetic fractionation during degassing) of the percentage of helium of mantellic origin, according to the formula of Clauser et al. (2002):

$$\%\ \mathrm{He}_{\mathrm{mantle}} = \left[\left(\frac{R}{\mathrm{Ra}}\right) * \frac{(R\mathrm{a} - R_{\mathrm{crust}})}{(R_{\mathrm{mantle}} - R_{\mathrm{crust}})}\right] * 100 \quad (9)$$

with R_a = 1.385 x 10^{-6} (Mamyrin and Tolstikhin, 1984), R_{mantle} = 1.2 x 10^{-5} (Craig and Lupton, 1981) for the MORB source and R_{crust} = 1.5 x 10^{-8} (Mamyrin and Tolstikhin, 1984). If we consider, according to Gautheron et al. (2005), that the mantle beneath the Massif Central has a different isotopic signature and that this signature of intra-plate volcanism is instead characterized by an $^3He/^4He$ ratio of the order of 6.3±0.3 *R*a, then we must take a value of 8.7 x 10^{-6} for the R_{mantle} isotope ratio.

The $^3He/^4He$ measured on the three gas samples associated with the Lavoir, Magnac and Montchanson thermo-mineral springs are, respectively: 0.828 ± 0.007, 1.119 ± 0.009 and 0.720 ± 0.02 (Table S7, SM), allowing us to estimate, for each source, helium percentages of mantle origin of the order of 13.0, 17.6 and 11.3%, if we consider a mantle signature of 6.3 Ra. Using a MORB signature for the mantle component, the values are 9.4, 12.8 and 8.2%, respectively.

These values can be compared with those compiled by Matthews et al. (1987), who positioned thermo-mineral water and gas samples from the Massif Central in relation to major European geothermal zones (Figure IV.11). As this work was carried out in 1987, the percentages of helium of mantle origin estimated by these authors are based on a MORB-type mantle helium ratio and are, in principle, somewhat underestimated in relation to the currently known context of the Massif Central. It should be noted that the contributions of mantle origin estimated in our study are relatively significant. In particular, they are much higher than those estimated for the Upper Rhine Graben (URG), where R/R_a values range from 0.1-0.2. The He contents associated with the Lavoir and Magnac thermal springs vary from 50 to 60 ppm. These He contents are low compared to non-condensable gases associated with waters originating from a known granitic reservoir such as Soultz, in the URG (He contents from 4500 to 22000 ppm; Sanjuan et al., 2010, 2011). This suggests a short residence time of these gases in the granite. If we compare the results for the two water samples on which $\delta^{13}C$ values were measured for both thermo-mineral water and gaseous CO_2 associated with thermo-mineral springs (Table S7, SM), we confirm that isotopic fractionation is greater at lower temperatures, since we

obtain: $\Delta(CO_2)_{gas}$-$(CO_2)_{solution}$ = $\delta^{13}C(CO_2)_{gas}$ - $\delta^{13}C(CO_2)_{solution}$ = -6.4‰ for Lavoir spring water, which indicates an emergence temperature of 67.7°C, and -10.5‰ for Magnac spring water, which has an emergence temperature of 10.5°C.

From these results and the $\delta^{13}C$ values measured on thermo-mineral waters (Table S7, SM), we can roughly estimate, the $\delta^{13}C$ values of gaseous CO_2 associated with these waters. Thus, for gaseous CO_2 from the Montchanson spring, we find a similar $\delta^{13}C$ value (-5.7‰) to that of gaseous CO_2 from the Magnac spring (-6.3‰), which is very close to a MORB-type signature of mantle origin.

For gaseous CO_2 from the Laval and Jenny thermal springs, $\delta^{13}C$ values would be between -8.0 and -10‰, suggesting a greater contribution of organic and atmospheric origin (mixing of the deep pole with a much more pronounced surface water input). The same type of remarks can be made for gaseous CO_2 from the waters of the Sainte-Marie, Fontanes and Moulinges spring group, for which we obtain $\delta^{13}C$ values ranging from -8.0 to -11‰, or for the waters of the Margeride spring group for which $\delta^{13}C$ values range from -9.5 to -13‰. For gaseous CO_2 from the La Chaldette borehole, the estimated value of $\delta^{13}C$ is around -12‰, which is compatible with a relatively superficial water.

By way of comparison, although the Massif Central shows a signature of intraplate volcanism, volatile compounds from MORBs, in most cases, have an average $CO_2/^3He$ ratio value of $2 \pm 1\ 10^9$ (Marty and Jambon, 1987).Values of these ratios higher than those of volatile MORB compounds are due to the mixing of a crustal compound rich in CO_2 and ^4He with gases from the upper mantle (Fiebig et al., 2004).

The $CO_2/^3He$ ratio can be calculated according to the following formula of Giggenbach et al., (1994) :

$$CO_2/\ ^3\mathrm{He} = \frac{X_{\mathrm{Co2}}}{\left(Ra * \left(\frac{R}{Ra}\right) * X_{\mathrm{He}}\right)} \qquad (10)$$

where X_{CO2} and X_{He} are the proportions of gas by volume. For gas samples from the Lavoir, Magnac and Montchanson springs, the $CO_2/^3He$ ratio values give, respectively: $1.4\ 10^{10}$, $1.10\ 10^{10}$, $> 4.4\ 10^{10}$.

These values, associated with an isotopic signature of intra-plate volcanism, are higher than those of the $CO_2/^3He$ ratio, of gases associated with mid-ocean ridge basalts (MORB). The values found for gases associated with the Lavoir and Magnac springs are comparable to those found on the Waitopu ($9.7\ 10^9$) and Wairakei ($1.4\ 10^{10}$) geothermal fields, characteristic of rift gas emissions. Furthermore, Brauer et al. (2016) support this interpretation by highlighting similar elevated $CO_2/^3He$ ratios in continental rift zones, linking them to deep magmatic CO_2 contributions and low mantle helium dilution, consistent with tectonic settings characterized by lithospheric extension. The Massif Central is known for its large quantities of carbon dioxide emissions, which are particularly visible in groundwater (Ricci et al., 2024). Many springs in the Massif Central are rich in carbon dioxide, such as those at Vichy (Michard et al., 1976), Limagne (Fouillac and Michard, 1979), Chaudes-Aigues and others

Conceptual model of Chaudes-Aigues hydrothermal system

The work here has not only confirmed the hypotheses previously established but has also provided new information to clarify the functioning of Chaudes-Aigues hydrothermal system.

Consequently, in the light of our results, the southern edge of the granite (see white dots line, Figure IV.6b) represents the best candidate to be the impluvium. The Chaudes-Aigues springs are spatially connected to this area by a N150E fault zone several kilometres thick (2.5 km according to the geological map, De Goer de Herve et al., 1994). Its southern part is covered by morainal sediments. Analyses have demonstrated that the surface water component of Chaudes-Aigues springs could correspond to that of La Chaldette. As the spring is located in the middle of the fault zone, this confirms that the water could infiltrate into the southern part of the MGC and could be then drained north-westwards towards the town. The meteoric component of the Chaudes-Aigues springs therefore comes from the MGC. Contrary to the model of Vasseur et al. (1997), no glacial origin is suggested here.

Once the water has reached the northern edge of the MGC, it could use the Couffour Granite as a vertical drain. This small granite is supposed to be younger (De Goer de Herve, 1991). This would explain the higher $^{87}Sr/^{86}Sr$ values compared to those of the East Margeride springs. Thanks to the topographic gradient and the numerous N50E faults, fluids flow through the valley carved out by the Remontalou and reach the emergence area. These faults are also responsible for the upwelling of mantle gases into the reservoir. Figure IV.14 summarises all the results for the Chaudes-Aigues hydrothermal system and the new reservoirs.

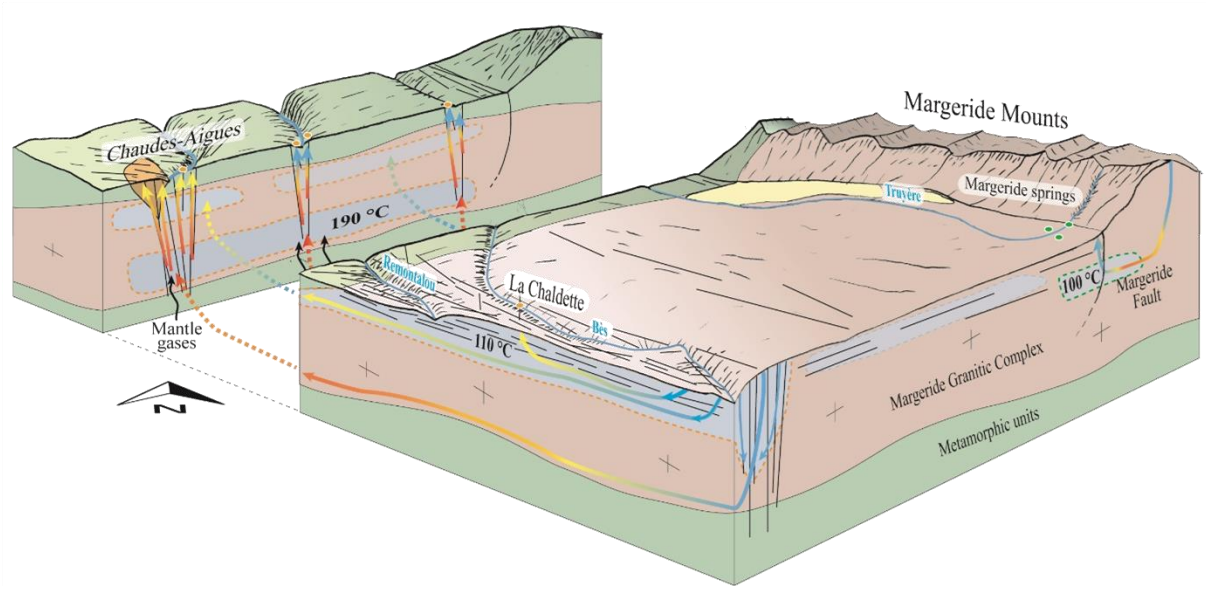

Figure IV.14: 3D block diagram (not to scale) summarizing fluid circulation and the various geothermal reservoirs within the Margeride Granitic Complex. Couffour granite, near Chaudes-Aigues, is represented in orange. The South Cantal group was not represented.

Conclusions and perspectives

Our study based on a “large-scale” sampling of thermo-mineral waters helped to characterise the hydrothermal system of Chaudes-Aigues but also revealed the presence of two others hydrothermal systems within the MGC.

Firstly, the largest reservoir could exist on the northern edge of the MGC. This would partly supply the springs of Chaudes-Aigues, Loubaresse, Laval, Magnac and Montchanson. The Montchanson spring is the closest in composition to this deep endmember. Our data enabled us to accurately estimate the temperature of this reservoir, which is 190 ± 10 °C, a value which is confirmed by geochemical and numerical models (Figure IV.8 and SM, S2). This initial component is supplemented by another component of cold surface water. Due to the high

density of faults and fractures around Chaudes-Aigues springs, fluids can rise in abundance and at high rates maintaining their high temperature. Conversely, the springs further East (Montchanson, Laval, Loubaresse, Magnac), with few faults, fluid ascent is limited, resulting in low flow rates and temperatures.

Further south, waters from La Chaldette spring are locally infiltrated and heat up to 110 ± 10 °C at depth without any mixing. This hydrothermal system could be associated with circulation in a horizon affected by both tectonics (fault zone) and supergene alteration (fluid circulation) such as the regolith.

Finally, the East Margeride group comes from a mixture of surface water from the Margeride Mounts, located just to the east, and waters from and a deep reservoir. Based on our data, the reservoir temperature is estimated at around 100 ± 10 °C. Their low surface temperature could be due to relatively low fracturing in the area.

Other fractured granites in France and Europe, such as the MGC, could host hydrothermal systems consisting of several reservoirs with multiple fluid pathways, which would be of interest for high-temperature geothermal exploration. A well-known European reference is the Soultz-sous-Forêts system, located in Alsace, France, in the Upper Rhine Graben (URG). Even if the geothermal system is developed within fractured Hercynian granite, it lacks sufficient natural permeability and active fluid circulation. In consequence, the system required hydraulic stimulation to artificially improve reservoir permeability (Genter et al., 2010). This highlights a key distinction: while Soultz-sous-Forêts is an Enhanced Geothermal System (EGS), Chaudes-Aigues represents a naturally functioning, amagmatic hydrothermal system, with no sedimentary cover, sustained by fluid flow through inherited fault and fracture networks without any artificial enhancement.

In terms of analogues, we can find systems with similar geological characteristics as our study area. In eastern France, Bains-les-Bains and Plombières-les-Bains are two towns known for their thermal springs, with temperatures ranging from 27 to 51°C and 43 to 80°C, respectively

(Desprez et al., 1971). Very few geological studies have been carried out on these systems, and the only information available is that the springs are linked to grabens bordered by Variscan faults (Desprez et al., 1971), and that the water would flow in the granite (Lefort and Jutier, 1862). Other cold springs have been found further east of these two systems. This area is made up of a granite massif covered by a thin layer of sediment, represents a direct analogue to the MGC. Another example is the Pietrapola thermal station in south-east Corsica, with several springs ranging from 27 to 54°C (Dupuy, 2021). Here, according to geochemical studies, after a long circulation through the Hercynian bedrock (monzogranite), waters spring up through faults (Dupuy, 2021). Similarly, the Karlovy Vary, formerly known as Karlsbad, springs in the Czech Republic, are also associated with a granitic basement (Vrba, 1996). The massif is rich in hot springs, indicating a potential geothermal reservoir.

The common point between all these systems is that despite their renown as thermal centers, few geological or hydrogeological studies have been carried out. The identification of blind geothermal system, that have no surface manifestations (Hanson et al., 2014; Dobson, 2016; Craig et al., 2021), remains challenging and happens often by accident (Garg et al., 2010; Faulds and Hinz, 2015; Dobson, 2016). In our case, the systems are not blind but hidden by unstudied surface indicators. The chemical composition of cold springs is already a favourable surface indicator. This exploration would need to be extended around known hydrothermal systems to identify hidden ones. This represents a fantastic opportunity for high-temperature geothermal exploration.

Funding

The financial support was provided by Bureau de Recherches Géologiques et Minières (BRGM), Institut des Sciences de la Terre d'Orléans (ISTO) and by the project « GERESFAULT » funded by the French Research Agency (ANR-19-CE05-0043).

Acknowledgements

Geochemical data from the 2012 field campaign were acquired by BRGM for a private company, which finally did not publish these data. We would like to thank both anonymous reviewers for their advice leading to a more concise and structured manuscript.

Supplementary Material

S1: Reservoir temperature: complementary chemical geothermometric calculations and geochemical modelling

For the Na-K geothermometer, the used thermometric relationship of Arnórsson et al. (1983) is that determined for geothermal waters with temperature values ranging from 25-250°C. The thermometric relationships determined by Fournier (1979) and Giggenbach (1988) give overestimated temperature values (223-232°C and 238-246°C, respectively). These values are similar to those estimated using the thermometric relationship determined by Arnórsson et al. (1983) for geothermal waters with temperature values ranging from 250 to 350°C, which are 221-229°C, suggesting that the thermometric relationships defined by Fournier (1979) and Giggenbach (1988) are better adapted for waters with such high temperatures. Conversely, the thermometric relationship defined by Michard (1990) for geothermal waters with temperatures between 50 and 150°C gives slightly lower estimates (173-181°C).

Indeed, according to several authors (White, 1965; Ellis, 1970; Fournier et al., 1979; Arnórsson et al., 1983; Giggenbach, 1988; Michard, 1990), it is widely accepted that the Na-K geothermometer is based on the chemical equilibrium between K-feldspar and Albite in most natural waters at temperatures greater than 100-150°C:

$$\mathrm{KAlSi_3O_8\ (K-Feldspar) + Na^+ = NaAlSi_3O_8\ (Albite) + K^+} \qquad (11)$$

with an equilibrium constant K (T) = $(K^+)/(Na^+)$, where (K^+) et (Na^+) are the activities of these two elements.

Depending on the temperature range between 100-150°C and 250°C, the thermodynamic data concerning the mineral phases, especially the degree of ordering and crystallinity of the precipitated Albite, can vary and slightly modify this equilibrium constant. At temperatures lower than 100-150°C, either equilibrium with these two minerals is not attained or other solid phases, such as clays, micas, and zeolites can control dissolved Na and K (Fournier and Truesdell, 1970; Fournier, 1979, 1991).

Michard et al. (1981) established a model for estimating the temperatures of geothermal reservoirs while explaining the chemical composition of the thermo-mineral waters in these reservoirs based on a chemical equilibrium with respect to the mineral association Quartz, Albite, Adularia, Calcite, Kaolinite or Illite, and Chlorite. They showed that the temperature is the main variable for determining the chemical composition of the thermo-mineral waters. This model can be considered as a chemical geothermometer using the overall chemical composition of the waters. They applied this model (with Illite instead to Kaolinite) to the Par thermal water, before mixing with the surface waters. They obtained a correct representation of the chemical composition of this water in terms of pH, Na, K, SiO_2, and HCO_3 concentrations, and estimate a reservoir temperature of 175°C.

This estimation is slightly lower than that recommended in this paper, but the observed difference is mainly due to the selected thermodynamic data, and their uncertainty. This discrepancy can be explained in the same way as those observed for the results using the different Na-K geothermometric relationships.

In order to confirm the consistency of our geothermometric results, which already suggest chemical equilibrium of the Par water with respect to Quartz (Silica geothermometer), Albite and K-feldspar (Na-K and Na-K-Ca geothermometers) in the deep geothermal reservoir at 190°C, before mixing with cold surface waters, we sought to estimate its pH value, assuming this water is also in equilibrium with respect to Illite, represented by Muscovite, as done by Michard et al. (1981). The concentrations of dissolved species such as Na, K, Ca, HCO_3 and SO_4 in this deep water can be calculated (see Table 2) in the same way as the concentration of dissolved silica was previously estimated, using the chloride concentrations.

Assuming the chemical equilibrium between K-Feldspar and Muscovite:

$$3\mathrm{KAlSi_3O_8\ (K-Feldspar)} + 2\ \mathrm{H^+} = \mathrm{K3Al3Si_3O_{10}(OH)_2(Muscovite)} + 6\ \mathrm{SiO_2\ (Quartz)} + 2\ \mathrm{K^+} \quad (12)$$

the equilibrium constant of this reaction is: $K(T) = (K^+)^2/(H^+)^2 = \gamma_K^2\ [K^+]^2/10^{-2pH}$.

Solving this equation at a temperature of 190°C, using the thermodynamic database proposed by Johnson et al. (1992) and the Extended Debye-Hückel equation for the γ_K activity coefficient calculation, gives a pH value close to 6.92 for the deep water of the geothermal reservoir. A neighbouring pH value of 7.08 is found using the thermodynamic database proposed by Michard (1983).

The pH values measured for the Par water samples vary from 6.26 to 6.35 at the discharge of the spring. As this water is mixed at relatively significant proportions with cold shallow waters before reaching the surface, we can assume that its pH is very little affected by outgassing. As discussed by Sarazin et al. (1986), the pH of very dilute waters is the best estimate of pH before outgassing. The more dilute the water, the smaller the outgassing and the smaller the pH change (Michard et al., 1986).

On the other hand, in order to compare the pH value under reservoir temperature conditions (190°C) estimated using that measured at the discharge of this spring, we can use the formulas:

$$\mathrm{pH}_{\mathrm{t°C discharge}} = \mathrm{pK}_{\mathrm{A1}}\left(\mathrm{t°C}_{\mathrm{discharge}}\right) + \log\left[\frac{(\mathrm{HCO}_3^-)}{(\mathrm{H_2CO_3})}\right] \quad (13)$$

$$\mathrm{pH}_{190°\mathrm{C}} = \mathrm{pK}_{\mathrm{A1}}\,(190°\mathrm{C}) + \log\left[\frac{(\mathrm{HCO}_3^-)}{(\mathrm{H_2CO_3})}\right] \quad (14)$$

where (HCO_3^-) and (H_2CO_3) are the activities of these species and pK_{A1} = - log K_{A1}, K_{A1} being the equilibrium constant of the chemical reaction: HCO_3^- + H^+ = H_2CO_3, which lead to the approximate relationship:

$$\mathrm{pH}_{190°\mathrm{C}} \approx \mathrm{pH}_{\mathrm{t°C discharge}} + \mathrm{pK}_{\mathrm{A1}}\,(190°\mathrm{C}) - \mathrm{pK}_{\mathrm{A1}}(\mathrm{t(°C)discharge}) \quad (15)$$

Indeed, the species HCO_3^- and H_2CO_3 can be considered as conservative species to a first approximation.

Using the thermodynamic database proposed by Johnson et al. (1992) and the pH values measured at the discharge of the Par Spring, we find pH values around of 6.99-7.13, which

are very close to those previously estimated using the equilibrium reaction between Muscovite and K-Feldspar (6.92-7.08).

S2: Numerical modeling

Modeling procedure and set-up

The uncertainty on the value of the reservoir temperature can be reduced by numerical modeling of hydrothermal circulation in a fault zone, from a depth of 5 km (Vasseur et al., 1997) to the surface,

where hot fluid emerges. To constrain the reservoir temperature, simplified 2D numerical experiments have been performed with the Comsol Multiphysics™ software. The main objectives consist at (i) simulating fluid circulation within a wide permeable faut zone, and (ii) reproducing both the regional surface heat flow value (100 – 120 $mW.m^{-2}$; Lucazeau et al., 1984) and the maximum spring temperature at Chaudes-Aigues (80°C). A vertical permeable fault zone, 800 m wide, 5 km deep, is embedded within granitic host rocks (Figure IV.15). These numerical values are consistent with surface observations and previous studies (Vasseur et al., 1997; Penhoët et al., 2025a). At a depth of 5 km, a fixed temperature value (the reservoir temperature) is imposed. At the surface, a fixed temperature T_0 of 10°C is imposed, except above the fault zone, where a mixed thermal condition allows variations in surface temperature. This condition is controlled by a heat transfer coefficient h, and the surface heat flow (Q) above the fault zone equals $h \times (T_0 - T)$. This kind of thermal condition (also called Robin boundary condition), has already been used by Magri et al. (2015) or Taillefer et al. (2018, 2024) to reproduce spring temperatures higher than the average surface temperature. Elevated temperatures and elevated vertical fluid velocity above the fault zones correspond to the emergence of hot fluid.

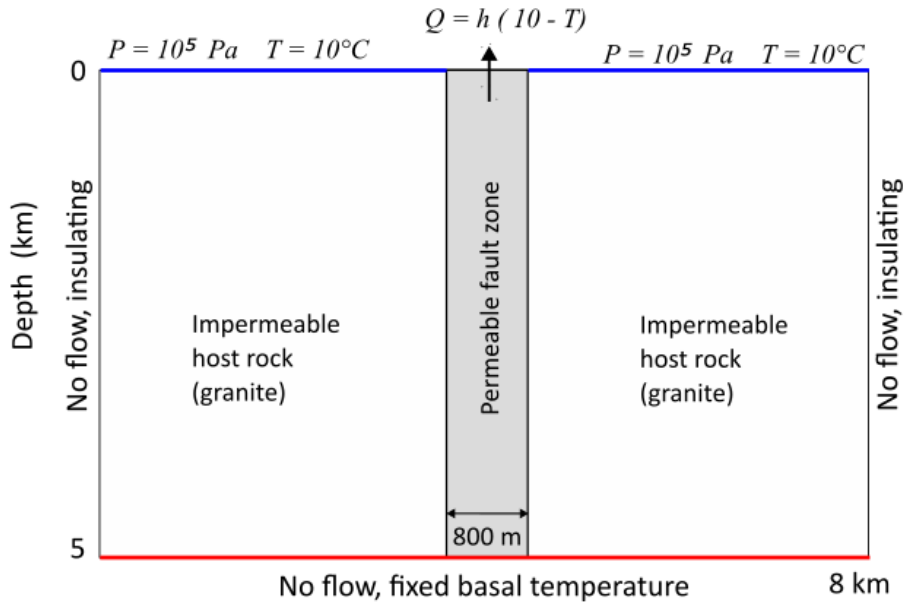

Figure IV.15: Model set-up and boundary conditions (see text). Blue and red lines correspond to fixed temperature conditions, where the red one represents the reservoir temperatures.

Heat transfer equation is coupled with Darcy law and mass conservation (see Guillou-Frottier et al., 2013 for details on governing equations). Fluid viscosity is temperature-dependent, and fluid density is temperature- and pressure-dependent, as detailed in Guillou-Frottier et al. (2020). Initial temperature field is conductive, and at time $t > 0$, permeability of the fault zone is set to k_{FZ}, which is varied from 10^{-14} m² to 10^{-13} m². Transient evolution of the temperature and velocity fields are recorded, and the presented results correspond to steady-state regimes (or pseudo steady-state in the case of pulsating fluid ascent, leading to periodic variations of surface temperature).

Petrophysical parameters have been taken from the literature (e.g. thermal conductivity and heat production values are from Vasseur, 1982, and Lucazeau et al., 1984). All properties are detailed in Table 3. Permeability of the fault zone, and value of the heat transfer coefficient are the main unknowns. However, it has been shown by several recent studies on fluid circulation in the subsurface, that high temperature values can be reproduced with permeability values around $10^{-14} - 10^{-13}$m² (e.g. Souche et al., 2014; Roche et al., 2018; Taillefer et al., 2018; Patterson et al., 2018; Wanner et al. 2019). A heat transfer coefficient of 0.02 W.m^{-2}.K^{-1} was chosen by Taillefer et al. (2018) according to a sensitivity study. Taillefer et al. (2024) used a

value of 0.025 $W.m^{-2}.K^{-1}$. Magri et al. (2015) used a volumetric value of 0.13 $W.m.K^{-1}$ (note the different unit) and suggest that the heat transfer coefficient corresponds the the thermal conductivity of surface rocks divided by the representative numerical element height. Since there is no clear definition to determine this coefficient, a range of values for h has been tested, from 10^{-1} $W.m^{-2}.K^{-1}$ to 5 10^{-4} $W.m^{-2}.K^{-1}$, with the objective of reproducing both the regional heat flow values (100 – 120 $mW.m^{-2}$) and the maximum spring temperature (80 °C).

If a regional heat flow Q of 110 $mW.m^{-2}$ is expected, then the basal temperature can be roughly estimated since thermal regime is conductive outside the fault zone. Neglecting the effect of radiogenic production, the basal temperature T_b obeys:

$$T_b - T_0 = \frac{H \times Q}{k_{eq}} \quad (16)$$

where T_0 is the surface temperature outside the fault zone (10°C), H is the thickness (5 km), Q the regional surface heat flow (0.11 $W.m^{-2}$), and k_{eq} is the equivalent thermal conductivity, which was measured on 10 water-saturated core samples (heat flow site « Estables », 30 km south-east of Chaudes-Aigues) and averages 2.5 $W.m^{-1}.K^{-1}$ (Vasseur, 1982 ; Lucazeau et al., 1984). A basal temperature of 230 °C is obtained from equation (16). For extreme values of surface heat flow (100 and 120 $mW.m^{-2}$) the basal temperature is estimated at 210 and 250°C, respectively. However, when crustal heat production is considered, temperature gradient decreases with depth and deep (basal) temperature should be lower than these rough estimates. Consequently, more precise values are computed with numerical models.

Properties	Host rocks	Fault zone	Fluid
Thermal conductivity ($W.m^{-1}.K^{-1}$)	2.6	2.6	0.6
Heat capacity ($J.kg^{-1}.K^{-1}$)	800	800	4180
Porosity	0.05	0.10	
Permeability (m^2)	10^{-20}	[10^{-14} – 10^{-13}]	
Density ($kg.m^{-3}$)	2700	2700	variable
Viscosity			variable
Heat production rate ($\mu W.m^{-3}$)	3.15	3.15	0

Table IV.4: Physical properties used in the numerical models. Host rock thermal conductivity value is chosen such as the equivalent thermal conductivity (which accounts for porosity) equals the measured values (2.5 $W.m^{-1}.K^{-1}$; Vasseur, 1982). The fluid density and fluid viscosity laws can be found in Guillou-Frottier et al. (2020). Heat production rates have been measured on core samples from the Margeride granite (Lucazeau et al., 1984).

Results

Tests on the heat transfer coefficient

Figure IV.16 illustrates the hot spring temperature as a function of fault zone permeability, for two different heat transfer coefficients and for two basal temperatures, 140 and 200°C. Clearly, spring temperature increases when permeability increases. Similar results were already obtained by Lopez and Smith (1995) who also observed a permeability threshold for which spring temperature begins to decrease. The role of the heat transfer coefficient does not seem fundamental when compared to the influence of the basal temperature. Indeed, spring temperature cannot reach 80°C for a basal temperature of 140°C. For a basal temperature of 200°C and a permeability greater than 6 10^{-14} m², spring temperature exceeds 80°C for both heat transfer coefficients.

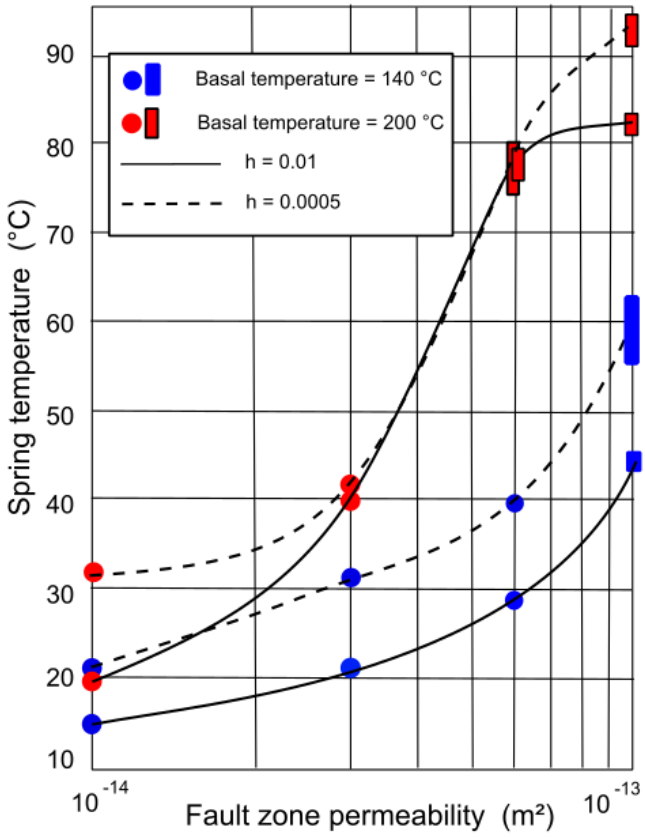

Figure IV.16: Spring temperature as a function of the fault zone permeability, for two distinct basal temperatures and two heat transfer coefficients. Rectangles indicate fluctuating spring temperatures due to periodic hydrothermal pulses. For a basal temperature of 200 °C, temperature around and above 80°C can be reached for a fault zone permeability greater than 6 10^{-14} m².

Figure IV.17 shows the role of the heat transfer coefficient on spring temperature for a fault zone permeability of 6 10^{-14} m². Computed regional heat flow values are reported in bold numbers. For a basal temperature of 140°C (in blue), and for all h values tested, regional heat flow does not reach 80 mW.m^{-2} and spring temperature remains below 40°C. For a basal temperature of 200°C (in red), regional heat flow values correspond to measured values, and spring temperature can reach 80°C for h = 0.001 W.m^{-2}.K-1.

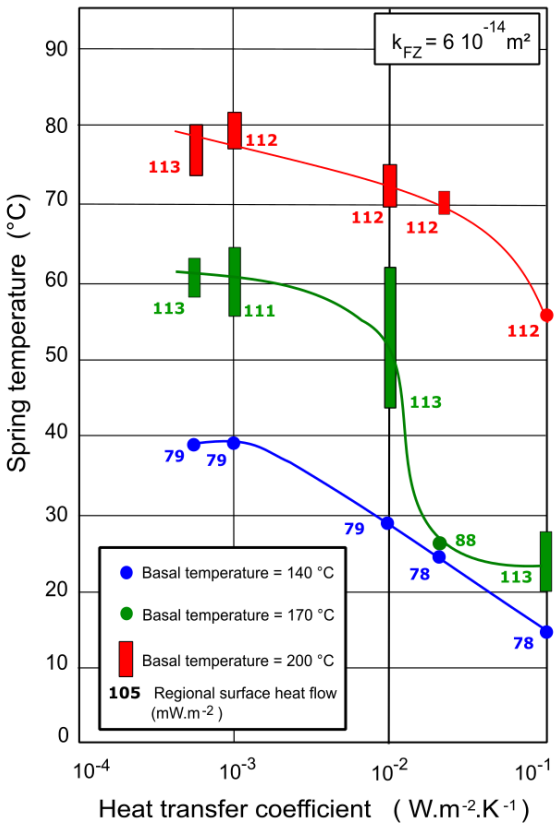

Figure IV.17: Spring temperature and regional heat flow values (bold numbers) as a function of the heat transfer coefficient, for a fault zone permeability of 6 10^{-14} m². Rectangles indicate fluctuating spring temperatures due to periodic hydrothermal pulses. Basal temperatures of 140 °C give regional heat flow values lower than the measured ones. For 170 °C, regional heat flow values are consistent with heat flow data, but spring temperature is too low. For a basal temperature of 200 °C, spring temperature around 70-80°C can be reached, and regional surface heat flow is consistent with measured values.

Tests on basal temperature values

As illustrated in the two previous Figures, there is a clear influence of the basal (reservoir) temperature on the spring temperature. Figure IV.18a shows that spring temperature around 80°C cannot be reached for basal temperatures lower than 190 °C (h = 0.01) or lower than 170 °C (h = 0.001). Figure IV.18b illustrates hydrothermal convection within the fault zone for k_{FZ} = 6 10^{-14} m², h = 0.0005 and for a basal temperature of 185°C. These parameters result in a spring temperature of 83°C with a regional heat flow of 112 mW.m^{-2}.

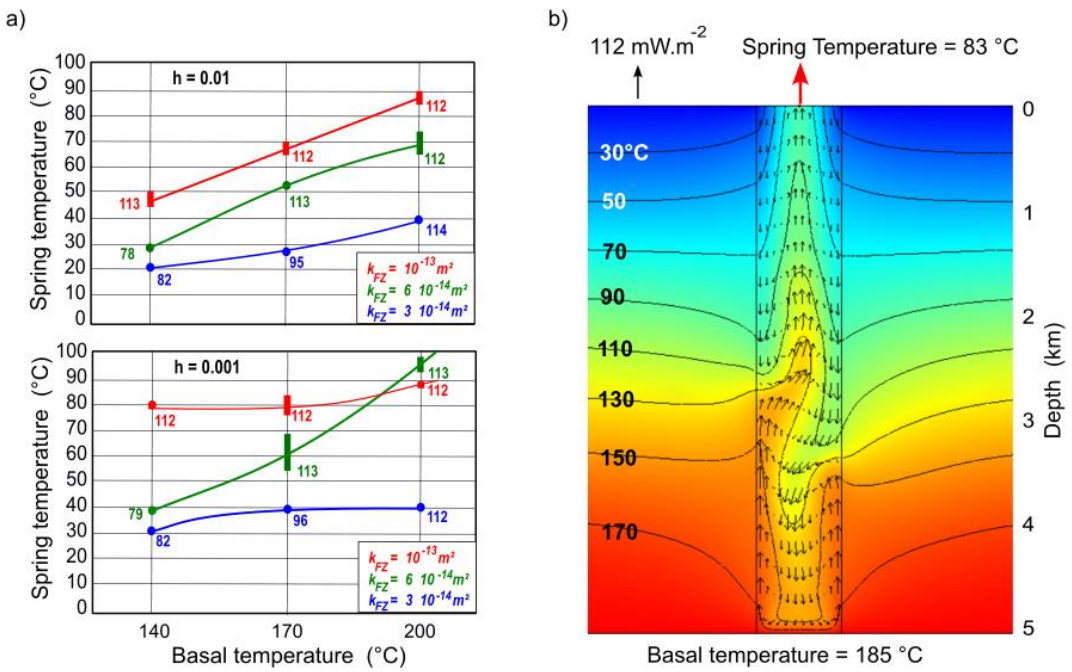

Figure IV.18: a) Role of basal temperature on spring temperature, for two heat transfer coefficients and two values for the fault zone permeability. Rectangles indicate fluctuating spring temperatures due to periodic hydrothermal pulses. b) illustration of hydrothermal convection within the fault zone, for an imposed basal temperature of 185°C, with a fault zone permeability of 6 10-14 m², and with a h value of 0.0005. The maximum recorded temperature at the surface equals 83°C. This image is a zoom around the fault zone and thus isotherms (black contours) are not horizontal on external edges. Color code corresponds to temperature values, from 10°C (blue) to 185°C (red).

Group	Sampling point	Name	Coordinates			Year	T	Cond. 25°C	pH	Eh	O_2	$Alk._{mes.\ site}$
			X-L93	Y-L93	Z		°C	µS/cm		mV	%	meq/l
Chaudes-Aigues	Source du Par	Par 2012	700198	6417140	750	2012	80.0	1407 (45°C)	6.35	-210	31.6 (45°C)	11.17
	Source du Lavoir	Lavoir 2012	700292	6416935	750	2012	67.7	1345 (27°C)	6.27	-132	71.2 (27°C)	11.15
	Forage du Ban	Ban 2012	700316	6416960	755	2012	74.4	1360 (31°C)	6.27	-252		11.27
	Source Magnac	Magnac	708877	6421504	740	2012	10.5	2240	6.12	-76.6	10.7	22.70
	Source Laval	Laval	708396	6420634	760	2012	10.2	692	6.18	320	76.2	4.81
	Source Montchanson	MTC 2012	711247	6422690	760	2012	11.0	2270	6.03	-102	8.5	21.60
	Loubaresse	Loubaresse	717621	6426057	765	2012	8.1	210	5.86	99	69.8	3.95
	Source Jenny	Jenny	719821	6426250	750	2012	6.4	623	5.70	46	62.4	5.34
	Forage Chaldette	LC 2012	703555	6408157	1010	2012	34.2	910	7.29	97	3.9	8.59
South Cantal	Fontaine minérale	Sainte Marie	690237	6419990	680	2012	11.0	1354	5.76	108	0.1	14.07
	Source Fontanes	Fontanes	687046	6420965	750	2012	8.2	2280	6.06	34	17.8	19.98
	Source Moulinges	Moulinges	684460	6422656	725	2012	6.1	1340	6.19	102	48.2	16.26
East Margeride	Mazel	Mazel	735927	6400733	1120	2012	2.2	1830	6.19	82	37.9	19.52
	Fontaine Haute	FH	735927	6400733	1120	2012	4.0	3700	6.35	72	9.5	43.54
	Fontaine Basse 1	FB1	735726	6400590	1080	2012	3.3	4680	6.40	62	30.6	56.65
	Fontaine Basse 2	FB2	735726	6400590	1080	2012	3.1	3340	6.87	40	49.8	48.19
	Ranc	Ranc	735630	6397662	1100	2012	2.7	3320	6.56	162	48.2	37.62
Chaudes-Aigues	Source du Par	Par 2023	700198	6417140	750	2023	80.0	1317 (55°C)	6.26	-72	43.4 (55°C)	9.43
	Source du Lavoir	Lavoir 2023	700292	6416935	750	2023	67.9	1294 (59°C)	6.14	-6.7	28.6 (59°C)	10.31
	Forage du Ban	Ban 2023	700316	6416960	755	2023	73.2	1314 (53°C)	6.44	38	43.5 (53°C)	9.40
	Source Boucharinc	Boucharinc	700216	6417151	755	2023	65.2	1254 (53°C)	6.46	172	59.6 (53°C)	8.75
	Source Condamines	Condamines	700754	6417789	750	2023	15.2	154 (15°C)	6.14	55	43.0 (15°C)	0.57
	Source La Poste	Poste	700263	6417108	750	2023	58.8	1312 (50°C)	6.99	172	87.0 (50°C)	10.06
	Source Vialard	Vialard	700374	6417241	750	2023	60.0	1306 (51°C)	6.39	19	51.0 (51°C)	11.26
	Source Tourette	Tourette	700197	6417091	750	2023	57.2	1292 (48°C)	6.39	-7.4	70.8 (48°C)	11.15
	Source Montchanson	MTC 2023	711247	6422690	760	2023	13.0	2130	6.00	-120	26.2	14.12
	Forage Chaldette	LC 2023	703555	6408157	1010	2023	35.5	919	7.181	-146	46.4	8.16
Surface	Rieubain Stream	Rieubain	663779	1989373	755	2012	5.7	72.5	7.05	286	100	0.27
	Truyère River	Truyère	652057	1987869	657	2012	8.7	88.2	6.93	333	92.4	0.48
	Truyère River	Truyère 2	686057	1965253	1020	2012	2.5	48.9	7.18	165	100	0.20
	Chazette Stream	Chazette	672161	1993666	751	2012	3.2	73.8	7.31	230	100	0.31
	Brozons River	Brozons	636924	1989133	720	2012	2.2	69.1	7.59	141	100	0.57

Table S3: Physico-chemical measurements of thermal waters collected from the Chaudes-Aigues area

Group	Name	T	Na	K	Ca	Mg	Cl	SO_4	NO_3	TIC	TOC	$Alk._{mes.\ site}$	$Alk._{labo}$	SiO_2	Cl/Br	TDS	B.I.
		°C	mg/l	mg/l	mg/l	mg/l	mg/l	mg/l	mg/l	mg/l	mg/l	meq/l	meq/l	mg/l	(weight)	g/l	%
Chaudes-Aigues	Par 2012	80.0	268	28.7	22.0	6.2	75.1	20.1	< 0.5	147	2.2	11.17	11.56	85.7	395	1.2	1.70
	Lavoir 2012	67.7	265	28.3	22.0	6.4	75.7	19.4	< 0.5	141	2.1	11.15	11.23	86.1	398	1.2	0.99
	Ban 2012	74.4	260	26.8	20.8	5.8	77.9	21.9	< 0.5	123	2.6	11.27	11.54	79.4	410	1.2	-3.64
	Magnac	10.5	397	60.4	61.5	38.5	109	3.7	< 0.5	324	4.6	22.70	22.70	40.1	389	2.1	-1.99
	Laval	10.2	107	15.7	13.1	8.3	41.5	9.4	3.8	86.6	1.1	4.81	5.28	28.9	472	0.5	3.69
	MTC 2012	11.0	411	66.5	47.5	32.0	147	10.2	< 0.5	315	4.8	21.60	21.18	42.2	397	2.1	-3.71
	Loubaresse	8.1	86.4	13.9	6.3	5.5	41.2	5.5	0.5	63.7	3.7	3.95	3.77	26.9	515	0.4	-0.67
	Jenny	6.4	65.2	10.5	14.3	16.3	25.5	4.4	< 0.5	62.0	2.4	5.34	5.23	58.5	510	0.5	0.75
	LC 2012	34.2	196	6.9	10.1	1.0	15.6	18.5	0.5	110	1.7	8.59	8.52	64.3	312	0.8	-4.04
South Cantal	Sainte Marie	11.0	194	15.2	52.1	36.8	35.5	16.0	< 0.5	180	3.3	14.07	14.23	42.0	507	1.3	-4.68
	Fontanes	8.2	290	15.4	101	66.0	150	51.6	< 0.5	265	3.8	19.98	20.44	66.5	484	2.0	-4.64
	Moulinges	6.1	225	27.9	43.0	50.5	46.6	8.8	1.3	203	4.1	16.26	16.67	65.30	518	1.5	-4.02
East Margeride	Mazel	2.2	173	10.1	35.7	13.6	9.7	6.1	< 0.5	115	9.0	10.10	9.89	17.1	323	0.9	3.61
	FH	4.0	783	39.0	128	50.0	29.0	18.2	< 0.5	451	8.7	43.54	44.98	40.2	171	3.8	2.68
	FB1	3.3	934	35.2	152	77.5	38.1	20.5	< 0.5	774	10.8	56.65	59.10	49.4	181	4.8	-3.55
	FB2	3.1	796	28.9	128	69.0	32.5	18.1	< 0.5	617	13.2	48.19	50.15	42.7	181	4.1	-3.09
	Ranc	2.7	709	83.2	46.3	30.0	29.8	16.9	1.3	462	8.9	37.62	38.25	42.6	199	3.3	-2.65
Chaudes-Aigues	Par 2023	80.0	250	29.7	22.1	6.8	75.3	21.1	< 0.5			11.06		92.4	299	1.2	-1.61
	Lavoir 2023	67.9	253	30	21.7	6.8	74.8	21.2	< 0.5			10.65		94	308	1.2	2.42
	Ban 2023	73.2	250	29	21.8	6.7	75.1	20.7	< 0.5			10.94		94.9	317	1.2	-0.89
	Boucharinc	65.2	233	27.5	21.5	6.6	75.7	17.9	< 0.5			10.4		88.2	329	1.1	-2.78
	Condamines	15.2	7.7	1.9	6.8	7	2.3	35.2	< 0.5			0.57		33.9	168	0.1	-4.85
	Poste	58.8	241	27.4	22.2	6.6	77.7	21.4	1			10.06		89.4	328	1.1	1.89
	Vialard	60.0	248	29	21.4	6.8	74.8	23.2	< 0.5			11.26		91.1	293	1.2	-4.30
	Tourette	57.2	249	29	22.1	6.8	73.6	23	< 0.5			11.25		90.4	300	1.2	-3.42
	MTC 2023	13.0	359	65	45	32.6	137	24.2	< 0.5			18.20		54.5	296	0.7	0.22
	LC 2023	35.5	207	6.3	10.2	1.1	15.2	17.7	< 0.5			8.75		66.8	133	0.3	2.70
Surface	Rieubain	5.7	6.5	1.3	4.2	1.5	5.1	4.8	2.8	4.2	4.9	0.27	0.38	16.5	> 51	0.06	3.94
	Truyère	8.7	6.2	1.3	5.7	2.4	7.5	3.4	2.4	5.1	3.1	0.48	0.39	9.5	> 75	0.07	2.90
	Truyère 2	2.5										0.20					
	Chazette	3.2										0.31					
	Brozons	2.2										0.57					

Table S4: Results of chemical analyses (major elements) of thermal waters collected from the Chaudes-Aigues area

Group	Name	NH_4	NO_2	PO_4	F	Br	B	Li	Sr	Ba	Mn	Fe	Al	As	Rb	Cs
		mg/l	mg/l	mg/l	mg/l	mg/l	µg/l	µg/l	µg/l	µg/l	µg/l	µg/l	µg/l	µg/l	µg/l	µg/l
Chaudes-Aigues	Par 2012	0.26		0.1	3.2	0.19	1359	700	449	265	26.3	358	2.99	355	183	93.6
	Lavoir 2012	0.26		< 0,1	3.0	0.19	1357	691	454	263	23.4	290	2.80	358	186	92.8
	Ban 2012	0.25		< 0,1	3.7	0.19	1125	682	403	238	26.5	58	1.85	355	176	91.6
	Magnac	0.48		< 0,1	3.4	0.28	2264	2304	831	1083	258	4072	238	185	341	182
	Laval	< 0,05		0.1	1.4	0.09	1144	534	228	262	2.39	< 20	91.3	1.75	94	54.5
	MTC 2012	0.59		< 0,1	3.9	0.37	2781	2827	384	792	181	6742	730	507	445	187
	Loubaresse	< 0,05		0.3	0.2	0.08	785	695	50.5	22.4	254	6242	62.7	261	102	62.2
	Jenny	0.12	< 0,01	< 0,1	0.5	0.05	335	656	29.4	5.50	1401	27200	131	195	89.5	53.2
	LC 2012	0.07	< 0,01	< 0,1	5.4	0.05	505	310	160	6.26	41.1	< 20	1.88	32.3	49.7	85.6
South Cantal	Sainte Marie	0.12	0.01	< 0,1	0.5	0.07	206	412	243	45.9	344	5630	40.6	1.82	78.3	16.3
	Fontanes	0.18	< 0,01	< 0,1	1.2	0.31	624	1209	539	35.3	547	15600	161	224	86.5	30.6
	Moulinges	0.47	0.01	< 0,1	0.3	0.09	172	966	345	56.2	327	3140	4.75	1.21	148.3	10.2
East Margeride	Mazel	< 0,05		< 0,1	0.7	0.03	103	1373	926	31.1	211	495	105	7.98	24.9	6.03
	FH	0.11		< 0,1	3.2	0.17	242	3131	2077	52.1	669	1681	43.4	36.0	54.8	16.0
	FB1	0.11	< 0,01	< 0,1	2.6	0.21	268	4464	3906	62.9	583	1290	23.4	19.7	40.0	20.0
	FB2	0.09	< 0,01	< 0,1	1.9	0.18	207	3765	3354	62.2	416	1550	19.2	14.0	33.9	16.1
	Ranc	0.08	< 0,01	< 0,1	4.9	0.15	219	2080	474	142	150	200	217	4.59	452	171
Chaudes-Aigues	Par 2023					0.19	1220	738	391							
	Lavoir 2023					0.18	1121	746	392							
	Ban 2023					0.18	1188	766	405							
	Boucharinc					0.17	1050	671	363							
	Condamines					0.01	2.48	22	51							
	Poste					0.18	1089	709	382							
	Vialard					0.19	1172	763	402							
	Tourette					0.2	1146	715	384							
	MTC 2023					0.38	2391	2777	328							
	LC 2023					0.06	568	311	143							
Surface	Rieubain	< 0,05		< 0,1	< 0,1	< 0,02	2.74	5.53	36.6	6.27	1.8	86	33.3	4.52	3.34	< 1
	Truyère	< 0,05		< 0,1	< 0,1	< 0,02	2.68	2.00	52.6	9.37	48	131	5.28	1.99	3.37	< 1
	Truyère 2						< 0,5	1.33	29.3							
	Chazette						< 0,5	3.44	41.6							
	Brozons						< 0,5	1.26	58.8							

Table S5: Results of chemical analyses (trace elements) of thermal waters collected from the Chaudes-Aigues area

Group	Name	Ge	Be	Co	Cr	Ni	Cu	Zn	Ag	Cd	Pb	U	Th	Nd
		µg/l	µg/l	µg/l	µg/l	µg/l	µg/l	µg/l	µg/l	µg/l	µg/l	µg/l	µg/l	ng/l
Chaudes-Aigues	Par 2012	6.39		< 0.05	< 0.1	< 0.1	< 0.1	< 0.5	< 0.01	0.07	< 0.05	0.010	< 0.1	4.82
	Lavoir 2012	6.32		0.08	< 0.1	0.35	0.31	1.28	< 0.01	0.15	< 0.05	0.015	< 0.1	2.91
	Ban 2012	6.91		< 0.05	< 0.1	< 0.1	< 0.1	< 0.5	< 0.01	0.02	< 0.05	0.010	< 0.1	1.45
	Magnac	6.60		0.22	< 0.1	0.93	0.33	0.89	< 0.01	0.05	< 0.05	0.988	< 0.1	10.4
	Laval	2.48		< 0.05	0.17	0.79	0.47	15.61	< 0.01	0.09	< 0.05	0.523	< 0.1	16.3
	MTC 2012	8.44		1.17	< 0.1	3.38	0.11	7.73	0.02	0.11	< 0.05	0.137	< 0.1	29.4
	Loubaresse	1.67		2.85	0.22	5.9	1.63	10.50	0.01	0.19	0.08	0.214	< 0.1	209
	Jenny	1.30	11.3	5.86	< 0.1	6.24	0.13	19.97	< 0.01	0.04	< 0.05	0.50	< 0.1	6.70
	LC 2012	7.70	0.80	0.18	< 0.1	< 0.1	< 0.1	< 0.5	< 0.01	0.01	< 0.05	1.42	< 0.1	2.80
South Cantal	Sainte Marie	2.50	2.45	0.78	< 0.1	2.03	< 0.1	3.81	< 0.01	< 0.01	< 0.05	0.31	< 0.1	166
	Fontanes	1.50	13.2	1.15	< 0.1	1.80	0.25	8.83	0.01	0.01	< 0.05	2.35	< 0.1	24.4
	Moulinges	< 0,5	0.14	6.3	< 0.1	24.61	0.34	8.28	< 0.01	0.04	< 0.05	0.28	< 0.1	10.6
East Margeride	Mazel	0.60		0.16	0.31	0.71	1.40	2.66	0.01	0.03	0.32	12.6	0.18	433
	FH	1.83		0.33	< 0.1	0.41	0.20	2.60	0.04	0.02	0.06	28.7	0.12	39.2
	FB1	1.10	41.6	0.99	< 0.1	0.53	< 0.1	4.05	0.19	0.01	< 0.05	39.1	< 0.1	8.30
	FB2	1.10	29.8	0.20	< 0.1	0.22	< 0.1	1.19	0.11	0.01	< 0.05	34.9	< 0.1	32.4
	Ranc	3.80	46.2	0.18	< 0.1	0.13	0.19	0.84	0.01	0.01	< 0.05	3.66	< 0.1	15.2
Surface	Rieubain	< 1		0.05	0.16	0.44	0.44	0.87	< 0.01	0.05	0.09	0.531	< 0.1	107
	Truyère	< 1		0.10	0.11	0.47	0.70	0.84	< 0.01	0.12	0.05	0.080	< 0.1	34.3
	Truyère 2													
	Chazette													
	Brozons													

Table S5 (continuation): Results of chemical analyses (trace elements) of thermal waters collected from the Chaudes-Aigues area

Group	Name	T	$\delta^{18}O_{SMOW}$	δD_{SMOW}	$\delta^{18}O_{SO4}$	$\delta^{34}S_{SO4}$	$\delta^{13}C_{PDB}$	$\delta^{11}B$	$\delta^{7}Li$	$^{87}Sr/^{86}Sr$
		°C	(‰)	(‰)	(‰)	(‰)	(‰)	(‰)	(‰)	
Chaudes-Aigues	Par 2012	80.0	-9.0	-63.2	3.6	15.7	0.7	-3.53	4.3	0.721996
	Lavoir 2012	67.7	-9.0	-62.9			1.4	-4.60	4.6	0.721948
	Ban 2012	74.4	-9.0	-62.6	5.2	17.5	-0.8	-3.19	3.9	0.721951
	Magnac	10.5	-9.4	-66.4	10.2	3.1	4.2	-7.67	4.1	0.718803
	Laval	10.2	-8.8	-62.5	6.7	14.0	2.6	-5.23	4.5	0.718279
	MTC 2012	11.0	-9.2	-65.1	4.8	7.8	4.8	-4.78	3.0	0.717339
	Loubaresse	8.1	-8.6	-59.8				-6.72	3.5	0.713437
	Jenny	6.4	-8.9	-62.4	11.2	11.4	1.7	-4.55	1.4	0.715157
	LC 2012	34.2	-9.6	-66.5	5.5	17.9	-4.3	-3.98	5.5	0.716400
South Cantal	Sainte Marie	11.0	-8.6	-57.5	9.8	14.5	0.9	6.18	4.2	0.716930
	Fontanes	8.2	-8.7	-57.1	5.8	18.4	1.7	10.38	2.1	0.715796
	Moulinges	6.1	-8.0	-53.3	10.0	28.7	2.6	3.28	2.6	0.711970
East Margeride	Mazel	2.2	-9.1	-62.2	12.7	28.3	-1.1	13.37	4.9	0.713222
	FH	4.0	-9.8	-66.6	17.3	30.9	-0.8	10.94	4.5	0.713142
	FB1	3.3	-9.8	-66.0	14.0	37.2	0.1	13.67	5.3	0.712964
	FB2	3.1	-9.6	-64.3					4.5	
	Ranc	2.7	-9.3	-63.0	13.1	40.4	1.1	11.73	3.9	0.716388
Chaudes-Aigues	Par 2023	80.0	-8.7	-62.0						
	Lavoir 2023	67.9	-8.7	-63.5						
	Ban 2023	73.2	-8.7	-61.7						
	Boucharinc	65.2	-8.6	-62.0						
	Condamines	15.2	-8.1	-59.5						
	Poste	58.8	-8.5	-61.4						
	Vialard	60.0	-9.1	-62.4						
	Tourette	57.2	-8.6	-63.0						
	MTC 2023	13.0	-8.7	-62.6						
	LC 2023	35.5	-9.2	-66.3						
Surface	Rieubain	5.7	-8.8	-60.1				22.64	10.1	0.715817
	Truyère	8.7	-8.8	-60.7				10.75	12.2	0.710789
	Truyère 2	2.5	-9.2	-62.3					6.1	0.714147
	Chazette	3.2	-8.7	-58.7			-8.0		10.4	0.710914
	Brozons	2.2	-8.8	-58.2					10.4	0.704792

Table S6: Results of isotopic analyses of thermal waters collected from the Chaudes-Aigues area

Spring	Units	Lavoir	Magnac	MTC 2012
T	**°C**	67.7	10.5	11.0
$\delta^{13}C_{PDB}$	**(‰)**	-5.0	-6.3	-1.6
$\delta^{18}O_{PDB}$	**(‰)**	-1.0		2.0
$\delta^{18}O_{SMOW}$	**(‰)**	29.8		33.0
$^{3}He/^{4}He$		0.828	1.119	0.720
CO_2	**(%)**	95.1	93.4	71.4
O_2	**(%)**	0.42	0.73	8.65
N_2	**(%)**	2.2	3.66	17.7
Ar	**(%)**	0.058	0.07	0.39
He	**(%)**	0.0061	0.0055	< 0,005
Ne	**(%)**		0.00069	
H_2	**(%)**	< 0,005	< 0,005	< 0,005
H_2S	**(%)**	< 0,005	< 0,005	< 0,005
CH_4	**(%)**	0.077	0.041	0.0007
C_2H_6	**(%)**	0.0006	0.0012	< 0,0002
C_3H_8	**(%)**	0.0004	< 0,0002	< 0,0002
SC_4H_{10}	**(%)**	< 0,0004	< 0,0004	< 0,0004
iso-C_4H_{10}	**(%)**	< 0,0002	< 0,0002	< 0,0002
n-C_4H_{10}	**(%)**	0.0003	< 0,0002	< 0,0002
SC_5H_{12}	**(%)**	< 0,0002	< 0,0002	< 0,0002
SC_6H_{14}	**(%)**	< 0,0002	< 0,0002	< 0,0002
Somme	**(%)**	97.9	97.9	98.1
N_2/Ar	**(vol.)**	38	52	45
He/Ar	**(vol.)**	0.105	0.079	< 0,013

Table S7: Analysis of non-condensable gases sampled from thermo-mineral springs in the Chaudes-Aigues area.

		T Qz (°C)	T Chalcedony (°C)	T Na/K 1 (°C)	T Na/K 2 (°C)	T Na/K 3 (°C)	T Na/K 4 (°C)	T Na/K/Ca (°C)	T K/Mg (°C)	T ^{18}O (°C)	T ^{18}O 2 (°C)	T ^{18}O 3 (°C)
Chaudes-Aigues	Par 2023	133	72	232	216	213	246	196	99	x	x	x
	Lavoir	134	73	228	211	208	242	194	98	x	x	x
	Ban 2023	134	74	230	213	211	244	195	99	x	x	x
	Boucharinc	130	70	232	215	213	246	195	98	x	x	x
	La Poste	131	71	228	211	208	243	193	98	x	x	x
	Vialard	132	72	231	214	212	245	196	99	x	x	x
	Tourette	132	71	230	214	211	245	195	99	x	x	x
	Par 2012	129	69	223	205	202	238	192	98	149	164	170
	Lavoir 2012	129	69	223	204	202	238	191	97	x	x	x
	Ban 2012	125	65	220	200	198	235	190	97	132	145	150
	MTC 2012	94	65	262	254	250	274	218	99	134	148	150
	MTC 2023	106	47	274	270	265	284	222	99	x	x	x
	Magnac	92	34	256	246	242	168	388	95	86	96	105
	Loubaresse	62	19	261	253	249	273	206	82	x	x	x
	Laval	65	22	252	242	237	264	197	80	119	132	135
	LC 2012	114	55	141	108	108	161	137	85	123	136	135
	LC 2023	116	57	133	98	99	152	132	83	x	x	x
	Deep EM	180	184	222	204	201	237	200	110	149	164	171
Margeride	Mazel	58	58	175	146	146	193	149	64	71	80	84
	FH	92	92	163	133	133	182	155	81	42	50	55
	FB 1	101	101	145	112	113	165	143	73	59	68	75
	FB 2	95	95	143	110	110	163	141	70	x	x	x
	Ranc	95	95	231	215	212	245	209	107	68	76	79
	Deep EM	122	125	146	123	113	165	147	100	68	76	80
Sainte-Marie	Sainte-Marie	94	36	197	173	171	213	162	62	95	105	110
	Fontanes	116	56	168	139	138	186	144	56	129	142	145
	Moulinges	115	55	236	221	218	250	191	72	98	109	112

Table S8: Reservoir temperatures estimated using chemical and isotopic geothermometers. T_{Qz}: Fournier (1977); $T_{Chalced.}$: Truesdell (1975); $T_{Na\text{-}K\ (1)}$: Fournier (1979) ; $T_{Na\text{-}K\ (2)}$: Michard (1979); $T_{Na\text{-}K\ (3)}$: Arnórsson et al. (1983), T < 250°C ; $T_{Na\text{-}K\ (4)}$ Giggenbach (1988) ; $T_{Na\text{-}K\text{-}Ca}$: Fournier and Truesdell (1973); $T_{K\text{-}Mg}$: Giggenbach (1988). Using $\delta^{18}O(SO_4)$: $T^{18}O_{(1)}$: Lloyd (1968) ; $T^{18}O_{(2)}$: Boschetti et al. (2011) ; $T^{18}O_{(3)}$: Zheng (1999).

Chapter V: Infiltration in a weathered granite: regolith impact on hydrothermal systems

V. Infiltration in a weathered granite: regolith impact on hydrothermal systems

V.1 Introduction

The infiltration zone of a hydrothermal system is located at the topographic high points. Infiltration of meteoric fluids is even more effective using permeable structures. Deep drains are then needed to allow the fluids to heat up at depth. Regolith, which results from the in-situ alteration of the underlying rocks and also from tectonics (faults), plays a key role in these processes. Consisting of a superposition of layers with specific characteristics, it controls the surface permeability of the system, thereby influencing the recharge and circulation of fluids. Its thickness, geometry and hydraulic properties can modulate exchanges between meteoric water and deeper fluids.

I.5.4 Infiltration, rainfall, runoff: calculating a water balance.

We calculated a water balance (Figure V.1) in the Chaudes-Aigues - La Chaldette fault cluster as far as the southern edge of the MGC (black rectangle, Figure V.2) to quantify infiltration. It is defined as follows:

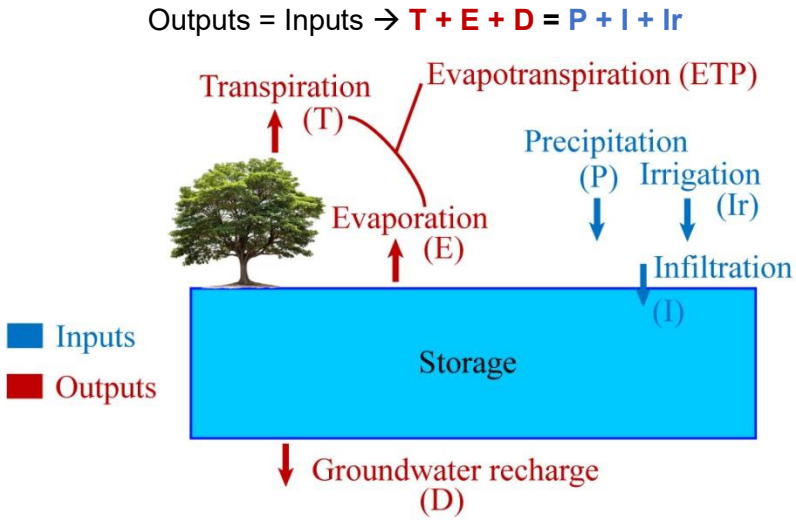

Figure V.1: Example of a water balance summarising the processes likely to affect the study area. Outputs are shown in red and inputs in blue.

Here, the inputs into the zone are simplified. These consist of rainfall estimated between 900 and 1400 mm/year (Bourrié, 1978; Chambre d'agriculture de l'Aveyron et du Cantal année 2020; Parc naturel régional de l'Aubrac; Syndicat des territoires de l'Est Cantal) and a small

stream, the Bès, with an upstream flow rate of 2.3 m^3/s (Fédération départementale de la pêche de Lozère). The outputs of the system, or losses, correspond to evapotranspiration (300 mm/year on average; Bourrié, 1978; Chambre de l'agriculture de l'Aveyron year 2020), runoff, which here is the variation in flow of the Bès, its downstream flow is 7.5 m^3/s (Fédération départementale de la pêche de Lozère) as well as infiltration I (unknown here). The result is:

$$P + Bès_{amont} = Bès_{aval} + ETP + I \text{ or } I = P + Bès_{amont} - Bès_{aval} – ETP$$

This gives an average infiltration of 30% (10 to 42% depending on P value) of precipitation in the study area. A simple calculation of the water balance (or mass balance) reveals a particularly high infiltration rate in the fault zone to the south of Chaudes-Aigues. This high infiltration rate suggests a predominant role of fracturing but also suggests a potential complementary role of a surface aquifer acting as a sponge. Understanding the structure and nature of the regolith in this context becomes essential to better constrain water transfer processes in the reservoir.

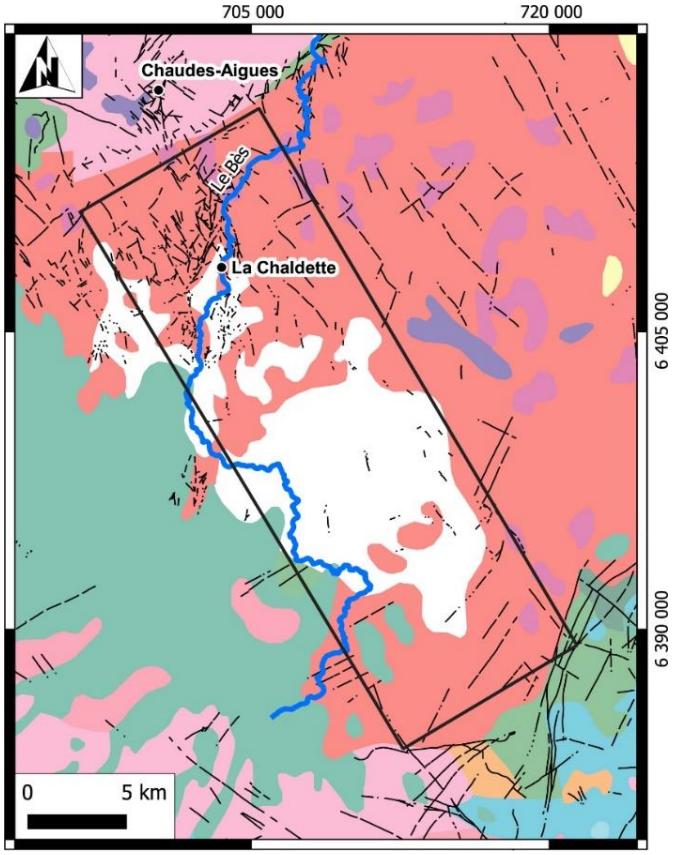

Figure V.2: Location of water balance calculation. Background corresponds to the 1M geological map of France. The ««amont»« Bès corresponds to the part outside the box to the south-west and the ««aval» Bès to the north-east.

I.5.5 Weathering profile: structure

The combined action of climate and tectonics generates supergene reactions leading to the formation of a weathered area, known as regolith. It is made up of different horizons:

- Saprolite or alterite. This horizon is divided into two sub-units (Wyns, 1999). The first, alloterite, is mainly made up of unconsolidated sandy-clay rocks. The original structure of the rock is no longer observable (Jones, 1985; White et al., 2001; Dewandel et al., 2006). Below this level, as the intensity of the weathering processes decreases, the structure of the rock is less affected and remains recognisable (White et al., 2001). This sub-division represents two-thirds of the saprolite (Dewandel et al., 2006), and its base is marked by laminated horizons made up of highly weathered blocks of the host rock. Thanks to its sandy composition, saprolite can have high porosity values ranging from 5 to 30% depending on the weathered lithology (Wyns, 1999, 2004; Dewandel et al., 2006). The hydraulic conductivity is low, at 10^{-6} m/s (Figure V.3). Once saturated, this level constitutes the main storage area of the overall composite aquifer (Dewandel et al., 2006).
- The fissured layer. It is characterised by a high density of horizontal and vertical fractures, which decrease in number with depth (Maréchal et al., 2003a; 2004; Wyns et al., 2004). The origin of these fractures is still debated, with some authors suggesting decompression (Acworth, 1987; Taylor and Howard, 2000), only weathering (Lachassagne et al., 2011), or tectonic processes. Thanks to these horizontal fractures, this layer ensures aquifer transmissivity and is mainly targeted for drilling. Its hydraulic conductivity is anisotropic, and fluid circulation is faster horizontally ($K_x = 10K_z$, Figure V.3) than vertically, with an average value of 10^{-5} m/s (Figure V.3). Even without its alterite layer, the fractured horizon can also accumulate high volumes of water (Dewandel et al., 2006).
- Fresh basement, only locally permeable due to fractures or faults.

Close to a fault zone or vein, this profile deepens. At depth, the fractures forming the fissured horizon become vertical and parallel to the fault (Lachassagne et al., 2011). The hydraulic properties of the different layers (with or without faults) are summarised in Figure V.3.

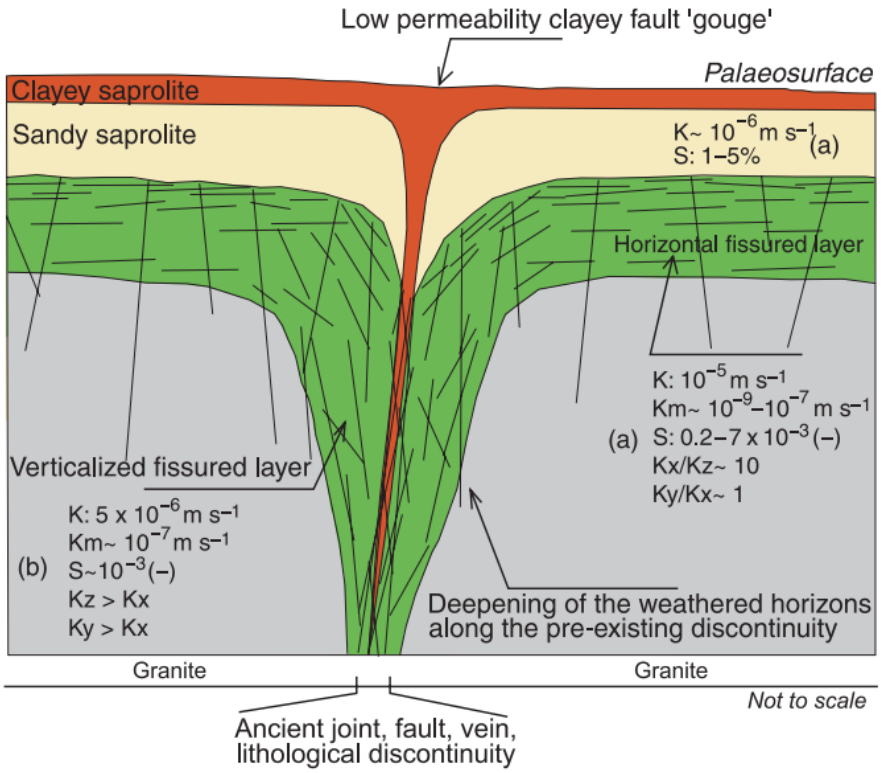

Figure V.3: Weathering profile structure and hydraulic characteristics close and outside a fault zone (faults, veins) according to Lachassagne et al., (2011). The deepening zone increases permeability and facilitates infiltration at depth.

In this context, this chapter proposes to study the MGC weathering to understand its impact on hydrothermal circulation. Through a field study, it was shown that the weathering profile was not equally preserved. These different configurations served as examples of geometries directly used in 3D thermal-hydraulic models. The purpose of these models is to quantify the hydraulic impact of the regolith on the functioning of the hydrothermal system.

V.2 Defining MGC weathering profile: field study

A field survey was devoted to determining the alteration of the MGC. This mainly involved characterising outcrops and landscapes. All the observation points are summarised in Figure V.4.

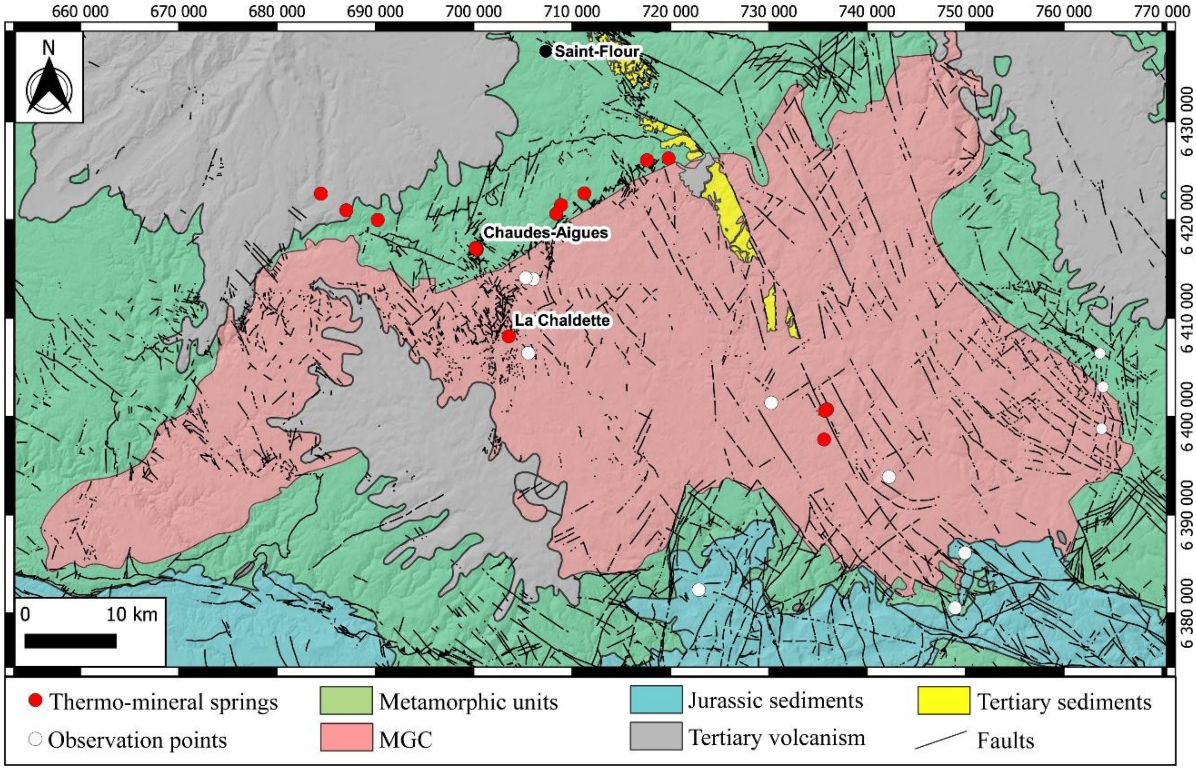

Figure V.4: Observation points spatial distribution. The thermo-mineral springs correspond to those previously sampled in chapter III.

I.5.6 Age and evolution of the weathering profile

Few studies exist on the MGC regolith. Most of it is thought to pre-date the Cenozoic (De Goër de Hervé et al., 1994) and even the Lias, to the south of the Granite, Liassic sediments can be seen lying directly on the alterites (Figure V.5a, Briand et al., 1979). Thanks to favourable climatic and topographical conditions, this pre-established profile could have been resumed at the end of the Cretaceous or Palaeocene up to the Miocene, leading to a thickening of the profile (Lachassagne et al., 2001). During the Würm glaciation, glaciers covered the Aubrac Massif and part of the MGC (De Goër de Hervé et al., 1994; Vasseur et al., 1997). As a result, alterites are supplemented in places by morainal sediments, acting as granite arenas, which have been identified as very good aquifers (De Goër de Hervé et al., 1994). In some places, glacial erosion washed away the established weathering profile.

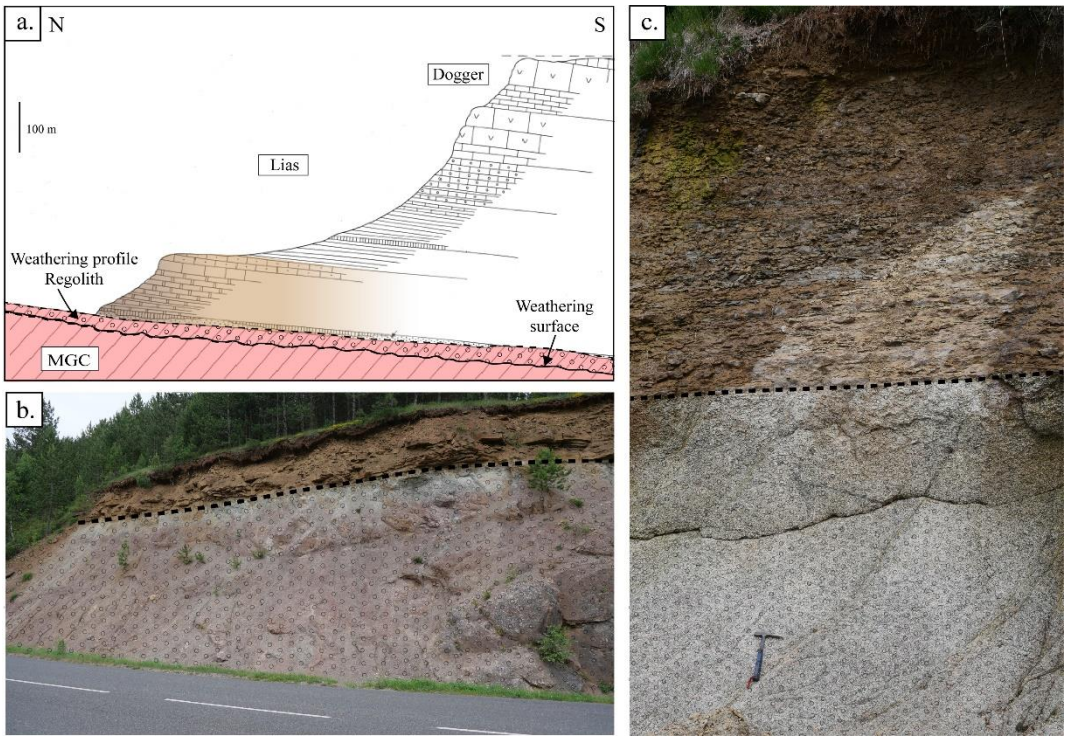

Figure V.5: Log representing Jurassic deposits on the MGC (modified from Briand et al., 1979). The weathering profile sealed by the Liassic sediments can be seen on these outcrops near Marvejols, (b) on the N88 (44.572, 3.629) and (c) on the D901 (44.540, 3.288).

I.5.7 MGC weathering profile spatial distribution

Preservation of the MGC weathering profile varies considerably from west to east.

To the west, beneath the Aubrac plateau (Aubrac, Figure V.7), the weathering profile has been largely preserved thanks to basaltic flows (De Goër de Hervé et al., 1994) preventing erosion. These volcanic formations acted like a shield, sealing the unconsolidated layers and limiting their remodelling. The weathering profile is at its thickest in this area.

Moving towards the centre of the MGC, in the vicinity of La Chaldette, the conservation of the profile is intermediate: the unconsolidated part of the profile is thinner than in the Aubrac. Erosion reduced the alterite part but did not completely remove it (Chaudes-Aigues, Figure V.7). This erosion is partly due to the Würm glaciation and the glaciers in place on the MGC (De Goër de Hervé et al., 1994). As this area is affected by a thick fault zone, a deepening of the weathering profile is indeed possible (Figure V.6d).

To the East, near Le Malzieu, by contrast, only the fissured layer remains. Here, erosive processes have completely stripped away the loose part of the profile (Malzieu, Figure V.6a).

The landscape is made up of huge, rounded blocks of granite. As the altitude is higher in the east of the MGC than in western part, the climatic and morphological conditions were more conducive to the erosion and transport of weathered materials. A study by Lachassagne et al (2001) estimates an average alterite thickness of 0 to 10 m and a fissured horizon of 15 to 40 m.

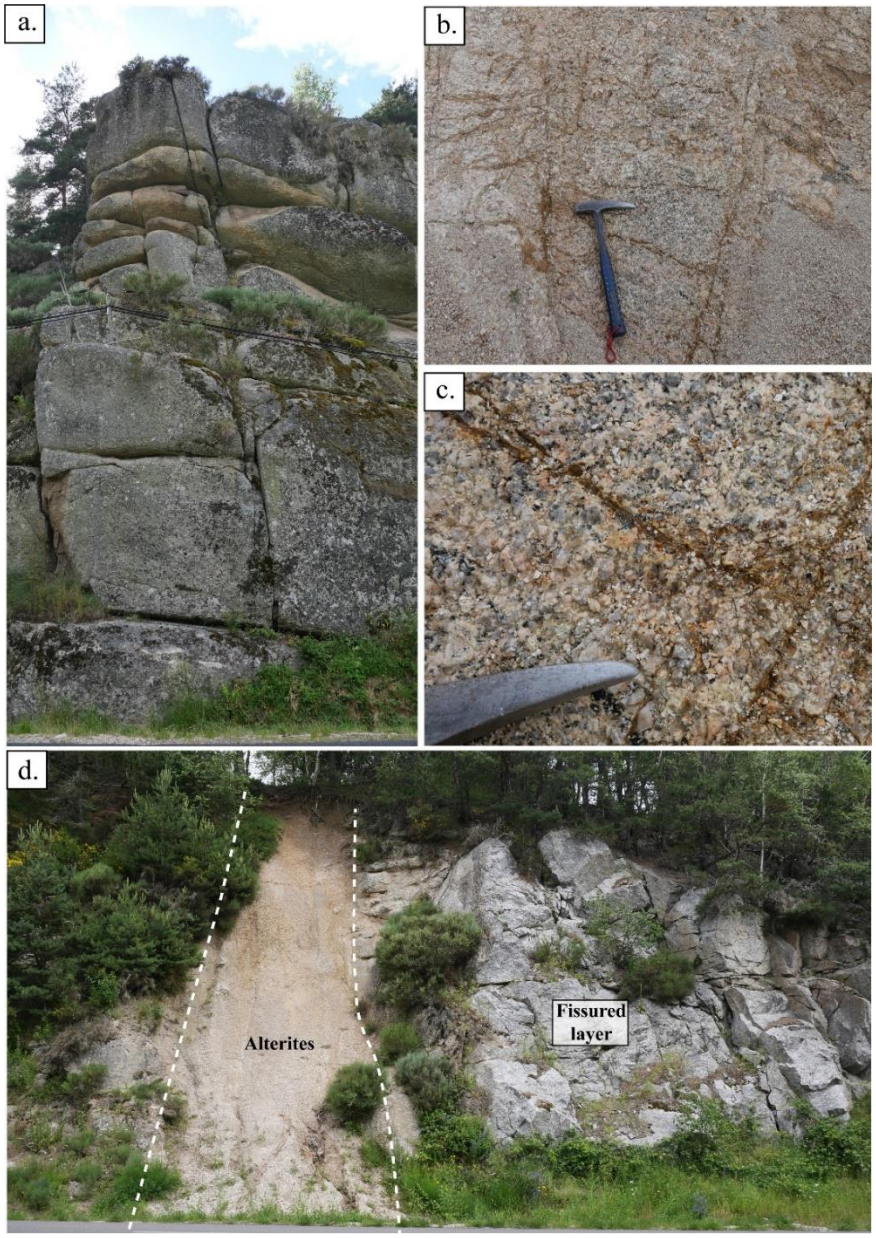

Figure V.6: (a) The fissured horizon (44.711, 3.382), characterised by its horizontal and vertical fractures, (b) the unconsolidated alterites located just above (44.824, 3.076) and (c) a zoom on these (44.826, 3.066), the main altered mineral biotite has disappeared, quartz and feldspars are visible. As mentioned above, near faults, there is a (d) deepening of the profile bringing alterites and fissured layer into contact (44.685, 3.805).

These different weathering profiles (Figure V.7), depending on the different horizons, directly possess unique hydraulic properties. The degree of consolidation or fracturing of each layer

affects permeability and water storage capacity, thus impacting the circulation of subsurface fluids.

To the west, the basaltic cover and preservation of the deep alteration are likely to favour greater storage dynamics, while in the centre, the reduction in the unconsolidated part could indicate intermediate permeability. To the east, on the other hand, the disappearance of the loose horizons and the predominance of the fissured layer suggest that fluid circulation is mainly controlled by the fracture network.

As a result, the MGC can be divided into three major areas with distinct hydraulic behaviours. This structural organisation will serve as a basis for the construction of our 3D thermal-hydraulic models, providing a better understanding of the interactions between surface and deep circulations.

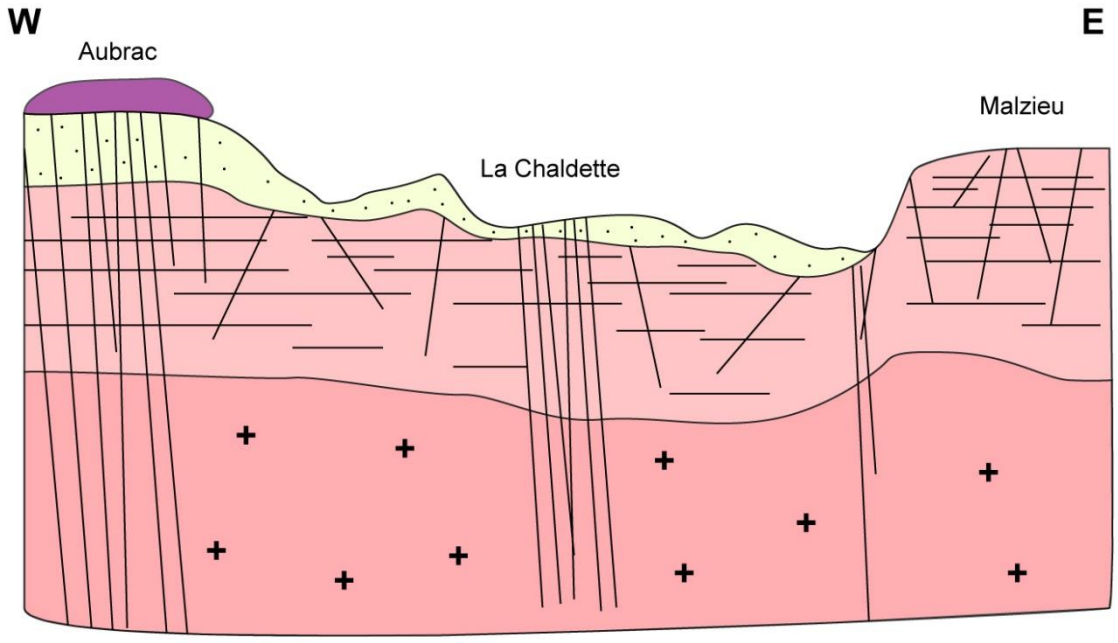

Figure V.7: Schematic cross-section (not to scale) of the MGC, the deepening of the profile in the fault zones has not been represented here. Dark pink with crosses corresponds to unweathered granite, light pink to fissured horizon, yellow to alterites (unconsolidated part) and purple to basalts.

V.3 Impact on fluid flow and thermal regime

In order to quantify the impact of the weathering profile, and more specifically the different configurations highlighted above, on the circulation of fluids at depth, 3D thermal-hydraulic models have been carried out.

I.5.8 Methods

Previously identified areas were used as models to create three different geometries. Firstly, the «Aubrac» zone with a complete weathering profile with alterites and a fissured horizon. The «Chaudes-Aigues» configuration with a thinner alteration profile and a complete fissured horizon. Finally, the «Malzieu» profile, made up solely of the fractured horizon. For each model, the weathering profile lies on a fault zone of constant thickness (1000 m) with varying permeability, all within a host rock assumed to be impermeable (Figure V.8). The thicknesses and permeabilities are summarised in Table V.1.

Formation	Thickness	Permeability
Alterites	Aubrac: 100 m La Chaldette: 50 m Malzieu: 0 m	10^{-13} m²
Fissured horizon	Aubrac, La Chaldette, Malzieu = 200 m	$K_{xy} = 7\ 10^{-12}$ m² $K_z = 10^{-12}$ m²

Table V.1: Properties of the different models (after Lachassagne et al., 2011).

A heat flow of 85 mW.m^{-2} is imposed at the base of the model. On the surface, a mixed thermal condition is imposed in order to reproduce temperature variations and therefore potentially thermal springs. That condition, previously used by Magri et al., (2015) or Taillefer et al., (2018), mainly depends on the transfer coefficient h (see Chapter 3). Its value is chosen to reproduce the measured regional heat flux (100 -120 mW.m^{-2} in the French Massif Central, Lucazeau et al., 1984) and a temperature of 10°C under conductive conditions. An appropriate value here is 0.03 mW/(m².K). Atmospheric pressure (10^5 Pa) is also imposed on the upper surface. The side surfaces are thermally insulated, and no fluid can pass through them.

Fluid viscosity depends on temperature, while density depends on both temperature and pressure (Guillou-Frottier et al., 2020). The permeability of the fault zone varies from 10^{-15} to 5 10^{-13} m², whereas the host rock is assumed to be impermeable (10^{-18} m²).

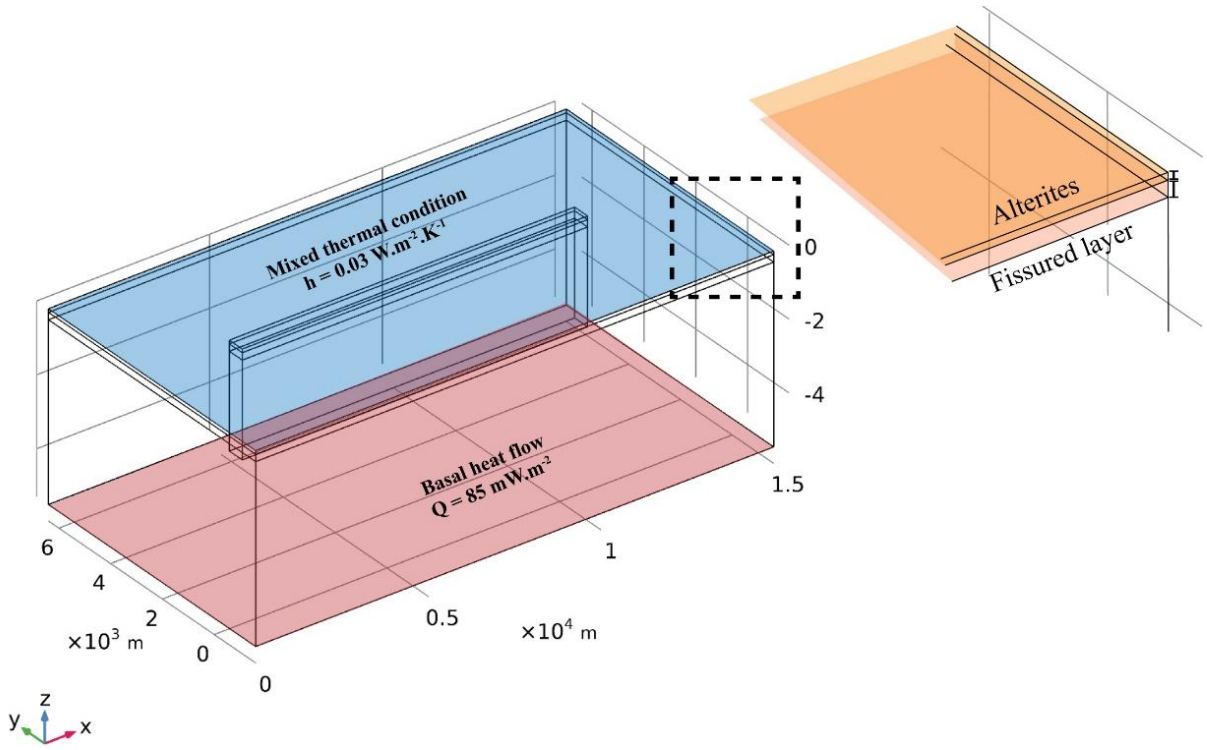

Figure V.8: Configuration of an Aubrac-type model with the complete weathering profile overlaying the fault zone, with boundary conditions shown (see text).

I.5.9 Results

Impact on deep fluid circulation

The different configurations described above do not have the same effects on the circulation of fluids at depth.

Regolith (partial or complete) influences the depth of positive temperature anomalies (the temperature difference between the obtained temperature and the one which would be obtained in the conductive regime). When the weathering profile is present, positive temperature anomalies do not exceed 1000 m in depth (Figure V.9a). The thicker the profile, the shallower the anomalies. The Aubrac-type models (yellow line, Figure V.9a) do not produce anomalies beyond a depth of 500 m, whereas the Malzieu-type models (red line, Figure V.9a) reach a depth of 900 m. Models with a partial weathering profile (La Chaldette-type) show behaviour intermediate to the two previous ones (Figure V.9a). Conversely, without weathering profile, anomalies can be very deep (2500 m, green line Figure V.9a). They become more superficial as permeability increases. In terms of positive temperature anomaly values, the opposite is observed. Models with a weathering profile produce higher anomalies than those

without (Figure V.9b). This time the structure of the weathering profile is not directly linked to the anomaly values. The Malzieu-type models produce the highest anomalies (16°C, Figure V.9b), followed by the Aubrac-type (15°C) and the La Chaldette-type (15°C). Models without a weathering profile, for any value of permeability, produce the lowest anomalies, which do not exceed 15°C.

If deep circulations are impacted, the temperatures of thermal springs potentially associated with these systems will also be affected. For low permeabilities (< 10^{-13} m²), models with a weathering profile produce the hottest springs (Figure V.9c). The Aubrac-type models have the highest values, at 26°C, compared with 17°C without any regolith (Figure V.9c). When permeability increases (> 10^{-13} m²), the results are reversed, with the granite-only models producing the warmest springs (35°C). Models with regolith (Aubrac-La Chaldette-Malzieu) peak at 31°C, 28°C and 28°C respectively. For all models, the higher the permeability, the higher the spring temperatures.

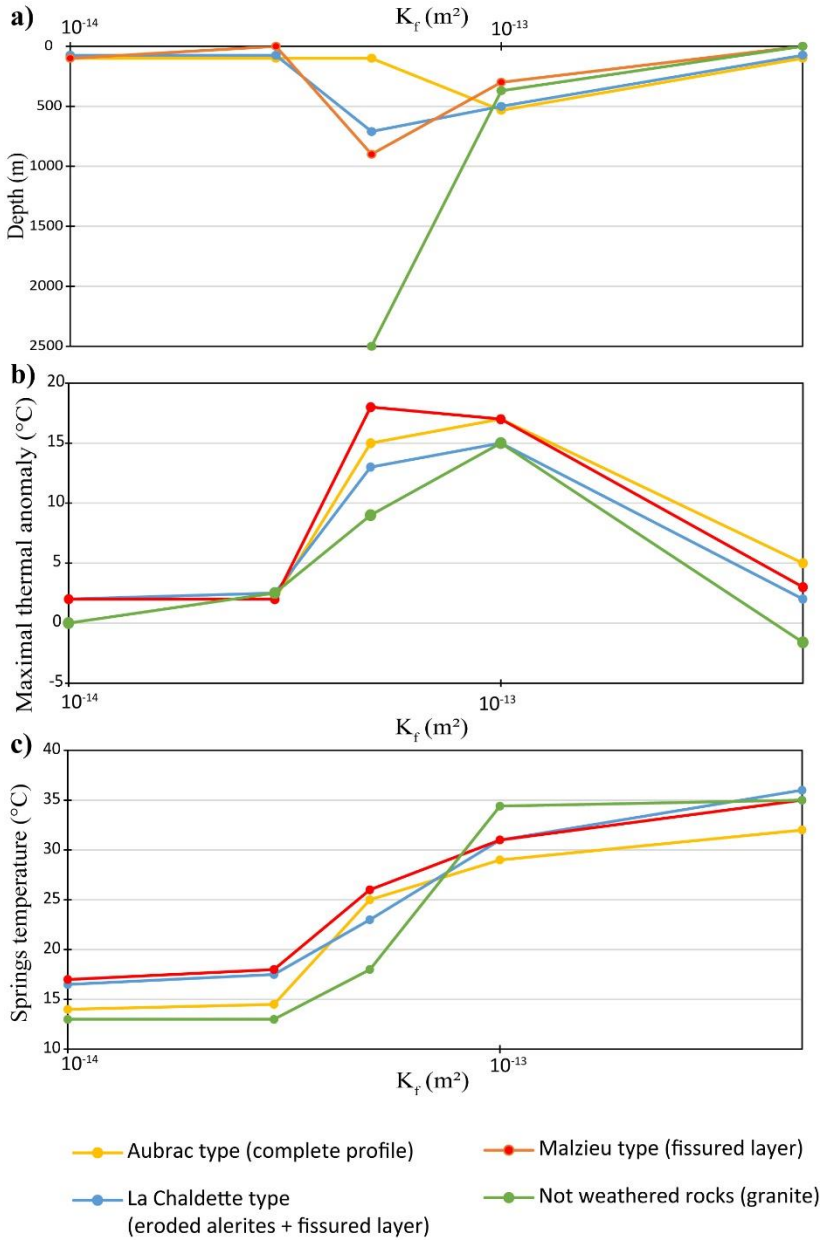

Figure V.9: (a) Temperatures of potential thermal springs on the surface, (b) depth of maximum temperature anomalies, (c) value of maximum temperature anomalies as a function of fault zone permeability.

Impact on surficial fluid circulation

The weathering profile, combined with a fault zone, modifies circulations at depth, but also at the surface. The interactions between the fault zone and this aquifer differ according to the structure of the weathering profile.

Complete weathering profile (Aubrac-type)

For a complete weathering profile (Figure V.7, Aubrac), water contained in both the weathering level and the fissured horizon is drained towards the fault zone (Figure V.10a). The arrows, symbolising Darcy velocity, converge at the ends but also at the centre of the fault zone. In the

upper part of the fault zone, corresponding to the regolith, small convection cells appear (Figure V.10b). Deep circulation can be seen, but also a shallow circulation along the length of the fault zone (Figure V.10b). This circulation is much faster. These small shallow cells develop close to the upwelling zones of the deep circulations and are perpendicular. Fluids can circulate both on the surface and infiltrate towards depth.

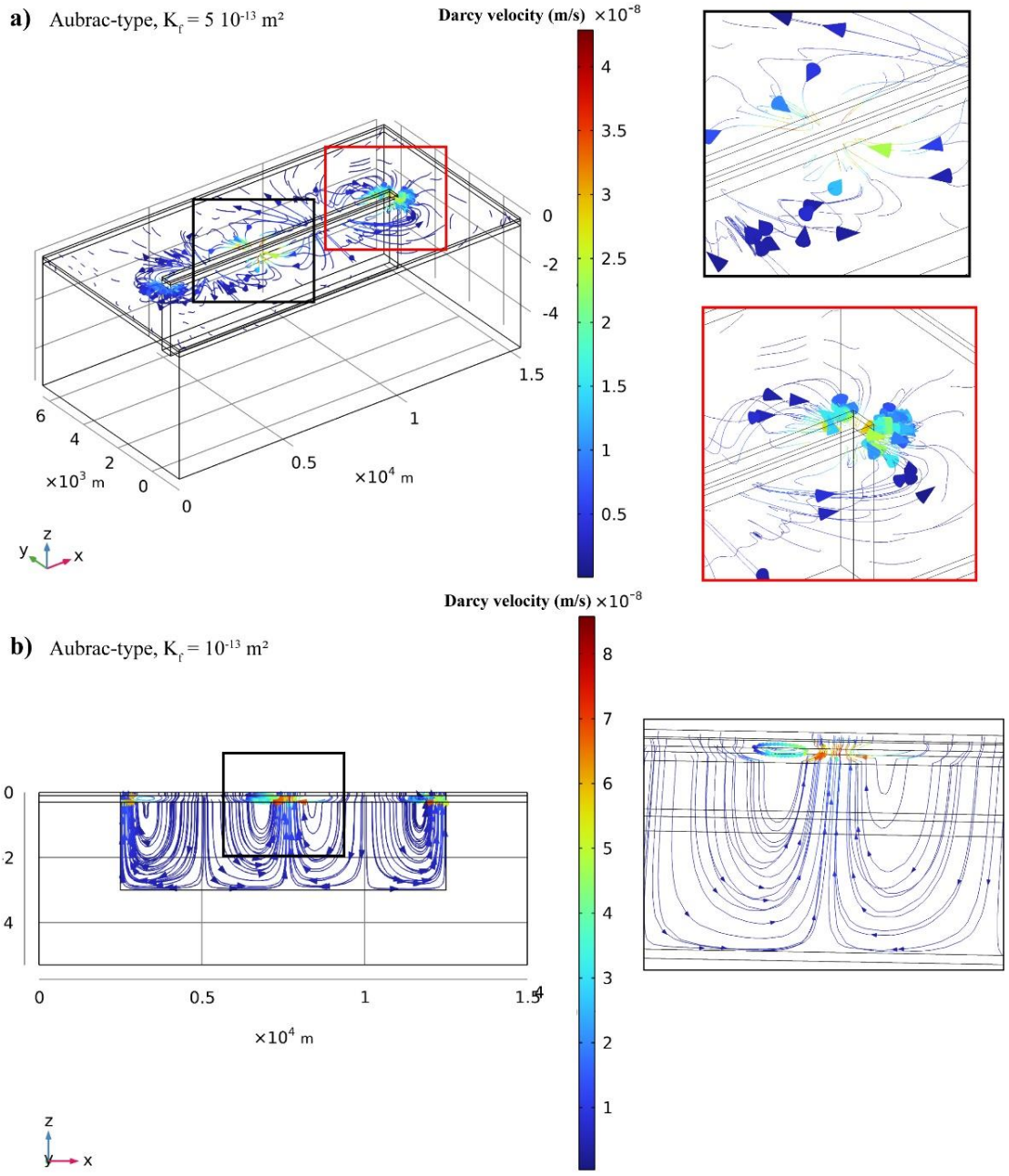

Figure V.10: Fluid circulation symbolised by the arrows (Darcy velocity) in the case of an Aubrac-type model. (a) Top view, circulation within the alteration profile and (b) cross-section showing interactions with depth.

Fissured layer (Malzieu-type)

The Malzieu-type configuration, made up only of the fissured horizon, has different hydrogeological and thermal characteristics. Firstly, several convection cells develop within the fractured level. This phenomenon does not require a fault zone and can be observed at very low permeabilities (Figure V.11a). No temperature anomalies are apparent in the fault zone, whereas they are in the fissured horizon. The cross-section view and the streamlines (black lines) highlight the cells (Figure V.11a). These, from the start to the end of the cells, involve only the fissured horizon and not the fault zone. Positive anomaly values are low, from 2.5 to 3°C, but are slightly higher above the fault zone, up to 5°C. This phenomenon was not observed when the fissured horizon is covered by alterites. When fault zone permeability increases ($< 10^{-13}$ m²), the convection cells mentioned above remain only outside the fault zone. Within, they disappear. In the fault zone, water infiltrate at depth (Figure V.11b). For higher permeability value ($> 10^{-13}$ m²), the water still infiltrates, but the interactions with the outside of the fault zone are different. Unlike in the previous case, water accumulated in the fault zone flows towards the fissured horizon (Figure V.11c).

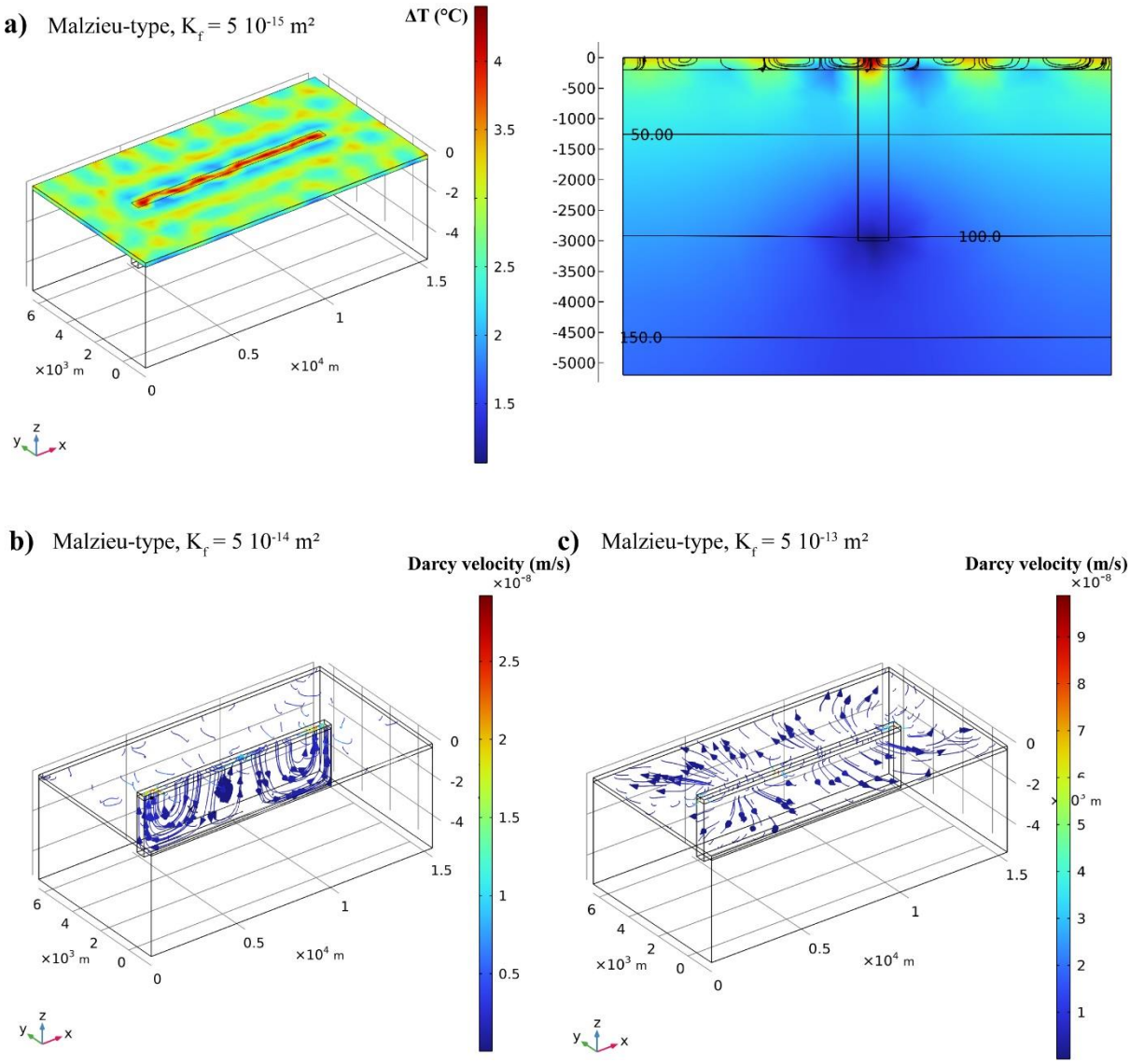

Figure V.11: (a) Convection cells in the fissured horizon, top view and cross-section. (b) Interactions between the surface and deep circulations for low permeabilities, (c) for higher permeabilities.

Partial weathering profile (La Chaldette-type)

Models with an intermediate weathering profile present intermediate results compared to the two previous ones (Aubrac-type and Malzieu-type). For low permeability (< 5 10^{-14} m²), convection cells form outside the fault zone in the fissured horizon. These are very small and perpendicular to the fault zone. Water contained in the immediate vicinity of the fault zone converges towards the ends, and interactions are limited (Figure V.12a). As the permeability of the fault zone increases, as in Aubrac-type models, convection cells form in the upper part of the fault zone (fractured horizon). These are longitudinal and correspond to the upwelling zones of deep circulations (Figure V.12b). Additionally, drainage around the fault zone is increasing.

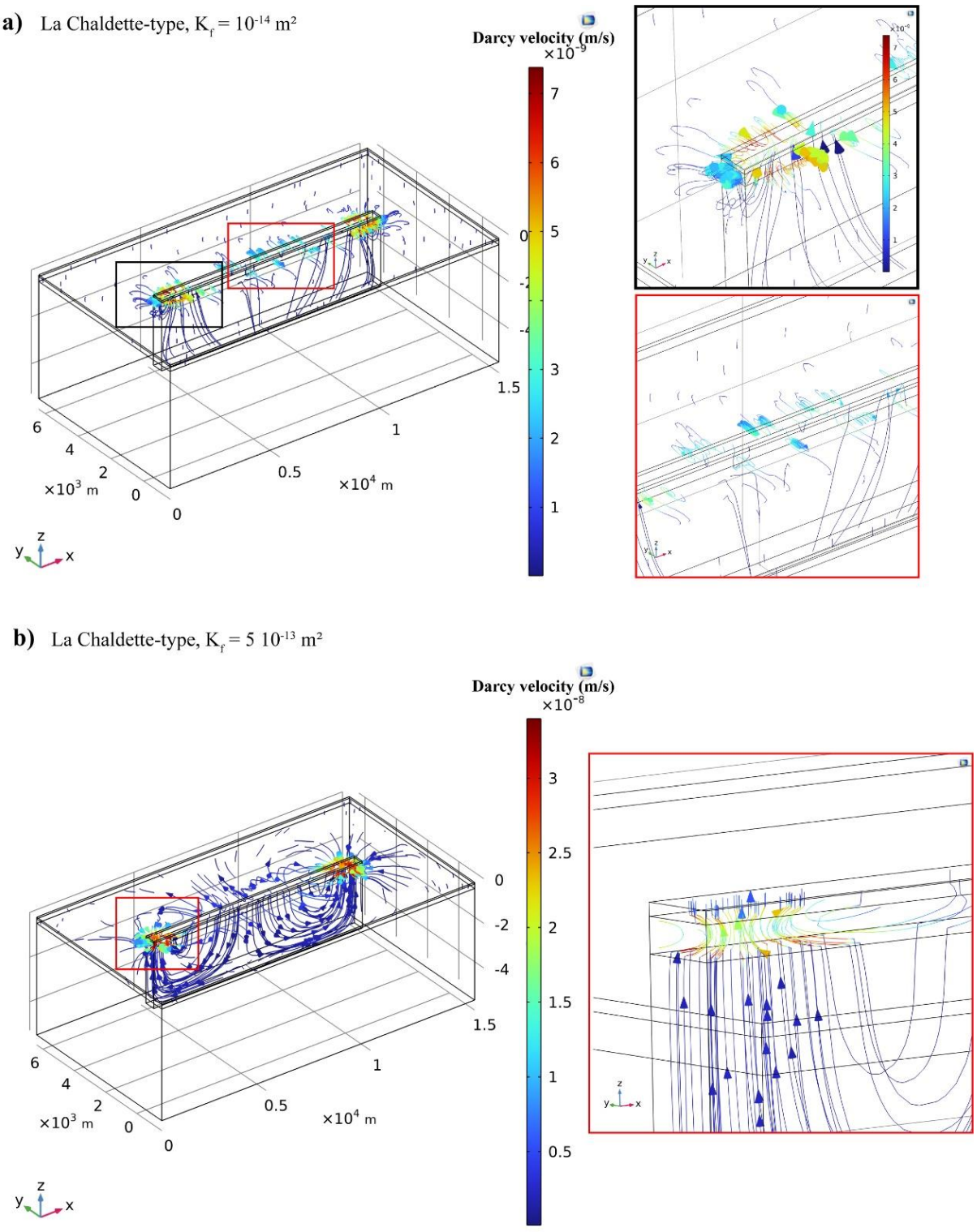

Figure V.12: Fluid circulation symbolised by the arrows (Darcy velocity) in the case of a La Chaldette-type model. (a) Top view, circulation within the alteration profile and (b) top view for higher permeability value.

V.4 Discussion

I.5.10 Regolith impact on the functioning of hydrothermal systems

The effect of weathering profiles in granite areas has been studied from a hydrogeological perspective (Edet and Okereke, 2005; Dewandel et al., 2011; Ifabiyi et al. 2016, Lachassagne et al., 2021) but not in terms of its thermal impact on fluid flow. These results indicate the influence of the weathering profile on both deep and shallow water flow. This particularly permeable layer allows a fault zone to reach a convective regime for lower permeability values than without weathering (Figure V.9a). This phenomenon, coupled with the increase of the intrinsic permeability of the fault zone, favours cold downward flow, so that the positive temperature anomalies associated with hot upwelling are limited. Cold, dense fluids then predominate over warm, low-density fluids. This geological configuration reproduces thermal springs, but with low temperatures (Figure V.9c). Conversely, depending on the lateral extension of the weathering profile and its configuration (layers), it could have a real influence on the flow rates of the thermal springs produced. Particularly in the case of a complete weathering profile (Aubrac-type), the convergence of the fluids around the fault zone could result in high flow rates. Without this layer, the impluvium is limited to the fault zone.

I.5.11 Implications for the Chaudes-Aigues hydrothermal system

With regard to the Chaudes-Aigues hydrothermal system, the weathering profile could play an key role. Indeed, water geochemistry has shown that most of the fluid circulation zone from the catchment area to the springs corresponds to MGC (Chapter 4). Two circulation circuits could exist within the pluton, as suggested by Vasseur et al. (1997). The first, deep, would explain the chemical signature of Chaudes-Aigues springs, while the second, more superficial could explain the La Chaldette spring. This spring is perfectly balanced with the surrounding rock (MGC) and reaches a temperature of 110°C at depth. Furthermore, it is exclusively meteoric water and corresponds to the surface component of the Chaudes-Aigues waters.

The common feature between the two circuits is the impluvium. With no weathering profile, the granite would have a low accumulation capacity, so the outflow rates would be low. In contrast,

the regolith is known for its excellent aquifer properties, which, coupled with the N150E fault zone, would allow both surface accumulation and circulation, followed by deep infiltration. The eastern part of the MGC, corresponding to the Magnac and Loubaresse springs (see Chapter 4), has a more limited weathering profile (Malzieu-type). As a result, the springs are cold and have a low surface flow rate. In addition, they are less diluted than those of Chaudes-Aigues. Apart from tectonics, the absence of regolith could be a factor inhibiting the presence of thermal springs.

I.5.12 Limits and perspectives

The study proposed here, combining field observations and 3D numerical thermo-hydraulic modelling, is still preliminary. In fact, these models offer an initial approach using a simplification of reality. For example, here we are assuming lateral continuity of the weathering profile, which may be discontinuous. The same phenomenon can occur with its thickness, which can be variable. Hydraulic parameters may therefore be over or underestimated. Moreover, as previously mentioned, these models are simplified and do not take into account all of the key parameters controlling fluid circulation, such as topography (Taillefer et al., 2018). These models require further study, but they can still be used to identify some of the phenomena that influence fluid circulation and the convective regime.

Chapter VI: Numerical modelling of the Chaudes-Aigues hydrothermal system: thermal springs simulation and controlling factors analysis.

VI. Numerical modelling of the Chaudes-Aigues hydrothermal system: thermal springs simulation and controlling factors analysis

VI.1 Introduction

3D numerical thermo-hydraulic modelling is a fundamental tool for representing, testing and refining our understanding of hydrothermal systems (Appold et al., 2007; Magri et al., 2012, 2016; Taillefer et al., 2018; Eldursi et al., 2023; Bock et al., 2024). In this study, it is used to coherently integrate data from field observations, geophysics and water geochemistry in order to simulate the hydrodynamic functioning of the springs. The aim of this numerical model is not only to reproduce the main characteristics of the system as observed, but also to assess its coherence, confirm certain hypotheses or, on the contrary, reveal new elements.

This chapter corresponds to a manuscript that will be submitted to G-cubed or Geofluids, some parts of which (mainly the introduction and discussion) have yet to be finalised. In order to model the hydrothermal system, the entire MGC and its various fault zones were modelled. The geometry is based on both the geological maps covered by the MGC and the geophysical study carried out by Talbot et al (2005). Some local details have been simplified such as the intersection zone of Chaudes-Aigues as a unique permeable zone. A deep reservoir, the location of which was determined in Chapter 4, was added at the northern edge of the MGC. Two parameters were tested to quantify and determine the control factors of the hydrothermal system: topography and the presence of a deep reservoir at a temperature of 190°C (see Chapter 4). Four series of models were produced, corresponding to the different combinations with/without topography and with/without deep reservoir. The aim of these models was to reproduce the characteristics of the Par Spring for Chaudes-Aigues, as well as La Chaldette, which was included in the hydrothermal system for the first time. These characteristics correspond to 7 key elements: the geographical location of the Par and La Chaldette springs, their temperatures (80 and 35°C), the total flow rate from Chaudes-Aigues (between 500 to 700 l/min), the mixing coefficients (see Chapter 4) and the infiltration area. The permeability, main unknown in the models, is supposed to be laterally homogeneous within a fault zone domains.

VI.2 Contribution of this chapter

The different numerical modelling configurations tested enabled an evaluation of the respective influence of topography and the presence of a deep reservoir on the Chaudes-Aigues hydrothermal system. The simplest models, with neither topography nor reservoir, fail to reproduce most of the observations (whatever permeability value), reproducing only the temperature and the approximate location of the La Chaldette spring. The addition of a deep reservoir partially improves the results, in particular by reaching the high temperature observed at the Par Spring, but this configuration can no longer reproduce the La Chaldette spring (location and temperature). Conversely, the configurations incorporating topography, even without a reservoir, better reproduce the total flows rate observed at Chaudes-Aigues (≥ 700 l/min), as well as the locations of the two springs and the infiltration zone. However, they are still insufficient to correctly reproduce the temperature of the Par Spring, and the mixing proportions derived from geochemistry (Chapter 4). It is only with the most complete configuration, including both topography and a deep reservoir, that all the criteria are met. This configuration reproduces the temperatures and flow rates measured at the thermal springs. The simulated mixing ratios are also consistent with the geochemical data. In addition, the deep circulations reach temperatures of 200°C, in line with the estimates provided by geothermometers (190 ± 10°C; Vasseur et al., 1997; Chapter 4).

Modelling has also enabled us to better constrain the location of the infiltration zone. Contrary to the hypothesis of Vasseur et al (1997), the models do not indicate any contribution from the Aubrac plateau. The infiltration actually seems to be closer, near the La Chaldette spring. The N150E-trending fault zone therefore includes all the system's functionalities: infiltration, deep circulation and emergence. It should be noted that slow, deep circulation from the south of the MGC cannot be ruled out. Finally, the La Chaldette spring also appears to be the result of circulation within this same N150E fault zone, with modelled circulation temperatures reaching 130°C at depth, in line with geochemical estimates (110 ± 10°C, Penhoët et al., 2025b).

These results confirm not only the preponderance of the fault zone, but also the robustness of the model in its ability to integrate all the geological, geochemical and hydrodynamic constraints of the system in order to reproduce the observed variables.

VI.3 Numerical modeling of thermal springs to investigate controlling factors in amagmatic hydrothermal systems: the Chaudes-Aigues case (French Massif Central) (to be submitted manuscript)

Numerical modeling of thermal springs to investigate controlling factors in amagmatic hydrothermal systems: the Chaudes-Aigues case (French Massif Central)

Emmy Penhoët[1,2], Laurent Guillou-Frottier[1,2], Laurent Arbaret[2], Bernard Sanjuan[1], Angélie Portal[1]

Manuscript submitted to Geochemistry Geophysics Geosystems

1 : BRGM, F-45060 Orléans, France.

2 : ISTO, UMR 7327, Université d'Orléans, CNRS, BRGM, F-45071 Orléans, France.

E-mail adresses : e.penhoet@brgm.fr , l.guillou-frottier@brgm.fr , laurent.arbaret@univ-orleans.fr, b.sanjuan@brgm.fr, a.portal@brgm.fr

Corresponding author at: Emmy Penhoët, BRGM, F-45060 Orléans, France.

E-mail address: e.penhoet@brgm.fr

Abbreviations :

Bureau de Recherches Géologiques et Minières : BRGM

Institut des Sciences de la Terre d'Orléans : ISTO

Lower Gneiss Unit: LGU

Upper Gneiss Unit: UGU

Margeride Granite Complex : MGC

Microgranite vein : MGV

Cantal volcanic complex: CVC

Supplementary material: SM

Abstract

Three-dimensional thermo-hydraulic numerical modelling is a key approach for improving our understanding of complex hydrothermal systems by integrating geological, geophysical and geochemical data. In this study, we investigate the hydrothermal functioning of the Chaudes-Aigues system (France) using a 3D model that incorporates the full structure of the Margeride Granitic Complex and its associated fault zones. Located in the southern Massif Central, Chaudes-Aigues is known for its 30 thermal springs counting one of the hottest in Europe : the Par spring (82°C). The thermal waters are thought to be the result of a double circulation within the granite: a superficial one, such as the Chaldette spring (10 km to the south, 35°C) and a deep one feeding a reservoir with an estimated temperature of 190°C. We tested the influence of two major factors: topography and the presence of a deep reservoir (190 °C) on the ability of the model to reproduce seven key observed features, including spring locations, temperatures, flow rates, mixing ratios, and recharge area. Four model configurations were tested: with/without topography and with/without the deep reservoir. Our results show that models excluding both topography and deep heat sources fail to reproduce most field observations. Including the deep reservoir improves thermal reproduction at the Par Spring but cannot replicate La Chaldette characteristics. Models that include topography reproduce spring locations, infiltration zones, and total flow rates but remain insufficient for replicating geochemical mixing ratios and high spring temperature of the Par Spring. Only the

configuration that includes both topography and a deep reservoir succeeds in reproducing all observed variables. It also aligns with geothermometric estimates, with deep circulations reaching 200 °C. Furthermore, the model revises the system recharge area, locating it near La Chaldette rather than the distant Aubrac Plateau, as previously hypothesized. Results also highlight the key role of the N150E-trending fault zone, which governs infiltration, deep flow, and spring emergence for both the Par and La Chaldette springs. This work demonstrates the critical importance of modelling constrained by a multidisciplinary approach and provides a robust tool for interpreting hydrothermal circulation in faulted crystalline terrains.

Keywords

Chaudes-Aigues, thermal springs, numerical modelling, flow rates, temperature, topography, reservoir.

Introduction

3D numerical thermo-hydraulic modelling is a fundamental tool for representing, testing and refining our understanding of hydrothermal systems (Appold et al., 2007; Magri et al., 2012, 2016; Taillefer et al., 2018; Eldursi et al., 2023; Bock et al., 2024). In this study, it is used to coherently integrate data from field observations, geophysics and water geochemistry in order to simulate the hydrodynamic functioning of the springs. The aim of this numerical model is not only to reproduce the main characteristics of the system as observed, but also to assess its coherence, confirm certain hypotheses or, on the contrary, reveal new elements.

The Chaudes-Aigues hydrothermal system, located near the northern edge of the Margeride Granitic Complex, is characterised by the presence of thirty thermal springs, including one of the hottest in Europe at up to 82°C: the Par spring. These springs are thought to be fed by two coexisting circuits in the MGC. This initial model was proposed by Vasseur et al. (1997) and then completed and updated by Penhoët et al (2025b). Surface water would infiltrate the southern edge of the MGC via a vast zone of Variscan faults N150E. This is where the two circulations separate. The deep circulation extends to the northern end of the MGC, where it penetrates deep into the gneisses (Penhoët et al., 2025b). At shallow depth beneath the town, the reservoir reaches temperatures estimated at around 190°C. As it rises, this warm water

mixes with colder surface water. This water comes from surface ciruclations similar to those at the La Chaldette spring (35°C). These circulations within the N150E fault zone are thought to reach 110°C (Penhoët et al., 2025b).

The aim of this work is to model the entire Chaudes-Aigues hydrothermal system in order to validate the geochemical hypotheses and also to identify the main factors controlling the system. To evaluate the influence of topography and the presence of this deep reservoir, four series of numerical models were developed, combining these parameters in different configurations. The models aim to reproduce the main features of the Par spring at Chaudes-Aigues and, for the first time, include the La Chaldette spring within the hydrothermal system. Key target characteristics include the geographic locations of the springs, their temperatures (80°C for Par and 35°C for La Chaldette), the total flow rate at Chaudes-Aigues (500-700 l/min), mixing coefficients derived from earlier analyses, and the infiltration area.

Factors influencing thermal spring distribution: example of France

For the following analysis, a spring is said to be thermal if its temperature exceeds the annual average. In France, the average annual temperature was 14.4°C and 14.5°C in 2022 and 2023 respectively (French National Temperature Indicator, Infoclimat), so any spring with a temperature above 15°C is considered thermal. Using this definition, more than 368 springs have been identified in France (BSSEAU BRGM, Annales des Mines 1998). The springs have been divided into two categories: between 15-50°C hot springs and between 50-85°C very hot springs.

Thermal springs are mainly located in the Pyrenees, the Massif Central and the Alps. However, there are also a few in eastern France and Corsica, and just one in Brittany (Figure VI.1). The aim here is to determine whether the distribution of these springs is purely random, or whether it is influenced by a number of specific geological factors. Tamburello *et al.* (2022) explored the distribution of hot springs in relation to endogenous factors (heat flow, volcanism, tectonic constraints, etc.) and exogenous factors (topography, precipitation values, climatic variations, etc.) on a global scale. Their work demonstrates that heat flow, topography and the presence

of volcanism, as well as an extensive stress regime, play a major role. Based on these results, this section aims to analyse the distribution of hot springs in mainland France using lithology, topography, fault density and heat flow.

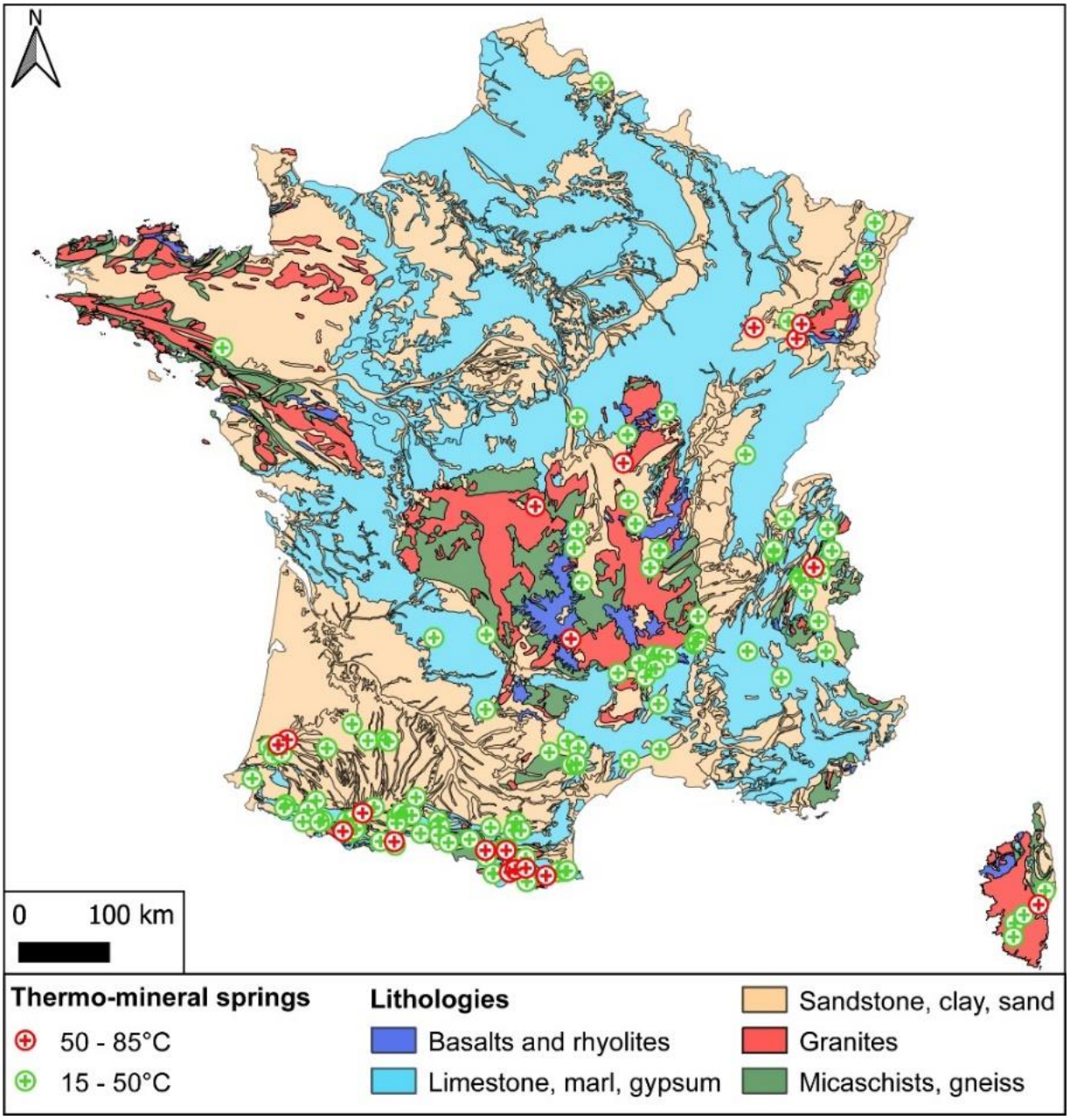

Figure VI.1: Distribution of thermo-mineral springs (according to the Banque du Sous-Sol, BSSEAU, BRGM) in France. The background map corresponds to the 2M geological map (BRGM).

Heat flow

Figure VI.2 illustrates the heat flow map of France based on the study of Vasseur (1982), supplemented by Lucazeau and Vasseur (1989). In France, some regions have an average heat flux, notably Brittany, the Pyrenees, Provence and the Alps, with values between 60-80

$mW.m^{-2}$. While these heat flux values are not very abnormal, the fact is that mountainous regions (Pyrenees, Alps) are very rich in thermal springs. Most of these springs have temperatures between 15-50°C, but some have temperatures above 50°C.

The Massif Central, the Rhône basin and Alsace have much higher heat flow values (90 - 110 $mW.m^{-2}$). These areas are characterised by numerous thermal springs, including one of the hottest in Europe (Source du Par, Chaudes-Aigues). In addition, there are thermal springs at Plombières-les-Bains, Luxeuil-les-Bains and Bourbonne-les-Bains, most of which exceed 50°C. The springs are less abundant than in the previous case, but on average hotter.

The thermal source-heat flux relationship is not that simple. When we compare the heat flow values, represented by the isolines, with the location of the thermal springs, we can see that a high heat flow value does not lead to a very high emergence temperature (Morbihan, Rhone basin). By contrast, regions with low heat flux can produce very hot springs, as in the Pyrenees ($T > 50$ °C). Although heat flow is an initial approach to analysing the distribution of thermal springs in France, it is not sufficient. In order to refine this analysis, other criteria such as fault density, topography and lithology of the hydrothermal system will also be taken into account in the following sections.

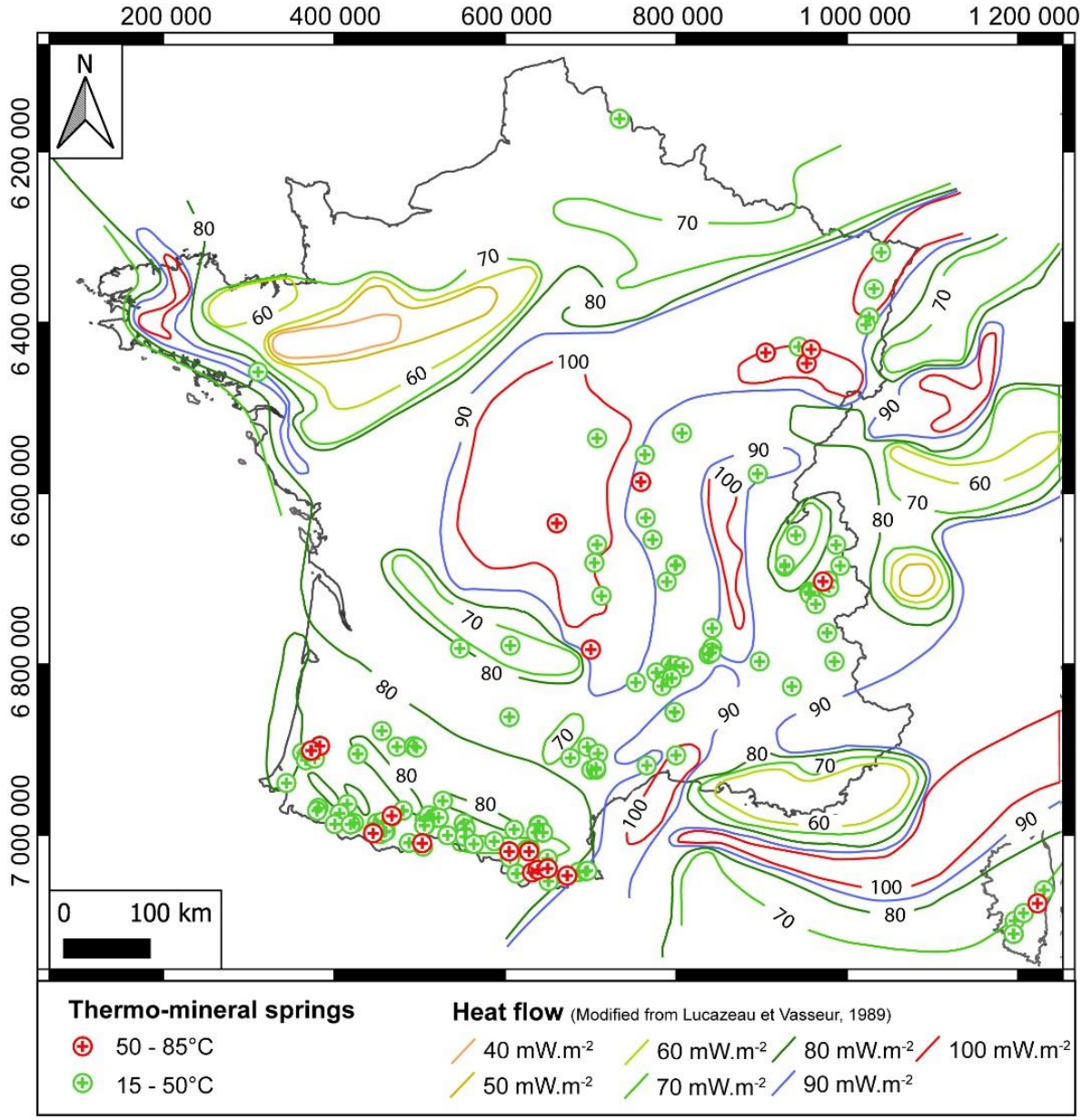

Figure VI.2: Distribution of thermal springs as a function of heat flow in France. Heat flow contours are extracted from the heat flow map of Lucazeau and Vasseur (1989).

Host lithology

The database used here indicates a potential hydrothermal system and a hot reservoir for each spring. Using the 2M geological map (Figure VI.1) and the lithologies cited in the inventory (BSSEAU BRGM, Annales des Mines 1998) four categories have been created: sedimentary rocks (sandstone, clay, sand, limestone, marl and gypsum), granites, metamorphic rocks (micaschists, gneiss, schists) and volcanic rocks (basalts and rhyolites). Of the 368 springs counted, 2 are volcanic, 159 granitic, 56 metamorphic and 151 sedimentary (Figure VI.2).

The granite hydrothermal system have both the largest number of springs and some of the highest temperatures, with a maximum of 77.8°C (Source Rossignol, Ax-Les-Thermes). The average temperature of these springs is 41°C (Figure VI.2). Metamorphic rocks also host very hot springs reaching 82°C (Source du Par, Chaudes-Aigues), with an average value of 37°C (Figure VI.2). Sedimentary rocks have many springs, but their temperatures are lower, averaging 30°C, with a maximum of 62°C (Bourbonne-les-Bains, Source no. 10) (Figure VI.2). The few springs associated with volcanic rocks are relatively cold (27°C on average), with a maximum temperature of 28°C (Source Saint-Martin, Chamalières).

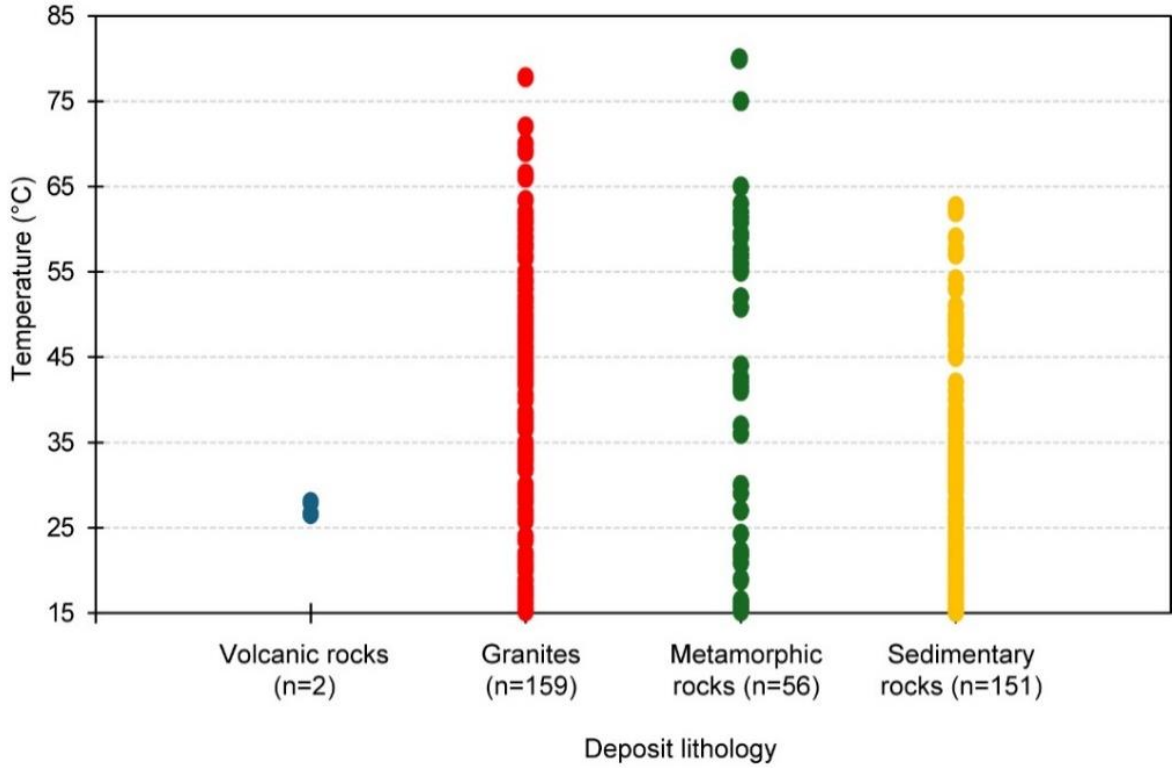

Figure VI.3: Temperature of the 368 springs according to the lithology of the hydrothermal system.

The host lithologies in the database (BSSEAU and Annales des Mines, 1998) are based on field reports carried out on each spring. When the data is available, it will be used. Conversely, when it is not provided, the spring lithology of the 2M geological map will be considered. This can lead to uncertainties such as the Chaudes-Aigues springs, which are located in metamorphic units but associated with a granitic reservoir (Vasseur *et al.*, 1997; Penhoët et al., 2025b). As the data does not appear in the inventory, these are considered to come from a metamorphic hydrothermal system rather than granitic.

Topography

Identified as a key parameter in fluid circulation, topography controls both fluid infiltration but also the distribution of thermal springs at the surface (Taillefer *et al.*, 2018). To identify the influence of topography, the maximum difference in altitude surrounding each spring was calculated. Within a 10 km radius, the difference between the maximum elevation and the spring elevation was calculated.

The results fall into two groups (Figure VI.3b). The first group covers small gradients (less than 1 500 m), with an average temperature of 32°C and a maximum temperature of 80°C (gradient of 644 m). All four types of lithologies are represented. The second group, with a higher elevation difference (between 1 500 and 2 900 m), has a higher average value (39 °C) and a maximum of 77.8 °C. Here, granitic and metamorphic rocks predominate.

It should be noted that the spring temperatures belonging to the sedimentary lithology type are not directly linked to topographic gradient, temperature varies little as the difference in altitude increases or decreases. Temperatures of springs linked to basement rocks (granites and metamorphic rocks), in contrast, do not behave in the same way. More springs emerge when the topographic gradient is high (the second group mentioned above) with higher temperatures. These types of system are therefore more influenced by the surrounding topography.

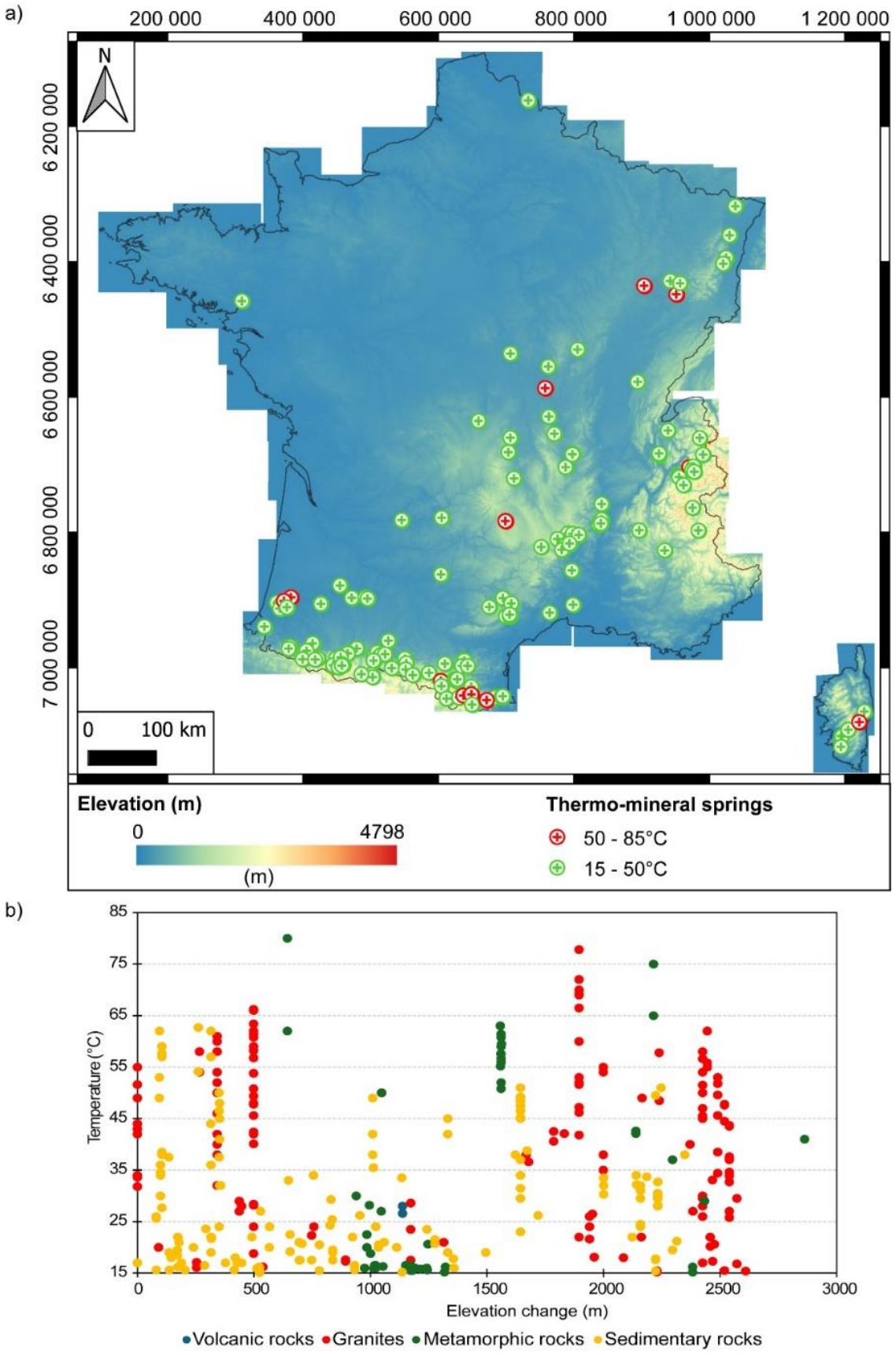

Figure VI.4: (a) Map showing the distribution of thermal springs in France as a function of topography. (b) Temperature of springs as a function of maximum difference in elevation within a 10km radius of each spring.

Fault density

The influence of fracturing density was studied using a fault density map (Figure VI.4a). Within a radius of 10 km, the average value of cumulative fault length has been calculated. The method is detailed in Penhoët *et al.* (2025).

The results show that an optimum fracturing density permits the highest source temperatures to be reached (Figure VI.4b). The highest temperatures (up to 82°C) are found between 50 km and 100 km of cumulative length. For lower densities, the springs are numerous but their maximum temperature decreases, with values not exceeding 65°C. Conversely, for more densely faulted areas (> 100 km), there are few springs and temperatures are even lower. These do not exceed 55°C. However, it should be noted that for these density values, the minimum temperatures are high (35°C compared with 15°C for the previous groups).

This phenomenon can be directly related to the concept of permeability. The calculated fault density therefore provides an initial estimate of the area permeability. Thermo-hydraulic modelling has shown that there is a window of optimal permeability values (of the host rock) that allows the highest spring temperature values to be reached (Lopez and Smith, 1995). In our case, using the fracture density calculated around the emergence zone, a similar behaviour appears. If the fault density is too low, the permeability is assumed to be low, and the hot fluids rise slowly, in small volumes, and cool. As a result, surface springs will be cold. Inversely, when the fracturing density is very high, the area becomes favourable to the infiltration of dense, cold fluids because it is very highly permeable. By contrast, with an intermediate fracturing density, the area becomes permeable enough to allow the fast ascent of hot fluids in large volumes, but not permeable enough to allow the infiltration of cold fluids. In this configuration, hot springs appear.

As regards reservoir lithologies, it can still be seen that the temperatures of springs in sedimentary environments are not directly affected by fracturing. They range over all values. Basement rocks, however, are confined within the window of optimum cumulative length

values mentioned above. Outside this range of values, the temperature of the springs falls significantly.

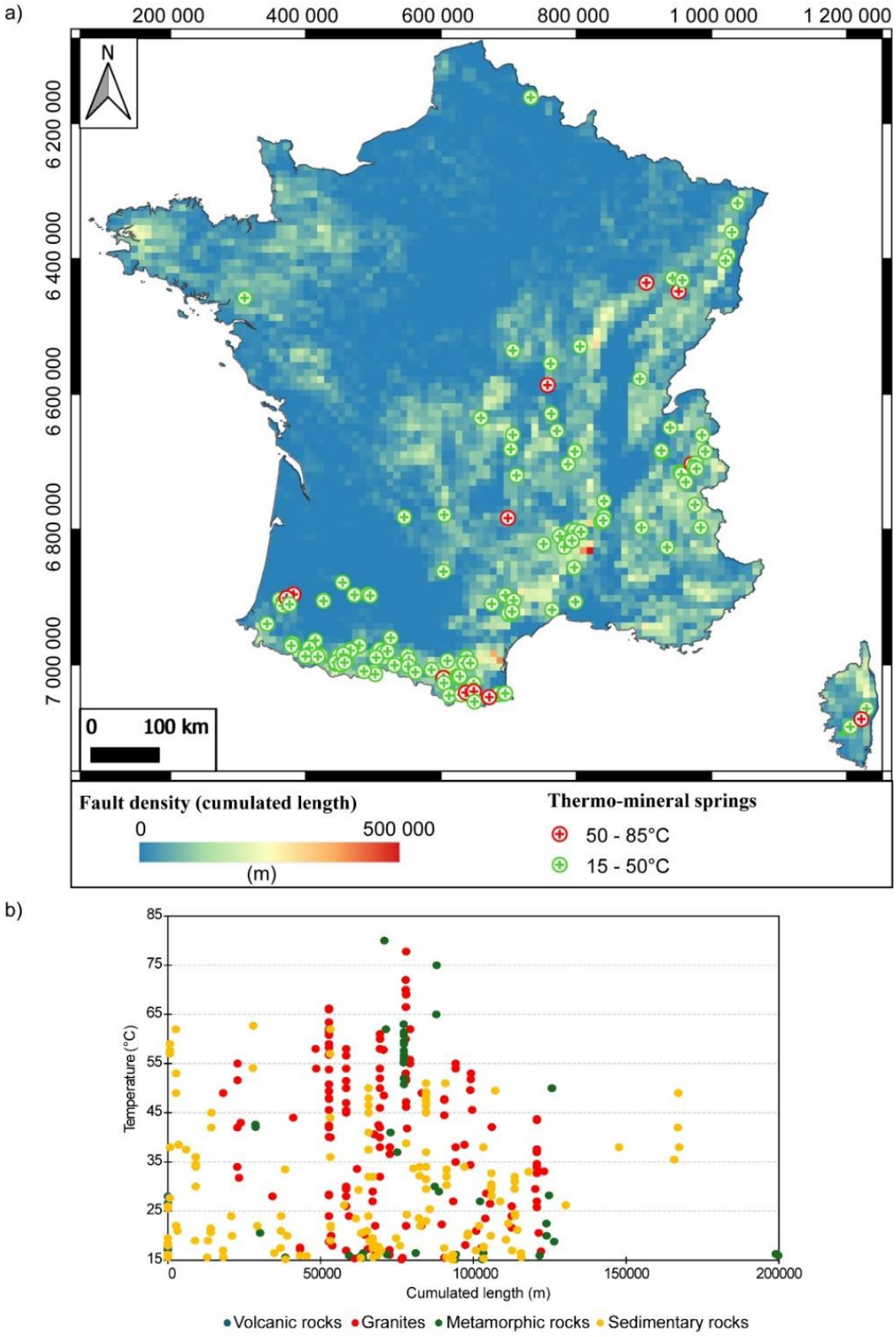

Figure VI.5: (a) Map showing the distribution of thermal springs in France as a function of fault density. (b) Temperature of springs as a function of average fault density within a 10 km radius of each spring.

The French Massif Central

Geology of the French Massif Central

Variscan history of the Massif Central will not be detailed, although it plays a fundamental role in the current structuring of the region. Indeed, the main fault orientations N030E-50E and N120E-150E structuring the study area, typical of regional fracturing, originate from this ancient heritage (Penhoët et al., 2025a). From a hydrothermal point of view, the key factor is the reactivation of these structures over geological time to maintain their high permeability values. From a thermal point of view, this period provides very little information, as the hydrothermal system lifetime is limited to thousand to hundreds of thousand years (Iwatsuki et al., 2000; Dupuy et al., 2021, Waber et al., 2017; Carbajal-Martinez et al., 2024; Wang et al., 2024), which is negligible compared with the time scale of Variscan events.

Tertiary events are fundamental to understanding the actual thermal state of our study area. At the end of the Cretaceous and during the Palaeocene, a compressive phase led to a lithospheric bulge in Europe (Ziegler et al., 2007). During the Eocene, an extensional phase developed across Europe, forming a series of sedimentary basins (European Cenozoic Rift System, Ziegler 1992). Evidence of this phase can be seen in the southern Massif Central such as the Limagne (Michon and Merle 2001; Dèzes et al. 2004; Merle et al. 2023) or the Malzieu basin (De Goer de Herve et al., 1990). The origin of this extensive phase is still discussed (Michon and Merle, 2001; Michon et al. 2003; Michon and Merle, 2005; Dèzes et al. 2004; 2005). Authors agree, however, that a mantle thermal anomaly caused crustal thinning beneath the Massif Central. This anomaly is particularly visible in section AB, Figure VI.6. To the west of the Houiller Sillon, the crust is about 30 km thick (Figure VI.6b). Towards the east it becomes progressively thinner, reaching 25 km beneath the Limagne basin (Figure VI.6a and b). Crust thickness returns to normal at the eastern edge of the profile (Figure VI.6b).

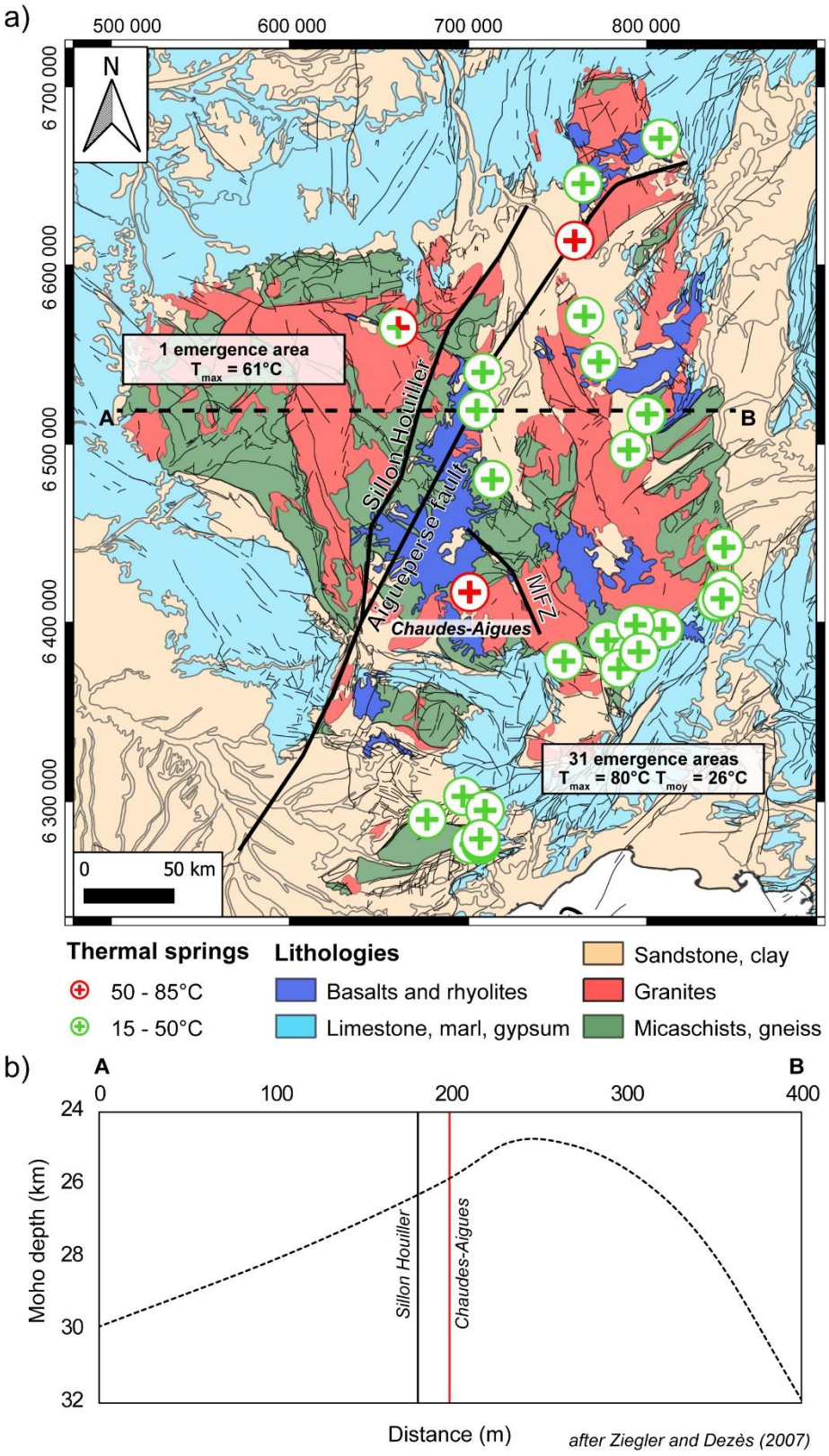

Figure VI.6: (a) Thermal springs distribution in the Massif Central on a 2M geological map (BRGM). (b) Depth of the Moho represented as the thickness of the crust along the AB profile (after Ziegler and Dezès, 2007).

Geodynamic setting

The French Massif Central (FMC) exhibits a large wavelength surface heat flow anomaly (greater than 90 $mW.m^{-2}$), as illustrated by the blue contour in Figure VI.2. At the scale of Western Europe, several surface heat flow maps clearly illustrate this ~800 km long anomalous surface heat flow signature, from the southwest Massif Central to the Upper Rhine graben in Germany (see Figure 2b in Cloetingh et al., 2010; Figure 5 in Majorowicz and Wybraniec, 2010, or Figure 3b in Guillou-Frottier et al., 2024). Even if radiogenic heat production of some granitoids of the French Massif Central can exceed 5 $mW.m^{-3}$, their thicknesses are too small to explain such anomalous surface heat flow. Based on several independent data, a large mantle heat flow value (up to 60 $mW.m^{-2}$) has been invoked by Lucazeau et al. (1984), who first suggested the presence of a mantle diapir. Additional analyses of seismic, gravity, petrologic and thermal observations led Sobolev et al. (1997) to suggest the presence of a mantle plume beneath the FMC, leading to temperatures of the upper mantle 150 to 200°C higher than the average temperature of the upper mantle.

Although different geodynamic processes (subduction-induced, shear-heating) have been suggested to cause this anomalous mantle heat flow, the main consequence is that the first kilometres of the crust are heated by a deep heat flow reaching 80-90 $mW.m^{-2}$ (i.e. a large mantle heat flow completed with the radiogenic component of the crust). This is the basal thermal boundary condition which will be assumed in the following models.

Thermal springs distribution

Thermal springs are unequally distributed throughout the Massif Central. To the north-west of the Sillon Houiller and the Aigueperse Fault, only one hydrothermal system is known (Figure VI.6a). The maximum temperature of these springs is 61°C. Nevertheless, in the south-east, on the opposite side of the Sillon Houiller, there are 31 hydrothermal systems. The average temperature of the springs is 26°C. The hottest of these is the Par Spring, part of the Chaudes-Aigues hydrothermal system. Our study is focused on this hydrothermal system which seems to be located on the most favorable part of the FMC.

Chaudes-Aigues

Geological settings

The thirty thermal springs of Chaudes-Aigues are located near the northern edge of the Margeride Granitic Complex (MGC). The MGC was emplaced into the Variscan basement, made of metamorphic units (LGU and UGU), during the late Carboniferous (~300 Ma) (Talbot et al., 2005). Its emplacement is associated with post-orogenic extension and is accompanied by a network of fractures and faults that have been reactivated during subsequent tectonic episodes (Talbot et al., 2005; Penhoët et al., 2025a). This geological context is further developed in Penhoët et al. (2025a) and Penhoët et al. (2025b). The springs are located at the edges of a major NW-SE fault system crosscut by 2 other Variscan fault zones (Gibert et al., 1975, De Goer de Hervé, 1991; Penhoët et al., 2025a). One of these clusters, N50 trending, is characterised by thick ductile faults reactivated in brittle dynamics over geological time (Penhoët et al, submitted). This, intersected by the N150E faults, creates a zone of very high permeability. Theses faults would crosscut the MGC beneath the town. Gravity studies have shown that the MGC is dipping to the north and lies at a shallow depth beneath the town (Penhoët et al, submitted).

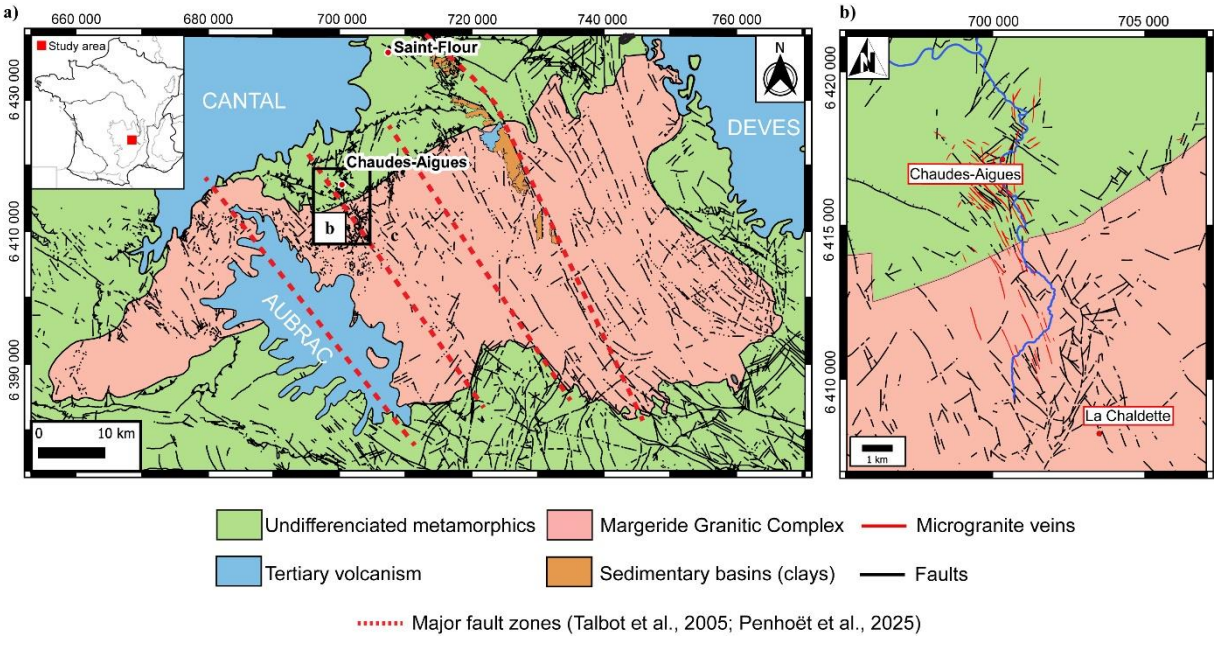

Figure VI.7: Geological maps of the (a) MGC cut by the various major fault zones and (b) zoom on the Chaudes-Aigues hydrothermal system.

Hydrogeological settings

The 30 thermal springs of the Chaudes-Aigues area reach temperatures between 50 and 80 °C, making the Par Spring one of the hottest natural springs in Europe. The total flow rate of the springs reaches more than 700 l/min and is constant over the year. The emergence area, in the gneissic units, is characterized by a high density of brittle structures (Figure VI.7). The springs are located at the edges of major NW-SE fault systems crosscut by 2 other Variscan fault zones (Gibert et al., 1975, De Goer de Hervé, 1991; Penhoët et al., 2025a). These NW-SE faults intersect the whole MGC, creating a favourable setting for hydrothermal activity. Further south in the MGC (10 km), located in the same fault zone, another thermal spring, the "La Chaldette" spring emerges at 35°C in the granite laccolith (Figure VI.7b).

Chaudes-Aigues springs are formed by a mixture of surface water and a contribution from a deep endmember (Penhoët et al, 2025b). The meteoric waters would infiltrate to the south via a N150E fault zone, within which lies the La Chaldette spring, the composition of which constitutes the surficial part of the circuit. This fault zone would allow meteoric waters to be drained at shallow depths, giving rise to thermal springs such as La Chaldette, but also at depth to supply a deep reservoir. Its temperature has been estimated at 190°C (Penhoët et al, 2025b). It is thought to lie on the northern edge of the MGC, which, although not present at the surface, dips to the north and lies at shallow depth beneath the town (Penhoët et al, submitted). The major Variscan faults N50, characterised by crushed mylonites, reactivated over geological time, are thought to be the main drains of the system (Penhoët et al, submitted). This fault orientation is intersected by a N150E fault zone, once again resulting in very high permeability around the thermal springs.

Numerical modeling

Methods

Model set up: simulations and parameters

As demonstrated in previous studies, the establishment of convective regimes depends directly on the fault zone geometry (Malkovsky and Margi, 2016; Duwiquet et al., 2021; Penhoët et al., 2025a) but also on the topography (Taillefer et al., 2018). Here, a parametric

study was carried out to determine the control factors of the Chaudes-Aigues hydrothermal system, consisting of models with or without topography and with or without deep reservoir. As in Guillou-Frottier et al. (2013), Darcy law was coupled with heat transfer equation and mass conservation. For each model configuration (topography, reservoir), two different simulations were computed. First, a simulation corresponding to a purely conductive regime: homogeneous basement, fault zones deactivated. This way, the initial conditions for the second simulation correspond to a purely conductive thermal state. Then a second simulation with the physical properties (permeability) of the fault zones.Several variables such as thermal conductivity, heat capacity, porosity, rock density (see Table 6.1) necessary for modeling were estimated thanks to field observations and literature data (Brace 1984; Lucazeau et al., 1984; Sonney and Vuataz, 2009; Moeck, 2014, Neuzil, 2019).

	Porosity	***Permeability (m^2)***	***Matrix thermal conductivity (W/m.K)***	***Density (kg/m^3)***	***Matrix heat capacity (J.kg.K)***	***Fluid thermal conductivity (W/m.K)***	***Fluid heat capacity (J/kg.K)***	***Heat production (W/m^3)***
Metam. units	0.05	10^{-18}	2.9					0
MGC	0.05	10^{-18}	2.7	2700	1000	0.6	4200	$3\ 10^{-6}$
Fault zones	0.1	10^{-15} – $5\ 10^{-14}$	3.1					x

Table VI.1: Physical parameters used for rocks and fluid in 3D modelling. These values have been obtained from different studies (Smith and Chapman 1983, Rabinowicz et al. 1998, McKenna and Blackwell 2004, Guillou-Frottier et al. 2013, Taillefer 2017, Duwiquet et al. 2019).

Fluid physical properties are dependent on pressure and/or temperature. The dynamic viscosity of the fluid is dependent on temperature and the density of water is dependent on both pressure and temperature. The equations used are the same as Penhoët et al (2025a).

The main unknown remains the permeability value for each formation. The MGC and the metamorphic units are considered, in the absence of fracturing, as impermeable. The increase in pressure at depth tends to seal the fractures and thus causes a decrease in the permeability of the units:

$$K_u(z) = K_{0_u}.e^{\frac{-z}{\delta}} \quad (1)$$

where $K_u(z)$ is the permeability of each unit (m²), K_{0_u} is the highest permeability (from 10^{-15} m² to 5 10^{-14} m² in the fault zone, and 10^{-18} m² in the host rocks) reached by the unit (at the surface) and z is the depth (m) (Garibaldi et al. 2010). The length δ (m) characterizes the intensity of the decrease in permeability with depth. A δ value of 1500m has been chosen.

Meshing and geometry

The models all have identical geometry, based on the geological maps covering the MGC (n°812 Vic-sur-Cere, 813 Chaudes-Aigues, 814 Saugues, 815 Cayres, 836 Entraygues-sur-Truyère, 837 Nasbinals, 838 Saint-Chély-D'Apcher, 839 Langogne, 859 Decazeville, 860 Espalion, 861 Saint-Geniez-D'Olt, 862 Mende, 863 Le Bleymard,) but also the emplacement model of the MGC proposed by Talbot et al. (2005). The major fault zones (see Figure VI.7) cross-cutting the MGC have been represented according to the geological maps (thickness, location) and Talbot et al. (2005) emplacement model: Aubrac (FZ 1), Chaudes-Aigues (FZ 2), Loubaresse (FZ 3), MFZ (FZ 4), East (FZ 5) fault zones (Figure VI.8a). Models therefore present 3 main domains: the MGC, fault zones and the host rock made up of metamorphic units (Figure VI.8a). On the northern edge, the reservoir proposed by geochemical studies (Penhoët et al., 2025b) was represented. Its lateral extension (SW-NE) was determined by the chemical composition of the springs present on the northern edge of the MGC (red dots, Figure VI.8b). Assumed to be in Granite, it has the same physical properties. The dimensions of these geometries are summarised in Table VI.2:

	L (km)	***H (km)***	***W (km)***
Host rock	106	8	70
MGC	91	5	50
FZ 1	5	5	38
FZ 2	3	5	39
FZ 3	2	5	34
FZ 4	0.2	5	50
FZ 5	0.1	5	15
Reservoir	22	1.5	5

Table VI.2: Dimensions of the different domains

The upper surface of the model corresponds to the actual topography of the study area. This 25 m resolution DEM comes from the IGN (BD-Alti). The highest altitude corresponds to the Cantal (1615 m a.s.l) and the lowest is in the south-west corner of the model (255 m a.s.l).

The size of mesh elements is based on the permeability value. In areas of low permeability (host rocks), the mesh element size is coarse (minimum size 100 m) but extremely fine in the fault zone (high permeability) (maximum 20 m).

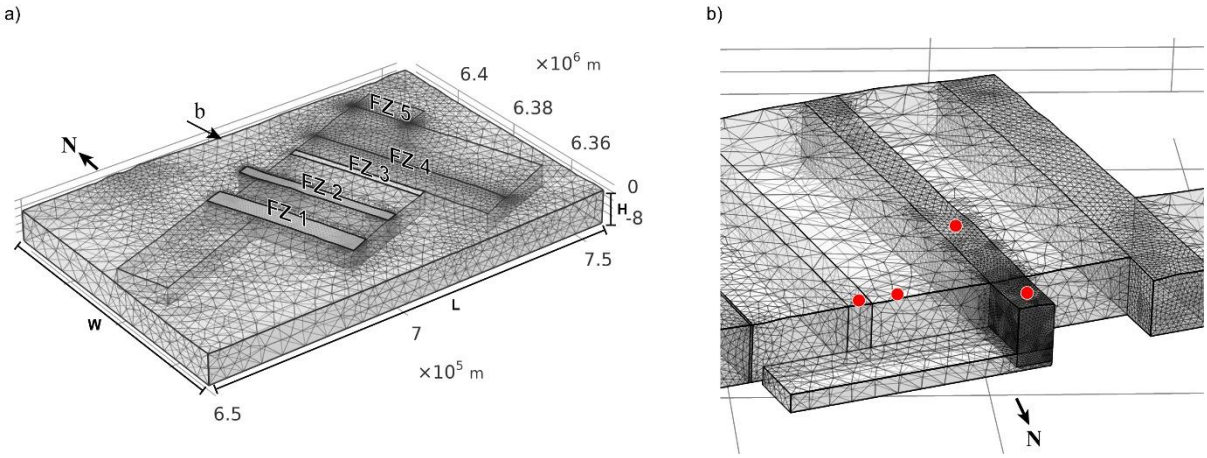

Figure VI.8: (a) Overall geometry of the model with the main faults cutting the Margeride Granite, (b) northern view of the Chaudes-Aigues fault zone crossing the assumed reservoir at depth. The red dots correspond to the thermal springs used to determine its location (Penhoët et al., 2025b).

Boundary conditions

Thermal conditions

At the upper surface of the model, a temperature of 10 °C was fixed except for the Chaudes-Aigues fault zone (FZ 2, Figure VI.9a). In order to reproduce temperature variations such as thermal springs, a mixed thermal boundary condition has been applied. This was previously used by Magri et al. (2016) or Taillefer et al. (2018):

$$Q = h(T_0 - T) \qquad 2$$

With Q the surface heat flow ($W.m^{-2}$), h a heat transfer coefficient ($W.m^{-2}.K^{-1}$) and T_0 the surface temperature (10°C). The value of h was selected on the basis of a parametric study to reproduce in a conductive regime (i) a surface temperature close to 10°C, (ii) a surface heat flow close to 100 $mW.m^{-2}$. Its value has to be between 0.01 and 0.07 $W.m^{-2}.K^{-1}$, for the

parametric study its value is fixed to 0.04 $W.m^{-2}.K^{-1}$. According to regional data, a constant heat fux of 85 $mW.m^{-2}$ is imposed at the base of the model (Lucazeau and Vasseur 1989). The lateral borders were thermally insulated (metamorphic units). At the northern edge of the model, the deep reservoir is characterised by imposing at its surface a fixed temperature of 190°C (Vasseur et al., 1997; Penhoët et al., 2025b) (Figure VI.9). This would reach 190°C (Vasseur et al., 1997; Penhoët et al., 2025b).

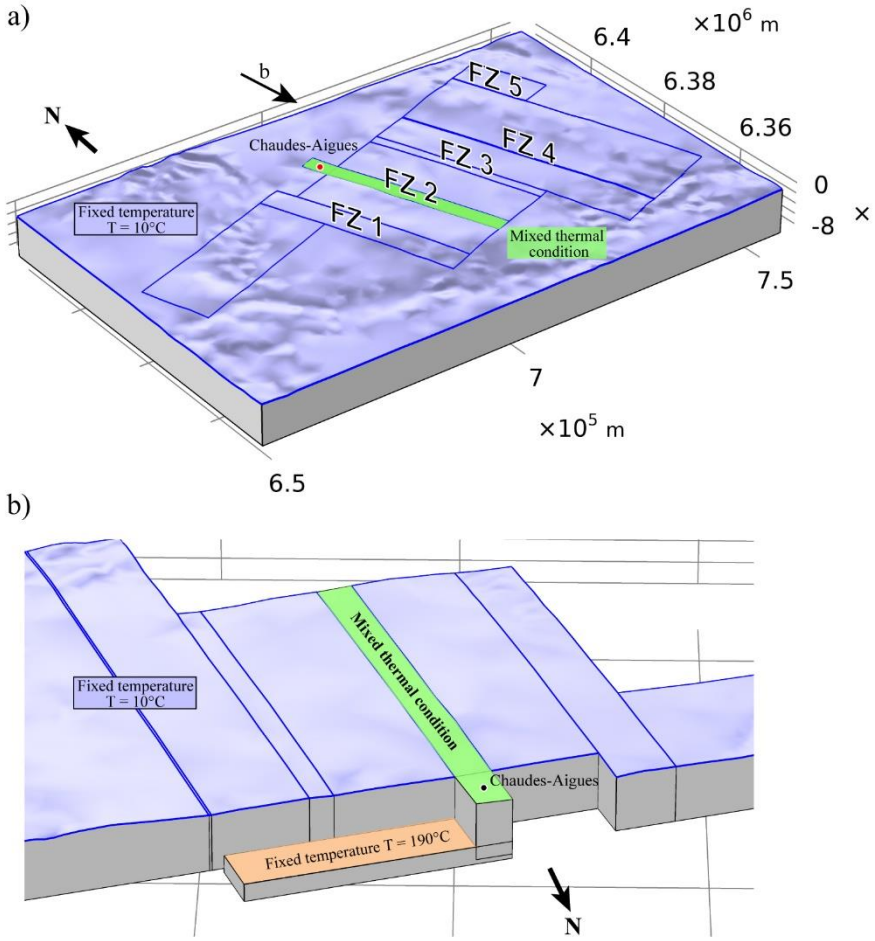

Figure VI.9: (a) Boundary conditions used for all models (with or without topography), (b) zoom on the northern edge of the granite with a reservoir represented as a surface with an imposed temperature. In the case of models without reservoir this condition disappears.

Flow conditions

The surface pressure is equivalent to the atmospheric pressure (10^5 Pa), and its value increases with depth. A no flow condition was imposed on lateral sides and bottom of the model (metamorphic units).

Constraint factors

In order to obtain results that are as robust as possible, a series of criteria and parameters will have to be reproduced by the 3D numerical models. Firstly, a geographical criterion: Chaudes-Aigues and La Chaldette springs will have to be spatially reproduced at locations close to reality. They are about 10 km apart in the metamorphic units and the MGC respectively. Their temperatures are also key criteria for validating the results. Concerning the Chaudes-Aigues area, which includes around 30 thermal springs, the objective is to reproduce the temperature of the Par Spring (the hottest, measured at 80°C). For the La Chaldette spring, the 35°C of the borehole (formerly a natural spring) will have to be reproduced.

Then, from a hydrogeological point of view, the global discharge of the 30 Chaudes-Aigues springs will have to be reproduced. This represents around 700 l/min. This flow will be decomposed into “deep” and “surface” components. The thermal waters of Chaudes-Aigues have been identified as a mixture of 65% meteoric water and 35% deep endmember contribution (Vasseur et al., 1997; Penhoët et al., 2025b). These different flow rates are calculated via Comsol Multiphysics™ as an integral of the Darcy velocity across a defined surface. These calculations are detailed in Figure VI.10. Finally, the impluvium, identified as the MGC and more precisely the N150E fault zone to the south of Chaudes-Aigues (Penhoët et al., 2025b) should also correspond.

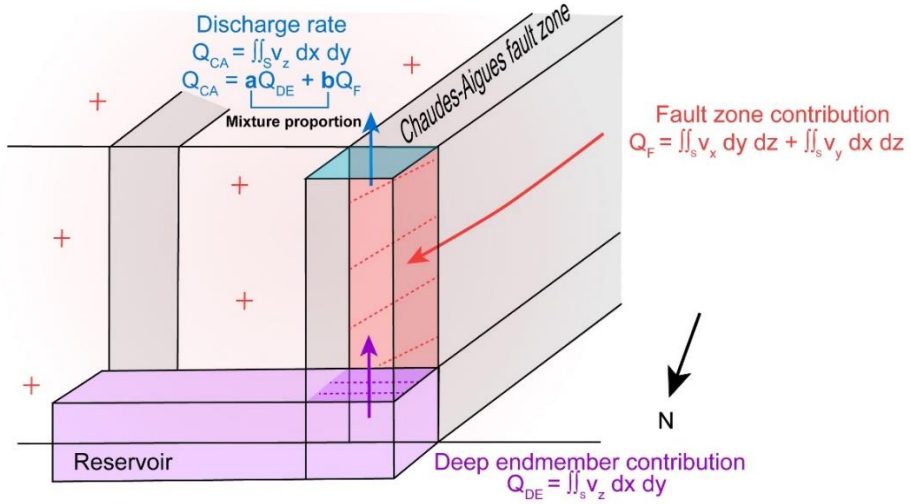

Figure VI.10: Calculation of different flow rates and mixing ratios in numerical models.

The following numerical results correspond to final state (steady state regime) of 500 kyr of transient evolution.

Results

Four quantified criteria are to be reproduced to determine the control factors of the hydrothermal system. The values to be reached are represented by a dot red line Figure VI.11. Spatial criteria also must be reproduced, such as the location of thermal springs or the recharge zone.

Spring temperatures

The first two criteria correspond to the temperature of the Par and La Chaldette springs. Concerning the Par Spring (Figure VI.11a), its temperature is only reproduced for two configurations involving the presence of the deep reservoir with (blue line) or without (red line) topography. The springs reproduced reach up to 90°C. Without the reservoir (yellow and green lines), the springs do not exceed 60°C, so the Par Spring is not reproduced (Figure VI.11a).

The Chaldette spring is easier to reproduce because of its lower temperature. Three configurations were successful: those with topography and with (blue line) or without (green line) reservoir, and the one without topography or reservoir (red line, Figure VI.11b). Temperatures ranged from 35 to 45°C. Nevertheless, without topography and with a reservoir (yellow line), the La Chaldette spring cannot be reproduced, whatever the permeability of the fault zone (Figure VI.11b).

Mixing coefficients

The mixing coefficients for Chaudes-Aigues springs vary between 30-40% deep endmember and 60-70% surface water (Penhoët et al., 2025b). The two configurations without deep reservoirs do not reproduce mixing coefficients close to those found in geochemical studies (yellow and green lines Figure VI.11c). Only 10% of the total flow would come from the deep reservoir, which is too low a value. The configuration without topography but with reservoir (red

line) reproduces the mixing coefficients for a single fault zone permeability value (9 10^{-15} m² < K < 10^{-14} m²). Below this value, the values are close to 0, and above, the values reach 90%. The configuration with topography and reservoir (blue line) reproduces proportions close to reality, 30-35%, for fault zone permeabilities greater than 9 10^{-15} m².

Flow rates

Total outflows from the Chaudes-Aigues area are the last quantified criterion to be reproduced. In the city, these are estimated at around 700 l/min. In the case of unknown springs, all higher values will be considered valid.

Configurations without topography do not achieve a flow rate of 700 l/min at Chaudes-Aigues, whatever the value of the permeability of the fault zone (yellow and red lines, Figure VI.11d). The two configurations with topography flow rates exceed 700 l/min for low permeability values (9 10^{-15} m²), when the fault zone permeability is very high (5 10^{-14} m²), 3500 l/min (blue line, Figure VI.11d) with reservoir and 3000 l/min without (green line, Figure VI.11d).

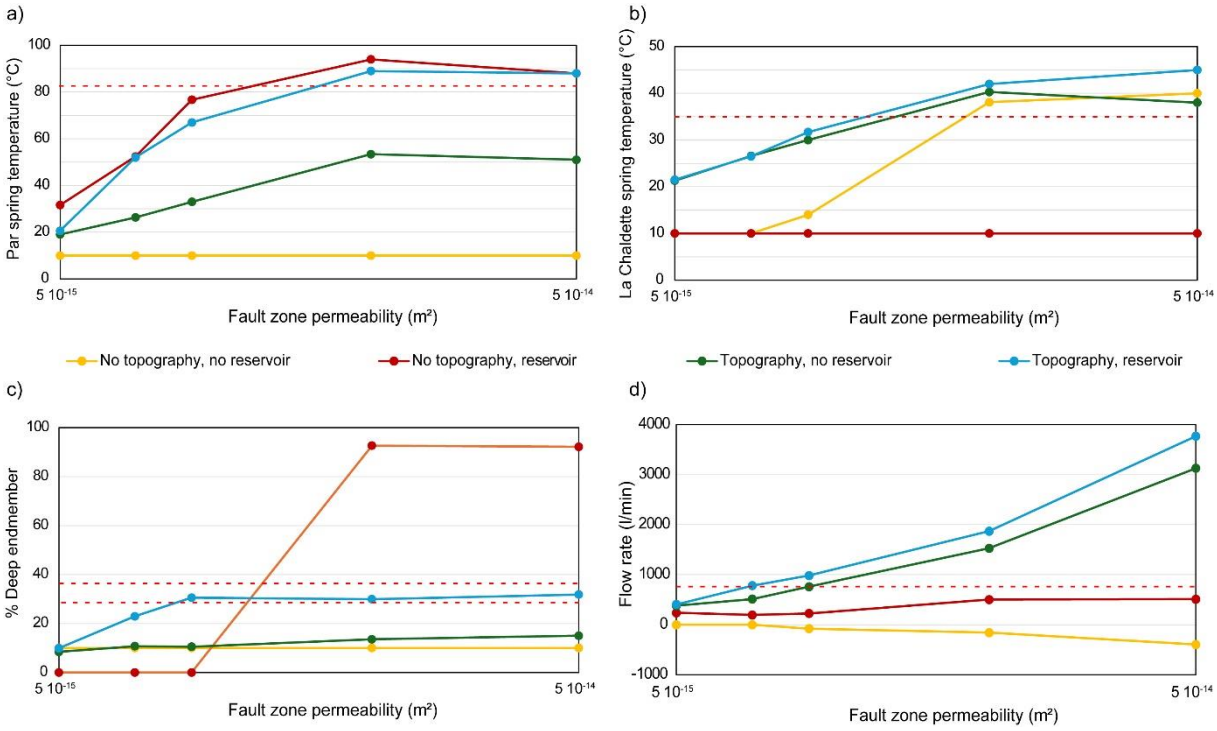

Figure VI.11: Results of the different models (with/without topography, reservoir): (a) Par spring temperature, (b) La Chaldette spring temperature, (c) mixing coefficients between surface water and deep endmember, and (d) discharge rates at Chaudes-Aigues (see Figure VI.7) as a function of the fault zone permeability. Red dot line indicates the Par Spring or La Chaldette spring values that must be reproduced.

Spring and impluvium locations

The geographical location of the Par Spring was reproduced for all configurations except the one without topography and without reservoir. Only the models without topography and with reservoir were unable to simulate the La Chaldette spring.

Synthesis

Table VI.3 summarises the results and the ability of the different configurations to reproduce the entire hydrothermal system.

The first configuration, with no topography or reservoir, only reproduces La Chaldette spring temperature and location. The rest of the criteria are absent. Then, if a reservoir is added, still without topography, the criteria concerning the Par Spring (location, temperature and flow rates) are validated. Nevertheless, the Chaldette spring is no longer reproduced.

The two configurations that include topography produced the best results. The first, which does not include a reservoir, meets all the criteria except for the Par Spring temperature (maximum of 50°C, green line in Figure VI.11a) and the mixing coefficients (90% surface contribution, green line in Figure VI.11c) for the Par. Despite these failures, the hydrothermal system is almost reproduced. The final configuration, which incorporates both a reservoir and topography, is the only one that successfully reproduces all criteria observed in the field and identified through geochemical studies.

Configurations				Par spring temperature	LC spring temperature	Par spring location	LC spring location	Impluvium location	Mixture proportion	Chaudes-Aigues flow rate	**Conclusion**
✗	Topography	✗	Reservoir								Not reproduced
✗	Topography	✓	Reservoir								Partially reproduced
✓	Topography	✗	Reservoir								Almost reproduced
✓	Topography	✓	Reservoir								Reproduced

Table VI.3: Results of the different modelling configurations in relation to the constraint parameters used. The conclusion column corresponds to the ability to reproduce the hydrothermal system at Chaudes-Aigues.

Discussion

Conclusions on Chaudes-Aigues hydrothermal system

In order to reproduce the exact temperatures and flows of the Chaudes-Aigues and La Chaldette springs, models with topography and reservoir were used.

The result is 80.9°C at the Par Spring for a total flow rate of 800 l/min. The proportions of the mixture remain close to those estimated by water geochemistry, with 30% of the water coming from the fault zone and 70% from the deep reservoir. In addition, the deep circulations reach a temperature of 200°C (Figure VI.12a), in line with the values given by geothermometers of 190 ± 10°C (Vasseur et al., 1997, Penhoët et al., 2025b). The infiltration zone has been clarified. Vasseur et al. (1997) assumed a possible deep connection with the Aubrac plateau. Numerical models have shown that this is not the case, as no circulation is visible even at very low velocities. Because of its great thickness, 5 km in the models, the Aubrac becomes more favourable to downward flow, which results in a downward deformation of the isotherms (Figure VI.12b). Nevertheless, the Chaudes-Aigues infiltration appears to be closer than the southern edge of the MGC, near La Chaldette spring. The N150E fault zone therefore includes the infiltration, circulation and emergence zones. However, deeper and slower circulations could also originate from the southern edge of the MGC. The residence time for the entire circuit was estimated between 50 000 and 200 000 years using numerical modelling, questioning the Würm origin proposed by Vasseur et al. (1997). This interval is consistent with other basement hydrothermal systems (Iwatsuki et al., 2000; Dupuy et al., 2021, Waber et al., 2017; Carbajal-Martinez et al., 2024; Wang et al., 2024).

La Chaldette spring also comes from circulation within this N150E fault zone, with models indicating circulation reaching 130°C (Figure VI.12a) at depth. This value is close to that estimated by Penhoët et al., (2025b) (110 ± 10°C).

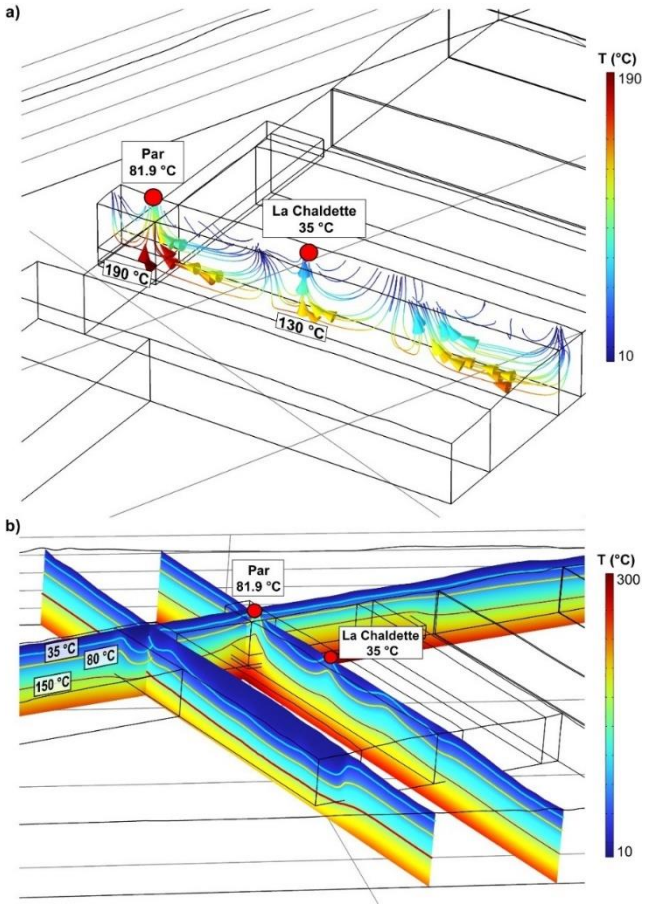

Figure VI.12: Final model representing the Chaudes-Aigues hydrothermal system with K_{CA} = 1 10^{-14} m², K_{Aubrac} = 5 10^{-14} m² and h = 0.01 $W.m^{-2}.K^{-1}$. (a) the arrows represent Darcy velocities (m/s) the colour code represents circulation temperatures in the fault zone. (b) Thermal state of the different fault zones in the model with associated isothermal deformations.

Limitations and perspectives.

The aim of this study was to assess the main factors controlling the Chaudes-Aigues (and La Chaldette) hydrothermal system, through modelling using thermo-hydraulic coupling. Only the configuration incorporating both topography and a deep reservoir can reproduce all the criteria observed in the field. This configuration therefore appears to be the most realistic for representing the current hydrothermal system.

Nevertheless, several limitations need to be highlighted. The first concerns the main unknown parameter in modelling: permeability. This fundamental parameter is not constrained by laboratory measurements in our study area, and the values used are based on assumptions and correspond to those in the literature (Brace 1984; Evans et al. 1997; Sonney and Vuataz 2009; Ranjram et al. 2015; Walter 2016; Achtziger-Zupancic et al. 2016; 2017; Neuzil 2019).

Furthermore, permeability is assumed to be laterally homogeneous in fault zones, without taking into account the alternation between fault core (impermeable) and damage zone (permeable). The value used is an average of these components.

The second limitation is the simplified representation of the fault network. The Chaudes-Aigues intersection zone is modelled as a single permeable domain. The actual orientations of the two fault zones are not taken into account. However, the orientation of a fault in relation to regional tectonic constraints is a key factor influencing fluid circulation (Barton et al. 1995; Mckenna and Blackwell 2004; Faulds et al. 2010; Haines et al. 2016, Duwiquet et al., 2022). These two parameters will have to be integrated to obtain more accurate results and reach a definitive conclusion on the nature of the upwelling drains at Chaudes-Aigues.

Finally, another important limitation is that the regolith is not taken into account in the model. This weathered surface layer, often characterised by very high permeability (Lachassagne et al., 2011), can play a key role in the interactions between deep and surface circulations, and can also have thermal impacts. Its exclusion from the model is a necessary compromise to avoid numerical instabilities and excessive complexity, but it limits the representation of interactions between deep flows and the infiltration zone.

Conclusions

This study highlights the value of three-dimensional thermo-hydraulic modelling for improving the understanding of complex hydrothermal systems. Through an evaluation of the respective influences of topography and a deep thermal reservoir, our results demonstrate that only the combined inclusion of both factors enables the model to reproduce all key hydrodynamic and thermal observations of the Chaudes-Aigues system. These findings support the hypothesis of a dual-flow regime, involving deep circulation feeding a 190 °C reservoir and a shallower meteoric component contributing to mixing processes at discharge zones. In addition, the modelling refines previous models regarding the recharge area, suggesting a more proximal zone near La Chaldette rather than the distant Aubrac Plateau. The N150E-trending fault zone is shown to play a key role centralizing recharge, deep circulation, and discharge.

Beyond its application to the Chaudes-Aigues system, this work highlights the importance of integrating structural, geophysical, and geochemical constraints in numerical simulations of fractured crystalline environments. This approach may serve as a valuable methodology for investigating similar geothermal systems and supporting resource assessment in analogous geological contexts.

Funding

The financial support was provided by Bureau de Recherches Géologiques et Minières (BRGM), Institut des Sciences de la Terre d'Orléans (ISTO) and by the project « GERESFAULT » (ANR-19-CE05-0043)

Chapters VII and VIII: Discussion, limits, perspectives and conclusions

VII. Discussion, limits and perspectives

In a context of energy transition, high-temperature geothermal energy is emerging as a strategic resource for producing renewable, local, low-carbon energy. To develop this resource, new targets need to be identified, particularly outside volcanic contexts or the major sedimentary basins that have been popular until now. The Chaudes-Aigues hydrothermal system, located in the Hercynian basement of the French Massif Central, is an example of an active reservoir in an amagmatic context, within a faulted granite. It is therefore a unique demonstrator for exploring the geothermal potential associated with zones of high permeability: crustal fault zones.

This system illustrates a new approach to geothermal exploration: targeting areas where the structure and fracturing of the basement allow the circulation of hot deep fluids, rather than relying solely on the presence of a high geothermal gradient. At Chaudes-Aigues, the presence of thermal springs reaching 80°C demonstrates the effectiveness of this type of reservoir, whose operation is based on the reactivation of inherited structures and the persistence of high permeability.

VII.1 Multidisciplinary approach

A comprehensive understanding of a hydrothermal system fundamentally requires a multidisciplinary approach. As highlighted above, there are many different types of control factors. Our work combines different methods namely, structural geology, water geochemistry, geophysics and hydrogeology. These data will serve both as a basis and as validation criteria for 3D thermal-hydraulic modelling. The interactions between these different disciplines ensure this comprehensive understanding of the studied system.

First, a structural study is needed to understand the fragile structure of the study area. This is a fundamental step, as it enables the orientation of the main fault families to be determined. This data is the first step in identifying the chronology of the faults, deducing potential reactivations in connection with the paleo and current tectonic stresses. This information has been used to determine the past and present evolution of the drains in the hydrothermal

system. This stage is the first estimate of the drain permeability, and only allows it to be quantified (high, low) spatially, but does not give a numerical value. Laboratory measurements of permeability could be used to refine and obtain a more constrained value, some have been used in Duwiquet et al. (2019) or Launay et al. (2019).

Second, geochemistry coupled with hydrogeology can be used to reconstruct the path taken by the water from the surface to depth. As shown here, the temperature of a spring at the surface is not a sufficient criterion for determining whether a hydrothermal system is present; only its chemical composition (geothermometric calculations) is a reliable criterion. Geochemical methods are needed to pinpoint the location of a deep reservoir.

Third, the gravimetric study carried out at a kilometre scale confirmed the geochemical observations. Nevertheless, to determine the precise location of the deep reservoir, a more detailed study would be required, in particular the acquisition of Magneto - Telluric data. This method is already widely used in geothermal exploration (Harinarayana et al., 2006; Heise et al., 2008; Newman et al., 2008; Patro, 2017; Duwiquet et al., 2021). This method maps electrical resistivity at depth and can be used to identify conductive bodies. For geothermal exploration, it can be used to identify reservoirs of hot fluids and hydrothermal alteration such as cap rocks characterised by high conductivity. As far as this method could identify fluid flow in depth, this could help to determine the geothermal potential of Chaudes-Aigues since it depends on the depth and volume of the reservoir.

The final stage involves 3D thermal-hydraulic modelling. Once the models have been constrained by the various techniques described above, they provide a dynamic visualization of the hydrodynamic functioning of the hydrothermal system. These were used to question or validate the results of other methods. Their construction and analysis require constant interaction with the natural object. In the models produced, permeability is assumed to be laterally homogeneous in a fault zone. This results in an ‘average’ between the fault core and the damage zone, potentially over- or under-estimating the permeability value. Other models

use a lateral variation in permeability, thus reproducing the succession of fault cores and damage zones within the fault zone (Duwiquet et al., 2019).

VII.2 Synthesis of key findings on Chaudes-Aigues hydrothermal system

This study has not only confirmed the hypotheses previously established but has also provided new information to clarify the functioning of Chaudes-Aigues hydrothermal system. Although in 2D, the first model provided by Vasseur et al. (1997) proposed a complete circulation diagram from the infiltration zone to the thermal springs (Figure VII.1). They proposed two parallel pathways in the MGC: one deep and another more superficial. In this model, the microgranite veins are the vertical pathways for fluids upwelling as they intersect, at a depth of 5 km, a deep reservoir at 190°C, (see chapter 1, I.5.3).

However, uncertainties needed to be clarified, such as the location of the impluvium, the deep reservoir geometry and extension, the deep-water pathways, time transfer and possible 3D circulation transfer. Last, the La Chaldette thermal spring has not been included in the model of Vasseur et al. (1997) whereas its atypic location within the reservoir was not yet explained.

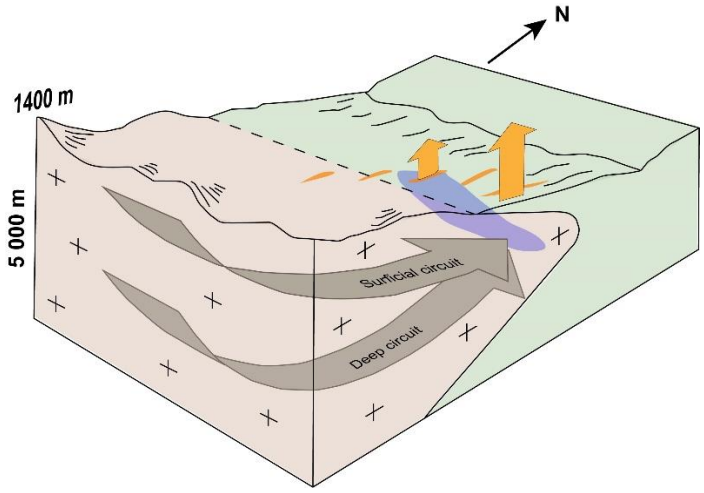

Figure VII.1: Block diagram illustrating the geothermal systemof Chaudes-Aigues springs (modified from Vasseur et al., 1997). The granitic reservoir is drained to the North thanks to two fluids pathways (greys arrows), while upwelling of hot fluids (orange arrows) is ensured by the dense network of microgranite veins (in orange).

I.5.13 Historical model validation

The results of this study validate some points supposed by Vasseur et al. (1997): Chaudes-Aigues springs originate from the mixing of meteoric waters and a deep reservoir, two distinct

pathways would coexist one surficial and the other deep (Chapter 4). Thanks to new geochemical data and numerical modelling, our study has reduced the uncertainty about the temperature of the reservoir, which is now estimated at 190°C.

I.5.14 New elements and global diagram

The complete path of the water, from the infiltration to the thermal springs, has been reconstructed thanks to new results in water geochemistry, structural geology, geophysics and 3D thermal-hydraulic modelling.

Uncertainties about the infiltration zone have been reduced. The southern edge of the granite and the N150E fault damage zone to the south of Chaudes-Aigues have been identified as the main impluvium. Within this, highly permeable, fault zone a convective regime allows hot fluids to rise locally the surface as well illustrated by the La Chaldette thermal spring (Figure VII.2). This locally infiltrated water has a long circulation in the MGC and is thought to reach 110°C at depth (Chapter 4).

Once infiltrated, water could flow through two different pathways. The first corresponds to a shallow circulation. This surficial part presents the same chemical composition than those measured in the La Chaldette spring. These waters are the results of near surface circulation that could take place within the weathered horizons of the MGC that comprise the alterite and fissured layers. This profil could reach greater depth within fault zones (Chapter 5). The physical continuity between these two sites (Chaudes-Aigues - La Chaldette) is ensured both by the N150E directed fault zone and potentially also by the weathering which is still present in the fault zone and ever deeper. These weathering layers may act as a surface aquifer, which could partly explain the high flow rates observed at Chaudes-Aigues.

The second, deeper circuit, feeds the granitic reservoir. The fluids are drained at depth and towards the northern edge of the MGC. The MGC plunges northwards and is present at a shallow depth beneath Chaudes-Aigues as inferred from our gravity measurements (Chapter 3).

Chaudes-Aigues area is characterised by the intersection of three fault zones (N0E, N050E and N150E) along with microgranite and quartz veins, some being mineralised, emplaced. Based on our structural survey, the main upwelling drains identified are the N050E-trending faults and, with a secondary importance, the N140E-trending faults. Initially ductile, these conjugate vertical fault networks are deep structures affecting both the LGU and the northern termination of the MGC at depth. All were continuously reactivated in a brittle domain since the late Variscan and in particular during the Cenozoic - and until now - ensuring a potential present-day high permeability of these damage zones. It is worth-noting that the spring swarm of Chaudes-Aigues is located at the intersection between the three set of faults network suggesting that the permeability is enhanced at this intersection in which damage zones appears highly developed. As a consequence, the fast upwelling of a large volume of hot waters is enhanced, ensuring spring temperature of more than 60°C. The concentration of the springs along the Remontalou river suggests that the final, near surface, fluid pathway is controlled by the minimum topographic level as often observed in many hydrothermal systems (Taillefer et al, 2018, Dupuy, 2021; Carbajal Martinez et al., 2024).

Vasseur et al. (1997) considered the microgranite veins as the main drains for the upwelling hots waters. Our structural survey suggests that the N050E thick damage fault zone are the best candidates while the microgranite veins are not affected by fluid circulation except for N050E fracture planes in which limited signs of dissolution indicate the passage of small quantities of fluids. By opposite, the high density of microgranite and quartz veins, and silicified mylonites, North of Chaude-Aigues may potentially act at depth as barriers preventing the fluid upwelling toward the North.

The residence time for the entire circuit was estimated between 50 000 and 200 000 years using numerical modelling, questioning the Würm origin proposed by Vasseur et al. (1997). This interval is consistent with other basement hydrothermal systems such as in Japan (Tono granite), Corisa (monzogranite) or Wugongshan region in China (orogenic belt), and their residence times have been estimated at between 6 500 and 100 000 years (Iwatsuki et al.,

2000; Dupuy et al., 2021, Waber et al., 2017; Carbajal-Martinez et al., 2024; Wang et al., 2024). The whole hydrothermal system is resumed in Figure VII.2.

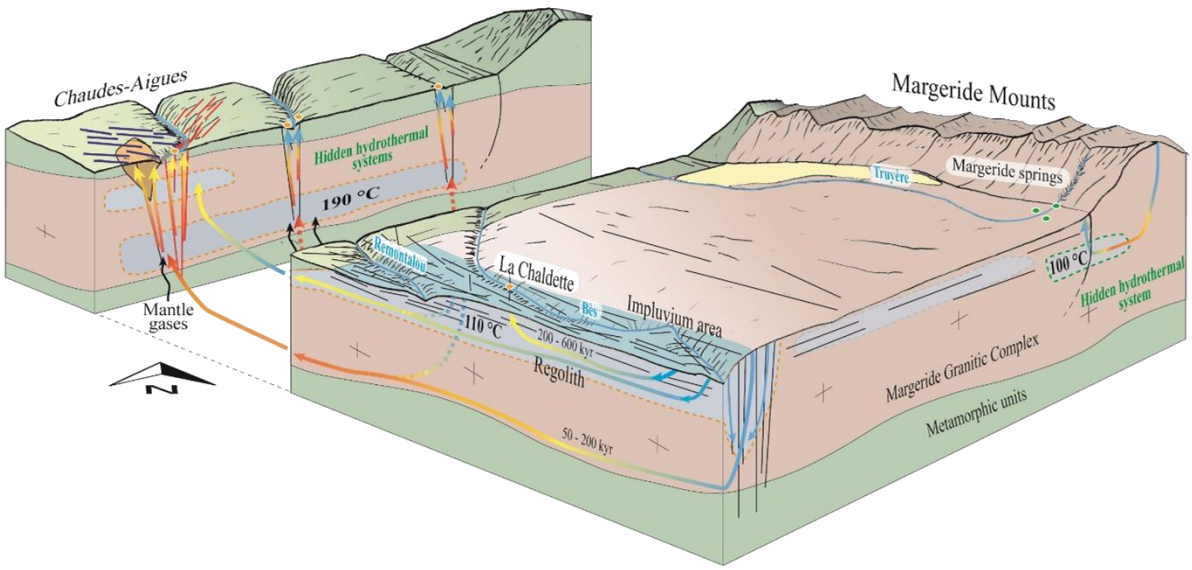

Figure VII.2: Functioning of the Chaudes-Aigues hydrothermal system and other hidden systems within the MGC. N50E faults are represented in red and N150E in blue.

Finally, this study has identified other potential hydrothermal systems within the MGC hidden by cold springs at the surface such as the Margeride springs reaching 100°C at depth (see Chapter 4).

VII.3 Perspectives for geothermal exploration

In France and around the world, geothermal exploration has been guided by previous oil exploration. In order to discover new deposits, oil companies have drilled extensively in Mesozoic and Cenozoic basins. These wells have provided precise information about the geology and geometry of these sedimentary basins, as well as providing temperature measurements at depth. These measurements have led to the discovery of the Soultz-Sous-Forêts temperature anomaly (Genter et al., 2010). Consequently, in France, the assessment of potential geothermal resources is often limited to sedimentary basins (mainly Parisian basin and Aquitain basin, Figure VII.3a)

Nevertheless, the hottest thermal springs in France (T > 50°C) are mostly located outside these areas with identified potential. Most of them are in basement areas (Pyrenees, Massif Central,

Alps, Vosges, Corsica, Figure VII.3b). These thermal springs are true surface indicators, suggesting high geothermal potential at depth. The presence of springs at 50°C at the surface is a clear indication of a potential reservoir at depth.

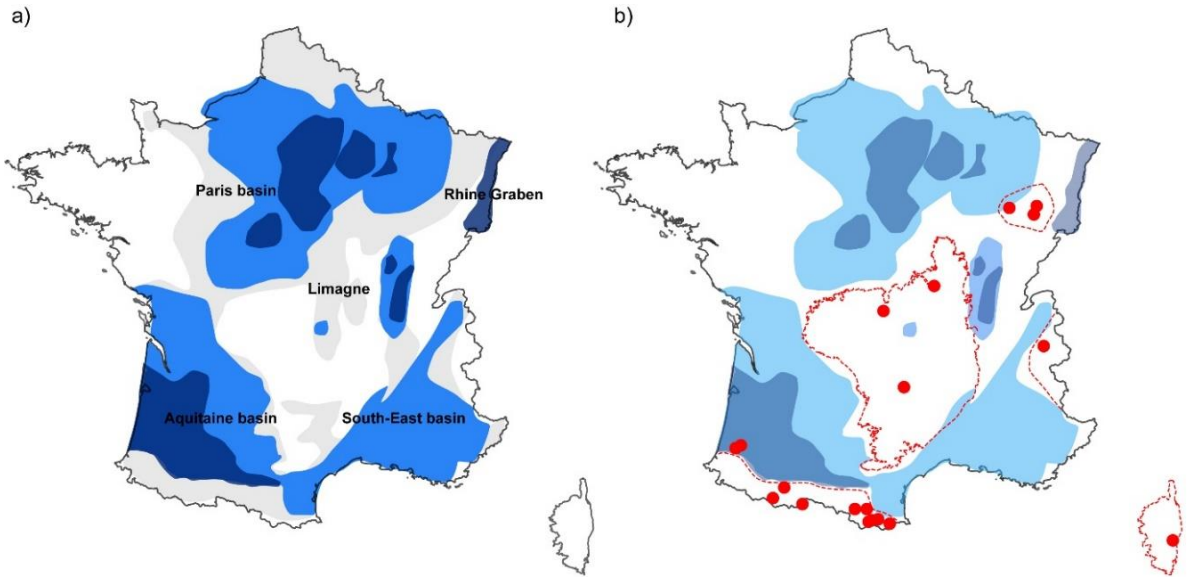

Figure VII.3: (a) Vision of French geothermal potential in 2018 (BRGM), the grey contours correspond to the main sedimentary basins, the light blue boundaries to continuous reservoirs indicating potential resources and the dark blue to resources assumed/proved to be above 70°C. (b) Vision of global geothermal potential including the sedimentary and crystalline domains. The red lines correspond to the contours of crystalline massifs hosting thermal springs (red dots, T > 50°C).

Other fractured granites in France and Europe, such as the MGC, could host hydrothermal systems consisting of several reservoir with multiple fluid pathways, which would be of interest for high-temperature geothermal exploration. In terms of analogues, we can find systems with similar geological characteristics. In the eastern part of France, Bains-les-Bains and Plombières-les-Bains are two towns known for their thermal springs, with temperatures ranging from 27 to 51°C and 43 to 80°C, respectively (Desprez et al., 1971). Very few geological studies have been carried out on these systems, and the only information available is that the springs are linked to grabens in Variscan directions (Desprez et al., 1971), and that the water would flow in the granite (Lefort and Jutier, 1862). Other cold springs have been found further east of these two systems. This area is made up of a granite massif covered by a very thin layer of sediment, represents a direct analogue to the MGC and its regolith. Another example is the Pietrapola thermal station in south-east Corsica, with several springs ranging from 27 to 54°C (Dupuy, 2021). Here, according to geochemical studies, after a long circulation through

the Hercynian bedrock (monzogranite), waters spring up through faults (Dupuy, 2021). Similarly, the Karlovy Vary, formerly known as Karlsbad, springs in the Czech Republic, are also associated with a granitic basement (Vrba, 1996). The massif is rich in hot springs, indicating a potential geothermal reservoir. Other example in the southeastern corner of British Columbia, Canada shows thermal springs ranging between 20 and 80°C. This hydrothermal system presents characteristics similar to Chaudes-Aigues: springs, fault zones, heat flow (80 – 120 $mW.m^{-2}$), no volcanism and a reservoir temperature up to 180°C (Finley et al., 2021).

VII.4 Spring temperature and generating potential: a misleading relation?

It may seem intuitive to consider that a hot spring at the surface directly reflects the presence of a high-temperature geothermal reservoir at depth, and conversely that a cold spring would indicate the absence of exploitable resources. However, this relationship is far from systematic.

I.5.15 High temperature: a good indicator for high-temperature geothermal energy?

As described in Chapter 1, thermal springs, whatever their temperature, are found in both sedimentary basins and crystalline massifs. Located in the aquitain basin, Dax springs reach temperature between 49 and 62°C, making these the hottest in sedimentary context. However, the deep dolomitic aquifer does not exceed 65°C (Alezine, 1987; Dupuy, 2001). The rapid ascent of fluids is thought to be made possible by the presence of faults. Similarly, in Bagnères-de-Bigorre, there are 16 springs with temperatures ranging from 23 to 51°C. Geochemical studies have shown that the water reaches a maximum of 55 to 64°C in the sedimentary aquifer (Cretaceous, Jurassic sediments and Triassic evaporites). The Bigorre-Adour fault is thought to be the main drain in the system. These examples illustrate that high surface temperatures do not necessarily guarantee a deep reservoir suitable for power generation (T > 150°C).

More generally, these exemples can be explained by the very characteristics of sedimentary basins, which are generally not conducive to the installation of deep, high-temperature hydrothermal systems. Their geometry, while offering great horizontal continuity, is often vertically heterogeneous (Figure VII.4a). The stacking of different sedimentary layers

(sandstones, limestones, clays, etc.) can act as a brake on flow due to the alternation of formations with very contrasting hydraulic properties. This vertical partitioning can greatly slow down deep-water circulation. These basin areas also have a relatively low density of faults, and those that do exist are often isolated, far from deep crustal fault zones, which reduces the presence of drains. In addition, the topography of the region is generally not very pronounced. If the difference in elevation between the infiltration zone and the source is small, the potential depth at which fluids can circulate is also limited, and therefore so is their heating. Finally, certain geological phenomena such as karstification can create very rapid, shallow circuits in carbonate rocks, short-circuiting any slow, deep circulation necessary for the development of high temperatures.

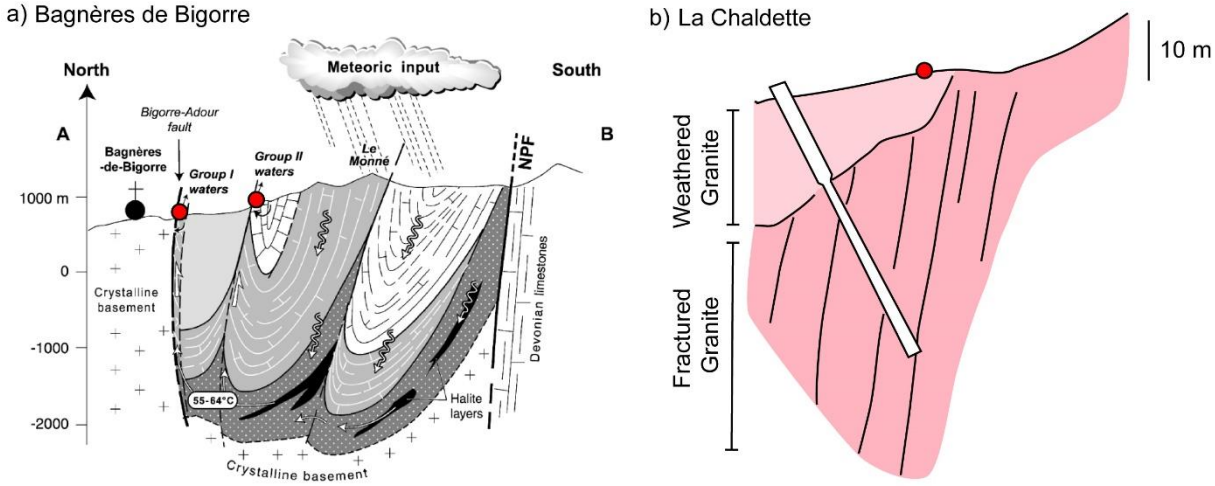

Figure VII.4: Comparison of vertical continuity through two examples: (a) Bagnères-de-Bigorre involving 5 lithologies (Levet et al., 2002) and (b) La Chaldette borehole only drilled in granite (Calvet et al., 2012). Thermal springs are highlighted by the red circles.

Nevertheless, in some cases, a hot spring may indicate a high-temperature reservoir. This was the case in our study, where the 80°C of the Source du Par was an indicator of the 190°C reservoir located beneath the town. The Plombières-les-Bains springs in eastern France, among the hottest in France, reach 70°C. They are thought to be associated with a deep reservoir with a temperature between 137 and 178°C (Gijbels et al., 1980). Basement rocks such as granites appear to be more suitable for this type of resource. Unlike sedimentary rocks, granite plutons can be continuous over great depths (in the case of the Granite de la Margeride, around 5 km, Talbot et al., 2005, Figure VII.4b). In addition, these massifs are often

characterised by a greater topography, which means that circulations can reach greater depths and therefore higher temperatures. Lastly, these areas are characterised by the presence of crustal fault zones, some of which are very deep and thick thus enhancing potential hydrothermal convection (Chapter 2). These systems then become predominantly convective, almost free of the pressure gradients offered by the topography.

I.5.16 Low temperatures: an absence of resources, or a misleading signal?

It is easy, almost intuitive, to assume that low-temperature or even cold springs automatically reflect the absence of interesting geothermal potential, or even the total absence of an exploitable resource. However, this idea needs to be revisited.

Our study has highlighted the existence of “hidden” hydrothermal systems within the Margeride granite: cold springs at the surface that are supported by deep reservoirs with temperatures higher than 100°C. La Chaldette spring, reaching 35°C at the surface, might seem of limited interest compared with the 82°C at Chaudes-Aigues. Although it does not reach 190°C at depth, its chemical composition indicates a deep reservoir at 110°C (Chapter 4, Penhoët et al., 2025b). Even more unexpectedly, the springs to the east of the Margeride Granite (Mazel, Fontaine Basse, Ranc) at 10°C are thought to come from a deep circulation reaching 100°C. Similarly, the Magnac and Montchanson springs, which come from the same reservoir as the Chaudes-Aigues waters, although cold at the surface, are closer in terms of chemical composition to the deep reservoir than their neighbours. They are much less diluted and more mineralised. All these discoveries were only made thanks to the presence of the 32 thermal springs of Chaudes-Aigues and to a “'random”' sampling, without which these systems would have remained hidden. Another example in the Massif Central is represented by the spring swarm of Saint Nectaire composed of more than a dozen springs whose temperatures do not exceed 40°C (Pauwels et al., 1997). Previous studies have shown that these waters come from a deep reservoir at a temperature between 160 and 200°C (Pauwels et al., 1997; Chaguéron et al., 2003). In addition, the town counts around thirty other springs, most of which are mineralised but cold. Other examples can be found throughout the Massif Central,

including Royat, Joze, Le Bard and Chaudefour springs, which do not exceed 35°C but are associated with a deep reservoir close to 200°C (Fouillac, 1983).

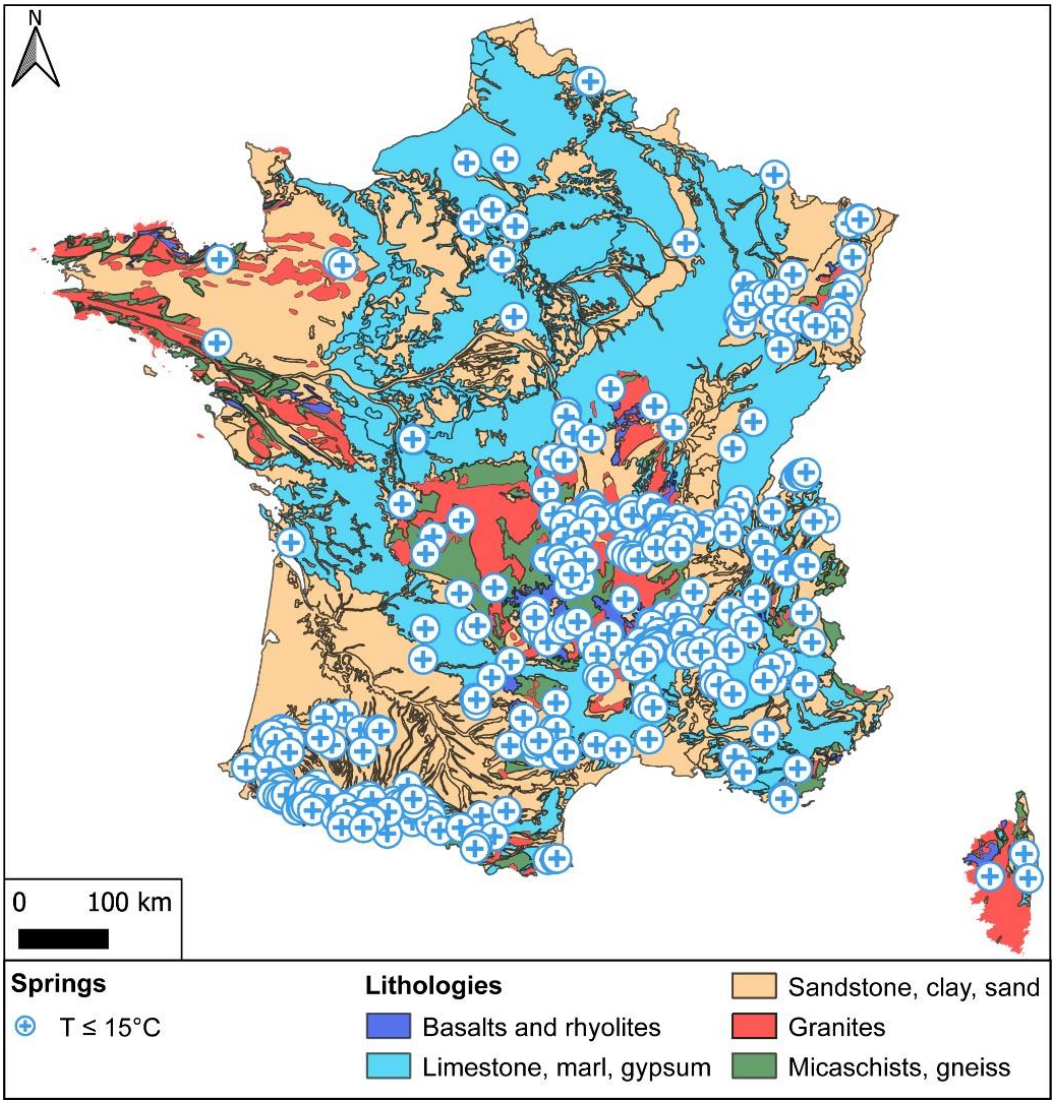

Figure VII.5: Cold springs locations in France (T ≤ 15°C), some are located close to thermal springs (T > 15°C) and could be the start of a new exploration.

VII.5 Hydrothermal systems vulnerability to climate change

I.5.17 An underground resource threatened by the surface

Climate change is profoundly disrupting the natural water cycle, affecting the availability and distribution of water resources both locally and globally (Rosenberg et al., 1999; Jaunat et al., 2016; Riedel et Weber, 2020; Atawneh et al., 2021). Rising temperatures at the surface means possibly more intense evaporation, possibly reducing vegetation and therefore water infiltration into the soil. In addition, a soil devoid of vegetation is more conducive to run-off. At the same

time, rainfall is becoming more irregular, with an increase in extreme events, alternating between prolonged drought and violent rain. As the infiltration capacity of the soil is limited and above all slow, infiltration and groundwater recharge are limited.

These changes directly affect the recharge of surface aquifers, which is essential for the renewal of underground resources, particularly hydrothermal systems. By modifying the balance between infiltration, storage and run-off, climate change threatens the chemical composition of thermal waters. In the case of Chaudes-Aigues, the water is made of 60% surface water and 40% from a deep reservoir. If infiltration were to decrease, the coefficients would change, as would the composition of the water, which could then fall outside the standards imposed. The shorter the residence time of the system, the greater the impact, with springs located in sedimentary zones under the greatest threat. As mentioned above, these circulations are more superficial and faster, and therefore more exposed to surface changes.

I.5.18 Socio-economic issues of hydrothermal vulnerability

In France, but also elsewhere in the world, many towns depend on the spa industry. Their entire economic model is based on spa visitors, between tourism and spa income. Global warming is a direct threat to these communities. It can change both the flow rates and the chemical composition of the water, which could jeopardise the centres ability to use thermal water. At the same time, more than 45% of French spas have to heat water collected from the surface or at depth (Pfund, 2024). Rising energy costs are creating an additional constraint for these local authorities. This means that spa towns are being forced to “reinvent themselves in order to survive” (Pfund, 2024) by diversifying their activities: for instance, installing heat exchangers to heat public areas, as it is already the case in Chaudes-Aigues. The thermal baths at Luchon have replaced their gas-fired generator with a heat exchanger in order to reduce their operating costs. These local adaptations reflect a broader need for scientific and technical support to ensure the long-term sustainability of spa towns. In particular, projects linking these spa towns with research institutions are emerging, one example of such support is the ongoing ThermEcoWat project, supported by BRGM and CNRS.

VIII. Conclusions

The point of this thesis was to gain a better understanding of the mechanisms controlling hydrothermal circulation in amagmatic systems, in order to identify and explore new targets for high-temperature geothermal energy (T > 150°C). The Chaudes-Aigues hydrothermal system, counting one of the hottest thermal springs in Europe, is located in a granitic context marked by a structuring inherited from the Variscan orogen. This hydrothermal system was studied using a multidisciplinary approach combining field observations, structural geology, geophysics, water geochemistry and 3D numerical modelling.

The results demonstrate that hydrothermal circulation at Chaudes-Aigues is mainly controlled by a combination of factors. Firstly, by the brittle structure and its dynamics over geological time. The faults inherited from the late-variscan period and reactivated since nowadays determine the permeability of the system. The topography, although low in our case, influences spring locations without significantly affecting their temperatures. Finally, the presence of the regolith, as a weathering and permeable layer particularly developed above the thick fault zones, could modulate exchanges between surface water and deep circulations, constituting an additional control factor to be taken into account.

These results confirm that crustal fault zones, inherited from major tectonic phases, are prime targets for high-temperature geothermal exploration, particularly in the granitic contexts of the Massif Central. In addition, cold springs, which are often studied separately from a hydrogeological perspective, should be re-examined from a geothermal point of view in order to identify new potential targets. Geothermal exploration now requires interaction between hydrogeology, geochemistry, structural geology, geophysics and numerical modelling.

By shedding light on the unknown dynamics of deep fluid circulation in crystalline terrains, this study paves the way for a new geothermal exploration that embraces the complexity of geological heritage rather than avoiding it. A key strategy emerging from this work is to prioritize the study of hydrothermal systems already expressed at the surface through thermal springs. These offer valuable natural laboratories to understand the functioning of amagmatic

hydrothermal system. Starting from these, exploration can then be extended to areas with only cold springs hiding potentially active hot reservoirs. This two-step exploration approach starting from obvious indicators moving towards hidden ones, increases the number of potential geothermal targets and consequently the associated resources.

Résumé étendu

IX. Résumé étendu

Chapitre I : Contexte et objectifs de l'étude

La géothermie haute température (HT) s'est historiquement développée dans des contextes volcaniques ou zone d'extension crustale, où les gradients géothermiques élevés assurent un apport thermique suffisant pour la production d'électricité. Ces zones étant plus que restreintes, l'exploration géothermale HT doit identifier de nouvelles cibles. Si la recherche de ressources géothermiques s'appuyait principalement sur des critères thermiques, l'accent est désormais mis sur l'identification de zones à perméabilité anormalement élevée, drains naturels permettant la remontée de fluides chauds. Dans ce sens, depuis une dizaine d'années, les zones de failles crustales deviennent de nouvelles zones d'intérêt, bien que leur exploration reste encore limitée. Cette thèse s'inscrit dans cette dynamique en étudiant un système hydrothermal situé dans un massif granitique fracturé célèbre pour ses sources thermales dont l'origine reste encore partiellement expliquée.

Une source est considérée comme thermale si sa température dépasse la moyenne annuelle. En France, une source peut donc être qualifiée de thermale à partir de 15 °C. En s'appuyant sur cette définition, plus de 368 sources thermales ont été recensées en France (Banque du Sous-Sol, *Annales des Mines*, 1998).

Ces sources thermo-minérales se concentrent principalement dans les Pyrénées, le Massif Central et les Alpes. Quelques-unes sont aussi visibles dans l'Est de la France, en Corse, et une seule en Bretagne (Figure IX.1). L'objectif est ici de déterminer si cette répartition est purement aléatoire ou guidée par des facteurs spécifiques. Les relations entre sources chaudes, flux de chaleur, lithologies, topographie et densité de failles sont en effet complexes. Aucun de ces paramètres ne suffit, à lui seul, à expliquer la présence ou la température d'une source. Un système hydrothermal semble être le résultat d'une combinaison complexes de plusieurs critères. Ainsi, les régions montagneuses constituées de roches de socle, avec un gradient thermique élevé et une forte fracturation, présentent un grand nombre de sources thermales. À l'inverse, les bassins sédimentaires peu fracturés et à faible relief (Aquitaine, Bassin Parisien) en comptent très peu, quel que soit le flux de chaleur mesuré. Des exceptions existent toutefois, comme les Alpes ou la Corse, où malgré des conditions a priori favorables (altitude, socle, fractures), les sources chaudes sont peu nombreuses.

Cette étude préliminaire souligne donc que l'apparition de sources thermales résulte d'interactions multiples. Par la suite, notre travail se concentrera sur le système hydrothermal de Chaudes-Aigues, comptant l'une des sources les plus chaudes d'Europe, afin de mieux comprendre les liens et interactions entre sources thermales, topographie, flux de chaleur et fracturation.

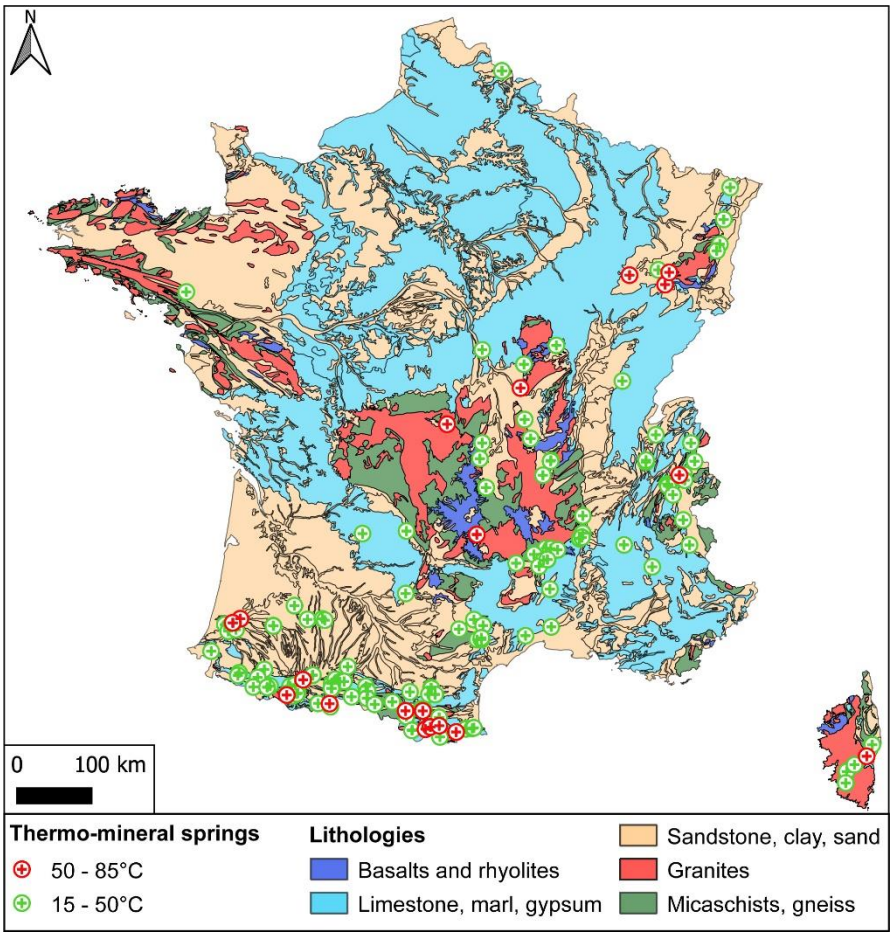

Figure IX.1: Distribution of thermo-mineral springs (according to the Banque du Sous-Sol, BSSEAU, BRGM) in France. The background map corresponds to the 2M geological map (BRGM).

Située dans le Massif Central, dans le département du Cantal (15), Chaudes-Aigues se distingue grâce à une singularité : ses 32 sources thermales dont les températures s'échelonnent entre 50 et 82 °C. La source du Par, indiquée comme la plus chaude d'Europe, présente, en plus de sa température élevée, un débit constant au cours de l'année de 250 $L.min^{-1}$ (Vasseur et al., 1997). L'ensemble des sources représentant un débit total d'environ 500 $L.min^{-1}$ (Vasseur et al., 1997) voire plus selon les estimations. La zone d'émergence de Chaudes-Aigues est située dans l'unité inférieure des gneiss à la terminaison d'un épais faisceau de failles N150E. L'environnement immédiat des sources est marqué par l'intersection de trois faisceaux de failles varisques (N0E, N030-050E, N120-150E), qui focalise de nombreuses minéralisations et filons de microgranite (Gibert et al., 1975 ; De Goer de Herve et al., 1990). A 10 km plus au Sud, la source thermale de la Chaldette (Figure IX.2a) était anciennement captée au niveau du lavoir du village. De nos jours, l'établissement thermal capte l'eau chaude (35°C) directement en profondeur via un forage incliné à 65 m de profondeur.

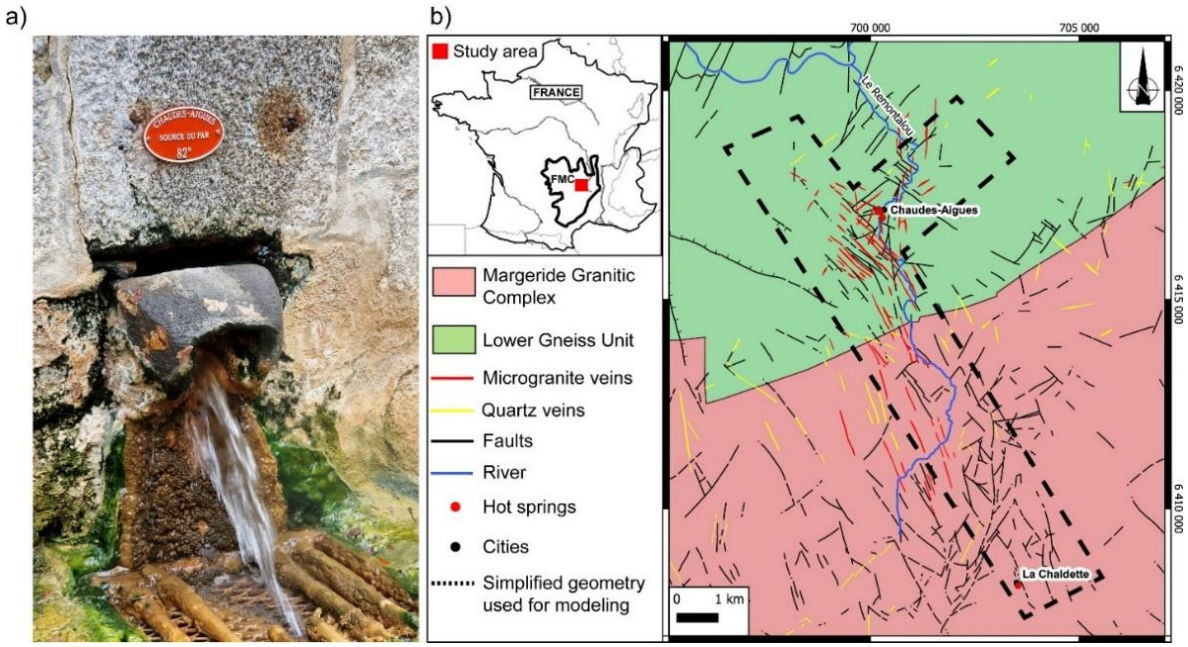

Figure IX.2: (a) La source du Par (82°C), l'une des plus chaudes d'Europe. (b) Localisation de la zone d'étude (Penhoët et al., 2025a).

L'étude de ce système hydrothermal tend à identifier de nouvelles cibles pour l'exploration géothermal haute température. Il s'agit ici de déterminer les facteurs de contrôle déterminant le fonctionnement des systèmes hydrothermaux en domaine de socle fracturé. Afin de caractériser ce système complexe, nous nous appuyons sur différentes approches complémentaires. La géologie structurale permet notamment d'identifier, comprendre la structuration fragile du système et d'évaluer qualitativement la perméabilité. La géochimie des eaux caractérise le fonctionnement du système hydrothermal en apportant des informations sur l'origine des eaux, la température, nature du réservoir et le temps de résidence des fluides. Les méthodes géophysiques (gravimétrie) permettent d'imager les structures en profondeur. Ces données issues du terrain permettront d'alimenter des modèles numériques thermo-hydrauliques en contraignant les paramètres clés du réservoir (perméabilité, structures importantes), afin de proposer un modèle conceptuel robuste du fonctionnement du système hydrothermal de Chaudes-Aigues.

Chapitre II : Influence de la géométrie des zones de failles sur la circulation des fluides, études des zones de failles du Granite de la Margeride

Ce chapitre explore l'influence de la géométrie des zones de failles sur la circulation des fluides et les anomalies thermiques dans le Massif Granitique de la Margeride (MGC), en s'appuyant sur deux zones d'étude : les sources thermales de Chaudes-Aigues et la zone de failles de la Margeride (MFZ).

La zone d'émergence de Chaudes-Aigues, à l'échelle régionale, est caractérisée par une très forte densité de fracturation (Penhoët et al., 2025a). Les sources sont situées à l'intersection

de trois zones de failles, dont deux principales formant une structure complexe en forme de Y. La première orientation, N150E, est caractérisée par la présence d'une autre source thermale (La Chaldette, 35°C). Elle présente une épaisseur de plus de 2,5 km sur une longueur de 10 km. La seconde, orientée N50, est relativement moins épaisse (1,5 km) mais est très marquée dans la topographie, comme en témoigne l'orientation de la vallée. La rivière, le Remontalou, est déviée de son orientation initiale (N150E). Ces directions varisques ont été réactivées à de nombreuses reprises depuis le Paléozoïque jusqu'à nos jours (Penhoët et al., 2025a). La troisième tendance, moins importante que les précédentes, correspond à plusieurs failles et fractures orientées N0E. La seconde zone, la MFZ, se distingue par une forte variation de son épaisseur, passant de 50 m au Sud à plus de 2,5 km au Nord, près de Saint-Flour. Dans sa portion Nord, la source minérale de Coren-Les-Eaux atteindrait 220°C en profondeur, suggérant une potentielle anomalie thermique cachée. Ces deux contextes permettent d'analyser deux paramètres géométriques majeurs : l'intersection de deux zones de failles (Chaudes-Aigues) et l'épaisseur d'une zone de faille (MFZ).

L'étude paramétrique sur la zone d'intersection montrent que les failles simples produisent des sources avec des températures plus élevées mais avec des débits faibles, tandis que les intersections (notamment avec de petits angles) permettent des débits plus élevés (jusqu'à 40 l/s) mais à des températures moindres. Le régime convectif démarre pour des perméabilités plus faibles, donc plus facilement, dans les configurations avec intersections. Appliqué à Chaudes-Aigues, le modèle simplifié en forme de Y reproduit la localisation de la source mais sous-estime à la fois la température et le débit (Figure IX.3).

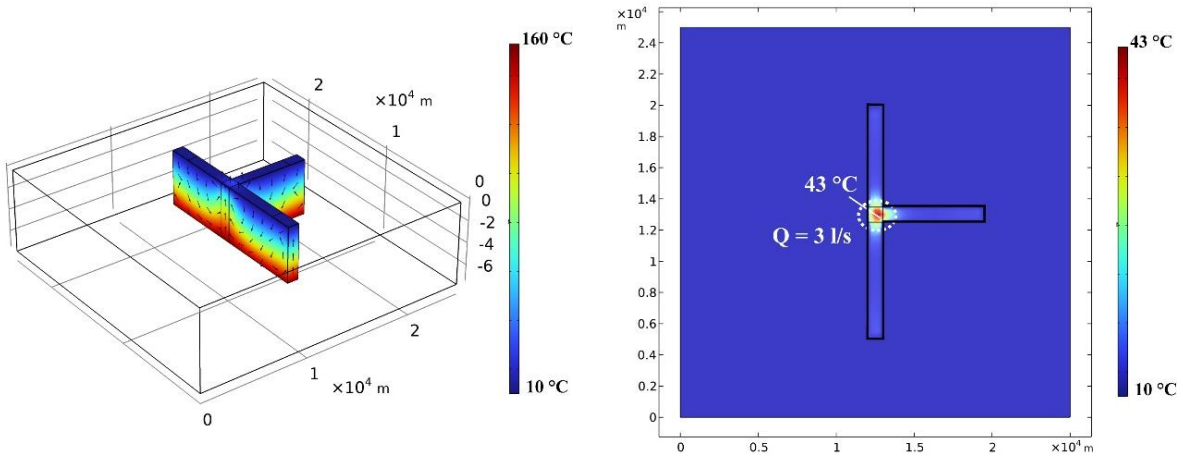

Figure IX.3: Configuration reproduisant la localisation de Chaudes-Aigues. Coupe à la surface du modèle.

Concernant la MFZ, l'étude démontre que l'épaisseur de la faille influence fortement le régime thermique : des failles fines produisent plusieurs anomalies peu profondes, de faible intensité, tandis que des failles épaisses génèrent une seule anomalie importante à plus grande profondeur. Une zone de faille épaisse offre un régime convectif plus stable et des anomalies

de température plus élevées. Ainsi, l'épaisseur devient, en plus de la perméabilité, un paramètre clé pour l'évaluation du potentiel géothermique.

En conclusion, la géométrie des zones de failles, tant leur épaisseur que leurs interactions, influence fortement la circulation des fluides et les anomalies thermiques associées. Les résultats obtenus permettent d'identifier deux zones à fort potentiel géothermique : Chaudes-Aigues, déjà connue pour ses sources chaudes en surface, et l'extrémité nord de la MFZ, où une anomalie thermique profonde pourrait être présente. Toutefois, des modèles numériques plus complets, intégrant la topographie et les contraintes tectoniques actuelles seront nécessaires pour affiner ces hypothèses.

Chapitre III : Structures héritées et drains de remontée : typologie des failles varisques réactivées.

La zone d'émergence de Chaudes-Aigues se caractérise par une forte densité de failles. Les sources thermales sont situées à l'intersection de trois zones de failles : N150E, N050E (principales) et N0E. Ces directions sont marquées par la présence de filons de microgranite, interprétés historiquement comme les principaux drains permettant l'ascension rapide des eaux chaudes profondes vers la surface (Vasseur et al., 1997). Toutefois, malgré certaines hypothèses anciennes, peu d'études ont précisément documenté l'architecture fragile de cette zone. Seule celle de Gibert et al. (1975) identifie clairement des zones de forte fracturation, attribuées à l'intersection des failles N050E et N150E, comme source de la perméabilité élevée responsable des nombreuses sources chaudes.

Une analyse structurale détaillée de la zone d'émergence des sources a été réalisée. Le but était d'identifier les principales familles de structures et leur dynamique de réactivation. Une campagne de mesures gravimétriques a également permis de connaître la géométrie en profondeur, notamment la position des granites de la Margeride et du Couffour, ainsi que les unités gneissiques sous-jacentes, afin de déterminer les formations susceptibles d'héberger un réservoir hydrothermal.

L'analyse des linéaments révèle une segmentation structurale nette entre les unités métamorphiques au nord et le granite de la Margeride au sud, où les failles sont plus longues et alignées principalement selon N150E. L'analyse microstructurale identifie des fractures majoritairement verticales, avec deux orientations dominantes (N020E et N140E), tandis que dans le granite, une fracture principale N170E est observée.

Trois groupes de failles ont été identifiés à proximité des sources, en particulier les failles N030E-N050E, caractérisées par des zones d'endommagement épaisses (Figure IX.4b), ces failles initialement ductiles ont été réactivées à plusieurs reprises en contexte fragile. Ces structures présentent des indices clairs de circulation fluides et en grande quantité. La

gravimétrie révèle une géométrie complexe du MGC, notamment la terminaison nord du granite à faible profondeur sous Chaudes-Aigues, et pour la première fois, l'image de la structure du granite de Couffour.

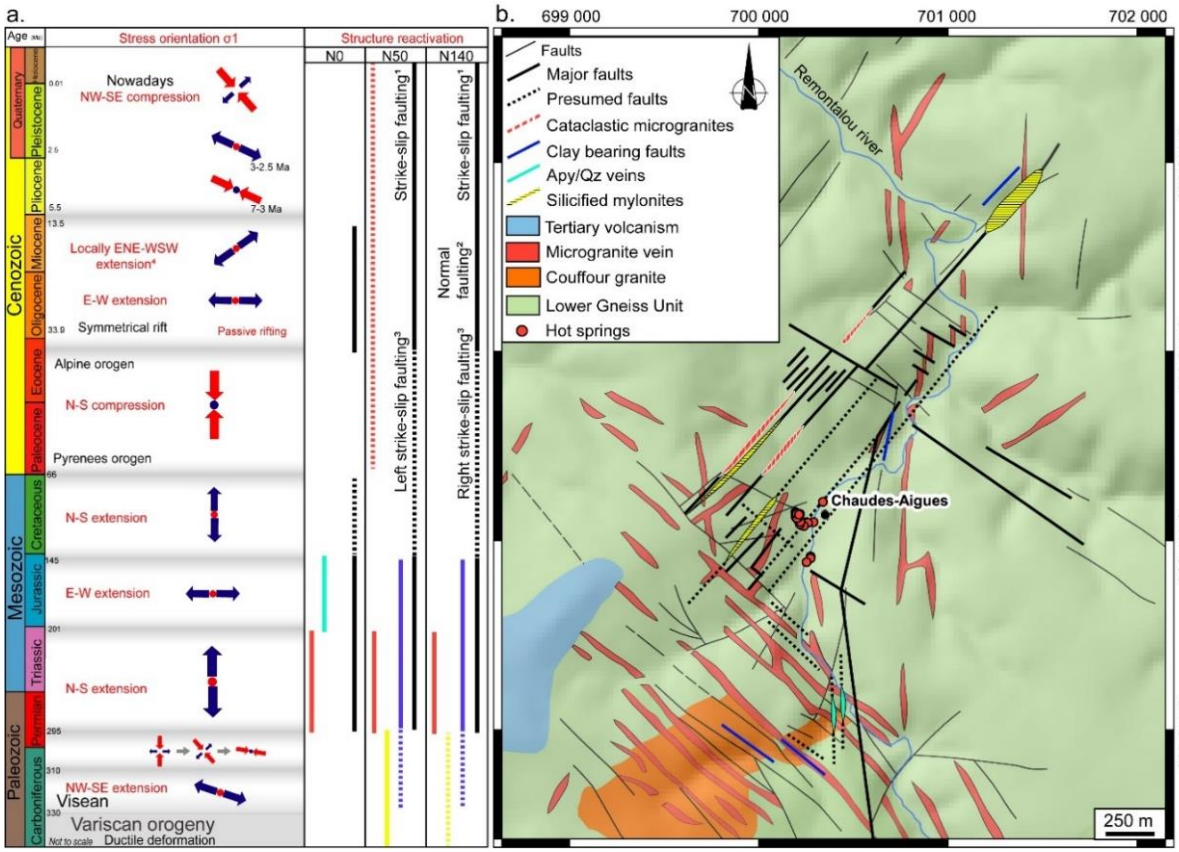

Figure IX.4: (a) Calendrier tectonique résumant les différents évènements (Daffos et al., 2024) et les jeux de failles associés, (b) Carte géologique simplifiées représentant les principales failles proches de la zone d'émergence.

Les données obtenues suggèrent que le système hydrothermal de Chaudes-Aigues est principalement contrôlé par l'héritage des failles varisques, en particulier les failles N050E, réactivées de nombreuses fois (Figure IX.4a). Ces failles profondes, épaisses et bréchifiées, traverseraient le toit du granite, qui agirait alors comme réservoir hydrothermal. La présence d'une faille mylonitisée sous la source du Ban, mentionnée dans un forage thermal, renforce cette hypothèse. L'orientation de la vallée du Remontalou, déviée de son tracé N150E, appuie également l'existence d'une grande faille N050E sous la ville. L'intersection avec les failles N150E renforcerait localement la perméabilité du système.

Bien que les filons de microgranite aient longtemps été considérés comme les principaux drains, peu de traces d'activité hydrothermale passée y ont été identifiées. Quelques figures de dissolution ont cependant pu être observées sur les plans de fractures N030E.

Chapitre IV : Un système hydrothermal peut en cacher un autre : étude géochimique des sources thermales de Chaudes-Aigues et celles environnantes

Les sources de Chaudes-Aigues ont fait l'objet de plusieurs études géochimiques. Celle-ci ont permis de mettre notamment en avant que les eaux des émergences seraient issues d'un mélange entre des eaux de surface et un réservoir profond dont la température a été estimée entre 175 et 200°C (Cailleaux et al., 1976 ; Michard et al., 1981, Vasseur et al., 1997). Le modèle de Vasseur et al. (1997) précise les proportions du mélange en indiquant une dilution de 62%. Les analyses isotopiques réalisées sur les eaux ne permettent pas de déterminer avec précision la zone d'impluvium des sources, l'altimétrie du Cantal, de l'Aubrac et du Granite de la Margeride étant relativement proches (Vasseur et al., 1997). Très peu de données sont disponibles sur la source de La Chaldette, sa relation avec les sources de Chaudes-Aigues reste donc indéterminée. Afin de lever ces incertitudes, plusieurs sources situées autour de la zone d'émergence de Chaudes-Aigues ont été échantillonnées.

Cet échantillonnage « à grande échelle » a mis en évidence que différents systèmes hydrothermaux existaient au sein du Granite de la Margeride. Un premier alimentant les sources du Sud de la Margeride (sources de Mazel, Fontaine Basse, Ranc) un second correspondant à la source de la Chaldette et le dernier relatif aux sources de Chaudes-Aigues (sources de la ville, Montchanson, Loubaresse, Magnac). Les sources de la Margeride, infiltrées dans les abords immédiats, proviennent d'un mélange entre des eaux de surface (45%) et un premier réservoir profond (55%), dont la température est estimée à environ 120°C. Le manque de failles pourrait expliquer leur température faible en surface. Ensuite, l'eau de la Chaldette, principalement météorique elle aussi, atteindrait 110°C en profondeur. La convergence des géothermomètres indique que les eaux infiltrées au niveau de la bordure Sud du granite sont en équilibre avec leur encaissant.

En ce qui concerne les sources de Chaudes-Aigues, comme évoqué par les études précédemment réalisées, les eaux sont issues d'un mélange entre une composante de surface et un réservoir chaud profond (Figure IX.5). Les différents résultats indiquent que les eaux météoriques s'infiltreraient principalement dans la bordure Sud de la Margeride et seraient drainées vers la ville à la faveur d'un gradient topographique favorable et d'un grand faisceau de failles N150E comme en témoigne la source de la Chaldette. En complément, une partie des eaux de Chaudes-Aigues provient d'un réservoir profond, situé en partie sous la ville, qui s'étendrait plus au Nord-Est sur une dizaine de kilomètres. Les différentes méthodes ont permis d'estimer sa température à 190°C.

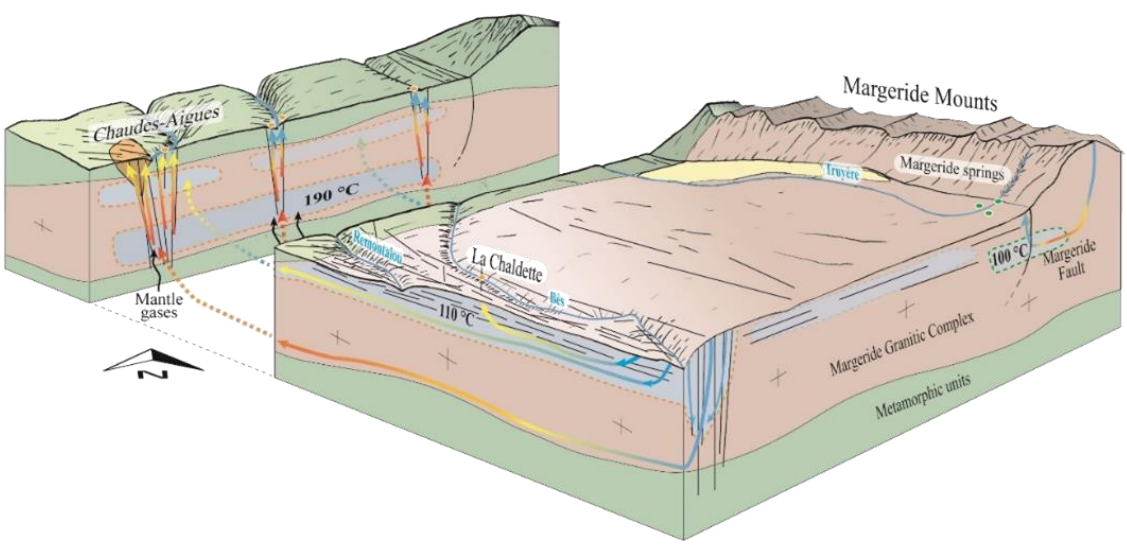

Figure IX.5: Schéma global de fonctionnement du système hydrothermal de Chaudes-Aigues.

Ces premiers résultats ont permis de mettre en évidence plusieurs réservoirs géothermaux supposés au sein du Granite de la Margeride (Figure IX.5). Cependant notre étude étant principalement ciblée sur Chaudes-Aigues, d'autres analyses et études de terrain seraient nécessaires pour caractériser d'avantage le potentiel géothermique du granite dans sa globalité. En ce qui concerne le système hydrothermal de Chaudes-Aigues, ce travail a permis de valider les travaux précédemment réalisés mais aussi de lever certaines incertitudes (zone d'infiltration, température et nature du réservoir) grâce à de nouveaux résultats (analyses isotopiques, modélisation numérique).

Chapitre V : Infiltration dans un granite altéré : l'impact thermique du régolithe sur les systèmes hydrothermaux.

Un bilan hydrique a été réalisé dans la zone incluant Chaudes-Aigues, La Chaldette jusqu'à la bordure sud du granite de la Margeride. Les entrées (précipitations de 900 à 1400 mm/an et débit amont du Bès de 2,3 m³/s) et les sorties (évapotranspiration de 300 mm/an, débit aval du Bès de 7,5 m³/s et infiltration) ont permis de calculer l'infiltration. Les résultats montrent qu'environ 30 % des précipitations s'infiltrent, pouvant atteindre jusqu'à 42 %. Ce taux élevé est lié à la fracturation intense de la région et possiblement à la présence d'un aquifère superficiel. Ainsi, la compréhension du régolithe (épaisseur, géométrie, propriétés hydrauliques) devient essentielle pour comprendre les interactions entre la surface et les écoulements profonds. Dans ce contexte, ce présente le Granite de la Margeride et son état d'altération afin de mieux comprendre l'impact du régolithe sur les circulations hydrothermales. À travers une étude de terrain, il a été possible de mettre en évidence que le profil d'altération n'a pas été préservé de manière homogène à la surface du pluton. Ces différentes configurations ont servi d'exemple de géométries directement utilisées dans des modèles

thermo-hydrauliques 3D visant à quantifier l'impact hydraulique du régolithe sur le fonctionnement du système hydrothermal.

Une mission de terrain a permis de caractériser l'altération du granite de la Margeride, révélant une grande variabilité spatiale du régolithe en lien avec l'histoire géologique, climatique et tectonique de la région (Figure IX.6). Ce profil d'altération, en grande partie antérieur au Lias, a été localement préservé entre le Crétacé et le Miocène, puis partiellement érodé durant la glaciation du Würm. À l'ouest, sous le plateau de l'Aubrac, les coulées basaltiques ont protégé le régolithe, permettant la conservation d'un profil épais favorable au stockage d'eau. Au centre, autour de La Chaldette, l'altération est encore présente mais plus mince, avec une érosion partielle. À l'Est, vers Malzieu, seul subsiste l'horizon fissuré, l'érosion ayant complètement décapé la couverture meuble. Cette répartition inégale de l'altération induit des comportements hydrauliques différents. Ces géométries constituent une base pour la modélisation thermo-hydraulique 3D des échanges entre eaux de surface et circulations profondes.

L'effet des profils d'altération dans les domaines granitiques a été largement étudié d'un point de vue hydrogéologique, mais rarement en ce qui concerne leur impact thermique sur la circulation des fluides. Nos résultats montrent pourtant que le régolithe influence à la fois les écoulements d'eau superficiels et profonds. Cette couche altérée, particulièrement perméable, permettrait à une zone de faille d'atteindre un régime convectif pour des perméabilités plus faibles que dans un contexte non altéré. Couplée à une perméabilité intrinsèque plus élevée dans la faille, cette configuration favorise la descente d'eaux froides denses, limitant ainsi les anomalies thermiques positives liées aux remontées d'eaux chaudes. Le système qui en résulte donne lieu à des sources thermales mais à température modérée.

Dans le cas du système hydrothermal de Chaudes-Aigues, le régolithe semble jouer un rôle essentiel. La géochimie des eaux indique deux circuits semblent coexister au sein du granite : un profond, responsable de la signature chimique des sources de Chaudes-Aigues, et un plus superficiel, associé à la source de La Chaldette, entièrement d'origine météorique, à l'équilibre avec le granite et atteignant 110 °C en profondeur. Ces deux circuits partagent un même impluvium. Sans régolithe, la capacité de stockage du granite serait faible, entraînant des débits réduits. À l'inverse, la présence de régolithe, bien connu pour ses propriétés aquifères, combinée à la faille N150E, permet l'accumulation en surface, la circulation et l'infiltration vers la profondeur.

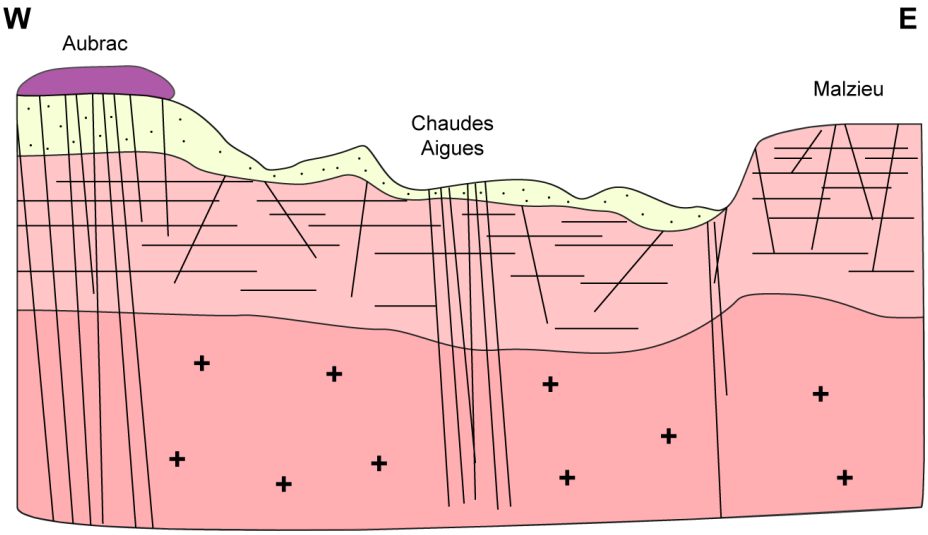

Figure IX.6: Coupe schématique (non à l'échelle) du Granite de la Margeride, l'approfondissement du profil dans les zones de failles n'a pas été représenté ici.

Chapitre VI : Modélisation numérique du système hydrothermal de Chaudes-Aigues : analyse des facteurs de contrôle grâce aux sources thermales.

Cette dernière étape correspond à la modélisation numérique thermo-hydraulique 3D du système hydrothermal de Chaudes-Aigues, dans le but de reproduire et de mieux comprendre son fonctionnement. En intégrant des données géologiques, géophysiques et géochimiques, le modèle permet de simuler le comportement des sources thermales, notamment celles du Par à Chaudes-Aigues et de La Chaldette, intégrée ici pour la première fois dans le système. Quatre configurations de modèles ont été testées, combinant ou non la topographie et la présence d'un réservoir profond à 190 °C. Ces modèles visent à reproduire sept critères clés : les localisations et les températures des sources du Par et La Chaldette, le débit total à Chaudes-Aigues, les proportions de mélange des eaux, et la zone d'infiltration.

Les résultats montrent que les modèles les plus simples (sans topographie ni réservoir) ne parviennent pas à reproduire correctement les caractéristiques des sources thermales. L'ajout du réservoir améliore certains aspects, comme la température de la source du Par, mais ne permet plus de représenter la source de La Chaldette. À l'inverse, l'intégration de la topographie permet de mieux simuler les débits et les localisations des sources, mais reste insuffisante pour reproduire les températures et proportions des mélanges d'eau.

C'est seulement en combinant la topographie et le réservoir profond que l'ensemble des observations est fidèlement reproduit : températures et débits des sources, coefficients de mélange cohérents avec les données géochimiques, et circulation profonde atteignant 200 °C (Figure 7a), en accord avec les estimations des géothermomètres. De plus, la modélisation permet de préciser la localisation de la zone d'infiltration. L'Aubrac, évoqué comme potentielle zone d'infiltration dans de précédents modèles (Vasseur et al., 1997), ne présente aucune

connexion avec le système de Chaudes-Aigues (Figure IX.7b). La zone d'infiltration se situe dans la zone de faille N150E, mais au lieu de la bordure sud du granite, elle serait à proximité de La Chaldette.

Cette étude met en évidence le rôle central de la zone failles orientée N150E, qui regroupe l'ensemble des fonctions du système : infiltration, circulation profonde et émergence (Figure 6). Cette approche confirme aussi la robustesse du modèle, capable d'intégrer de manière cohérente toutes les contraintes géologiques, hydrodynamiques et géochimiques du système hydrothermal de Chaudes-Aigues.

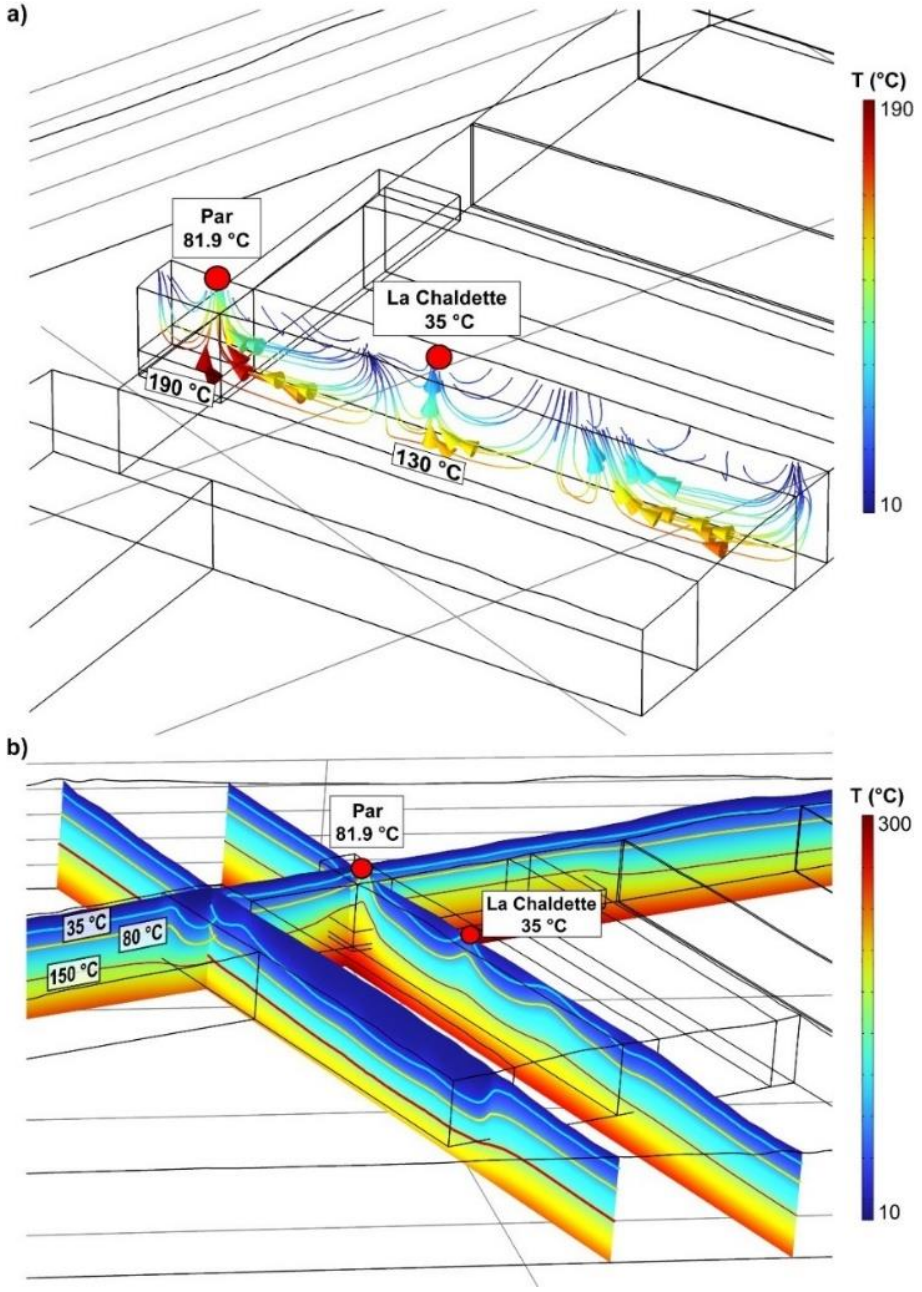

Figure IX.7: (a) Circulations de fluide au sein de la zone de failles de Chaudes-Aigues, les flèches représentent les vitesses de Darcy et leur code couleur correspond aux températures atteintes. (b) Interactions entre les différents faisceaux de failles et le réservoir.

Discussion et conclusion

Cette étude a permis une d'obtenir un schéma de fonctionnement global du système hydrothermal de Chaudes-Aigues, validant et complétant le modèle initial de Vasseur et al. (1997). Grâce à une approche multidisciplinaire combinant géologie structurale, géochimie, géophysique gravimétrique et modélisation thermique-hydraulique 3D, plusieurs incertitudes majeures ont été levées, notamment sur la localisation précise de l'impluvium, la localisation et température du réservoir profond et les différents circuits.

Les résultats confirment que les sources thermales de Chaudes-Aigues résultent du mélange d'eaux météoriques infiltrées dans la zone de failles située au sud de la ville. Les principaux drains de remontée ont été identifiés, notamment les failles N050E, tandis que les microgranites jouent un rôle limité dans la circulation des fluides. Le temps de résidence des eaux est estimé entre 50 000 et 200 000 ans.

Cette étude montre que le système de Chaudes - Aigues est principalement contrôlé par la structure fragile héritée du Varisque, réactivée jusqu'à nos jours, qui gouverne la perméabilité. La topographie quant à elle contrôle la localisation des sources thermales. La présence d'un régolithe épais, augmenté par la présence des failles, modulerait également les échanges entre eaux superficielles et profondes. Ces résultats confirment que les zones de failles crustales héritées des grandes phases tectoniques sont des cibles privilégiées pour l'exploration géothermique haute température, notamment dans les contextes granitiques comme le Massif Central.

Enfin, cette thèse préconise une stratégie d'exploration en deux temps, partant des systèmes hydrothermaux manifestés par des sources chaudes visibles à la surface, pour ensuite étendre l'exploration aux sources froides, potentiellement révélatrices de réservoirs profonds actifs. Cette approche, intégrant pleinement la complexité géologique, ouvre la voie à une exploration géothermique plus efficace et à l'identification de nouvelles ressources potentielles.

References

References

Achtziger-Zupančič, P., Loew, S., Hiller, A., Mariethoz, G., 2016. 3D fluid flow in fault zones of crystalline basement rocks (Poehla-Tellerhaeuser Ore Field, Ore Mountains, Germany). Geofluids 16, 688–710. https://doi.org/10.1111/gfl.12192

Achtziger-Zupančič, P., Loew, S., Mariéthoz, G., 2017. A new global database to improve predictions of permeability distribution in crystalline rocks at site scale. Journal of Geophysical Research: Solid Earth 122, 3513–3539. https://doi.org/10.1002/2017JB014106

Acworth, R.I., 1987. The development of crystalline basement aquifers in a tropical environment. Quarterly Journal of Engineering Geology 20, 265–272. https://doi.org/10.1144/GSL.QJEG.1987.020.04.02

Aghshahi, E., 1979. Etude gravimétrique du diapir de Qum (Iran) et du massif granitique de la Margeride (France). Université de Montpellier 2.

Albert-Llorca, M., 2005. Eaux thermales et eaux miraculeuses. La Ricerca Folklorica 65. https://doi.org/10.2307/30033274

Alt-Epping, P., Diamond, L., Wanner, C., Hammond, G., 2021. Effect of Glacial/Interglacial Recharge Conditions on Flow of Meteoric Water Through Deep Orogenic Faults: Insights Into the Geothermal System at Grimsel Pass, Switzerland. Journal of Geophysical Research: Solid Earth 126, e2020JB021271. https://doi.org/10.1029/2020JB021271

Appold, M.S., Garven, G., Boles, J.R., Eichhubl, P., 2007. Numerical modeling of the origin of calcite mineralization in the Refugio-Carneros fault, Santa Barbara Basin, California. Geofluids 7, 79–95. https://doi.org/10.1111/j.1468-8123.2006.00165.x

Arlhac, P., Becq-Giraudon, J.F., 1989. Carte géologique de la France à 1/50 000, feuille 860 Espalion.

Arnórsson, S., 1983. Chemical equilibria in icelandic geothermal systems—Implications for chemical geothermometry investigations. Geothermics 12, 119–128. https://doi.org/10.1016/0375-6505(83)90022-6

Atawneh, D., Cartwright, N., Bertone, E., 2021. Climate change and its impact on the projected values of groundwater recharge: A review. Journal of Hydrology 601, 126602. https://doi.org/10.1016/j.jhydrol.2021.126602

Aubignat, A., 1949. Hydrologie de Chaudes-Aigues, Note technique du 29 janvier 1949 et PV de visite du 4 février 1949.

Aubignat, A., Blanquet, L., Tronche, 1949. Le bassin hydrothermal de Chaudes-Aigues (Cantal). Ann. Inst. Hydro 2ème fasc., 119 à 136.

Bächler, D., Kohl, T., Rybach, L., 2003. Impact of graben-parallel faults on hydrothermal convection—Rhine Graben case study. Physics and Chemistry of the Earth, Parts A/B/C, Heat Flow and the Structure of the Lithosphere 28, 431–441. https://doi.org/10.1016/S1474-7065(03)00063-9

Baietto, A., Cadoppi, P., Martinotti, G., Perello, P., Perrochet, P., Vuataz, F.-D., 2008. Assessment of thermal circulations in strike-slip fault systems: the Terme di Valdieri case (Italian western Alps). SP 299, 317–339. https://doi.org/10.1144/SP299.19

Barth, S., 1993. Boron isotope variations in nature: a synthesis. Geol Rundsch 82, 640–651. https://doi.org/10.1007/BF00191491

Bayer, R., 1982. Résultats géophysiques récents sur le Granite de la Margeride.

Bayer, R., Couturie, J.P., Vasseur, G., 1982. Résultats géophysiques récents sur le granite de la Margeride. Annales de géophysique 38, 431–447.

BCSF-Rénass, 2022. Instrumental seismicity in mainland France (1962-2021). https://www.doi.org/10.25577/fv3f-sq09

Bellon, H., Gibert, J.P., 1975. Absolute dating of the geological components of the exit area of the Chaudes-Aigues hyperthermal waters, Massif Central, France. C. R. Hebd. Seances Acad. Sci., Ser. D; (France) 280:16.

Bense, V.F., Gleeson, T., Loveless, S.E., Bour, O., Scibek, J., 2013. Fault zone hydrogeology. Earth-Science Reviews 127, 171–192. https://doi.org/10.1016/j.earscirev.2013.09.008

Bense, V.F., Person, M.A., 2006. Faults as conduit-barrier systems to fluid flow in siliciclastic sedimentary aquifers. Water Resources Research 42, 2005WR004480. https://doi.org/10.1029/2005WR004480

Bense, V.F., Person, M.A., Chaudhary, K., You, Y., Cremer, N., Simon, S., 2008. Thermal anomalies indicate preferential flow along faults in unconsolidated sedimentary aquifers. Geophysical Research Letters 35. https://doi.org/10.1029/2008GL036017

Bérard, P., Loiseau, M., Vigouroux, P., 2002. Amélioration de la connaissance des ressources en eau souterraine des sites thermaux – Région Auvergne – Site de Chaudes-Aigues (15). (Rapport BRGM No. RP-51722-FR). BRGM.

Berkowitz, B., 2002. Characterizing flow and transport in fractured geological media: A review. Advances in Water Resources 25, 861–884. https://doi.org/10.1016/S0309-1708(02)00042-8

Bézèlgues-Courtade, S., Bes-De-Berc, S., 2007. Étude réalisée dans le cadre des projets de Service public du B R G M 2005 06EAUH07.

Bischoff, A., Heap, M.J., Mikkola, P., Kuva, J., Reuschlé, T., Jolis, E.M., Engström, J., Reijonen, H., Leskelä, T., 2024. Hydrothermally altered shear zones: A new reservoir play for the expansion of deep geothermal exploration in crystalline settings. Geothermics 118, 102895. https://doi.org/10.1016/j.geothermics.2023.102895

Blés, J.L., Bonijoly, D., Castaing, C., Gros, Y., 1989. Successive post-Variscan stress fields in the French Massif Central and its borders (Western European plate): comparison with geodynamic data. Tectonophysics 169, 79–111. https://doi.org/10.1016/0040-1951(89)90185-6

Blum, J., Erel, Y., Brown, K., 1993. 87Sr/86Sr ratios of sierra nevada stream waters: Implications for relative mineral weathering rates. Geochimica et Cosmochimica Acta 57, 5019–5025. https://doi.org/10.1016/S0016-7037(05)80014-6

Bock, K., Branquet, Y., Boulvais, P., Duretz, T., 2024. Surface-derived fluid percolation along detachment systems enhanced by syn-kinematic granites: uranium mineralization as an application. Bulletin de la Société Géologique de France 195, 13. https://doi.org/10.1051/bsgf/2024010

Boschetti, T., Cortecchi, G., Toscani, L., Iacumin, P., 2011a. Sulfur and oxygen isotope compositions of Upper Triassic sulfates from Northerm Apennines (Italy): palaeogeographic and hidrogeochemical implications. Geologica Acta 129–147.

Boschetti, T., Toscani, L., Shouakar-Stash, O., Iacumin, P., Venturelli, G., Mucchino, C., Frape, S., 2011b. Salt Waters of the Northern Apennine Foredeep Basin (Italy): Origin and Evolution. Aquat Geochem 17, 71–108. https://doi.org/10.1007/s10498-010-9107-y

Bouiller, R., Cornen, G., Burg, J.P., Lasnier, B., 1986. Carte géologique de la France à 1/50 000, feuille 790 Langeac.

Bouiller, R., Couturie, J.P., Kornprobst, J., 1978. Carte géologique de la France à 1/50 000, feuille 815 Cayres.

Bourlier, P.-Y., Lachassagne, P., Desprats, J.-F., Gille, E., 2005. Nouveaux éléments sur la structure et le fonctionnement hydrogéologique du plateau basaltique de l'Aubrac (Massif central, France). Première évaluation des potentialités en eau souterraine. Comptes Rendus Geoscience 337, 663–673. https://doi.org/10.1016/j.crte.2005.01.014

Bourrié, G., 1978. Acquisition de la composition chimique des eaux en climat tempéré. Application aux granites des Vosges et de la Margeride.

Brace, W.F., 1984. Permeability of crystalline rocks: New in situ measurements. J. Geophys. Res. 89, 4327–4330. https://doi.org/10.1029/JB089iB06p04327

Brantley, S.L., Chesley, J.T., Stillings, L.L., 1998. Isotopic ratios and release rates of strontium measured from weathering feldspars. Geochimica et Cosmochimica Acta 62, 1493–1500. https://doi.org/10.1016/S0016-7037(98)00082-9

Bräuer, K., Geissler, W.H., Kämpf, H., Niedermannn, S., Rman, N., 2016. Helium and carbon isotope signatures of gas exhalations in the westernmost part of the Pannonian Basin (SE Austria/NE Slovenia): Evidence for active lithospheric mantle degassing. Chemical Geology 422, 60–70. https://doi.org/10.1016/j.chemgeo.2015.12.016

Braun, J., Mercier, J., Guillocheau, F., Robin, C., 2016. A simple model for regolith formation by chemical weathering. Journal of Geophysical Research: Earth Surface 121, 2140–2171. https://doi.org/10.1002/2016JF003914

Briand, B., Legendre, C., Prax, J.Y., 2009. Carte géologique de la France à 1/50 000, feuille 861 St-Geniez-d'Olt.

Briand, B., Negron, J., Viard, M., Combémorel, R., Couturié, J.P., 1994. Carte géologique de la France à 1/50 000, feuille 863 Le Bleymard.

Briand, B., Peyretti, G., Couturié, J.P., 1979. Carte géologique de la France à 1/50 000, feuille 862 Mende.

Brousse, R., de Peyronnet, P., de Saint-Ours, P., 1977. Carte géologique de la France à 1/50 000, feuille 787 Pleaux.

Brousse, R., Gibert, J.P., Park, F., 1975. Carte géologique de la France à 1/50 000, feuille 812 Vic-sur-Cère.

Brousse, R., Larroque, P., Gibert, J.P., 1980. Carte géologique de la France à 1/50 000, feuille 811 Aurillac.

Brown, S., Coolbaugh, M., DeAngelo, J., Faulds, J., Fehler, M., Gu, C., Queen, J., Treitel, S., Smith, C., Mlawsky, E., 2020. Machine learning for natural resource assessment: An application to the blind geothermal systems of Nevada. Transactions - Geothermal Resources Council 44.

Bucher, K., Zhang, L., Stober, I., 2009. A hot spring in granite of the Western Tianshan, China. Applied Geochemistry 24, 402–410. https://doi.org/10.1016/j.apgeochem.2008.12.021

Burg, J.P., Matte, P., 1978. A Cross Section through the French Massif Central and the Scope of its Variscan Geodynamic Evolution. Z. Dtsch. Geol. Ges. 129, 429–460. https://doi.org/10.1127/zdgg/129/1978/429

Caballero, Y., Gironde, C., Ladouche, B., Le Goff, E., 2012. Ressources thermales de la station d'Amélie-les-Bains. (No. RP-60618-FR). BRGM.

Cailleaux, P., Fouillac, C., Michard, G., Ouzounian, G., 1976a. Etude géochimique des sources thermales de Chaudes-Aigues (Cantal). Conséquences géothermiques. C.R Acad. Sci. 282, 1237–1240.

Cailleaux, P., Fouillac, C., Michard, G., Ouzounian, G., 1976b. Etude géochimiques des sources thermales de Chaudes-Aigues (Cantal). Conséquences goéthermiques. C. R. Acad. Sci. 282, 1237–1240.

Caine, J.S., Evans, J.P., Forster, C.B., 1996. Fault zone architecture and permeability structure. Geol 24, 1025. https://doi.org/10.1130/0091-7613(1996)024<1025:FZAAPS>2.3.CO;2

Calcagno, P., Baujard, C., Guillou-Frottier, L., Dagallier, A., Genter, A., 2014. Estimation of the deep geothermal potential within the Tertiary Limagne basin (French Massif Central): An integrated 3D geological and thermal approach. Geothermics 51, 496–508. https://doi.org/10.1016/j.geothermics.2014.02.002

Calvet, A., Aunay, B., Ladouche, B., 2012. Ressource en eau thermale de la station de La Chaldette - Etat des lieux - Rapport Final (No. RP-61434-FR). BRGM.

Carbajal-Martínez, D., Wanner, C., Diamond, L.W., Peiffer, L., Fletcher, J., Inguaggiato, C., Contreras-López, M., 2024. Behavior of Amagmatic Orogenic Geothermal Systems: Insights From the Agua Blanca Fault, Baja California, Mexico. Geochemistry, Geophysics, Geosystems 25, e2023GC011145. https://doi.org/10.1029/2023GC011145

Caspari, E., Greenwood, A., Baron, L., Egli, D., Toschini, E., Hu, K., Holliger, K., 2020. Characteristics of a fracture network surrounding a hydrothermally altered shear zone from geophysical borehole logs. Solid Earth 11, 829–854. https://doi.org/10.5194/se-11-829-2020

Charguéron, C., Bertin, C., Rouzaire, D., Vigouroux, P., 2003. Amélioration de la conaissances des ressources en eau souterraine des sites thermaux en Auvergne. Site Saint-Nectaire (63) (No. RP-52469-FR). BRGM.

Chassang, P., 1982. Chaudes-Aigues : une description, une histoire.

Chaussidon, M., Albarède, F., 1992. Secular boron isotope variations in the continental crust: an ion microprobe study. Earth and Planetary Science Letters 108, 229–241. https://doi.org/10.1016/0012-821X(92)90025-Q

Chen, B., Huang, C., Zhao, H., 2020. Lithium and Nd isotopic constraints on the origin of Li-poor pegmatite with implications for Li mineralization. Chemical Geology 551, 119769. https://doi.org/10.1016/j.chemgeo.2020.119769

Choubert, B., Girod, M., 1974. Carte géologique de la France à 1/50 000, feuille 839 Langogne.

Cirodde, J.L., Feybesse, J.L., 1989. Carte géologique de la France à 1/50 000, feuille 835 Maurs.

Clemenceau, G., 1896. Note de voyage.

Cloetingh, S., van Wees, J.D., Ziegler, P.A., Lenkey, L., Beekman, F., Tesauro, M., Förster, A., Norden, B., Kaban, M., Hardebol, N., Bonté, D., Genter, A., Guillou-Frottier, L., Ter Voorde, M., Sokoutis, D., Willingshofer, E., Cornu, T., Worum, G., 2010. Lithosphere tectonics and thermo-mechanical properties: An integrated modelling approach for Enhanced Geothermal Systems exploration in Europe. Earth-Science Reviews 102, 159–206. https://doi.org/10.1016/j.earscirev.2010.05.003

Cloos, E., 1932. “Feather Joints” as Indicators of the Direction of Movements on Faults, Thrusts, Joints and Magmatic Contacts. Geology 18, 387–395. https://doi.org/10.1073/pnas.18.5.387

Couturié, J.-P., 1977. Le massif granitique de la Margeride (Massif Central Français). PhD Thesis, Université de Clermont II.

Couturié, J.P., 1974. Carte géologique de la France à 1/50 000, feuille 838 St-Chély-d’Apcher.

Couturié, J.P., 1972. Carte géologique détaillée de la France à 1/50 000, feuille 814 Saugues.

Couturié, J.P., Vachette Caen, M., Vialette, Y., 1979. Age Namurien d’un laccolite granitique différencié par gravité : Le granite de la Margeride (Massif Central Français). Acad. Sci. 289, 449–452.

Cox, S.E., 2003. Estimates of Residence Time and Related Variations in Quality of Ground Water Beneath Submarine Base Bangor and Vicinity, Kitsap County, Washington : U.S Geological Suvrey Watter-Resources investigations Report (No. 03–4058).

Craig, J., Absar, A., Bhat, G., Cadel, G., Hafiz, M., Hakhoo, N., Kashkari, R., Moore, J., Ricchiuto, T.E., Thurow, J., Thusu, B., 2013. Hot springs and the geothermal energy potential of Jammu & Kashmir State, N.W. Himalaya, India. Earth-Science Reviews 126, 156–177. https://doi.org/10.1016/j.earscirev.2013.05.004

Craig, J.W., Faulds, J.E., Hinz, N.H., Earney, T.E., Schermerhorn, W.D., Siler, D.L., Glen, J.M., Peacock, J., Coolbaugh, M.F., Deoreo, S.B., 2021. Discovery and analysis of a blind geothermal system in southeastern Gabbs Valley, western Nevada, USA. Geothermics 97, 102177. https://doi.org/10.1016/j.geothermics.2021.102177

Crosbie, R.S., Scanlon, B.R., Mpelasoka, F.S., Reedy, R.C., Gates, J.B., Zhang, L., 2013. Potential climate change effects on groundwater recharge in the High Plains Aquifer, USA. Water Resources Research 49, 3936–3951. https://doi.org/10.1002/wrcr.20292

Curewitz, D., Karson, J., 1997. Structural settings of hydrothermal outflow: Fracture permeability maintained by fault propagation and interaction. Journal of Volcanology and Geothermal Research 79, 149–168. https://doi.org/10.1016/S0377-0273(97)00027-9

Daffos, C., Arbaret, L., Bourdier, J.L., Gumiaux, C., 2024. Regional structural control on the Mont-Dore Plio-Quaternary volcanism (France). J. Volcanol. Geotherm. Res. 447, 108029. https://doi.org/10.1016/j.jvolgeores.2024.108029

D’Arcy, D., 1972. Etude hydrogéologique du périmètre thermal d’Evaux les Bains (No. 72 SGN 230 MCE). BRGM.

Darcy, H., 1856. Les fontaines publiques de la ville de Dijon : exposition et application des principes à suivre et des formules à employer dans les questions de distribution d’eau.

De Goer de Herve, A., 1991. Carte géologique de la France à 1/50 000, feuille 813 Chaudes-Aigues.

De Goer de Herve, A., Bogdanoff, S., Couturié, J.P., 2006. Carte géologique de la France à 1/50 000 ; feuille 836 Entraygues sur Truyère.

De Goer de Herve, A., Couturié, J.P., Galvier, J., 1994. Carte géologique de la France à 1/50 000, feuille 837 Nasbinals.

De Goer de Herve, A., Tempier, P., Boudon, G., 1990. Carte géologique de la France à 1/50 000, feuille 789 Saint-Flour.

De Launay, L., 1906. Observations géologiques sur quelques sources thermales : Chaudes-Aigues - Mont Dore. Ann. des Mines IX 10, 5.

Desprez, N., Durand, M., Jurain, G., Minoux, G., 1971. Carte géologique détaillée de la France à 1/50 000, feuille [375] Plombières-les-Bains. Plombières-les-Bains.

Deveaud, S., Millot, R., Villaros, A., 2015. The genesis of LCT-type granitic pegmatites, as illustrated by lithium isotopes in micas. Chemical Geology 411, 97–111. https://doi.org/10.1016/j.chemgeo.2015.06.029

Dewandel, B., Lachassagne, P., Wyns, R., Maréchal, J.C., Krishnamurthy, N.S., 2006. A generalized 3-D geological and hydrogeological conceptual model of granite aquifers controlled by single or multiphase weathering. Journal of Hydrology, Hydro-ecological functioning of the Pang and Lambourn catchments, UK 330, 260–284. https://doi.org/10.1016/j.jhydrol.2006.03.026

Dewandel, B., Lachassagne, P., Zaidi, F., Chandra, S., 2011. A conceptual hydrodynamic model of a geological discontinuity in hard rock aquifers: Example of a quartz reef in granitic terrain in South India. Journal of Hydrology 405, 474–487. https://doi.org/10.1016/j.jhydrol.2011.05.050

Dèzes, P., Schmid, S.M., Ziegler, P.A., 2005. Reply to comments by L. Michon and O. Merle on bEvolution of the European Cenozoic Rift System: interaction of the Alpine and Pyrenean orogens with their foreland lithosphere. Tectonophysics 257–262. https://doi.org/10.1016/j.tecto.2005.01.006.

Dèzes, P., Schmid, S.M., Ziegler, P.A., 2004. Evolution of the European Cenozoic Rift System: interaction of the Alpine and Pyrenean orogens with their foreland lithosphere. Tectonophysics 389, 1–33. https://doi.org/10.1016/j.tecto.2004.06.011

Dobson, P.F., 2016. A Review of Exploration Methods for Discovering Hidden Geothermal Systems.

Dupuy, A., 2001. Global modeling of the behavior of a complex geothermal system: example of Dax area, S-W of France - heuristic model. pp. 931–934.

Dupuy, M., 2021. Caractérisation hydrogéologique, hydrogéochimique et isotopique des eaux souterraines thermo-minérales de la Corse orientale. Université Pascal Paoli.

Duwiquet, H., Arbaret, L., Guillou-Frottier, L., Heap, MJ., Bellanger, M., 2019. On the geothermal potential of crustal fault zones: a case study from the Pontgibaud area (French Massif Central, France). Geotherm Energy 7, 33. https://doi.org/10.1186/s40517-019-0150-7

Duwiquet, H., Genter, A., Guillou-Frottier, L., Donzé, F.V., Ledru, P., Magri, F., Guillon, T., Horne, R.N., Arbaret, L., Souque, C., 2024. Advanced 3D TH and THM Modeling to Shed Light

on Thermal Convection in Fault Zones With Varying Thicknesses. Journal of Geophysical Research: Solid Earth 129. https://doi.org/10.1029/2023JB028205

Duwiquet, H., Guillou-Frottier, L., Arbaret, L., Bellanger, M., Guillon, T., Heap, M.J., 2021. Crustal Fault Zones (CFZ) as Geothermal Power Systems: A Preliminary 3D THM Model Constrained by a Multidisciplinary Approach. Geofluids 2021, 1–24. https://doi.org/10.1155/2021/8855632

Duwiquet, H., Magri, F., Lopez, S., Guillon, T., Arbaret, L., Bellanger, M., Guillou-Frottier, L., 2022. Tectonic Regime as a Control Factor for Crustal Fault Zone (CFZ) Geothermal Reservoir in an Amagmatic System: A 3D Dynamic Numerical Modeling Approach. Nat Resour Res 31, 3155–3172. https://doi.org/10.1007/s11053-022-10116-w

Edet, A., Okereke, C., 2005. Hydrogeological and hydrochemical character of the regolith aquifer, northern Obudu Plateau, southern Nigeria. Hydrogeol J 13, 391–415. https://doi.org/10.1007/s10040-004-0358-9

Eichhubl, P., Davatzes, N., Becker, P., 2009. Structural and diagenetic control of fluid migration and cementation along the Moab fault, Utah. AAPG Bulletin 93, 653–681. https://doi.org/10.1306/02180908080

Eldursi, K., Scholtes, L., Conin, M., Golfier, F., Ledru, P., Mercadier, J., Collon, P., Chemillac, R., 2023. 3-D hydromechanical simulation of intersecting faults: Influences on fluid circulation and formation of oriented-orebodies. Journal of Structural Geology 171, 104864. https://doi.org/10.1016/j.jsg.2023.104864

Ellis, A.J., 1970. Quantitative interpretation of chemical characteristics of hydrothermal systems. Geothermics 2, 516–528. https://doi.org/10.1016/0375-6505(70)90050-7

Evans, J., Forster, C., Goddard, J., 1997. Permeability of fault-related rocks, and implications for hydraulic structure of fault zones. Journal of Structural Geology 19, 1393–1404. https://doi.org/10.1016/S0191-8141(97)00057-6

Evans, J.P., Forster, C.B., Goddard, J.V., 1997. Permeability of fault-related rocks, and implications for hydraulic structure of fault zones. Journal of Structural Geology 19, 1393–1404. https://doi.org/10.1016/S0191-8141(97)00057-6

Faulds, J., Coolbaugh, M., Bouchot, V., Moek, I., Oguz, K., 2010. Characterizing Structural Controls of Geothermal Reservoirs in the Great Basin, USA, and Western Turkey: Developing Successful Exploration Strategies in Extended Terranes.

Faulds, J., Hinz, N., 2015. Favorable tectonic and structural settings of geothermal systems in the Great Basin region, western USA: Proxies for discovering blind geothermal systems. Proceedings World Geothermal Congress, Melbourne, Australia.

Faulkner, D.R., Jackson, C.A.L., Lunn, R.J., Schlische, R.W., Shipton, Z.K., Wibberley, C.A.J., Withjack, M.O., 2010. A review of recent developments concerning the structure, mechanics and fluid flow properties of fault zones. Journal of Structural Geology, Fault Zones 32, 1557–1575. https://doi.org/10.1016/j.jsg.2010.06.009

Faure, M., 1995. Late orogenic carboniferous extensions in the Variscan French Massif Central. Tectonics 14, 132–153. https://doi.org/10.1029/94TC02021

Faure, M., Lardeaux, J.-M., Ledru, P., 2009. A review of the pre-Permian geology of the Variscan French Massif Central. Comptes Rendus Geoscience, Mécanique de l'orogénie

varisque : Une vision moderne de le recherche dans le domaine de l'orogénie 341, 202–213. https://doi.org/10.1016/j.crte.2008.12.001

Feybesse, J.-L., Couturie, J.-P., Ledru, P., Johan, V., 1995. Les granites de la Margeride, de Chambon-le-Château et de Saint-Christophe-d'Allier (Massif Central) : des laccolites synchrones des derniers stades de l'épaississement varisque. Géologie de la France 27–45.

Finley, T., Johnston, S., Unsworth, M., Banks, J., Pana, D., 2021. The structural settings of convective hydrothermal systems in southeastern British Columbia, Canada.

Fintley, H.O., Eberle, A.R., Rodden, C.J., 1962. Isotopic boron composition of certain boron minerals. Geochimica et Cosmochimica Acta 26. https://doi.org/10.1016/0016-7037(62)90064-9

Fleming, A., 1994. The hydrogeology of Allen County, Indiana: a geologic and ground-water atlas (1994). Indiana Geological & Water Survey, Special Reports;57. https://doi.org/10.5967/dyna-cr60

Forster, C., Smith, L., 1989. The influence of groundwater flow on thermal regimes in mountainous terrain: A model study. J. Geophys. Res. 94, 9439–9451. https://doi.org/10.1029/JB094iB07p09439

Fouillac, C., 1983. Chemical geothermometry in CO2-rich thermal waters. Example of the French massif central. Geothermics 12, 149–160. https://doi.org/10.1016/0375-6505(83)90025-1

Fouillac, C., Michard, G., 1981. Sodium/lithium ratio in water applied to geothermometry of geothermal reservoirs. Geothermics 10, 55–70. https://doi.org/10.1016/0375-6505(81)90025-0

Fournier, R.O., 1977. Chemical geothermometers and mixing models for geothermal systems. Geothermics 5, 41–50. https://doi.org/10.1016/0375-6505(77)90007-4

Fournier, R.O., Potter, R.W., 1979. Magnesium correction to the Na-K-Ca chemical geothermometer. Geochimica et Cosmochimica Acta 43, 1543–1550. https://doi.org/10.1016/0016-7037(79)90147-9

Fournier, R.O., Rowe, J.J., 1966. The deposition of silica in hot springs. Bull Volcanol 29, 585–587. https://doi.org/10.1007/BF02597179

Fournier, R.O., Truesdell, A.H., 1973. An empirical Na/K/Ca geothermometer for natural waters. Geochimica et Cosmochimica Acta 37, 1255–1275. https://doi.org/10.1016/0016-7037(73)90060-4

Franklyn, M.T., McNutt, R.H., Kamineni, D.C., Gascoyne, M., Frape, S.K., 1991. Groundwater 87Sr/86Sr values in the Eye-Dashwa Lakes pluton, Canada: Evidence for plagioclase-water reaction. Chemical Geology: Isotope Geoscience section 86, 111–122. https://doi.org/10.1016/0168-9622(91)90057-4

Franzson, H., Kristjánsson, B.R., Gunnarsson, G., Björnsson, G., Hjartarson, A., Steingrímsson, B., Gunnlaugsson, E., Gíslason, G., 2005. The Hengill-Hellisheiði Geothermal Field. Development of a Conceptual Geothermal Model.

Froulikova, L., 2008. Les villes d'eau dans les Pays tchèques: de la cure à la culture et au multiculturalisme. Culture des villes d'eau 61–67.

Garcia, J., Hartline, C., Walters, M., Wright, M., Rutqvist, J., Dobson, P.F., Jeanne, P., 2016. The Northwest Geysers EGS Demonstration Project, California: Part 1: Characterization and reservoir response to injection. Geothermics, Enhanced Geothermal Systems: State of the Art 63, 97–119. https://doi.org/10.1016/j.geothermics.2015.08.003

Garg, S.K., Pritchett, J.W., Combs, J., 2010. Exploring for hidden geothermak systems. Proceedings World Geothermal Congress, Bali, Indonesia 7.

Garibaldi, C., Guillou-Frottier, L., Lardeaux, JM., Bonté, D., Lopez, S., Bouchot, V., Ledru, P., 2010. Thermal anomalies and geological structures in the Provence basin: Implications for hydrothermal circulations at depth. Bulletin de la Société Géologique de France 181, 363–376. https://doi.org/10.2113/gssgfbull.181.4.363

Geirsson, S.B., 2008. Hellisheiði Power Plant. European Investment Bank.

Genter, A., Evans, K., Cuenot, N., Fritsch, D., Sanjuan, B., 2010. Contribution of the exploration of deep crystalline fractured reservoir of Soultz to the knowledge of enhanced geothermal systems (EGS). Comptes Rendus. Géoscience 342, 502–516. https://doi.org/10.1016/j.crte.2010.01.006

Géochimie des interactions entre les eaux, les minéraux et les roches, 1980. . Éditions Éléments, Tarbes.

Gibert, J.P., Sorel, D., Vergely, P., 1975. Tectonique cassante polyphasée et émergences d'eaux hyperthermales; le site de Chaudes-Aigues (Cantal). Bulletin de la Société Géologique de France S7-XVII, 629–636. https://doi.org/10.2113/gssgfbull.S7-XVII.4.629

Giggenbach, W., 1988. Geothermal solute equilibria. Derivation of Na-K-Mg-Ca geoindicators. Geochimica et Cosmochimica Acta 52, 2749–2765. https://doi.org/10.1016/0016-7037(88)90143-3

Giggenbach, W., Minissale, A.A., Scandiffio, G., 1988. Isotopic and chemical assessment of geothermal potential of the Colli Albani area, Latium region, Italy. Applied Geochemistry 3, 475–486. https://doi.org/10.1016/0883-2927(88)90020-0

Gijbels, R., Van Grieken, R., Blommaert, W., Vandelannoote, R., Van't Dack, L., 1980. Trace Element Geochemistry in Thermal Waters from Plombieres and Bains (Vosges). Advances in European Geothermal Research 396–409. https://doi.org/10.1007/978-94-009-9059-3_35

Girod, M., Bouiller, R., Weber, F., Larqué, P., Giot, D., 1979. Carte géologique de la France à 1/50 000, feuille 791 Le Puy.

Gleeson, T., Smith, L., Moosdorf, N., Hartmann, J., Dürr, H., Manning, A., Van Beek, L., Jellinek, A.M., 2011. Mapping permeability over the surface of the Earth: Mapping global permeability. Geophys. Res. Lett. 38, 607–615. https://doi.org/10.1029/2010GL045565

Gölke, M., Coblentz, D., 1996. Origins of the European regional stress field. Tectonophysics, Dynamics of Extensional Basins and Inversion Tectonics 266, 11–24. https://doi.org/10.1016/S0040-1951(96)00180-1

Graham, R.C., Anderson, M.A., Sternberg, P.D., Tice, K.R., Schoeneberger, P.J., 1997. Morphology, Porosity, and Hydraulic Conductivity of Weathered Granitic Bedrock and Overlying Soils. Soil Science Society of America Journal 61, 516–522. https://doi.org/10.2136/sssaj1997.03615995006100020021x

Granet, M., Wilson, M., Achauer, U., 1995. Imaging a mantle plume beneath the French Massif Central. Earth and Planetary Science Letters 136, 281–296. https://doi.org/10.1016/0012-821X(95)00174-B

Gudmundsson, A., 2000. Active fault zones and groundwater flow. Geophysical Research Letters 27, 2993–2996. https://doi.org/10.1029/1999GL011266

Guillou-Frottier, L., Carrė, C., Bourgine, B., Bouchot, V., Genter, A., 2013. Structure of hydrothermal convection in the Upper Rhine Graben as inferred from corrected temperature data and basin-scale numerical models. Journal of Volcanology and Geothermal Research 256, 29–49. https://doi.org/10.1016/j.jvolgeores.2013.02.008

Guillou-Frottier, L., Duwiquet, H., Launay, G., Taillefer, A., Roche, V., Link, G., 2020. On the morphology and amplitude of 2D and 3D thermal anomalies induced by buoyancy-driven flow within and around fault zones. Solid Earth 11, 1571–1595. https://doi.org/10.5194/se-11-1571-2020

Guillou-Frottier, L., Milesi, G., Roche, V., Duwiquet, H., Taillefer, A., 2024. Heat flow, thermal anomalies, tectonic regimes and high-temperature geothermal systems in fault zones. C. R. Geosc. 356, 1–33. https://doi.org/10.5802/crgeos.213

Guo, Q., Liu, M., Luo, L., Yan, K., Guo, W., Wu, G., Yan, W., Wang, Y., 2019. Geochemical controls on magnesium and its speciation in various types of geothermal waters from typical felsic-rock-hosted hydrothermal systems in China. Geothermics 81, 185–197. https://doi.org/10.1016/j.geothermics.2019.05.006

Haines, S., Lynch, E., Mulch, A., Valley, J.W., Van Der Pluijm, B., 2016. Meteoric fluid infiltration in crustal-scale normal fault systems as indicated by δ ^{18} O and δ ^{2} H geochemistry and ^{40} Ar/ ^{39} Ar dating of neoformed clays in brittle fault rocks. Lithosphere 8, 587–600. https://doi.org/10.1130/L483.1

Hanson, M.C., Oze, C., Horton, T.W., 2014. Identifying blind geothermal systems with soil CO2 surveys. Applied Geochemistry 50, 106–114. https://doi.org/10.1016/j.apgeochem.2014.08.009

Harinarayana, T., Abdul Azeez, K.K., Murthy, D.N., Veeraswamy, K., Eknath Rao, S.P., Manoj, C., Naganjaneyulu, K., 2006. Exploration of geothermal structure in Puga geothermal field, Ladakh Himalayas, India by magnetotelluric studies. Journal of Applied Geophysics, Electrical and Electromagnetic Studies in Geothermally Active Regions 58, 280–295. https://doi.org/10.1016/j.jappgeo.2005.05.005

Heise, W., Caldwell, T.G., Bibby, H.M., Bannister, S.C., 2008. Three-dimensional modelling of magnetotelluric data from the Rotokawa geothermal field, Taupo Volcanic Zone, New Zealand. Geophysical Journal International 173, 740–750. https://doi.org/10.1111/j.1365-246X.2008.03737.x

Henou, B., 1973. Les sources minérales et thermales du Cantal : leur cadre géologique Massif Central Français. Université de Clermont-Ferrand.

Hickman, S., Sibson, R., Bruhn, R., 1995. Introduction to Special Section: Mechanical Involvement of Fluids in Faulting. Journal of Geophysical Research: Solid Earth 100, 12831–12840. https://doi.org/10.1029/95JB01121

Houston, J.F.T., Lewis, R.T., 1988. The Victoria Province Drought Relief Project, II. Borehole Yield Relationships. Groundwater 26, 418–426. https://doi.org/10.1111/j.1745-6584.1988.tb00407.x

Ifabiyi, I.P., Ashaolu, E.D., Omotosho, O., 2016. Hydrogeological Characteristics of Groundwater Yield in Shallow Wells of the Regolith Aquifer: a Study from Ilorin, Nigeria. Momona Ethiopian Journal of Science 8, 23–36. https://doi.org/10.4314/mejs.v8i1.2

IGN, 2011. BD ALTI® | Géoservices. Institut National de l'Information Géographique et Forestière, France Géoservices IGN, BD ALTI 25m, V2.0. https://geoservices.ign.fr/bdalti

IMA–CNMNC approved mineral symbols | Mineralogical Magazine | Cambridge Core [WWW Document], n.d. URL https://www.cambridge.org/core/journals/mineralogical-magazine/article/imacnmnc-approved-mineral-symbols/62311F45ED37831D78603C6E6B25EE0A (accessed 11.18.24).

Indicateur national climatologique - Infoclimat [WWW Document], n.d. URL https://www.infoclimat.fr/climato/indicateur_national.php#2025;,1981-2010,1,-3.65,368.65,,y,desc,1929.05,2025.95

Ingebritsen, S.E., Appold, M.S., 2012. The Physical Hydrogeology of Ore Deposits. Econ. Geol. 107, 559–584. https://doi.org/10.2113/econgeo.107.4.559

Iwatsuki, T., Xu, S., Itoh, S., Abe, M., Watanabe, M., 2000. Estimation of relative groundwater age in the granite at the Tono research site, central Japan. Nuclear Instruments and Methods in Physics Research Section B: Beam Interactions with Materials and Atoms, 8th International Conference on Accelerator Mass Spectrometry 172, 524–529. https://doi.org/10.1016/S0168-583X(00)00149-X

Jarrassé, D., 1992. Les thermes romantiques: bains et villégiatures en France de 1800 à 1850. Presses Univ Blaise Pascal.

Jaunat, J., Dupuy, A., Huneau, F., Celle, H., Le Coustumer, P., 2016. Groundwater flow dynamics of weathered hard-rock aquifers under climate-change conditions: an illustrative example of numerical modeling through the equivalent porous media approach in the north-western Pyrenees (France). Hydrogeology Journal 24. https://doi.org/10.1007/s10040-016-1408-9

Jaupart, C., Labrosse, S., Mareschal, J.-C., 2007. 7.06 Temperatures, Heat and Energy in the Mantle of the Earth 223–270.

Jaupart, C., Mareschal, J.-C., 2010. Heat Generation and Transport in the Earth. Cambridge University Press.

Jazé-Charvolin, M.-R., 2014. Les stations thermales : de l'abandon à la renaissance. Une brève histoire du thermalisme en France depuis l'Antiquité. In Situ. Revue des patrimoines. https://doi.org/10.4000/insitu.11123

Jenks, G.F., 1967. The Data Model Concept in Statistical Mapping. International Yearbook of Cartography 7, 186–190.

Johnson, J., Oelkers, E., Helgeson, H., 1992. SUPCRT92: A software package for calculating the standard molal thermodynamic properties of minerals, gases, aqueous species, and reactions from 1 to 5000 bar and 0 to 1000°C. Computers & Geosciences 18, 899–947. https://doi.org/10.1016/0098-3004(92)90029-Q

Jolie, E., Scott, S., Faulds, J., Chambefort, I., Axelsson, G., Gutiérrez-Negrín, L., Regenspurg, S., Ziegler, M., Ayling, B., Richter, A., Zemedkun, M., 2021. Geological controls on geothermal resources for power generation. Nat Rev Earth Environ 2, 324–339. https://doi.org/10.1038/s43017-021-00154-y

Jones, M.J., 1985. The weathered zone aquifers of the basement complex areas of Africa. Quarterly Journal of Engineering Geology 18, 35–46. https://doi.org/10.1144/gsl.qjeg.1985.018.01.06

Kerrich, R., 1986. Fluid infiltration into fault zones: Chemical, isotopic, and mechanical effects. PAGEOPH 124, 225–268. https://doi.org/10.1007/BF00875727

Kharaka, Y., Lico, M., Law, L., 1982. Chemical Geothermometers Applied to Formation Waters, Gulf of Mexico and California Basins: ABSTRACT. AAPG Bulletin 66, 588–588.

Kim, Y.S., Peacock, D., Sanderson, D.J., 2004. Fault damage zones. Journal of Structural Geology 26, 503–517. https://doi.org/10.1016/j.jsg.2003.08.002

Kircher, A., 1668. Mundus subterraneus, in XII libros digestus.

Knipe, R.J., Jones, G., Fisher, Q.J., 1998. Faulting, fault sealing and fluid flow in hydrocarbon reservoirs: an introduction. SP 147. https://doi.org/10.1144/GSL.SP.1998.147.01.01

Lachassagne, P., Wyns, R., Bérard, P., Bruel, T., Chéry, L., Coutand, T., Desprats, JF., Strat, P., 2001. Exploitation of High-Yields in Hard-Rock Aquifers: Downscaling Methodology Combining GIS and Multicriteria Analysis to Delineate Field Prospecting Zones.

Lachassagne, P., Wyns, R., Dewandel, B., 2011. The fracture permeability of Hard Rock Aquifers is due neither to tectonics, nor to unloading, but to weathering processes. Terra Nova 23, 145–161. https://doi.org/10.1111/j.1365-3121.2011.00998.x

Lapwood, E.R., 1948. Convection of a fluid in a porous medium. Math. Proc. Camb. Phil. Soc. 44, 508–521. https://doi.org/10.1017/S030500410002452X

Larousse, P., 1874. Grand dictionnaire universel du XIXe siècle : français, historique, géographique, mythologique, bibliographique.... T. 1 A / par M. Pierre Larousse.

Launay, G., 2018. Hydrodynamique des systèmes minéralisés péri-granitiques: étude du gisement à W-Sn-(Cu) de Panasqueira (Portugal). Université d'Orléans.

Launay, G., Sizaret, S., Guillou-Frottier, L., Fauguerolles, C., Champallier, R., Gloaguen, R., 2019. Dynamic Permeability Related to Greisenization Reactions in Sn-W Ore Deposits: Quantitative Petrophysical and Experimental Evidence. Geofluids 2019, 5976545. https://doi.org/10.1155/2019/5976545

Launay, L., 1906. Observations géologiques sur quelques sources thermales : Chaudes-Aigues—Mont-Dore. Ann. des Mines p.5.

Le Grand d'Aussy, P.J.-B., 1794. Voyage fait, en 1787 et 1788, dans la ci-devant Haute et Basse Auvergne, aujourd'hui départemens du Puy-de-Dôme, du Cantal et partie de celui de la Haute-Loire.

Ledésert, B., Hebert, R., Genter, A., Bartier, D., Clauer, N., Grall, C., 2010. Fractures, hydrothermal alterations and permeability in the Soultz Enhanced Geothermal System. Comptes Rendus. Géoscience 342, 607–615. https://doi.org/10.1016/j.crte.2009.09.011

Ledésert, B., Hebert, R., Genter, A., Bartier, D., Clauer, N., Grall, C., 2009. Fractures, hydrothermal alterations and permeability in the Soultz Enhanced Geothermal System. Comptes Rendus. Géoscience 342, 607–615. https://doi.org/10.1016/j.crte.2009.09.011

Lefort, J., Jutier, P., 1862. Études sur les eaux minérales et thermales de Plombières., Librairie de l'académie impériale de médecine.

Lei, X., Romer, R., Glodny, J., Jiang, S., 2023. Geochemical significance of lithium and boron isotopic heterogeneity evolving during the crystallization of granitic melts. Geology 51, 581–585. https://doi.org/10.1130/G50983.1

Lemoine, L., Schneider-Manuch, E., 2014. Chaudes-Aigues - Inventaire du patrimoine thermal. Route des Villes d'Eaux - Massif Central.

Les eaux souterraines (BSSEAU) | InfoTerre, n.d.

Levet, S., Toutain, J.P., Munoz, M., Berger, G., Negrel, P., Jendrzejewski, N., Agrinier, P., Sortino, F., 2002. Geochemistry of the Bagnères-de-Bigorre thermal waters from the North Pyrenean Zone (France). Geofluids 2, 25–40. https://doi.org/10.1046/j.1468-8123.2002.00030.x

Li, L., Wang, L., Romer, R., Ma, C., Cao, L., Tian, Y., 2025. Using tourmaline to trace Li mineralization in the Mufushan granitic batholith, South China. Chemical Geology 671, 122485. https://doi.org/10.1016/j.chemgeo.2024.122485

Licour, L., 2014. The geothermal reservoir of Hainaut: the result of thermal convection in a carbonate and sulfate aquifer. Geol. Belg.

Littré, E., 1877. Dictionnaire de la langue française.

Lloyd, R.M., 1968. Oxygen isotope behavior in the Sulfate-Water System. Journal of Geophysical Research (1896-1977) 73, 6099–6110. https://doi.org/10.1029/JB073i018p06099

López, D., Smith, L., 1995. Fluid Flow in Fault Zones: Analysis of the Interplay of Convective Circulation and Topographically Driven Groundwater Flow. Water Resources Research 31, 1489–1503. https://doi.org/10.1029/95WR00422

Lopoukhine, M., 1994. Réflexion concernant les critères de définition des gisements d'eau minérale.

Lothe, A., Emmel, B., Bergmo, P.E., Akervoll, I., Todorovic, J., Bhuiyan, M.H., Knies, J., 2018. Porosity, permeability and compaction trends for Scandinavian regoliths. Marine and Petroleum Geology 92, 319–331. https://doi.org/10.1016/j.marpetgeo.2017.10.027

Lowell, R.P., 1975. Circulation in Fractures, Hot Springs, and Convective Heat Transport on Mid-ocean Ridge Crests. Geophysical Journal International 40, 351–365. https://doi.org/10.1111/j.1365-246X.1975.tb04137.x

Lucazeau, F., 2019. Analysis and Mapping of an Updated Terrestrial Heat Flow Data Set. Geochem Geophys Geosyst 20, 4001–4024. https://doi.org/10.1029/2019GC008389

Lucazeau, F., Vasseur, G., 1989. Heat flow density data from France and surrounding margins. Tectonophysics 164, 251–258. https://doi.org/10.1016/0040-1951(89)90018-8

Lucazeau, F., Vasseur, G., 1981. Production de chaleur et régime thermique de la croûte du Massif Central. Production de chaleur et régime thermique de la croûte du Massif Central.

Lucazeau, F., Vasseur, G., Bayer, R., 1984. Interpretation of heat flow data in the French Massif Central. Tectonophysics, Terrestrial Heat Flow Studies and the Structure of the Lithosphere 103, 99–119. https://doi.org/10.1016/0040-1951(84)90077-5

Mack Kennedy, B., Truesdell, A.H., 1996. The Northwest Geysers high-temperature reservoir: evidence for active magmatic degassing and implications for the origin of the Geysers geothermal field. Geothermics 25, 365–387. https://doi.org/10.1016/0375-6505(96)00005-3

Magri, F., Akar, T., Gemici, U., Pekdeger, A., 2012. Numerical investigations of fault-induced seawater circulation in the Seferihisar-Balçova Geothermal system, western Turkey. Hydrogeol J 20, 103–118. https://doi.org/10.1007/s10040-011-0797-z

Magri, F., Inbar, N., Siebert, C., Rosenthal, E., Guttman, J., Möller, P., 2015. Transient simulations of large-scale hydrogeological processes causing temperature and salinity anomalies in the Tiberias Basin. Journal of Hydrology 520, 342–355. https://doi.org/10.1016/j.jhydrol.2014.11.055

Majorowicz, J., Wybraniec, S., 2011. New terrestrial heat flow map of Europe after regional paleoclimatic correction application. Int J Earth Sci (Geol Rundsch) 100, 881–887. https://doi.org/10.1007/s00531-010-0526-1

Malkovsky, V., Magri, F., 2016. Thermal convection of temperature-dependent viscous fluids within three-dimensional faulted geothermal systems: Estimation from linear and numerical analyses. Water Resources Research 52, 2855–2867. https://doi.org/10.1002/2015WR018001

Manning, C.E., Ingebritsen, S.E., 1999. Permeability of the continental crust: Implications of geothermal data and metamorphic systems. Reviews of Geophysics 37, 127–150. https://doi.org/10.1029/1998RG900002

Maréchal, J.C., Dewandel, B., Subrahmanyam, K., 2004. Use of hydraulic tests at different scales to characterize fracture network properties in the weathered-fractured layer of a hard rock aquifer. Water Resources Research 40. https://doi.org/10.1029/2004WR003137

Maréchal, JC., Wyns, R., Lachassagne, P., Subrahmanyam, K., Touchard, F., 2003. Anisotropie verticale de la perméabilité de l'horizon fissuré des aquifères de socle : concordance avec la structure géologique des profils d'altération. Comptes Rendus. Géoscience 335, 451–460. https://doi.org/10.1016/S1631-0713(03)00082-8

Margat, J., 1972. Terminologie Hydrogéologique (No. 72 SGN 2003 AME). Bureau de Recherches Géologiques et Minières.

Marques, J.M., Carreira, P.M., Goff, F., Eggenkamp, H.G.M., Antunes da Silva, M., 2012. Input of 87Sr/86Sr ratios and Sr geochemical signatures to update knowledge on thermal and mineral waters flow paths in fractured rocks (N-Portugal). Applied Geochemistry 27, 1471–1481. https://doi.org/10.1016/j.apgeochem.2012.03.007

Marre, J., 1986. The Structural Analysis of Granitic Rocks. North Oxford Academic, London.

Martin, C., Ponzevera, E., Harlow, G., 2015. In situ lithium and boron isotope determinations in mica, pyroxene, and serpentine by LA-MC-ICP-MS. Chemical Geology 412, 107–116. https://doi.org/10.1016/j.chemgeo.2015.07.022

Martínez, D.E., Fourré, E., Londoño, O.M.Q., Jean-Baptiste, P., Galli, M.G., Dapoigny, A., Grondona, S.I., 2016. Residence time distribution in a large unconfined–semiconfined aquifer in the Argentine Pampas using 3H/3He and CFC tracers. Hydrogeol J 24, 1107–1120. https://doi.org/10.1007/s10040-016-1378-y

Maubec, N., Deneele, D., Ouvrard, G., 2017. Influence of the clay type on the strength evolution of lime treated material. Applied Clay Science 137, 107–114. https://doi.org/10.1016/j.clay.2016.11.033

Mazabraud, Y., Béthoux, N., Guilbert, J., Bellier, O., 2004. Evidence for short-scale stress field variations within intraplate central-western France: Intraplate short-scale stress field variations. Geophysical Journal International 160, 161–178. https://doi.org/10.1111/j.1365-246X.2004.02430.x

McKenna, J., Blackwell, D., 2004. Numerical modeling of transient Basin and Range extensional geothermal systems. Geothermics 33, 457–476. https://doi.org/10.1016/j.geothermics.2003.10.001

McNutt, R., Gascoyne, M., Kamineni, D., 1987. 87Sr/86Sr values in groundwaters of the East Bull Lake pluton, Superior Province, Ontario, Canada. Applied Geochemistry, Isotope Geochemistry of Groundwater and Fracture Material in Plutonic Rock 2, 93–101. https://doi.org/10.1016/0883-2927(87)90064-3

Merle, O., Aumar, C., Labazuy, P., Merciecca, C., Buvat, S., 2023. Structuration tertiaire et quaternaire du Plateau des Dômes (Chaîne des Puys, Massif central, France). Géologie de la France.

Merle, O., Michon, L., 2001. The formation of the West European Rift; a new model as exemplified by the Massif Central area. Bull. Soc. Geol. Fr. 172, 213–221. https://doi.org/10.2113/172.2.213

Michard, A., Beaucaire, C., Michard, G., 1987. Uranium and rare earth elements in CO2-rich waters from Vals-les-Bains (France)∗. Geochimica et Cosmochimica Acta 51, 901–909. https://doi.org/10.1016/0016-7037(87)90103-7

Michard, G., 1990. Behaviour of major elements and some trace elements (Li, Rb, Cs, Sr, Fe, Mn, W, F) in deep hot waters from granitic areas. Chemical Geology 89, 117–134. https://doi.org/10.1016/0009-2541(90)90062-C

Michard, G., 1983. Compilation of thermodynamic data on water-mineral equilibria in hydrothermal reservoirs. Final report. Recueil des donnees thermodynamiques concernant les equilibres eaux-mineraux dans les reservoirs hydrothermaux.

Michard, G., 1979. Géothermomètres chimiques. Bull. Bur. Rech. Geol. Min 183–189.

Michard, G., Beaucaire, C., 1993. Les eaux thermales des granites de Galice (Espagne): des eaux carbogazeuses aux eaux alcalines (Thermal waters from granites of Galicia (Spain): from CO2-rich to high-pH waters). Chemical Geology 110, 345–360. https://doi.org/10.1016/0009-2541(93)90328-G

Michard, G., Fouillac, C., Grimaud, D., Denis, J., 1981. Une méthode globale d'estimation des températures des réservoirs alimentant les sources thermales. Exemple du Massif Central Français. Geochimica et Cosmochimica Acta 45, 1199–1207. https://doi.org/10.1016/0016-7037(81)90143-5

Michard, G., Ouzounian, G., Fouillac, C., Sarazin, G., 1979. Contrôle des concentrations d'aluminium dissous dans les eaux des sources thermales. Geochimica et Cosmochimica Acta 43, 147–155. https://doi.org/10.1016/0016-7037(79)90054-1

Michard, G., Roekens, E., 1983. Modelling of the chemical composition of alkaline hot waters. Geothermics 12, 161–169. https://doi.org/10.1016/0375-6505(83)90026-3

Michon, L., Merle, O., 2001. The evolution of the Massif Central rift: Spatio-temporal distribution of the volcanism. Bull. Soc. Geol. Fr. 172, 201–211. https://doi.org/10.2113/172.2.201

Michon, L., Merle, P., 2005. Discussion on “Evolution of the European Cenozoic Rift System: interaction of the Alpine and Pyrenean orogens with their foreland lithosphere” by P. Dèzes, S.M. Schmid and P.A. Ziegler, Tectonophysics 389 (2004) 1–33. Tectonophysics 401, 251–256. https://doi.org/10.1016/j.tecto.2005.01.006

Michon, L., Van Balen, R.T., Merle, O., Pagnier, H., 2003. The Cenozoic evolution of the Roer Valley Rift System integrated at a European scale. Tectonophysics 367, 101–126. https://doi.org/10.1016/S0040-1951(03)00132-X

Micklethwaite, S., Cox, S.F., 2004. Fault-segment rupture, aftershock-zone fluid flow, and mineralization. Geology 32, 813–816. https://doi.org/10.1130/G20559.1

Millot, R., Scaillet, B., Sanjuan, B., 2010. Lithium isotopes in island arc geothermal systems: Guadeloupe, Martinique (French West Indies) and experimental approach. Geochimica et Cosmochimica Acta 74, 1852–1871. https://doi.org/10.1016/j.gca.2009.12.007

Mitjanas, G., Walsh, J.J., Roca, E., Alías, G., Queralt, P., Ledo, J., Piña-Varas, P., 2024. The importance of structural complexity in the localization of geothermal systems: A case study along the Vallès-Penedès Fault in the Catalan Coastal Ranges (NE Spain). Geothermics 116, 102855. https://doi.org/10.1016/j.geothermics.2023.102855

Mizutani, Y., 1969. Oxygen isotopioc composition of sulphates. Part 3. Oxygen isotopic fractionation in the bisulphate ion-water system. N. Z. J. Sci. 12, 54–59.

Moeck, I., 2014. Catalog of geothermal play types based on geologic controls. Renewable and Sustainable Energy Reviews 37, 867–882. https://doi.org/10.1016/j.rser.2014.05.032

Morrow, C.A., Moore, D.E., Lockner, D.A., 2001. Permeability reduction in granite under hydrothermal conditions. Journal of Geophysical Research: Solid Earth 106, 30551–30560. https://doi.org/10.1029/2000JB000010

Négrel, P., 2006. Water–granite interaction: Clues from strontium, neodymium and rare earth elements in soil and waters. Applied Geochemistry 21, 1432–1454. https://doi.org/10.1016/j.apgeochem.2006.04.007

Négrel, P., Guerrot, C., Cocherie, A., Azaroual, M., Brach, M., Fouillac, C., 2000. Rare earth elements, neodymium and strontium isotopic systematics in mineral waters: evidence from the Massif Central, France. Applied Geochemistry 15, 1345–1367. https://doi.org/10.1016/S0883-2927(00)00008-1

Nehlig, P., Leyrit, H., Arnaud, N., 2001a. Carte géologique de la France à 1/50 000, feuille 788, Murat.

Nehlig, P., Leyrit, H., Dardon, A., Freour, G., de Goer de Herve, A., Huguet, D., Thieblemont, D., 2001b. Constructions et destructions du stratovolcan du Cantal. Bulletin de la Société Géologique de France 172, 295–308. https://doi.org/10.2113/172.3.295

Neuzil, C.E., 2019. Permeability of Clays and Shales. Annu. Rev. Earth Planet. Sci. 47, 247–273. https://doi.org/10.1146/annurev-earth-053018-060437

Newman, G., Gasperikova, E., Hoversten, M., Wannamaker, P., 2008. Three-dimensional magnetotelluric characterization of the Coso geothermal field. Geothermics 37, 369–399. https://doi.org/10.1016/j.geothermics.2008.02.006

Palabiyik, Y., Serpen, U., 2008. Geochemical assessment of Simav geothermal field, Turkey. Revista Mexicana de Ciencias Geológicas, ISSN 1026-8774 25, 408–425.

Palissy, B., 1580. Discours admirables de la nature des eaux et fontaines, tant naturelles qu'artificielles, des métaux, des sels et salines, des pierres, des terres, du feu et des émaux.

Patro, P., 2017. Magnetotelluric Studies for Hydrocarbon and Geothermal Resources: Examples from the Asian Region. Surv Geophys 38, 1005–1041. https://doi.org/10.1007/s10712-017-9439-x

Patterson, J.W., Driesner, T., 2021. Elastic and Thermoelastic Effects on Thermal Water Convection in Fracture Zones. Journal of Geophysical Research: Solid Earth 126, e2020JB020940. https://doi.org/10.1029/2020JB020940

Patterson, J. W., Driesner, T., Matthai, S., Tomlinson, R., 2018. Heat and Fluid Transport Induced by Convective Fluid Circulation Within a Fracture or Fault. Journal of Geophysical Research: Solid Earth 123, 2658–2673. https://doi.org/10.1002/2017JB015363

Patterson, J.W., Driesner, T., Matthai, S.K., 2018. Self-Organizing Fluid Convection Patterns in an en Echelon Fault Array. Geophysical Research Letters 45, 4799–4808. https://doi.org/10.1029/2018GL078271

Pauwels, H., Fouillac, C., Goff, F., Vuataz, F.-D., 1997. The isotopic and chemical composition of CO2-rich thermal waters in the Mont-Dore region (Massif-Central, France). Applied Geochemistry 12, 411–427. https://doi.org/10.1016/S0883-2927(97)00010-3

Peacock, J.R., Earney, T.E., Mangan, M.T., Schermerhorn, W.D., Glen, J.M., Walters, M., Hartline, C., 2020. Geophysical characterization of the Northwest Geysers geothermal field, California. Journal of Volcanology and Geothermal Research 399, 106882. https://doi.org/10.1016/j.jvolgeores.2020.106882

Penhoët, E., Arbaret, L., Guillou-Frottier, L., Duwiquet, H., Gumiaux, C., Bellanger, M., 2025. Fluid flow in crustal fault zones with varying lengthwise thickness: application to the Margeride fault zone (French Massif Central). Geotherm Energy 13, 6. https://doi.org/10.1186/s40517-025-00334-9

Penhoët, E., Sanjuan, B., Guillou-Frottier, L., Arbaret, L., Moreira, M., 2025. One hydrothermal system may hide another: Insights from a geochemical exploration of Chaudes-Aigues and nearby springs (French Massif Central). Geothermics 133, 103476. https://doi.org/10.1016/j.geothermics.2025.103476

Penhoët, E., Guillou-Frottier, L., Arbaret, L., 2024a. Naturally Fractured Granites as Promising Targets for HT Geothermal Exploration: Impact of Fault Network Geometry. Fifth EAGE Global Energy Transition Conference & Exhibition (GET 2024) 2024, 1–5. https://doi.org/10.3997/2214-4609.202421065

Penhoët, E., Guillou-Frottier, L., Arbaret, L., Sanjuan, B., Caritg, S., 2024b. Des thermes romains à la géothermie électrogène, que connaissons-nous réellement du système géothermal de Chaudes-Aigues ? Géologues, Société Géologique de France Les ressources des fluides hydrothermaux, 62–68.

Pentecost, A., 2005. Hot springs, thermal springs and warm springs. What's the difference? Geology Today 21, 222–224. https://doi.org/10.1111/j.1365-2451.2005.00536.x

Pentecost, A., Jones, B., Renaut, R.W., 2003. What is a hot spring? Can. J. Earth Sci. 40, 1443–1446. https://doi.org/10.1139/e03-083

Pétrequin, M., 1979. Etude gravimétrique du massif de la Margeride et de sa bordure méridionale. Université de Montpellier 2.

Pfund, G., 2024. Les stations thermales doivent se réinventer pour survivre à la crise énergétique. The Conversation.

Pollack, H., Hurter, S., Johnson, J., 1993. Heat flow from the Earth's interior: Analysis of the global data set. Reviews of Geophysics 31, 267–280. https://doi.org/10.1029/93RG01249

Pouchan, P., Canellas, J., Nguyen Ba, C., Pelissier-Hermitte, G., Courtes, C., 1991. Aspects de l'hydrothermalisme landais. Journal français d'hydrologie 22, 9–16. https://doi.org/10.1051/water/19912201009

Rabinowicz, M., Boulègue, J., Genthon, P., 1998. Two- and three-dimensional modeling of hydrothermal convection in the sedimented Middle Valley segment, Juan de Fuca Ridge. J. Geophys. Res. 103, 24045–24065. https://doi.org/10.1029/98JB01484

Ranjram, M., Gleeson, T., Luijendijk, E., 2015. Is the permeability of crystalline rock in the shallow crust related to depth, lithology or tectonic setting? Geofluids 15, 106–119. https://doi.org/10.1111/gfl.12098

Ricard, J., 1999. Examen des ouvrages thermaux délaissés de Midi-Pyrénées : Station Thermale de Ax-Les-Thermes (No. R 40914). BRGM.

Ricci, L., Frondini, F., Morgavi, D., Zuccolini, M., Boudoire, G., Laumonier, M., Caliro, S., Cardellini, C., Ionescu, A., Ariano, A., Chiodini, G., 2024. CO2 flux from the French Massif Central groundwaters: Modelling and quantitative estimation of the degassing process. Chemical Geology 652, 122012. https://doi.org/10.1016/j.chemgeo.2024.122012

Richards, H.G., Savage, D., Andrews, J.N., 1992. Granite-water reactions in an experimental Hot Dry Rock geothermal reservoir, Rosemanowes test site, Cornwall, U.K. Applied Geochemistry 7, 193–222. https://doi.org/10.1016/0883-2927(92)90038-5

Riedel, T., Weber, T., 2020. Review: The influence of global change on Europe's water cycle and groundwater recharge. Hydrogeol J 28, 1939–1959. https://doi.org/10.1007/s10040-020-02165-3

Roche, V., Sternai, P., Guillou-Frottier, L., Menant, A., Jolivet, L., Bouchot, V., Gerya, T., 2018. Emplacement of metamorphic core complexes and associated geothermal systems controlled by slab dynamics. Earth and Planetary Science Letters 498, 322–333. https://doi.org/10.1016/j.epsl.2018.06.043

Roig, J.Y., Alabouvette, B., Collomb, P., Bogdanoff, S., Monchoux, P., Genna, A., Ciszak, R., 2001. Carte géologique de la France à 1/50 000, feuille 859, Decazeville.

Rosenberg, N., Epstein, D., Wang, D., Vail, L., Srinivasan, R., Arnold, J., 1999. Possible Impacts of Global Warming on the Hydrology of the Ogallala Aquifer Region. Climatic Change 42, 677–692. https://doi.org/10.1023/A:1005424003553

Roux, L., 2009. Le thermalisme européen au XVIIIe siècle Étude comparative de quelques villes d'eaux. France, Angleterre, Belgique, Suisse, Italie, Allemagne.

Santoni, S., Huneau, F., Garel, E., Vergnaud-Ayraud, V., Labasque, T., Aquilina, L., Jaunat, J., Celle-Jeanton, H., 2016. Residence time, mineralization processes and groundwater origin within a carbonate coastal aquifer with a thick unsaturated zone. Journal of Hydrology 540, 50–63. https://doi.org/10.1016/j.jhydrol.2016.06.001

Sarazin, G., Michard, G., Rakotonindrainy, Pastor, L., 1986. Geochemical study of the geothermal field of Antsirabé (Madagascar). Geochemical Journal 20, 41–50. https://doi.org/10.2343/geochemj.20.41

Schmidt, R.B., Bucher, K., Stober, I., 2018. Experiments on granite alteration under geothermal reservoir conditions and the initiation of fracture evolution. European Journal of Mineralogy 30, 899–916. https://doi.org/10.1127/ejm/2018/0030-2771

Scibek, J., 2020. Multidisciplinary database of permeability of fault zones and surrounding protolith rocks at world-wide sites. https://doi.org/10.1038/s41597-020-0435-5

SHOM-Service Hydrographique Et Océanographique De La Marine, 2015. MNT Bathymétrique de façade du Golfe du Lion - Côte d'Azur (Projet Homonim). https://doi.org/10.17183/MNT_MED100M_GDL_CA_HOMONIM_WGS84

Sibson, R., 1996. Structural permeability of fluid-driven fault-fracture meshes. Journal of Structural Geology 18, 1031–1042. https://doi.org/10.1016/0191-8141(96)00032-6

Sibson, R., 1987. Earthquake rupturing as a mineralizing agent in hydrothermal systems. Geol 15. https://doi.org/10.1130/0091-7613(1987)15<701:ERAAMA>2.0.CO;2

Sigfússon, B., Arnarson, M., Snæbjörnsdóttir, S., Karlsdóttir, M.R., Aradóttir, E.S., Gunnarsson, I., 2018. Reducing emissions of carbon dioxide and hydrogen sulphide at Hellisheidi power plant in 2014-2017 and the role of CarbFix in achieving the 2040 Iceland climate goals. Energy Procedia, Carbon in natural and engineered processes: Selected contributions from the 2018 International Carbon Conference 146, 135–145. https://doi.org/10.1016/j.egypro.2018.07.018

Simms, M.A., Garven, G., 2004. Thermal convection in faulted extensional sedimentary basins: theoretical results from finite-element modeling. Geofluids 4, 109–130. https://doi.org/10.1111/j.1468-8115.2004.00069.x

Smith, L., Chapman, D.S., 1983. On the thermal effects of groundwater flow: 1. Regional scale systems. J. Geophys. Res. 88, 593–608. https://doi.org/10.1029/JB088iB01p00593

Sobolev, S.V., Zeyen, H., Granet, M., Achauer, U., Bauer, C., Werling, F., Altherr, R., Fuchs, K., 1997. Upper mantle temperatures and lithosphere-asthenosphere system beneath the French Massif Central constrained by seismic, gravity, petrologic and thermal observations. Tectonophysics 275, 143–164. https://doi.org/10.1016/S0040-1951(97)00019-X

Sonney, R., Vuataz, F.-D., 2009. Numerical modelling of Alpine deep flow systems: a management and prediction tool for an exploited geothermal reservoir (Lavey-les-Bains, Switzerland). Hydrogeol J 17, 601–616. https://doi.org/10.1007/s10040-008-0394-y

Souche, A., Dabrowski, M., Andersen, TB., 2014. Modeling thermal convection in supradetachment basins: example from western Norway. Geofluids 58–74. https://doi.org/10.1111/gfl.12042

Stettler, A., Allègre, C.J., 1978. 87Rb-87Sr studies of waters in a geothermal area: The Cantal, France. Earth and Planetary Science Letters 38, 364–372. https://doi.org/10.1016/0012-821X(78)90110-3

Stober, I., Bucher, K., 2007. Hydraulic properties of the crystalline basement. Hydrogeol J 15, 213–224. https://doi.org/10.1007/s10040-006-0094-4

Stober, I., Giovanoli, F., Wiebe, V., Bucher, K., 2022. Deep hydrochemical section through the Central Alps: evolution of deep water in the continental upper crust and solute acquisition

during water–rock-interaction along the Sedrun section of the Gotthard Base Tunnel. Swiss J Geosci 115, 9. https://doi.org/10.1186/s00015-022-00413-0

Stober, I., Zhong, J., Zhang, L., Bucher, K., 2016. Deep hydrothermal fluid–rock interaction: the thermal springs of Da Qaidam, China. Geofluids 16, 711–728. https://doi.org/10.1111/gfl.12190

Swihart, G., Moore, P., 1989. A reconnaissance of the boron isotopic composition of tourmaline. Geochimica et Cosmochimica Acta 53, 911–916. https://doi.org/10.1016/0016-7037(89)90035-5

Taillefer, A., 2017. Interactions entre tectonique et hydrothermalisme : rôle de la faille normale de la Têt sur la circulation hydrothermale et la distribution des sources thermales des Pyrénées Orientales. (These de doctorat). Montpellier.

Taillefer, A., Guillou-Frottier, L., Soliva, R., Magri, F., Lopez, S., Courrioux, G., Millot, R., Ladouche, B., Le Goff, E., 2018. Topographic and Faults Control of Hydrothermal Circulation Along Dormant Faults in an Orogen. Geochem Geophys Geosyst 19, 4972–4995. https://doi.org/10.1029/2018GC007965

Taillefer, A., Truche, L., Audin, L., Donzé, F.-V., Tisserand, D., Denti, S., Manrique Llerena, N., Masías Alvarez, P., Braucher, R., Zerathe, S., Monnin, C., Dutoit, H., Taipe Maquerhua, E., Apaza Choquehuayta, F., 2024. Characterization of Southern Peru Hydrothermal Systems: New Perspectives for Geothermal Exploration Along the Andean Forearc. Geochemistry, Geophysics, Geosystems 25, e2023GC011344. https://doi.org/10.1029/2023GC011344

Talbo, H., Bos, P., 1993. Valorisation des ressources en eau dans le socle breton : les manifestations thermales du Moulin de Quip à Allaire (56) (Rapport BRGM No. RR 37289).

Talbot, J.Y., 2003. Apport des études ASM et gravimétriques des plutons cévenols à la caractérisation structurale de l'évolution tardi-hercynienne du Massif Central. Université d'Orléans.

Talbot, J.Y., Faure, M., Chen, Y., Martelet, G., 2005. Pull-apart emplacement of the Margeride granitic complex (French Massif Central). Implications for the late evolution of the Variscan orogen. Journal of Structural Geology 27, 1610–1629. https://doi.org/10.1016/j.jsg.2005.05.008

Tamburello, G., Chiodini, G., Ciotoli, G., Procesi, M., Rouwet, D., Sandri, L., Carbonara, N., Masciantonio, C., 2022. Global thermal spring distribution and relationship to endogenous and exogenous factors. Nat Commun 13, 6378. https://doi.org/10.1038/s41467-022-34115-w

Taylor, J., 2021. Laboratory Measurement of Electrical and Hydraulic Properties of Regolith Over Granitic Bedrock (Master of Science in Hydrologic Sciences). Boise State University, Boise, ID. https://doi.org/10.18122/td.1860.boisestate

Taylor, R., Howard, K., 2000. A tectono-geomorphic model of the hydrogeology of deeply weathered crystalline rock: Evidence from Uganda. Hydrogeology Journal 8, 279–294. https://doi.org/10.1007/s100400000069

Teng, F.-Z., McDonough, W.F., Rudnick, R.L., Dalpé, C., Tomascak, P.B., Chappell, B.W., Gao, S., 2004. Lithium isotopic composition and concentration of the upper continental crust. Geochimica et Cosmochimica Acta 68, 4167–4178. https://doi.org/10.1016/j.gca.2004.03.031

Trévoux, Papin, 1771. Dictionnaire universel françois et latin, vulgairement appelé Dictionnaire de Trévoux : contenant la signification et la définition des mots de l'une et de l'autre langue.

Truesdell, A., 1975. Geochemical techniques in exploration, summary of section III. Proc. Second U. N. Symp. on the Development and Use of Geothermal Resources, 1975.

Turcotte, D., Schubert, G., 2002. Geodynamics. Cambridge University Press.

Van De Meulebrouck, J., 1983. Reconnaissance géophysique des structures crustales de deux segments de chaîne de collision: le Haut Allier (Massif Central français) et le sud du Tibet (Himalaya). Université de Montpellier 2.

Vanderhaeghe, O., Laurent, O., Gardien, V., Moyen, J.F., Gébelin, A., Chelle-Michou, C., Couzinié, S., Villaros, A., Bellanger, M., 2020. Flow of partially molten crust controlling construction, growth and collapse of the Variscan orogenic belt: the geologic record of the French Massif Central. BSGF - Earth Sci. Bull. 191, 25. https://doi.org/10.1051/bsgf/2020013

Vasseur, G., 1982. Synthèse des résultats de flux géothermique en France. Ann. Geophys. 38, 189–201.

Vasseur, G., Michard, G., Fouillac, C., 1997. Contraintes sur la structure profonde et le fonctionnement du système hydrothermal de Chaudes-Aigues (France) 3–17.

Vieira, F.P., Hamza, V.M., Alexandrino, C.H., 2014. Obliteration of thermal springs by groundwater flows in sedimentary basins of Brazil. Hydrogeol J 22, 69–86. https://doi.org/10.1007/s10040-013-1081-1

Vrba, J., 1996. Thermal mineral water springs in Karlovy Vary. Geo 27, 120–125. https://doi.org/10.1007/BF01061684

Waber, H.N., Schneeberger, R., Mäder, U.K., Wanner, C., 2017. Constraints on Evolution and Residence time of Geothermal Water in Granitic Rocks at Grimsel (Switzerland). Procedia Earth and Planetary Science, 15th Water-Rock Interaction International Symposium, WRI-15 17, 774–777. https://doi.org/10.1016/j.proeps.2017.01.026

Walter, B., 2017. Réservoirs de socle en contexte extensif: genèse, géométries et circulations de fluides: exemples du rift intracontinental du lac Albert (Ouganda) et de la marge proximale d'Ifni (Maroc). Université de Lorraine.

Wang, L., Liu, K., Ma, Y., Zhang, Y., Tong, J., Jia, W., Zhang, S., Sun, J., 2024. Geochemical and Isotopic Techniques Constraints on the Origin, Evolution, and Residence Time of Low-enthalpy Geothermal Water in Western Wugongshan, SE China. Acta Geologica Sinica - English Edition 98, 801–818. https://doi.org/10.1111/1755-6724.15161

Wanner, C., Diamond, L.W., Alt-Epping, P., 2019. Quantification of 3-D Thermal Anomalies From Surface Observations of an Orogenic Geothermal System (Grimsel Pass, Swiss Alps). Journal of Geophysical Research: Solid Earth 124, 10839–10854. https://doi.org/10.1029/2019JB018335

Warr, L., 2021. IMA–CNMNC approved mineral symbols. Mineralogical Magazine 85, 291–320. https://doi.org/10.1180/mgm.2021.43

White, A.F., Bullen, T.D., Schulz, M.S., Blum, A.E., Huntington, T.G., Peters, N.E., 2001. Differential rates of feldspar weathering in granitic regoliths. Geochimica et Cosmochimica Acta 65, 847–869. https://doi.org/10.1016/S0016-7037(00)00577-9

White, D., 1965. Saline Waters of Sedimentary Rocks1, in: Young, A., Galley, J. (Eds.), Fluids in Subsurface Environments. American Association of Petroleum Geologists, p. 0. https://doi.org/10.1306/M4360C14

Wibberley, C., Shimamoto, T., 2003. Internal structure and permeability of major strike-slip fault zones: the Median Tectonic Line in Mie Prefecture, Southwest Japan. Journal of Structural Geology 25, 59–78. https://doi.org/10.1016/S0191-8141(02)00014-7

Williams, L., Hervig, R., Holloway, J., Hutcheon, I., 2001. Boron isotope geochemistry during diagenesis. Part I. Experimental determination of fractionation during illitization of smectite. Geochimica et Cosmochimica Acta 65, 1769–1782. https://doi.org/10.1016/S0016-7037(01)00557-9

Williams, L., Turner, A., Hervig, R., 2007. Intracrystalline boron isotope partitioning in illite-smectite: Testing the geothermometer. American Mineralogist 92, 1958–1965. https://doi.org/10.2138/am.2007.2531

Wu, Y., Zhou, X., 2023. Structural control effects on hot springs' hydrochemistry in the northern Red River Fault Zone: Implications for geothermal systems in fault zones. Journal of Hydrology 623, 129836. https://doi.org/10.1016/j.jhydrol.2023.129836

Wu, Y., Zhou, X., Zhuo, L., Tao, G., Ma, J., Wang, Y., 2023. Structural controls of the northern Red River Fault Zone on the intensity of hydrothermal activity and distribution of hot springs in the Yunnan-Tibet geothermal belt. Geothermics 109, 102641. https://doi.org/10.1016/j.geothermics.2022.102641

Wunder, B., Meixner, A., Romer, R., Feenstra, A., Schettler, G., Heinrich, W., 2007. Lithium isotope fractionation between Li-bearing staurolite, Li-mica and aqueous fluids: An experimental study. Chemical Geology 238, 277–290. https://doi.org/10.1016/j.chemgeo.2006.12.001

Wunder, B., Meixner, A., Romer, R., Heinrich, W., 2006. Temperature-dependent isotopic fractionation of lithium between clinopyroxene and high-pressure hydrous fluids. Contrib Mineral Petrol 151, 112–120. https://doi.org/10.1007/s00410-005-0049-0

Wunder, B., Meixner, A., Romer, R., Wirth, R., Heinrich, W., 2005. The geochemical cycle of boron: Constraints from boron isotope partitioning experiments between mica and fluid. Lithos 84, 206–216. https://doi.org/10.1016/j.lithos.2005.02.003

Wyns, R., 2002. Climat, eustatisme, tectonique: quels contrôles pour l'altération continentale? Exemple des séquences d'altération cénozoïques en France. Bulletin d'information des géologues du bassin de Paris 39, 5–16.

Wyns, R., Baltassat, J.-M., Lachassagne, P., Legchenko, A., Vairon, J., Mathieu, F., 2004. Application of proton magnetic resonance soundings to groundwater reserve mapping in weathered basement rocks (Brittany, France). Bulletin de la Société Géologique de France 175, 21–34. https://doi.org/10.2113/175.1.21

Wyns, R., Gourry, J.C., Baltassat, J.-M., Lebert, F., 1999. Caractérisation multiparamètres des horizons de subsurface (0-100 m) en contexte de socle altéré. 2ème Colloque GEOFCAN 105–110.

Yokochi, R., Ram, R., Zappala, J., Jiang, W., Adar, E., Bernier, R., Burg, A., Dayan, U., Lu, Z., Mueller, P., Purtschert, R., Yechieli, Y., 2019. Radiokrypton unveils dual moisture sources of a deep desert aquifer. Proc Natl Acad Sci U S A 116, 16222–16227. https://doi.org/10.1073/pnas.1904260116

Zhang, Y., Schaubs, P.M., Zhao, C., Ord, A., Hobbs, B.E., Barnicoat, A.C., 2008. Fault-related dilation, permeability enhancement, fluid flow and mineral precipitation patterns: numerical

models. Geological Society, London, Special Publications 299, 239–255. https://doi.org/10.1144/SP299.15

Zhao, C., Hobbs, B.E., Mühlhaus, H.B., Ord, A., Lin, G., 2003. Convective instability of 3-D fluid-saturated geological fault zones heated from below. Geophysical Journal International 155, 213–220. https://doi.org/10.1046/j.1365-246X.2003.02032.x

Zheng, Y.-F., 1999. Oxygen isotope fractionation in carbonate and sulfate minerals. Geochemical Journal 33, 109–126. https://doi.org/10.2343/geochemj.33.109

Zhou, J., Wang, Q., Xu, Y., Cempírek, J., Wang, H., Ma, J., Wei, G., Huang, T., Zhu, G., Zhang, L., 2021. Geochronology, petrology, and lithium isotope geochemistry of the Bailongshan granite-pegmatite system, northern Tibet: Implications for the ore-forming potential of pegmatites. Chemical Geology 584, 120484. https://doi.org/10.1016/j.chemgeo.2021.120484

Ziegler, P.A., 1992. European Cenozoic rift system. Tectonophysics, Geodynamics of rifting, volume 1 Case history studies on rifts: Europe and Asia 208, 91–111. https://doi.org/10.1016/0040-1951(92)90338-7

Ziegler, P.A., Dèzes, P., 2007. Cenozoic uplift of Variscan Massifs in the Alpine foreland: Timing and controlling mechanisms. Global and Planetary Change 58, 237–269. https://doi.org/10.1016/j.gloplacha.2006.12.004

Zuddas, P., Seimbille, F., Michard, G., 1995. Granite-fluid interaction at near-equilibrium conditions: Experimental and theoretical constraints from Sr contents and isotopic ratios. Chemical Geology 121, 145–154. https://doi.org/10.1016/0009-2541(94)00159-6

Appendices

Appendices

Appendix A: Fault density map methodology

In order to characterise the fracturation of an area, a fault density map has been produced. To do this, a geological map is needed, and more specifically the linear structures (faults). In our example, the map is produced at the scale of France. At this scale, the faults used are the vectorised faults associated with the 1M map.

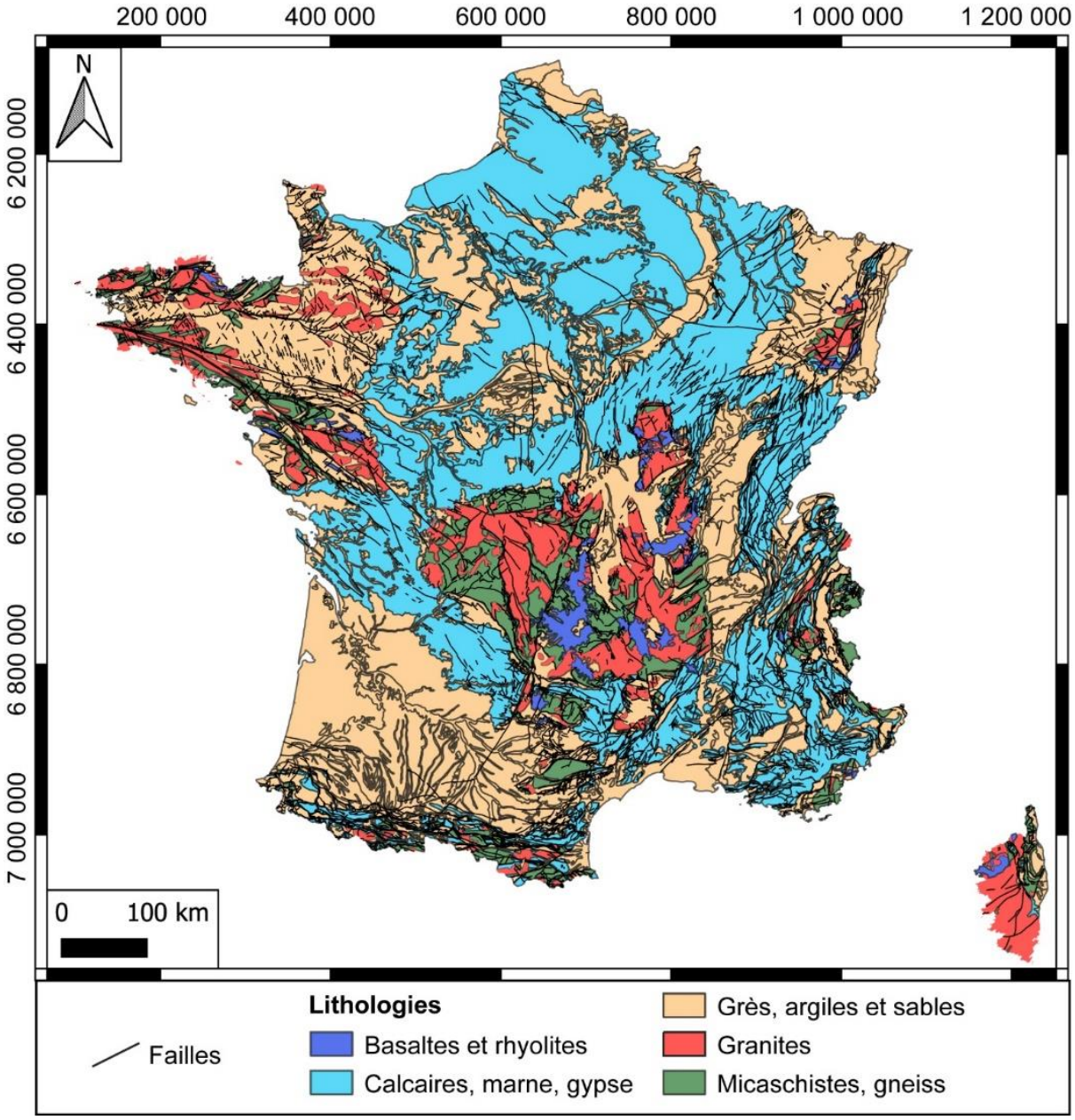

Fig. 1: 2M geological map of France (BRGM), the faults superimposed are taken from the 1M geological map (BRGM).

The next step is to generate a grid, made up of squares, to create the cells for the statistical analysis that will follow. The tool can be found in QGIS ‘Create a grid’, and here we will use a width and length of 10km.

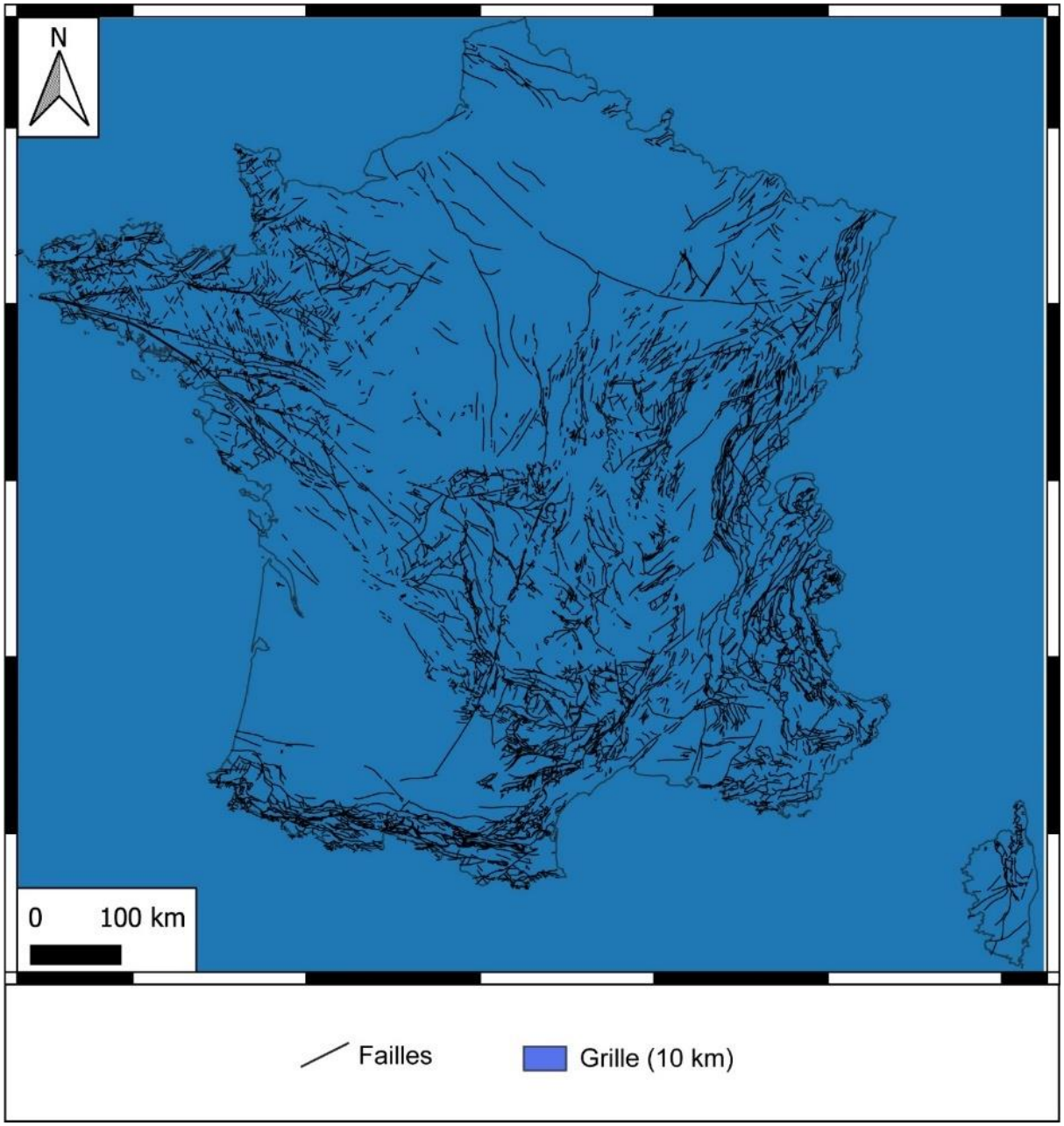

Fig. 2: Definition of a 10 km grid to count the faults and sum their length per cell.

Once the grid has been created, in ‘Analysis tools’ on QGIS there is a ‘Sum of line lengths’ window. In this window, all you need to do is indicate the grid as ‘Polygons’ and the faults on the 1M map as ‘Lines’. Two new fields appear in the grid attribute table: ‘Count’, which counts the linear units in each cell, and ‘Length’, which is the cumulative length of the lines per cell.

The last step uses the layer's ‘Symbology’, with the ‘Graduated’ tab providing a visual representation by classifying the zones from least to most fractured when the Length or Count fields are used. To associate the intervals (fracture values) with the colours, the most reliable way is to use the natural breaks in the histogram (Jenks' method). These will then give the values corresponding to very low, low, high and very high densities.

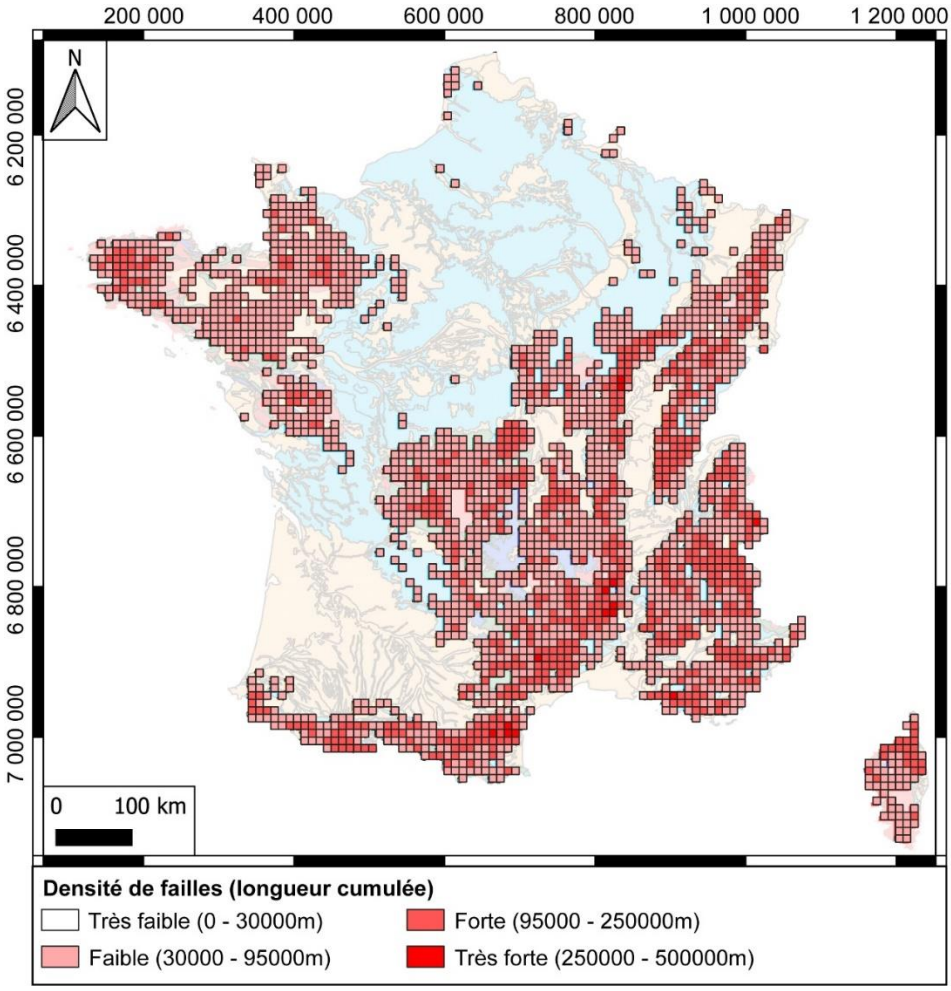

Fig. 3: Fault density map based on the 2M geological map. Each cell represents the cumulative length of the faults. The delineation of fracturing intensities is deduced from the histogram using Jenks natural rupture method.

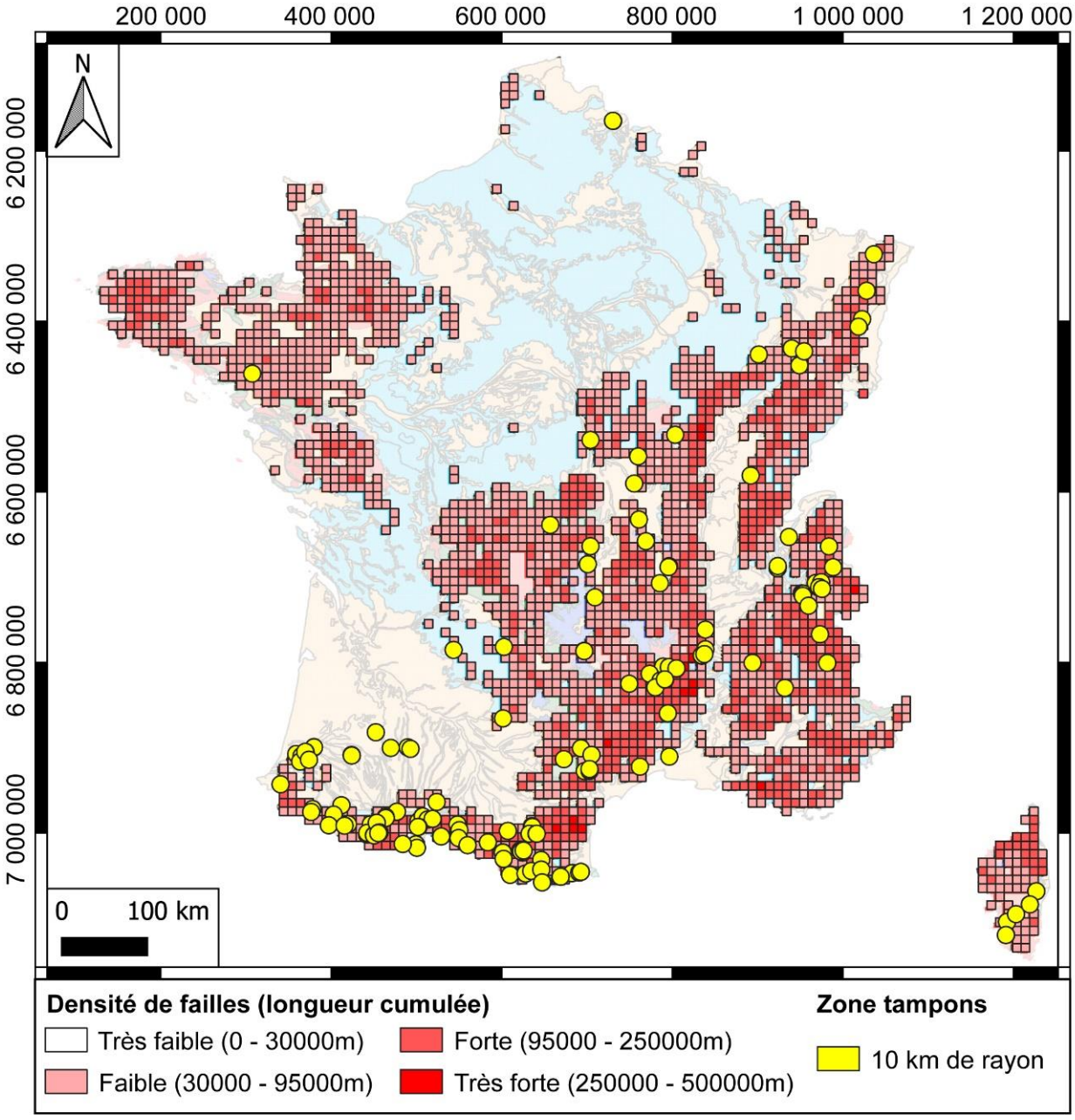

Fig. 4: Fault density map with buffers, faults are vectorised form 1M geological map (BRGM).

To obtain the fault density associated with a thermal source, a circle with a radius of 10 km is drawn around each one (Fig. 4). Then, the maximum value of the cumulative length of faults (density) is assigned to each source. This calculation is performed once the vector layer has been converted to a raster (Fig. 5).

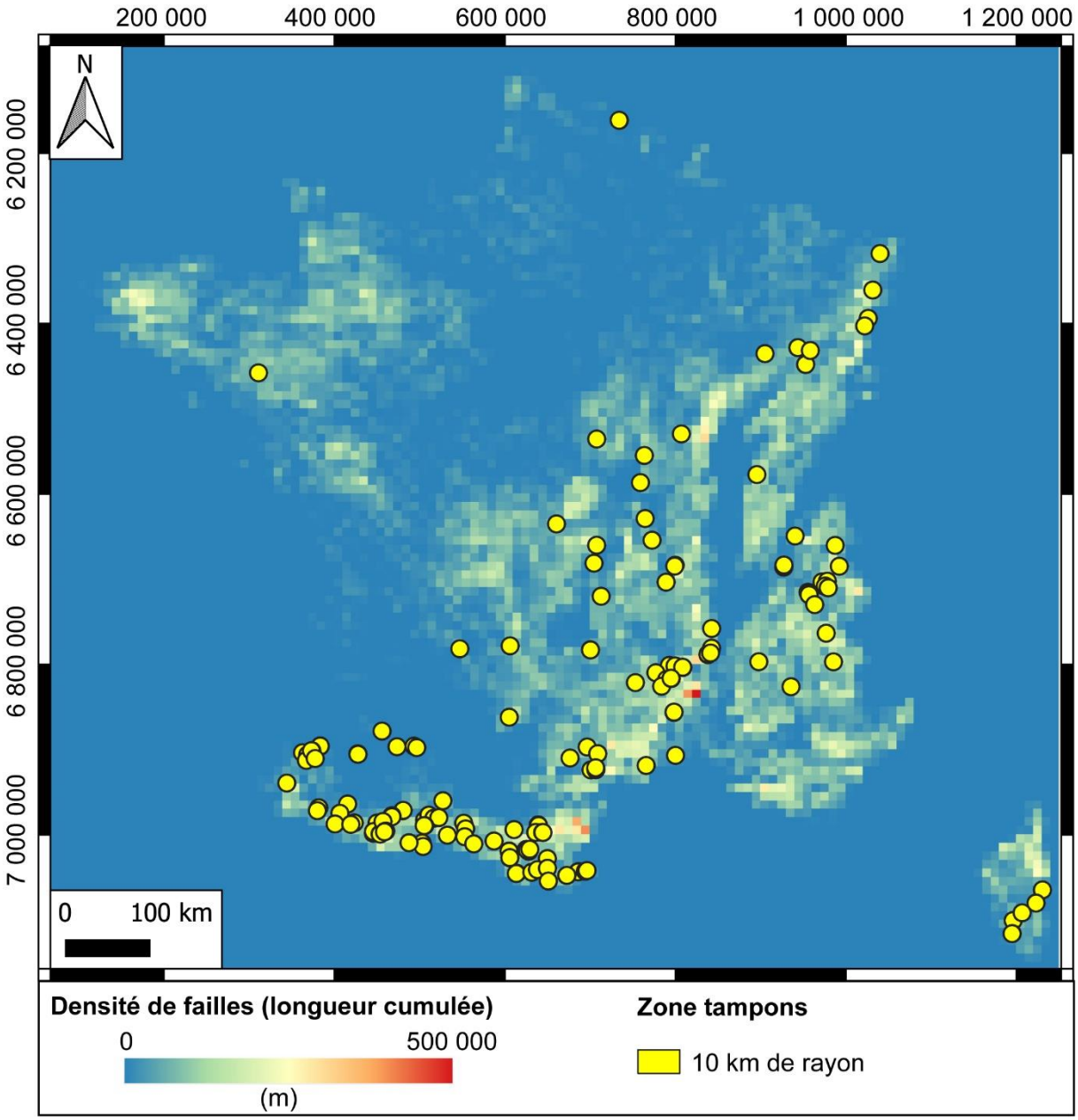

Fig. 5: Raster version of the fault density map based on the 2M geological map with buffer zones. The cells previously used have been merged to form a raster.

Appendix B: Methodology used for 3D thermo-hydraulic modelling.

All the numerical models presented here were produced using Comsol Multiphysics™ software. The circulation of fluids in porous media is described by Darcy's law. This can be written as:

$$\vec{v} = -\frac{k}{\mu_f}\left(\nabla\vec{P} - \rho_f\vec{g}\right) \quad 1$$

With v the Darcy velocity (m/s), k (m²) the permeability of the flow medium, μ_f (Pa.s) the dynamic viscosity of the fluid, ρ_f (kg.m^{-3}) the density of the fluid and g the acceleration of gravity (by convention, 9.81 m²/s). A coupling between the Darcy law and the heat equation was performed according to the procedure of Guillou-Frottier et al. (2013), it gives:

$$\rho Cp\,\frac{\partial T}{\partial t} = \nabla\left(\lambda \cdot \vec{\nabla}T\right) - \rho_L C_L\vec{v}\cdot\vec{\nabla}T \quad 2$$

Where T (°C) is temperature, t is time and $\vec{v}$ (m/s) the Darcy velocity, ρ (kg.m^{-3}) is the rock density, Cp (J/kg.K) is the specific heat, λ (W/m.K) is the thermal conductivity, ρ_L is the fluid density and C_L the fluid specific heat.

For the fuid, here supposed as pure water, the dynamic viscosity (Pa.s) is a function of temperature T(°C), such that:

$$\mu(T) = 2.414.10^{-5}.e^{\frac{570}{(T+133)}} \quad 3$$

following Smith and Chapman (1983) and Rabinowicz et al. (1998). The density of water is also a function of pressure and temperature, such that:

$$\begin{aligned}\rho_f(T,P) = {} & 1006 + (7.424 \times 10-7 \times P) \\ & + (-0.3922 \times T) \\ & + (-4.441 \times 10-15 \times P^2)) \\ & + (4.547 \times 10-9 \times P \times T) \\ & + (-0.003774 \times T^2) \\ & + (1.451 \times 10-23 \times P^3) \\ & + (-1.793 \times 10-17 \times P^2 \times T)\end{aligned}$$

$$+ (7.485 \times 10 - 12 \times P \times T^2)$$
$$+ (2.955 \times 10 - 6 \times T^3)$$
$$+ (-1.463 \times 10 - 32 \times P^4)$$
$$+ (1.361 \times 10 - 26 \times P^3 \times T)$$
$$+ (4.018 \times 10 - 21 \times P^2 \times T^2)$$
$$+ 7.372 \times 10 - 15 \times P \times T^3)$$
$$+ (5.698 \times 10 - 11 \times T^4) \quad (4)$$

This equation is based on a polynomial fit of experimental data, as developped by Launay (2018) and published in Guillou-Frottier et al. (2020). The permeabilities of the different rock units and the fault zone are the main unknowns in the models. The increase in pressure at depth tends to seal the fractures and thus causes a decrease in the permeability of the units. This phenomenon can be described by the following equation:

$$K_u(z) = K_{0_u} . e^{\frac{-z}{\delta}} \quad (5)$$

where $K_u(z)$ is the permeability of each unit (m²), K_{0_u} is the highest permeability (from 10^{-15} m² to 5 10^{-13} m² in the fault zone, and 10^{-18} m² in the host rocks) reached by the unit (at the surface) and z is the depth (m) (Garibaldi et al. 2010). The length δ (m) characterizes the intensity of the decrease in permeability with depth.

At the upper surface of the model, a temperature of 10 °C is fxed or a mixed condition is used (Q=h(T0-T)). According to regional data, a constant heat fux of 85 mW m^{-2} is imposed at the base of the model (Lucazeau and Vasseur 1989). The lateral borders are thermally insulated (host rocks). A geothermal gradient of 30 °C km^{-1} is imposed as an initial condition. The surface pressure is equivalent to the atmospheric pressure (105 Pa), and its value increases gradually with depth. A no flow condition is imposed on lateral sides and bottom of the model.

Appendix C: Article published in the review Géologues, June 2024.

Des thermes romains à la géothermie électrogène, que connaissons-nous réellement du système géothermal de Chaudes-Aigues ?

Emmy Penhoët,[1,2] Laurent Guillou-Frottier,[1,2] Laurent Arbaret,[2] Bernard Sanjuan,[1] Séverine Caritg [1]

[1]BRGM, Direction des Géoressources, Orléans, France.

[2]ISTO, UMR 7327, Université d'Orléans, CNRS, BRGM, Orléans, France.

Connues depuis l'époque romaine, la ville de Chaudes-Aigues (Cantal) et ses trente sources dépeignent un parfait exemple du thermalisme français. Depuis 1906, plusieurs auteurs ont tenté d'expliquer l'origine de la source du Par, l'une des plus chaudes d'Europe (82°C) mais de nombreuses incertitudes persistent quant aux caractéristiques du système hydrothermal (origine des fluides, réservoir et circulation, drains et émergences). Cet article présente un état des connaissances géologiques, géochimiques, hydrogéologiques ainsi que les perspectives concernant le système hydrothermal de Chaudes-Aigues.

Introduction

Historiquement, l'exploration géothermique était guidée principalement par la présence d'anomalies thermiques. Par exemple, les centrales géothermiques de Bouillante en Guadeloupe ou Soultz-sous-Forêts en Alsace se situent dans des contextes géodynamiques favorables à la formation d'anomalies thermiques (contexte volcanique et extensif, respectivement). Depuis une quinzaine d'années, plusieurs projets d'exploration se tournent davantage vers les anomalies de perméabilité, et la présence de drains devient primordiale (Garg *et al.*, 2010 ; Craig *et al.*, 2021). Les nouvelles cibles correspondent à des régions fortement affectées par des déformations fragiles comme les zones de failles crustales (Bellanger *et al.*, 2017). Les domaines de socle ne présentant pas nécessairement d'anomalies thermiques, et restent donc sous exploités. Cependant ces grands accidents tectoniques entaillent la roche jusqu'à des profondeurs kilométriques, favorisent l'altération hydrothermale, et peuvent augmenter significativement la perméabilité (e.g. Bischoff *et al.*, 2024). Ainsi, les circulations de fluides sont favorisées dans les zones de failles crustales, phénomène d'autant plus important en contexte extensif (Barton *et al.* 1995; Faulds *et al.* 2010; McKenna and Blackwell 2004; Haines *et al.* 2016).

Située dans le sud du Massif Central, la commune de Chaudes-Aigues constitue une manifestation remarquable du thermalisme français. En plus d'abriter l'une des sources les plus chaudes d'Europe (source du Par) à une température de 82°C et un débit constant de 500 $L.min^{-1}$, 29 autres sources ayant une température entre 25 et 68°C ont été recensées. La zone d'émergence est localisée à proximité d'un dense réseau de dykes de microgranite mis en place dans le socle gneissique. En outre, elle est également à l'intersection de trois grands systèmes de failles varisques formant une « structure en Y » (Figure 1b). Comme cela va être détaillé par la suite, les études antérieures, notamment celles de géochimie des eaux et d'hydrogéologie (Cailleaux *et al.*, 1976 ; Fouillac et Michard, 1981 ; Vasseur *et al.*, 1997), semblent indiquer la présence d'un important potentiel géothermique en profondeur, mais soulèvent encore de nombreuses interrogations en termes de circulation des eaux et de température du réservoir profond. En ce sens, la région de Chaudes-Aigues constitue un laboratoire naturel idéal pour l'exploration de ce type de réservoirs géothermiques, que l'on peut qualifier de non-conventionnels (Jolie *et al.,* 2021). Nos premiers travaux de modélisation semblent confirmer le fort potentiel géothermique de la zone, mais il est nécessaire de progresser pour mieux comprendre la circulation des eaux (aire de recharge, processus de mélange de l'eau profonde avec des eaux superficielles, etc.) et le fonctionnement du système hydrothermal de Chaudes-Aigues, avant de pouvoir passer à l'exploitation de ce potentiel.

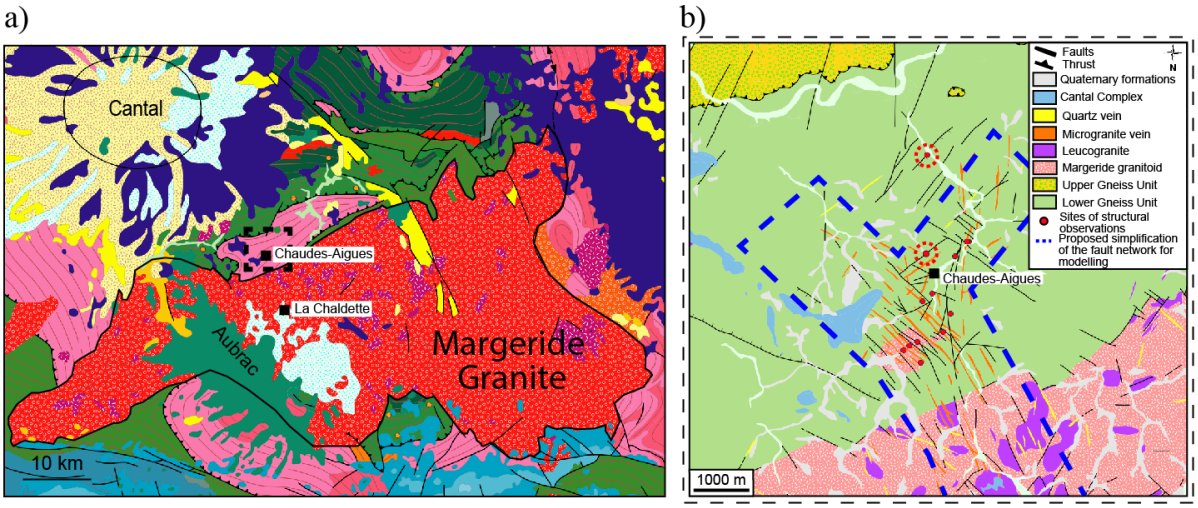

Figure 1. (a) Carte géologique au millionième, (b) zoom sur la région de Chaudes-Aigues sur fond de la carte géologique au 50 000ème. Les pointillés soulignent la structure de la zone faillée en Y. Les pointillés rouges indiquent les affleurements présentés en Figure 4.

Etat des connaissances sur le système géothermique de Chaudes-Aigues.

Aquae Calidae, Calidas Aquas, Chaldas Aigues et maintenant Chaudes-Aigues, la ville a changé plusieurs fois de nom, mais tous renvoient à la même caractéristique hydrologique : ses eaux thermales. La première utilisation des sources remonte à l'époque romaine : des vestiges d'établissements thermaux ont été retrouvés à proximité de la source du Par (baignoire en lave volcanique, piscine). Les eaux étaient connues pour leurs vertus curatives notamment contre les maladies du foie. C'est au Moyen-Age que Chaudes-Aigues devient un centre thermal de grande renommée, et la ville connait une période prospère du XIII^{ème} au XVI^{ème} siècle (Bédard *et al.*, 2002). En 1332, les sources deviennent privées, les habitations sont construites directement au-dessus des émergences, ce qui permet de mettre en place un système de chauffage utilisant l'eau circulant sous les dallages du rez-de-chaussée. Initialement étudiées pour leurs vertus curatives, les eaux thermales ont intéressé les scientifiques qui se sont interrogés sur leur origine ainsi que sur le fonctionnement du système hydrothermal.

La première hypothèse est formulée en 1906 par De Launay (Figure 2a). Il propose que l'eau proviendrait du plateau gneissique aux abords immédiats de la ville. Le moteur de l'écoulement serait un dénivelé altimétrique de 300 m. A la faveur des joints de l'unité métamorphique l'eau s'infiltrerait jusqu'à 2500 m de profondeur pour rejoindre un réservoir situé juste sous la ville. Les filons de microgranites, bien qu'individualisés à l'affleurement se rejoindraient en profondeur afin de former un conduit unique. Sous l'effet de la pression, l'eau chaude rejoindrait alors la surface.

En 1949, Aubignat (Figure 2b) complète les travaux précédents en précisant que selon lui, les sources dateraient du Pliocène, les contraintes étant favorables à l'ouverture de structures d'orientation similaires à celle des filons de microgranite. Il ajoute que la structure du volcan du Cantal serait propice à l'infiltration rapide d'eau vers la profondeur, ce qui le conduit à l'identifier comme la zone d'impluvium. La source de chaleur proviendrait des matériaux volcaniques présents en profondeur. En 1973, Henou (Figure 2c) reprendra ces concepts en précisant que, selon lui, le réservoir se situerait à 2000 m de profondeur. Il ajoute aussi qu'il semble peu probable que l'ensemble des filons se rejoigne en profondeur pour former un conduit unique, il propose que seuls certains atteignent le réservoir.

Les études réalisées par Cailleaux *et al.* (1976) reprises par Fouillac et Michard (1981) se focalisent principalement sur la composition chimique des eaux. Des calculs de géothermométrie ont mis en évidence que l'eau des sources de Chaudes-Aigues serait issue d'un mélange entre une composante chaude profonde et une eau dite de surface, plus froide. En identifiant la composition chimique du pôle profond, les auteurs s'accordent entre eux sur une température de réservoir de 175 à 200°C.

En 1997, Vasseur *et al.* complètent les travaux précédents avec de la géologie, de la géophysique et une modélisation analytique simplifiée pour proposer un schéma complet de fonctionnement du système hydrothermal (Figure 2d). Deux circuits de circulation d'eau cohabiteraient au sein du pluton de la Margeride, comme détaillé ci-dessous.

Sur le terrain, les sources se situent à proximité d'un réseau de filons de microgranites et de plusieurs faisceaux de failles assez denses. Les émergences sont sans aucun doute liées aux discontinuités mais comme mentionné précédemment les maisons étant construites directement dessus les relations structurales sont impossibles à établir directement. Selon Vasseur *et al.* (1997), les filons seraient les drains ascendants permettant la remontée de l'eau. Le granite de la Margeride situé au sud de Chaudes-Aigues est lui-même découpé par plusieurs réseaux de failles (Figure 2b) qui ont permis durant le Cénozoïque la remontée de magmas basaltiques pour former le massif volcanique de l'Aubrac. Ce phénomène témoigne d'une valeur de perméabilité localement élevée, qui combinée à la continuité physique du granite jusqu'à 5 km de profondeur en fait un très bon candidat pour héberger un réservoir hydrothermal.

Le circuit superficiel drainerait les eaux de surface froides s'infiltrant d'une part au niveau du massif volcanique de l'Aubrac et d'autre part dans les monts de la Margeride. Ce chemin s'établirait à une profondeur d'environ 2000 m et amènerait les eaux sous Chaudes-Aigues. Selon les auteurs, le fonctionnement ainsi que la structure du réservoir intermédiaire restent toutefois à déterminer. Le second circuit suivrait le même itinéraire que le premier mais cette fois-ci jusqu'à 5000m de profondeur ce qui permettrait aux eaux de se réchauffer et de se charger en ions au contact avec la roche encaissante (contact prolongé par rapport au premier). Le circuit profond viendrait se mélanger avec le premier dans un réservoir intermédiaire situé 2000 m sous la ville, constituant ainsi une zone de mélange, avant de remonter vers les différentes sources. Les proportions du mélange correspondraient à 40% du pôle chaud profond entre 180 et 200°C et 60% d'eau superficielle.

Cependant plusieurs éléments restent à consolider comme par exemple l'emplacement de la zone d'impluvium ou le cheminement de l'eau en profondeur. La glaciation du Würm (ayant duré jusqu'à 11 700 ans AP), entraînant de grandes étendues recouvertes par des glaciers pourrait expliquer les volumes d'eau émergeant dans la ville. L'eau aurait pu s'infiltrer lentement et en grande quantité. Les auteurs proposent ainsi une datation hypothétique du système d'environ 10 000 ans qui elle aussi devra être étoffée.

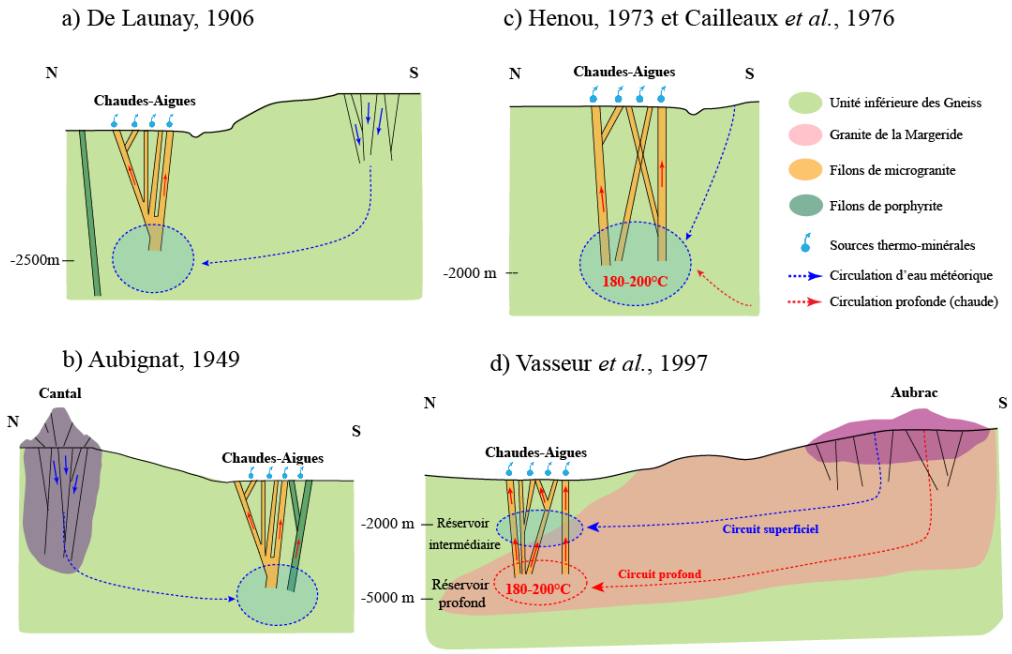

Figure 2. Récapitulatif des différents schémas de fonctionnement proposés depuis 1906 d'après Bédard (2002).

En 2011, un industriel français a souhaité évaluer le potentiel géothermique de la zone pour l'installation d'une centrale géothermique électrogène. Une vaste étude d'exploration géothermique alliant géologie structurale, géochimie (eaux, gaz), ainsi que géophysique (gravimétrie et magnétotellurie) et modélisation géologique fut confiée au BRGM. Les résultats de cette étude ont été consignés dans des rapports confidentiels (Caritg *et al.*, 2013).

Depuis octobre 2022, une thèse encadrée par une équipe composée à la fois de numériciens, géologues structuralistes, géochimistes et hydrogéologues tentent de lever les dernières incertitudes autour du système hydrothermal de Chaudes-Aigues. Comprendre ce type de système en milieu granitique permettrait d'accroître le potentiel géothermique français en s'intéressant cette fois-ci au territoire métropolitain, voire européen (Guillou-Frottier *et al.*, 2024). En effet, les domaines de socle viendraient compléter les contextes géologiques favorables (volcanique ou extensif) pour développer la géothermie profonde électrogène. Ainsi, puisque les plutons granitiques sont nombreux (e.g. Bretagne, Vosges, Massif Central) et souvent affectés par de grands accidents fragiles augmentant fortement leur perméabilité, de nouvelles cibles potentielles sont peut-être à considérer. Il existerait notamment un analogue à Chaudes-Aigues dans les Vosges, la ville de Plombières-les-bains, qui compterait plusieurs sources thermales dont une à 85°C (Source Vulcain, Minoux *et al.*, 1977).

Nouveaux éléments

Pour mieux comprendre le fonctionnement du système de Chaudes-Aigues deux missions de terrain ont été réalisées. Des mesures structurales ainsi que des prélèvements d'eau ont été effectués.

a) Identification des drains : une nouvelle hypothèse

Présentés historiquement comme canaux de remontée des fluides chauds et profonds, les nombreux filons de microgranites n'ont fait l'objet d'aucune observation de terrain indiquant une circulation ou paléo-circulation de fluides. Le seul argument de leur nombre important ne permet pas de les distinguer des failles elles aussi fortement représentées dans la zone. Au cours d'une mission de terrain récente, l'attention fut portée sur ces dykes de microgranite (Figure 3a et 3b). Bien que densément fracturés, les microgranites ne présentent pas d'indices de circulation massive de fluides chauds. A l'affleurement, des petites cavités sont visibles (Figure 3b), celles-ci sont liées à des dissolutions de minéraux et ne donnent pas de conditions de températures précises. De plus, celles-ci sont uniquement présentes sur les plans de fracture orientés N030E. Cette frange d'altération se propage sur quelques centimètres mais n'affecte pas la roche dans son entièreté (Figure 3a). Les épontes des filons présentent une fracturation dense mais il n'y a pas de traces d'une potentielle circulation de fluides à haute température.

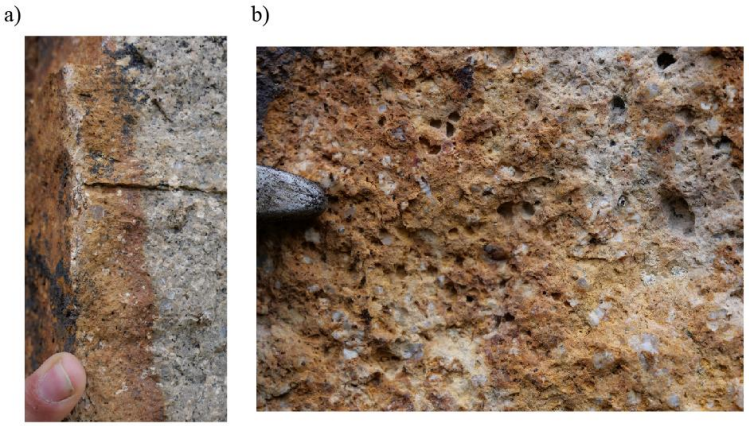

Figure 3. Photos d'un filon de microgranite, vue en coupe de la frange d'altération (a) et des cavités sur les plans N030E (b).

Les autres structures perméables potentielles présentes sont les failles. Aux abords de la ville deux familles sont très bien représentées, et peuvent être individualisées dans les deux directions N150E et N030E. Contrairement aux filons, les failles orientées N030E présentent des traces de circulation massive de fluides chauds. Deux affleurements en témoignent particulièrement. Le premier présente un plan de faille totalement silicifié, la structure originelle des gneiss n'est plus du tout reconnaissable (Figure 4a). Ce phénomène se propage sur plusieurs dizaines de mètres et affecte la roche dans son volume. Des oxydes ainsi que des argiles sont visibles dans les plans de fracture. Le second affleurement est encore plus parlant puisqu'il présente une zone de faille très développée avec une zone d'endommagement de plus de 120m de puissance. D'autre part, au sein du cœur de faille de plus de 25m de large (Figure 4b), les unités métamorphiques sont totalement broyées. Quelques blocs sains subsistent mais restent discrets. Des suintements d'eau sont visibles tout le long de l'affleurement ce qui indique une perméabilité encore relativement élevée à ce jour. La proximité de failles normales pourrait laisser supposer un rejeu et donc une réactivation au tertiaire de cette grande structure. Ces observations sont communes à de nombreuses failles orientées entre N030E et N050E.

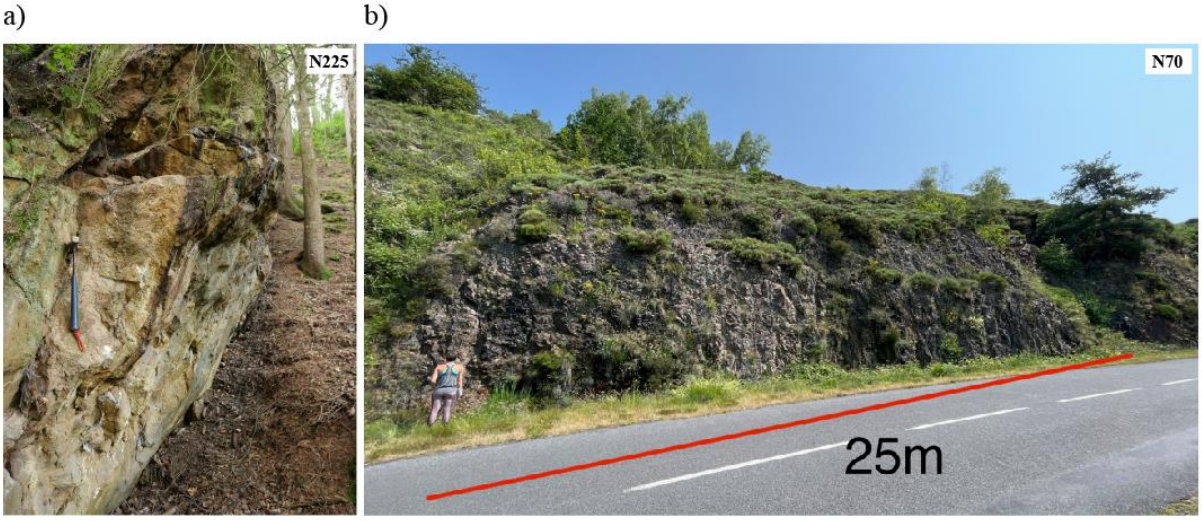

Figure 4. Affleurements de deux failles orientées N050E (a) plan silicifié et (b) la grande faille de plus de 100m de zone d'endommagement.

b) Caractérisation du réservoir : impluvium et température.

La température du réservoir des eaux thermales ainsi que sa profondeur sont deux paramètres fondamentaux à déterminer en vue d'une potentielle exploitation. Dans le cas de l'eau thermale de la source du Par et de sources voisines, les géothermomètres à cations ont indiqué une température d'environ 200°C contre 130°C pour celui de la silice (Cailleaux *et al.* 1976 ; Vasseur *et al.* 1997). Il était donc nécessaire de refaire des analyses chimiques de l'eau de ces sources pour valider et mieux appréhender la divergence de ces estimations de température. En plus de cela, la zone d'alimentation en surface n'a pas été clairement identifiée ; aucun des deux massifs volcaniques n'a pu être réellement écarté. En dernier lieu, une source n'a jamais été intégrée dans les travaux précédents, la source thermale de La Chaldette. Située à 10 km au sud de Chaudes-Aigues, dans le même couloir de failles (Figure 1a), avec une température à l'émergence de 34°C, elle pourrait représenter un élément clé dans la compréhension du système de Chaudes-Aigues.

Neuf sources ont été échantillonnées afin d'étudier leur composition chimique. Huit d'entre elles sont des sources thermales qui se situent dans le bourg même de Chaudes-Aigues, et une correspond à celle de La Chaldette plus au Sud.

Les valeurs de $\delta^{18}O$ permettent de déduire une altitude d'infiltration en les comparant à des gradients isotopiques régionaux. Etant donné la grande quantité de données nécessaire à leur élaboration, ici deux

gradients calculés dans le Massif Central (Cézallier et Sancy) ont été utilisés. Les valeurs des différentes sources s'échelonnent entre -9.8 ‰ et -9.4 ‰ ce qui indiquerait une altitude d'infiltration comprise entre 1400 et 1700 m comme représenté en Figure 5. En tenant compte de la topographie entourant la zone de Chaudes-Aigues les valeurs données par le premier gradient déterminé par Vuataz *et al.* (1987) semblent plus cohérentes. Nous retiendrons donc que l'impluvium se situerait entre 1400 et 1550 m d'altitude. Ces données laissent donc deux candidats, d'un côté l'Aubrac complété par la bordure sud du Granite de la Margeride et de l'autre le Cantal. Or, la présence de la rivière de La Truyère entre l'édifice volcanique et la ville constitue une barrière hydrographique à l'eau potentiellement infiltrée au niveau du Cantal. De plus, la fabrique ductile des gneiss, présentant une foliation relativement plate à légèrement pentée vers le Nord, n'est pas favorable à l'acheminement des fluides vers Chaudes-Aigues. Enfin, le chevauchement présent entre les deux unités métamorphiques, également penté vers le nord constitue un frein aux écoulements.

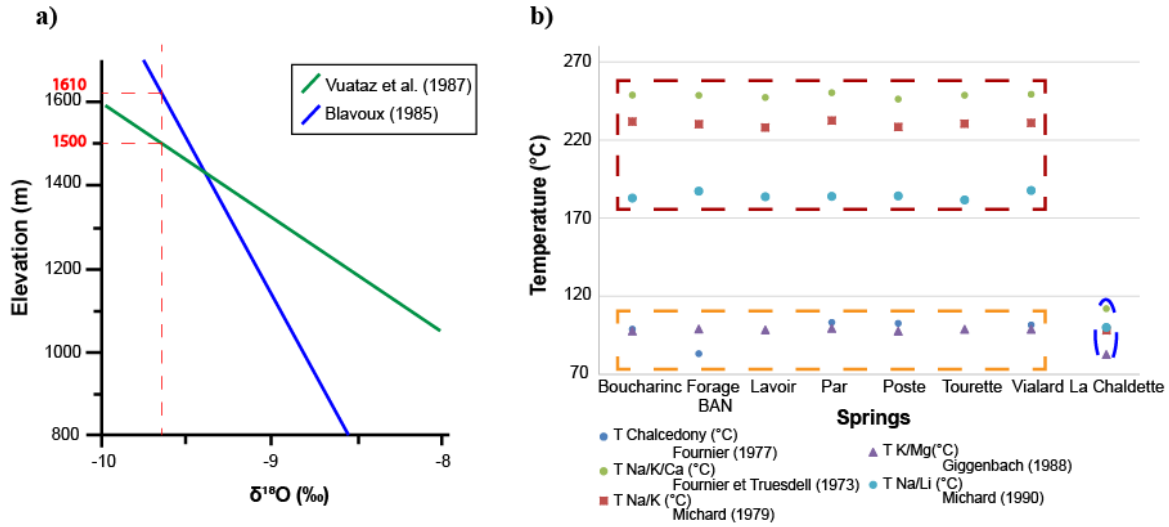

Figure 5. Graphiques représentant (a) les isotopes stables de l'eau et (b) les différents géothermomètres chimiques calculés ainsi que les températures obtenues.

Plusieurs géothermomètres chimiques ont été utilisés afin d'estimer la température du réservoir profond. Comme présenté en Figure 5b, les résultats se répartissent selon deux groupes. Le premier, regroupant les températures les plus élevées, indiquerait que l'eau atteindrait 180 à 230°C. L'autre groupe, lui, suggère une température beaucoup plus faible avec des valeurs de 80 à 110°C. Afin de départager ces deux hypothèses, des modélisations thermo-hydrauliques simples ont été réalisées. En se basant sur l'hypothèse de Vasseur *et al.* (1997), le réservoir intermédiaire se situerait à 2500 m de profondeur. Les modèles reprennent cette géométrie en simulant les sources de Chaudes-Aigues en surface (condition thermique mixte permettant d'atteindre 82°C en surface pour reproduire la source du Par). Une zone perméable représentant le couloir de fracturation rejoint le réservoir supposé. A la base du couloir une température fixe est imposée. Le but des simulations consiste à tester les deux hypothèses pour retrouver les paramètres observés. Les résultats montrent qu'il est impossible de retrouver les 82°C en surface (avec des vitesses de circulation réalistes et applicables au cas naturel) pour une température de réservoir comprise entre 90-110°C. En revanche, dans le second cas, à partir de 170°C jusqu'à 220°C, les tests reproduisent une température de 82°C à Chaudes-Aigues.

Seules les températures indiquées par quatre géothermomètres différents, utilisés sur la source de la Chaldette, convergent vers une valeur unique de 110°C (Figure 5b). Ces résultats suggèrent que l'eau chaude profonde est complètement à l'équilibre chimique avec la roche encaissante de son réservoir (le granite de la Margeride) et qu'il n'y a eu aucun mélange avec des eaux plus superficielles au cours de sa remonté vers la surface.

c) Fonctionnement du réservoir : modélisation dynamique simplifiée en 3D.

Les observations de géologie structurale tendent à suggérer que le réservoir du système hydrothermal de Chaudes-Aigues se situerait dans le granite de la Margeride. Pour comprendre et quantifier les circulations de fluides au sein du pluton un premier modèle simple en 3D a été réalisé. Ce modèle numérique couple l'équation de la chaleur, la loi de Darcy, la conservation de la masse, et prend en compte la dépendance de la température de la densité et de la viscosité du fluides (e.g. Guillou-Frottier *et al.*, 2024). Par souci de simplification, le granite de la Margeride est découpé en parallélépipèdes symbolisant les zones d'alimentation lors de sa mise en place décalés par des faisceaux de failles plus perméables (Talbot *et al.* 2005).

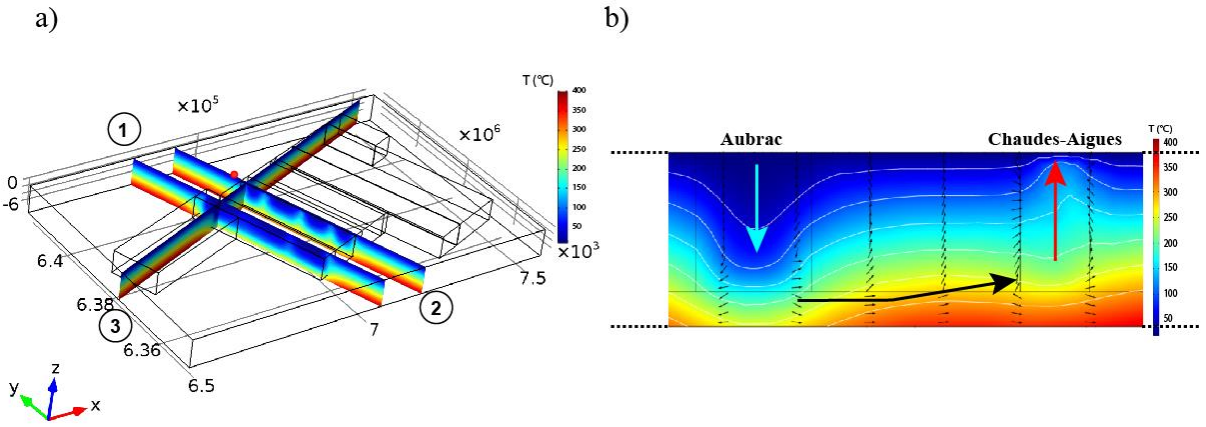

Figure 6. (a) Modèle dynamique 3D simplifié avec (b) un extrait de la coupe n°3. Les flèches mettent en évidence l'infiltration (bleue), la circulation en profondeur (noire) et la remontée des fluides chauds (rouge). Le point rouge indique la localisation de la ville de Chaudes-Aigues.

Trois coupes ont été extraites du bloc thermique 3D, une première recoupant le massif de l'Aubrac, une seconde dans le faisceau situé au sud des émergences puis une troisième recoupant les deux premières et parallèle à la bordure Nord du granite.

La coupe la plus à l'Ouest (n°1), majoritairement bleue foncé, témoigne d'une zone dominée par des écoulements froids descendants ce qui indique une forte infiltration. En revanche, sur la seconde (n°2) plusieurs zones de remontées de fluides chauds sont visibles (bleu ciel). En effet, différentes boucles convectives se mettent en place dans le faisceau. Au niveau de la source de La Chaldette, la température obtenue par le modèle dynamique est de 38°C. C'est en bonne cohérence avec la valeur réelle de 34°C mesurée à la source. Pour terminer, il est aussi possible de voir grâce à la coupe transversale n°3 (Figure 6b) une circulation profonde et lente (vitesse avoisinant les 10^{-12} m.s^{-1}) entre l'Aubrac et le faisceau de Chaudes-Aigues : les fluides seraient donc drainés du massif volcanique vers l'Est.

Vers un nouveau modèle du système hydrothermal ?

Les différentes données acquises lors des missions de terrain ainsi que celles des modélisations dynamiques 2D et 3D tendent à mieux contraindre le système hydrothermal de Chaudes-Aigues par rapport aux modèles précédemment proposés. En effet, présentés depuis 1906 comme des drains, les filons de microgranite ne seraient pas impliqués dans le système hydrothermal. En revanche, de nombreuse failles N030E affleurant dans le secteur de Chaudes-Aigues semblent former un faisceau perméable que la rivière emprunte au niveau de la ville et qui pourrait être le drain majeur du système hydrothermal. De plus l'intersection avec l'autre famille N150E permettrait d'accroître localement la perméabilité et de faciliter la remontée des fluides. Toutefois, aucune trace de circulation n'a été vue le long de cette orientation.

Le circuit du système hydrothermal de Chaudes-Aigues débuterait au niveau du granite de la Margeride depuis l'Aubrac. Les eaux météoriques s'infiltreraient en profondeur *via* le grand faisceau de failles

N150E situé juste au sud de la ville. Celui-ci étant un parfait drain pour acheminer les eaux météoriques de la bordure Sud du Granite de la Margeride vers Chaudes-Aigues. Cette circulation profonde permettrait à l'eau de se réchauffer (Figure 7b). Sous la ville se produirait un mélange avec une eau plus profonde et plus chaude (180-200°C). Le tout remonterait à la faveur des failles N030E (Figure 7d), au niveau du point topographique le plus bas constitué par la vallée du Remontalou.

En parallèle de cela, d'autres boucles convectives se mettent en place comme imagée avec la modélisation numérique 3D. La source de la Chaldette est issue d'une autre remontée d'eau profonde en amont de Chaudes Aigues, et donc la composition chimique de celle-ci ainsi que sa température diffèrent (environ 110°C). Elle ne présente aucune trace de mélange avec des eaux plus superficielles. Au niveau du massif volcanique de l'Aubrac, l'eau météorique s'infiltre en utilisant le réseau de failles précédemment emprunté par le basalte. Par effet de gradient de pression, les fluides sont drainés lentement vers le faisceau de failles de Chaudes-Aigues (Figure 7c). Le volume ajouté est cependant inconnu à ce jour.

Il reste encore des éléments à éclaircir. La provenance des eaux reste encore une vaste question, les volumes des émergences étant difficilement explicables par une simple infiltration des eaux de pluie. D'autre part, il serait fondamental d'identifier les proportions du mélange d'eaux au niveau de Chaudes-Aigues et de déterminer l'origine du pôle chaud. Ces réponses pourraient, en partie, être apportées par un modèle dynamique 3D plus réaliste en modifiant, notamment, la géométrie pour qu'elle soit plus proche du cas naturel et en prenant en compte la topographie, ce qui permettrait notamment de valider ou non la contribution de l'Aubrac, bien que très lente, mise en évidence dans le premier modèle.

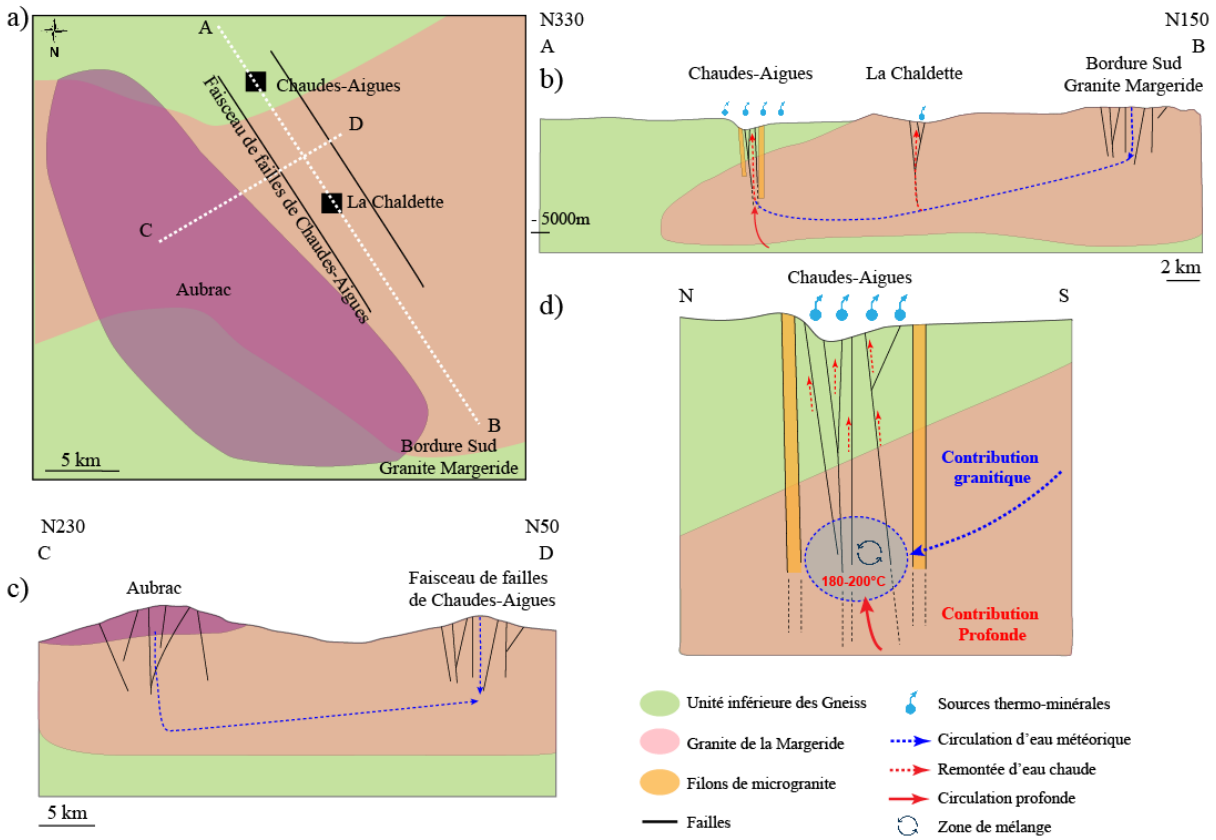

Figure 7. (a) Schéma structural de la zone d'études indiquant l'emplacement des deux coupes résumant le fonctionnement hydrodynamique du système géothermal. La première dans l'axe du faisceau de failles (b) et une seconde perpendiculaire (c) complétées par un zoom sur la ville De Chaudes-Aigues (d).

Bibliographie

Aubignat A., 1949. Hydrologie de Chaudes-Aigues. Note technique du 29 janvier 1949. 5 p., ET pv de visite du 4 février 1949.
Barton C.-A., Zoback M.-D., Moos D., 1995. Fluid fow along potentially active faults in crystalline rock. Geology 23(8), 683-686.
Bellanger M., 2017. High temperature geothermal resources of crustal fault zones: a dedicated approach. In: 79th EAGE conference and exhibition. https://doi.org/10.3997/2214-4609.201701771.
Bérard P., Loizeau M., Rouzaire D., Vigouroux P., 2002. Amélioration de la connaissance des ressources en eau souterraine des sites thermaux – Région Auvergne – Site de Chaudes-Aigues (15). Rapport BRGM n°RP-51722-FR, 152 p.
Blavoux B., 1995. Apport des techniques isotopiques à la connaissance des gisements d'eau minérale. La Houille Blanche 2/3, 51-58.
Cailleaux P., Fouillac C., Michard G., Ouzounian C., 1976. Etude géochimique des sources thermales de Chaudes-Aigues (Cantal). Conséquences géothermiques. C.R. Acad. Sc. Fr. 282, 1237-1240.
Caritg S., Baltassat J.-M., Bouchot V., Calcagno P., Coppo N., Martelet G., Sanjuan. B. (2013) – Projet PEGASE - Exploration géothermique de surface des régions de Chaudes-Aigues et de Coren (Massif central français). Étape 4 - Modèle(s) conceptuel(s) 3D d'exploration et proposition de zone(s) favorable(s) à l'implantation de forage(s) d'exploration. Rapport final. BRGM/RC-62436-FR, 75 p., 18 fig., 2 tabl., 3 ann.
Craig J.W., Faulds J.E., Hinz N.H., Earney T.E., Schermerhorn W.D., Siler D.L., Glen J.M., Peacock J., Coolbaugh M.F., Deoro S.B., 2021. Discovery and analysis of a blind geothermal system in southeastern Gabbs Valley, western Nevada, USA. Geothermics 97, 102177.
Faulds J., Coolbaugh M., Bouchot V., Moek I., Oguz K., 2010. Characterizing structural controls of geothermal reservoirs in the Great Basin, USA, and western turkey: Developing successful exploration strategies in extended terranes. In: Proceedings world geothermal congress Bali, Indonesia, April 25-30th 2010.
Fouillac C., Michard M., 1981. Geochemistry of waters from Chaudes-Aigues. Massif Central. France. Manuscrit inédit.
Garg S.K., Pritchett J.W., Combs J., 2010. Exploring for hidden geothermal systems, Proc. World Geothermal Congress 2010, Bali, Indonesia, 25-29th April, 7 p., 2010.
Guillou-Frottier L., Milesi G., Roche V., Duwiquet H., Taillefer A., 2024. Heat flow, thermal anomalies, tectonic regimes and high-temperature geothermal systems in fault zones. Comptes-Rendus des Géosciences, Online first (2024), pp. 1-33. doi:10.5802/crgeos.213.
Haines S., Lynch E., Mulch A., Valley J.-W., van der Pluijm B., 2016. Meteoric fluid infiltration in crustal-scale normal fault systems as indicated by $\delta^{18}O$ and $\delta^{2}H$ geochemistry and $^{40}Ar/^{39}Ar$ dating of neoformed clays in brittle fault rocks. Lithosphere 8(6), 587-600.
Henou B., 1973. Les sources minérales et thermales du Cantal : leur cadre géologique. Massif Central français. Thèse 3e cycle, Clermont-Ferrand, 133 p., 2 cartes ann.
Jolie, E., Scott, S., Faulds, J. *et al.* Geological controls on geothermal resources for power generation. *Nat Rev Earth Environ* **2**, 324–339 (2021). https://doi.org/10.1038/s43017-021-00154-y
Launay L. de, 1906. Sources de Chaudes-Aigues. Géologie. Ann. Des Mines, 10 p.
Mckenna J.-R., Blackwell D.-D., 2004. Numerical modeling of transient basin and range extensional geothermal systems. Geothermics 33(4), 457-76.
Michard G., Fouillac C., Grimaud D., Denis J., 1981. Une méthode globale d'estimation des températures des réservoirs alimentant les sources thermales. Exemple du Massif central français. Geochim. Cosmochim. Acta 45, 1199-1207.
MINOUX G. (1973) - Etude Hydrogéologique du Bassin Thermal de Plombières-les-Bains (Vosges): Campagne d'études 1962-1973. Rapport 73-SGN-385-NES, BRGM Ed. 234 pp.
Talbot J.-Y., Faure M., Chen Y., Martelet G., 2005. Pull-apart emplacement of the Margeride granitic complex (French Massif Central). Implications for the late evolution of the Variscan orogen. Journal of Structural Geology 27(9), 1610-1629.
Vasseur G., Michard G., Fouillac C., 1997. Contraintes sur la structure profonde et le fonctionnement du système hydrothermal de Chaudes-Aigues (France). BRGM, Bull. Hydrogéologie 4, 3-17.
Vuataz F.D., Fouillac A.M., Fouillac C., Michard G., Brach M., 1987. Etude isotopique et suivi géochimique des eaux des sondages de Chassole et de quelques sources minérales du Cézallier. Géologie de la France 4, 121-132.

Appendix D: Extended abstract EAGE GET 2024.

Naturally fractured granites as promising targets for HT geothermal exploration: Impact of fault network geometry.

Emmy Penhoët[1,2] , Laurent Guillou-Frottier[1,2], Laurent Arbaret[2], Charles Gumiaux[2].

1 : BRGM, Georesources Division, 45060 Orléans, France.

2 : ISTO, UMR 7327, Université d'Orléans, CNRS, BRGM, 45071 Orléans, France.

Introduction

Currently, French geothermal power plants are limited to tectonically active areas such as the Rhine graben (Soultz-sous-Forêts) or magmatic zones (Bouillante, Guadeloupe). In order to increase the production of resources (heat or power), geothermal exploration must move towards other geological contexts, such as basement areas. However, direct exploitation remains complex because of low porosity and permeability values (Achtziger-Zupancic 2017). However, the tectonic history of these areas including fault reactivations, may promote the formation of major fault zones, whose impact on fluid flow has already been demonstrated in numerous studies (Barton et al. 1995; Faulds et al. 2010). Although they may represent significant geothermal reservoirs, their exploration and exploitation remain limited. It has been demonstrated that fault zones may host positive temperature anomalies at shallow depths (Duwiquet et al. 2021, Penhoët et al. 2024), resulting in lower drilling costs.

To enhance the understanding of the geothermal potential of these unusually permeable targets, our study will concentrate on two fault zones located in a crystalline basement : the Margeride Granitic Complex (MGC), in the south of the French Massif Central. Vasseur et al (1997) identifies its northern edge as a potential geothermal reservoir that would feed the 30 hot springs in the village of Chaudes-Aigues (e.g. the Par spring, with an emerging fluid temperature of 82°C). According to different geothermometers, the fluids would reach 200°C at a depth estimated at 2 500 metres by Vasseur et al. (1997). A 2.5 km wide N140 fault zone drains surface water to depth and then towards Chaudes-Aigues. The N140 fault zone intersects another N030E fault zone at the location of Chaudes-Aigues. Twenty kilometers east of the Chaudes-Aigues area, various geothermometers applied to the Coren-les-Eaux spring (Saint-Flour area, Figure 1) have also identified a potential reservoir of up to 220°C (Fouillac 1983). This spring would be associated with our second case study, the Margeride Fault Zone (MFZ).

Geological settings

The basement is composed of metamorphic gneissic formations (Vanderhaeghe et al. 2020; green in Figure1). The MGC emplaced around 323 Ma ago by NW-SE faults (feeder zones) (Talbot 2005). During the extension phase at the Eocene, small sedimentary basins visible in the western part of the MGC have been formed (De Goer De Herve et al. 1990; yellow in Figure 1). The MGC and gneiss units have suffered successive tectonic brittle events from the late Paleozoic to present-day (Faure 1995).

Methods

1. Field and GIS

A regional scale fault density analysis has been performed after assembling the 15 geological maps covering the study area. The method consists in creating a grid of 500-metre squares and adding up the length of the faults in each cell. Results were divided into 5 classes using the natural breaks of the

distribution histogram (Jenks algorithm implemented in QGIS). These results were compared with observations made in the field.

2. Numerical modelling

The MGC offers two sectors with a possible high geothermal potential: the Chaudes-Aigues fault clusters and the Margeride fault zone (MFZ, Figure 1). As demonstrated in previous studies, the geometry of the fault, more specifically its thickness over height ratio, directly influences the setting up of thermal convection (Malkovsky and Magri 2016). These two sites will be used for parametric studies: firstly, a Y-shape model to represent the intersection of the fault clusters in the Chaudes-Aigues area; secondly, a prism model to study the impact of the varying thickness in the longitudinal direction. As in Guillou-Frottier et al. (2013) Darcy law was coupled with heat transfer equation and mass conservation. Thanks to field observations and literature data, several variables necessary for the modeling were estimated.

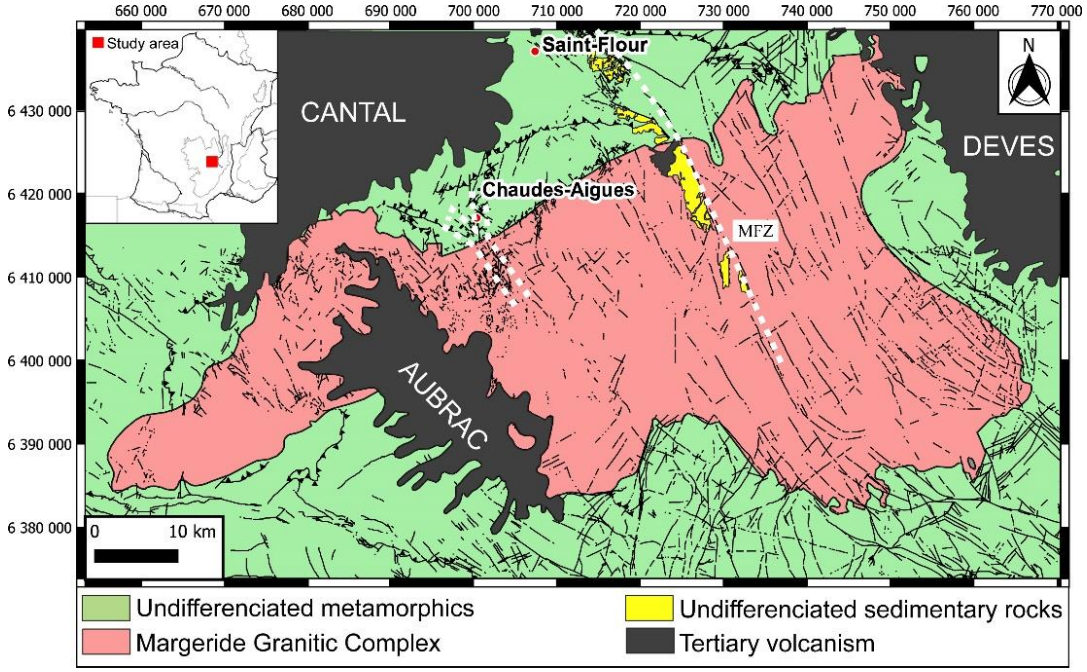

Figure 6: Simplified geological map of the Margeride Granitic Complex (MGC) White dashed lines indicate the simplified geometry used for 3D models. Coordinate system: Lambert 93 – RGF93 EPSG:2154.

Results

1. A densely fractured granite.

An analysis of fault density on a regional scale highlights the main damaged zones. Most of the MGC is characterised by densities ranging from very low to moderate. However, large alignments corresponding to N140 faults can be seen. These structures displace the feeding zones of the granite during its emplacement (Talbot 2005).

The village of Chaudes-Aigues is characterised by high fault density. This zone corresponds to a thick N140 fault zone extending into the granite (Figure 1). Its extent is minimised here because the southern part is covered by morainic sediments.

Another area of high density can be seen around Saint-Flour, corresponding to the thick part of the MFZ. It is more difficult to identify the southern part (low density value) because of its reduced thickness (Penhoët et al., 2024).

The very high fault densities located in the south of the MGC are mainly due to a change in lithologies (Jurassic sediments), which do not have the same rheology as the basement rocks. The same observation

can be applied to the southern part of the Cantal volcanic complex and Tertiary sediments. The highly faulted section to the east of Saint-Flour corresponds to the thrust between the two gneissic units.

1. **Two potential geothermal reservoirs.**

Numerical models using a prismatic model have shown that there is always a positive temperature anomaly in the thickest part of the MFS. At Saint-Flour, a temperature of 100°C could be expected at a depth of 1000m (positive temperature anomaly of 60°C) (Penhoët et al., 2024).

To investigate the influence of fault intersections, as at Chaudes-Aigues, Y-shaped models were carried out. The results indicate a positive thermal anomaly at the point where the fault zones intersect. At the surface temperature reaches 82°C, reproducing the Par spring temperature (Figure 3a). At a depth of 1000 m, the anomaly intensifies to reach 108°C (Figure 3b). As a result, the 150°C isotherm (target temperature for exploitation) rises more than 3 000 m to reach a depth of 1 500 m (Figure 3c). Over time, the anomaly moves towards the extremities of the fault zones and its intensity decreases.

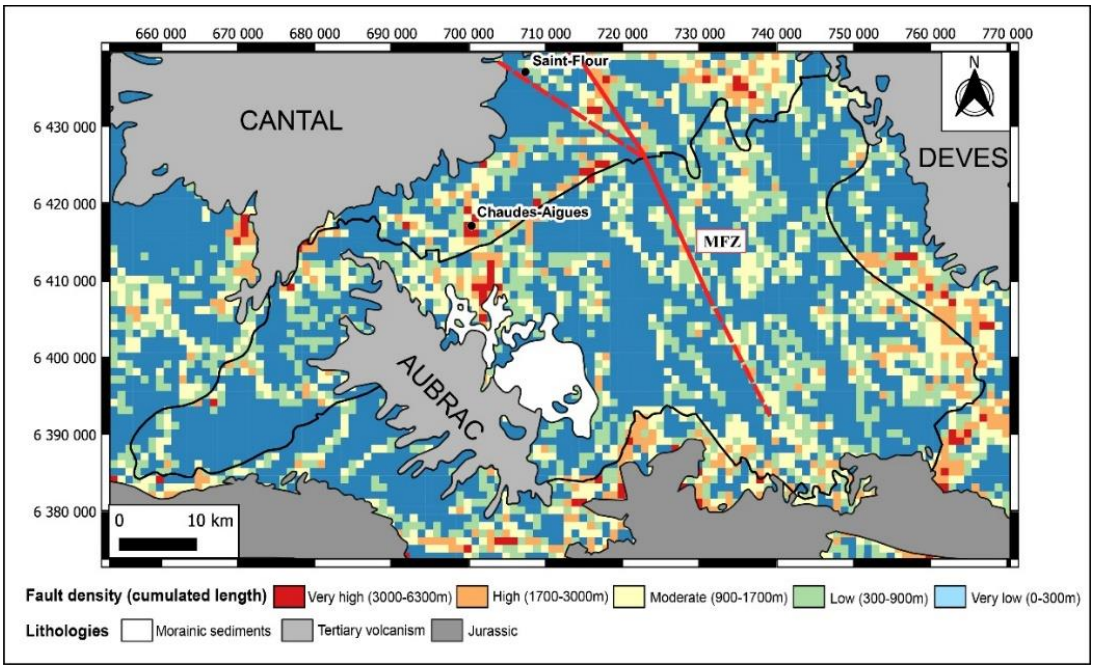

Figure 7: Fault density map of the study area, the contact between lithologies (black) correspond to those shown in Figure 1. Coordinate system: Lambert 93 – RGF93 EPSG:2154.

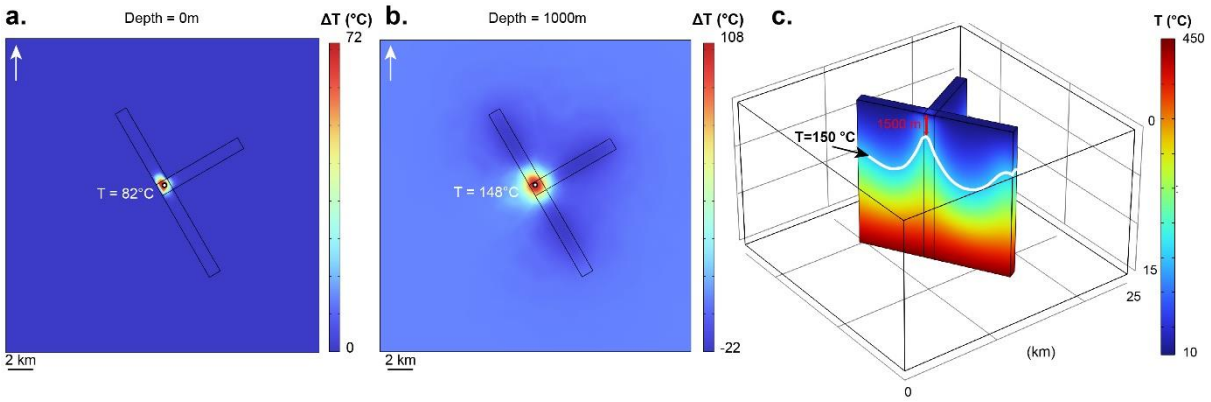

Figure 8: 3D model showing thermal anomalies ΔT and values of temperature at the intersection (a) section at the surface, (b) at 1000m depth; (c) 3D view showing isotherm 150°C (white line). All were produced at t=400 kyr and for permeability values of 10^{-14} m² in the fault zone and 10^{-18} m² in the basement.

Conclusions

New targets for geothermal exploration can be suggested thanks to this study. The Margeride granite has two potential geothermal reservoirs, offering a resource at much shallower depths than those already identified in sedimentary contexts (Soultz-sous-Forêts, 165°C at 4000 depth). As naturally fractured basement zones are abundant throughout Europe, the high-temperature geothermal potential could be underestimated.

References

Achtziger-Zupančič, P., Loew, S., and Mariéthoz, G. [2017]. A new global database to improve predictions of permeability distribution in crystalline rocks at site scale. Journal of Geophysical Research: Solid Earth, 122(5), 3513–3539.

Barton, C. A., Zoback, M. D., and Moos, D. [1995]. Fluid flow along potentially active faults in crystalline rock. Geology, 23, 683–668.

De Goer de Herve, A., Tempier, P., and Boudon, G. [1990]. Carte géologique de la France à 1/50 000, feuille 789 Saint-Flour. Saint-Flour [Carte géologique]. BRGM.

Duwiquet, H., Guillou-Frottier, L., Arbaret, L., Bellanger, M., Guillon, T., and Heap, MJ. [2021]. Crustal Fault Zones (CFZ) as Geothermal Power Systems: A Preliminary 3D THM Model Constrained by a Multidisciplinary Approach. Geofluids, 2021, 1–24.

Faulds, J., Coolbaugh, M., Bouchot, V., Moek, I., and Oguz, K. [2010]. Characterizing Structural Controls of Geothermal Reservoirs in the Great Basin, USA, and Western Turkey: Developing Successful Exploration Strategies in Extended Terranes.

Faure, M. [1995]. Late orogenic carboniferous extensions in the Variscan French Massif Central. Tectonics, 14(1), 132–153.

Fouillac, C. [1983]. Chemical geothermometry in CO2-rich thermal waters. Example of the French massif central. Geothermics, 12(2–3), 149–160.

Guillou-Frottier, L., Carrė, C., Bourgine, B., Bouchot, V., and Genter, A. [2013]. Structure of hydrothermal convection in the Upper Rhine Graben as inferred from corrected temperature data and basin-scale numerical models. Journal of Volcanology and Geothermal Research, 256, 29–49. https://doi.org/10.1016/j.jvolgeores.2013.02.008

Malkovsky, V. I., and Magri, F. [2016]. Thermal convection of temperature-dependent viscous fluids within three-dimensional faulted geothermal systems: Estimation from linear and numerical analyses. Water Resources Research, 52(4), 2855–2867. https://doi.org/10.1002/2015WR018001

Penhoët E., Arbaret L., Guillou-Frottier L., Duwiquet H., Gumiaux C., Bellanger M. [2024]. Fluid flow in crustal fault damage zones with varying lengthwise thickness: application to the Margeride Fault System (French Massif Central). Geothermal Energy. Submitted.

Talbot, J.-Y., Faure, M., Chen, Y., and Martelet, G. [2005]. Pull-apart emplacement of the Margeride granitic complex (French Massif Central). Implications for the late evolution of the Variscan orogen. Journal of Structural Geology, 27(9), 1610–1629.

Vanderhaeghe, O., Laurent, O., Gardien, V., Moyen, J.-F., Gébelin, A., Chelle-Michou, C., Couzinié, S., Villaros, A., and Bellanger, M. [2020]. Flow of partially molten crust controlling construction, growth and collapse of the Variscan orogenic belt: the geologic record of the French Massif Central. BSGF - Earth Sciences Bulletin, 191, 25.

Vasseur, G., Michard, G., and Fouillac, C. [1997]. Contraintes sur la structure profonde et le fonctionnement du système hydrothermal de Chaudes-Aigues (France). Hydrogéologie, (4), 3–17.

Appendix E: Comsol report.

Test 3D final test reservoir2

Définitions globales

Date	28 mars 2025 à 09:12:26

RÉGLAGES GLOBAUX

Nom	Test 3D final test reservoir2.mph
Chemin	D:\Modélisation\Test 3D FINAL\Test_3D_final_test_reservoir2.mph
Version	COMSOL Multiphysics 6.2 (Build: 290)

PRODUITS UTILISÉS

COMSOL Multiphysics
Subsurface Flow Module

INFORMATIONS SUR L'ORDINATEUR

CPU	Intel64 Family 6 Model 154 Stepping 3, 10 coeurs, 31,69 Go RAM
Système d'exploitation	Windows 10

Variables

Variables 1

SÉLECTION

Niveau géométrique	Modèle entier

Nom	Expression	Unité	Description
gradi	0.030249[degC/m]	K/m	
rhoF	1006 + (7.424e-7*p) + (-0.3922*(T - 273.15)) + (-4.441e-15*p^2) + (4.547e-9*p*(T - 273.15)) + (-0.003774*(T - 273.15)^2) + (1.451e-23*p^3) + (-1.793e-17*p^2*(T - 273.15)) + (7.485e-12*p*(T - 273.15)^2) + (2.955e-6*(T - 273.15)^3) + (-1.463e-32*p^4) + (1.361e-26*p^3*(T - 273.15)) + (4.018e-21*(p^2)*((T - 273.15)^2)) + (-7.372e-15*p*(T - 273.15)^3) + (5.698e-11*(T - 273.15)^4)		
Prof	exp((z)/1500)		
Profondeur	exp((z)/1000)		

Composant 1

Définitions

Fonctions

Elévation (DEM) 1

Nom de la fonction	elev1
Type de fonction	Elévation (DEM)

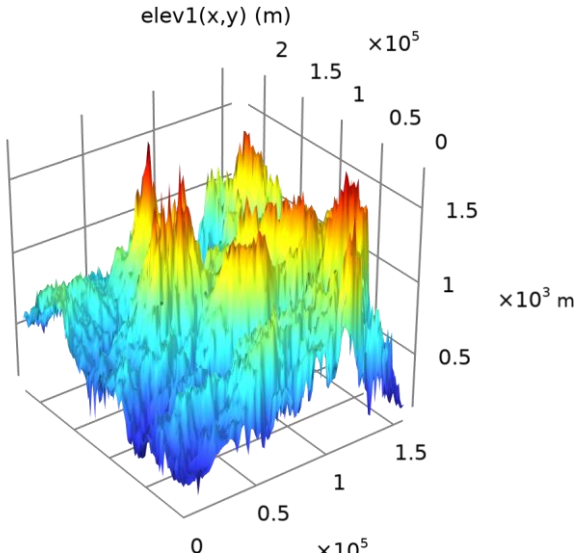

Elévation (DEM) 1

Sondes

Sonde sur un point de domaine 1

Type de sonde	Sonde sur un point de domaine

Repères

Repère sur frontière 1

Type de système de coordonnées	Repère sur frontière
Etiquette	sys1

NOMS DES COORDONNÉES

Première	Deuxième	Troisième
t1	t2	n

Géométrie 1

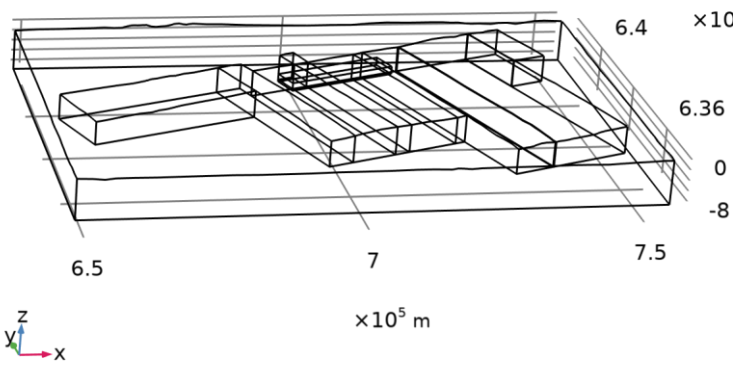

Géométrie 1

UNITÉS

Unité de longueur	m
Unité d'angle	deg

Loi de Darcy

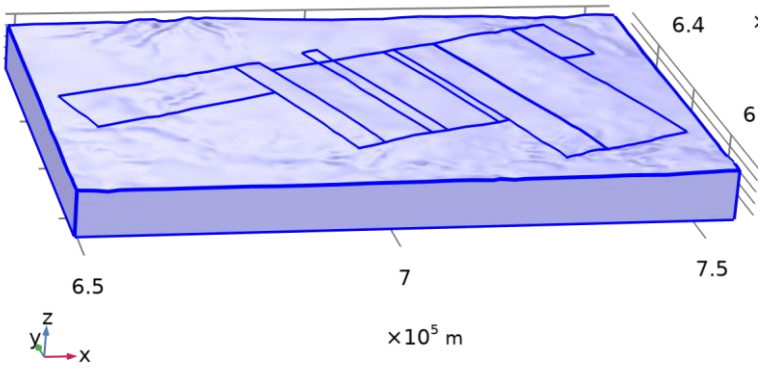

Loi de Darcy

EQUATIONS

$$\frac{\partial}{\partial t}(\epsilon_p \rho) + \nabla \cdot (\rho \mathbf{u}) = Q_m$$

$$\mathbf{u} = -\frac{\kappa}{\mu}(\nabla p - \rho \mathbf{g})$$

FONCTIONNALITÉS

Nom	Niveau
Encaissant	Domaine
Pas d'écoulement	Frontière
Gravité	
Valeurs initiales	Domaine
Pression	Frontière
Faisceau CA Nord	Domaine
Réservoir	Domaine
Faisceau CA	Domaine
Faisceau A	Domaine

Transfert de chaleur en milieu poreux

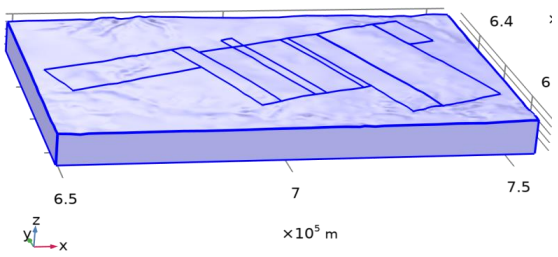

Transfert de chaleur en milieu poreux

EQUATIONS

$$(\rho C_p)_{\text{eff}}\frac{\partial T}{\partial t} + \rho_f C_{p,f}\mathbf{u}\cdot\nabla T + \nabla\cdot\mathbf{q} = Q + Q_p + Q_{\text{vd}} + Q_{\text{geo}}$$
$$\mathbf{q} = -k_{\text{eff}}\nabla T$$

FONCTIONNALITÉS

Nom	Niveau
Encaissant (Gneiss)	Domaine
Valeurs initiales	Domaine
Isolation thermique	Frontière
Flux de chaleur	Frontière
Température (surface)	Frontière
Source de chaleur 1	Domaine
Failles	Domaine
Granite	Domaine
Condition mixte CA	Frontière
Condition mixte CA Nord	Frontière
Réservoir	Frontière

Maillage 1

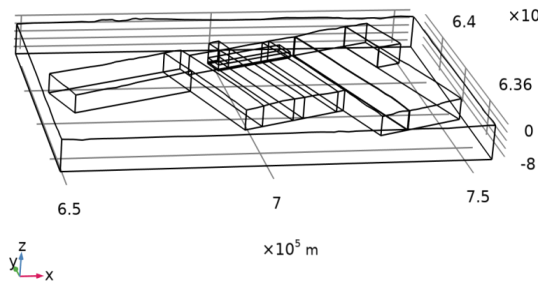

Maillage 1

Etude 1

INFORMATION SUR LE CALCUL

Temps de calcul	33 min 41 s

Test (propriétés actives)

Temps	Unité
range(0,1,10) range(10,10,100) range(100,100,1000) range(1000,500,10000) range(10000,1000,1e5) range(1e5,2500, 5e5)	a

RÉGLAGES DE L'ÉTUDE

Description	Valeur
Inclure la non-linéarité géométrique	Désactivé

RÉGLAGES DE L'ÉTUDE

Description	Valeur
Unité de temps	a
Instants de sortie	{0, 1, 2, 3, 4, 5, 6, 7, 8, 9, 10, 10, 20, 30, 40, 50, 60, 70, 80, 90, 100, 100, 200, 300, 400, 500, 600, 700, 800, 900, 1000, 1000, 1500, 2000, 2500, 3000, 3500, 4000, 4500, 5000, 5500, 6000, 6500, 7000, 7500, 8000, 8500, 9000, 9500, 10000, 10000, 11000, 12000, 13000, 14000, 15000, 16000, 17000, 18000, 19000, 20000, 21000, 22000, 23000, 24000, 25000, 26000, 27000, 28000, 29000, 30000, 31000, 32000, 33000, 34000, 35000, 36000, 37000, 38000, 39000, 40000, 41000, 42000, 43000, 44000, 45000, 46000, 47000, 48000, 49000, 50000, 51000, 52000, 53000, 54000, 55000, 56000, 57000, 58000, 59000, 60000, 61000, 62000, 63000, 64000, 65000, 66000, 67000, 68000, 69000, 70000, 71000, 72000, 73000, 74000, 75000, 76000, 77000, 78000, 79000, 80000, 81000, 82000, 83000, 84000, 85000, 86000, 87000, 88000, 89000, 90000, 91000, 92000, 93000, 94000, 95000, 96000, 97000, 98000, 99000, 1E5, 1E5, 1.025E5, 1.05E5, 1.075E5, 1.1E5, 1.125E5, 1.15E5, 1.175E5, 1.2E5, 1.225E5, 1.25E5, 1.275E5, 1.3E5, 1.325E5, 1.35E5, 1.375E5, 1.4E5, 1.425E5, 1.45E5, 1.475E5, 1.5E5, 1.525E5, 1.55E5, 1.575E5, 1.6E5, 1.625E5, 1.65E5, 1.675E5, 1.7E5, 1.725E5, 1.75E5, 1.775E5, 1.8E5, 1.825E5, 1.85E5, 1.875E5, 1.9E5, 1.925E5, 1.95E5, 1.975E5, 2E5, 2.025E5, 2.05E5, 2.075E5, 2.1E5, 2.125E5, 2.15E5, 2.175E5, 2.2E5, 2.225E5, 2.25E5, 2.275E5, 2.3E5, 2.325E5, 2.35E5, 2.375E5, 2.4E5, 2.425E5, 2.45E5, 2.475E5, 2.5E5, 2.525E5, 2.55E5, 2.575E5, 2.6E5, 2.625E5, 2.65E5, 2.675E5, 2.7E5, 2.725E5, 2.75E5, 2.775E5, 2.8E5, 2.825E5, 2.85E5, 2.875E5, 2.9E5, 2.925E5, 2.95E5, 2.975E5, 3E5, 3.025E5, 3.05E5, 3.075E5, 3.1E5, 3.125E5, 3.15E5, 3.175E5, 3.2E5, 3.225E5, 3.25E5, 3.275E5, 3.3E5, 3.325E5, 3.35E5, 3.375E5, 3.4E5, 3.425E5, 3.45E5, 3.475E5, 3.5E5, 3.525E5, 3.55E5, 3.575E5, 3.6E5, 3.625E5, 3.65E5, 3.675E5, 3.7E5, 3.725E5, 3.75E5, 3.775E5, 3.8E5, 3.825E5, 3.85E5, 3.875E5, 3.9E5, 3.925E5, 3.95E5, 3.975E5, 4E5, 4.025E5, 4.05E5, 4.075E5, 4.1E5, 4.125E5, 4.15E5, 4.175E5, 4.2E5, 4.225E5, 4.25E5, 4.275E5, 4.3E5, 4.325E5, 4.35E5, 4.375E5, 4.4E5, 4.425E5, 4.45E5, 4.475E5, 4.5E5, 4.525E5, 4.55E5, 4.575E5, 4.6E5, 4.625E5, 4.65E5, 4.675E5, 4.7E5, 4.725E5, 4.75E5, 4.775E5, 4.8E5, 4.825E5, 4.85E5, 4.875E5, 4.9E5, 4.925E5, 4.95E5, 4.975E5, 5E5}
Tolérance	Contrôlé par l'utilisateur
Tolérance relative	1E-4

SELECTION DE LA PHYSIQUE ET DES VARIABLES

Interface physique	Résoudre pour	Forme des équations
Loi de Darcy (dl)	Activé	Automatique (Temporel)
Transfert de chaleur en milieu poreux (ht)	Activé	Automatique (Temporel)

VALEURS DES VARIABLES DÉPENDANTES

Description	Valeur
Réglages	Contrôlé par l'utilisateur
Méthode	Solution
Etude	Etude 2
Réglages	Contrôlé par l'utilisateur
Méthode	Solution
Etude	Etude 2

CONSERVER DANS LE MODELE A L'ISSUE DU CALCUL

Interface	Sortie	Sélection
Loi de Darcy (dl)	Contrôlé par la physique	
Transfert de chaleur en milieu poreux (ht)	Contrôlé par la physique	

SÉLECTION DU MAILLAGE

Composant	Maillage
Composant 1	Maillage 1

Etude 2

INFORMATION SUR LE CALCUL

Temps de calcul	19 min 23 s

Conduction

Temps	Unité
range(0,1,10) range(10,10,100) range(100,100,1000) range(1000,500,10000) range(10000,1000,1e5) range(1e5, 100000, 5e6)	a

RÉGLAGES DE L'ÉTUDE

Description	Valeur
Inclure la non-linéarité géométrique	Désactivé

RÉGLAGES DE L'ÉTUDE

Description	Valeur
Unité de temps	a
Instants de sortie	{0, 1, 2, 3, 4, 5, 6, 7, 8, 9, 10, 10, 20, 30, 40, 50, 60, 70, 80, 90, 100, 100, 200, 300, 400, 500, 600, 700, 800, 900, 1000, 1000, 1500, 2000, 2500, 3000, 3500, 4000, 4500, 5000, 5500, 6000, 6500, 7000, 7500, 8000, 8500, 9000, 9500, 10000, 10000, 11000, 12000, 13000, 14000, 15000, 16000, 17000, 18000, 19000, 20000, 21000, 22000, 23000, 24000, 25000, 26000, 27000, 28000, 29000, 30000, 31000, 32000, 33000, 34000, 35000, 36000, 37000, 38000, 39000, 40000, 41000, 42000, 43000, 44000, 45000, 46000, 47000, 48000, 49000, 50000, 51000, 52000, 53000, 54000, 55000, 56000, 57000, 58000, 59000, 60000, 61000, 62000, 63000, 64000, 65000, 66000, 67000, 68000, 69000, 70000, 71000, 72000, 73000, 74000, 75000, 76000, 77000, 78000, 79000, 80000, 81000, 82000, 83000, 84000, 85000, 86000, 87000, 88000, 89000, 90000, 91000, 92000, 93000, 94000, 95000, 96000, 97000, 98000, 99000, 1E5, 1E5, 2E5, 3E5, 4E5, 5E5, 6E5, 7E5, 8E5, 9E5, 1E6, 1.1E6, 1.2E6, 1.3E6, 1.4E6, 1.5E6, 1.6E6, 1.7E6, 1.8E6, 1.9E6, 2E6, 2.1E6, 2.2E6, 2.3E6, 2.4E6, 2.5E6, 2.6E6, 2.7E6, 2.8E6, 2.9E6, 3E6, 3.1E6, 3.2E6, 3.3E6, 3.4E6, 3.5E6, 3.6E6, 3.7E6, 3.8E6, 3.9E6, 4E6, 4.1E6, 4.2E6, 4.3E6, 4.4E6, 4.5E6, 4.6E6, 4.7E6, 4.8E6, 4.9E6, 5E6}
Tolérance	Contrôlé par l'utilisateur
Tolérance relative	1E-4

SELECTION DE LA PHYSIQUE ET DES VARIABLES

Interface physique	Résoudre pour	Forme des équations
Loi de Darcy (dl)	Activé	Automatique (Temporel)
Transfert de chaleur en milieu poreux (ht)	Activé	Automatique (Temporel)

CONSERVER DANS LE MODELE A L'ISSUE DU CALCUL

Interface	Sortie	Sélection
Loi de Darcy (dl)	Contrôlé par la physique	
Transfert de chaleur en milieu poreux (ht)	Contrôlé par la physique	

SÉLECTION DU MAILLAGE

Composant	Maillage
Composant 1	Maillage 1

Emmy PENHOËT

Exploration de nouvelles cibles géothermiques en domaine de socle fracturé : étude multidisciplinaire du système hydrothermal de Chaudes-Aigues (Massif Central)

Les systèmes hydrothermaux en domaine de socle fracturé constituent des cibles prometteuses pour l'exploration géothermique haute température. Cependant l'exploration de ces zones restent limitée et le fonctionnement de ces systèmes mal contraint. A travers l'exemple du système hydrothermal de Chaudes-Aigues, hébergeant l'une des sources les plus chaudes d'Europe, le but de cette étude consiste à déterminer les principaux facteurs de contrôle et le fonctionnement global du système. Une approche combinant géologie structurale, géochimie des eaux, géophysique (gravimétrie) et modélisation numérique 3D a été mise en œuvre. L'analyse structurale a permis d'identifier les principales zones de failles (N0, N50, N150E), de caractériser leur perméabilité relative et leurs interactions. La géochimie des eaux thermales a fourni des informations essentielles sur la nature, la température du réservoir, l'origine des eaux et leurs zones d'infiltration. Des données gravimétriques ont permis de contraindre les géométries profondes. Ces observations de terrain ont ensuite alimenté des modélisations numériques thermo-hydrauliques 3D afin de simuler la circulation des fluides et d'imager les processus en profondeur. Les résultats confirment l'existence d'un double circuit de circulation, initialement proposé par Vasseur et al. (1997), au sein du Granite de la Margeride. Deux grands types de circulation sont identifiés : un écoulement superficiel au sein du régolithe altéré, illustré par la source de La Chaldette, qui pourrait agir comme un aquifère de surface et expliquer les forts débits à Chaudes-Aigues (500 l/min). En parallèle, un circuit profond alimente un réservoir, dont la température atteint 190°C sous la ville. La remontée rapide des fluides chauds est favorisée par la présence des failles varisques réactivées au cours des temps géologiques. Cette perméabilité est localement renforcée par leur intersection avec un autre faisceau de failles varisques. L'impluvium principal a pu être localisé au sud de Chaudes-Aigues, principalement dans une zone de faille N150E dans le Granite de la Margeride. Contrairement aux modèles antérieurs, les filons de microgranite n'apparaissent plus comme des vecteurs majeurs de la circulation des fluides. Ceux-ci peuvent même constituer des barrières hydrauliques, de même que les veines de quartz ou mylonites observées au nord du site. Ces structures contribuent à concentrer les émergences au centre de la vallée. Enfin, les modèles numériques estiment un temps de résidence des fluides compris entre 20 000 et 200 000 ans, ce qui remet en cause une origine glaciaire récente. L'intégration de données multidisciplinaires et la modélisation 3D ont permis de reconstituer le trajet complet de l'eau, de l'infiltration à l'émergence, tout en reproduisant le flux de chaleur régional, les températures et les débits des sources. En parallèle, une étude paramétrique a été réalisée sur l'impact de la géométrie du réseau de failles. Les deux zones de failles principales du Granite de la Margeride ont été utilisées : Chaudes-Aigues et la faille de la Margeride. Ces deux exemples particuliers ont permis de comprendre l'impact de la géométrie sur la formation d'anomalies thermiques par le biais de la convection hydrothermale. Cette approche constitue un outil efficace pour l'exploration géothermique en domaine de socle fracturé. Cette étude a notamment permis d'identifier d'autres systèmes hydrothermaux cachés au sein du granite de la Margeride. En outre, d'autres systèmes analogues, en France ou en Europe, pourraient faire l'objet d'une exploration similaire.

Mots clés : Chaudes-Aigues, Sources thermales, Géologie structurale, Modélisation numérique, Géochimie des eaux, Gravimétrie

Exploration of new geothermal targets in fractured basement context: a multidisciplinary study of the hydrothermal system of Chaudes-Aigues (French Massif Central)

Hydrothermal systems in fractured basement domains are promising targets for high-temperature geothermal exploration. However, exploration of these zones remains limited and the functioning of these systems poorly constrained. Using the example of Chaudes-Aigues, which hosts one of the hottest springs in Europe, the aim is to determine the main control factors and the overall functioning of the hydrothermal system. An approach combining structural geology, water geochemistry, geophysics (gravimetry) and 3D numerical modelling was used. The structural analysis identified the main fault zones (N0, N50, N150E) and characterised their relative permeability and interactions. The geochemistry of the thermal waters provided essential information on the nature and temperature of the reservoir, the origin of the waters and their infiltration zone. Gravity data was used to constrain the deep geometry. These field observations were then implemented into 3D thermo-hydraulic numerical modelling to simulate fluid circulation and image processes at depth. The results confirm the existence of a dual circulation circuit, initially proposed by Vasseur et al (1997), within the Margeride Granite. Two main types of circulation are identified: a surface flow within the weathering regolith, illustrated by the La Chaldette spring, which could act as a surface aquifer and explain the high flow rates at Chaudes-Aigues. In parallel, there is a deep circuit feeding a reservoir, reaching 190°C, located beneath the town. The rapid ascent of hot fluids is favoured by the presence of Variscan faults that have been reactivated over geological time. This permeability is locally enhanced by their intersection with another Variscan fault cluster. The main impluvium has been located to the south of Chaudes-Aigues, mainly in an N150E fault zone in the Margeride Granite. Contrary to previous models, the microgranite veins do not appear to be major vectors of fluid circulation. They may even constitute hydraulic barriers, as do the quartzified or mylonitised veins observed to the north of the site. These structures help to concentrate discharge in the centre of the town. Finally, numerical models estimate a residence time for the fluids of between 20,000 and 200,000 years, which questions a recent glacial origin. By integrating multidisciplinary data and 3D modelling, we were able to reconstruct the entire path of the water, from infiltration to emergence, and propose a predictive model of the system. This approach is an effective tool for geothermal exploration in fractured basement areas.

Keywords: Chaudes-Aigues, Thermal spring, Structural geology, Numerical modeling, Water geochemistry, Gravity study

Géosciences pour une Terre durable
brgm

**ISTO, 1A rue de la Ferollerie
Campus Geoscience,
45100 Orléans**

ISTO